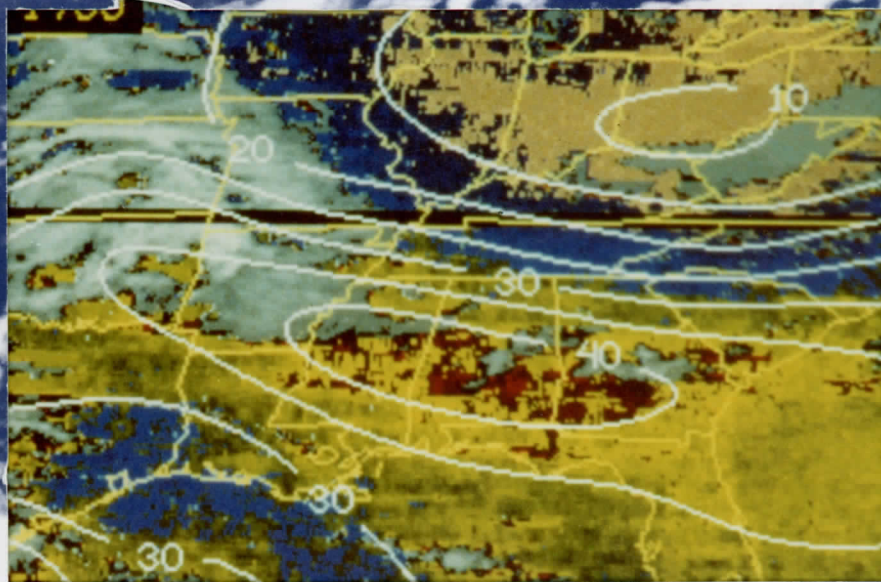


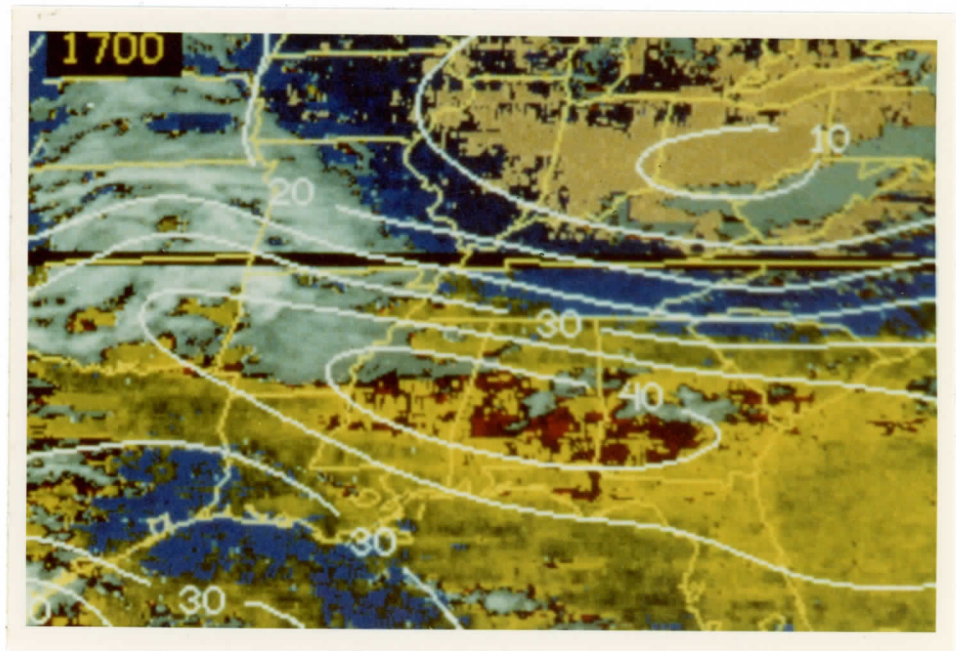
1984 Annual Report of CIMSS  
Scientific Contributions

# A REPORT from the

# Cooperative Institute for Meteorological Satellite Studies



1984 Annual Report of CIMSS  
Scientific Contributions



VAS total-precipitable water vapor/cloud imagery and contours of total-precipitable water vapor over the southeastern U.S. on May 14, 1700 GMT

## Table of Contents

	Page
Forward.....	i
CIMSS Board of Directors and CIMSS Council Members.....	iii
Ongoing CIMSS Projects.....	1
List of Publications.....	2
Author Index.....	5
1984 Publications.....	7

## Forward

The Cooperative Institute for Meteorological Satellite Studies (CIMSS) conducts research and development to advance the peaceful use of weather satellite technology for the benefit of mankind. This work is performed by a joint University, Federal, and visiting scientist research group through base funding to the University of Wisconsin (UW) by the National Oceanic and Atmospheric Administration (NOAA) and additional funding from contracts and grants awarded by NOAA, the National Aeronautics and Space Administration (NASA), and the National Science Foundation (NSF). The University scientists associated with CIMSS are from the Space Science and Engineering Center (SSEC) and the Department of Meteorology at the UW-Madison. The NOAA scientists are employees of the National Environmental Satellite Data and Information Service (NESDIS) and the National Weather Service (NWS). During 1984, visiting scientists from Australia, New Zealand, the United Kingdom, and the Peoples Republic of China were associated with CIMSS. Students at the UW also participate in CIMSS scientific programs.

The broad charter of CIMSS encompasses research for improving our understanding of the earth's weather and climate through the development of techniques for interpreting remote sensing data from advanced weather satellites. Particular attention is concentrated on the transition of new satellite data interpretation techniques into operational practice both at NOAA within the United States as well as at other weather forecast centers around the world.

During 1984, CIMSS research focused on five areas:

### 1. Retrieval Technique Development

Techniques are developed for achieving accurate determinations of atmospheric temperature and moisture profiles, cloud and water vapor motion "winds", land and sea surface temperature, atmospheric stability, ozone, and cloud and radiation parameters as needed for weather and climate research and operations. Particular emphasis has been placed on the interpretation of radiometric data from the VISSR Atmospheric Sounder (VAS) on the geostationary weather satellite GOES. Research conducted by CIMSS under the NOAA VAS Assessment program (NOVA) is oriented toward providing NOAA with applications software that will enable the effective operational use of the data soon after the VAS becomes fully operational during 1986. Methods have been advanced for interpreting sounding data from the polar orbiting NOAA satellites. These refinements have been used to improve a CIMSS developed software package, which has been made available to the world meteorological satellite direct readout user community.

### 2. Subjective Severe Weather Forecast Methods

Methods are developed for combining satellite and conventional data products in order to improve severe weather forecasts, including tornadic storms and hurricanes. The methods have been tested with real-time satellite and conventional data and evaluated for their operational utility at several NOAA forecast centers.

### 3. Numerical Data Assimilation and Forecasting

A numerical analysis and prediction facility is under development at the CIMSS for assimilating the wide variety of satellite and conventional meteorological data available on the UW McIDAS system. During 1984 the numerical prediction system has been used to assess the forecast impact of new satellite data types and retrieval algorithms.

### 4. Advanced Satellite Instrument Development and Testing

A High spectral resolution Interferometer Spectrometer (HIS) is under construction and associated data retrieval techniques are being developed for observing soundings with high vertical resolution and for monitoring surface and atmospheric constituents from high flying aircraft and satellites. Preliminary verification of the HIS observation technique was achieved using high spectral resolution interferometer data obtained during a University of Denver balloon flight experiment.

### 5. Low-cost Satellite Data Work-station

Satellite data processing and product display software is being developed for the IBM personal computer to enable this new, very low cost, video-graphic interactive computer technology to be used for meteorological satellite research and weather forecast operations. A menu-driven software package is near completion for distribution to the meteorological satellite data user community.

The scientific papers presented in this report provide the technical details on the accomplishments achieved within the five program areas noted above. The results illustrate the productivity of scientists associated with CIMSS during 1984. In addition to their scientific research and developments, the CIMSS associates have contributed greatly to the World Weather Watch program through their unselfish training of visitors from all parts of the world and through their participation in national and international workshops and symposia.



William L. Smith  
Director, CIMSS

CIMSS Board of Directors

Robert Bock  
Christopher Hayden  
John McElroy  
William Smith  
Verner Suomi  
John Young

William Bishop (representative for Dr. McElroy)  
Robert Fox (participant)

CIMSS Council Members

Robert Fox  
Christopher Hayden  
David Houghton  
Donald Johnson  
John Kutzbach  
John Lewis  
David Martin  
Paul Menzel  
William Smith  
Verner Suomi  
Harold Yates

Ongoing CIMSS Projects

Alpine Experiment (Alpex)

P.I. W. L. Smith  
P.M. A. J. Schreiner

Cooperative Institute Base Funding

P.I. W. L. Smith  
P.M. L. M. Parker

Earth Radiation Budget Experiment (ERBE)

P.I. W. L. Smith  
P.M. L. A. Stromovsky

High Resolution Interferometer Sounder (HIS)

P.I. W. L. Smith  
P.M. H. E. Revercomb

Marshall VAS Cooperative Program

P.I. V. E. Suomi  
P.M. G. R. Diak

Measurement of Skin Temperature

P.I. V. E. Suomi  
P.M. G. R. Diak

Monsoon Experiment (MONEX)

P.I. V. E. Suomi  
P.M. A. J. Schreiner

NOAA Operational VAS Assessment (NOVA)

P.I. W. L. Smith  
P.M. P. Raphael

Severe Weather Initiative

P.I. W. L. Smith  
P.M. A. J. Schreiner

LIST OF PUBLICATIONS

Technique Development

- 1 COMBINED ATMOSPHERIC SOUNDING/CLOUD IMAGERY: A NEW FORECASTING TOOL. W.L. Smith, G.S. Wade and H.M. Woolf. Submitted to Bulletin of the American Meteorological Society, September 1984.
- 2 APPLICATIONS OF VAS AND TOVS TO TROPICAL CYCLONES. C.S. Velden, W.L. Smith and M. Mayfield. Bulletin of the American Meteorological Society v.65, no.10, October 1984
- 3 THE ADVANTAGES OF SOUNDING WITH THE SMALLER DETECTORS OF THE VISSR ATMOSPHERIC SOUNDER. W.P. Menzel, T.H. Achtor, C.M. Hayden and W.L. Smith. Washington, D.C., NOAA. National Environmental Satellite, Data, and Information Service, 1984. 22p. (NOAA Technical Memorandum NESDIS 6).
- 4 THE CLOUDS AND VAS. C.M. Hayden, W.P. Menzel and A.J. Schreiner. Reprinted from Conference on Satellite Meteorology/Remote Sensing and Applications, Clearwater Beach, FL, 25-29 June 1984. Preprints. Boston, MA, American Meteorological Society, 1984. Pp49-54.
- 5 ESTIMATING THE WIND FIELD FROM VAS TEMPERATURE SOUNDINGS. C.M. Hayden. To be submitted to Journal of Climate and Applied Meteorology, 1984.
- 6 IMPROVED VERTICAL SOUNDINGS FROM AN AMALGAMATION OF POLAR AND GEOSTATIONARY RADIANCE OBSERVATIONS. W.L. Smith and H.M. Woolf. Reprinted from Conference on Satellite/Remote Sensing and Applications, Clearwater Beach, FL, 25-29 June 1984. Preprint volume. Boston, MA, American Meteorological Society, 1984. Pp45-48.
- 7 AN INVESTIGATION OF THE EFFECTS OF SPATIALLY AVERAGING SATELLITE BRIGHTNESS MEASUREMENTS ON THE CALCULATION OF INSOLATION. C. Gautier, G. Diak and S. Masse. To be published in Journal of Climate and Applied Meteorology.
- 8 A NOTE ON THE COVERAGE AND ACCURACY OF WATER VAPOR WIND TRACKING USING VAS DATA ON McIDAS. C.M. Hayden, T.R. Stewart and W.L. Smith. To be submitted to Bulletin of the American Meteorological Society, 1984.
- 9 NOWCASTING: ADVANCES WITH McIDAS III. W.L. Smith, G.S. Wade, W.P. Menzel, V.E. Suomi, R.J. Fox, C.S. Velden and J.F. LeMarshall. Presented at Nowcasting 2, Norrkoping, Sweden, 3-7 September 1984.
- 10 SEA SURFACE TEMPERATURE: OBSERVATIONS FROM GEOSTATIONARY SATELLITE. J.J. Bates and W.L. Smith. Submitted to Journal of Geophysical Research - Oceans, August 1984.
- 11 TOTAL OZONE FROM NOAA SATELLITES: A PHYSICAL MODEL FOR OBTAINING MEASUREMENTS WITH HIGH SPATIAL RESOLUTION. X.-L. Ma, W.L. Smith and H.M. Woolf Journal of Climate and Applied Meteorology v.23, no.9, September 1984.
- 12 LIMB EFFECTS IN SATELLITE TEMPERATURE SOUNDING. J.F. LeMarshall and A.J. Schreiner. Submitted to Journal of Climate and Applied Meteorology, May 1984.



- 13 GEOSTATIONARY SATELLITE SOUNDER (VAS) OBSERVATIONS OF LONGWAVE RADIATION FLUX. W.L. Smith and H.M. Woolf. To be submitted to Journal of Climate and Applied Meteorology, 1984.

#### New Instrumentation and Systems

- 14 THE INTERACTIVE VIDEOGRAPHIC COMPUTER: A REVOLUTIONARY TOOL FOR METEOROLOGICAL RESEARCH. W.L. Smith. Abstracted in Conference on Interactive Meteorological Processing, 3rd, Greenbelt, MD, 23-25 October 1984. Greenbelt, MD, NASA. Goddard Space Flight Center, 1984. 52p.
- 15 PASSIVE REMOTE SOUNDING FROM METEOROLOGICAL SATELLITES. W.L. Smith. Presented at Australasian Conference on the Physics of Remote Sensing of Atmosphere and Ocean, 1st, Melbourne, Australia, 13-16 February 1984.
- 16 RECENT ADVANCES IN SATELLITE REMOTE SOUNDING. W.L. Smith, H.E. Revercomb, H.B. Howell and H.M. Woolf. Presented at International Radiation Symposium '84, Perugia, Italy, 21-29 August 1984.
- 17 VAS DATA ACQUISITION AND PROCESSING SYSTEM FOR A PERSONAL COMPUTER. R.G. Dedecker, R.N. Green and H.B. Howell. Abstracted in Conference on Interactive Meteorological Processing, 3rd, Greenbelt, MD, 23-25 October 1984. Greenbelt, MD, NASA. Goddard Space Flight Center, 1984. 52p.

#### VAS Assessment

- 18 REAL TIME METEOROLOGICAL APPLICATIONS OF THE GEOSTATIONARY SATELLITE SOUNDER ON GOES-6: BATTLING THE COMPUTER, CODE AND CLOCK. C.M. Hayden and A.J. Schreiner. Presented at SPIE Technical Symposium East '84, Arlington, VA, 29 April - 4 May 1984.
- 19 ACARS WIND MEASUREMENTS: AN INTERCOMPARISON WITH RADIOSONDE, CLOUD MOTION AND VAS THERMALLY DERIVED WINDS. R.J. Lord, W.P. Menzel and L.E. Pecht. Journal of Atmospheric and Oceanic Technology., v.1, no.2, pp131-137, June 1984.
- 20 ROUTINE GENERATION OF VAS PRODUCTS FOR NATIONAL CENTER EVALUATION. A.L. Siebers, W.P. Menzel and R.L. Sorensen. Abstracted in Conference on Interactive Meteorological Processing, 3rd, Greenbelt, MD, 23-25 October 1984. Greenbelt, MD, NASA. Goddard Space Flight Center, 1984. 52p.
- 21 SEA SURFACE TEMPERATURES FROM VAS MSI DATA. J.J. Bates. Final report. Madison, University of Wisconsin-Madison. Space Science and Engineering Center, 1984. [10p.]

### Data Assimilation

- 22 THE USE OF ADJOINT EQUATIONS TO SOLVE A VARIATIONAL ADJUSTMENT PROBLEM WITH ADVECTIVE CONSTRAINTS. J.M. Lewis and J.C. Derber. Submitted to Tellus, August 1984.
- 23 AN EXTENDED LAGRANGIAN THEORY OF SEMI-GEOSTROPHIC FRONTOGENESIS. M.J.P. Cullen and R.J. Purser. Journal of Atmospheric Sciences v.41, no.9, pp1477-1497, 1 May 1984.
- 24 HURRICANE DEBBY: ANALYSIS AND NUMERICAL FORECASTS USING VAS SOUNDINGS. J.F. LeMarshall, W.L. Smith and G.M. Callan. Reprinted from Conference on Hurricanes and Tropical Meteorology, 15th, Miami, FL, 9-13 January 1984. Postprint volume. Boston, MA, American Meteorological Society, 1984. Pp140-144.
- 25 THE INFLUENCE OF VARIATIONS IN SURFACE TREATMENT ON 25-HOUR FORECASTS WITH A LIMITED AREA MODEL, INCLUDING A COMPARISON OF MODELLED AND SATELLITE-MEASURED SURFACE TEMPERATURES. G. Diak, S. Heikkinen and J. Bates. Submitted to Monthly Weather Review, October 1984.
- 26 A NEW APPROACH TO THE OPTIMAL ASSIMILATION OF METEOROLOGICAL DATA BY ITERATIVE BAYESIAN ANALYSIS. R.J. Purser. Reprinted from Conference on Weather Forecasting and Analysis, 10th, Clearwater Beach, FL, 25-29 June 1984. Proceedings. Boston, MA, American Meteorological Society, 1984.
- 27 THE USE OF VAS WINDS AND TEMPERATURES AS INPUT TO BAROTROPIC HURRICANE TRACK FORECASTING. J.M. Lewis, C.M. Hayden, C.S. Velden, T.R. Stewart, R.J. Lord, L. Shapiro and S. Goldenberg. Accepted for presentation at the Conference on Tropical Meteorology and Hurricanes, Houston, Texas, May 1985.

### Special Field Programs

- 28 THE REGIONAL CLOUD DISTRIBUTION DURING THE ONSET PHASE OF THE 1979 SUMMER MONSOON BASED ON GOES-1 IMAGERY. H. Virji and L.D. Herman. Submitted to Journal of Climate and Applied Meteorology. 1984.
- 29 SATELLITE OBSERVED THERMODYNAMICS DURING FGGE. W.L. Smith. Lecture prepared for the FGGE Workshop, Woods Hole, MA, 9-20 July 1984.

### International Cooperative Programs

- 30 The International TOVS Study Conference, 1st, Igls, Austria, 29 August - 2 September 1983. Technical proceedings. W.P. Menzel, editor. Madison, University of Wisconsin-Madison. Space Science and Engineering Center. Cooperative Institute for Meteorological Satellite Studies, March 1984. 352p.
- 31 The International TOVS Study Conference, 1st, Igls, Austria, 29 August - 2 September 1983. Report. W.P. Menzel and M.J. Lynch, editors. Madison, University of Wisconsin-Madison. Space Science and Engineering Center. Cooperative Institute for Meteorological Satellite Studies, December 1983. 32p., appendices.

INDEX

<u>AUTHOR</u>		<u>PAPER #</u>
Achter, Thomas H.	CIMSS	3
Bates, John J.	CIMSS	10, 21, 25
Callan, Geary M.	NOAA/NESDIS	24
Cullen, M.J.P.	Bracknell M.D.	23
Dedecker, Ralph G.	CIMSS	17
Derber, John C.	CIMSS	22
Diak, George R.	CIMSS	7, 25
Fox, Robert J.	SSEC	9
Gautier, C.	SCRIPPS	7
Goldenberg, S.	NOAA/HRD	27
Green, R.N.	NOAA/NESDIS	17
Hayden, Christopher M.	NOAA/NESDIS	3, 4, 5, 8, 18, 27
Heikkinen, Stacy	CIMSS	25
Herman, Leroy D.	NOAA/NESDIS	28
Howell, H. Benton	NOAA/NESDIS	16, 17
LeMarshall, John F.	Australian B.M.	9, 12, 24
Lewis, John M.	NOAA/NESDIS	22, 27
Lord, Raymond J.	CIMSS	19, 27
Lynch, M.J.	W.A.I.T.	31
Ma, Xia-Lin	CIMSS	11
Masse, S.	SCRIPPS	7
Mayfield, M.	NHC	2
Menzel, W. Paul	NOAA/NESDIS	3, 4, 9, 19, 20, 30, 31
Pecht, L.E.	ANSER	19
Purser, R. James	CIMSS	23, 26
Revercomb, Henry E.	CIMSS	16
Schreiner, Anthony J.	CIMSS	4, 12, 18

INDEX

<u>AUTHOR</u>		<u>PAPER #</u>
Shapiro, L.	NOAA/HRD	27
Siebers, Anthony L.	NOAA/NESDIS	20
Smith, William L.	CIMSS	1, 2, 3, 6, 8, 9, 10, 11, 13, 14, 15, 16, 24, 29
Sorensen, Roney L.	NOAA/NESDIS	20
Stewart, Tod R.	CIMSS	8, 27
Suomi, Verner E.	CIMSS	9
Velden, Christopher S.	CIMSS	2, 9, 27
Virji, H.	NSF	28
Wade, Gary S.	NOAA/NESDIS	1, 9
Wolf, Harold M.	NOAA/NESDIS	1, 6, 11, 13, 16

1984 Publications

COMBINED ATMOSPHERIC SOUNDING/CLOUD IMAGERY--A NEW FORECASTING TOOL

William L. Smith  
Cooperative Institute for Meteorological Satellite Studies  
University of Wisconsin-Madison

Gary S. Wade and Harold M. Woolf  
NOAA/NESDIS Development Laboratory

1225 West Dayton Street  
Madison, Wisconsin 53706

To be Submitted to the Bulletin of the American Meteorological Society

SEPTEMBER 1984

## Abstract

A method for displaying sounding and cloud information in a composite image is described. Examples are shown to illustrate how a forecaster can use a time sequence of these images to monitor changes in atmospheric moisture and stability antecedent to convective weather and at the same time monitor the cloud developments resulting from these atmospheric moisture and stability tendencies. The image products are now being produced in real time at the University of Wisconsin for an assessment of their operational utility as a part of the NOAA Operational VAS Assessment (NOVA) program. Initial response has been favorable such that it is likely that the sounding/cloud imagery product will be available to all forecast centers in 1986 after the VAS data acquisition and processing system becomes fully operational.

## 1. Introduction

The VISSR Atmospheric Sounder (VAS) on the GOES series of satellites provides atmospheric water vapor and temperature sounding information with 7 km spatial resolution. Because the VAS operates in the infrared, the sounding information is compromised by cloudiness to a degree dependent upon the cloud height and amount. Experience has shown that useful soundings can be achieved in cloud free or low level cloud overcast conditions.

Consequently, large gaps in the coverage of vertical soundings from VAS will occur across areas of extended middle and high level cloudiness. These breaks in sounding coverage cause errors in objectively produced contour displays of the sounding data and consequently limit their utility for subjective weather forecasting. Also since the cloudiness can undergo rapid evolution and movement in convective or fast moving frontal situations, it is very difficult to achieve time continuity of objective analyses of the one to three hourly interval VAS sounding data.

For the numerical analysis/forecast application of VAS soundings, the cloud gap problem can be alleviated through the use of ancillary data, for example, cloud and water vapor motion tracer winds (Le Marshall et al., 1984) and/or by imposing physical constraints on the space and time structure permitted in the analysis (Lewis et al., 1983). Furthermore, a forecast field can be used as a control of the analysis across data void regions. However, for real time subjective use of the sounding information, for example, for nowcasting convective weather, a high resolution image presentation is more appropriate than a low resolution contour analysis. Chesters et al. (1983) devised a technique for creating images of low level moisture from VAS window and water vapor channel data. However, there were blanks in their images where clouds existed. For general forecast use a presentation technique is



required which: (1) preserves the full resolution of the data, (2) does not display any artificial information as might arise from an objective analysis across data sparse regions, and (3) provides a real time image display of the data. To achieve this nowcasting product, a scheme was devised to:

(1) produce 7 km resolution sounding information as part of the current 80 km resolution sounding production process, (2) put the sounding values in an image (i.e., grey scale) format and combine it with the cloud image information provided by the VAS infrared window (11  $\mu$ m) radiance observations, and (3) enhance the combined sounding/cloud image in such a manner that the cloud portion of the image can be easily distinguished from the atmospheric sounding portion of the image. This note describes the technique and illustrates two examples of the resulting product as produced on the Man-computer Interactive Data Access System (McIDAS) at the University of Wisconsin (Suomi et al., 1983).

## 2. Sounding Determination

It is beyond the scope of this paper to describe the VAS sounding retrieval algorithm in detail (see Smith et al., 1984a and 1984b for such a description). It suffices here to state that the method is a physical and direct analytical solution of the radiative transfer equation. The retrieval system is set up to produce soundings with a resolution and spacing of about 80 km. This is achieved by inspecting the radiances for an 11 x 11 array of 7 km fields of view, eliminating the cloud contaminated ones, and averaging the remaining ones to achieve a cloud filtered spatially averaged set of spectral radiances for each sounding area of 80 km linear resolution.

The solutions for the temperature,  $T$ , and water vapor mixing ratio,  $q$ , profiles can be written in the form

$$T(p) = T^0(p) + \sum_{i=1}^M \alpha_i(p) [T_B(v_i) - T_B^0(v_i)]$$

and

(1)

$$q(p) = q^0(p) + q^0(p) \sum_{i=1}^M \beta_i(p) [T_B(v_i) - T_B^0(v_i)]$$

where  $p$  is pressure and  $M$  is the number of VAS spectral channels (12). The  $\alpha_i(p)$  and  $\beta_i(p)$  retrieval coefficients are in this case solely dependent upon the atmospheric transmittance, its dependence on water vapor, the Planck radiance dependence on temperature, and the expected errors of the radiance observations (Smith et al., 1984). The retrieval coefficients are solved for by matrix inversion, where the transmittance and Planck radiance terms are specified from initial profiles,  $T^0(p)$  and  $q^0(p)$ .

For the purpose of the sounding image generation, the retrieval coefficients,  $\alpha_i$  and  $\beta_i$ , are assumed to be representative of each individual VAS field of view. Consequently, individual field of view soundings are produced by applying the 80 km area average retrieval coefficients to the individual cloud free field of view radiances. In this case  $T^0(p)$ ,  $q^0(p)$ , and  $T_B^0(v_i)$  are specified as the area average retrieval values and the area average brightness temperature observations. Since most of the computational work is performed in achieving the retrieval coefficients, and not in their application, the production of individual retrievals does not result in a significant increase of computer time in the sounding retrieval process.

### 3. Combined Sounding/Cloud Image Generation .

Once the soundings are produced for each individual cloud free field of view any desired sounding product (e.g., total precipitable water) can be combined with the 11  $\mu\text{m}$  window radiance observed in the cloud contaminated fields of view. The sounding value is allocated to the first half of the dynamic range of the grey scale used for the image presentation whereas the 11  $\mu\text{m}$  cloud radiance is allocated to the second half of the grey scale range. The sounding portion of the grey scale is then color enhanced in order to distinguish the clear atmosphere characteristics from the cloud features.

Figure 1 is presented as an illustration of the image generation. Shown on the right side is an 11  $\mu\text{m}$  (VAS band 8) infrared cloud image for 1400 GMT on April 10, 1984 over east-central Texas. On the left is a plot of the 80 km resolution total precipitable water vapor values corresponding to the soundings derived from the 11 x 11 field of view radiance arrays. Total precipitable water vapor values corresponding to the individual cloud free fields of view are denoted by the colored resolution elements, with the color scale given at the bottom of the image. The resolution elements corresponding to cloud contaminated fields of view have been filled with the 11  $\mu\text{m}$  radiance values, and this portion of the grey scale has a black and white enhancement. Although the individual field of view values appear noisy due to the fact that the single field of view radiances are noisy relative to their area average values, coherent small scale features can be seen, particularly in regions where strong horizontal gradients exist.

### 4. Sample Results

Two of the sounding/cloud imagery products which have been found to be useful for monitoring convective storm developments are the total precipitable

water vapor and the total-totals stability index. The total precipitable water vapor (U) is calculated using the relation

$$U = - \int_{p_s}^p \frac{q(p)}{g} dp$$

where  $g$  is the acceleration due to gravity and  $p_s$  is the earth's surface pressure. The total-totals index (TT) is given by

$$TT = T_d(850) + T(850) - 2*T(500)$$

where 850 and 500 refer to the 850 mb and 500 mb pressure levels, respectively. The dewpoint temperature at 850 mb is calculated from the 850 mb mixing ratio using Tietjens' formula.

Figures 2 and 3 show three hour interval images of total precipitable water vapor/cloud images and total-totals/cloud images for April 10, 1984. The contours displayed correspond to an objective analysis of the 80 km resolution retrievals, using the Barnes scheme (Barnes, 1964), resident on the McIDAS system. As can be seen, a large convective system located over Nebraska, Oklahoma, and northern Texas associated with an upper level cut-off low is moving eastward during the day. The precipitable water/cloud imagery shows a maximum water vapor concentration over eastern Texas, propagating eastward with the convective system (Figure 2). Strong horizontal gradients of moisture can be seen to the east and west of the storm complex. The area extent of high moisture values over Texas diminishes somewhat as the system moves eastward. At 1700 GMT the moisture imagery indicates that the largest moisture values are over the Texas-Louisiana border. On the other hand, the atmospheric stability imagery (Figure 3) shows destabilization occurring during the day across eastern Texas and western Louisiana. Severe storm

stability conditions (total-totals in excess of 60 degrees) exist in this region at both 1700 and 2000 GMT. The destabilization is presumably due to increases in the temperature lapse rate of the lower troposphere since the water vapor is steady or decreasing in magnitude during this period as shown in Figure 2. Both the stability trends and the location of the maxima total-totals index values are in good correspondence to the afternoon and early evening (2000-0200 GMT) severe weather reports shown plotted in Figure 3a.

Another situation is shown in Figures 4 and 5 for May 14, 1984. In this case at 1100 GMT there is a small total precipitable water maximum over Arkansas along a cold front stretching across the south-eastern United States in a northwest flow aloft situation. This area of high water vapor concentration extends eastward with time and increases in magnitude during the day with isolated values in excess of 45 mm occurring along a narrow line stretching from eastern Mississippi across central Alabama and Georgia and into southern South Carolina. The stability of the atmosphere (Figure 5) decreases dramatically over the southeastern states with severe weather stabilities (total-totals in excess of 60 degrees) occurring over southern Alabama, southern Georgia, and southern South Carolina at the 1400 and 1700 GMT VAS sounding observation times. Once again areas of maximum instability and the trends in both moisture and stability provide good indication of the potential for and the locations of afternoon and early evening severe weather as shown in Figure 5a.

## 5. Summary

A method has been developed for displaying geostationary satellite sounding information in an image format. Clear air water vapor and stability are combined with cloud radiance to provide to a weather forecaster, in real time, a comprehensive image of the state of the atmosphere. A time sequence of these images allows the forecaster to monitor water vapor convergence and atmospheric stability changes usually antecedent to intense convective weather developments. At the same time the forecaster can monitor the cloud developments associated with these atmospheric water vapor and stability tendencies.

The utility of the sounding/cloud imagery product is currently being evaluated on a routine basis by forecasters at the National Severe Storms Forecast Center in Kansas City, Missouri. The initial response has been very favorable. As a result, this image product will most likely be available to all forecast centers, beginning in 1986, when the VAS data acquisition and processing system becomes fully operational.

## References

- Barnes, S. L., 1964: A technique for maximizing details in numerical weather map analysis. J. Applied Meteor., 3, 396-409.
- Chesters, D., L. W. Uccellini, and W. D. Robinson, 1983: Low-level water vapor fields from the VISSR Atmospheric Sounder (VAS) "split window" channels. J. Clim. and Applied Meteor., 22, 725-743.
- Le Marshall, J. F., W. L. Smith, and G. M. Callan, 1984: Hurricane Debby--An illustration of the complimentary nature of VAS soundings and cloud and water vapor motion winds. Accepted for publication in the Bull. Amer. Meteor. Soc.
- Lewis, J. M., C. M. Hayden, and A. J. Schreiner, 1983: Adjustment of VAS and RAOB geopotential analysis using quasi-geostrophic constraints. Mon. Wea. Rev., 111, 2058-2067.
- Smith, W. L., and H. M. Woolf, 1984: Improved vertical soundings from an amalgamation of polar and geostationary radiance observations. Preprint Volume: Conference on Satellite Meteorology/Remote Sensing and Applications, June 25-29, 1984, Clearwater Beach, Florida. Published by the American Meteorological Society, Boston, Massachusetts, pp. 45-48.
- Smith, W. L., H. E. Revercomb, H. B. Howell, and H. M. Woolf, 1984: Recent advances in satellite remote sounding. Presented at International Radiation Symposium '84, August 21-29, 1984, Perugia, Italy.
- Suomi, V. E., R. Fox, S. S. Limaye, and W. L. Smith, 1983: McIDAS III: A modern interactive data access and analysis system. J. Clim. and Applied Meteor., 22, 766-778.

Figure 1 Side-by-side display of VAS total precipitable water vapor/cloud imagery (left) and VAS 11 $\mu$ m imagery (right) at 1400 GMT on April 10, 1984 over east central Texas. Plot of total precipitable water vapor values from VAS retrievals obtained by cloud filtering and spatially averaging 11 x 11 fields of view (sample boxes shown).

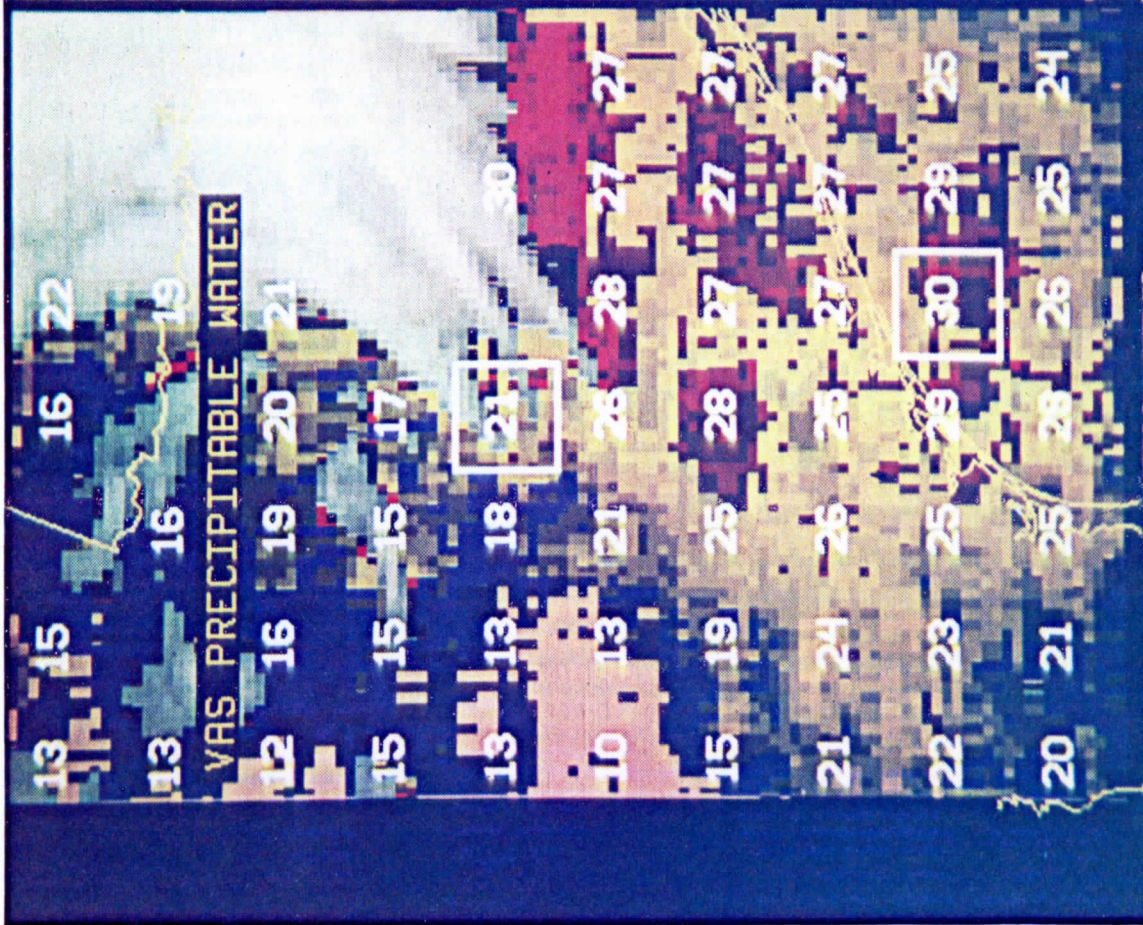
Figure 2 Time sequence of VAS total precipitable water vapor/cloud imagery and contours of total precipitable water vapor from the 11 x 11 field of view average VAS retrievals over the central U.S. on April 10, 1984 at 1100, 1400, 1700, and 2000 GMT.

Figure 3 Time sequence of VAS total-totals/cloud imagery and contours of total-totals index from the 11 x 11 field of view average VAS retrievals over the central U.S. on April 10, 1984 at 1400, 1700, and 2000 GMT. Severe weather reports (T = tornado, H = hail) from 2000 to 0200 GMT are plotted in the upper left panel.

Figure 4 Time sequence of VAS total-precipitable water vapor/cloud imagery and contours of total-precipitable water vapor from the 11 x 11 field of view average VAS retrievals over the southeastern U.S. on May 14, 1984 at 1100, 1300, 1400, and 1700 GMT.

Figure 5 Time sequence of VAS total-totals/cloud imagery and contours of total-totals index from the 11 x 11 field of view average VAS retrievals over the southeastern U.S. on May 14, 1984 at 1300, 1400, and 1700 GMT. Severe weather reports (H = hail, W = damaging wind) from 1900 to 0100 GMT are plotted in the upper left panel.



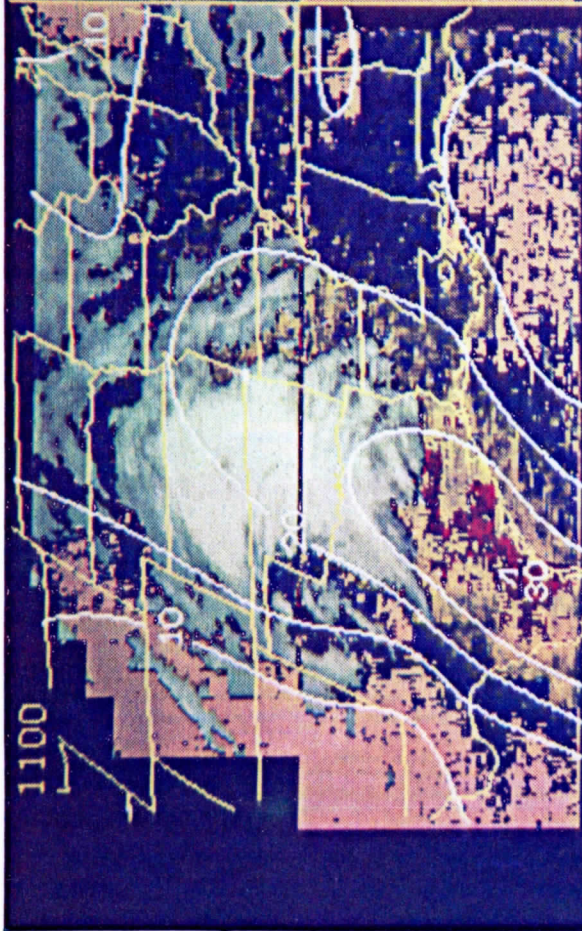
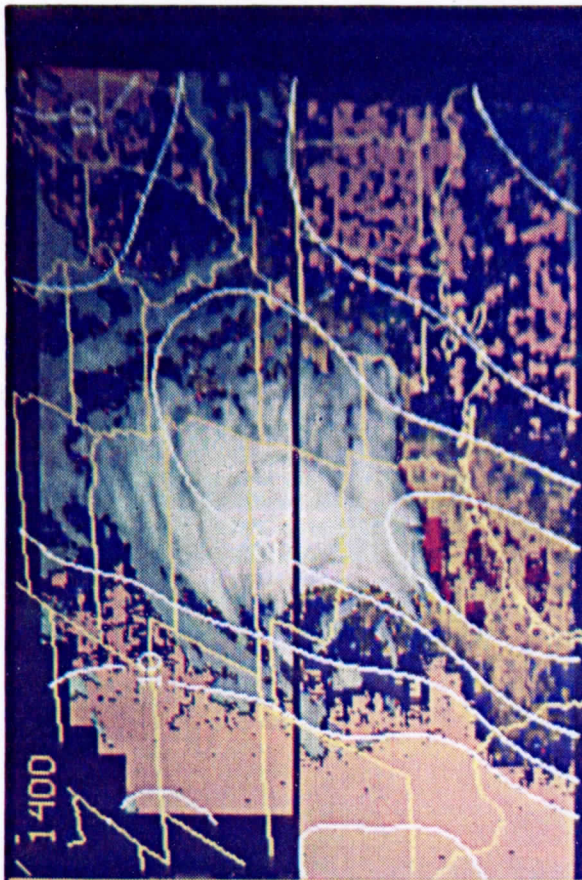


VAS PRECIPITABLE WATER

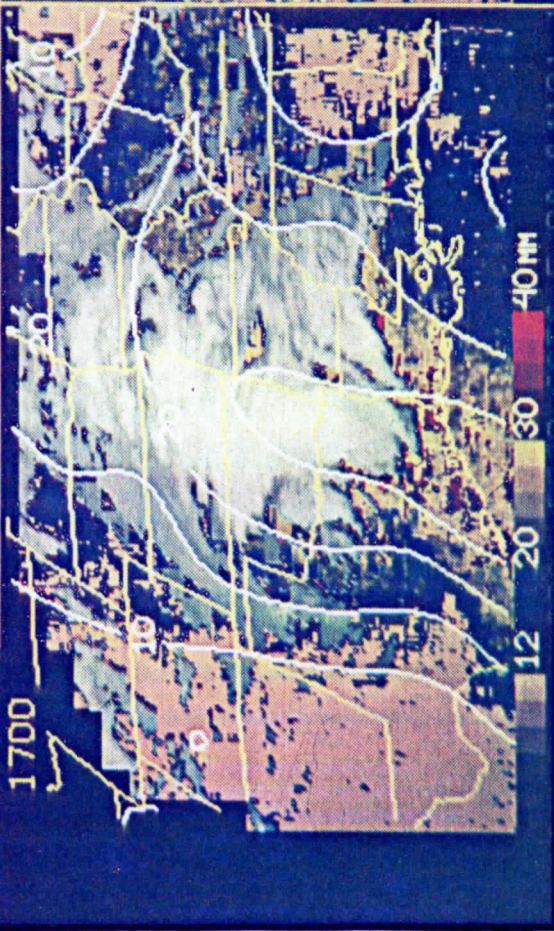
VAS BAND-8

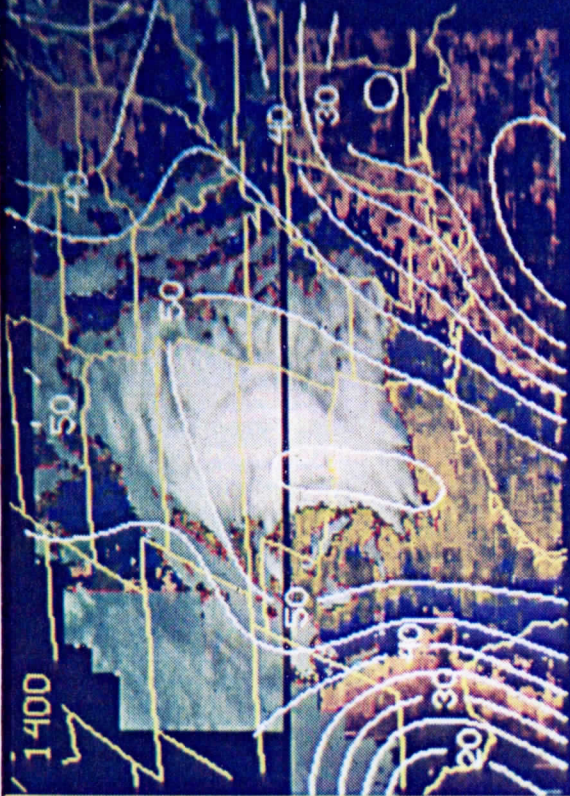
1400 GMT 10 APR 84

007 5560 GOES-5 08 84101 134800 03053 04571 02 00

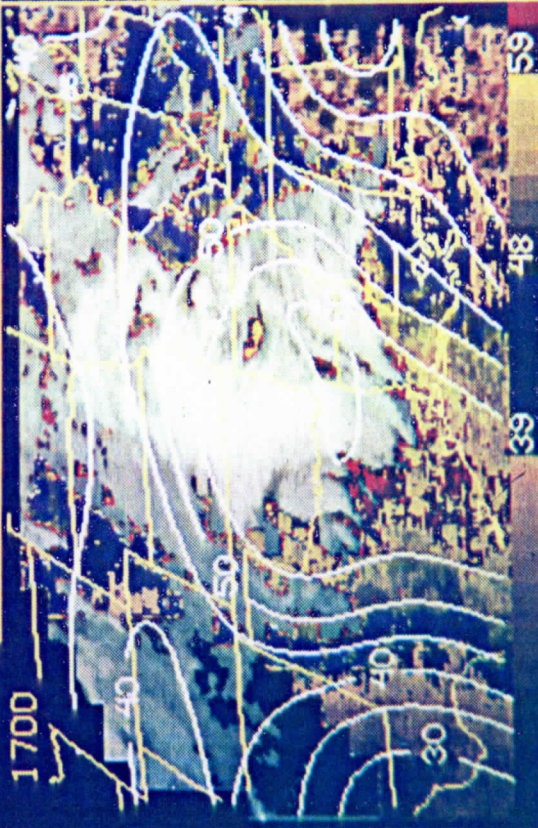


VAS PRECIPITABLE WATER 10 APRIL 1984





VAS TOTAL-TOTALS INDEX 10 APRIL 1984

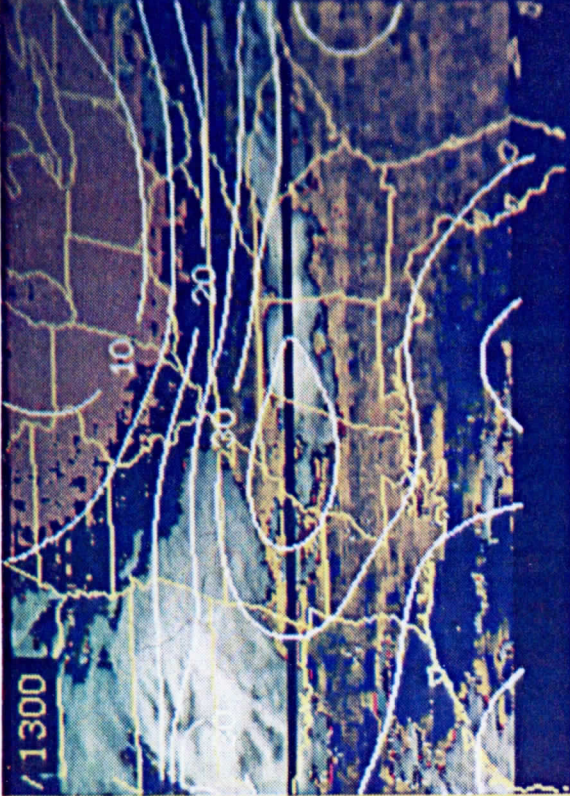


65 DEG-C

59

48

33

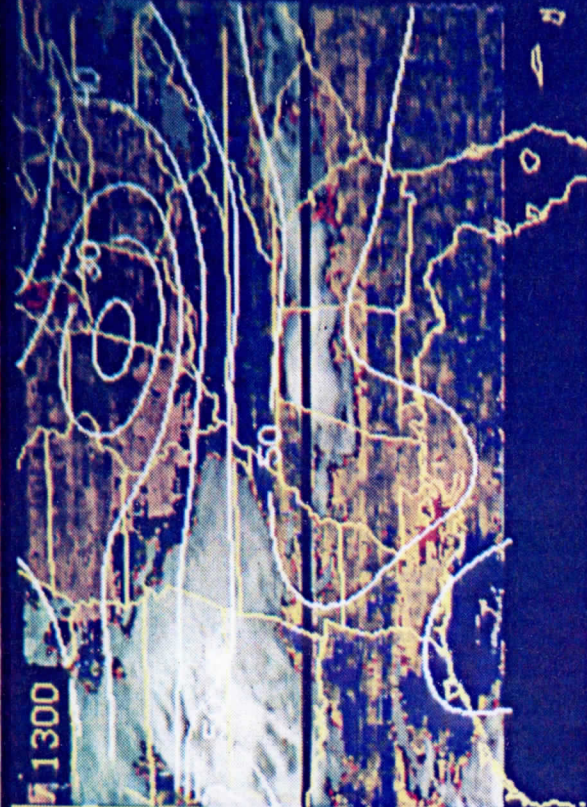
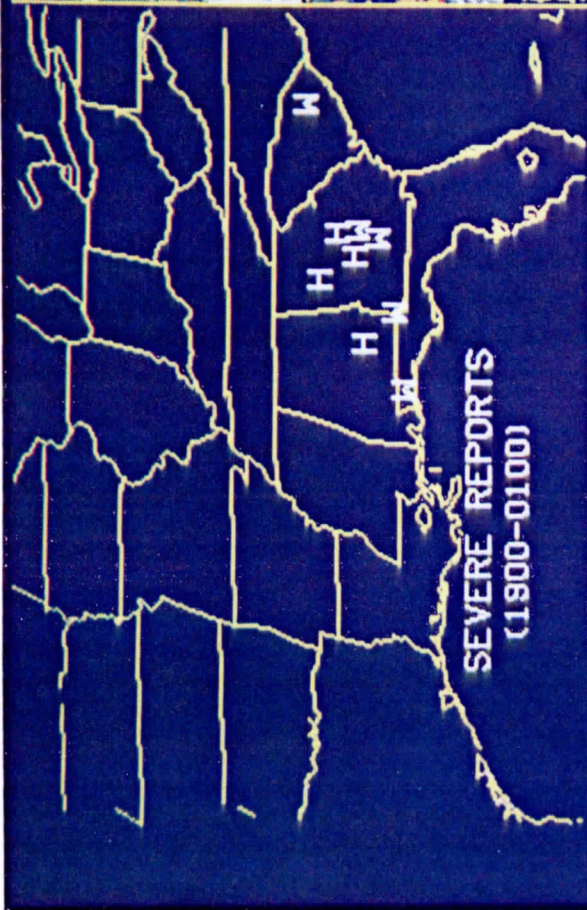


VAS PRECIPITABLE WATER 14 MAY 1984

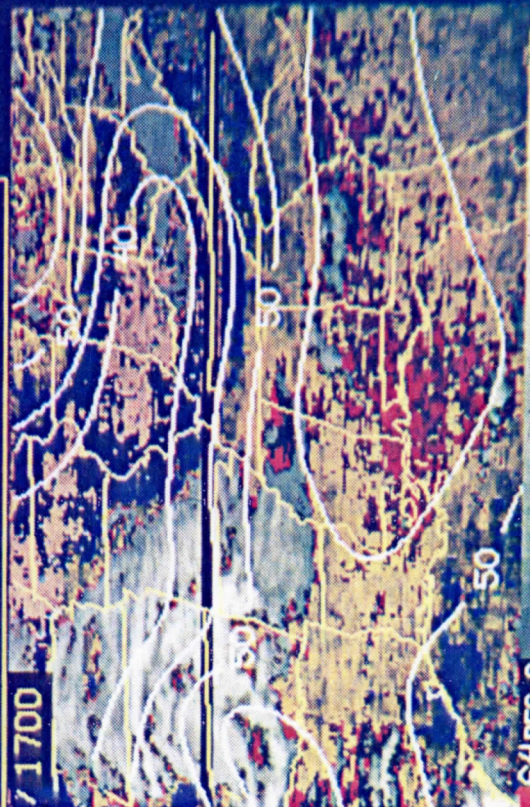


14 28 42 52mm

104800 02510 04856 03



VAS TOTAL-TOTALS INDEX 14 MAY 1984



APPLICATIONS OF VAS AND TOVS TO TROPICAL CYCLONES

Christopher S. Velden  
Space Science and Engineering Center  
1225 West Dayton Street  
Madison, Wisconsin 53706

William L. Smith  
NOAA/NESDIS Development Laboratory  
1225 West Dayton Street  
Madison, Wisconsin 53706

Max Mayfield  
NOAA/NWS Satellite Field Services Station  
1320 South Dixie Highway, 6th Floor  
Coral Gables, Florida 33146

Submitted to the Bulletin of the American Meteorological Society

February 1984  
Revised June 1984

## Abstract

Initial results are presented on research designed to evaluate the usefulness of Visible Infrared Spin Scan Radiometer Atmospheric Sounder (VAS) data in tropical cyclone applications. It is part of the National Aeronautics and Space Administration funded VAS demonstration, and the National Oceanic and Atmospheric Administration (NOAA) Operational VAS Assessment (NOVA) program. The University of Wisconsin (UW) Space Science and Engineering Center (SSEC) and the National Environmental Satellite, Data, and Information Service (NESDIS) Development Laboratory at the SSEC have been working with the National Hurricane Center (NHC), and the NOAA/Environmental Research Laboratories Atlantic Oceanographic and Meteorological Laboratory-Hurricane Research Division (HRD) to explore the different uses of geostationary satellite VAS data in tropical cyclone analysis and forecasting. Because of the cloud penetrating capability of the microwave component of the TIROS Operational Vertical Sounder (TOVS), polar orbiting satellite TOVS soundings in cloudy regions are used in some cases to enhance the VAS products along with cloud drift and water vapor motion winds derived from VAS imagery. This report describes some of the VAS/TOVS products being generated and evaluated on the Man-computer Interactive Data Access System (McIDAS) at the UW-SSEC and the NHC.

## 1. Introduction

The 1982 and 1983 hurricane seasons served as a "test ground" for McIDAS software (Suomi et al., 1983), display programs, subjective analysis, and editing at the UW-SSEC of VAS data over the North Atlantic Ocean area for use by the NHC in tropical cyclone applications. Initially, several problems were encountered in the processing and displaying phase of the operation. However, by the end of the 1983 season considerable progress had been made toward providing timely (quasi-real time, within 2-5 hours of data reception) high quality analyses and displays of mass, motion, and moisture patterns for NHC evaluation.

The VAS radiometer contains eight visible channel detectors and six thermal detectors that sense infrared radiation in 12 spectral bands. Retrieval of accurate temperature and moisture profiles from these radiances can be accomplished using the radiative transfer equation and solutions which rely on the physical properties of the measurements (Smith, 1983). Associated thicknesses can then be derived from these profiles, height fields can be built from the thickness fields and a lower (1000 mb) reference field discussed in the next section, and winds derived from these height fields (also discussed in the next section). More complete descriptions of the VAS and TOVS instruments, their retrieval algorithms, and operating modes are given by Smith (1983) and Smith et al. (1979).

Routine daily VAS coverage for NHC evaluation began in June of 1982. Normally, one data set at approximately 1300 GMT was provided to the NHC in near real time. Coverage normally included most of the Geostationary Operational Environmental Satellite (GOES)-East viewing area between 17-55°N and 30-110°W. To fit in with VISSR operational imaging commitments, the data were obtained in two ten minute swaths separated by approximately 30 minutes.



(Details of the VAS measurement characteristics and mode of operations are summarized by Smith et al., 1981.) On specifically designed hurricane research days, coverage was considerably expanded. Three ten minute swaths, each about a half hour apart, are combined to cover the tropical disturbance. An example of data coverage on a hurricane research day for tropical storm Beryl of 1982 is shown in Fig. 1. The figure shows 6.7  $\mu\text{m}$  (mid tropospheric) water vapor imagery with plotted radiosonde identification numbers (there are a few more stations not shown in the Caribbean Sea area); note the lack of conventional upper air data in this region. Data sets of smaller areal extent (Figure 2) centered on a significant tropical disturbance were processed up to three times a day in quasi-real time to provide the NHC with analyses of the storm environment. The imagery shown in Fig. 2 is constructed from a combination of the VAS 6.7  $\mu\text{m}$  mid tropospheric  $\text{H}_2\text{O}$  emission observations and 11  $\mu\text{m}$  atmospheric window cloud and surface emission observations. Clouds are delineated by white areas, high water vapor concentrations by blue and green areas, and dry, cloud free regions by dark brown and black areas. Figure 2 shows a plot of upper level (approximately 200 mb) winds (in knots) around hurricane Debby for 0000 GMT on September 16, 1982 from a combined wind data set which will be described in section 4.

A display program on McIDAS was developed to facilitate a quick look by NHC at selected fields derived from the VAS data. As improvements in retrieval, analysis, and display procedures were developed together with a better understanding of the VAS measurements qualities, including its limitations, the NHC personnel were better able to evaluate the capabilities of the VAS over oceanic areas for its tropical storm analysis and forecasting operation. Evaluation efforts to determine optimum use of these data are

expected to continue on a near real time basis through the 1984 hurricane season.

## 2. Comparisons with radiosondes

Comparisons of the VAS temperature and moisture profile retrievals with selected tropical radiosondes (Bermuda, San Juan, and West Palm Beach) were made by the NHC during the 1983 hurricane season (for details of VAS sounding retrieval methods, see Smith, 1983). Temperatures, dewpoints, thicknesses, heights, and winds were evaluated; the results for a combination of all comparisons are summarized in Table 1. Most comparisons were made at 1200 GMT, and wherever the radiosonde and VAS soundings were sufficiently close in time and space (within approximately 2 hour and approximately 100 km, respectively). Winds which accompany the VAS temperature retrievals are derived from geopotential heights analyzed at constant pressure levels. The height data used to construct the analyses are provided from the VAS temperatures and mixing ratios, and a lower reference level which is a surface height estimated from a topography file and a surface pressure field produced from objective analyses of mean sea level temperature and 1000 mb heights (Hayden, 1983, personal communication; Montgomery, 1984). The latter are based on conventional surface observations and a global forecast field. The curvature term is included in these gradient winds. The VAS gradient winds had a mean directional difference of about 30 degrees (not shown). Several factors may contribute to these differences such as deficient lower reference 1000 mb height fields due to inadequate conventional surface reports across some oceanic regions. Confidence in the gradient wind accuracy is higher in clear areas where sounding precision and density are the greatest. However, these results suggest that gradient winds computed in this manner are generally less

useful than cloud motion winds (when both are available) in the NHC tropical analyses. The VAS temperature observations, however, were considered good. The standard deviations of the difference between the VAS and radiosonde values were on the order of 1 to 1.5 degrees. Associated thicknesses derived from the temperature profiles were excellent when compared with the radiosonde observations. The NHC expressed confidence in the temperature and thickness parameters. As expected, the differences are larger for moisture because the VAS lower vertical resolution moisture profiles cannot capture highly structured vertical features as well as the radiosonde.

### 3. Comparisons with dropsondes

A comprehensive meteorological data set, including VAS data, is being constructed from observations of hurricane Debby from September 13-17, 1982. NOAA Office of Aircraft Operations aircraft flew prescribed tracks throughout the environment of hurricane Debby on two missions (September 14/15, and September 15/16, 1982). During this time a dropwindsonde experiment was performed by the HRD providing an opportunity to compare the VAS soundings produced in real time with Omega dropwindsonde (ODW) observations. Figure 3a shows an example comparison of the 500 mb temperatures at 0000 GMT on September 16, 1982 observed by the dropsondes and the VAS (dropsondes circled). Figure 3b shows a comparison of objective analyses of the VAS and dropwindsonde 700 mb temperature values for 0000 GMT on September 15, 1983. As may be seen the thermal patterns indicated by the independent observations are in close agreement. Figure 4 illustrates a specific VAS retrieval/dropwindsonde comparison on a skew-t/log-p diagram. Except for the height of the moist layer, the comparison is quite good. Numerical comparisons, similar to the previously noted radiosonde comparisons, were made by the NHC and are shown in

Table 2. Comparisons were made wherever the ODW and the VAS soundings were sufficiently close in time and space. The results of the comparisons were quite similar to the radiosonde comparisons, with the temperatures and thicknesses having the smallest differences. (No VAS gradient winds were generated in real time for September 14/15 so that the comparisons shown are for the September 15/16 case only).

4. Circulation from the VAS cloud drift, water vapor motion, and gradient wind observations

Studies have indicated that the deep layer mean wind field around a tropical cyclone is one of the best indicators of the storm's steering current (Chan and Gray, 1982). One of the main goals of the cooperative program is to provide the NHC with an analysis of the satellite derived deep layer mean wind "steering current" for forecasting hurricane movement. For tropical cyclone Debby, three VAS data sets were processed each day (0000, 1200, and 1800 GMT on September 13-17, 1982) covering a large area centered on the hurricane. To further enhance the VAS derived data sets, selected NOAA-6 and NOAA-7 polar orbiting satellite passes over Debby were processed to take advantage of the TOVS microwave profile retrievals and derived gradient winds in the cloudy regions of the hurricane not achievable from the VAS infrared data. These microwave soundings were combined with the VAS soundings into a single data set and manually edited for consistency using the McIDAS. To enhance further the atmospheric circulation information, high and low level cloud drift (Mosher, 1979) and mid level water vapor motion (Mosher and Stewart, 1981) winds were derived from the VAS imagery and added to the gradient wind data set, with further manual editing of the winds for consistency. The water vapor motion winds were derived from a 3 hour loop of the 6.7  $\mu\text{m}$  water vapor imagery which

has peak radiance contributions originating from about 400 mb. Radiosondes were used for quality control in the editing process where available. The final wind set consisting of VAS gradient, TOVS gradient (in some cases), cloud drift, and water vapor motion winds for three levels (approximately 850 mb, 400 mb, and 200 mb (Fig. 2)) was used to derive a deep layer (850-200 mb) mean (dlm) wind analysis. These three levels actually represent layers, since the cloud drift and water vapor motion data are not all exactly at the indicated heights ( $\pm 50$  mb and  $\pm 100$  mb, respectively). The small number of TOVS gradient winds shown in Fig. 2 is due to the fact that these winds are used only in areas void of cloud drift and VAS gradient winds. These areas usually correspond to the storm center and adjacent featureless heavy cloud areas where cloud drift winds are difficult. The cloud penetrating capabilities of the microwave radiances (after careful editing of precipitation attenuation) make soundings and derived gradient winds possible in these areas. However, due to the relatively poor resolution of the microwave radiances (5 km vertical and 110 km spatial), the TOVS gradient winds are subject to larger errors than the VAS gradient winds and should be used with discretion. Regression equations were derived by Sanders et al. (1980) based on tropical radiosonde data for estimating the tropospherically averaged flow from information at three levels (850, 500, and 250 mb), and a similar set of equations derived for the three levels in this study (850, 400, and 200 mb) were used to produce the dlm analysis (Goldenberg, 1984, personal communication). The entire process from data ingest to the completion of the dlm analysis for an area the size of Fig. 2 can be accomplished on the McIDAS in 2 to 2½ hours.

Combined wind vectors for the three levels over hurricane Debby's environment for 0000 GMT on September 16, 1982 are shown in Fig. 5a to 5c. The cyclonic circulation of Debby is present at all three levels with the strongest

winds at low levels as would be expected. The circulation quickly becomes anticyclonic away from the center at upper levels with a large ridge providing an outflow channel to the east of Debby. The amplitude of this ridge was under-forecast by the global analysis, with the result that many models forecast the storm to move on a more northeasterly path rather than more northerly path that the storm followed before turning to the northeast once over the ridge. Debby can be seen embedded in a mid-latitude trough with a closed center at mid and upper levels to the north of the storm.

The combination of high density cloud drift winds in cloudy areas, high density gradient winds derived from VAS retrievals in clear areas, water vapor motion winds at mid levels, and gradient winds derived from TOVS microwave retrievals (when available) provide a much better than normally available description of the wind fields surrounding tropical cyclones in a typically data sparse region. A Barnes objective map analysis scheme (Barnes, 1973) is used to derive the three individual level streamline analyses from the raw data. The deep layer mean wind analysis is then derived from the three individual level analyses using the regression equations on a 1.0 degree mesh grid. A final step is to remove the tropical cyclone vortex, if one is present, and define the mean wind steering current over the storm. This is first done by determining the position of the storm and its radius of influence. The radius of influence, as determined by the NHC, is the average distance from the storm center to the outermost analyzed closed isobar around the storm. This is compared to the outermost closed streamline in the dlm analysis. Whichever is greater is used, however, they usually are very close. The grid values within this radius of influence are then zeroed out. The current storm direction and speed, as determined by the NHC, are inserted into the grid at the storm position. The grid points within the radius of influence

are then given values using bi-linear interpolation between the surrounding data and the storm position value. While it is recognized that the determination of current storm direction and speed can be fairly subjective, especially in storms with non-descript centers and no reconnaissance support, this technique was used and will be evaluated in the next section. An example of the final dlm streamline and speed analyses with the vortex removed for Debby on September 16, 1982 is shown in Fig. 6.

Deep layer mean wind analyses are being provided to the AOML-HRD for all the time periods processed around Debby, and also for all 1983 Atlantic tropical cyclones, for comparisons with conventional atmospheric analyses of the North Atlantic Ocean area to assess the forecast utility of greatly enhanced wind observations over this area which is virtually void of conventional observations. Testing and numerical comparisons will be done with a modified version (Goldenberg, 1983, personal communication) of the SANBAR (SANDers BARotropic) model (Sanders et al., 1975). In the meantime, a simpler procedure has been tested at the UW-SSEC as described in the following section.

##### 5. Prediction of tropical cyclone motion

As may be seen in Fig. 6 from the locations of hurricane Debby at 12 hour intervals beginning at 0000 GMT on 16 September 1982, the tropical cyclone follows the satellite derived deep layer mean wind analysis streamlines (from 0000 GMT on 16 September 1982 data) fairly closely out to 72 hours. Greater deviations from the streamline pattern obviously can be expected at longer durations from the analysis time since steady state is assumed and the streamline fields in reality are constantly changing and evolving with time. This streamline field however serves as a good approximation of the steering current and subsequent short range storm track forecast. With assumptions that

the deep layer mean wind steering current theory holds, and also that the abundance of wind data in a normally data sparse region would improve the dlm analysis, a simple trajectory model was developed at the UW-SSEC to test on the hurricane Debby data. While it is recognized that trajectory forecasting of tropical cyclone movement is not a new concept, the method was employed using the satellite derived deep layer mean wind analyses to assess the accuracy of the streamline field as an approximate steering current, and as an initial analysis for more sophisticated forecast models (Le Marshall et al., 1984). The purpose of this exercise is not so much as to devise a hurricane forecast model but to evaluate the impact of the VAS data in combination with the TOVS and cloud drift data in the simplest way possible.

The streamlines are given by the solution to the following equations

$$dx/dt = u(x,y)$$

$$dy/dt = v(x,y)$$

These equations are solved numerically by using the Adams method (Hildebrand, 1962). This method assumes that  $u(x,y)$  and  $v(x,y)$  vary linearly between mesh points on the grid analysis and results in the following formula for the path:

$$x_{k+1} = x_k + hU_k + \frac{h}{2}(U_k - U_{k-1})$$

$$y_{k+1} = y_k + hV_k + \frac{h}{2}(V_k - V_{k-1})$$

where  $(x_k, y_k)$  and  $(x_{k-1}, y_{k-1})$  are the previous positions of the source point with corresponding velocities  $(U_k, V_k)$  and  $(U_{k-1}, V_{k-1})$ , and  $h$  is the time step. The velocity components at an arbitrary point in the grid analysis field are found using bi-linear interpolation. A typical model run takes only a few



seconds on the McIDAS. An example forecast for hurricane Alicia landfall is shown in Fig. 7.

Comparisons of mean forecast errors (MFE) for several different operational models used by the NHC, the official forecasts, and the VASTRA (VASTRA TRAjectory) model for selected homogeneous cases when satellite derived deep layer mean wind data were available from Debby of 1982, and Alicia, Barry and Chantal of 1983, are shown in Table 3. Initial positioning error (Neumann and Pelissier, 1981) was removed from the MFE in all cases. Performance of specified models relative to the CLIPER model is shown in Fig. 8. From Table 3 and Fig. 8 it can be seen that the VASTRA forecasts compare favorably with the official forecasts and the other operational models. While it is recognized that these data represent a relatively small statistical set, it is believed that the good quality and much improved density of wind data over the oceanic regions are at least in part responsible for the encouraging results. Several VASTRA forecasts (Debby cases) included in these results were not run in real time. However, more importantly, the data were collected, edited and analyzed for the most part in quasi-real time. VASTRA forecasts from 1983 storms were acutally made in real time in a quasi-operational testing mode, and made available to the NHC. It is the intent of the authors to show what is possible but not yet what is currently achieved in an operational mode. Further testing is being conducted by the NHC in the 1984 Atlantic hurricane season.

The model was also run on the same cases without inserting current storm motion (not shown) and using simple bi-linear interpolation of the surrounding data within the radius of influence with slightly poorer (5 to 10%) results. However, these case study storms had fairly good reconnaissance flight coverage, and steady storm tracks, so that initialized storm motion estimates provided by the NHC on the average were good. It is suggested that the current

storm motion be used when there is a high confidence in it by NHC, either by a clearly defined center and steady motion, or by continuous reconnaissance flight reports. It should not be used when confidence in the estimate is low due to a heavy overcast over the center, lack of reconnaissance data, etc.

#### 6. Intensity from TOVS soundings

Atlantic tropical cyclone intensities were also monitored at the UW-SSEC utilizing the NOAA polar orbiting satellite microwave measurements to provide an estimate of the strength of the upper tropospheric warm core, which is statistically correlated to the surface central pressure and maximum winds (Kidder et al., 1978; Grody and Shen, 1983; Velden and Smith, 1983). Figure 9 is an example of the agreement between the surface pressure and maximum sustained wind speed estimates from the TOVS microwave technique, with the NHC official best track data for tropical cyclone Barry. Scatter diagrams relating  $\Delta T_{250}$  with central pressure and maximum winds (as estimated by NHC) are shown in Fig. 10a and b. Included in the statistics shown in Fig. 10, which are an update from previous findings, are comparisons from the 1982 and 1983 hurricane seasons. Experimental use of the TOVS microwave intensity estimates by the NHC to augment existing methods was continued in the 1984 Atlantic hurricane season.

#### 7. Concluding remarks and future work

Future cooperative research using the VAS and TOVS data with the NHC and the AOML-HRD is planned through the 1984 hurricane season. Daily VAS and TOVS data sets were again processed and sent to the NHC in near real time for their evaluation.

An effort is currently underway to use trajectory analyses from consecutive deep layer mean wind analyses in a numerical model. In order to help generate the initial wind analysis for the barotropic model (SANBAR), the sequence of previous wind analyses will be used to augment the field at the initial time ( $t=0$ ), in effect, an extrapolation of the analyses to  $t=0$  in order to fill in the satellite data void areas. These ideas have been used successfully on the VAS geopotential data in conjunction with quasi-geostrophic models (Lewis, et al., 1983). In the context of hurricane tracking, the barotropic constraint of absolute vorticity conservation will be used to couple the wind fields in time.

Continued research into hurricane track forecasting using the satellite derived deep layer mean wind analyses in the SANBAR model and the complete VAS/TOVS sounding and wind data sets in primitive equation forecast models is planned as part of the NOAA Operational VAS Assessment (NOVA) program.

### Acknowledgments

The authors wish to thank the personnel of UW-SSEC, NESDIS/DL, NHC, and AOML-HRD who contributed to the research reported here. Special thanks are extended to Professor Verner E. Suomi for his enthusiastic support and guidance, Dr. Robert Burpee of HRD for providing the dropsonde data, Drs. Robert Fox and Paul Menzel for providing the McIDAS/VAS facility support necessary for the application reported here, Stan Goldenberg, Robert E. Kohler, Dr. John Lewis, Gary Wade, Dr. Christopher Hayden, Tod Stewart, and Dr. Arthur Pike for their contributions to the software and data processing aspects of this project, and to Mrs. Gail Turluck for the handling of the manuscript. The continued enthusiastic support of Dr. R. Sheets of the NHC is responsible for much of the rapid progress toward defining the tropical storm applications of VAS. This research was supported by NASA Grant #NAS5-21965.

## References

- Barnes, S. L., 1973: Mesoscale objective analysis using weighted time series observations. NOAA Technical Memorandum ERL NSSL-62, National Severe Storms Laboratory, 1313 Halley Circle, Norman, Oklahoma, 70369, 60 pp.
- Chan, J. C. L., and W. M. Gray, 1982: Tropical cyclone movement and surrounding flow relationships. Mon. Wea. Rev., 110, 1354-1374.
- Goldenberg, S., 1983: Personal communication. NOAA/ERL Atlantic Oceanographic and Meteorological Laboratories, Hurricane Research Division, 4301 Rickenbacker Causeway, Miami, Florida, 33149.
- Goldenberg, S., 1984: Personal communication. NOAA/ERL Atlantic Oceanographic and Meteorological Laboratories, Hurricane Research Division, 4301 Rickenbacker Causeway, Miami, Florida, 33149.
- Grody, N. and W. C. Shen, 1982: Observations of Hurricane David (1979) using the Microwave Sounding Unit. NOAA Technical Report NESS 88, National Oceanic and Atmospheric Administration, National Earth Satellite Service, Washington, D.C., 20233, 52 pp.
- Hayden, C. M., 1983: Personal communication. NOAA/NESDIS Development Laboratory, 1225 West Dayton Street, 2nd Floor, Madison, Wisconsin, 53706.
- Hildebrand, F. B., 1962: Advanced Calculus for Applications. Prentice-Hall, Inc., 646 pp.
- Kidder, S. Q., W. M. Gray and T. H. Vonder Haar, 1978: Estimating tropical cyclone central pressure and outer winds from satellite microwave sounder data. Mon. Wea. Rev., 108, 1458-1464.
- Le Marshall, J. F., W. L. Smith, and G. M. Callan, 1984: Hurricane Debby--An illustration of the complimentary nature of VAS soundings and cloud and water vapor motion winds. To be submitted to the Bulletin of the American Meteorological Society.
- Lewis, J. M., C. M. Hayden, and A. J. Schreiner, 1983: Adjustment of VAS and RAOB geopotential analysis using quasi-geostrophic constraints. Mon. Wea. Rev., 111, 2058-2067.
- Montgomery, H., 1984: VAS demonstration description, summary and final report. NASA Publication forthcoming in 1984.
- Mosher, F. R., 1979: Cloud drift winds from geostationary satellites. Atmospheric Technology, 10, 53-60.
- Mosher, F. R. and T. R. Stewart, 1981: Characteristics of water vapor tracked winds. NAVENVPREDRSCHFAC Contractor Report, CR 81-06, 51 pp.
- Neumann, C. J., and J. M. Pelissier, 1981: Models for the prediction of tropical cyclone motion over the North Atlantic: An operational evaluation. Mon. Wea. Rev., 109, 522-538.

- Sanders, F., A. C. Pike, and J. P. Gaertner, 1975: A barotropic model for operational prediction of tracks of tropical storms. J. Applied Meteor., 14, 265-280.
- Sanders, F., A. L. Adams, N. J. B. Gorden, and W. D. Jensen, 1980: Further development of a barotropic operational model for predicting paths of tropical storms. Mon. Wea. Rev. 108, 642-654.
- Smith, W. L., H. M. Woolf, C. M. Hayden, D. Q. Wark, and L. M. McMillin, 1979: The TIROS-N operational vertical sounder. Bull. Amer. Meteor. Soc., 60, 1177-1187.
- Smith, W. L., V. E. Suomi, W. P. Menzel, H. M. Woolf, L. A. Sromovsky, H. E. Revercomb, C. M. Hayden, D. N. Erickson, and F. R. Mosher, 1981: First sounding results from VAS-D. Bull. Amer. Meteor. Soc., 62, 232-236.
- Smith, W. L., 1983: The retrieval of atmospheric profiles from VAS geostationary radiance observations. J. Atmos. Sci., 40, 2025-2035.
- Suomi, V. E., R. Fox, S. S. Limaye, and W. L. Smith, 1983: McIDAS III: A modern interactive data access and analysis system. J. Clim. and Applied Meteor., 22, 766-778.
- Velden, C. S., and W. L. Smith, 1983: Monitoring tropical cyclone evolution with NOAA satellite microwave observations. J. Clim. and Applied Meteor., 22, 714-724.

TABLE I  
 SUMMARY OF COMPARISONS BETWEEN VAS AND RADIOSONDE DATA  
 FOR BERMUDA, SAN JUAN, AND WEST PALM BEACH  
 (1 AUGUST-30 NOVEMBER 1983)

Parameter	Mean (VAS-RAOB)	Standard Deviation	Range	Number of Cases
T850 (°C)	1.4	1.2	-1.6 to 4.7	70
T700	0.2	1.3	-2.3 to 3.4	70
T500	0.4	1.2	-2.4 to 2.7	69
T400	1.2	1.5	-3.0 to 4.0	66
T300	0.9	1.7	-3.6 to 4.3	66
T200	0.0	1.6	-5.5 to 3.4	63
TD850 (°C)	2.7	4.5	-5.8 to 21.8	70
TD700	4.6	8.3	-8.1 to 29.7	70
TD500	0.9	9.9	-9.0 to 21.9	69
TD400	2.8	7.8	-9.8 to 23.8	66
TD300	4.1	8.1	-18.2 to 24.1	66
Z850 (m)	7	10	-23.0 to 31.0	68
Z700	13	13	-21.0 to 36.0	67
Z500	18	19	-26.0 to 38.0	67
Z400	22	20	-37.0 to 66.0	65
Z300	30	27	-52.0 to 71.0	63
Z200	32	37	-63.0 to 110.0	62
Z500-850 (m)	12	15	-31.0 to 63.0	69
Z400-850	16	18	-42.0 to 50.0	67
Z300-850	23	26	-63.0 to 71.0	65
Z500-700	6	12	-28.0 to 52.0	68
Z400-700	10	16	-39.0 to 35.0	66
Z200-400	9	28	-78.0 to 60.0	63
Z200-850	24	41	-114.0 to 106.0	63
Magnitude of vector wind difference (ms <sup>-1</sup> )				
850	4	2	0.0 to 14.0	64
700	4	3	0.0 to 11.0	64
500	4	2	1.0 to 13.0	61
400	5	3	1.0 to 19.0	62
300	7	5	1.0 to 27.0	59
200	10	7	2.0 to 40.0	54

TABLE 2  
 SUMMARY OF COMPARISONS BETWEEN VAS AND ODW FOR  
 14/15 AND 15/16 SEPTEMBER 1982

Parameter	Mean (VAS-ODW)	Standard Deviation	Range	Number of Cases
T850 (°C)	1.4	1.3	-1.4 to 4.9	42
T700	-0.3	1.2	-2.7 to 2.6	42
T500	-0.1	1.3	-2.4 to 2.3	35
T400	0.2	1.4	-3.1 to 3.3	24
TD850 (°C)	1.6	3.2	-5.0 to 9.8	42
TD700	3.6	5.2	-8.9 to 14.9	42
TD500	-12.5	7.0	-36.4 to 6.0	35
TD400	-8.9	7.6	-25.3 to 7.5	24
Z850 (m)	-6	23	-68 to 26	42
Z700	0	22	-58 to 41	42
Z500	1	24	-56 to 44	35
Z400	2	27	-54 to 47	24
Z400-850 (m)	11	17	-16 to 45	24
Z500-850	6	14	-18 to 43	35
Z400-700	4	14	-16 to 34	24
location (nm)	29	15	6 to 54	42
time (min)	38	29	2 to 108	42
Magnitude of vector wind difference ( $\text{ms}^{-1}$ )				
850	7	4	1 to 14	23
700	7	4	1 to 16	23
500	5	3	1 to 12	22
400	7	4	3 to 16	13



TABLE 3  
 COMPARISONS OF MFE (nm) FOR SELECTED HOMOGENEOUS CASES  
 DURING HURRICANE DEBBY OF 1982 AND  
 HURRICANES ALICIA, BARRY, AND CHANTAL OF 1983  
 (OFFICIAL AND MFM FORECASTS ARE NOT ISSUED FOR 36 AND 72 h, RESPECTIVELY)

Model	FORECAST INTERVALS (h)									
	12	(# of cases)	24	(# of cases)	36	(# of cases)	48	(# of cases)	72	(# of cases)
Official Forecasts	54	(20)	126	(17)	--	--	289	(12)	305	(9)
VASTRA	53	(20)	111	(17)	--	--	232	(12)	311	(9)
NHC 67	52	(18)	110	(15)	195	(12)	269	(10)	393	(8)
NHC 72	50	(18)	114	(15)	178	(12)	224	(10)	530	(8)
CLIPER	59	(18)	137	(15)	251	(12)	318	(10)	430	(8)
VASTRA	51	(18)	104	(15)	146	(12)	201	(10)	375	(8)
HURRAN	72	(16)	171	(12)	287	(10)	358	(9)	356	(8)
VASTRA	56	(16)	115	(12)	151	(10)	208	(9)	297	(8)
NHC 73	57	(15)	125	(13)	155	(9)	206	(8)	528	(7)
VASTRA	52	(15)	112	(13)	164	(9)	194	(8)	362	(7)
SANBAR	66	(16)	141	(14)	269	(10)	373	(9)	570	(7)
VASTRA	56	(16)	107	(14)	167	(10)	231	(9)	362	(7)
MFM	54	(9)	95	(7)	123	(5)	191	(5)	--	--
VASTRA	45	(9)	85	(7)	134	(5)	187	(5)	--	--

## Figure legends

- Fig. 1: Example of data coverage on a hurricane research day for tropical storm Beryl of 1982. Plotted in yellow are radiosonde identification numbers over  $6.7 \mu\text{m}$  water vapor (mid tropospheric) imagery.
- Fig. 2: Final edited combined wind set (upper level, approximately 200 mb) consisting of VAS gradient (blue), TOVS gradient (red), and cloud motion (yellow) vectors (kts) for hurricane Debby September 16, 1982 at 0000 GMT.
- Fig. 3: (a) Comparison of the 500 mb temperatures ( $^{\circ}\text{C}$ ) observed by the dropwindsondes (circled numbers) and VAS near hurricane Debby for 0000 GMT on September 16, 1982.  
(b) Comparison of objective analyses of VAS (solid) and dropwindsonde (dashed) 700 mb temperature ( $^{\circ}\text{C}$ ) values for hurricane Debby on September 15, 1982 at 0000 GMT.
- Fig. 4: Example skew t/log p VAS retrieval/dropwindsonde comparison.
- Fig. 5: (a) Upper tropospheric (approximately 200 mb) edited combined wind vectors (kts) around hurricane Debby for 0000 GMT on September 16, 1982.  
(b) Same as (a) except for mid tropospheric (approximately 400 mb).  
(c) Same as (a) except for lower tropospheric (approximately 850 mb).  
The + indicates calm to east of Debby.
- Fig. 6: Final 850-200 mb satellite derived deep layer mean wind streamline (solid) and speed (dashed in m/sec) analysis for hurricane Debby at 0000 GMT on September 16, 1982. Solid squares indicate Debby's storm track every 12 hours.

- Fig. 7: Final 850-200 mb satellite derived deep layer mean wind streamline analysis for hurricane Alicia at 1200 GMT on August 16, 1983. Solid squares indicate Alicia's storm track every 12 hours. Open squares indicate the VASTRA forecast out to 48 hours.
- Fig. 8: Performance of specified models relative to the performance of the CLIPER model for 1982 and 1983 cases studied. The sample is homogeneous, with the numbers in parentheses giving sample size. Forecasts are unavailable for any model at 60 hours and for official forecasts at 36 hours.
- Fig. 9: Comparison of the National Hurricane Center "best track" versus the satellite microwave estimates of (a) central pressure (b) maximum winds for Barry.
- Fig. 10: Comparison of  $\Delta T_{250}$  versus National Hurricane Center estimated (a) central surface pressure, (b) maximum winds.  $P_E$  is average environmental surface pressure surrounding the storm at a  $6^\circ$  radius,  $n$  is number of cases in the sample,  $r$  is correlation coefficient, and  $\sigma$  is standard deviation.

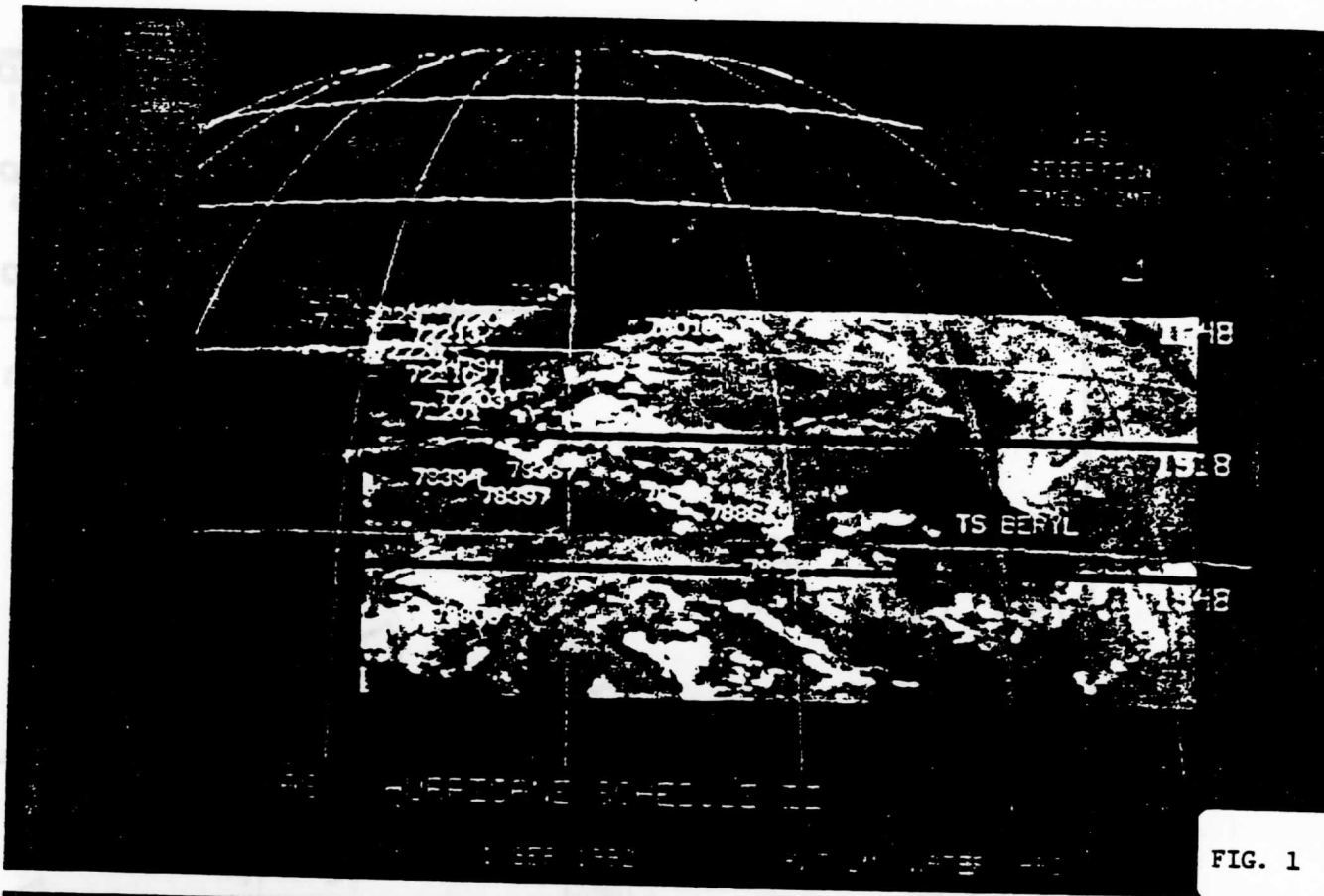


FIG. 1

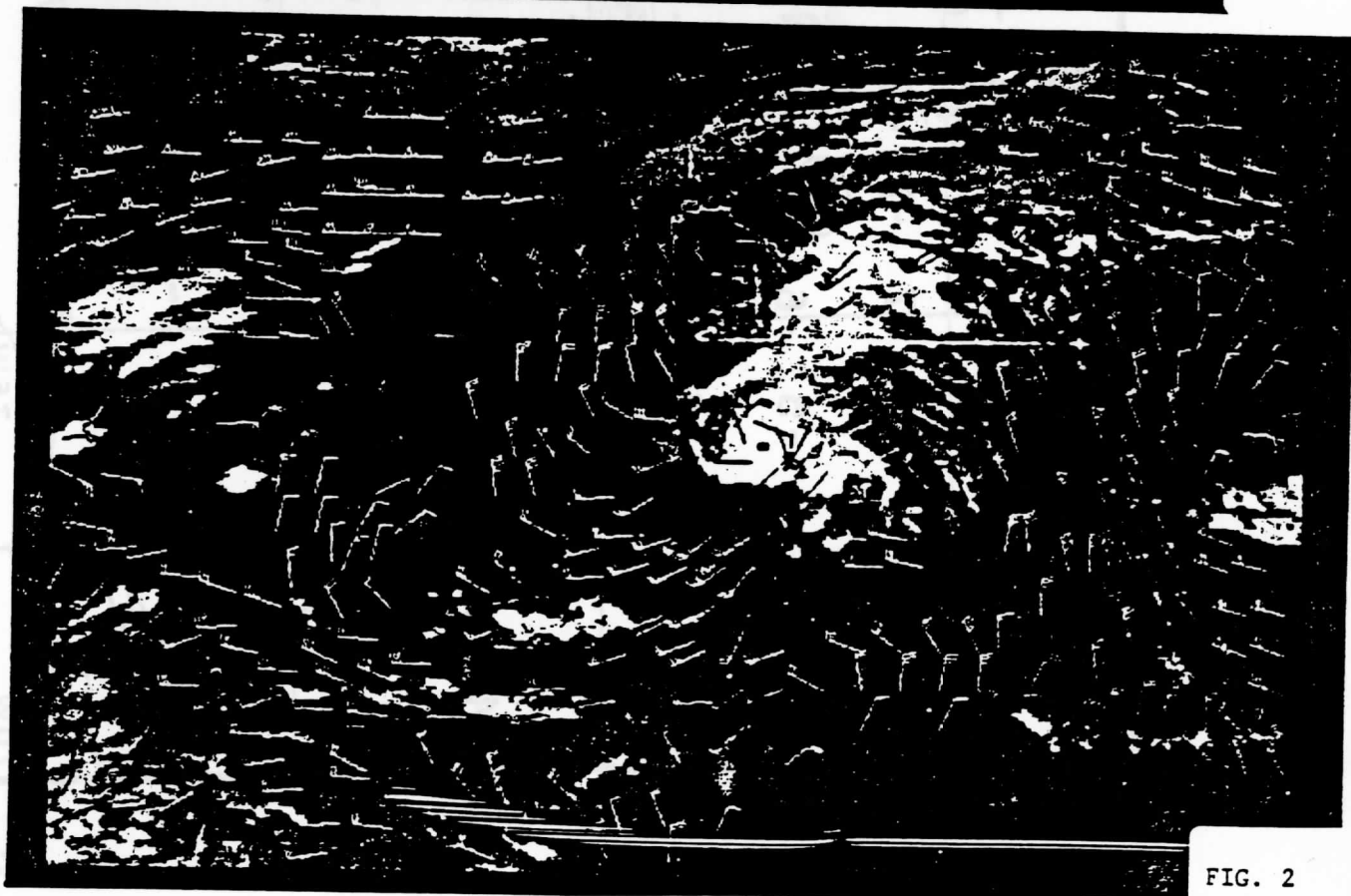


FIG. 2

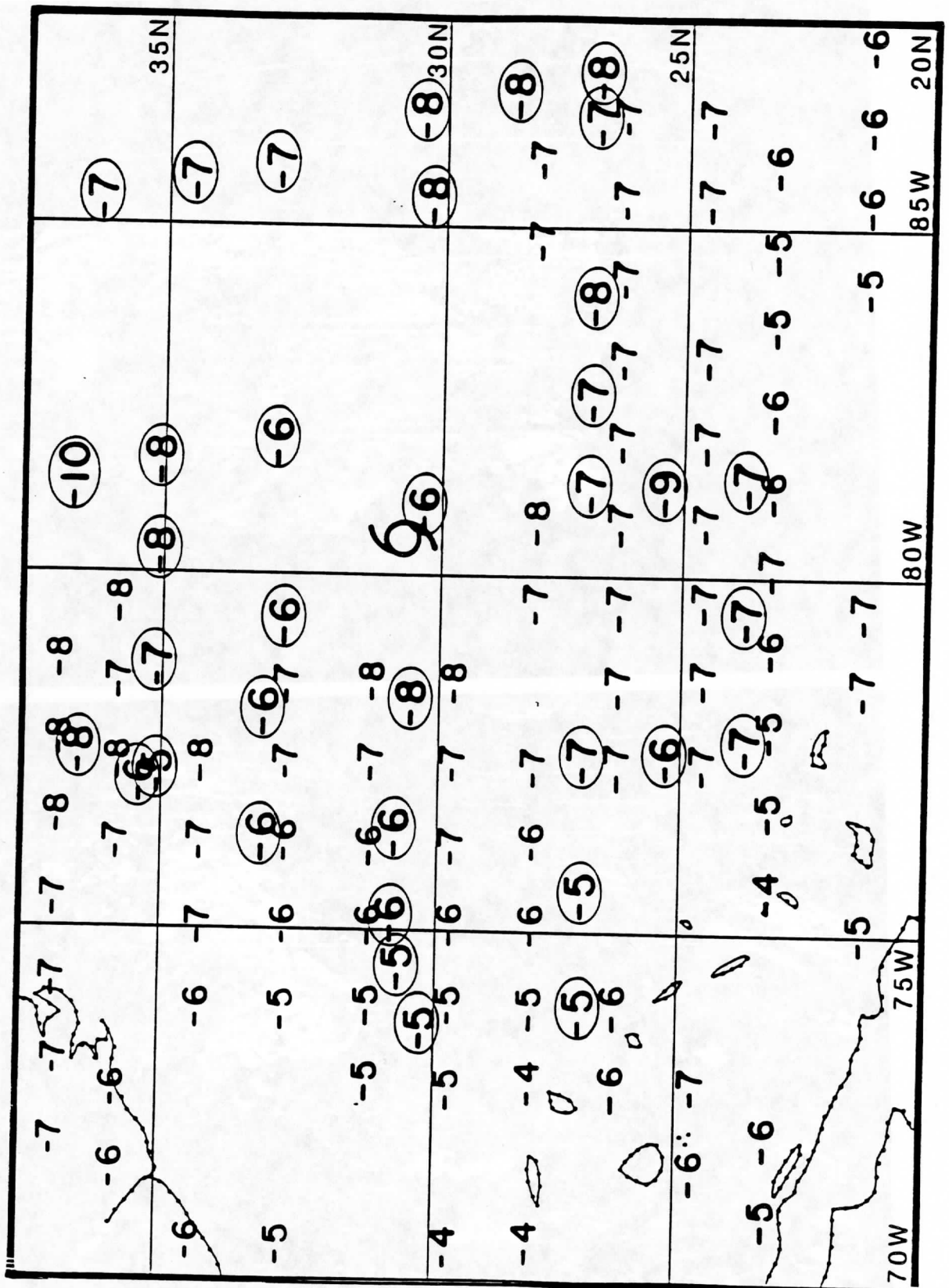


FIG. 3a  
Paper 2

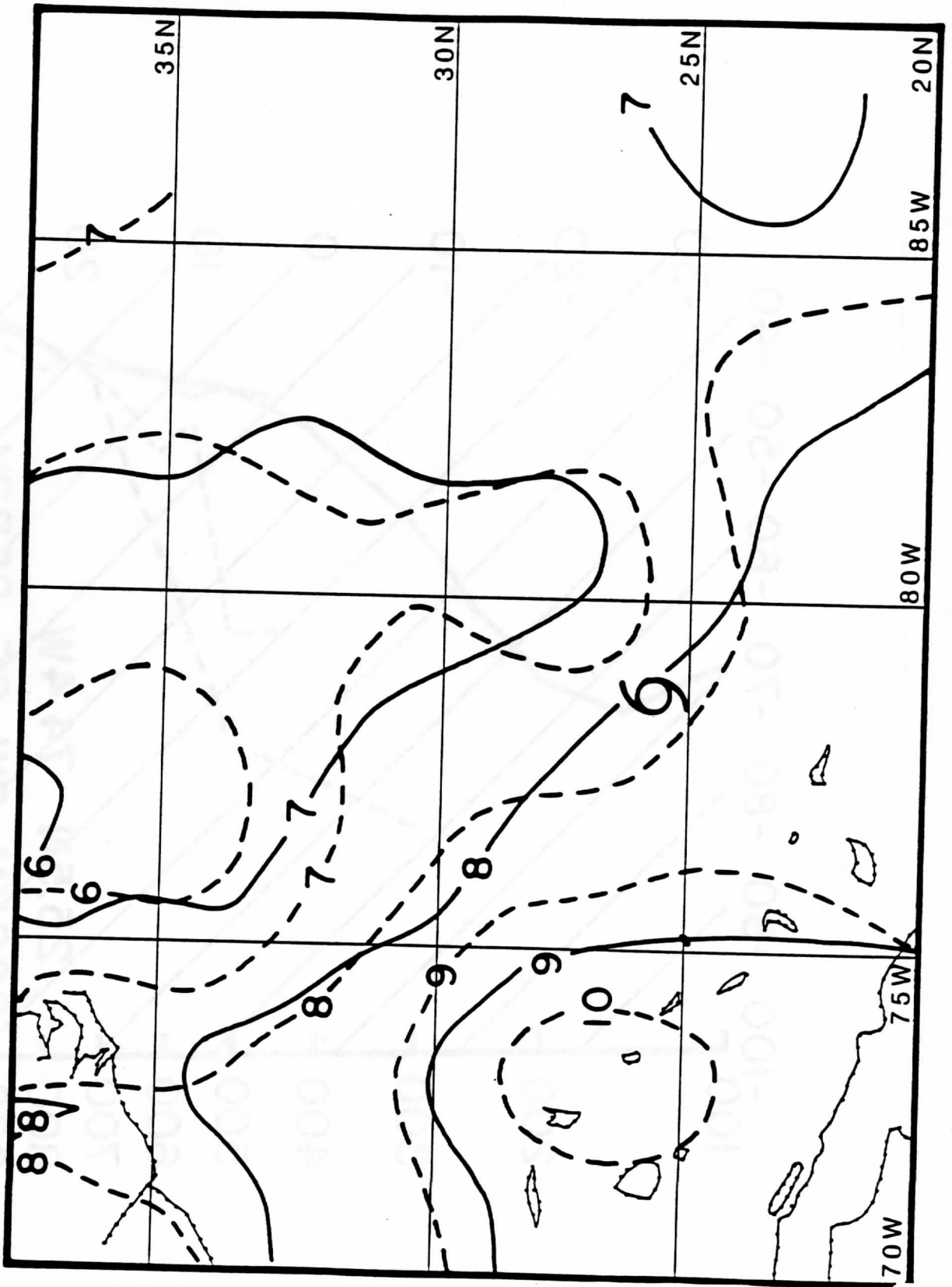


FIG. 3b  
Paper 2

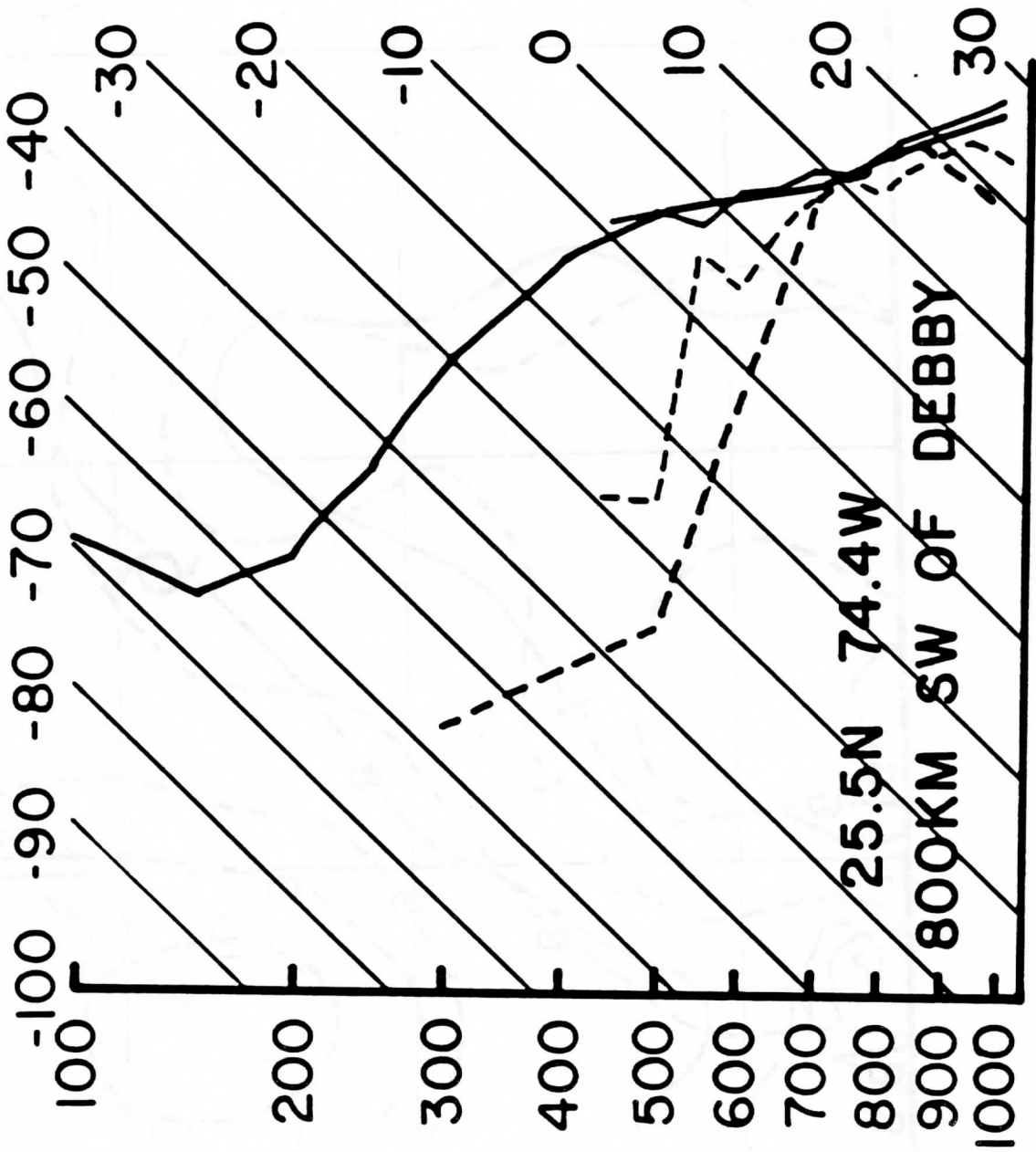
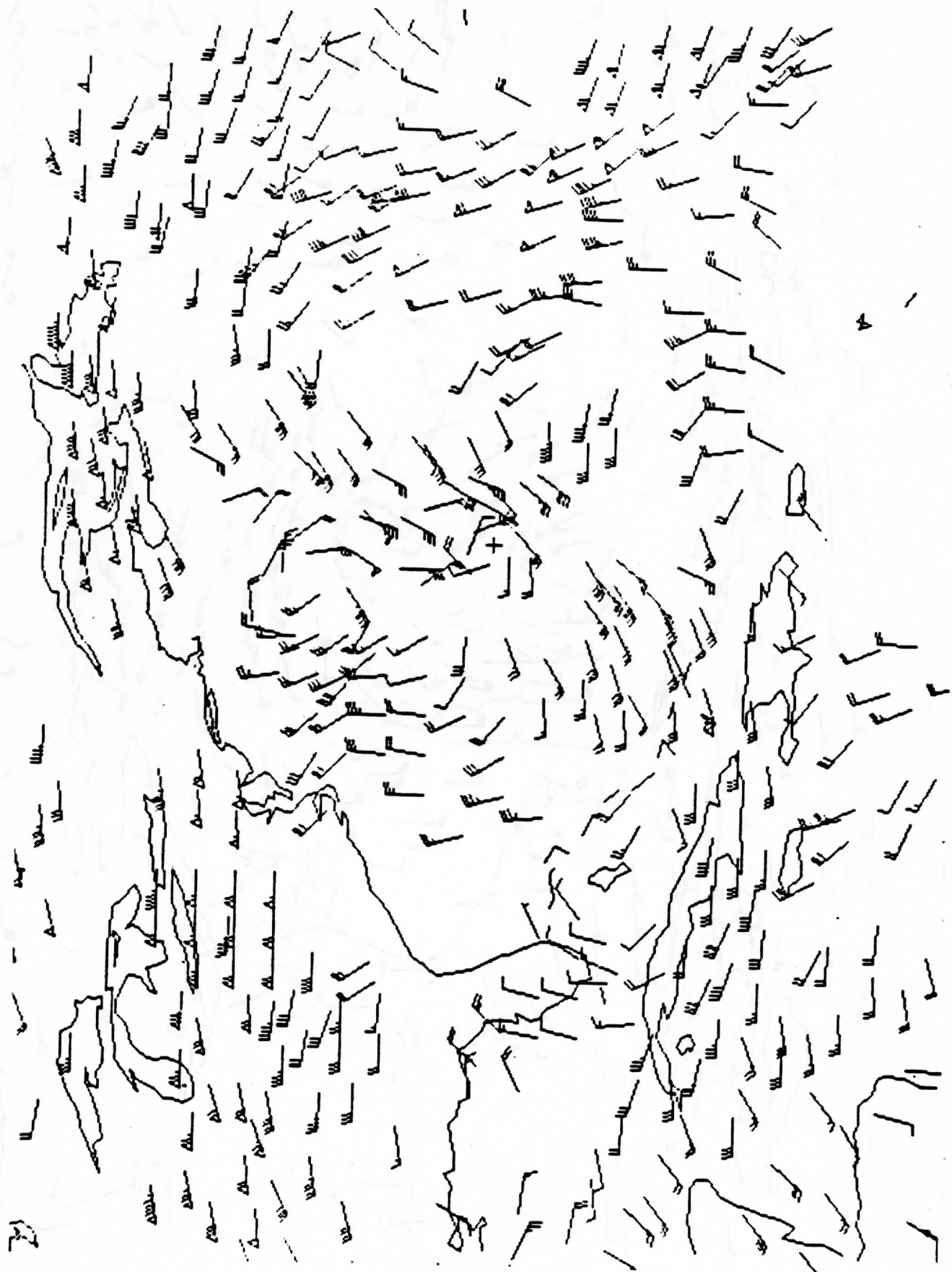


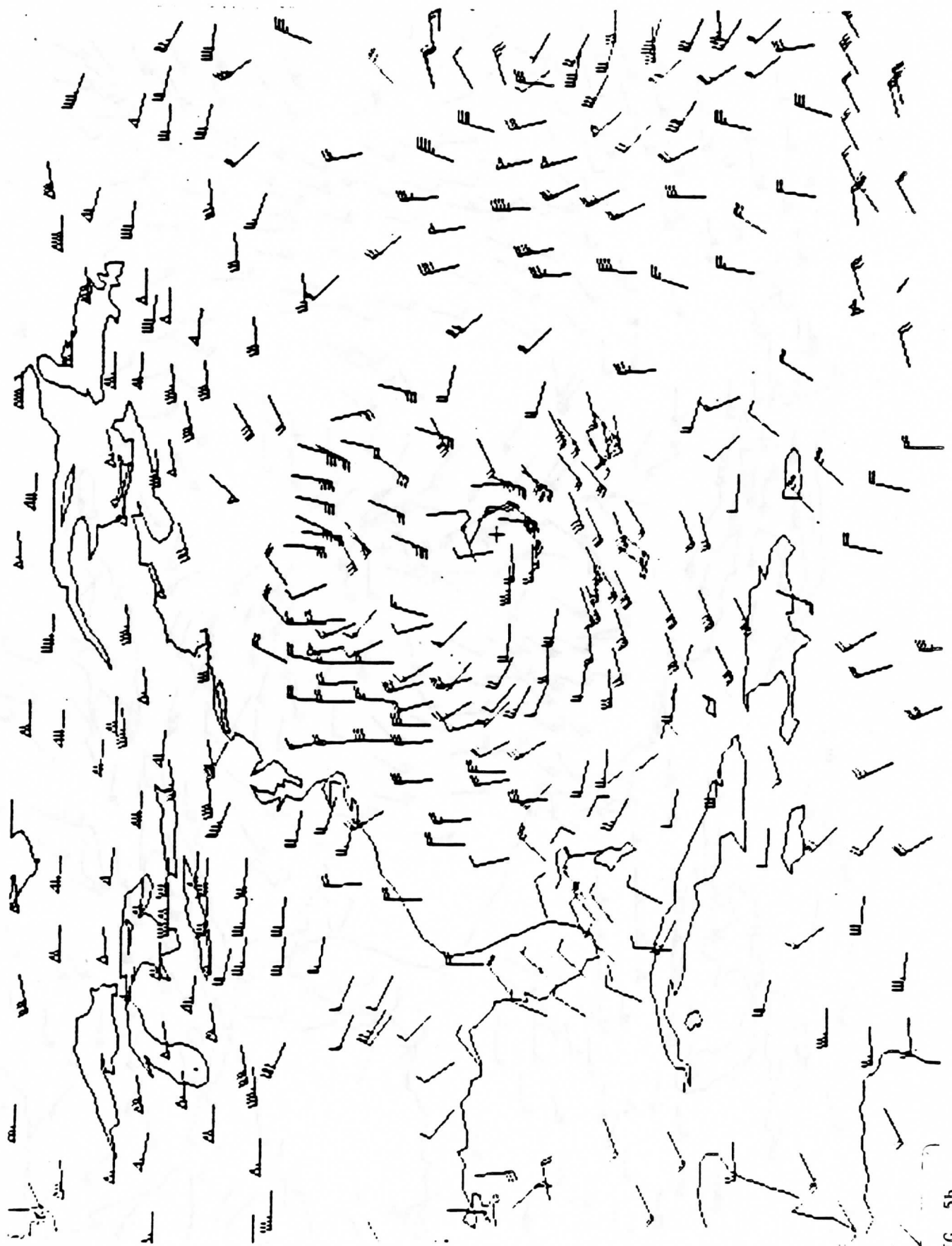
FIG. 4



Paper 2

FIG. 5a







Paper 2

FIG. 5c

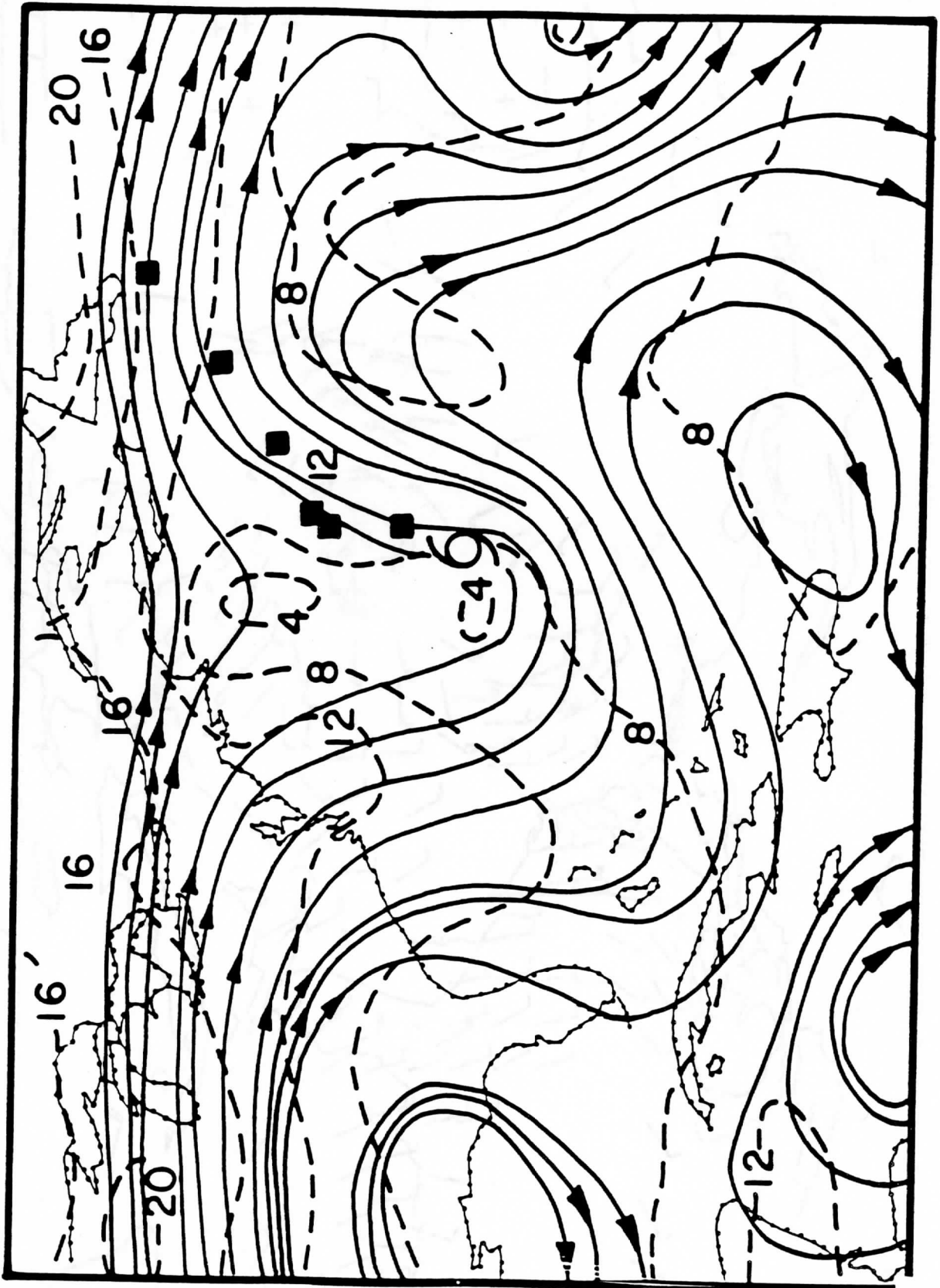


FIG. 6  
Paper 2

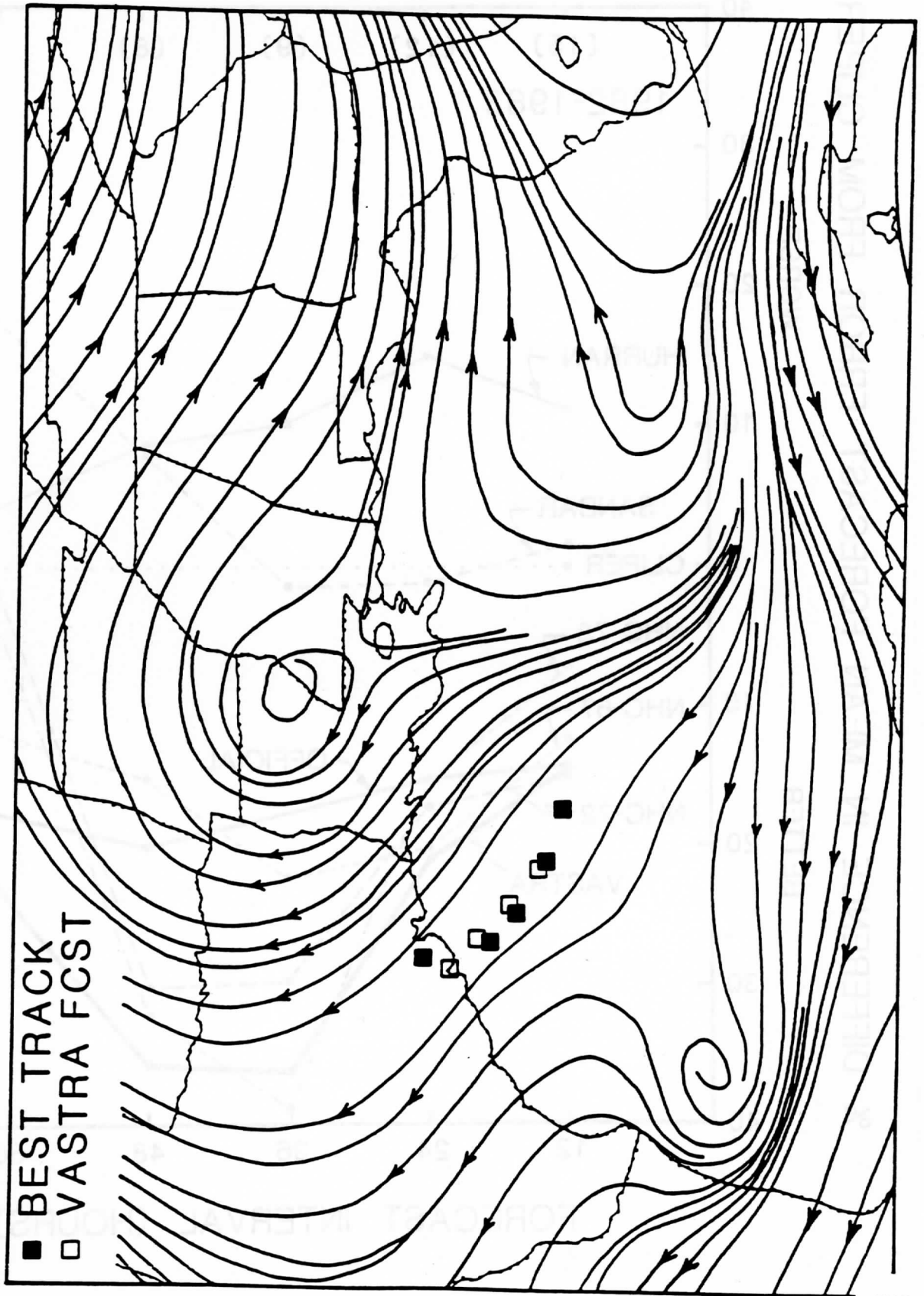


FIG. 7

% DIFFERENCE IN MEAN FORECAST ERROR FROM CLIPER

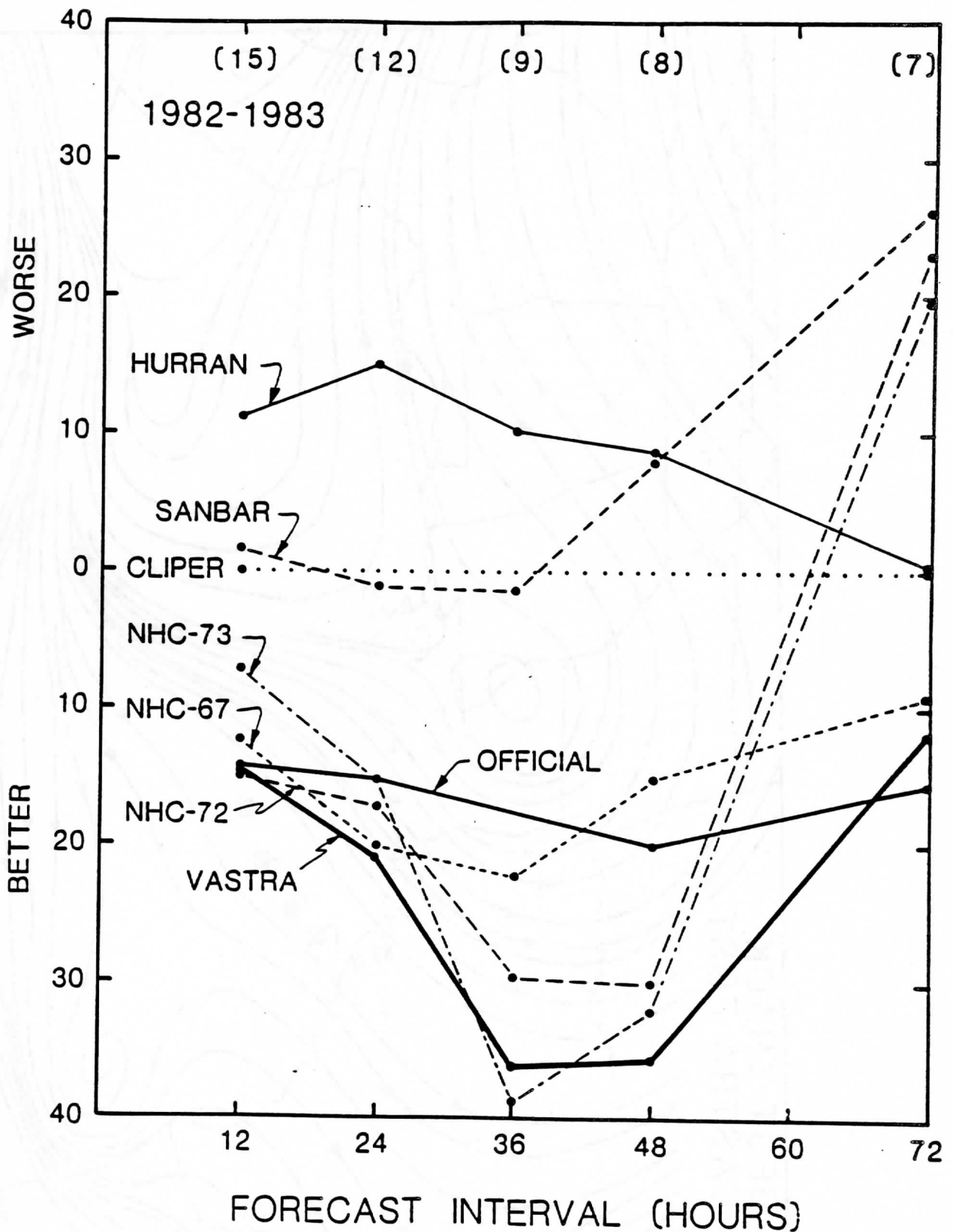
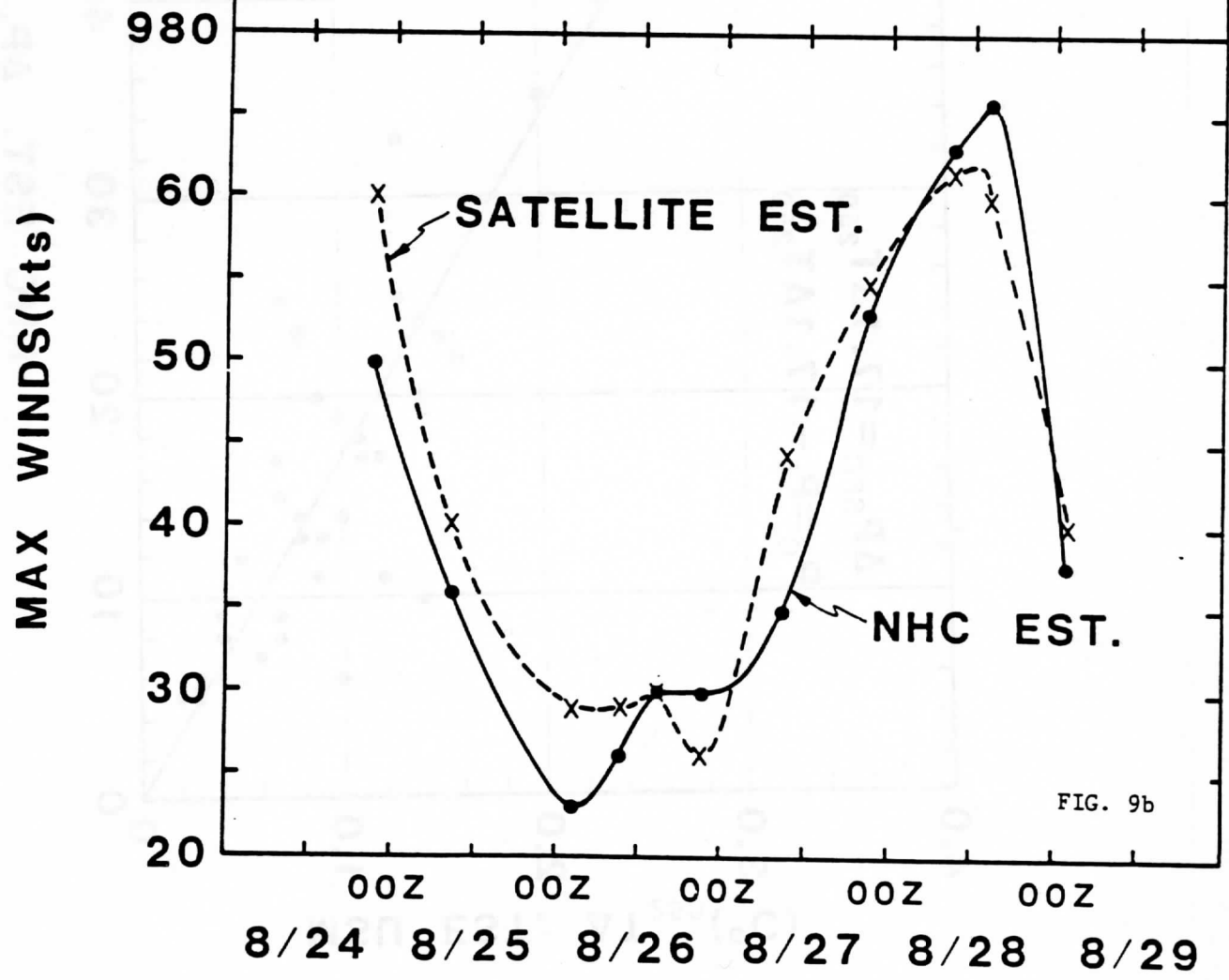
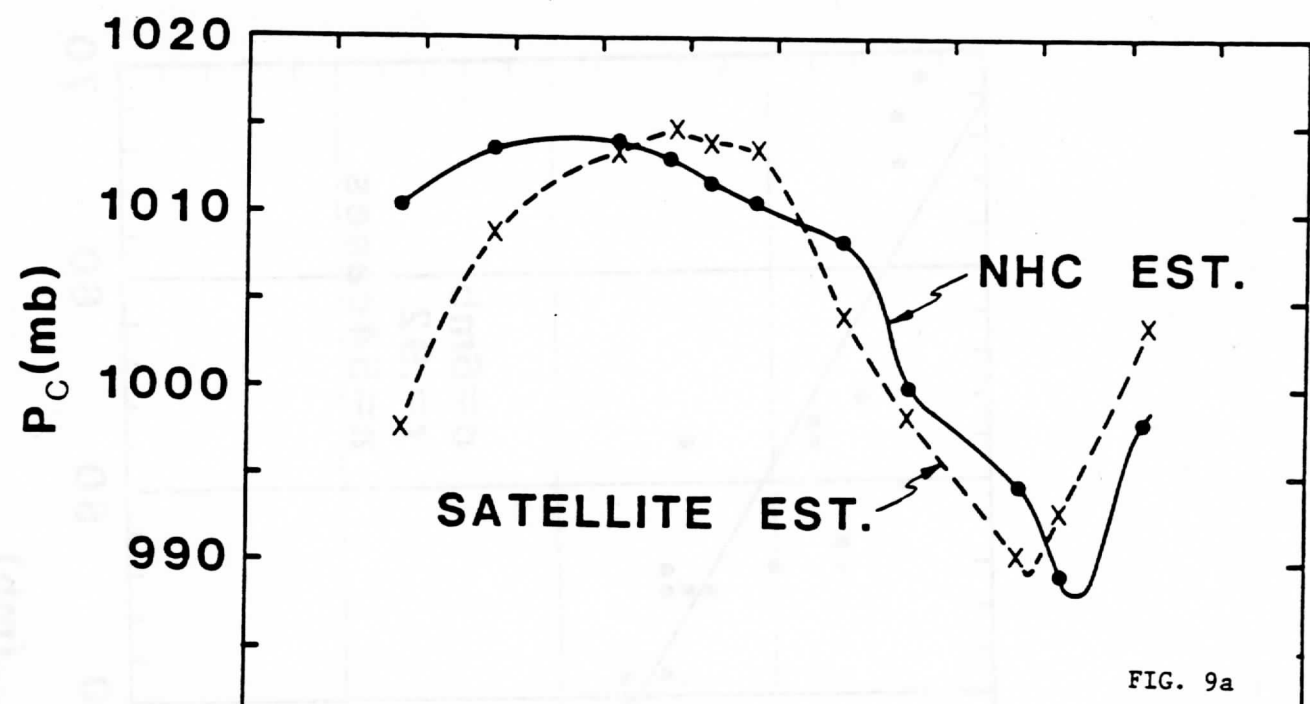


FIG. 8  
Paper 2



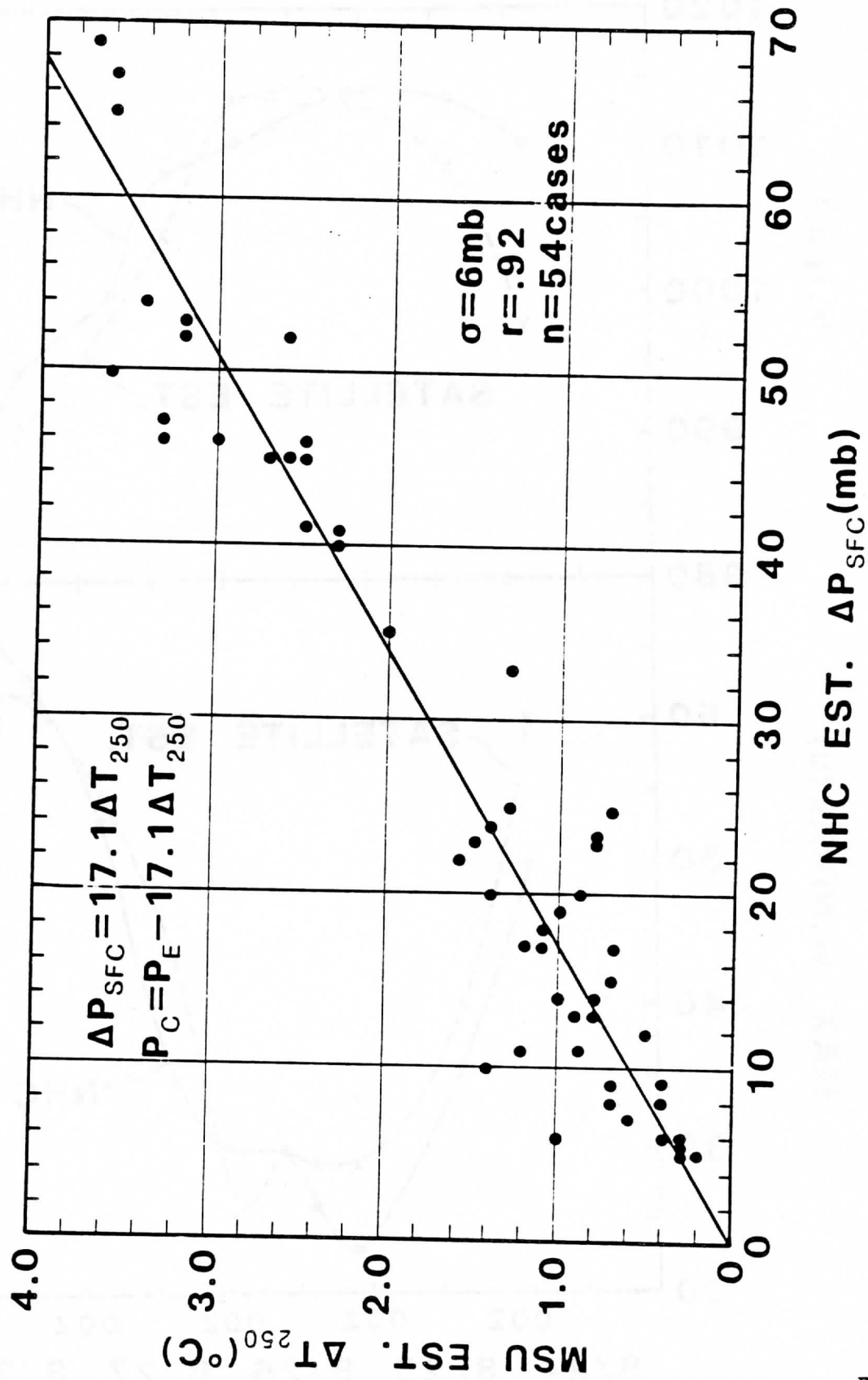


FIG. 10a  
Paper 2

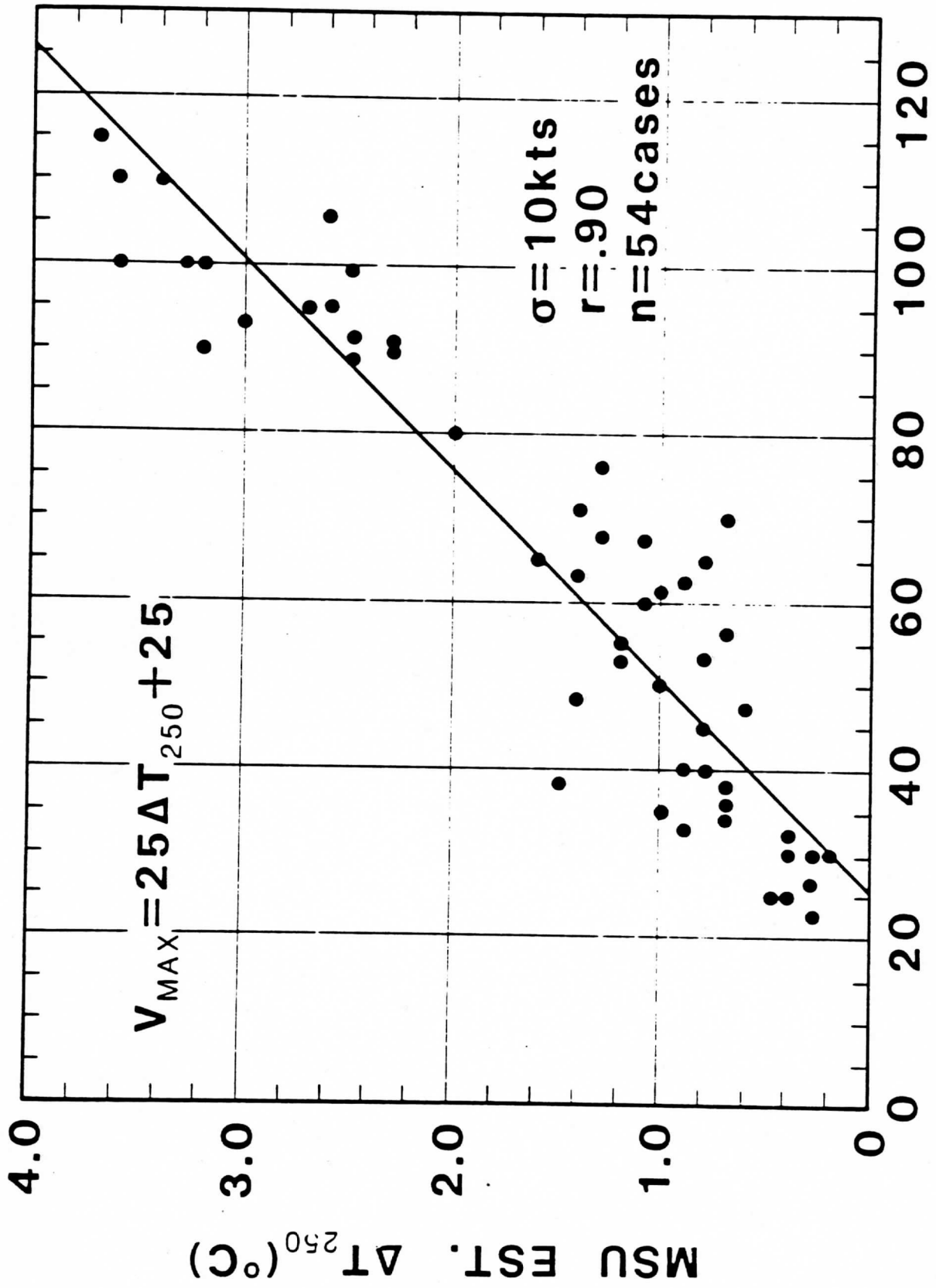


FIG. 10b  
 Paper 2



NOAA TECHNICAL MEMORANDUM NESDIS 6

THE ADVANTAGES OF SOUNDING WITH THE SMALLER DETECTORS  
OF THE VISSR ATMOSPHERIC SOUNDER

W. Paul Menzel

Thomas H. Achtor

Christopher M. Hayden

William L. Smith

Washington, D.C.

June 1984

2/WPM2/07

CONTENTS

	Page
Abstract . . . . .	iv
1. Introduction . . . . .	1
2. VAS data characteristics . . . . .	1
3. Clear column radiance determination . . . . .	2
4. Clear field of view statistics . . . . .	3
5. Retrievals . . . . .	3
6. Conclusions . . . . .	4
Acknowledgments . . . . .	5
References . . . . .	6
Tables . . . . .	7
Figures . . . . .	10
Appendix . . . . .	18

THE ADVANTAGES OF SOUNDING WITH THE SMALLER DETECTORS  
OF THE VISSR ATMOSPHERIC SOUNDER

W. Paul Menzel

NOAA/NESDIS Satellite Applications Laboratory  
Advanced Satellite Products Project

Thomas H. Achtor

Space Science and Engineering Center  
University of Wisconsin

Christopher M. Hayden

NOAA/NESDIS Development Laboratory  
Systems Design and Applications Branch

William L. Smith

NOAA/NESDIS Development Laboratory

1225 West Dayton Street, 2nd Floor  
Madison, Wisconsin 53706

**Abstract**

Results are presented that show sounding with the small detectors on the VAS produces more temperature profile retrievals of good quality in partly cloudy conditions than was possible with the large detectors. The increased ability to find clear fields of view outweighs the disadvantage of greater detector noise.

## 1. Introduction

With the launch of three VISSR Atmospheric Sounders (VAS) since late 1980, the era of time continuous sounding from a geostationary platform has begun. The results of the last three years have been well documented in the literature (Smith et al., 1981; Menzel et al., 1981; Chesters et al., 1982; Smith et al., 1982, Smith, 1983; Chesters et al., 1983; Petersen et al., 1983). All of the sounding data from this time period exclusively employed the large detectors on VAS (horizontal resolution of 13.8 km at subsatellite point); this study explores the advantages of sounding with the small detectors (horizontal resolution of 6.9 km at subsatellite point). While the small detector noise is roughly double that of the large detector, the doubled horizontal resolution compensates so that soundings representing equivalent areas have the same radiometric noise (4 small samples are equivalent to one large sample). However, the small detector has a great advantage in partly cloudy areas, as it is capable of finding clear fields of view in and around the clouds and thus can provide more soundings.

## 2. VAS data characteristics

The VAS instruments, on board the GOES-4 (now defunct), GOES-5, and GOES-6 satellites, are radiometers with eight visible detectors and six thermal detectors that sense infrared radiation in 12 spectral bands. The spectral bands cover the range of  $678.7 \text{ cm}^{-1}$  ( $14.73 \text{ }\mu\text{m}$ ) through  $2535 \text{ cm}^{-1}$  ( $3.94 \text{ }\mu\text{m}$ ) and are presented in Table 1. A filter wheel in front of the detector package enables spectral selection. The horizontal resolution at subsatellite point is .9 kilometers in the visible and 6.9 and 13.8 kilometers in the infrared depending on which detectors are used. Figure 1 shows the VAS Detector Package Array. Although there are six VAS infrared detectors, only two are in use during any satellite spin period. The selected mode of operation will dictate which detector pair is used--the small HgCdTe channels, the large HgCdTe channels, or the InSb channels.

In the sounding mode, up to twelve spectral bands on the filter wheel can be positioned into the optical path while the scan mirror is dwelling on a single earth swath (scan line). The filter wheel can be programmed so that each spectral band is sampled on the same earth swath from 0 to 255 spacecraft spins. For seven of the spectral bands either the high resolution (6.9 km) or low resolution (13.8 km) detectors can be selected. The remaining five spectral bands are limited to the low resolution detectors (see Table 1).

Table 2 shows the single sample noise observed for the VAS channels. A single sample is the voltage accumulated on the detector every 8  $\mu\text{sec}$ , which is then calibrated to a radiance value (Menzel et al., 1981; Menzel et al., 1983). The noise was estimated by taking the standard deviation of 200 successive samples from outer space. The GOES-5 and GOES-6 noise characteristics are very similar and have been averaged to produce Table 2. The noise equivalent radiance of the small detectors is roughly twice that of the large detectors for a single sample.

Temporal averaging of the VAS radiances, i.e., multiple sampling of the same earth swath in the same spectral band, is necessary to enhance the

ratio of the radiance signal to detector noise. Further enhancement of radiance signal to noise can be accomplished by spatial averaging of the radiances from several adjacent satellite fields of view, but thus reducing the horizontal resolution of the sounding radiances. This trade-off between signal to noise and horizontal resolution is the primary issue of small detector sounding. Table 3 indicates a nominal spin budget, the number of satellite spins allocated to the 12 spectral bands to reduce the radiometric noise to a level suitable for temperature sounding.

Appendix A describes several scan patterns used to achieve contiguous and non-contiguous dwell sounding data. Obviously the latitude coverage accomplished with the small detectors is half that accomplished with the large detectors in the same time period using the same spin budget. Comparable extent of latitude coverage can be achieved only if the small detectors are sampled with the venetian blind scan pattern (described in the Appendix).

Temperature profile retrievals from multi-spectral infrared radiance measurements are based on the assumption that the instrument field of view is cloud free. Infrared measurements are highly susceptible to cloud attenuation, thus special efforts need to be made to avoid or correct for cloud contamination. Higher horizontal resolution increases the probability of finding clear fields of view in and around clouds. The principle question that is addressed by this report is whether the advantage of the smaller detectors, higher horizontal resolution, and thus more clear fields of view, outweighs the disadvantages, higher single sample noise and decreased latitude coverage.

### 3. Clear column radiance determination

Techniques for clear column radiance determination are discussed at length in the literature (Smith, 1968; McMillin, 1978; Hayden, 1984). A brief summary follows.

Clear fields of view are screened by comparing each measurement with the warmest measurement in an area of interest, accepting that the warmest measurement is indeed clear. Since this assumption is incorrect under some circumstances, it remains for the retrieval program or the post retrieval editing programs to catch the error. However, accepting that the warmest is clear, samples are collected for cloud sensitive spectral bands as shown in Table 4. In the area of interest, a minimum sample of five is required for a successful clear column radiance determination. Otherwise the adjacent field view technique is employed.

The adjacent field of view technique for correcting for broken cloud is an extrapolation method, where two measurements of cloud contaminated radiances for a given spectral band are adjusted to give a single estimate of the clear value. This extrapolation is performed for all pairs of fields of view in the area of interest. The degree of extrapolation is controlled by the value assigned to the clear window spectral band. This is a critical choice. One can use any *a priori* estimate of the surface skin temperature to assign it. In our applications, in order to be consistent with the choice of clear fields of view, we have chosen to use the warmest measurement, rather than a manipulation of the surface air

temperature analysis. An analysis of surface air temperature is used as a filter, and the correction is not attempted unless the clearest 11 micron brightness temperature measurement is within 3° of the value expected from the surface temperature analysis.

#### 4. Clear Field of View Statistics

For the small detector sounding to be feasible, one must have a sufficiently greater number of clear small detector fields of view than large detector fields of view to compensate for the increased noise of the small detectors. Using VAS data over the United States from 16 September 1982, the small detector 11 micron image at 1731 GMT was compared to the large detector 11 micron image at 1749 GMT. For different cloud types and altitudes, clear fields of view for 12 areas of 100 x 100 km were investigated. Figures 2 and 3 show the images and the areas selected. Table 5 shows the comparison. There are roughly six times more small detector clear fields of view than large detector clear fields of view; if the scene had been totally clear there would have been four times as many. Thus the signal improvement from using small detectors is  $(6-4)/4$  or 50%. In addition clear soundings are calculable in all twelve areas with the small detectors, whereas clear soundings are calculable in only four areas with the large detectors (at least five adjacent fields of view must be clear).

For spatial averaging to overcome the greater small detector noise, four times as many fields of view must be usable. We showed six times as many are available in this case study. Clearly the small detector sounding is an attractive option. In the next section we compare small detector and large detector retrieval results.

#### 5. Retrievals

A comparison of the VAS large and small detector generated retrievals was performed utilizing radiance data from 9 December 1983. The large detector radiance measurements (using scan pattern A.1 in the Appendix) over the eastern Pacific (EPAC) region are from adjacent ten minute dwell soundings at 1333 and 1403 GMT, while the small detector measurements (using scan pattern A.3 in the Appendix) are from 1633 and 1703 GMT. Two synoptic scale cyclones are located within the EPAC region where retrievals were generated (see Figure 4). Since there are areas of considerable cloudiness associated with these cyclones, it is possible to conduct a test of the small detector capability to produce retrievals within a partly cloud region.

To initialize the retrieval algorithm (see Smith, 1983), the first guess field utilized the 12 hour LFM model forecast valid at 1200 GMT 9 December 1983 for all sounding periods. Thus, any differences in retrieval quantity are due either to atmospheric variability or instrument measurement differences. Retrievals were attempted over a region bordered by 50°N, 150°W in the northwest and 25°N, 120°W in the southeast. The algorithm used a 5 x 5 field of view box for the large detectors (25 fields of view) and a 9 x 9 box for the small detectors (81 fields of view of which 36 have no data due to the venetian blind coverage) to determine the clear column radiance, from which the retrieval algorithm is implemented.

The 1333-1403 GMT large detector VAS radiance measurements yielded 116 retrievals over the EPAC region, while the 1633-1703 GMT small detector radiance yielded 143 retrievals as shown in Table 6. The greater number of retrievals from the small detector radiance measurements represents a 23% increase in retrievals over the large detector set. Furthermore, in the northern dwell sound locations (1333, 1633 GMT), where most of the clouds are located, the small detector produced 34% more retrievals. Visual inspection of the 500 mb retrieval temperatures (Figures 5 and 6) indicate the small detector was able to resolve sufficiently clear fields of view in the cellular convection near 40°N, 150°W to produce soundings, whereas the large detector sample produced fewer retrievals in this region. Also, the small detector sample produced a number of partly cloudy (N\*) retrievals in the vicinity of the frontal boundary near 35°N, 140°W and off the west coast of the United States. Over the large area of mostly clear skies to the south of the cyclones the data sets produced an equal number of retrievals. It is evident that in regions of cloudiness the higher spatial resolution of the small detector instrument provides the capability of generating a significant increase in the number of retrievals.

The 500 mb temperature fields analyzed for each data set are shown in Figure 7. Examination of the fields indicates very close correspondence between large and small detector 500 mb retrieval temperatures. The gridpoint difference between the two fields is contoured in Figure 8, with an edited plot of large detector 500 mb temperatures which indicate the data coverage. All retrieval temperatures lie within the 1°C contour, indicating the close correspondence between the two 500 mb retrieval fields. It should be pointed out that the retrieval temperature differences from large and small detector radiances shown in this case are not always this close.

In summary, the small detector radiance measurement data set from 1633-1703 GMT 9 December 1983 produced 23% more retrievals than the 1333-1403 GMT large detector data set. Most of the additional retrievals were produced in areas of partial cloud cover. The higher resolution of the VAS small detector instrument is able to provide a considerable increase in the number of soundings in partly cloudy regions. A comparison of 500 mb temperatures indicates a very close correspondence in the quality of the soundings, indicating the small detector is as capable of providing the same quality retrievals as the large detector.

## 6. Conclusions

Based on the results reported here, and several other studies, it has become obvious that sounding with small detectors of higher horizontal resolution enables more temperature profile retrievals of good quality in partly cloudy conditions. As of January 1984 daily VAS operations have scheduled the CO<sub>2</sub> absorption spectral bands (3, 4, and 5) and the split window bands (7 and 8) to be sensed with the small detectors during dwell sounding (using scan pattern A.3 of the Appendix).

## Acknowledgments

This work was performed on the Man-computer Interactive Data Access System (McIDAS) at the University of Wisconsin as part of the NOAA Operational VAS Assessment under NOAA Contract Number NA83SAC00098.



## References

- Chesters, D., L. W. Uccellini, and A. Mostek, 1982: VISSR Atmospheric Sounder (VAS) simulation experiment for a severe storm environment. Mon. Wea. Rev., 110, 198-216.
- Chesters, D., L. W. Uccellini, and W. D. Robinson, 1983: Low-level water vapor fields from the VISSR Atmospheric Sounder (VAS) split window channels. J. Clim. Applied Meteor., 22, 725-743.
- Hayden, C. M., W. P. Menzel, and A. J. Schreiner, 1984: The clouds and VAS. Proceedings of the Conference on Satellite Meteorology/Remote Sensing and Applications, June 25-29, 1984, Clearwater Beach, Florida, Published by the American Meteorological Society, Boston, Massachusetts.
- McMillin, L. M., 1978: An improved technique for obtaining clear radiances from cloud contaminated radiances. Mon. Wea. Rev., 11, 1590-1597.
- Menzel, W. P., W. L. Smith, and L. D. Herman, 1981: Visible infrared spin-scan radiometer atmospheric sounder radiometric calibration: an inflight evaluation from intercomparisons with HIRS and radiosonde measurements. Applied Optics, 20, 3641-3644.
- Menzel, W. P., W. L. Smith, G. S. Wade, L. D. Herman, and C. M. Hayden, 1983: Atmospheric soundings from a geostationary satellite. Applied Optics, 22, 2686-2689.
- Petersen, R. A., L. W. Uccellini, D. Chesters, and A. Mostek, 1983: The use of VAS satellite data in weather analysis, prediction, and diagnosis. National Weather Digest, 8, 12-23.
- Smith, W. L., 1968: An improved method of calculating tropospheric temperature and moisture from satellite radiometer measurements. Mon. Wea. Rev., 96, 387-396.
- Smith, W. L., 1983: The retrieval of atmospheric profiles from VAS geostationary radiance observations. J. Atmos. Sci., 40, 2025-2035.
- Smith, W. L., V. E. Suomi, W. P. Menzel, H. M. Woolf, L. A. Sromovsky, H. E. Revercomb, C. M. Hayden, D. N. Erickson, and F. R. Mosher, 1981: First sounding results from VAS-D. Bull. Amer. Meteor. Soc., 62, 232-236.
- Smith, W. L., V. E. Suomi, F. X. Zhou, and W. P. Menzel, 1982: Nowcasting applications of geostationary satellite atmospheric sounding data. Nowcasting, (K. A. Browning, ed.), Academic Press, New York, pp. 123-135.

TABLE 1

## CHARACTERISTICS OF THE VAS SPECTRAL BANDS

VAS Channel Number	Spectral Center		Bands Width cm <sup>-1</sup>	Purpose for Sounding	Main Absorbing Gas
	μm	cm <sup>-1</sup>			
1	14.7	678	10	temp	CO <sub>2</sub>
2	14.5	691	16	temp	CO <sub>2</sub>
3*	14.3	699	16	temp	CO <sub>2</sub>
4*	14.0	713	20	temp	CO <sub>2</sub>
5*	13.3	750	20	temp	CO <sub>2</sub>
6	4.5	2209	45	temp+cloud	N <sub>2</sub> O
7*	12.7	787	20	moisture	H <sub>2</sub> O
8*	11.2	892	140	surface	-
9*	7.3	1370	40	moisture	H <sub>2</sub> O
10*	6.8	1467	150	moisture	H <sub>2</sub> O
11	4.4	2254	40	temp+cloud	CO <sub>2</sub>
12	3.9	2540	140	surface	-

\* Available at 6.9 km as well as 13.8 km resolution

TABLE 2

SINGLE SAMPLE RADIANCE NOISE OBSERVED IN THE  
VAS SPECTRAL BANDS

Band	Large Detector	Small Detector
1	2.8	n.a.
2	1.6	n.a.
3	1.2	2.5
4	1.0	2.0
5	0.8	1.6
6	0.022	n.a.
7	0.8	1.4
8	0.2	0.3
9	0.6	1.3
10	0.2	0.3
11	0.025	n.a.
12	0.008	n.a.

TABLE 3

SPIN BUDGET USED ON VAS

Band	Large Detector Only	Large Detector and Small Detectors
1	1	1
2	4	4
3	5	5 S
4	3	4 S
5	2	4 S
6	4	1
7	2	4 S
8	1	1 S
9	3	1
10	1	1
11	0	0
12	1	1

TABLE 4

"CLEAR" TOLERANCES FOR VAS SPECTRAL BANDS MEASURED AGAINST THE WARMEST SAMPLE OF THE POPULATION. ANY VALUE COLDER THAN TOLERANCE ELIMINATES ALL CHANNELS LISTED. LEVEL 2 IS TESTED ONLY IF LEVEL 1 FAILS.

Spectral Band		Frequency cm <sup>-1</sup>	Tolerance K	Bands Eliminated
Level 1	Level 2			
6	2	2214	1.0	6,12
	9	1380	Band 6 T <sub>B</sub> minus 20 <sup>B</sup>	9,10
8		890	2.0	5,6,7,8,12
	5	751	1.5	4,9
	4	715	1.0	3,10

TABLE 5  
CLEAR FIELD OF VIEW STATISTICS

Area <sup>a</sup>	Cloud Altitude	Number of Small Cloud <sup>b</sup>	Number of Large Clouds	Ratio
1	Clear	100	25	4.0
2	Middle	15	4	3.7
3	Low	41	10	4.1
4	Middle/High	5	2	2.5
5	High	9	1	9.0
6	Middle	14	2	7.0
7	Low	14	3	4.7
8	Low/Middle	21	1	21.0
9	Low/Middle	14	1	14.0
10	Middle/High	15	4	3.7
11	High	7	0	7/0
12	Low	47	6	7.8
<b>Total</b>		<b>202</b>	<b>34</b>	<b>5.9</b>

<sup>a</sup>Sounding area includes 10 x 10 small detector fields of view and 5 x 5 large detector fields of view.

<sup>b</sup>Clear threshold was chosen to be the maximum brightness temperature of the 100 small detector fields of view less 2°K.

TABLE 6  
NUMBER OF RETRIEVALS  
SMALL VERSUS LARGE DETECTOR

Time (GMT)	Detector	Number of boxes (100 x 100 km <sup>2</sup> )	Number of Retrievals	Retrieval Piece
1333-1403	Large	101	70	N
		56	46	S
		<u>157</u>	<u>116</u>	TOTAL
1633-1703	Small	106	94	N
		52	49	S
		<u>158</u>	<u>143</u>	TOTAL

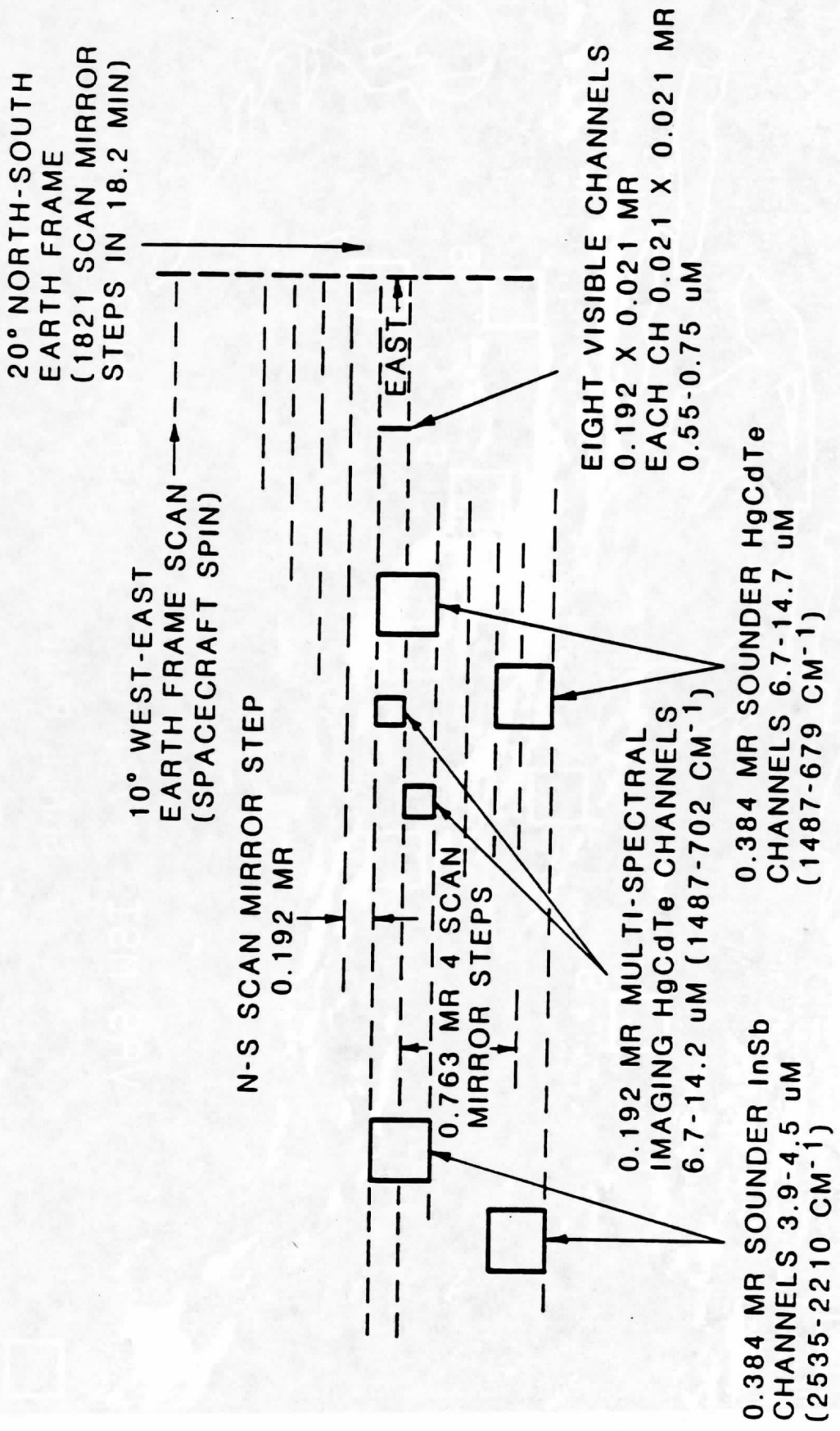


Figure 1: VAS-D detector package array.

DETECTOR INSTANTANEOUS GEOMETRIC FIELD OF VIEW (IGFOV)

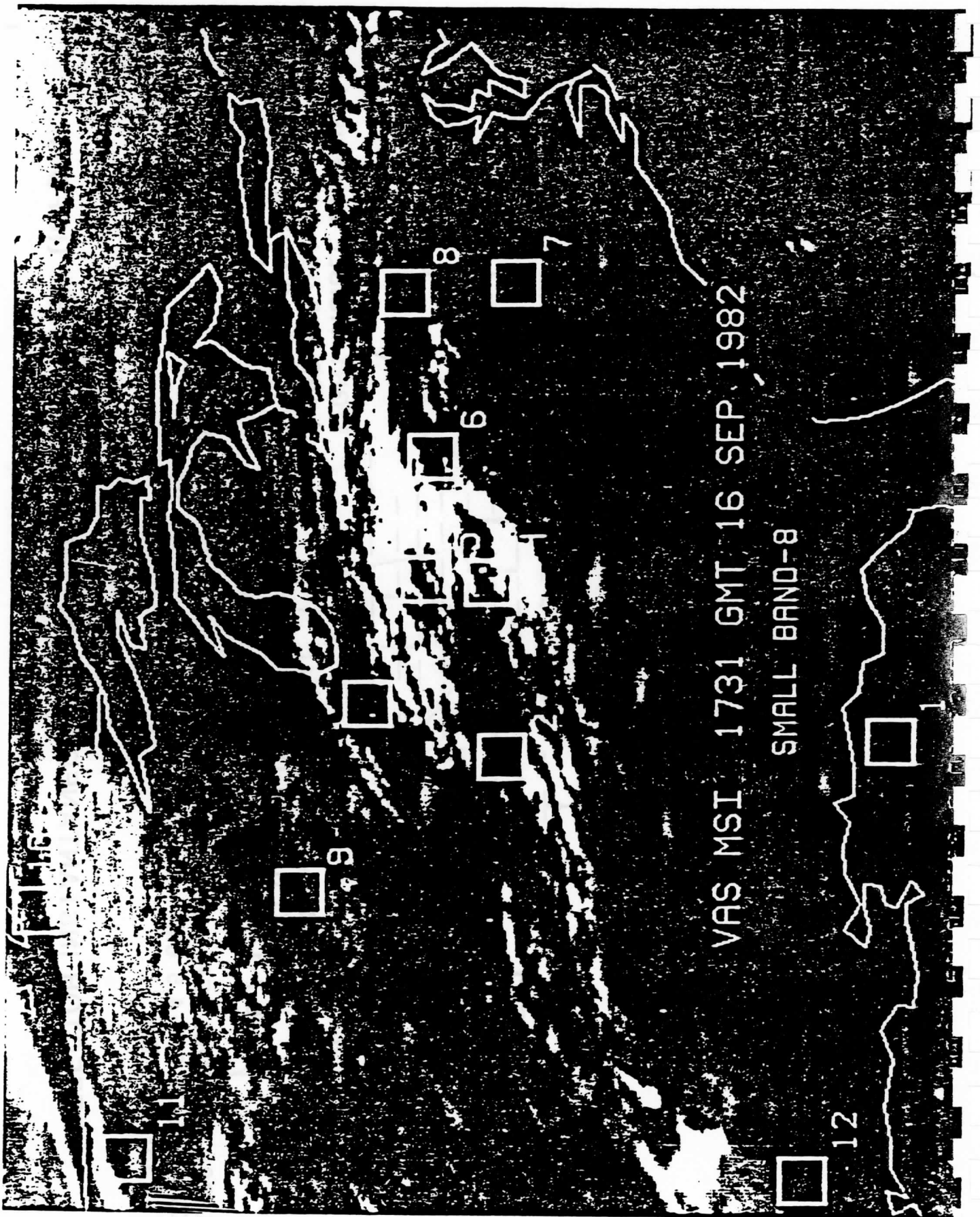


Figure 2: VAS small detector band 8 image for 1731 GMT 16 September 1982 showing areas (boxes) where soundings were made.

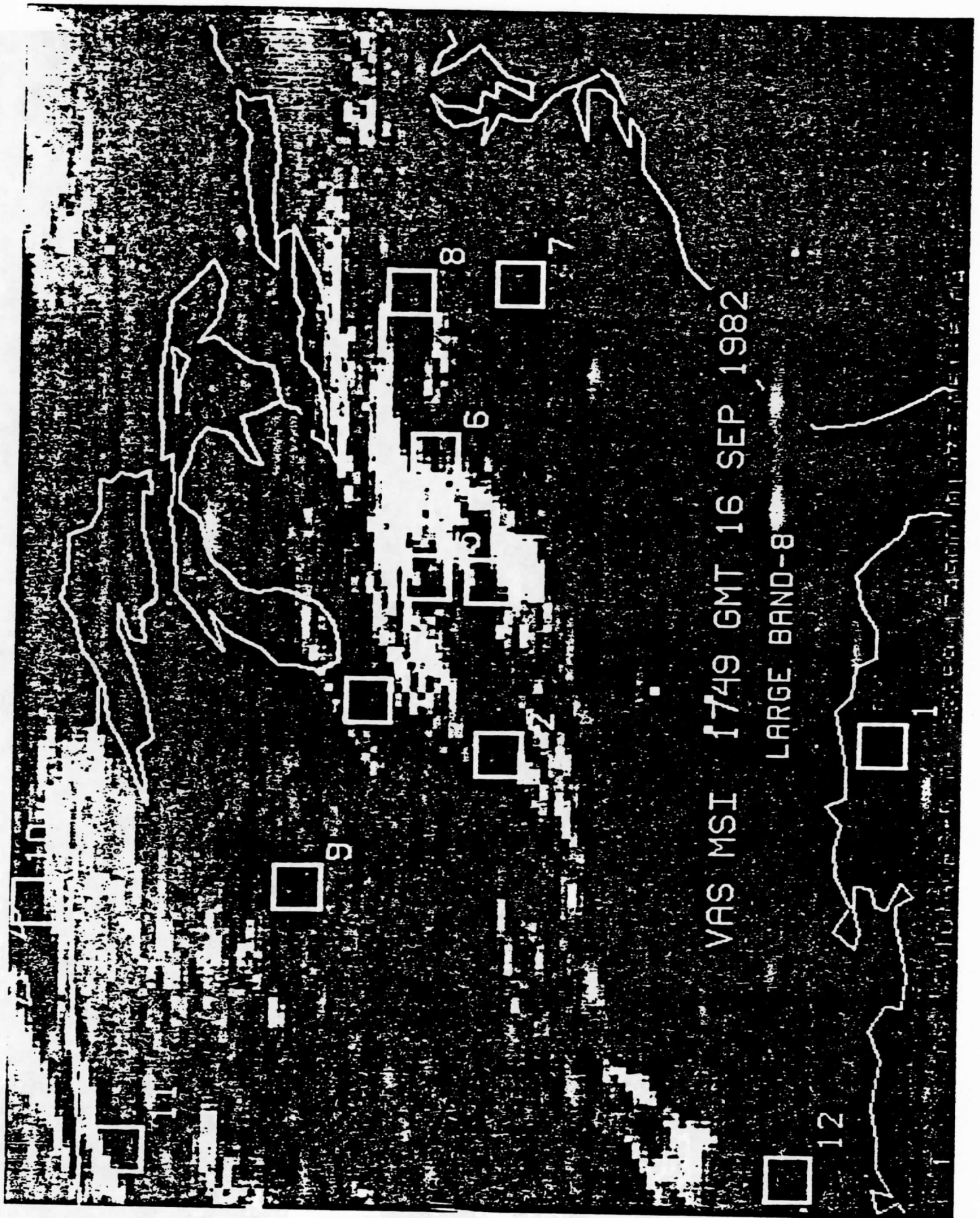


Figure 3: VAS large detector band 8 image for 1749 GMT showing areas (boxes) where soundings were made.

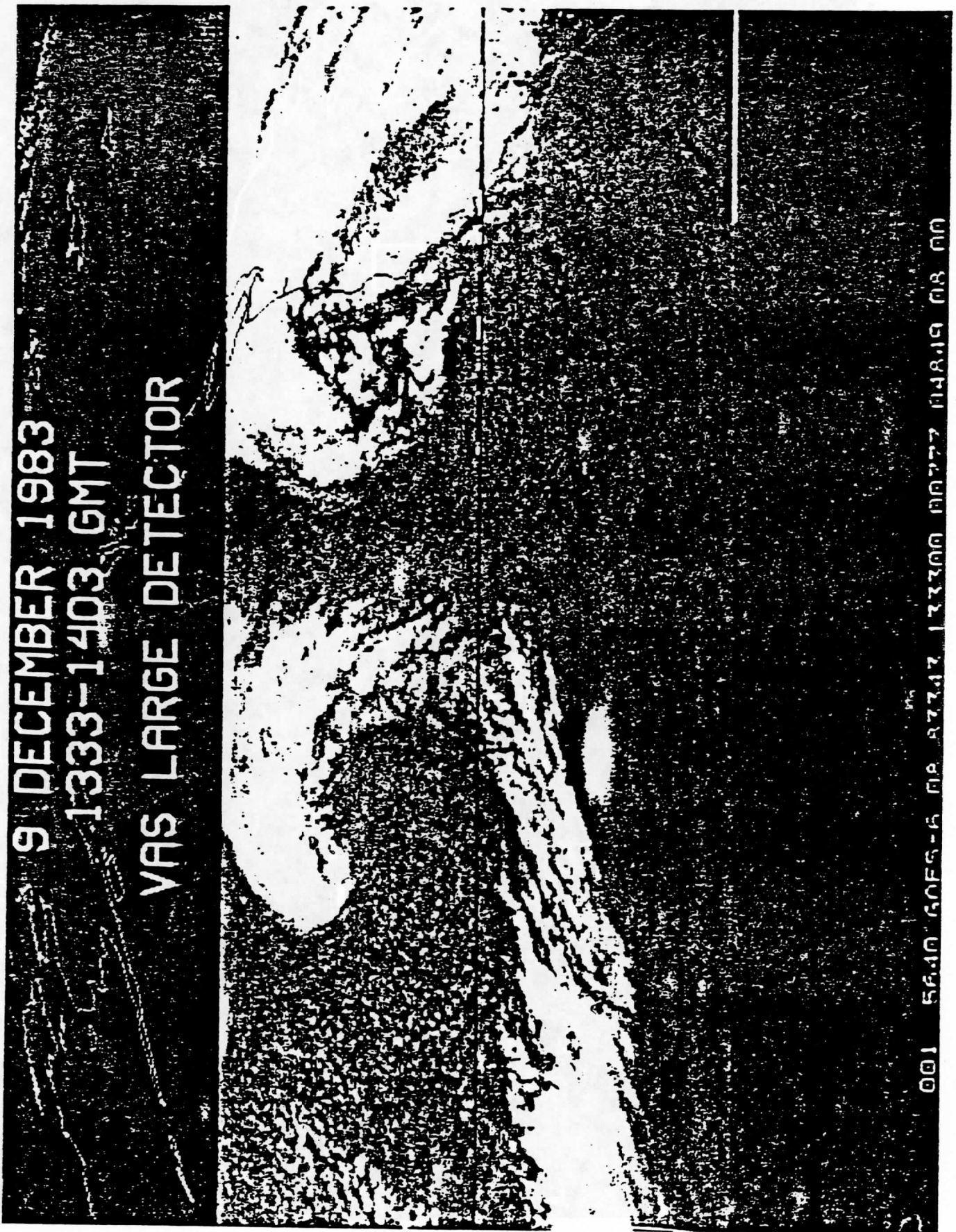


Figure 4: VAS large detector band 8 images for 1333 and 1403 GMT  
9 December 1983.

*Paper 3*





Figure 5: VAS large detector 500 mb temperatures (°C) for 1333-1403 GMT 9 December 1983.

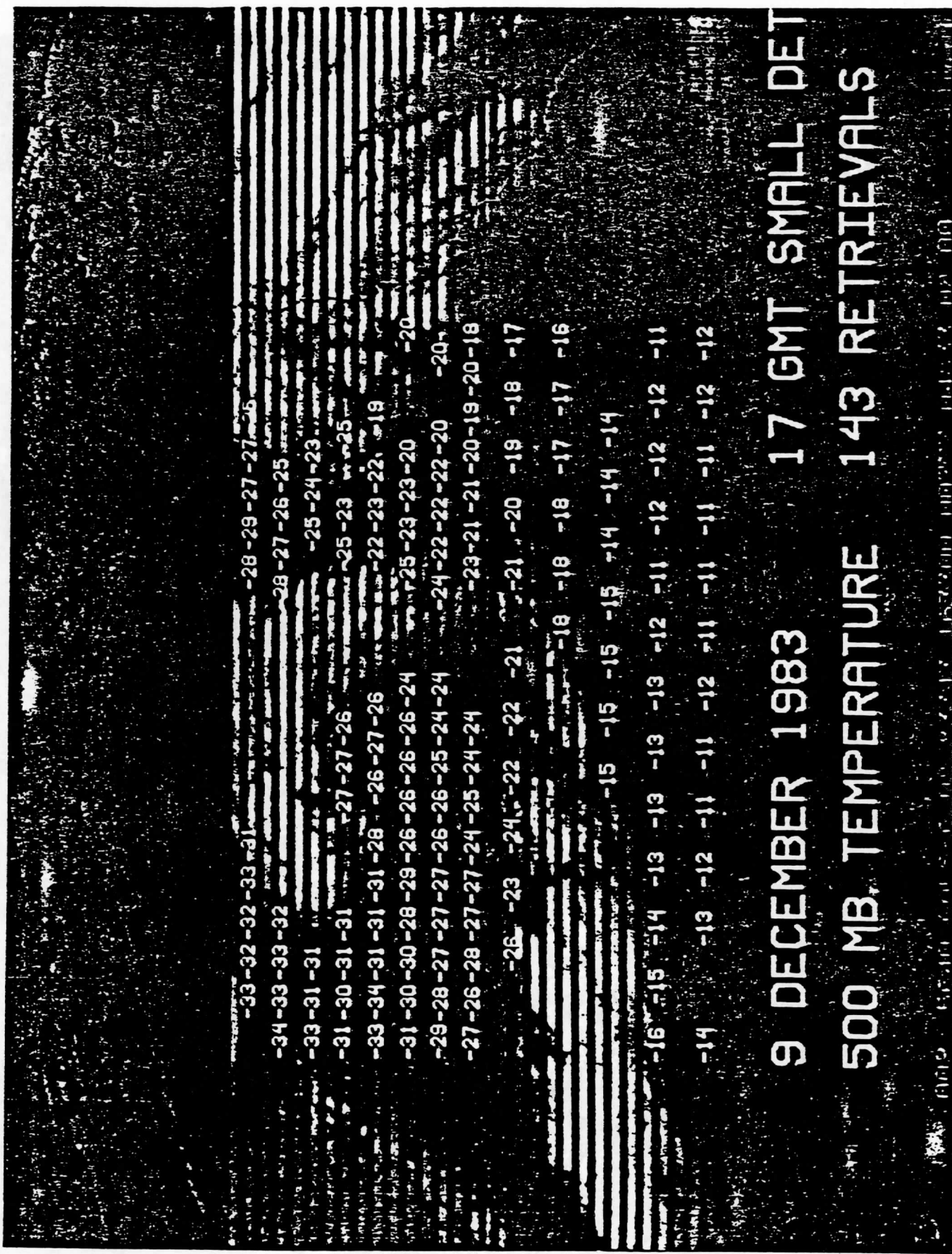


Figure 6: VAS small detector 500 mb temperatures (°C) for 1633-1703 GMT 9 December 1983.

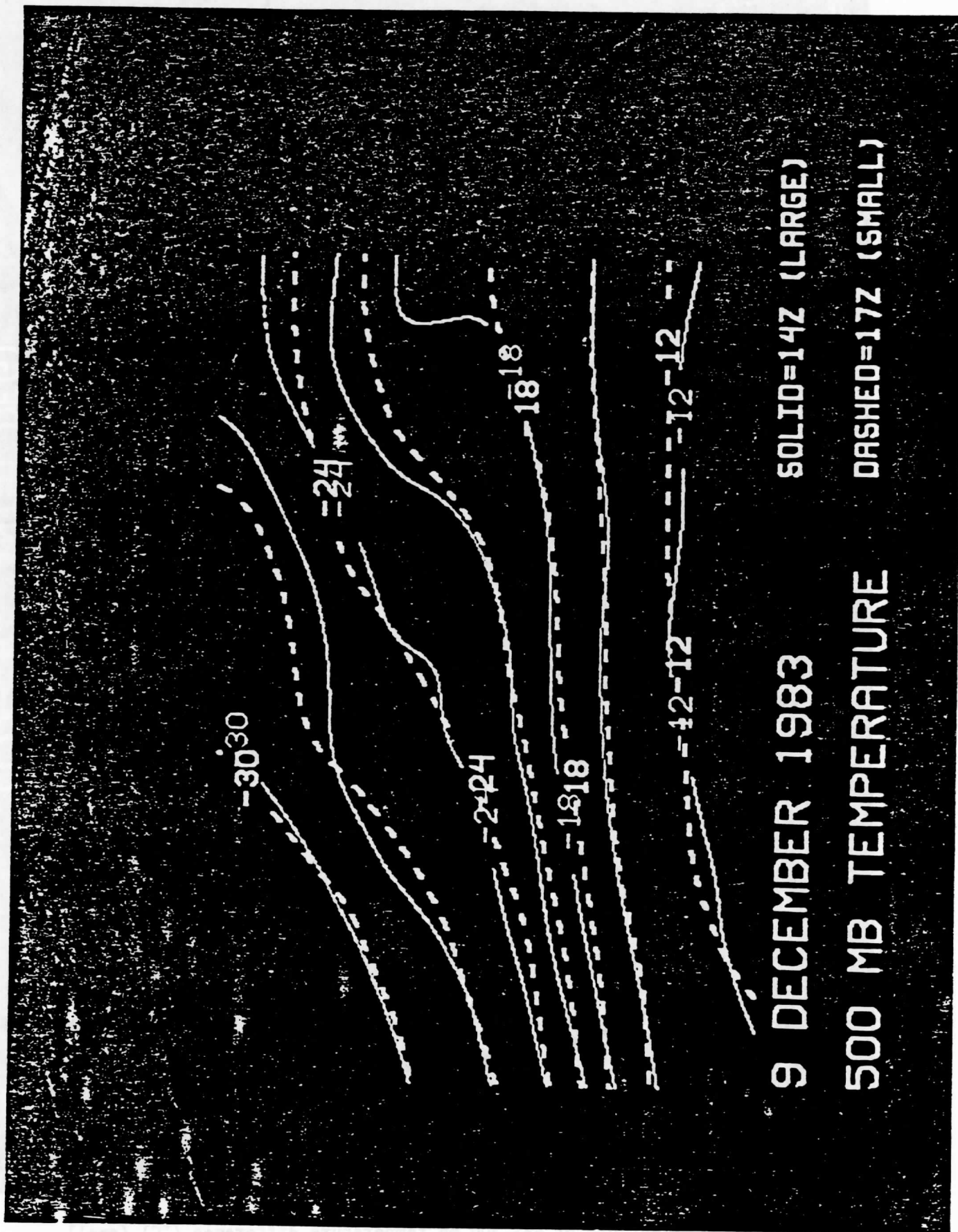


Figure 7: VAS 500 mb temperature contours ( $^{\circ}\text{C}$ ) for large detector (solid) and small detector (dashed).

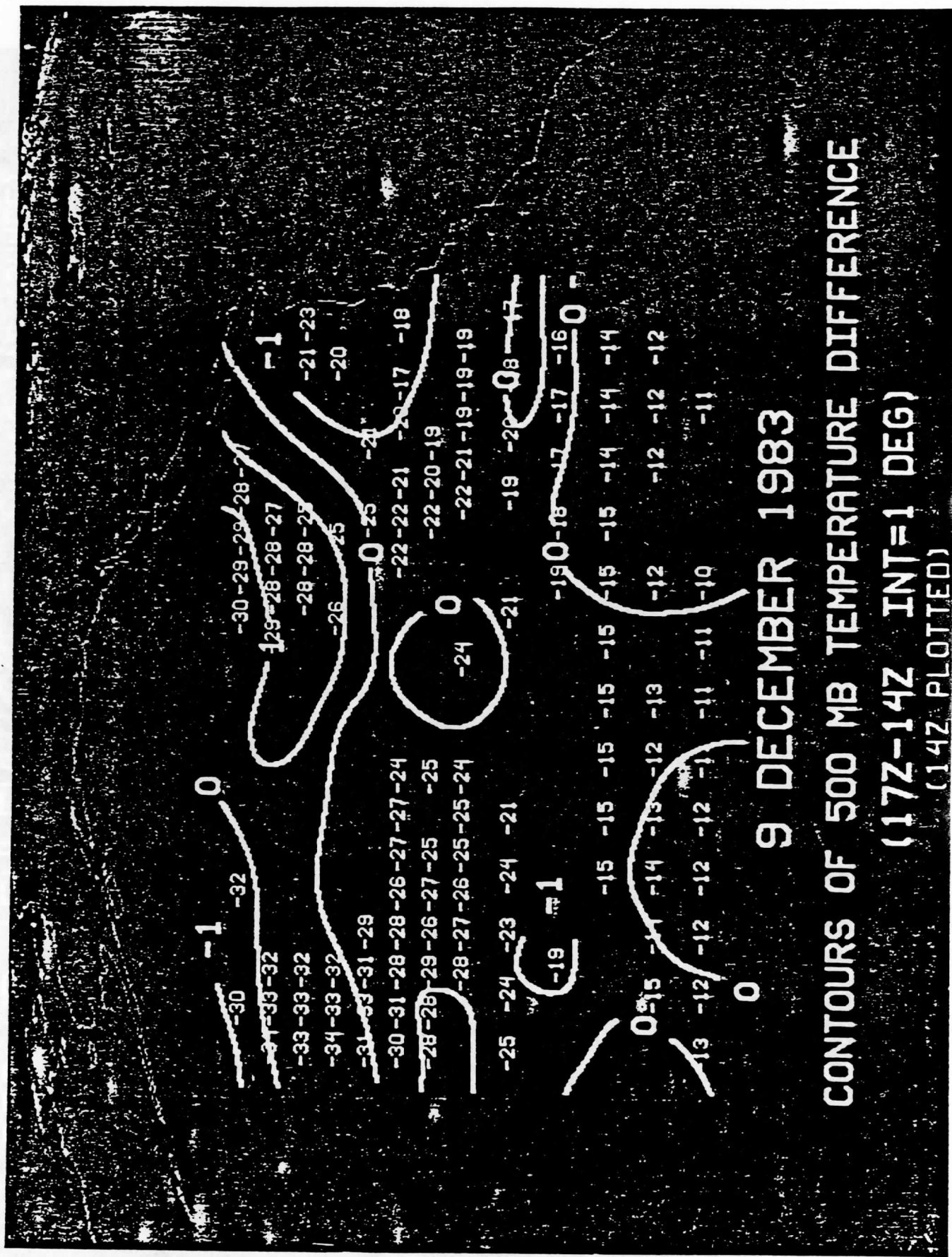


Figure 8: Contours of VAS 500 mb temperature difference (°C) (small detector-large detector) with plot of large detector 500 mb temperatures.

## Appendix A

The dwell sounding mode has three submodes. They are submode 1, submode 2, and submode 3. They occur in the cyclic order 1, 2, 3, 2, 1, 2, 3, 2, etc., throughout the frame. A brief explanation of the submodes follows.

### Submode 1

One satellite spin occurs per scan mirror step. After each mirror step, data is transmitted from the two small (6.9 km) band 8 (11 micron) channels. This mode is programmable to have one to eight scan mirror steps.

### Submode 2

This is the dwell mode. The scan mirror does not step during this mode. During this mode each of the 12 spectral filters may be put into the optical train and held there for from 0 to 255 satellite spins. The number of spins for each spectral band is programmable.

### Submode 3

This is the same as submode 1, except the number of scan mirror steps may be different than submode 1.

If  $S_1$  ( $S_3$ ) is the number of scan mirror steps in submode 1 (3) and  $S_2$  is the number of dwell spins in submode 2, then the time required for each (1, 2, 3, 2) sounding cycle is

$$T = (S_1 + 2S_2 + S_3)t \quad (\text{A.1})$$

where  $t$  is the nominal spin period of the satellite (.01 minutes). The north-south spatial coverage of each scan mirror step at the subsatellite point is 6.9 km, so the north-south extent of a latitude swath covered during one sounding cycle is

$$X_{NS} = (S_1 + S_3) 6.9 \text{ km} . \quad (\text{A.2})$$

The sounding rate is the ratio

$$S = 6.9(S_1 + S_3)/(S_1 + 2S_2 + S_3)/t \text{ km/min} . \quad (\text{A.3})$$

Figures A.1 through A.3 illustrate three scan patterns that enable dwell sounding using the spin budget presented in section 2. Scan pattern A.1 provides contiguous dwell sounding coverage from the large detectors; the sounding rate is 89 km/min. Scan pattern A.2 provides contiguous dwell sounding coverage from the small detectors; the sounding rate is 47 km/min.

Scan pattern A.3 provides venetian blind dwell sounding coverage from the small detectors; the sounding rate is 44 km/min covering the latitude extent at 89 km/min (half the latitude extent is not covered in a sounding mode).

LARGE DETECTOR DWELL SOUNDING SCAN PATTERN  
 MIRROR STEPPING-FILTER SELECTION SUBROUTINE SET AT  
 (6-DWELL-2-DWELL)

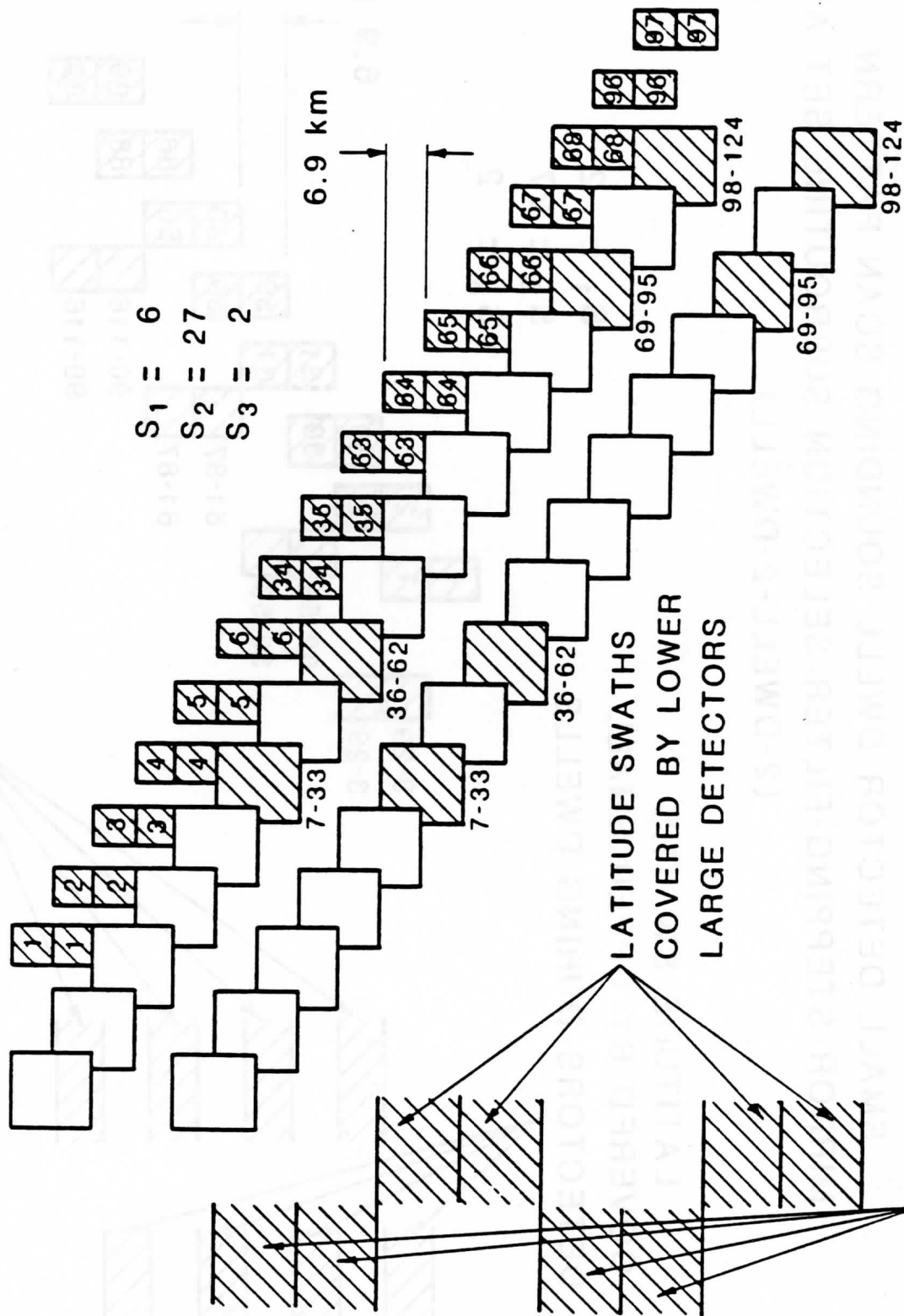


Figure A-1: Scan pattern for contiguous sounding with the large detectors.

SMALL DETECTOR DWELL SOUNDING SCAN PATTERN  
 MIRROR STEPPING-FILTER SELECTION SUBROUTINE SET AT  
 (2-DWELL-2-DWELL)

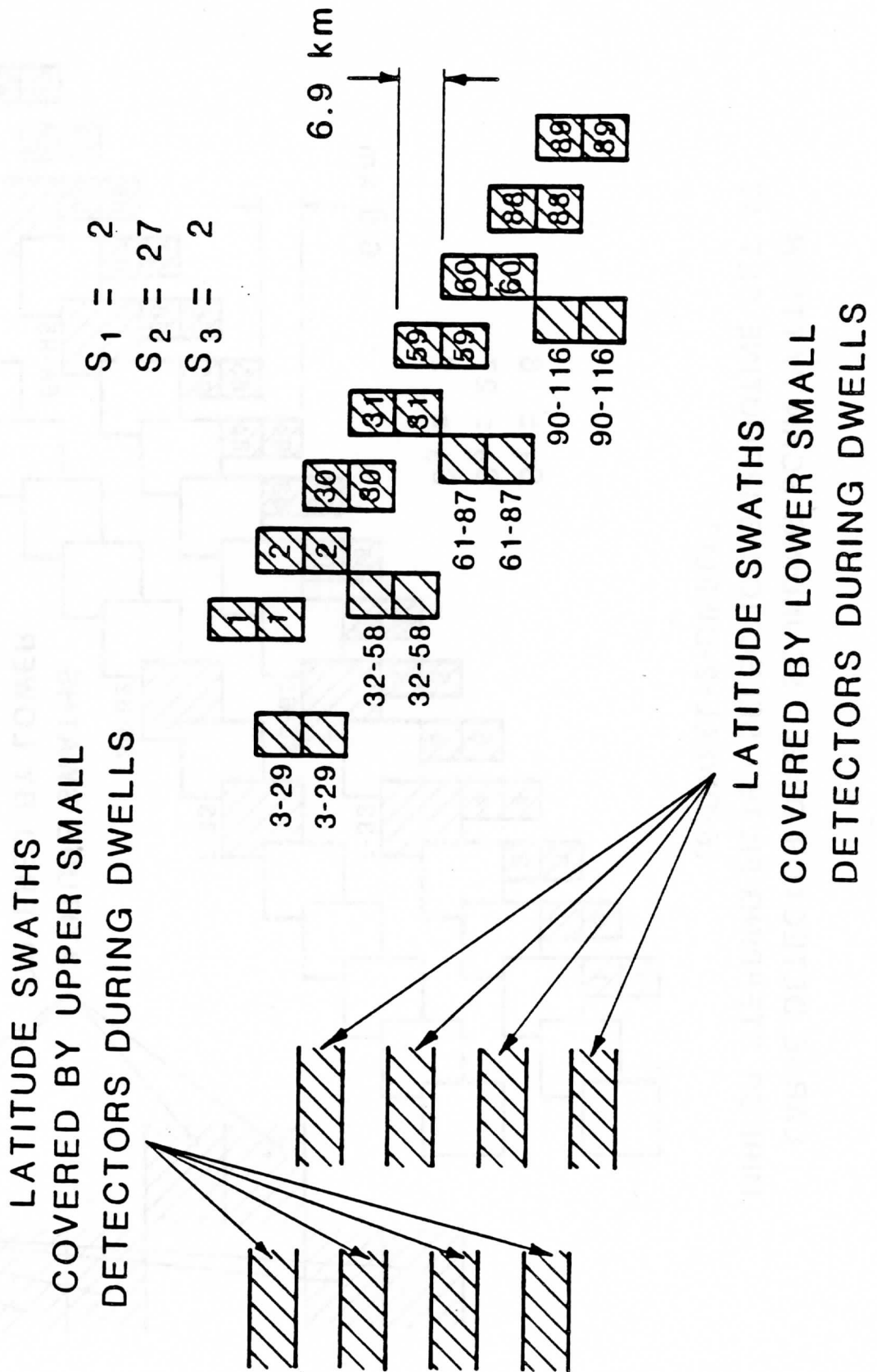


Figure A-2: Scan pattern for contiguous sounding with the small detectors.



SMALL DETECTOR DWELL SOUNDING SCAN PATTERN  
 MIRROR STEPPING-FILTER SELECTION SUBROUTINE SET AT  
 (6-DWELL-2-DWELL)

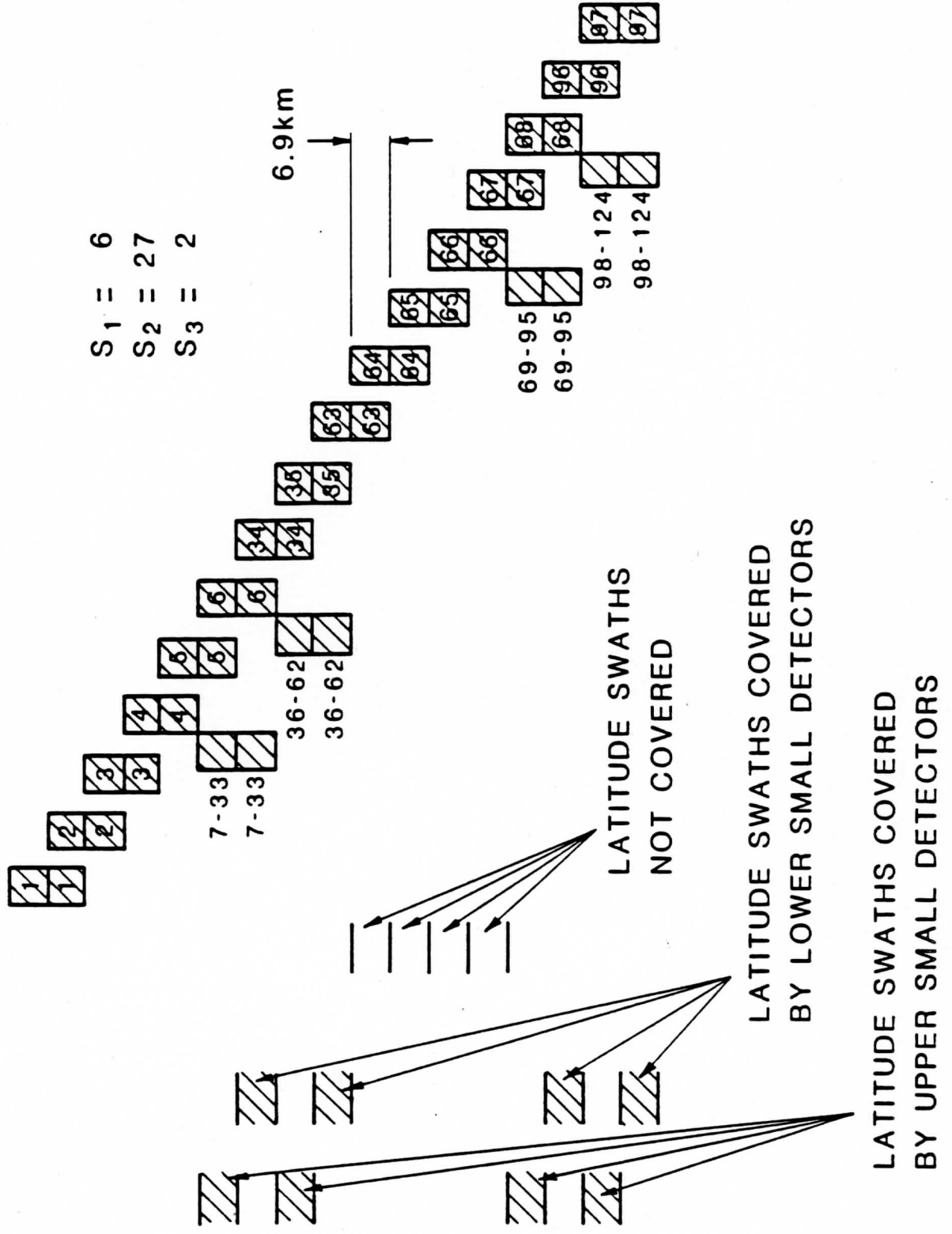


Figure A-3: Scan pattern for venetian blind sounding with the small detectors.

## THE CLOUDS AND VAS

Christopher M. Hayden  
NOAA/NESDIS Development Laboratory  
1225 West Dayton Street, 2nd Floor  
Madison, Wisconsin 53706

W. Paul Menzel  
NOAA/NESDIS Satellite Applications Laboratory  
1225 West Dayton Street, 2nd Floor  
Madison, Wisconsin 53706

Anthony J. Schreiner  
Space Science and Engineering Center  
University of Wisconsin  
1225 West Dayton Street, 2nd Floor  
Madison, Wisconsin 53706

### 1. INTRODUCTION

The VISSR Atmospheric Sounder (VAS) has been operating on the geostationary satellites, GOES 4-6 since September 1980. This instrument has the capability of measuring radiance in 12 infrared spectral channels which permits vertical temperature and moisture profile definition. Since the infrared measurements are highly susceptible to cloud attenuation, special care must be taken to avoid or correct for cloud interference. Techniques used in this process are essentially an extension of methods used with the polar orbiter instruments except that the absence of microwave measurements place a higher premium on a predetermined surface skin temperature. Partially offsetting this deficiency is the improved horizontal resolution of the VAS, which permits a greater probability of finding holes in the clouds.

Whereas the clouds are an impediment to the depiction of the atmosphere's temperature structure they are of benefit in determining the motion field. Cloud motion vectors have been determined from the geostationary satellites since the earliest ATS series (Hubert and Whitney, 1971) and are reputed to be very useful to numerical forecasting. Height assignment for these vectors has always been a problem (Bengtsson et al., 1982), but the multispectral capability of the VAS can reduce the uncertainty (Menzel et al., 1983).

In the following we shall describe the current techniques and results for both avoiding the cloud for temperature sounding and measuring the cloud height for wind derivation. A case study taken from a recent episode in the north Pacific is used to demonstrate and discuss method sensitivity and error sources.

### 2. CLEAR COLUMN RADIANCE DETERMINATION

It has been the policy of National Environmental Satellite, Data, and Information Service (NESDIS) operations and the Cooperative Institute for Meteorological Satellite Studies (CIMSS) to separate the task of determining clear column radiance values from the temperature retrieval problem. Our motivation is largely one of computer limitations; but there are also advantages in the production of clear radiance fields for editing and even for possible use in defining cloud heights as will be discussed in

the next section. In obtaining clear column radiances there are two options: avoid the clouds or correct for them. Our approach has been to emphasize the former, and to employ the adjacent field of view (McMillin, 1978) technique for the latter. In all cases the problem is approached with a sample of measurements coming from 3 x 3 up to 11 x 11 fields of views (25 up to 90 km on a side) according to the desired final resolution of the temperature retrievals.

It should be emphasized that both our approaches are extremely dependent on ancillary knowledge of the surface skin temperature, since comparison of the window channel with this "a priori" information ultimately determines the cloud contamination. In the following we shall briefly discuss the methods and examine the effectiveness of the second option in enhancing the representation of the meteorology.

For an estimate of the surface skin temperature we rely on an objective analysis of the surface air temperature. This is not an ideal technique since the data coverage is frequently inadequate (especially over the ocean) and since the surface air is frequently not representative of the surface skin. It would be considerably better for an operator to make a subjective determination of "clear," using images of high resolution visible and infrared with a capability of looping several images in time. However, such a manpower intensive operation is not practical. The basic criterion used in comparing the VAS measurement with the surface analysis is:

- Reject any sample whose warmest 11 micrometer value is more than 10°C colder than the surface air temperature.

If the sample passes the initial test it will follow a "probably clear" filter path unless either of two additional tests send it to the adjacent field of view filter. These tests are:

- The variance of the 11 micrometer sample must be less than 9°C.
- The warmest value must be accompanied by measurements in all the channels.

## 2.1 Probably Clear Filter

The philosophy behind this filter is to collect the largest sample for each measurement accepting that the warmest measurement is indeed clear. Since the assumptions is certainly incorrect under some circumstances, it remains for the retrieval program or the post retrieval editing programs to catch the error. Their success in this area will be treated later. However, accepting that the warmest is "clear," samples are collected for cloud sensitive channels as shown in Table I. A minimum sample of five is required for retention, otherwise the program reroutes to the partly cloudy, adjacent field of view option.

TABLE I  
"CLEAR" TOLERANCES FOR VAS CHANNELS MEASURED AGAINST THE WARMEST SAMPLE OF THE POPULATION. ANY VALUE COLDER THAN TOLERANCE ELIMINATES ALL CHANNELS LISTED. LEVEL 2 IS TESTED ONLY IF LEVEL 1 FAILS.

Channel Level	Frequency Level	Frequency cm <sup>-1</sup>	Tolerance K	Channels Eliminated
1	2			
6	9	2214 1380	1.0 (Temp. Chan 6-20.0)	6,12 9,10
8	5	890 751	2.0 1.5	5,6,7,8,12 4,9
	4	715	1.0	3,10

## 2.2 Partly Cloudy Filter

The adjacent field of view technique for correcting for broken field of view is an extrapolation method as shown in Figure 1 where the line joining two cloud contaminated radiances is

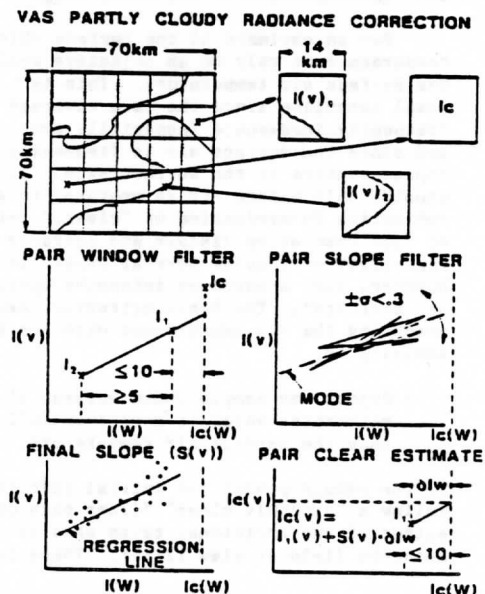


Figure 1: The adjacent field of view (NSTAR) filter. See text for details.

extended to give an estimate of the clear value. The degree of extrapolation is controlled by the value assigned to the clear window. This is a critical choice. One can use any "a priori"

estimate of the surface skin temperature to assign it. In our applications, in order to be consistent with the "probably clear" filter, we have chosen to use the warmest measurement, rather than a manipulation of the surface air temperature analysis. The surface air temperature analysis is used as a filter, and the NSTAR correction is not attempted unless the clearest 11 micrometer measurement is within 3 degrees of the value expected from the surface temperature analysis.

The partly cloudy algorithm is not as complicated as a quick glance at Figure 1 would suggest. Note first that all fields of view are compared to each other (not just adjacent pairs) yielding a sample of  $N(N-1)/2$  partly cloudy pairs where  $N$  is the number of observations. The suitability of each pair is tested in a number of ways:

- The warmest 11 micrometer value of a pair must be within 10 degrees of the warmest sample (to limit extrapolation).
- The colder of the pair must be at least 5 degrees colder than the warmer (to achieve a reasonable "slope" estimate).
- The slope formed by a pair must be within 0.3 of the modal slope (checked for two of the more transparent 15 micrometer channels). For all pairs that meet these restrictions a single slope is calculated by least squares, and a final clear sample is derived by extrapolating all the warmest values.

## 2.3 Example of Filters

Figure 3 gives an example of a) the radiances obtained from the "mostly clear" path, b) the "partly cloudy" path, and c) the residual



Figure 2: 11 micrometer window image of eastern Pacific, 18 February 1984.

remaining after retrieval and editing. In terms of quantity, the "partly cloudy" typically adds about 20% to the total radiance sample, but these

are somewhat noisier and more susceptible to later elimination. A net increase of 10% in the number of final retrievals is a rough average. Comparison with the 11 micrometer picture of the clouds (Figure 2) shows that the sample increase does indeed occur in the partly cloudy areas. Generally, however, the additional soundings occur around the edges of the large cloud systems.

Figure 3 shows that the rather forgiving "probably clear" criterion let through a considerable number of radiances which are later rejected during the temperature retrieval (based on channel consistency). For this example about 17% of the mostly clear were subsequently filtered. Of the partly cloudy selections, almost 45% were eliminated.

The most important consideration in evaluating the cloud filters is whether the results capture the meteorology of the situation. There is no question that large cloud masses continue to be a problem. The partly cloudy filtering helps, but not dramatically. The greatest improvement we have observed with the VAS has come from processing with the small (8 km) as opposed to large (16 km) field of view, simply because of the increased probability of finding cloud free fields of view. Even with this "small detector," however, occasions of obtaining soundings within large cloud masses are infrequent, and the case shown in Figure 2 is typical.

### 3. MULTISPECTRAL CLOUD HEIGHT ASSIGNMENT

The assessment of cloud height and amount by infrared sounder retrieval methods has been considered by Chahine (1975), Smith and Platt (1978), Weilicki and Coakley (1981), and Menzel et al., (1983). There are two basic techniques, a "direct" method and a "ratio" method. In the "direct" method a candidate group of assumed effective cloud amounts and cloud pressures is used to calculate outgoing radiances in two or more channels from a presumed temperature moisture structure. These radiances are compared to observations in the same channels and by some minimization criteria the most probable cloud pressure and amount are selected. The "ratio" method is a form of the direct method for 2 channels. Its advantage is that by ratioing the channels the effective cloud amount can be separated from the solution for cloud pressure. Thus the cloud pressure can be found efficiently. For application in determining wind tracer pressure altitude, the ratio method is an obvious choice since cloud amount is of no significance.

The mathematical expression for the ratio technique is given by

$$\frac{I(u_1) - I_{CL}(u_1)}{I(u_2) - I_{CL}(u_2)} = \frac{E_1 \int_{P_s}^P \tau(u_1, p) \frac{dB(u_1, T(p))}{dp} dp}{E_2 \int_{P_s}^P \tau(u_2, p) \frac{dB(u_2, T(p))}{p} dp}$$

where  $u_1$  and  $u_2$  are spectral frequencies,  $\tau$  the respective transmittance functions, and  $E$  the effective cloud amounts (assumed equal when the frequencies are chosen close together).  $I$

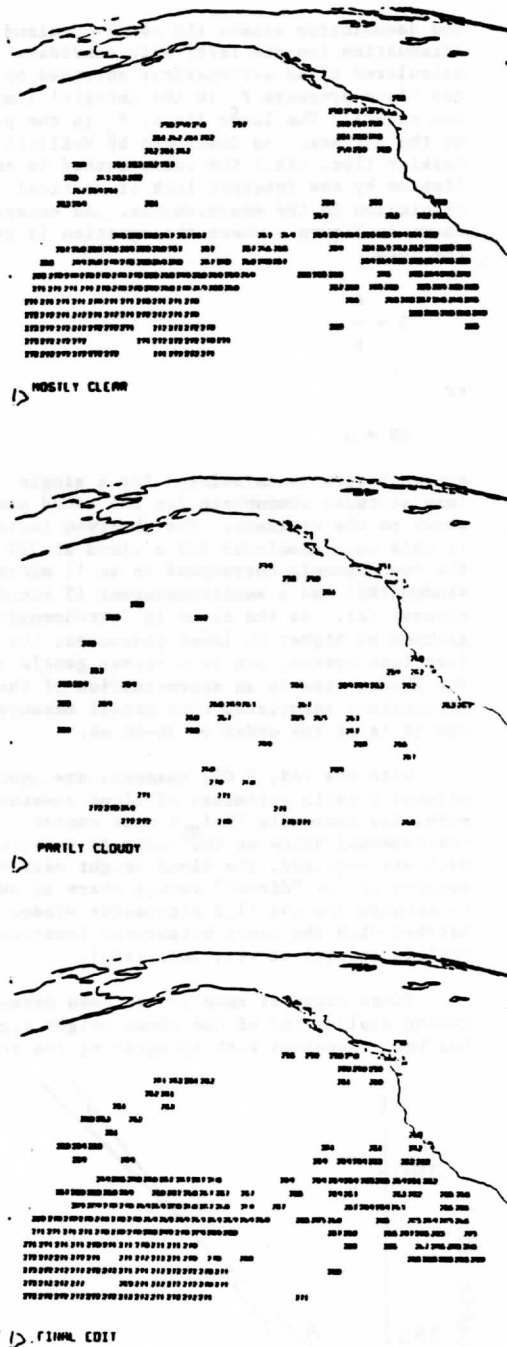


Figure 3: Top--radiance observations obtained as "mostly clear." Middle--radiance observations obtained as "partly cloudy." Bottom--final sample of clear column radiances.

represents the measured radiance whereas  $I_{CL}$  is the radiance which would be observed in the absence of cloud. In other words, both numerator

and denominator equate the observed cloud attenuation (on the left) with candidate calculated cloud attenuations obtained by varying the cloud pressure  $P$  in the integral limits (on the right). The lower limit,  $P$  is the pressure at the surface. As described by Weilicki and Coakley (loc. cit.) the ratio method is somewhat limited by the inherent lack of vertical resolution in the measurements. An example is shown in Figure 4 where the equation is recast in the form

$$R = \frac{A}{B}$$

or

$$RB = A$$

and each side is calculated for a single (midlatitude) atmosphere for the cloud pressures shown on the ordinate. The observed radiance is in this case simulated for a cloud at 320 mb, and the two channels correspond to an 11 micrometer window (RB) and a semitransparent 15 micrometer channel (A). As the cloud is (erroneously) assumed at higher or lower pressures, the two functions spread, but at a rather gentle rate. The shaded area is an approximation of the uncertainty associated with actual measurement and it is of the order of 30-40 mb.

With the VAS, 3  $CO_2$  channels are used to attempt 2 ratio estimates of cloud pressure. For both, the residuals ( $I - I_{CL}$ ) must exceed instrumental noise or the ratio is rejected. If both are rejected, the cloud height determination reverts to the "direct" method where an overcast is assumed and the 11.2 micrometer window is matched with the guess brightness temperature profile (Menzel et al., loc. cit.).

Since proof of concept has been established, recent application of the cloud height algorithm has been concerned with integrating the scheme

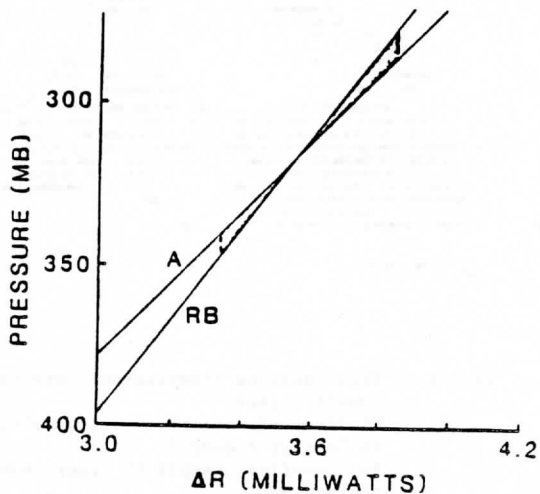


Figure 4: Sensitivity of the ratio method for determining cloud pressure. This example involves measurements at 750 and 890 wavenumber.

into routine VAS processing. To do this within the limitations of the Man-computer Interactive Data Access System (McIDAS), it has been necessary to dissociate the cloud height algorithm from the wind derivation procedure. This is accomplished by preparing a data set of cloud heights which can be plotted over the infrared (visible) images used to derive wind vectors. An example is shown as Figure 5. The operator assigns the pressure altitude of the wind vector from his interpretation of the plotted values. The figure separates the cloud assignments according to the choice made by the algorithm. The top shows results defaulting to the direct method. It is apparent that the ratio method is more successful in thicker, higher cloud where the attenuation is well in excess of probable measurement noise. Note further, however, that there is reasonably good correspondence between cloud pressures achieved by the different methods where both occur. There does appear to be a slight bias in that the direct estimates are systematically lower (higher pressure) than the ratio estimates. A true cloud emissivity of less than one would lead to this result.

Apart from the fundamental uncertainty of measurement accuracy as shown in Figure 4, there are other sources of error in practical

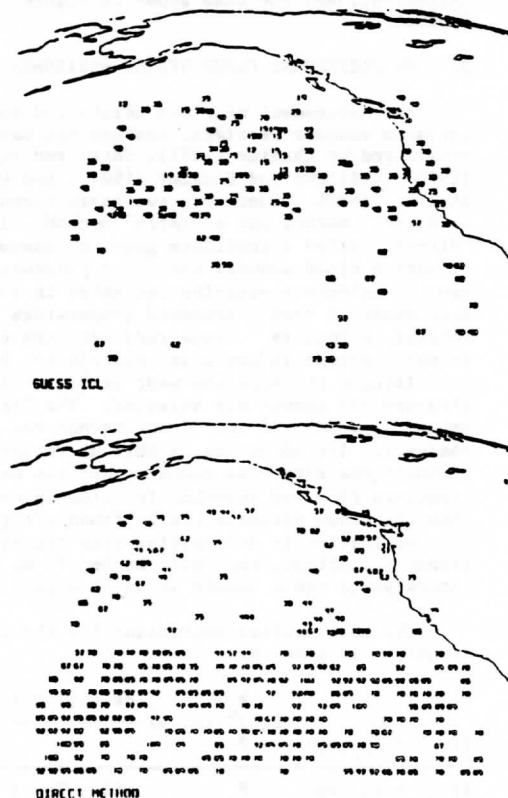


Figure 5: Cloud pressures derived for 18 February 1984. Top: cloud pressures achieved by the ratio technique. Bottom: cloud pressures defaulting to the "direct" method. NMC global temperature forecast used for calculating radiances.

application of the cloud height ratio algorithm. A major one is the determination of clear column radiance ( $I_{CL}$ ). We have investigated two options for the estimation of this quantity: calculate the value by the radiative transfer equation from a temperature/moisture profile estimate; select the value from a gridpoint analysis of observed clear values. The error associated with the first choice is the accuracy of the temperature estimate at high levels, and the accuracy of the transmittance properties for each channel. The errors in the transmittance are potentially more serious, but in practice one maintains a running account of the bias error associated with each measurement and minimizes its effect. The accuracy of the temperature profile will vary with location and synoptic situation, but its effect is smoothed by the averaging properties of the radiative transfer integral. Also, since  $I_{CL}$  appears in both numerator and denominator of the ratio there is a tendency for the temperature profile error to compensate. The error involved in the second option of choosing  $I_{CL}$  is directly related to the accuracy of cloud filtering as discussed in the previous section. The major source of uncertainty is in large regions of

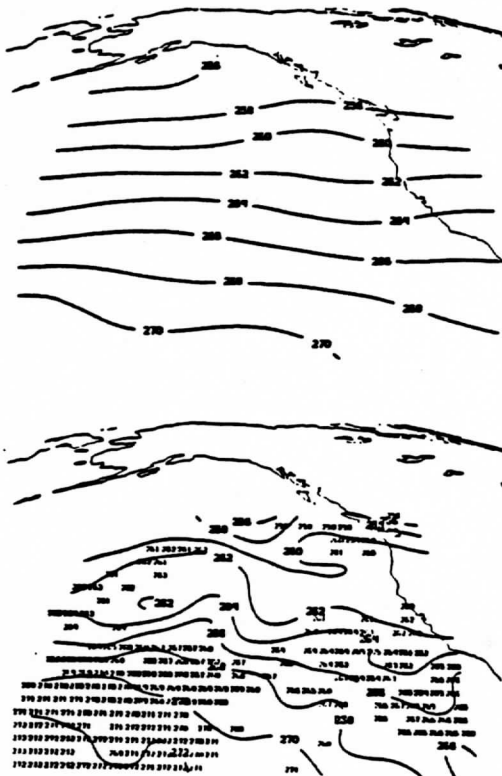


Figure 6: Clear  $I_{CL}$  estimates for the VAS 750 wavenumber channel as obtained from an integration of the NMC global forecast (top) and from cloud filtering of observations.

dense cloud where sampling is difficult. Figure 6 is an example of the clear brightness temperatures obtained from the NMC global forecast valid at 1200 GMT for 18 February 1984 and from VAS observations made at approximately the same time. Note that there is a considerable discrepancy in the amount of detail portrayed. Some of the finer scale given by the measurements seems reasonable where there are supporting observations, but the trough ridge pattern in the heavy cloud is an invention of the analysis algorithm. The discrepancies in the analyses are carried over to the determination of cloud pressures as shown by comparing Figures 5 and 6, and a comparison of analyzed fields of cloud pressures from the two sources shows an rms difference of approximately 100 mb. The statistic is somewhat misleading inasmuch as the operator using the plotted values will subjectively smooth the discontinuities. However, the choice of a source for  $I_{CL}$  remains a significant source of uncertainty. It is perhaps worth noting that use of clear radiance fields approximately doubles the CPU effort to produce the cloud heights.

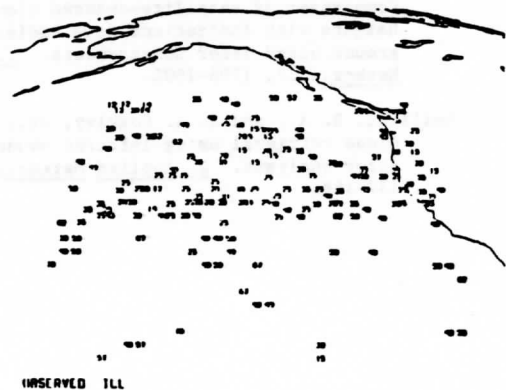


Figure 7: Cloud pressures derived from the ratio technique using analyses of observed clear column brightness temperatures.

#### 4. SUMMARY

The foregoing has described the current status in dealing with the clouds seen by the VAS. We are reasonably satisfied with the methods for avoiding cloud contamination in the radiances used temperature retrieval. The higher horizontal resolution of the small detector array is especially valuable. We are somewhat less satisfied with the method of cloud pressure assignment, but the technique is limited by the vertical resolution of a radiometric measurement. It does not appear that much more can be done to avoid the cloud. One suggestion has been to sample frequently over a short interval so that the clouds will "move out of the way." However, for large cloud masses which cause most of the problem, the cloud stays in about the same place relative to the meteorological situation. Future work will concentrate on better amalgamation of the wind and temperature derivations since they are truly complementary, and there seems little further progress to be made in avoiding or correcting for the clouds.

5. REFERENCES

- Bengtsson, L., M. Kanamitsu, P. Kallberg, and S. Uppala, 1982: FGGE 4-dimensional data assimilation at ECMWF. Bull. Amer. Meteor. Soc., 69, 29-43.
- Chahine, M. T., 1975: An analytical transformation for remote sensing of clear column atmospheric temperature profiles. J. Atmos. Sci., 32, 1946-1952.
- Hubert, L. F., and L. F. Whitney, Jr., 1971: Wind estimates from geostationary satellite pictures. Mon. Wea. Rev., 99, 665-672.
- McMillin, L. M., 1978: An improved technique for obtaining clear radiances from cloud contaminated radiances. Mon. Wea. Rev., 11, 1590-1597.
- Menzel, W. P., W. L. Smith, and T. R. Stewart, 1983: Improved cloud motion wind vector and altitude assignment using VAS. J. Clim. and Applied Meteor., 22, 377-384.
- Smith, W. L., and C. M. R. Platt, 1978: Comparison of satellite-deduced cloud heights with indications from radiosonde and ground based laser measurements. J. Applied Meteor., 17, 1796-1802.
- Weilicki, B. A., and J. A. Coakley, Jr., 1981: Cloud retrieval using infrared sounder data: error analysis. J. Applied Meteor., 20, 157-169.

**Estimating the Wind Field From VAS Temperature Soundings**

**Christopher M. Hayden  
NOAA/NESDIS Development Laboratory  
University of Wisconsin-Madison  
1225 W. Dayton Street, 2nd Floor  
Madison, WI 53706**

**November 12, 1984**



## Abstract

For purposes of rapid application of satellite data to the short term forecast problem it is useful to have access to both wind and mass information. This study examines the feasibility of deriving "pseudo" wind vectors to accompany VAS temperature profiles by using simple dynamic laws relating wind to geopotential. The reliability of the "pseudo" winds is determined by comparison with high density rawinsondes, cloud-drift measurements and winds generated by a forecast model. It is demonstrated that winds derived using the gradient approximation are slightly better at upper levels than either the geostrophic or ageostrophic estimates and competitive with all other estimates. At low levels the "pseudo" winds by all methods are only marginally useful.

### 1. Introduction

The high spatial and temporal resolution of the VISSR Atmospheric Sounder (VAS) has generated a quiet interest in using temperature gradient information to estimate the wind field, and to present VAS observations as a temperature profile with an associated profile of wind vectors. This interest springs from the concept that a primary user of the VAS data is the field forecaster who requires a data base including both mass and wind information. A distinction is drawn here between the "real-time" user and the center who applies the data as input to a numerical forecast model. For the latter, it is more appropriate that the model assimilate the temperature profiles in the course of initializing the distributions of mass and motion. The model should implicitly determine the motion field without resorting to "pseudo" winds which may have been provided with the VAS data. In fact, it is quite conceivable that the VAS winds could be

detrimental to the initialization process since their generation might involve statistical or dynamical relationships not in concert with the model dynamics. But, as noted, not all users of VAS data are numerical modelers, and for timely application to small scale and short-lived events, a "pseudo" wind is highly desirable. Given the growing application of graphical display terminals in central and regional forecast offices it is easy to give examples: delineation of the jet stream (Petersen and Horn, 1977); application of simple trajectory models for short term forecasting (Keller, 1984). This study presents three simple techniques which have been investigated to provide "pseudo" winds at the Cooperative Institute for Meteorological Satellite Studies (CIMSS) at the University of Wisconsin. The winds are evaluated against rawinsondes, cloud-drift measurements, and finally winds generated by a primitive equation forecast model.

## 2. Data sets

Two data sets from the 1982 NASA AVE VAS assessment program (Hill and Turner, 1983) have been used in this study. These are from 6 March and 24 April, 1982. On these days rawinsondes were released every 3 hours beginning at 1100 GMT to coincide with scheduled VAS sounding. The regular radiosonde network over the midwest was enhanced with high density sites over central Texas (Hill and Turner, 1983). In this study the first four time periods from each case were used.

Special network rawinsonde data were provided to CIMSS by the Marshall Space Flight Center. These data have been adjusted to a common release time (10 minutes after the beginning of satellite coverage) corresponding to 1100, 1445, 1745, and 2045 GMT. The method for adjustment is described in Fuelberg and Jedlovec (1982). The satellite soundings were processed

using a physical, iterative algorithm described by Smith (1984). The retrieval begins with a first guess temperature/moisture profile which in this case was time interpolated from the LFM 1200 GMT analysis and the 12-hour forecast from that analysis. The regular network of surface hourly observations was used to provide boundary conditions of temperature, moisture, and pressure.

### 3. Synoptic Conditions

On 6 March 1982, a well-defined cold front moved through central Texas during the AVE experiment. Thermal gradients over the region of special observations were approximately 15 degrees centigrade at the surface. A large amplitude trough at 500 mb with strong thermal gradient rotated rapidly through the network between 1200 GMT on 6 March and 0000 GMT on 7 March. A well-defined jet was positioned at the base of the trough. Clouds associated with the system initially covered a part of the special observing network but moved out during the day. Cloudy conditions persisted throughout the period over southeastern Texas, Arkansas and Louisiana, and satellite temperature retrievals in this areas were severely restricted.

The situation of 24 April 1982 was much less dynamic than that of 6 March. A weak warm front over the Gulf of Mexico combined with a high pressure system over the east maintained east to northeast surface flow over eastern Texas. In eastern Colorado a lee-side trough gave more southerly flow to western Texas. At upper levels a weak trough over the Rockies moved very slowly, but not into the special observation network. This case is characterized by a great deal of cloudiness which caused large gaps in the VAS sounding coverage.

#### 4. Procedure

In this experiment the rawinsonde measured winds are compared to 3 wind estimates derived from gridpoint fields of geopotential; a geostrophic estimate, a gradient estimate, and a quasi-geostrophic estimate. These were calculated according to the formulae:

$$\bar{v}_g = -\frac{1}{f} \nabla\phi \times \hat{k} \quad (\text{geostrophic}) \quad (1)$$

$$\bar{v}_{gr} = 2f\bar{v}_g / [f + (f^2 + 4|\bar{v}_g|K)^{1/2}] \quad (\text{gradient}) \quad (2)$$

$$\bar{v}_{ag} = \bar{v}_{gr} + \frac{1}{f} \hat{k} \times \frac{\partial \bar{v}_g}{\partial t} \quad (\text{ageostrophic}) \quad (3)$$

where  $\phi$  is the geopotential,  $K$  is the curvature of the trajectory (approximated by the geostrophic streamline), and  $f$  is the Coriolis parameter.

Since the wind estimates of (1)-(3) are sensitive to the numerical procedures invoked in deriving them, some of the details must be mentioned here. A more complete account can be found in Montgomery et al. (1984). The first step involves derivation of a gridpoint field of geopotential. This was accomplished on a  $0.8^\circ$  latitude/longitude grid using a standard 2-pass Barnes (Koch et al., 1984) analysis where the first pass results were replaced by a space and time-interpolated LFM product. Input data were the 3-hourly radiosonde or satellite-derived geopotentials. The choice of grid mesh size is a compromise between the desire for accuracy in the finite differencing, data densities problems (outside of the special

observing network), and the choice of horizontal smoothing chosen as an analysis parameter. After considerable experimenting, the gridlength of 0.8 degrees latitude with light smoothing was selected. Winds were derived at the locations of the observations using gradients represented by the analyses. Derivatives implicit in the calculations of (1)-(3) were determined from a least squares polynomial fit to 5x5 gridpoints centered nearest each observation.

Geopotentials to accompany the satellite temperature profiles were derived using a surface elevation and pressure as a reference level. Because this is a rather critical part of the eventual wind derivation, the details of the procedure need to be considered. The surface pressure is obtained from an objective (Barnes) analysis of the 1000 mb geopotential and the mean sea level temperature which are in turn derived from data reported by the surface network. In the derivation, reported station temperatures are reduced to sea level using the reported elevation and a constant lapse rate of 6.5 C/km. From the reported altimeter setting, the sea level pressure is estimated using:

$$\text{MSLP} = P_s (1. - .0000226Z_s)^{5.256} \quad (4)$$

where P is the altimeter setting and subscript s refers to the surface.

The 1000 mb geopotential is estimated from:

$$Z_{10} = Z_s - \frac{RT}{g} \ln(1013/P_s) \quad (5)$$

where the mean temperature  $\bar{T}$  is given by the average of the sea level and surface temperatures. The reference level pressure for each retrieval is

obtained from the 1000 mb geopotential analysis using (4) and (5) in reverse. The elevation required by (4) is obtained by interpolation in a topography file with 10 minute latitude/longitude resolution.

There is some error associated with assigning the reference level depending on the density of surface observations and the roughness of the topography. In the case studies presented here the error is not large from either source. RMS differences between independent radiosonde measurements of surface pressure and the satellite estimates are in the neighborhood of 8 mb. The degree to which this translates into an error in reference height, caused by the difference between assumed and actual lapse rates, is tolerably small.

Time derivatives for estimating the isallobaric component of the wind were formed by simple differencing between geopotential analyses of the three hourly observations periods. An attempt was made to introduce dynamic consistency between the analyses by applying an adjoint adjustment (Lewis and Derber, 1984). The adjoint model constrains the geopotential analyses at 850 and 300 mb by enforcing conservation of potential vorticity over several time periods. This procedure builds in continuity as portrayed in Fig. 1. The example is for 3 time periods on 6 March showing 300 mb geopotential and potential vorticity (dashed), before and after the adjustment. It is apparent that the adjoint procedure acts as a gentle, dynamic smoother, especially in the southern part of the area. The magnitude of the adjustments at 300 mb is typically of the order of 15 (RMS) mps.

## 5. Rawinsonde-"pseudo" wind comparisons

The observed 300 mb winds for 1800 GMT for 6 March and 24 April are shown in fig. 2. Both cases have good curvature, but the former is clearly the more dynamic with a sharp gradient in both speed and direction over central Texas and a strong jet extending from Texas to the northeast. The rapid movement of the upper level trough shown in Fig. 1 suggest that 6 March case is highly appropriate for testing the ageostrophic correction. The weaker synoptic conditions of 24 April should prove more challenging.

Figures 3 and 4 show wind barbs corresponding to "pseudo" winds derived from the objective analyses of radiosonde geopotentials for the two days at 1800 GMT. The first panel of each figure gives the geostrophic wind. The other panels of each figure show vector discrepancies between observation and each of the 3 types of derived wind. Figures 5 and 6 are similar to 3 and 4 except that the satellite "pseudo" winds replace those derived from the radiosonde. Conclusions which can be drawn visually are similar for the two sets. The derived winds compare quite well with the measured winds (Fig. 2), with respect to the location of wind maximum and horizontal shear in both speed and direction. Clearly the geostrophic wind is an overestimate of the speed in the trough, an error which is alleviated by the gradient correction (Fig. 7). However, the gradient estimate also shows systematic error over the special network in the 6 March case. Specifically, the estimate is too slow in the southern regions of higher wind speed and too fast in the northern regions of lesser speed. The derived horizontal shear is too smooth. To some extent this result is an artifact of the choices for grid mesh, smoothing, and finite differencing described earlier. Experiment showed that the shear in this

small area could be improved by increasing the grid resolution. However, areas poorly represented by observations suffered accordingly.

The isallobaric correction implied by comparing the gradient and ageostrophic discrepancies is clearly not successful. In the 6 March case the correction reinforced the gradient error whereas in the weaker 24 April case it had almost no effect. This is somewhat surprising in the 6 March case where the isallobaric component is significant, exceeding 10 mps in one instance. However, this component is shown in Fig. 7 and it is obvious to the eye that there is little correspondence with the gradient wind error shown in Fig. 3.

Statistical estimates of vector error comparing the observed and "pseudo" winds are given in Tables 1 and 2 for the radiosonde and satellite derivations respectively. In these comparisons the observed wind served as the standard to which any "pseudo" wind within a gridlength was compared. For the winds derived from radiosonde geopotentials the matching was obviously 1:1. For the satellite comparisons, occasionally two winds were compared to the same rawinsonde. Also, for a number of rawinsondes no satellite "pseudo" wind was available as cloud contamination precluded a temperature retrieval. The locations of the compared values for the 1800 GMT periods are shown in Fig. 3 and 4. These distributions are typical of the other time periods as well. Because the samples for the two types of "pseudo" winds are not identical, some care must be taken in comparing their relative accuracy in the tables.

The numbers of Tables 1 and 2 show that the 300 mb "pseudo" winds are a good representation of the measured winds. At 850 mb, however, the "pseudo" winds seem only marginally useful. The degradation at lower levels might have been anticipated since the wind "laws" are known to be



less well obeyed, and satellite temperature retrievals are known to be less accurate at lower levels of the atmosphere.

The statistical results with respect to comparing the 3 wind laws support comments made earlier from Fig. 3-6. At the 300 mb level there is evidence that the gradient approximation improves over the geostrophic, particularly with respect to the bias error. There is no evidence that the ageostrophic or isallobaric correction make any additional improvement. At 850 mb it clearly does not matter which of the laws is used. There may be a hint of an advantage to using the geostrophic approximation, but all estimates are significantly and almost equally different from the rawin observations.

Tables 1 and 2 permit an evaluation of the radiosonde and satellite "pseudo" winds relative to each other although, as cautioned earlier, some attention must be paid to the difference in samples. In particular, the extraordinary result obtained in correlating the satellite "pseudo" winds at 850 mb on 6 March requires a further look. The correlation of zero suggests that there is precisely no information in the satellite derivation, but the reader is invited to consider Fig. 8 and draw his own conclusion. The correlation results from a directional bias of nearly 90 degrees in areas where the data sets are compared. Visually a conclusion of "no information" over the whole field does not seem justified. In addition to the poor correlation, there is a significant bias error of 8 mps. This represents an inability of the retrieval algorithm to correct a rather poor first guess approximation as can be explained from Table 3. It shows that the bias error implicit in the guess at 850 mb on 6 March is 16 mps.

Table 3 can be used to evaluate the sample differences since statistics for the first guess are given for both radiosonde and satellite observation sites. From this comparison it appears that some of the deficiency of the 850 mb satellite "pseudo" winds in terms of correlation on 6 March is attributable to the lack of coverage over the eastern portion of the area, which reduces the total sample variance. On the other hand, an apparent slight RMS improvement in the satellite over the radiosonde representation at 300 mb on 6 March (Table 2) is also a reflection of less variance in the sample. Most importantly, Table 3 shows that the retrievals provide information over what is available from the first guess, especially with respect to bias error.

#### 6. Rawinsonde-cloud drift wind comparison

Another and more widely recognized method of obtaining winds from satellite measurements is the tracking of tracers in images of visible, infrared, and 6.7 micron radiation (Mosher, 1979, 1981). For 1800 GMT on 6 March, images were collected to provide cloud-drift winds to compare with the true and pseudo wind estimates. Cloud tracking is known to yield reliable results under controlled conditions and has been used previously to evaluate VAS "pseudo" winds at upper levels (Lord et al., 1984). Figure 9 shows both high and low level vectors, nominally at 200 and 970 mb respectively. Table 4 compares these winds with the rawin measurements and the two types of "pseudo" winds. At 850 mb the samples are too small to be meaningful, but there is the suggestion that the cloud-drift compare better to the radiosonde than do the "pseudo" winds. At 300 mb the cloud-drift winds have a standard deviation and correlation which are similar to the "pseudo" winds (Table 1), although they seem to underestimate, rather than

overestimate the observed velocity. Note by comparison with Fig. 4 that the cloud-drift winds complement, spatially, the satellite gradient winds which are necessarily in relatively cloud-free areas. While desirable in terms of forming a complete data set, this feature makes comparison difficult. Most comparisons are the trailing edge of the clouds where the wind shear is very strong; the very large error shown in column c of Table 4 is probably not representative, and is considerably poorer than results reported by Lord et al. (loc. cit.).

#### 7. Rawinsonde-SSM comparison

The final comparison offered here is between the rawinsonde measurements and the winds generated by a primitive equation forecast model. The model used is the Subsynoptic Model (SSM) which has been implemented on the McIDAS at CIMSS. It is a version of the Australian Meteorological Research Center limited area model with 10 levels in the vertical and a horizontal resolution of 67 km (McGregor et al., 1978; Le Marshall et al., 1984). The SSM was initiated with the rawinsonde data at 1200 GMT, and the forecasts were post-processed at 1500, 1800, and 2100 to provide winds for comparison. Although significantly more complicated dynamics are implicit in the SSM winds as compared to the simple "pseudo" winds, the advantage is not obvious with respect to the measured winds. This can be seen by comparing Tables 5 and 1. Here the statistical samples are identical, so the comparison is not ambiguous. Note that the SSM product is only slightly better than the gradient wind estimated at 850 mb and barely equivalent at 300 mb. Apparently the error of the forecast is commensurate with the error of the gradient approximation, or, equivalently, the advantage of later data equalizes the advantage of the

better dynamics. The significant bias in the SSM winds at upper levels is disturbing inasmuch as it seems to indicate excessive smoothing in areas of high gradient. The wind "errors" for the SSM are shown in Figure 10 for both levels, and the bias error at upper levels is obvious.

#### 8. Summary

The aim of this study has been to describe and evaluate winds which can be quickly generated to accompany VAS temperature retrievals. This has been accomplished by considering three levels of complexity in approximating the wind from geopotential, and matching these "pseudo" winds to rawinsonde measurements, cloud-drift winds and finally the output winds of the SSM forecast model. Several conclusions stand out. First, at high levels, any of the "pseudo" winds generated with the VAS data appear to be competitive with the other available estimates and perhaps even with the rawinsonde. This conclusion corroborates the finding of Lord et al. (1984). At low levels the "pseudo" winds are not competitive, apparently because of poorer relative accuracy in the geopotential. No estimate is comparable to the rawinsonde. The attempts made here to improve the VAS "pseudo" winds by adding a gradient and ageostrophic correction showed varying success. At high levels, some advantage is gained by the gradient correction, especially for the 6 March case. No such advantage is seen at low levels. In no instance was the ageostrophic correction noticeably favorable although it generally didn't do any harm either. This result is somewhat disappointing, but it must be recognized that even in the 6 March situation the isallobaric correction is close to the expected error of the rawinsonde (Lenhardt, 1973). It is concluded that the VAS winds have applications, but they are limited. The upper level winds are certainly

adequate for the determination of steering currents. For example, they should be useful in short term forecasts of vorticity advection or cloud movement. They are capable of delineating the position and strength of the upper level jet and jet streaks. However, the "pseudo" winds should be used with caution in applications at low levels. They should not be expected to produce accurate estimates of low level advection; for example to forecast low level stability. They will certainly not delineate a low level jet, at least not until they can be generated in concert with more sophisticated models, perhaps a model like the SSM.

## References

- Fuelberg, H.E. and G.J. Jedlovec, 1982: A subsynoptic-scale kinetic energy analysis of the Red River Valley tornado outbreak (AVE SESAME I). Mon. Wea. Rev., 110, 2005-20024
- Hill, C.K. and R.E. Turner, 1983: NASA's AVE/VAS Program. Bull. Amer. Meteor. Soc., 64, 796-797.
- Keller, D. L. and W. L. Smith, 1983: A statistical technique for forecasting severe weather from vertical soundings by satellite and radiosonde. NOAA Technical report NESDIS 5, 35 pp.
- Koch, S.E., M. DesJardins, and P.J. Kocin, 1984: An ineractive Barnes objective map analysis scheme for use with satellite and conventional data. J. of Clim. and Appl. Meteor. 22, 1487-1503.
- LeMarshall, J.T., W.L. Smith, G.R. Diak, and G.M. Callan, 1984: The use of a mesoscale numerical weather prediction model for nowcasting. To be submitted to Mon. Wea. Rev.
- Lenhardt, R.W., 1973: Variability of wind over a distance of 16.25 km. J. Appl. Meteor., 12, 1075-1078.
- Lewis, J.M. and J.C. Derber, 1984: The use of adjoint equations to solve a variational adjustment problem with advective constraints. Submitted to Tellus.

- Lord, R. J., W. P. Menzel, and L. E. Pecht, 1984: ACARS wind measurements: An intercomparison with radiosonde, cloud motion, and VAS thermally derived winds. J. Atmos. and Oceanic Tech., 1, 131-137.
- McGregor, J.L., L.M. Leslie, and D.J. Gauntlett, 1978: The ANMRC limited area model: consolidated formulation and operational results. Mon. Wea. Rev., 106, 427-438.
- Montgomery, H., 1984: VAS demonstration description, summary, and final report. NASA publication in process.
- Mosher, F.R., 1979: Cloud drift winds from geostationary satellites. Atmos. Tech., 10, 53-60.
- and T.R. Stewart, 1981: Characteristics of water vapor-tracked winds. NAVENPERRSCHFAC Contractor reporter. CR-81- 06, 51 pp.
- Petersen, R.A. and L.H. Horn, 1977: An evaluation of 500mb height and geostrophic wind fields derived from Nimbus-6 soundings. Bull. Amer. Meteor. Soc., 64, 1195-1201.
- Smith W.L., 1983: The Retrieval of atmospheric profiles from VAS geostationery radiance observations. J. Atmos. Sci., 40, 2025-2035.

Table 1. Comparison of observed winds with "pseudo" winds derived from objective analyses of geopotential. "Pseudo" winds are created from a) radiosonde measurements and, b) satellite estimates of geopotential obtained from temperature/moisture retrievals. Sample is for 1500, 1800, and 2100 GMT 6 March 1982. Mean vector difference (ms), standard deviation of the difference, and vector correlation coefficient are presented for 3 estimates of "pseudo" wind.

		a. Radiosonde			b. Satellite		
		GEOS	GRAD	AGEO	GEOS	GRAD	AGEO
	mean	-3.0	-2.9	-3.4	-7.6	-7.6	-8.1
850 mb	sigma	4.5	4.6	4.7	5.1	5.1	5.2
	cc	68	66	64	-01	-01	00
	sample	76			64		
	mean	-12.7	-3.6	-6.2	-9.6	-1.0	-3.8
300 mb	sigma	14.9	10.7	11.8	9.9	9.4	9.0
	cc	88	90	89	91	91	91
	sample	86			77		

Table 2. Same as Table 1 but for case of 24 April 1982

		a. Radiosonde			b. Satellite		
		GEOS	GRAD	AGEO	GEOS	GRAD	AGEO
	mean	-1.5	-0.8	-1.1	-1.8	-0.6	-1.8
850 mb	sigma	4.2	4.3	4.3	4.7	4.7	4.6
	cc	69	67	67	58	54	56
	sample	91			68		
	mean	-3.5	1.6	0.3	-5.0	0.2	-2.9
300 mb	sigma	7.9	7.6	7.6	8.5	8.6	8.4
	cc	91	89	89	88	87	87
	sample	105			97		



Table 3. Comparison of observed winds with gradient "pseudo" winds generated from retrieval "first guess" information at (a) radiosonde sites and (b) satellite retrieval sites. Comparisons are as in Table 1.

		a. Radiosonde sites		b. Satellite sites	
		6 March	24 April	6 March	24 April
	mean	-12.2	-1.3	-14.1	-0.9
850 mb	sigma	6.0	4.5	5.4	4.2
	cc	37	64	08	56
	sample	76	91	64	68
	mean	-7.6	2.7	-6.7	3.4
300 mb	sigma	13.1	8.8	11.6	8.7
	cc	85	85	84	86
	sample	86	105	77	86

Table 4. Comparison of cloud drift winds with rawinsondes and satellite derived gradient winds for 1800 GMT on 6 March. Units as in Table 1.

		a. Rawinsonde	b. Raob grad.	c. Satellite
	mean	-5.6	-1.5	-1.5
850 mb	sigma	3.6	6.5	8.2
	cc	87	43	69
	sample	4	4	5
	mean	8.2	16.2	16.3
300 mb	sigma	11.4	13.0	17.5
	cc	86	81	77
	sample	12	12	16

Table 5. Comparison of SSM with observed rawinsondes. Units are same as in Table 1.

	mean	0.6
850 mb	sigma	4.4
	cc	71
	sample	76

	mean	12.4
300 mb	sigma	11.5
	cc	89
	sample	86

## Figure Captions

Figure 1. 300 mb geopotential analyses and potential vorticity (300-850, dashed) for 1200, 1500, and 1800 GMT, 6 March 1982. Fields were derived from NASA AVE radiosonde reports with (right) and without (left) adjoin time continuity adjustment.

Figure 2. 300 mb winds observed by rawinsondes, 1800 GMT 6 March and 24 April 1982.

Figure 3. Top, left geostrophic winds calculated from radiosonde analysis of 300 mb geopotential, derived at locations of radiosonde reports. Other panels show errors implied by comparison to the observed winds of the geostrophic, gradient, and ageostrphic estimates. 6 March 1982

Figure 4. Same as Figure 5 but for 24 April 1982.

Figure 5. Same as Figure 3 except satellite-derived estimates of 300 mb geopotential replace radiosonde measurements. Difference plots represent satellite/radiosonde matches with 0.8 degrees of latitude.

Figure 6. Same as Figure 5 but for 24 April 1982.

Figure 7. 300 mb gradient and isallobaric corrections for winds derived from radiosonde geopotential measurements. 1500-1800 GMT geopotential change shown as solid contours for 6 March and 24 April 1982.

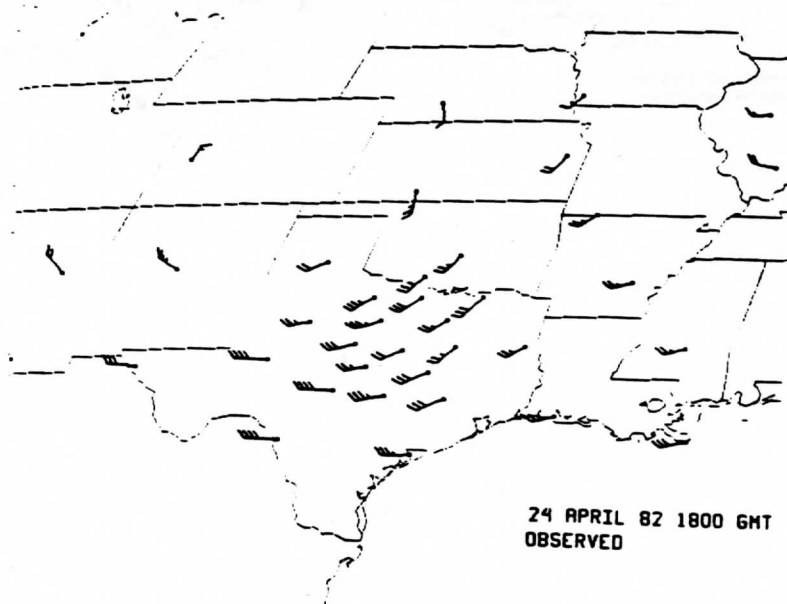
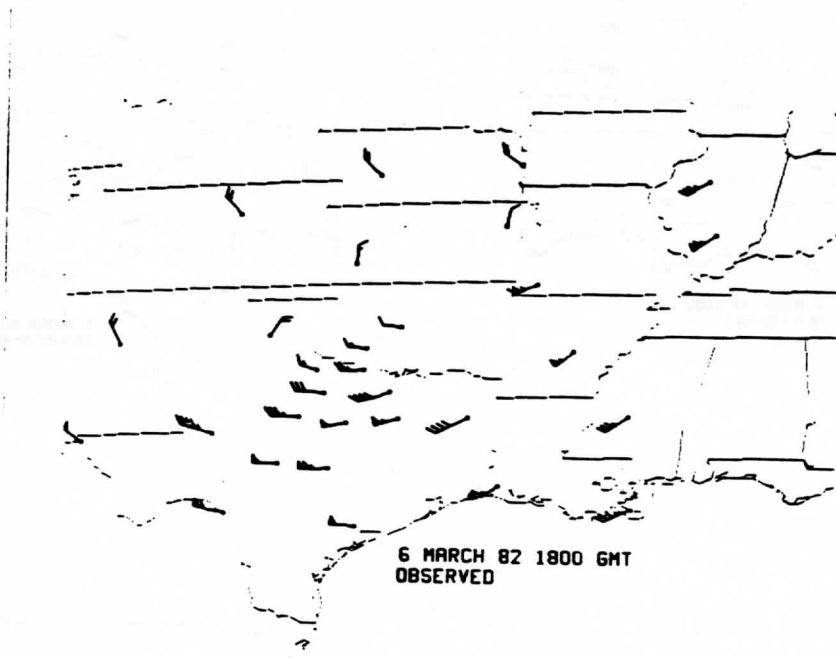
Figure 8. 850 mb observed wind; satellite derived gradient estimates and vector difference for 6 March 1982.

Figure 9. Cloud drift winds for 1800 GMT 6 March 1982 at high and low levels and their vector difference from rawinsonde observations.

Figure 10. Vector wind differences between rawinsonde and SSM forecast at 300 (top) and 850 (bottom) mb for 1800 GMT, 6 March 1982.

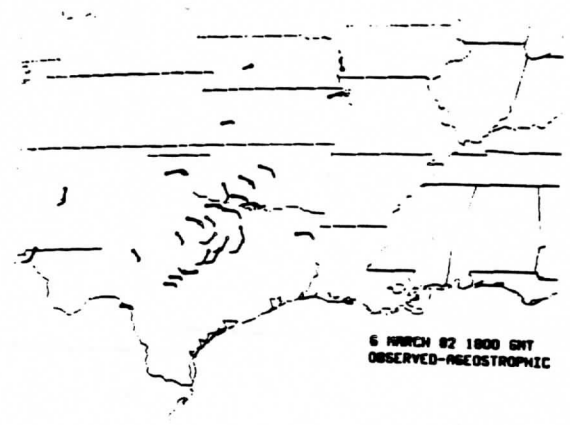
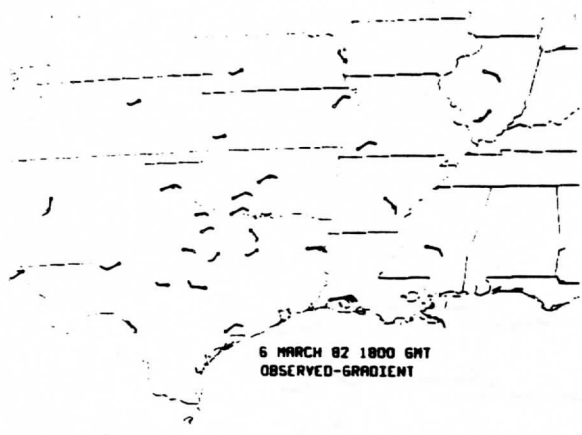
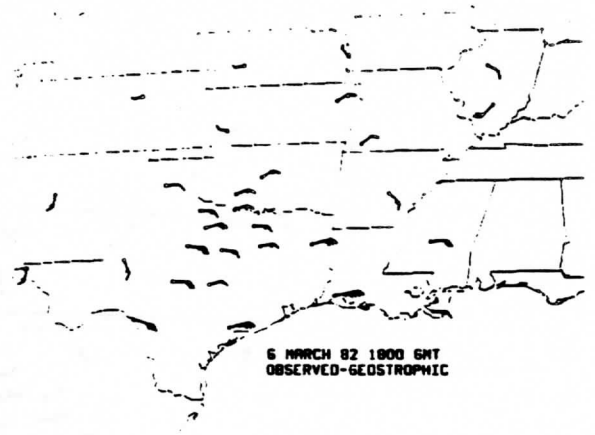
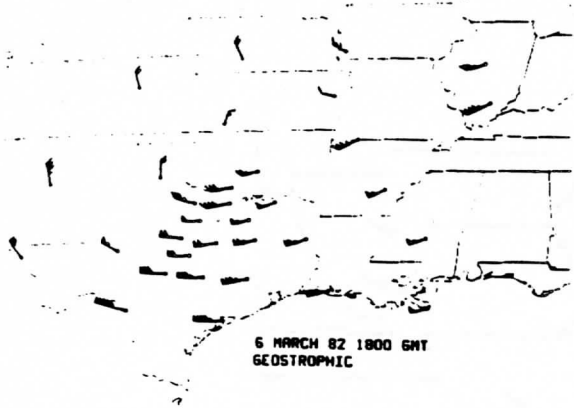
4/TOME/wind





paper 5

Fig. 2



5

Fig. 3  
paper 5

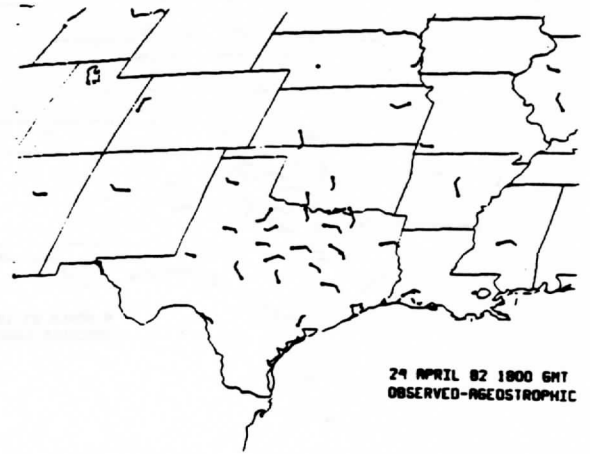
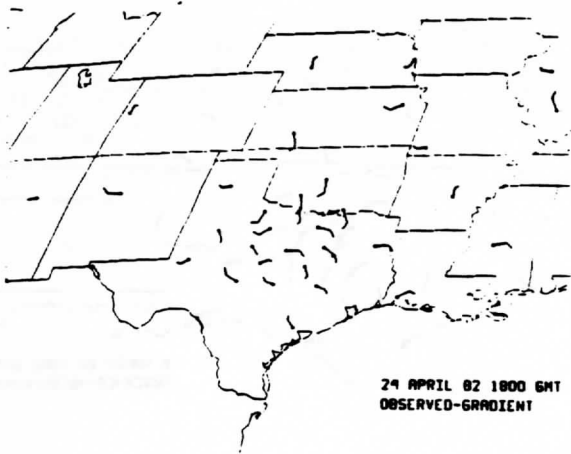
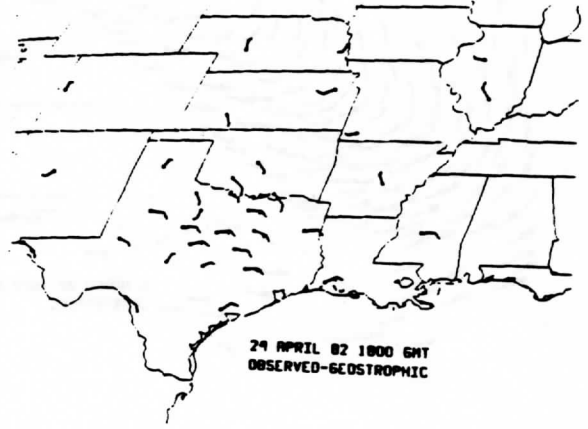
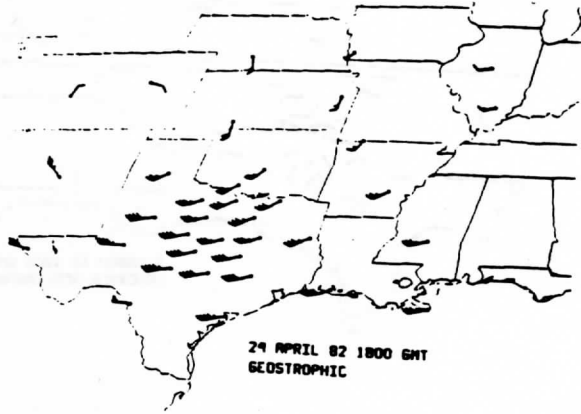


Fig. 4  
Paper 5



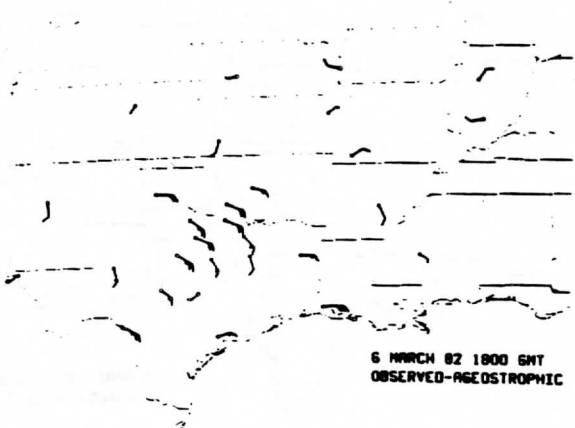
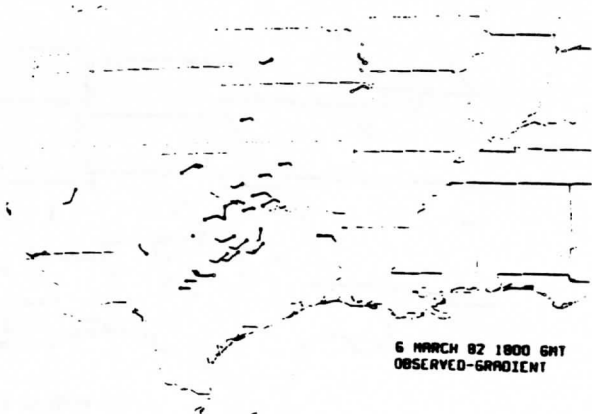
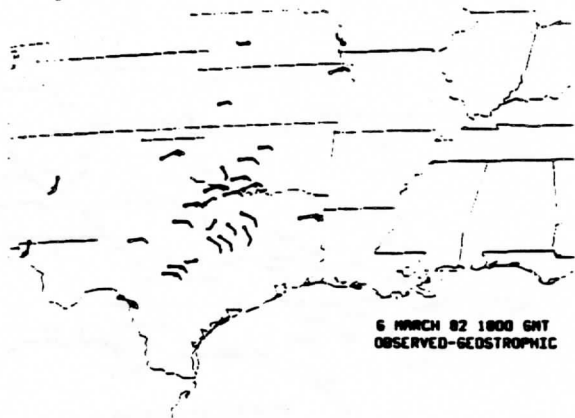
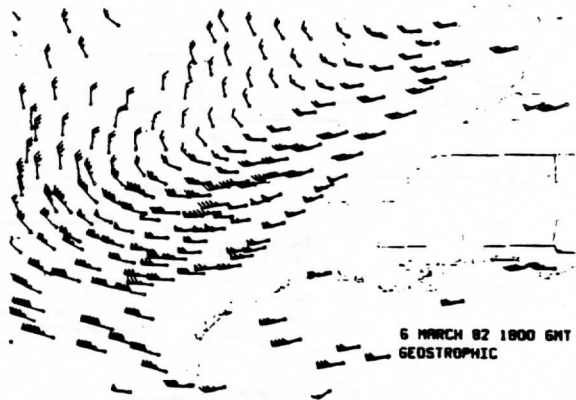


Fig. 5  
paper 5

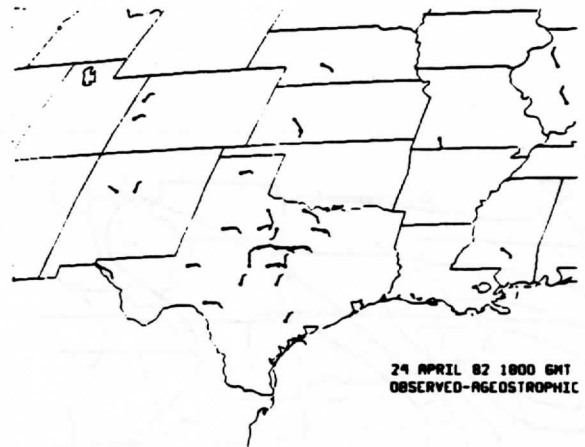
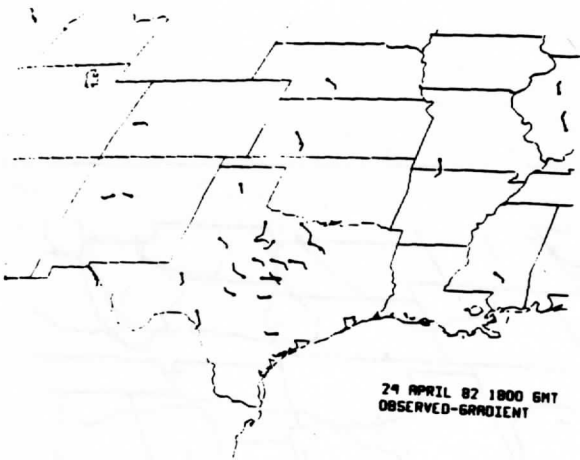
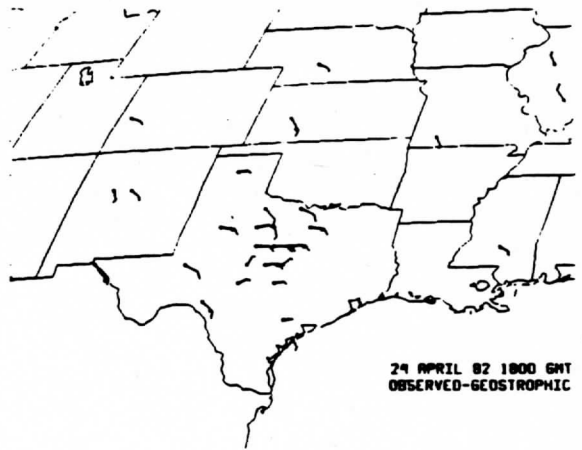


Fig. 6  
paper 5

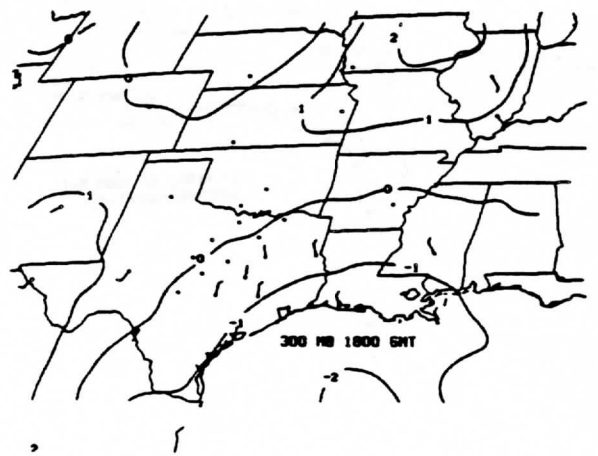
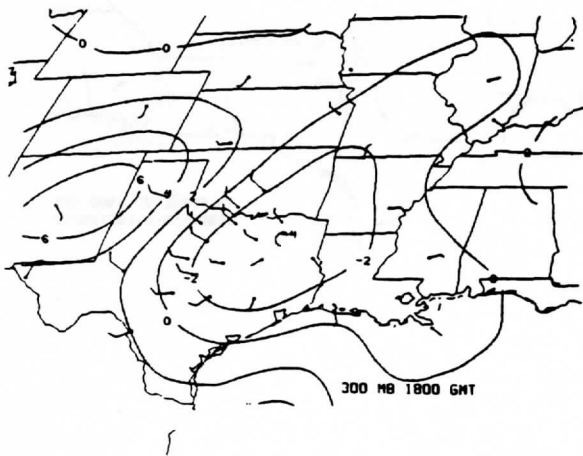
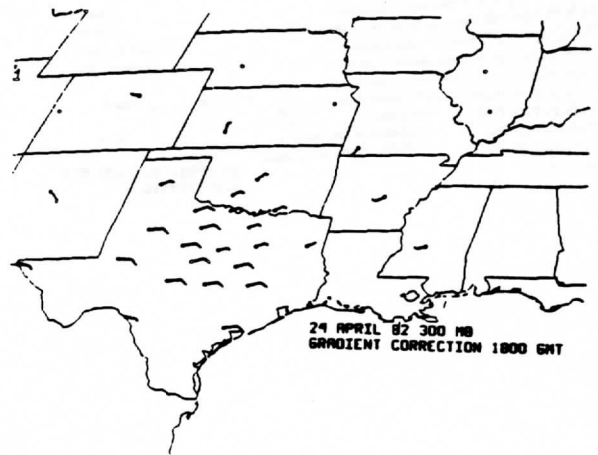


Fig 7 paper 5

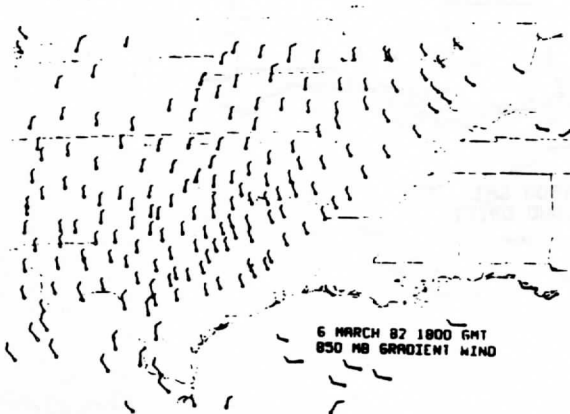
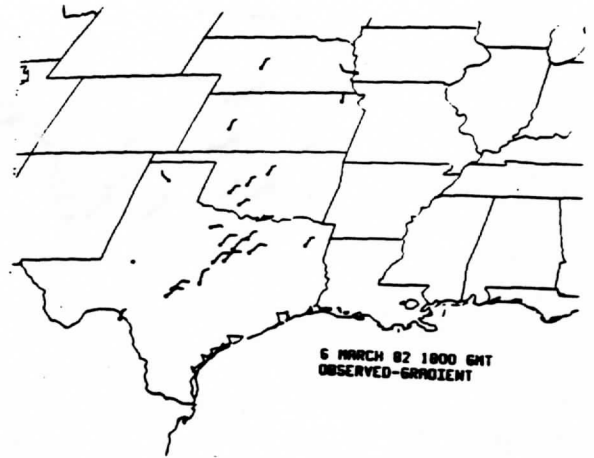
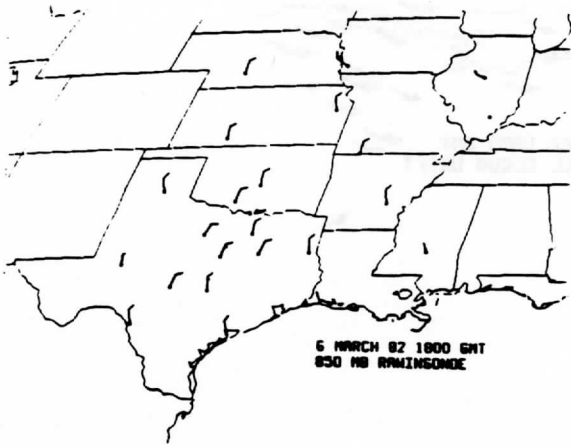
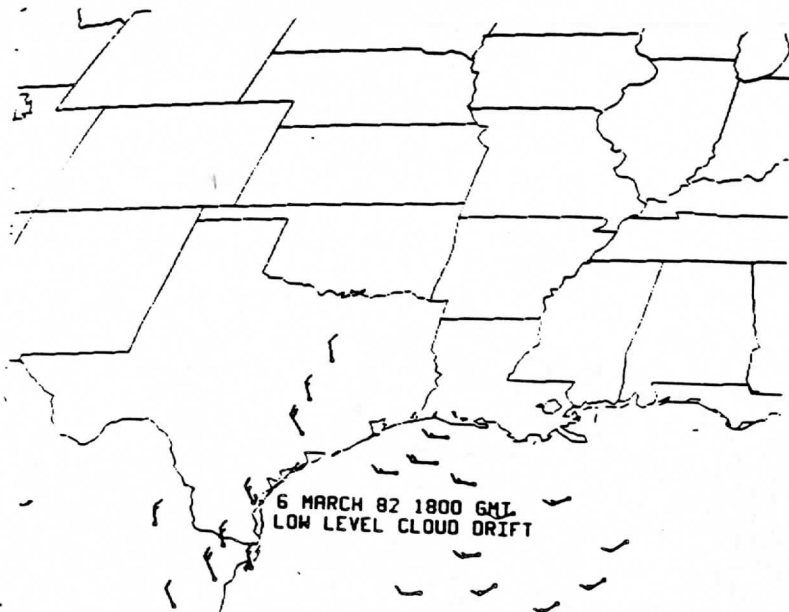
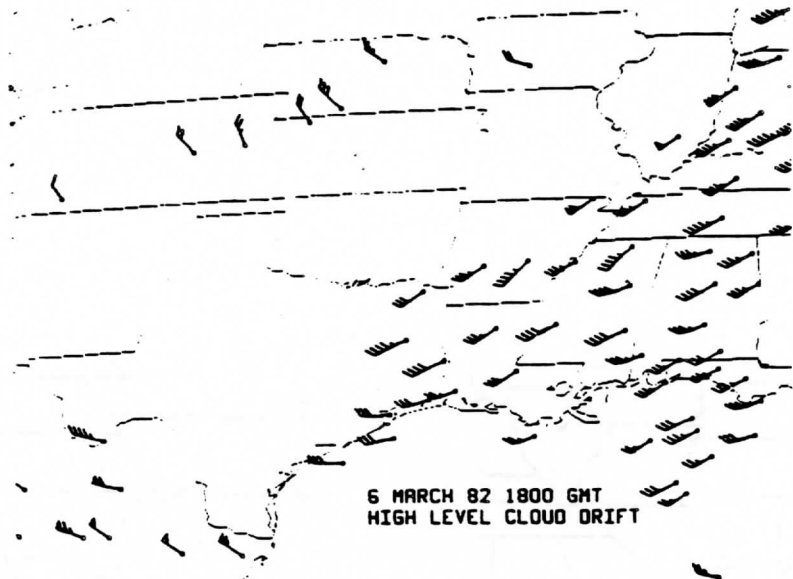
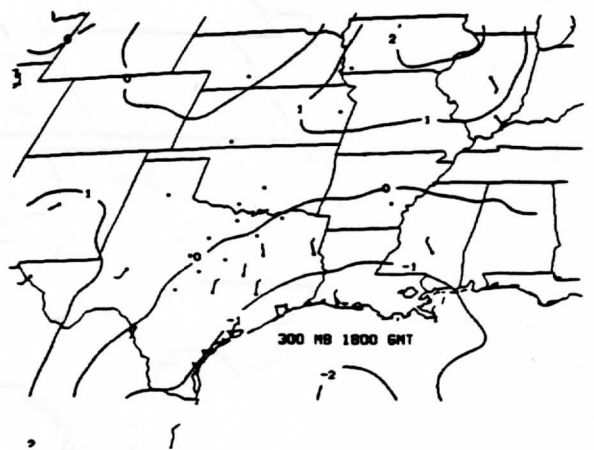
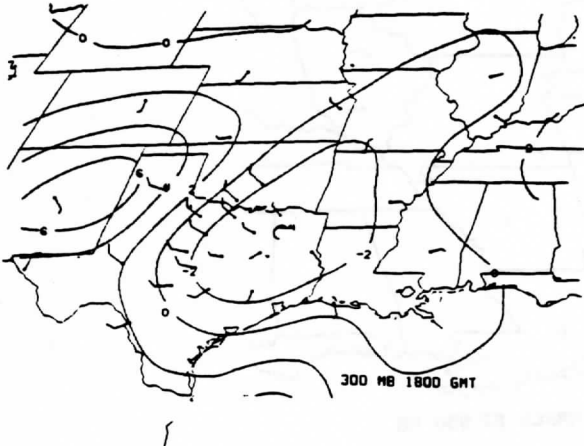
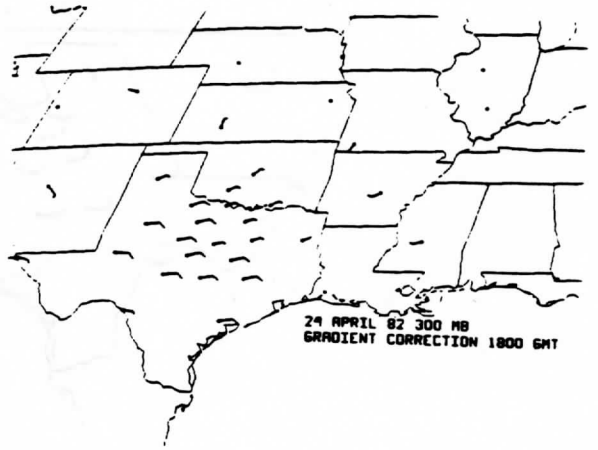
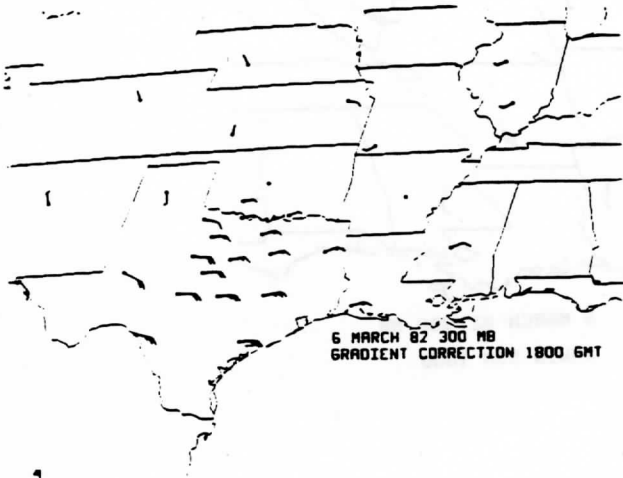


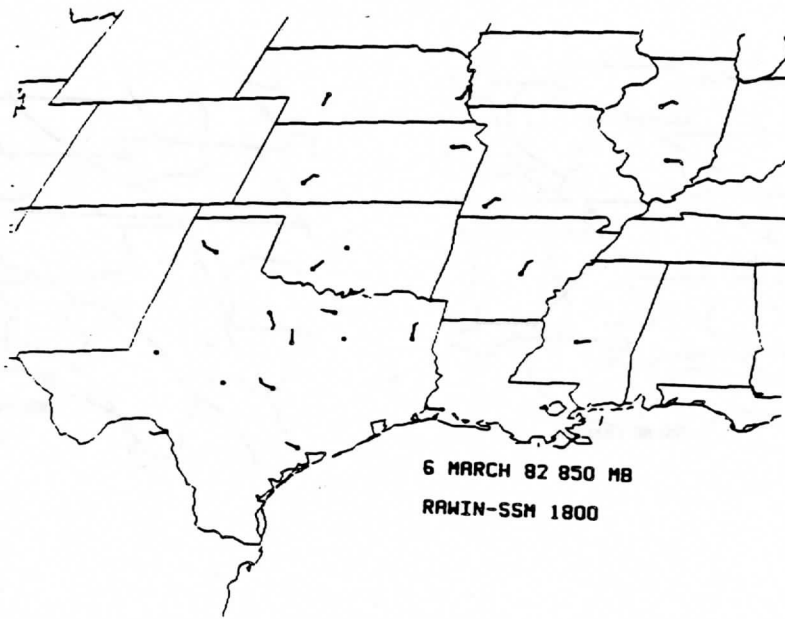
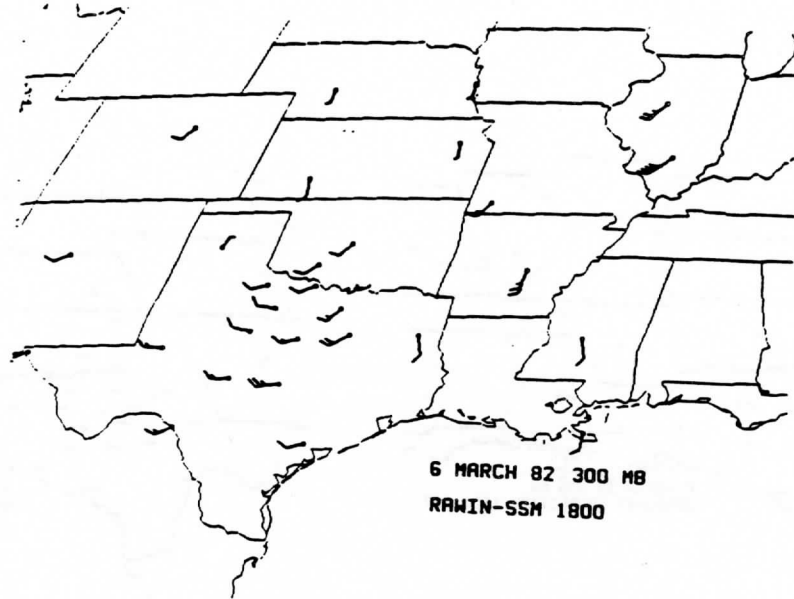
Fig 7  
paper 5



Paper 5

Fig. 8





Paper 5

Fig. 10

B.3

IMPROVED VERTICAL SOUNDINGS FROM AN AMALGAMATION OF POLAR AND GEOSTATIONARY RADIANCE OBSERVATIONS

William L. Smith and Harold M. Woolf  
NOAA/NESDIS Development Laboratory  
1225 West Dayton Street, 2nd Floor  
Madison, Wisconsin 53706

1. INTRODUCTION

The VISSR Atmospheric Sounder (VAS) on the current operational geostationary satellites is capable of sounding the atmosphere's temperature and water vapor distribution with either 14 km or 7 km horizontal resolution. However, the instrument operates in the infrared (Table 1) and therefore soundings to the ground cannot be achieved in cloud overcast situations. On the other hand, the TIROS Operational Vertical Sounder (TOVS) on the current polar orbiting satellites operates in the microwave as well as in the infrared (Table 1) and is therefore capable of sounding through most cloud overcasts.

For synoptic scale analysis/forecast applications, TOVS alone provides the necessary initial data. However, for subsynoptic scale applications, the six or twelve hour sampling interval of one or two polar orbiting satellites is too long; the higher frequency soundings (e.g., one to two hour) over certain geographical regions (e.g., North America) achievable from the geostationary satellites are required. Because of gaps in geostationary sounding coverage produced by extended cloud, it is desirable to utilize the less frequently sampled TOVS information, particularly the microwave radiances, together with the VAS sounding radiances for deducing atmospheric profiles down to the earth's surface across extended cloud areas. The importance of microwave sounding data in cloudy regions is exemplified in Figure 1 which shows the locations of reliable soundings to the ground achieved from VAS and TOVS radiance observations at 1600 GMT on 26 April 1982 over the southeastern United States. The locations are superimposed on a visible cloud image obtained within the hour of the sounding observations.

TABLE 1

CHARACTERISTICS OF VAS AND TOVS (HIRS AND MSU) SOUNDING CHANNELS

VAS channel number	Channel central wavenumber	Principal absorbing constituents	Level of peak energy contribution
1	679	CO <sub>2</sub>	60
2	691	CO <sub>2</sub>	100
3	702	CO <sub>2</sub>	400
4	714	CO <sub>2</sub>	600
5	751	CO <sub>2</sub>	950
6	2214	CO <sub>2</sub>	900
7	789	H <sub>2</sub> O	surface
8	889	window	surface
9	1379	H <sub>2</sub> O	600
10	1486	H <sub>2</sub> O	400
11	2254	CO <sub>2</sub>	500
12	2538	window	surface
HIRS channel number	Channel central wavenumber	Principal absorbing constituents	Level of peak energy contribution
1	668	CO <sub>2</sub>	30 mb
2	679	CO <sub>2</sub>	60 mb
3	691	CO <sub>2</sub>	100 mb
4	704	CO <sub>2</sub>	400 mb
5	716	CO <sub>2</sub>	600 mb
6	732	CO <sub>2</sub> /H <sub>2</sub> O	800 mb
7	748	CO <sub>2</sub> /H <sub>2</sub> O	900 mb
8	898	window	surface
9	1028	O <sub>2</sub>	25 mb
10	1217	H <sub>2</sub> O	900 mb
11	1364	H <sub>2</sub> O	700 mb
12	1484	H <sub>2</sub> O	500 mb
13	2190	N <sub>2</sub> O	1000 mb
14	2213	N <sub>2</sub> O	950 mb
15	2240	CO <sub>2</sub> /N <sub>2</sub> O	700 mb
16	2276	CO <sub>2</sub> /N <sub>2</sub> O	400 mb
17	2361	CO <sub>2</sub>	5 mb
18	2512	window	surface
19	2671	window	surface
20	14367	window	cloud
MSU channel number	Frequency (GHz)	Principal absorbing constituents	Level of peak energy contribution
1	50.31	window	surface
2	53.73	O <sub>2</sub>	700 mb
3	54.96	O <sub>2</sub>	300 mb
4	57.95	O <sub>2</sub>	90 mb

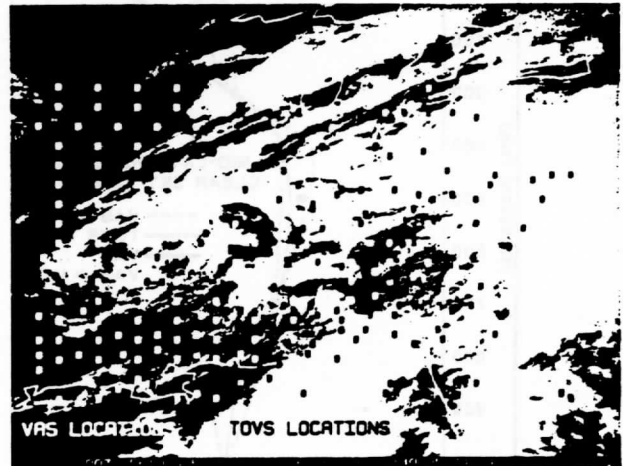


Figure 1: Locations of reliable 75 km resolution soundings from VAS and TOVS at 1600 GMT on 26 April 1982. White circles indicate VAS sounding locations and black circles indicate the TOVS sounding locations.

Finally, since the combination of VAS and TOVS provides many more radiances for the retrieval of atmospheric profiles than is provided by either system alone, improved sounding performance is expected.

In this paper the expected accuracy of sounding retrievals achieved from combined VAS



and TOVS radiance observations is compared to that achieved by each system alone. A new physical matrix inverse retrieval algorithm is formulated for retrieving simultaneously the temperature and water vapor profile from VAS and/or TOVS sounding radiances. The case study results achieved from the application of the new retrieval algorithm to actual radiance observations from VAS and TOVS are to be presented at the conference.

## 2. EXPECTED PERFORMANCE

The performance expected from a combined VAS-TOVS sounding system was estimated using multiple linear regression analysis of radiances simulated from a large statistical sample of radiosondes. Three latitude zones were considered (polar, mid-latitude, and tropical) with 300 soundings being used to formulate the dependent set from which regression equations are derived and 100 soundings being used as the independent set for testing the regression relations. For this performance analysis clear sky conditions and nominal instrument noise were assumed for simulating the VAS and TOVS sounding radiances. Furthermore, a spatial resolution of 75 km was assumed so that a spatial sample of 25 VAS, 9 HIRS, and 1 MSU fields of view were assumed to be associated with each sounding, thereby reducing the nominal instrument noise by the square-root of the number of fields of view available.

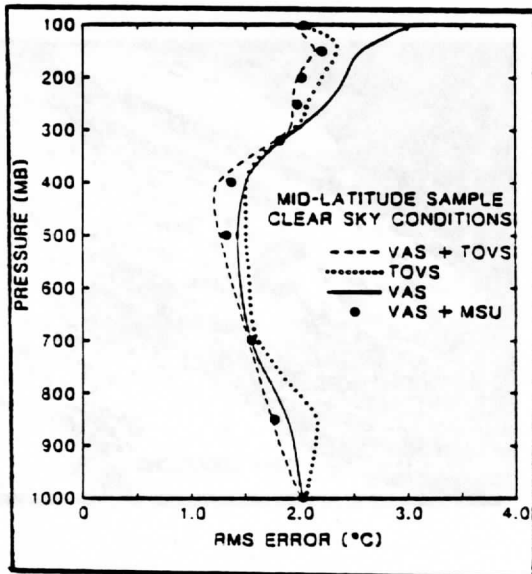


Figure 2: Accuracy of statistical regression retrievals of atmospheric temperature for various instrument configurations. The results shown are for the mandatory pressure levels only.

Figure 2 shows the performance at mandatory pressure levels for mid-latitude conditions. (The polar and tropical zone results are similar.) The combined set of VAS and TOVS radiances provides greater accuracy than either system alone, particularly in the lower troposphere (e.g., near 850 mb) and in the upper troposphere (300-100 mb). It is interesting to

note that for these clear sky conditions VAS contributes more than TOVS to the accuracy of the lower tropospheric temperatures (1000-700 mb layer) because of the higher signal-to-noise ratio of average radiances achieved for a 75 km sounding area. In the mid-troposphere (700-300 mb), VAS and TOVS performance is similar while in the upper troposphere (300-100 mb) TOVS is superior to VAS because of the sharper vertical resolution in this region provided by the monochromatic microwave observations. Thus the VAS and the Microwave Sounding Unit (MSU) portion of the TOVS provide highly complementary observations. As can be seen from Figure 2, VAS and MSU provide a system that yields a performance almost equal to that of the entire VAS-TOVS combination. This result was expected because of the similarity between VAS and TOVS infrared channels (Table 1). It should be remembered that the major enhancement of sounding retrieval accuracy by MSU observations is expected to be in cloud covered regions where VAS sounding information is restricted to the atmosphere above the cloud.

## 3. RETRIEVAL PROCEDURES

A recently developed (by the authors) "one step" simultaneous temperature/water vapor profile retrieval method will be used to calculate soundings from the VAS and/or TOVS radiances used for this study. As can be easily shown, the radiative transfer equation is expressible in the perturbation form:

$$\begin{aligned} \delta T^* = & \int_0^{P_S} \delta U \left[ \frac{\partial T}{\partial p} \frac{\partial \tau}{\partial U} \frac{(\partial B / \partial T)}{(\partial B / \partial T^*)} \right] dp \\ & - \int_0^{P_S} \delta T \left[ \frac{\partial \tau}{\partial p} \frac{(\partial B / \partial T)}{(\partial B / \partial T^*)} \right] dp + \delta T_S \left[ \frac{(\partial B / \partial T_S)}{(\partial B / \partial T^*)} \right] \tau_s \end{aligned} \quad (1)$$

where  $T^*$  is brightness temperature,  $U$  is precipitable water vapor,  $B$  is Planck radiance,  $T$  is temperature,  $T_S$  is surface-skin temperature,  $\tau$  is transmittance, and  $p$  is pressure. The perturbation,  $\delta$ , is with respect to an a priori estimated or mean condition. The pressure dependence of all integrand variables is to be understood. In order to solve (1) for  $\delta U$ ,  $\delta T$ , and  $\delta T_S$  from a set of spectrally independent radiance observations, we make the following profile representations in terms of arbitrary pressure functions,  $\phi(p)$ :

$$\delta q(p) = g \sum_{i=1}^N \alpha_i q_0(p) \phi_i(p) \quad (2a)$$

$$\delta T(p) = - \sum_{i=N+1}^N \alpha_i \phi_i(p) \quad (2b)$$

where  $q(p)$  is the water vapor mixing ratio and  $g$  is gravity. The zero subscript indicates the a priori condition. Equation 2a implies from the gas law and hydrostatic equation that

$$\delta U(p) = \sum_{i=1}^N \alpha_i \int_0^P q_0(p) \phi_i(p) dp \quad (2c)$$

Substituting representations (2b) and (2c) into (2) and letting  $\alpha_0 = \delta T_s$  yields for each spectral radiance observation,  $\delta T_j^*$ , for a set of K spectral channels:

$$\delta T_j^* = \sum_{i=0}^M \alpha_i \phi_{i,j} \quad j=1,2,\dots,K \quad (3)$$

where

$$\begin{aligned} \phi_{0,j} &= \frac{\partial B_j / \partial T_s}{\partial B_j / \partial T_j^*} \tau_{S,j} \\ \phi_{i,j} &= \int_0^P \int_0^P q_0 \phi_{i,j} dp \left[ \frac{\partial T}{\partial p} \frac{\partial \tau_j}{\partial U} \frac{\partial B_j / \partial T}{\partial B_j / \partial T_j^*} \right] dp \quad i < N \quad (4) \\ \phi_{i,j} &= \int_0^P \int_0^P \phi_{i,j} \left[ \frac{\partial \tau_j}{\partial p} \frac{\partial B_j / \partial T}{\partial B_j / \partial T_j^*} \right] dp \quad N < i < M \end{aligned}$$

The  $\phi_{i,j}$  quantities are calculated from the a priori estimated or mean profile conditions. Written in matrix form

$$t^* = \phi \alpha \quad (5)$$

where  $t^*$  is a row vector of K radiance observations,  $\alpha$  is a row vector of M+1 coefficients, and  $\phi$  is a matrix having dimensions (K x M+1). Assuming that K > M+1, then the least squares solution of (5) is employed to give stability to the solution, so that

$$\alpha = (\phi^T \phi)^{-1} \phi^T t^* \quad (6)$$

where  $( )^T$  indicates matrix transposition and  $( )^{-1}$  indicates matrix inverse. Once the  $\alpha_i$ 's are determined,  $\delta T_s$ ,  $\delta q$ , and  $\delta T$  are specified from (2) and added to the a priori estimates to yield the final solutions for surface-skin temperature and the water vapor mixing ratio and temperature profiles.

### 3.1. Choice of Basis Functions

The choice of pressure functions  $\phi(p)$  is arbitrary, although the accuracy of the solution will ultimately depend upon them. For example, empirical orthogonal functions (i.e., eigenvectors of the water vapor and temperature profile covariance matrices) can be used. In this study natural functions, the profile weighting functions ( $d\tau/d\ln p$ ) of the radiative transfer equation, are to be used. One of the temperature and water vapor functions is for  $\phi_i(p)=1$  in order to account for any vertically constant displacement between the true and a priori profiles.

### 3.2. Incorporating Ancillary Data

Ancillary information such as surface observations can be easily incorporated into the profile solutions. For example for surface observations it follows from (2) that

$$q(p_S) - q_0(p_S) = g \sum_{i=1}^N \alpha_i q_0(p_S) \phi_i(p_S)$$

and

$$T(p_S) - T_0(p_S) = - \sum_{i=N+1}^M \alpha_i \phi_i(p_S)$$

have the same form as (3) and therefore can be added to the set to yield K+2 equations to solve for M+1 unknowns ( $\alpha$ ).

### 3.3. Accounting for Observational Errors

Observational errors are accounted for in the solution by dividing both  $t^*$  and  $\phi$  by the expected errors for each radiance (or surface) observation. The result is an inverse error weighted least squares solution for  $\alpha$  where the more accurate observations receive the greater weights in the determinations.

Furthermore, the matrix inverse is stabilized by adding a small diagonal element to  $\phi^T \phi$  prior to inversion. That is, the matrix to be inverted in (6) is

$$\phi^T \phi + \gamma I$$

where  $\gamma$  is a scalar (nominally 0.1) and  $I$  is the identity matrix.

### 3.4. Handling the Influences of Clouds

To be discussed at the conference.

### 3.5. Advantages of "One Step" Procedure

The main advantage of the "one step" retrieval method is that it enables the temperature and water vapor profiles and the surface skin temperature to be determined simultaneously using all the radiance information available. This solution alleviates the problem associated with water vapor radiance dependence upon temperature and the dependence of several of the carbon dioxide channel radiance observations used for temperature profiling, on the water vapor concentration. The dependence of the radiance observations on surface emissions is accounted for in the simultaneous solution by the inclusion of surface temperature as an unknown. Also, since only a single matrix inversion is required for the specification of all parameters, the solution is computationally efficient. Finally, ancillary observations of temperature and/or moisture from surface sensors or aircraft, for example, can be readily incorporated in the solution.

### 3.6. Simulation Test of "One Step" Method

The "one step" retrieval method was applied to the VAS data synthesized for the independent sample of radiosonde/radiance sets described in section 2. The temperature and water vapor profile basis functions were taken as the weighting functions for carbon dioxide channels 2 through 5 and water vapor channels 7, 9, and 10, respectively. All spectral VAS radiances with the exception of channels 11 and 12 together with surface temperature and mixing ratio were used for the retrieval thus providing a system of twelve equations and ten unknowns. The errors of surface air temperature and mixing ratio were assumed to be 1°C and 10%, respectively, for

these simulations. The statistical regression solution was used as the a priori estimate for the "one step" retrieval. Figure 3 shows that the "one step" retrieval provides a significant improvement of the profile accuracy achieved by multiple linear regression, particularly for the lower troposphere and for water vapor mixing ratio. These improvements are due to the interdependencies of the water vapor retrieval upon temperature and the influence of water vapor on temperature (carbon dioxide) sounding radiance observations which are accounted for in the "one step" method. (Low latitude results are not shown because of their similarity to those for mid-latitudes.)

daily VAS and TOVS observations obtained in real time at the UW-Madison. Performance evaluations will be made from the daily sounding products produced at the UW-Madison for (a) VAS-only and (b) VAS + MSU. Particular emphasis will be placed on those products which are being evaluated for their operational forecast utility as part of the NOAA Operational VAS Assessment (NOVA) program. Also, the influence of the retrievals on the analyses used to initialize mesoscale forecast models is being evaluated. A comparison between mesoscale numerical weather forecasts generated from (a) VAS alone and (b) VAS + MSU produced soundings will be presented at the conference.

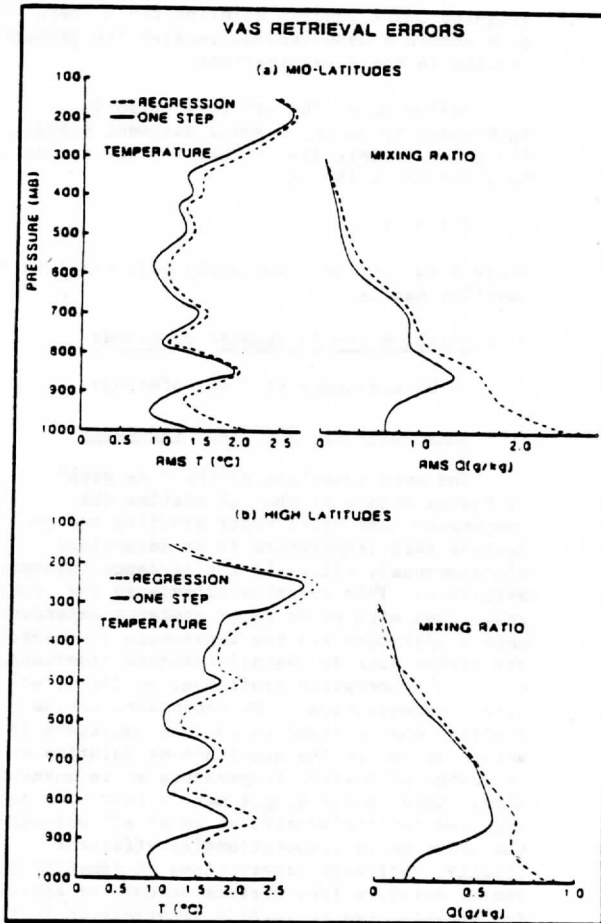


Figure 3: Comparison of retrieval accuracy using multiple linear regression and the "one step" matrix inverse methods. Results are presented for 20 levels between 100 and 1000 mb.

#### 4. VAS/TOVS STUDIES

The "one step" retrieval algorithm is just now being tested as part of the National Environmental Satellite, Data, and Information Service/University of Wisconsin-Madison (UW-Madison) VAS and TOVS sounding retrieval systems. A special retrieval module has been constructed to enable soundings to be performed from the combination of coincident VAS and MSU radiance observations under all cloud conditions. This new retrieval system is to be used with

AN INVESTIGATION OF THE EFFECTS  
OF SPATIALLY AVERAGING SATELLITE BRIGHTNESS MEASUREMENTS  
ON THE CALCULATION OF INSOLATION

by

Catherine Gautier\*

George Diak<sup>†</sup>

and

Serge Masse\*

---

\* California Space Institute, Scripps Institution of Oceanography  
University of California, San Diego La Jolla, CA 92093

<sup>†</sup> Space Science and Engineering Center, University of Wisconsin-Madison  
Madison, WI 53706

### Abstract

An investigation of the effects of spatially averaging brightness measurements from a geostationary satellite on the calculation of insolation is presented. The calculation of insolation from calibrated hourly visible GOES satellite data is based on the model described in Gautier et al., 1980.

A series of experiments are reported in which averaging over scales varying by a factor of 8 to 64 from the initial resolution as well as averaging within the model itself have been performed. Results from these experiments have been intercompared and compared with surface measurements. They indicate that spatially averaged daily insolation can be estimated from mean hourly brightness measurements at an eight-times reduced resolution. Furthermore, the mean insolation is not sensitive to averaging of the physical processes up to the largest spatial averaging of 64.

This result is important, since it may allow a sizable reduction of the data processing necessary to obtain accurate estimations of insolation for various climate studies.

## 1. Introduction

Geostationary satellite data have been shown to be superior to polar orbiter data for insolation estimation due to their increased sampling frequency (Tarpley 1979). Both a statistical method developed by Tarpley (1979) and a physical method developed by Gautier et al. (1980) have yielded very similar result statistics (error of about 10% of the mean of surface measurements). However, the requirement of dense time sampling (5-10 images per day) for large geographical areas means massive amounts of data processing and calculation even for simple models. A reduction of this data processing burden, if it could be accomplished with a minimal loss of accuracy, would greatly benefit the utility of the methods, especially for climate studies where results with high accuracy and over large areas and long durations are required.

Spatial averaging of the raw geostationary satellite data is one potential method to reduce the costs of estimating insolation from geostationary satellites. The purpose of this study is to investigate the effects of such spatial averaging on the calculation of insolation from the simple physical model described in Gautier et al. (1980)

## 2. Methodology

Details of the simple physical model (henceforth referred to as the GDM method for Gautier, Diak, and Masse) are given in Gautier et al. (1980) and will be only minimally reviewed here as it pertains to this study. Our nominal approach in originally testing the GDM method against surface pyranometer measurements was to use a sampling box size of 8 x 8 GOES full resolution pixels. Since there are 8 GOES visible sensors which scan sequential lines, this had the practical advantage of allowing us to use an

average calibration for the eight sensors, which in reality have response functions and calibrations which differ slightly from one another. Angles and physical quantities entering into the physical model were calculated for the center of each 8 x 8 box and assumed not to vary within the area of the box. Within the box for the pixels designated cloudy (i.e., those above a pre-calculated brightness threshold for cloud), a transformation was made from digital brightness counts to energy using the average calibration. An average reflectance for the cloudy pixels within the box was computed from the average energy from these cloudy pixels. An estimate of the insolation for clear pixels within the box (pixels with brightness values below the threshold) was also calculated and then the total insolation for the box estimated as the area weighted sum of clear and cloudy insolation values. The daily insolation is then obtained by integrating in time the hourly insolation estimates. This integration is accomplished by using the trapezoidal method, which requires the determination of the sunset and sunrise times for each box of 8x8.

All averaging experiments were performed over a box size of 64 x 64 full resolution pixels (approximately 100 km square). Experiment one is the previously described "nominal" mode of operation of our model to date. No brightness averaging is performed prior to model processing and angles and atmospheric are recalculated at the centers of sub-boxes of 8 x 8 full-resolution pixels within the original 64 x 64 dimension.

In the subsequent experiments (2-5), the average brightnesses for boxes of 8 x 8 full-resolution pixels are first calculated from the full resolution data. Such a choice of input data was made because it corresponds to the averaging routinely performed by the National Environmental Satellite Data and Information Service (NESDIS) on

geostationary satellite data. In this way the original 64 x 64 image is degraded in resolution by a factor of eight to a dimension of 8 x 8 reduced resolution pixels. In experiments two through five, the sub-box area within this 8 x 8 area at which angles and atmospheric are recalculated is quadrupled until in experiment five, only one value of each physical parameter represents the entire 100 km square box. Logistics of the experiment are detailed in Table 1.

Table 1.

Experiment	Input Data Averaging	Model's param. Averaging	# of Sub Box in Area
1	no averaging	averaging	64
2	8x8 averaging	no averaging	64
3	8x8 averaging	2x2 averaging	16
4	8x8 averaging	4x4 averaging	4
5	8x8 averaging	8x8 averaging	1

### 3. Results

The results of these experiment have been intercompared, and also compared to insolation measured from a pyranometer located somewhere within that 64 x 64 box. The reason why the pyranometer is not located in the center of the 64 x 64 box results from processing restraints (i.e., the processing always started from the top of the image). Such processing was chosen for computational speed. Fig. 1 shows the time series of the three



pyranometers used in the following comparisons. The expected error on individual pyranometer insolation value is about 5% since the calibration accuracy given by manufacturers is 4-5%.

Fig. 2a, b, and c present a comparison between the satellite daily insolation estimates for two (one and two) of the five experiments run, and the pyranometer measurements located within the 64 x 64 pixel box for three stations in Canada over a 28-day period in May 1978. The comparisons are presented in terms of the normalized difference between the pyranometer measurements and the satellite estimates, expressed in percentile. Additionally, the variance of the 64 boxes used to compute the insolation of experiment one is plotted on the same graph, in the same format.

The statistics of the entire data set are presented in Table 2. The first column indicates the module of the mean percentile difference, the second the r.m.s. value of the difference, and the third column the square root of the mean variance, expressed in  $W\cdot m^{-2}$ .

Table 2.

	$ \bar{\Delta}  (\%)$	r.m.s ( $\Delta$ )	$\sqrt{\sigma}$ (I)
1	12.2	12.7	17.3
2	12.5	12.7	19.1
3	12.2	12.7	-
4	12.0	-	11.5
5	12.2	-	-
closest	11.8	14.1	-

mean insolation from pyranometer =  $246.8 W/m^2$

Table 2 represents the distribution of the difference between the satellite estimates and the pyranometer measurements for three of the five tested combinations. From Fig. 2a, b, and c, Fig. 3, and Table 2, it is clear that the difference between the pyranometer measurements and the satellite estimates is relatively small (r.m.s. of 9 to 10% of the mean pyranometer measurements for all of the five experiments). It was not expected, however, to find the close agreement obtained between the results from the full resolution calculations and the results obtained using mean input 8 x 8 brightness. This indicates a quasi-linearity between brightness and insolation for that space scale (about 100 km at this latitude). This could explain the quality of the results obtained from a statistical model, which uses mean brightness and takes into account the geometry of the problem (i.e., Tarpley's approach).

This quasi-linearity could result from the fact that, in the cases tested, the values of satellite-retrieved brightnesses had values within a very limited range (e.g., either relatively spatially homogeneous cloud cover or small clouds that were not much brighter than the underlying surface). A simple examination of the spatial brightness variability eliminated, however, the first possibility. To discount the second possibility we closely examined the region of Lake Ontario, which during the time period of the experiment, was clear of ice and a region of consistently low surface albedo. Over this surface any existing clouds produce a large brightness contrast. Table 3 shows the summary of the results obtained in this lake area for experiments one and five, which represent no data or parameter averaging and the coarsest data and parameter averaging experiments respectively (i.e., the experimental extremes).

Shown are the average satellite-measured 24-hour insolation for the two experiments ( $W\text{-m}^{-2}$ ) and the spatial variance of insolation ( $W\text{-m}^{-2}$ ) for experiment one. Clearly the insolation estimates for these two combinations are very similar in all cases (i.e., even with large spatial variability as indicated by the second term in the column of Table 3, which represents the spatial variance).

Table 3.

Lake Ontario									
Exp. #1	$I(W/m^2)$	Day 122	$\sigma(W/m^2)$	Day 123		Day 124		Day 125	
	323.9		16.7	274.3	10.9	305.0	7.6	88.7	16.3
5	319.2	-	-	271.1	-	300.7	-	91.4	-
		128		129		130		131	
1	141.3		21.1	139.9	20.6	240.8	42.0	327.8	64.0
5	134.7	-	-	126.9	-	237.8	-	359.8	-
		133		135		136		137	
1	159.8		37.2	136.2	39.2	141.0	14.0	131.7	15.2
5	161.1	-	-	133.2	-	138.8	-	123.1	-
		138		141		140		142	
1	181.3		58.2	352.2	17.2	250.9	17.1	380.1	2.0
5	179.8	-	-	347.9	-	247.6	-	375.2	-
		143		144		145		146	
1	365.9		7.9	327.8	11.3	379.7	3.3	354.5	4.2
5	361.2	-	-	323.1	-	374.4	-	348.9	-
		148		149		150		151	
1	347.5		3.9	340.3	4.0	373.9	5.6	287.6	10.7
5	342.9	-	-	335.7	-	369.3	-	283.7	-
		129		147		132			
1	144.0		24.7	354.2	4.7	67.2	7.8		
5	134.6	-	-	349.3	-	56.4	-		

To this point we have only intercompared satellite estimates obtained using different methods, but all averaged over a 64 x 64 box. It is possible that the close correspondence between the results of the two methods (averaged data/averaged insolation) when compared with pyranometer measurements is a consequence of the averaging procedure. This reasoning can be verified by comparing the pyranometer measurements to the estimates made using full resolution input brightness for the box located the closest to the pyranometer location. Such comparisons are presented in Table 4 and statistically in Table 2.

Table 4.

	Ottawa	Montreal	Toronto	Ottawa	Montreal	Toronto
Day	122			123		
pyr (W/m <sup>2</sup> )	229.3	197.0	317.5	144.9	120.1	333.7
closest	219.4	201.9	332.4	90.6	123.8	316.7
Δ(%)	4	2	5	37	3	5
Δ(W/m <sup>2</sup> )	9.9	-4.8	-14.9	-54.3	-3.7	17.0
Day	124			125		
pyr	310.3	-	251.4	276.5	-	52.1
closest	318.6	-	281.2	305.7	-	50.7
Δ(%)	3	-	12	11	-	3
Δ	-8.3	-	-29.8	-29.2	-	1.4
Day	128			129		
pyr	240.3	-	59.9	148.9	-	176.5
closest	248.6	-	49.8	127.8	-	155.3
Δ(%)	3	-	17	14	-	12
Δ	-8.3	-	10.1	21.1	-	21.2

Table 4., Continued

	Ottawa	Montreal	Toronto	Ottawa	Montreal	Toronto
Day	130			131		
pyr	126.5	85.1	182.3	333.4	333.5	298.8
closest	112.1	88.5	175.4	361.5	364.9	324.3
$\Delta(\%)$	11	4	4	8	9	9
$\Delta$	14.4	-3.4	6.9	-28.1	-31.8	-25.5
Day	133			135		
pyr	140.2	183.6	94.4	119.2	130.1	96.9
closest	107.8	224.9	84.5	117.8	124.5	97.7
$\Delta(\%)$	23	23	11	1	3	1
$\Delta$	32.5	-41.4	9.9	1.4	5.6	-0.8
Day	136			137		
pyr	321.0	286.1	130.6	55.4	187.2	164.2
closest	343.1	180.4	155.0	69.3	149.8	223.8
$\Delta(\%)$	7	37	19	25	20	36
$\Delta$	-22.1	105.7	-24.3	-13.8	37.4	-59.6
Day	138			141		
pyr	188.8	195.6	1982.0	333.8	292.9	348.6
closest	192.4	182.7	186.5	377.3	326.3	365.1
$\Delta(\%)$	2	7	2	13	11	5
$\Delta$	-3.6	12.9	-4.5	-43.5	-33.3	-16.5
Day	139			140		
pyr	329.8	310.8	329.8	218.5	239.7	116.8
closest	376.3	375.9	376.2	263.2	255.1	97.8
$\Delta(\%)$	14	21	14	20	6	16
$\Delta$	-46.5	-65.1	-46.4	-44.7	-15.4	19.0
Day	142			143		
pyr	346.5	353.4	343.1	327.3	332.5	308.7
closest	371.9	375.3	382.2	376.1	368.8	334.4
$\Delta(\%)$	7	6	11	15	11	8
$\Delta$	-25.4	-21.9	-39.1	-48.8	-36.2	-25.8

Table 4., Continued

	Ottawa	Montreal	Toronto	Ottawa	Montreal	Toronto
Day	144			145		
pyr	328.8	329.9	310.4	325.5	334.0	347.6
closest	376.0	383.7	363.5	379.2	386.6	386.7
$\Delta(\%)$	14	16	17	17	17	11
$\Delta$	-47.2	-53.8	-53.1	-53.8	-56.6	-39.0
Day	146			148		
pyr	298.0	285.5	337.7	320.6	324.7	344.9
closest	342.8	344.1	375.0	339.2	343.9	354.1
$\Delta(\%)$	15	21	11	6	6	3
$\Delta$	-44.8	-58.5	-37.3	-18.6	-19.3	-9.2
Day	149			150		
pyr	302.8	327.2	325.1	299.7	264.9	324.5
closest	342.2	386.3	343.1	356.3	359.3	368.9
$\Delta(\%)$	13	18	6	19	36	14
$\Delta$	-39.4	-59.0	-18.0	-56.6	-94.3	-44.4
Day	151			147		
pyr	176.5	234.5	302.2	319.8	337.1	337.5
closest	171.7	271.7	321.0	352.9	359.3	357.3
$\Delta(\%)$	3	16	6	10	7	6
$\Delta$	4.8	-37.4	-18.8	-33.2	-22.3	-19.8
Day	132					
pyr	84.0	183.6	64.6			
closest	89.9	201.2	54.1			
$\Delta(\%)$	7	10	16			
$\Delta$	-5.9	-17.6	10.5			

The first column in Table 4 indicates the pyranometer measurement, the second is the "closest", the third gives the difference between the "closest" and the pyranometer, and the fourth column the same difference expressed in percentage of the pyranometer measurements. Again, the results were not anticipated since the r.m.s. of the difference for the

"closest" full resolution box is even larger than that for the spatial averages over 64 x 64. This can be understood from the intercomparison approach. In the intercomparison, instantaneous satellite estimates are averaged over space equivalent to time averaged pyranometer measurements. This is correct only if the cloud drift over the time averaging period is equivalent to the spatial averaging. Thus, the comparison with the "closest" for a 12 to 14 km box would probably provide better results if the pyranometer measurements were averaged over a shorter time period. Unfortunately, pyranometer measurements are provided in the form of hourly averages. We can, however, understand the previous results by looking in more detail at each individual case to infer the causes.

We carefully examined the cases for which the difference (in percent) of the previous comparisons ("closest" vs. pyranometers) were larger than 15%. We found two classes of errors. First, a class for which the spatial variability was very large (as deduced from the estimated spatial variance). In these cases it was always possible to find an adjacent box for which the satellite insolation estimate was within a few percent of the pyranometer measurements. Second, a class for which the discrepancy between the satellite estimates and the pyranometer measurements occur when the insolation is large; most of the time larger than  $312.5 \text{ W/m}^2$ . In these cases the spatial variability was relatively small and the conditions were almost clear, although not entirely. Examination of the cloud albedos obtained in the intermediary calculations of the model showed that they were in the vicinity of 3 to 6%. We interpreted this as corresponding to partial filling of the 1 km pixel. Visual examinations of the images corresponding to these cases enhanced our confidence in this explanation.

From these types of results it became evident to us that it was necessary to improve our modeling in the quasi-clear air conditions.

This has been done, and the results obtained by improving the model were reported in Diak and Gautier, 1983.

#### 4. Conclusions and Recommendations

The results presented and discussed above indicate that spatially averaged daily insolation can be estimated from mean hourly brightness at a resolution of about 14 km (averages of eight full resolution pixels at about 40 latitude). These results have been obtained by spatially averaging original full resolution (about 1.7 km) brightness data, but the same conclusions would probably hold for implicit sensor-averaged brightness provided that the sensor averaging procedure is sufficiently isotropic.

Since our results indicate a quasi-linearity between linear combinations of hourly brightness and daily insolation at the 100 km scale, and since the results of experiment 5 are comparable to the other results for the mean insolation, it appears that it may even be possible to use input hourly brightness averaged over as large an area as 100 km to obtain adequate mean insolation values. Therefore, we conclude that the optimal averaging combinations of the input data and within the model which require the least amount of computation but retain the important spatial characteristics of the field analyzed are an average of eight (8) of the input brightness with an average of four (4) within the model to calculate hourly and daily insolation.



Acknowledgements

This research has been supported by NOAA grant NA81AA-H-00024, mod. 2 and by a joint NSF-NOAA grant ATM-8019529.

We would like to thank the Space Science and Engineering Center staff for its continuous support during the realization of this work. We also thank Dan Tarpley from NOAA for his interest in our work and for suggesting that we use our model in NOAA operational conditions. Finally, we thank Ellen Barnier for having typed the tables which form a large part of this paper.

## REFERENCES

- Coulson, K.L., 1959: Characteristics of the radiation emerging from the top of a Rayleigh atmosphere, 1 and 2. Planet. Space Sci. 1, 256-284.
- Diak, G.R. and C. Gautier, 1983: Improvements to a simple physical model for estimating insolation from GOES data. Jour. Clim. and Appl. Meteor. 22, 505-508.
- Gautier, C., 1982: Mesoscale insolation variability derived from satellite data. Jour. Appl. Meteor. 21, 51-58.
- Gautier, C., G. Diak, and S. Masse, 1980: A simple physical model to estimate incident solar radiation at the surface from GOES satellite data. Jour. Appl. Meteor. 19, 1005-1012.
- Lacis, A.A. and J.E. Hansen, 1974: A parameterization for the absorption of solar radiation in the earth's atmosphere. J. Atmos. Sci. 31, 118-133.
- Paltridge, G.W., 1973: Direct measurement of water vapor absorption of solar radiation in the free atmosphere. J. Atmos. Sci. 30, 156-160.
- Tarpley, J.D., 1979: Estimating incident solar radiation at the surface from geostationary satellite data. J. Appl. Meteor. 18, 1172-1181.

## FIGURES

Fig. 1: Pyranometers Daily Insolation Time Series for Ottawa, Montreal, and Toronto during the Time Period of the Experiments (May 1978).

Fig. 2a: Normalized Difference:  $(\text{Pyranom. Meas.} - \text{Satellite est.}) / \text{Pyranom. meas.}$  for Ottawa.

Fig. 2b: Same as a, but for Montreal.

Fig. 2c: Same as A, but for Toronto.

Fig. 3: Distribution of the Normalized Difference: for experiments one and two.

## TABLES

- Table 1. Details of input data averaging and model parameters for experiments one through five.
- Table 2. Result statistics for experiments one through five. Shown are the module of mean percentile difference between pyranometer and satellite daily insolation estimates  $|\Delta|$  (%), r.m.s. value of this difference (%), and the square root of the mean variance  $\sqrt{\sigma}$  ( $\text{W-m}^{-2}$ ).
- Table 3. Comparison of satellite insolation calculations between experiment one (no data or parameter averaging) and experiment five (coarsest data and parameter averaging). Shown are 24 hour average insolation  $I$  ( $\text{W-m}^{-2}$ ) for experiments one and two, and the spatial variance of insolation  $\sigma$  ( $\text{W-m}^{-2}$ ) for experiment 1.
- Table 4. Comparisons between pyranometer insolation measurements and "closest" satellite measurement. Shown are 24-hour average insolation from pyranometer and satellite measurements ( $\text{W-m}^{-2}$ ) and  $\Delta$ , the difference between the two expressed both in  $\text{W-m}^{-2}$  and as a percent of the pyranometer measurement.

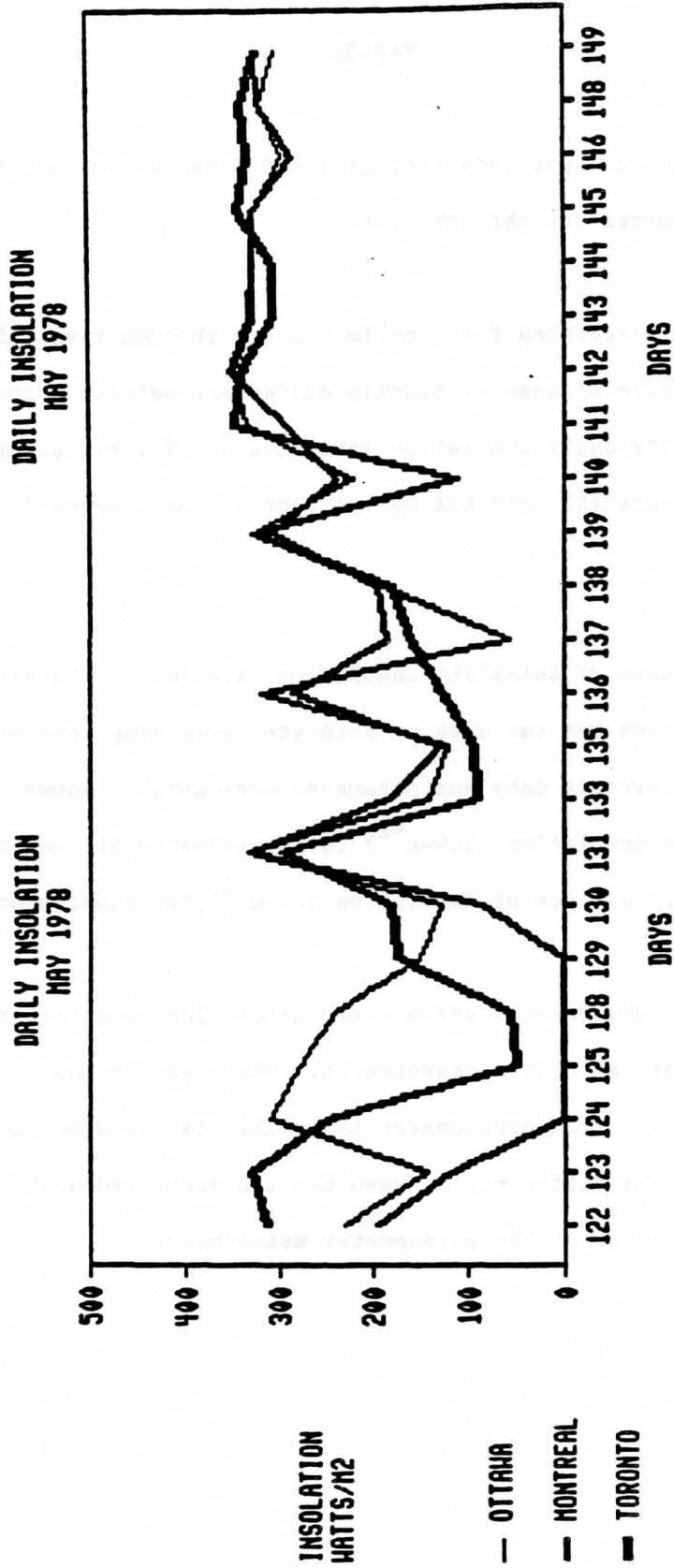


Figure 1

## TABLES

- Table 1. Details of input data averaging and model parameters for experiments one through five.
- Table 2. Result statistics for experiments one through five. Shown are the module of mean percentile difference between pyranometer and satellite daily insolation estimates  $|\Delta|$  (%), r.m.s. value of this difference (%), and the square root of the mean variance  $\sqrt{\sigma}$  ( $W\text{-m}^{-2}$ ).
- Table 3. Comparison of satellite insolation calculations between experiment one (no data or parameter averaging) and experiment five (coarsest data and parameter averaging). Shown are 24 hour average insolation  $I(W\text{-m}^{-2})$  for experiments one and two, and the spatial variance of insolation  $\sigma(W\text{-m}^{-2})$  for experiment 1.
- Table 4. Comparisons between pyranometer insolation measurements and "closest" satellite measurement. Shown are 24-hour average insolation from pyranometer and satellite measurements ( $W\text{-m}^{-2}$ ) and  $\Delta$ , the difference between the two expressed both in  $W\text{-m}^{-2}$  and as a percent of the pyranometer measurement.

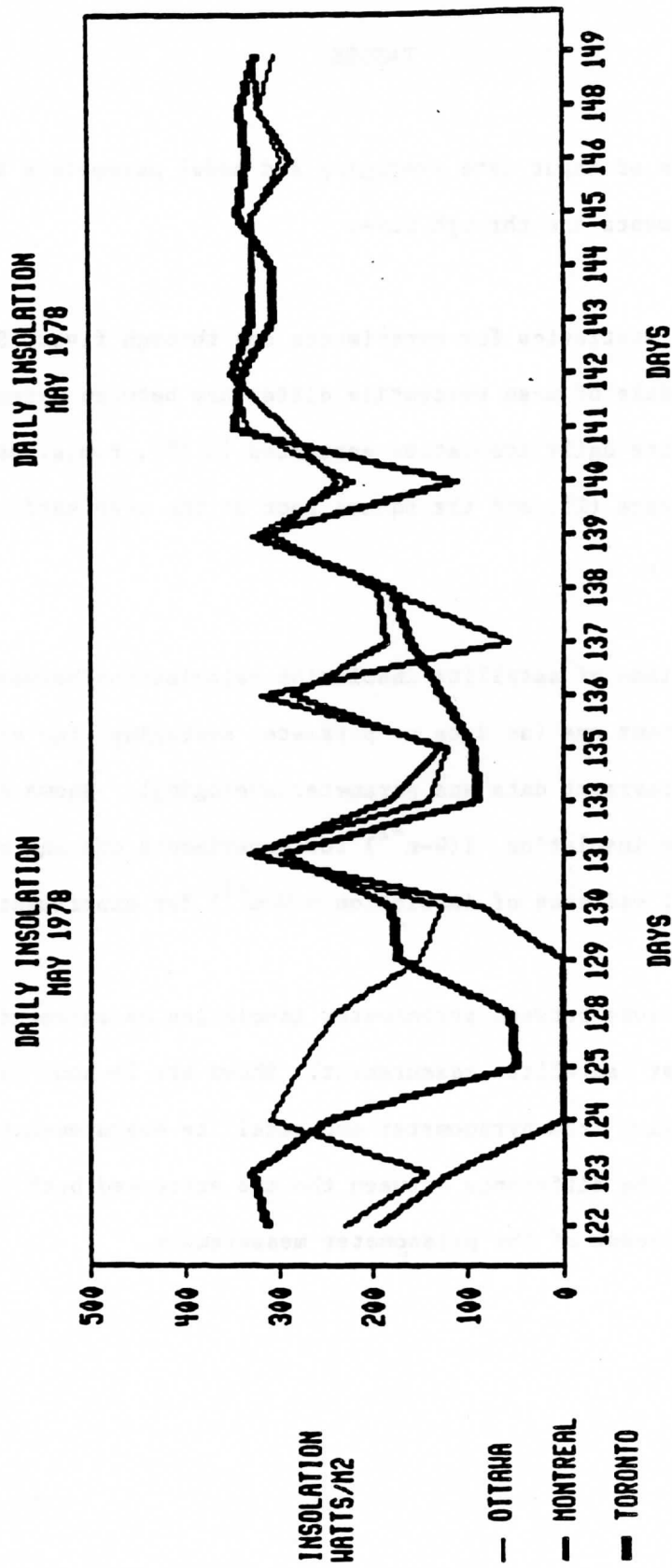


Figure 1

**DIFFERENCE PYRANOMETER-SATELLITE (MEAN)  
AND SPATIAL VARIANCE (MEAN)**

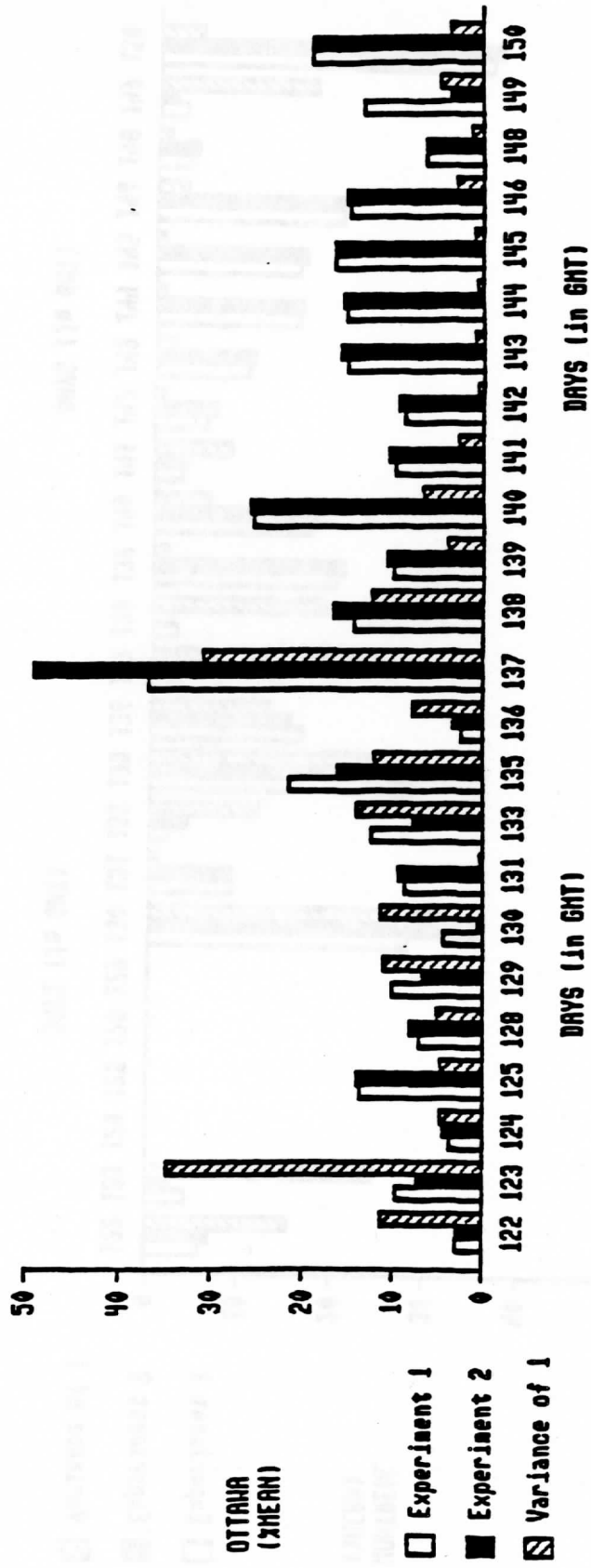


Figure 2a



**DIFFERENCE PYRANOMETER-SATELLITE ( $\lambda$ MEAN)  
AND SPATIAL VARIANCE ( $\lambda$ MEAN)**

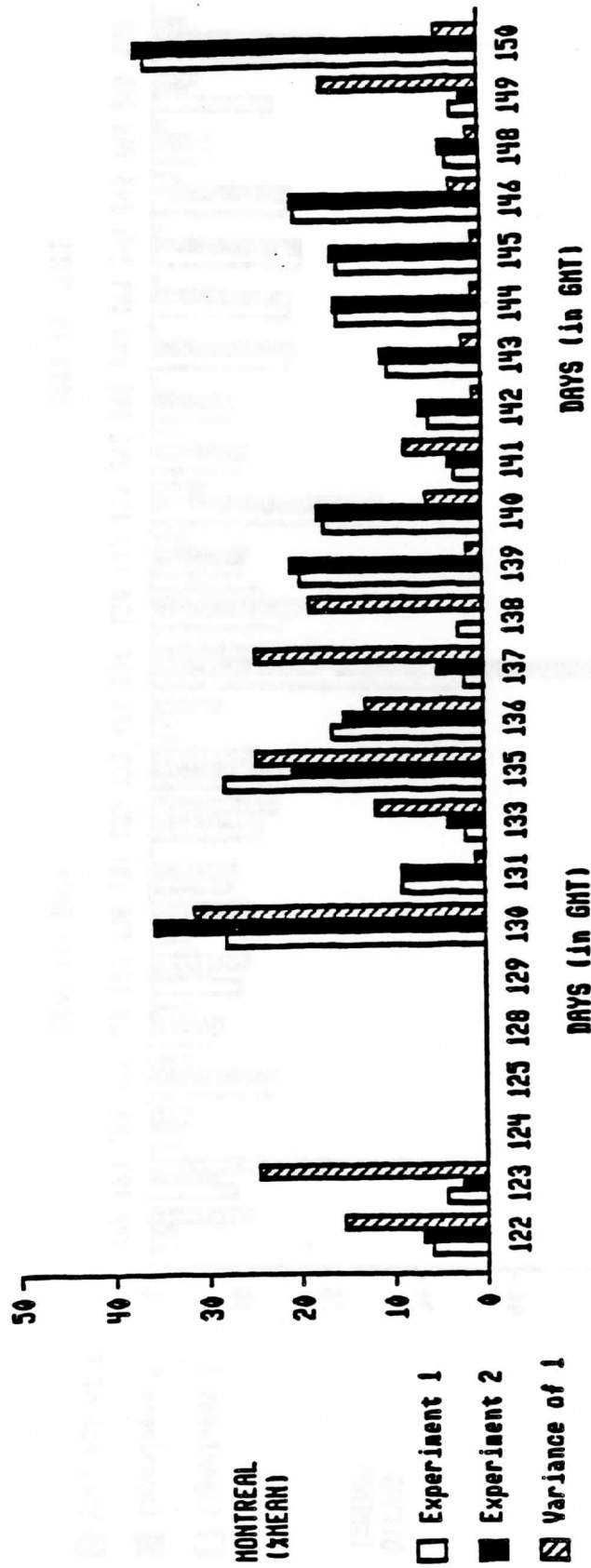


Figure 2b

**DIFFERENCE PYRANOMETER-SATELLITE ( $\Delta$ MEAN)  
AND SPATIAL VARIANCE ( $\Delta$ MEAN)**

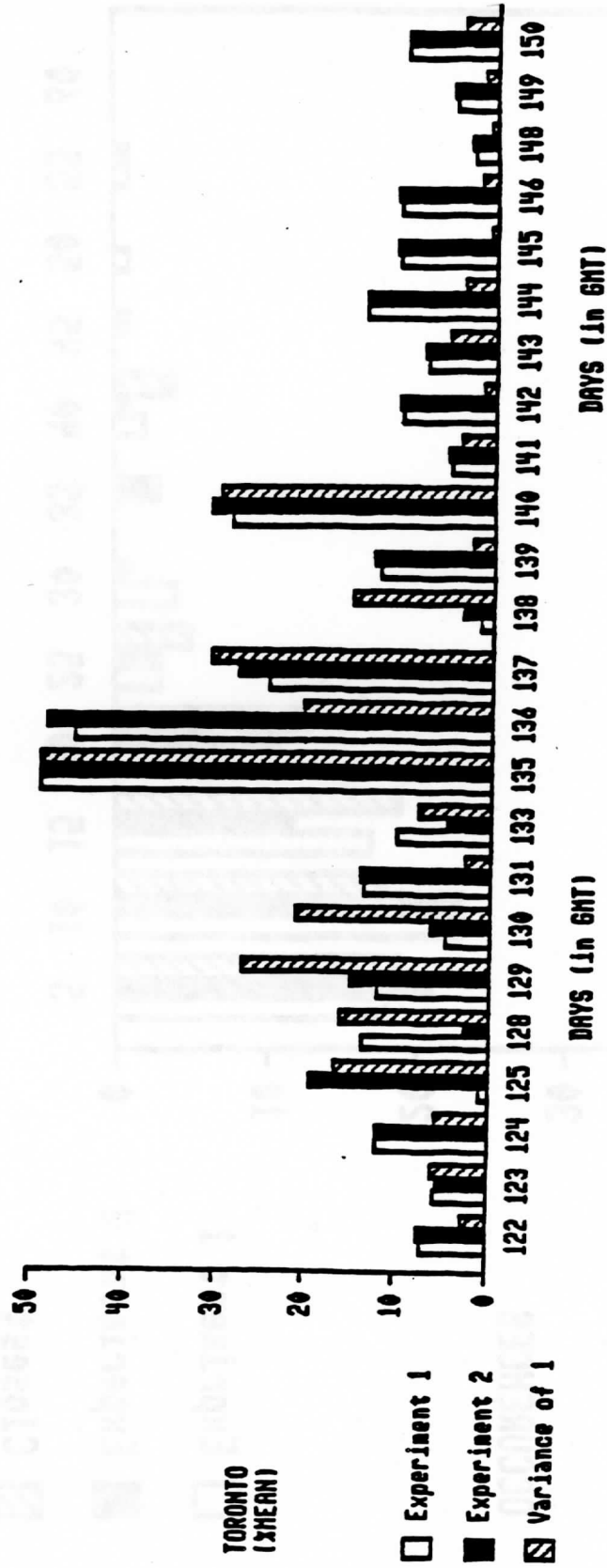


Figure 2c

# DISTRIBUTION OF DIFFERENCE (%MEAN)

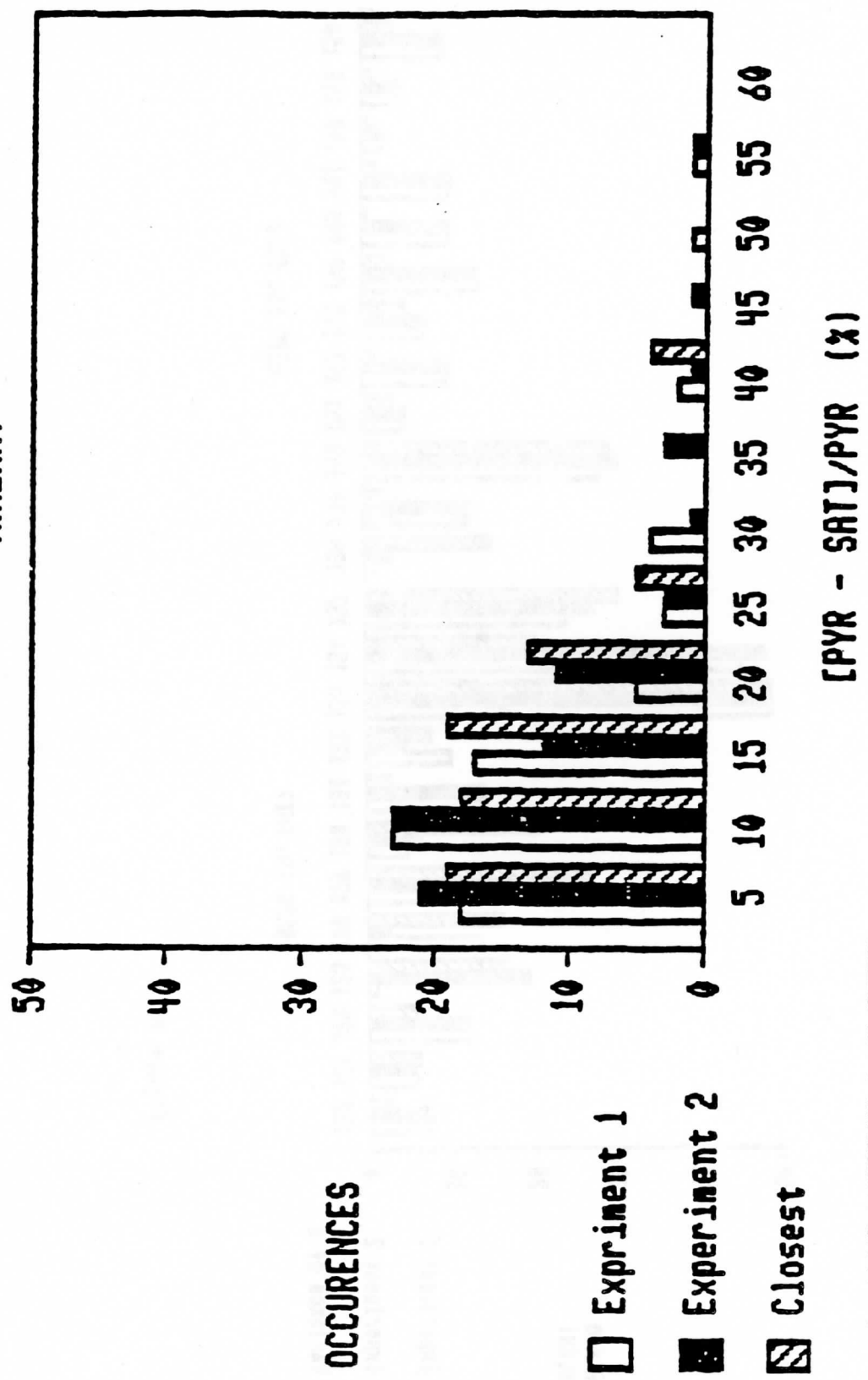


Figure 3

# A Note on Water Vapor Wind Tracking Using VAS Data on McIDAS

Tod R. Stewart  
Christopher M. Hayden  
William L. Smith

## Abstract

Eleven data sets where water vapor winds were obtained from the GOES-5 6.7 micrometer measurement over the U. S. are compared with rawinsondes. Over 2000 point comparisons are made for a) an arbitrary height assignment of 400 mb and b) a height assignment determined by matching the measured brightness temperature to the temperature structure represented in the LFM analysis. It is shown that the water vapor winds provide uniform horizontal coverage of midlevel flow with high accuracy (8 mps vector RMS). Furthermore, the radiometric height assignment significantly improves the accuracy.

## 1. Introduction

It has been recognized for some time that water vapor structure visible in infrared imagery offers a potential for obtaining motion vectors when several images are considered in sequence. The earliest attempts were made with data obtained from the Nimbus-5 Temperature/Humidity Infrared Radiometer (Allison et al., 1972). Of course the polar orbiting Nimbus satellite did not offer a suitable basis for obtaining wide or timely coverage, but the feasibility of the concept was demonstrated, and possibly encouraged inclusion of a water vapor channel on the METEOSAT geostationary satellite. Research with these data led Eigenwillig and Fischer (1982) to conclude that mid-level wind vectors could be successfully obtained with an RMS speed accuracy compared to rawinsondes of 5 m/s. GOES-4 followed METEOSAT with water vapor measuring channels on the VISSR Atmospheric Sounder, VAS; channels which can be used either for sounding or for imaging. Moser and Stewart (1981) investigated the latter as a source for wind vectors, examining in particular the trade-offs involved in the choice of time lapse between images. These efforts were limited insofar as only a single data set was considered and the data themselves were poor; GOES-4 had one bad sensor (of two) which caused every other line of data to be missing.

Water vapor imaging has continued with GOES-5 and 6, and found great favor among operational meteorologists to the extent that they replace the usual infrared image four times each day at 530, 1130, 1730, and 2030 GMT. These images are used for synoptic interpretation. Water vapor winds are not generated operationally, but they have been processed routinely on a research basis at the Cooperative Institute for Meteorological Satellite Studies (CIMSS) at the University of Wisconsin.

## 2. Measurement technique.

The tracking of water vapor structure to obtain wind vectors is an extension of the technology developed to obtain winds from cloud motions on geostationary satellite images. Two or three images separated in time are loaded in the McIDAS computer with geometric fidelity ensured by navigation algorithms implicit in the system (Suomi et al., 1983). Changes in the cloud (water vapor) field are followed in time, either by a direct, operator controlled tracking or by a cross correlation method which matches small patterns in the successive images. For the case of water vapor, only the first method has so far proved viable. The imagery is too amorphous (especially given the 16 km resolution) to be unambiguous to correlation methods. In this study all winds were determined by single pixel tracking over 3 images individually separated by an hour. The three images yield two estimates of the wind which are objectively compared and rejected if they differ by greater than 5 mps.

To be a valid tracer of the wind, a feature must be a quasi-passive, shallow body drifting with the wind during the time of the series of images being used. Clouds have been shown to be suitable tracers even though there is some shape evolution during the tracking period. Water vapor inhomogeneities also prove to be valid tracers. The "trackability" depends on the operators' distinguishing features which are small enough to represent a uniform flow of air and yet large enough to have a lifetime sufficient for identification over the interval of several images. The lifetime depends on their dissipation by atmospheric turbulence, and is therefore a function of the size of the tracer and the eddy diffusivity of the atmosphere. Bauer (1974) in a review of experimental data on the horizontal spreading of inert tracers shows that a tracer with 100 km width will have, on the average, a lifetime of one day. However, depending on the eddy diffusivity this feature can have a lifetime from 3 hours to more than three days. By contrast, a 10 km feature will have an average lifetime of only 1 hour.

An example of the imagery used to generate water vapor winds in this study is given in Figure 2. This picture is taken from the McIDAS television screen with the 6.7 micrometer image enhanced to delineate the moisture features. Bright white represents cloud. Gray features are areas of high water vapor concentration which give way to the dark or dry areas associated with midlevel subsidence. Winds derived from this (and two subsequent images) are shown in Figure 2a. Note the uniform coverage obtained, even in areas which appear dark and featureless in the image. This coverage, which is typically obtained by the experienced operator, has been the source of some skepticism. One might reasonably ask, "Is the operator not really following the bright cloud tracers and using his imagination, tempered by synoptic experience, to fill in between?" Certainly to some extent these suspicions are true (which helps to explain the failure of objective correlation techniques). The operator undoubtedly has a good conception of the midlevel flow based on the observable motion of the clouds, the synoptic systems portrayed, and on his meteorological knowledge. He uses this filter in perceiving motions in the moisture field. But however it is accomplished, the important consideration is whether or not his perceptions yield realistic wind vectors. This can and will be verified in the results discussed below.

### 3. Height Assignment

The radiance sensed by the 6.7 micrometer water vapor channel corresponds to a layer-averaged "Planck" radiance emerging from a portion of the atmosphere whose location is determined by two factors: 1) the profile of the emissivity of the radiating water vapor, and 2) the profile of the transmissivity of the entire depth of water vapor above each radiating level. The emissivity profile varies with the profile of water vapor mixing ratio while the transmissivity profile varies with the profile of integrated precipitable water vapor. Thus radiation measured from space is primarily representative of the uppermost moist region (high emissivity) with dry air (high transmissivity) above. The thickness of the layer radiating to space increases as the mixing ratio profile becomes more uniform (i.e., the emissivity and transmissivity profiles are more slowly varying with altitude).

The magnitude of the radiance observed is proportional, through Planck's law, to the mean temperature of the atmosphere as weighted by the product of the emissivity and transmissivity profiles (the temperature profile weighting function). The VAS 6.7 micrometer weighting function is gaussian with a half-width of about 300 mb and a peak ranging in pressure altitude between the 200 and 500 mb levels, depending on the water vapor profile characteristics. Examples for a similar channel on the METEOSAT can be found in Fischer et al., 1981). Since the mid to upper troposphere region contributing to the 6.7 micrometer radiance usually exhibits a constant lapse rate in temperature, the radiometric temperature observed (i.e., the brightness temperature) is generally close to the atmospheric temperature at the pressure level where the weighting function (and moisture as seen from above) is a maximum. Figure 1 shows a scatter diagram relating brightness temperatures measured with GOES-5 to temperature observed by radiosonde at the level where the water vapor wind vector agreed most closely with the rawinsonde wind observation. Given the considerable noise associated with the matching (especially since winds were considered only at mandatory pressure levels for the rawinsonde), the correspondence justifies assigning the pressure altitude of the vapor wind vector as the pressure where the observed brightness temperature matches the environmental air temperature. In the CIMSS water vapor tracking program, the same software used to provide a first guess temperature profile for temperature retrievals is used to provide the environmental temperature.

It is important to note that the margin for altitude assignment error is smaller for the water vapor winds than for the conventional cloud winds which use an 11 micrometer "window" brightness measurement. This is because the range of 6.7 micrometer brightness temperatures due to water vapor emissivity variations is small (approx. 10 C), since the radiance always emanates from the upper troposphere. 11 micrometer window brightness temperatures can vary with cloud emissivity from values close to the earth's surface temperature to the cloud top temperature (as much as 100 C variation for the case of cirrus).

#### 4. Results

Eleven data sets were produced for this study. Ten of these originated from July 1984 and the eleventh from August 1983; a case study of hurricane Alicia. Typically, 600 water vapor winds were generated for each case over the geographical area shown in Fig. 2. Figure 3 shows the derived vectors and the pressure altitudes assigned. From these winds, approximately 2000 were matched with and compared with radiosondes measurements, in two ways designed to evaluate a) their generic accuracy, and b) the advantage of brightness temperature cloud height assignment. Any vapor wind within a 2 degree (latitude) radius of a rawinsonde is candidate for verification. It is compared to the rawinsonde measurement at the "standard" 400 mb level and at the "assigned" level. For the latter, the nearest rawinsonde mandatory level was chosen. Thus vapor winds from 226-274 mb are compared with the 250 mb rawinsonde, 275-350 mb are compared with the 300 mb etc.

Tables 1b and 2b presents statistics where all all vapor winds are compared at 400 mb. Tables 1a and 2a treats the same winds at "assigned" levels. Comparisons are given for both speed and vector differences. The outstanding result is that the height assignment clearly improves the comparison. The RMS difference for speed is reduced from 6.8 to 4.4 mps whereas that for vector difference is lowered from 8.8 to 7.9 mps. An even more dramatic indication of the value of height assignment is shown by the sample standard deviations. For the "assigned" vectors the variance of the vapor winds closely follows that of the rawinsonde for the 11 samples. For the 400 mb vectors the variance is in every case too low, frequently by a large amount. Figure 3b clearly shows how the improvement is obtained. This figure shows the pressures at which the vapor winds were assigned. The darker (drier) areas show winds at higher pressures whereas the brighter (wetter) areas show winds at upper levels. The high wind speeds at higher levels largely account for the improvement in vector variance mentioned above.

In terms of absolute accuracy the water vapor winds appear to be more than competitive with cloud drift winds which have received wide acceptance in operational application. Table 3 gives some of the recent verification statistics gathered for the latter over the last two years (Whitney, 1983). In general, the vector difference for the cloud drift winds is given as 10 mps or greater whereas that for the water vapor winds studied here is approximately 8 mps.

#### 5. Conclusion

This study has demonstrated that water vapor features observed at 6.7 micrometers permit the derivation of accurate midlevel wind vectors with uniform horizontal coverage at the synoptic scale. These vectors are a valuable addition to cloud motion vectors because they generally represent a level of flow unobtainable with the latter. Also, the water vapor winds are often able to define jet cores where there are no visible clouds. It furthermore appears from these results than the vapor winds are more accurate than cloud vectors, chiefly because of a

relatively unambiguous height assignment obtainable from the measured brightness temperature.

This study may be criticized on the grounds of showing only the result of a highly skilled operator's acting under "research" conditions with a sophisticated tracking system. It has been shown at CIMSS (though not in these results) that equivalent water vapor winds can be produced under operational time constraints by a number of different operators. As a word of caution, however, it certainly helps to have an experienced operator with meteorological insight. There appears to be considerable art involved in the generation of these data. A consequence is that it will be difficult to fully automate the water vapor wind extraction technique. But a similar situation has not precluded the operational use of manually generated high level cloud vectors with good success. It appears that with the implementation of an operational VAS, the generation of water vapor winds should receive a high priority.



References:

Allison, L. J., J. Steranka, G. T. Cherrix, and E. Hilsenrath, 1972: Meteorological application of the NIMBUS 4 Temperature Humidity Infrared Radiometer, 6.7 micron channel data. Bull. Amer. Meteor. Soc. 53, 526-535.

Eigenwillig, N., and H. Fischer, 1982: Determination of midtropospheric wind vectors by tracking pure water vapor structure in METEOSAT water vapor image sequences. Bull. Amer. Meteor. Soc. 63, 44-57.

Fischer, H., N. Eigenwillig, and H. Maller, 1981: Information content of METEOSAT and NIMBUS/THIR water vapor channel data; altitude association of observed phenomena. J. Appl. Meteor. 20, 1344-1352.

Mosher, F. R., and T. R. Stewart, 1981: Characteristics of water vapor tracked winds. NAVENPERRSCHFAC Contractor Report, CR-81-06, 51pp.

Suomi, V. E., R. Fox, S. S. Limaye, and W. L. Smith, 1983: McIDAS III: A modern interactive data access and analysis system. J Climate Appl. Meteor., 22, 765-778.

Whitney, L. F., 1983: International comparison of satellite winds-an update. Advances in Space Research, 2, 73-77.

Figure captions:

Figure 1. Scatter diagram of radiosonde temperatures vs. VAS 6.7 micrometer brightness temperature measurements for matched samples of water vapor tracked and rawinsonde measured winds.

Figure 2: GOES-5 6.7 micrometer imagery for 1031 GMT 16 August 1983.

Figure 3. a) Water vapor winds tracked from GOES 6.7 micrometer measurements at 1031, 1131, and 1231 GMT 16 August 1983. b) Pressure levels associated with water vapor winds (cb). Brighter values in darker (drier) areas discriminate higher pressures.

TIME	WIND	TEMP	WIND	TEMP	WIND	TEMP
08.0	42.0	857	13.0	885	8558	
09.11	47.1	857	13.0	885	8558	
10.2	52.2	857	13.0	885	8558	
11.3	57.3	857	13.0	885	8558	
12.4	62.4	857	13.0	885	8558	
13.5	67.5	857	13.0	885	8558	
14.6	72.6	857	13.0	885	8558	
15.7	77.7	857	13.0	885	8558	
16.8	82.8	857	13.0	885	8558	
17.9	87.9	857	13.0	885	8558	
19.0	93.0	857	13.0	885	8558	
20.1	98.1	857	13.0	885	8558	
21.2	103.2	857	13.0	885	8558	
22.3	108.3	857	13.0	885	8558	
23.4	113.4	857	13.0	885	8558	
24.5	118.5	857	13.0	885	8558	
25.6	123.6	857	13.0	885	8558	
26.7	128.7	857	13.0	885	8558	

Table 1. Water-vapor winds compared with rawinsondes; speed RMS differences.

Water Vapor winds compared with nearest Mandatory Level

<u>Day</u>	<u>#Comparisons</u>	<u>RMS(m/s)</u>	<u>corr coef</u>	<u>Data <math>\sigma</math></u>	<u>STND <math>\sigma</math></u>
83228	282	3.69	.871	7.40	6.68
84192	153	4.60	.935	12.37	11.46
84193	148	4.23	.838	7.62	6.47
84194	159	4.64	.808	7.60	6.74
84198	169	5.32	.884	11.15	9.18
84199	226	6.61	.815	9.21	10.91
84201	164	4.15	.901	9.44	8.08
84202 (00 Z)	170	3.25	.882	6.62	6.66
84202 (12 Z)	179	3.13	.889	6.72	6.52
84208 (00 Z)	181	4.58	.896	10.30	9.47
84208 (12 Z)	275	4.67	.855	8.97	7.88
Total # of comparisons		2106			
Avg. Speed Diff. RMS (m/s)		4.44			

All Water Vapor winds compared with 400 mb.

<u>Day</u>	<u>#Comparisons</u>	<u>RMS(m/s)</u>	<u>corr coef</u>	<u>Data <math>\sigma</math></u>	<u>STND <math>\sigma</math></u>
83228	282	6.21	.729	5.54	6.68
84192	153	8.38	.799	7.93	11.46
84193	148	7.06	.660	6.52	6.47
84194	159	5.70	.802	7.15	6.74
84198	169	8.33	.747	7.88	9.18
84199	226	8.66	.801	8.22	10.91
84201	164	7.62	.859	8.16	8.08
84202 (00 Z)	170	5.55	.802	5.75	6.66
84202 (12 Z)	179	4.98	.795	5.25	6.52
84208 (00 Z)	181	6.48	.864	8.93	9.47
84208 (12 Z)	275	5.85	.791	7.24	7.88
Total # of comparisons		2106			
Avg. Speed Diff. RMS (m/s)		6.80			

Table 2. Water-vapor winds compared with rawinsondes; vector differences.

<u>Day</u>	<u>#Comparisons</u>	<u>RMS(m/s)</u>	<u>corr coef</u>	<u>Data <math>\sigma</math></u>	<u>STND <math>\sigma</math></u>
83228	269	6.84	.858	12.45	12.65
84192	147	7.79	.926	17.40	18.23
84193	144	7.22	.866	13.81	13.89
84194	155	6.45	.873	12.63	11.94
84198	165	9.10	.860	16.87	16.31
84199	225	9.22	.862	15.20	16.90
84201	152	9.01	.831	15.74	15.17
84202 (00 Z)	159	5.59	.874	10.53	10.97
84202 (12 Z)	174	6.27	.869	11.65	12.02
84208 (00 Z)	177	7.26	.910	16.15	15.97
84208 (12 Z)	256	6.94	.872	13.52	13.36
Total # of comparisons		2023			
Avg. Vector Diff. RMS (m/s)		7.88			

All Water Vapor winds compared with 400 mb.

<u>Day</u>	<u>#Comparisons</u>	<u>RMS(m/s)</u>	<u>corr coef</u>	<u>Data <math>\sigma</math></u>	<u>STND <math>\sigma</math></u>
83228	269	7.99	.808	8.98	12.65
84192	147	10.51	.871	11.57	18.23
84193	144	9.05	.765	10.14	13.89
84194	155	7.52	.820	10.66	11.94
84198	165	10.31	.811	12.20	16.31
84199	225	10.58	.823	12.31	16.90
84201	152	10.72	.746	11.31	15.17
84202 (00 Z)	159	6.95	.810	8.03	10.97
84202 (12 Z)	174	6.83	.834	9.24	12.02
84208 (00 Z)	177	8.55	.864	12.73	15.97
84208 (12 Z)	256	7.88	.811	10.67	13.36
Total # of comparisons		2023			
Avg. Vector Diff. RMS (m/s)		8.81			

Table 3. Computability of cloud-drift and water-vapor winds.

Data Set	Avg. Vector Mag. Diff. RMS (m/s) Level			#Comparisons Level		
	Low	Mid	High	Low	Mid	High
1/15/83 - 2/13/83						
GMS (Japan)	4.3	-	15.2	263	-	332
GOES (NESDIS)	5.3	-	16.0	604	-	92
METEOSAT (ESA)	9.6	11.1	12.4	516	389	411
JULY 1983						
GMS (Japan)	3.8	-	11.3	196	-	860
GOES (NESDIS)	5.5	-	9.2	571	-	166
METEOSAT (ESA)	7.1	10.8	10.3	184	180	631
1/21/84 - 2/13/84						
GMS (Japan)	4.9	-	10.7	339	-	171
GOES (NESDIS)	4.9	-	11.5	428	-	90
METEOSAT (ESA)	6.2	10.3	10.6	370	381	693
JULY 1984						
GMS (Japan)	-	-	-	-	-	-
GOES (NESDIS)	5.5	-	9.2	554	-	169
METEOSAT (ESA)	5.9	8.3	10.3	292	328	534
Water Vapor	-	-	7.9	-	-	2023
Water Vapor*	-	8.8	-	-	2023	-

\* Comparisons are made with 400 mb rawinsonde measurements.

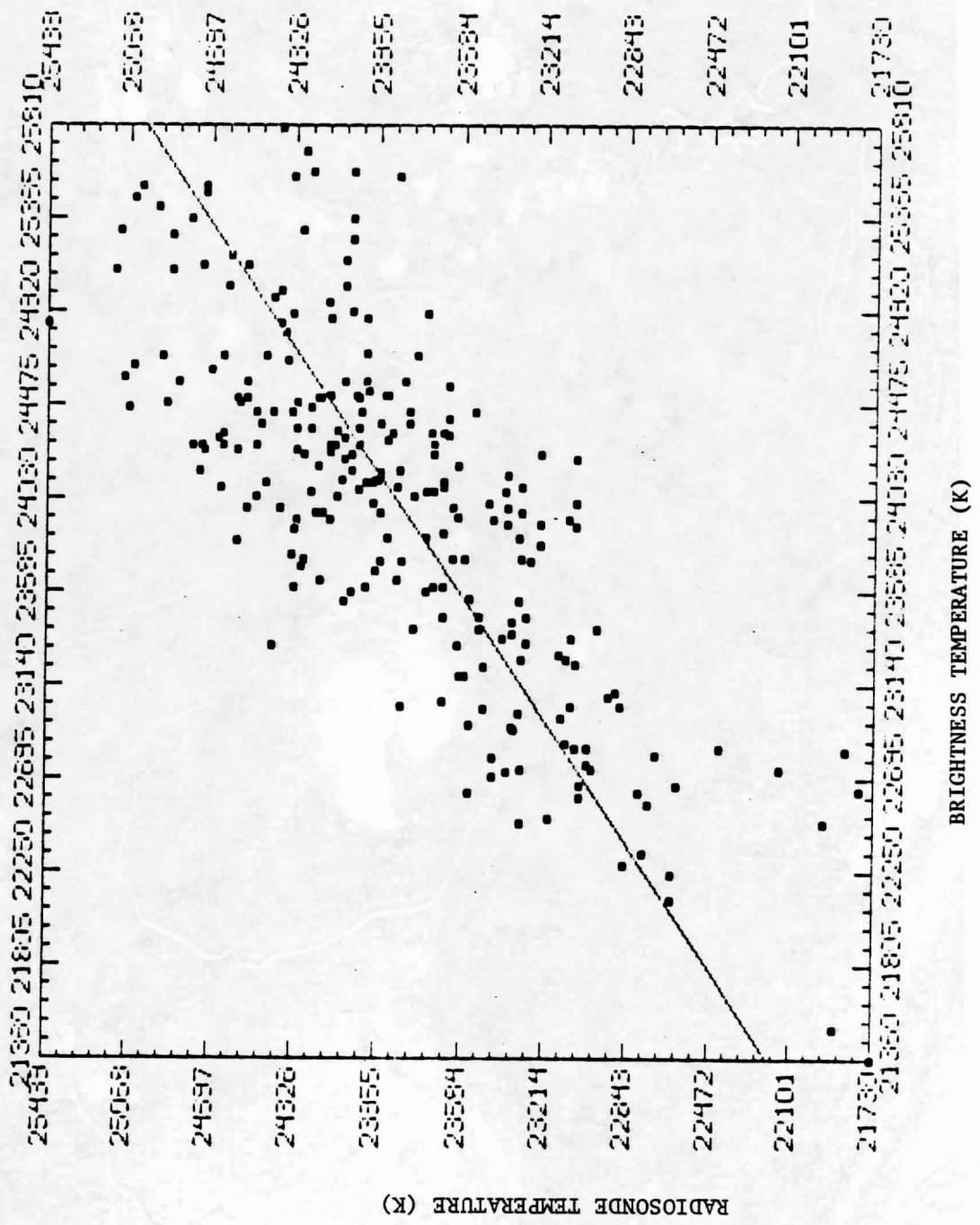


Figure 1.



VAS 6, 7 MICRON 1031 GMT 16 AUGUST 1983

Figure 2.

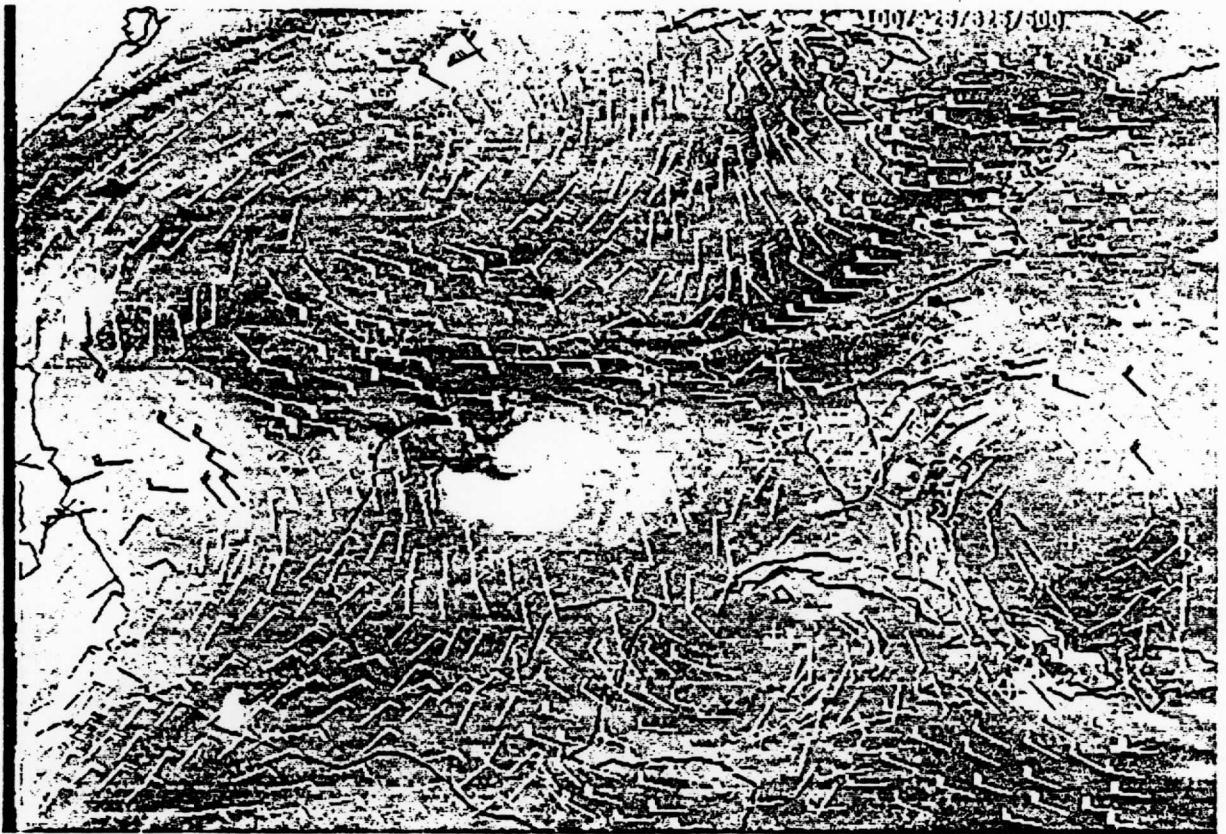


Figure 3a.



Figure 3b.



NOWCASTING—ADVANCES WITH McIDAS III

W. L. Smith G. S. Wade W. P. Menzel V. E. Suomi R. J. Fox C. S. Velden J. F. Le Marshall

NOAA/NESDIS  
1225 West Dayton Street  
Madison, Wisconsin 53706  
United States of America

Space Science and Engineering Center  
1225 West Dayton Street  
Madison, Wisconsin 53706  
United States of America

Visiting Scientist  
Bureau of Meteorology  
Melbourne, Victoria  
Australia

ABSTRACT

McIDAS III is capable of performing a wide range of nowcasting functions. These vary in computational difficulty from the video display of animated satellite or radar imagery to the execution of a mesoscale primitive equation forecast model. The model is initialized with locally processed satellite vertical soundings and tracer winds blended with conventional observations in order to provide objective limited area weather forecasts out to 24 hours.

McIDAS III is operated on a routine basis to provide experimental nowcast products to the National Severe Storms Forecast Center (NSSFC) and the National Hurricane Center (NHC) in the United States. In this presentation, an overview of McIDAS III is given and the nowcast products developed for experimental use by operational severe weather forecast centers are described.

Keywords: videographic interactive computer, satellite observations, mesoscale analysis and forecasting, nowcasting, tropical storms, severe weather.

1. McIDAS III

The McIDAS III is the latest generation of the Man-computer Interactive Data Access System which is under continual development at the University of Wisconsin (Suomi et al., 1983). Its real time data base includes conventional surface and upper air data, polar and geostationary satellite imagery and sounding data, radar, lightning detector data, Mesonet and Profiler data in eastern Colorado from the Prototype Regional Observing and Forecasting Service (PROFS), and global observations and forecast data from the National Meteorological Center (NMC). Software has been developed for processing and displaying mesoscale meteorological information in real time for a variety of short term forecast applications. Simple barotropic forecast models resident on the system are used for predicting the trajectory of tropical cyclones. A statistical model has been implemented for short term predictions of the probability of severe convective storms. A mesoscale primitive equation forecast model is initialized with conventional surface data and satellite soundings and cloud and water vapor tracer winds for providing objective limited area weather forecasts out to 24 hours.

McIDAS III uses an IBM-4341 computer as its mainframe CPU. Standard user terminals consist of interactive keyboard, cursor, data tablet control, CRT, and high resolution 28 frame color image and 14 frame color graphic monitor. Firmware has been developed to provide image and graphic animation, multi-image (e.g., satellite and radar) amalgamation, stereo image and graphic display, image-graphic overlays, etc. The McIDAS III system is now being used routinely for experimental nowcasting of intense weather (e.g., severe convective weather and tropical cyclones).

2. TROPICAL CYCLONES

The 1982 and 1983 hurricane seasons served as a test and development period for McIDAS III tropical cyclone applications software. Software was developed for processing and displaying polar orbiting satellite microwave imagery, and algorithms were tested for estimating the surface pressure and maximum sustained surface wind of tropical cyclones from upper tropospheric temperature patterns (Velden and Smith, 1983). Techniques were also developed for analyses of tropical cyclone steering currents from a combination of geostationary satellite derived thermal winds and cloud and water vapor tracer winds (Velden, Smith and Mayfield, 1984). By the end of the 1983 hurricane season, timely high quality analyses and displays of temperature, moisture, and motion patterns were being provided to the National Hurricane Center (NHC) for evaluation of their operational utility. NHC forecasters in Miami could view the McIDAS III products using a videographic display terminal on-line to the McIDAS mainframe computer in Madison, Wisconsin.

Figure 1 shows Hurricane Debby viewed in the NOAA-6 Microwave Sounding Unit (MSU) 55 GHz channel 3 which senses upper tropospheric thermal emission. Superimposed are 250 mb temperature contours derived from observations in all four MSU radiance channels. The upper tropospheric warm core anticyclone is clearly evident. Analyses of numerous tropical storms show good correlation between the temperature perturbation of the MSU derived 250 mb warm core and the central surface pressure and maximum winds (Figure 2) as measured by the NHC. In this example, the four degree temperature deviation indicates that Hurricane Debby has maximum sustained surface wind speeds of more than 100 kts.



Fig. 1: Image of radiance to space emitted by upper tropospheric oxygen observed by NOAA-6 over hurricane Debby. Contours of the 250 mb temperature derived from Microwave Sounding Unit (MSU) observations are superimposed.

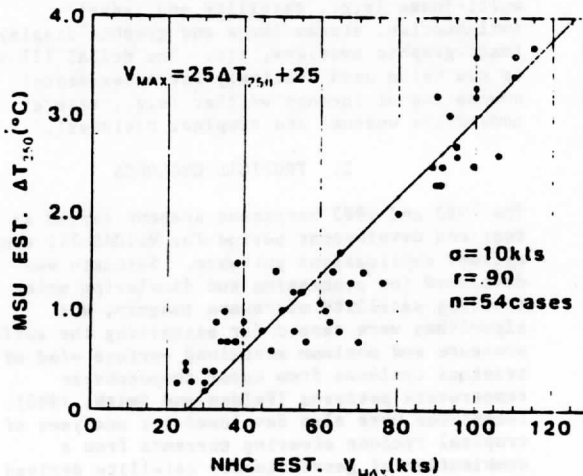


Fig. 2: Statistical relation between tropical storm warm core temperature deviation from the environment (as derived from MSU observations) and maximum wind speed (as measured by NHC).

Studies have indicated that the deep layer mean wind field around a tropical cyclone is one of the best indicators of the storm's steering current (Chan and Gray, 1982). One of the important applications of McIDAS III is to analyze the deep layer mean wind "steering current" for forecasting hurricane movement. To provide this product, soundings from the geostationary VISSR Atmospheric Sounder (VAS) are processed several times each day covering a large area centered on a tropical disturbance. To further enhance the VAS derived data sets, NOAA-6 and NOAA-7 polar orbiting satellite passes are processed in order to include the TOVS microwave profile retrievals and derived gradient winds in the cloudy regions of the hurricane which the VAS infrared data cannot provide. These microwave soundings are combined with the VAS soundings into a single data set and manually edited for consistency using the McIDAS III. To delineate the atmospheric

circulation more clearly, high and low level cloud drift (Mosher, 1979) and mid level water vapor motion (Mosher and Stewart, 1981) winds are determined from the VAS imagery and added to the gradient wind data set, with further manual editing of the winds for consistency. Radiosondes are used for quality control in the editing process where available.

An example of combined wind vectors for mid-tropospheric levels over Hurricane Debby's environment for 0000 GMT on September 16, 1982 is shown in Figure 3. The combination of high density cloud drift winds in cloudy areas, high density gradient winds from VAS retrievals in clear areas, water vapor motion winds at mid levels, and gradient winds from TOVS microwave retrievals (when available) provide an excellent description of the wind fields surrounding tropical cyclones in a what is a conventional data sparse region.

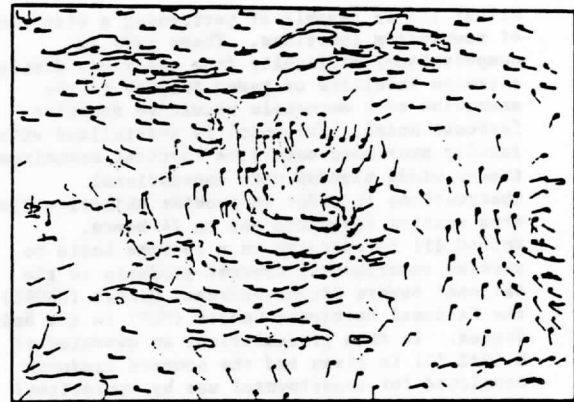


Fig. 3: Composite of cloud tracer, water vapor tracer and gradient wind estimates associated with Hurricane Debby over the western Atlantic (16 September 1982).

The final wind set consisting of VAS gradient, TOVS gradient (when available), cloud drift, and water vapor motion winds for three levels (approximately 850 mb, 400 mb, and 200 mb) are used to derive a pressure weighted deep layer (850-200 mb) mean wind analysis. Once the deep layer mean wind field is defined, simple trajectory models can be applied to forecast the future storm position (Velden, Smith and Mayfield, 1984). A typical model run takes a few seconds on the McIDAS III. An example forecast for Hurricane Alicia landfall is shown in Figure 4.

Comparisons of mean forecast errors (MFE) were made for several different operational models used by the NHC, the official forecasts, and the VASTRA (VAS TRAjectory) model for selected homogeneous cases when VAS deep layer mean wind data were available (from Hurricanes Debby of 1982, and Alicia, Barry and Chantal of 1983). Initial positioning error (Neumann and Pelissier, 1981) was removed from the MFE in all cases. Performance of specified models relative to the CLIPER (climatology and persistence) model is shown in Figure 5. It can be seen that the VASTRA forecasts compare favorably with the official forecasts and the other operational models. While

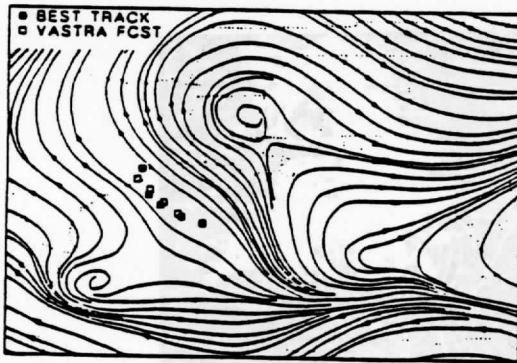


Fig. 4: Final 850-200 mb satellite derived deep layer mean wind streamline analysis for Hurricane Alicia at 1200 GMT on 16 August 1983. Solid squares indicate Alicia's storm track every 12 hours. Open squares indicate the VASTRA forecast out to 48 hours.

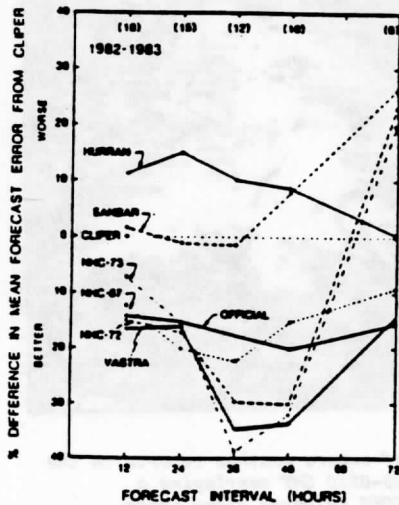


Fig. 5: Performance of specified models relative to the performance of the CLIPER model for 1982 and 1983 cases studied. The sample is homogeneous, with the numbers in parentheses giving sample size. Forecasts are unavailable for any model at 60 hours and for official forecasts at 36 hours.

It is recognized that these data represent a relatively small statistical set, it is believed that the good quality and much greater density of wind data over the oceanic regions are responsible for the encouraging results. Good nowcasts of tropical cyclones are being achieved with McIDAS III.

### 3. SEVERE STORMS

One of the primary functions of McIDAS III is to demonstrate the severe weather nowcasting capabilities of the VAS (Smith et al., 1982). For this purpose vertical temperature and moisture soundings and cloud and water vapor tracer winds are produced at one to three hour intervals.

Severe storm forecast products are provided for real-time evaluation to forecasters at the National Severe Storms Forecast Center (NSSFCC) in Kansas City. The products include upper and lower level wind analyses produced from combined thermal and cloud tracer winds, plots and analyses of the "lifted" stability index, analyses of 850 and 500 mb temperature fields and total precipitable water content. The sounding and wind data are generally produced with a horizontal resolution of 80 km. However, two sounding products are generated at the full 7 km resolution of the VAS instrument: (a) total precipitable water, and (b) the "total-totals" thermodynamic stability index. These full resolution products are displayed to the forecasters in an image format in order to portray all the mesoscale detail of the observations. Finally, a statistical probability estimate of severe weather (Keller and Smith, 1983) is generated from each VAS sounding data set. This probability of severe weather is based on the three dimensional temperature and moisture structure diagnosed by VAS and conventional surface observations and their expected time variations due to advection. These objectively determined severe probability estimates usually resemble the subjective outlooks for severe weather generated by skilled forecasters at the NSSFCC.



Fig. 6: Statistical probability (%) of severe weather based on surface observations and VAS upper air soundings at 1100 GMT on 10 April 1984.

Examples of McIDAS III severe weather nowcast products are shown in Figures 6-10 for 10 April 1984. Figure 6 shows the severe weather probability generated from early morning (1100 GMT) VAS sounding data overlaying a 6.7  $\mu$ m upper tropospheric water vapor image. As can be seen, significant probabilities exist for eastern Texas. Figure 7 shows a full resolution (7 km) image for the same hour of the VAS derived total-totals stability index with a contour analysis of 80 km horizontally average values superimposed. As can be seen, the total-totals indicate very unstable atmospheric conditions over eastern Texas. As the day progressed the atmosphere over eastern Texas rapidly destabilized due to the differential advections of warm moist air from the gulf at low levels and cold drier air aloft from the northwest. Figure 8 shows the total-totals product for 1700 GMT. The very unstable air over northeastern Texas is quite noticeable. By 2000 GMT the VAS

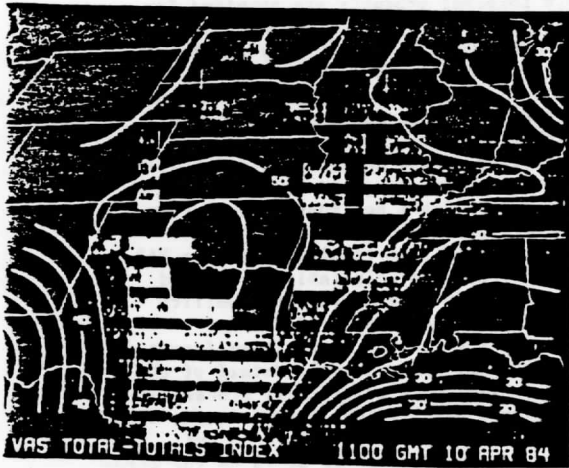


Fig. 7: Image of VAS derived atmospheric stability (total-totals) for 1100 GMT, 10 April 1984 portrayed at 7 km resolution with contours of horizontally averaged values superimposed. White areas indicate unstable conditions while dark regions indicate either stable air or sounding voids (black areas) due to cloud obstruction.

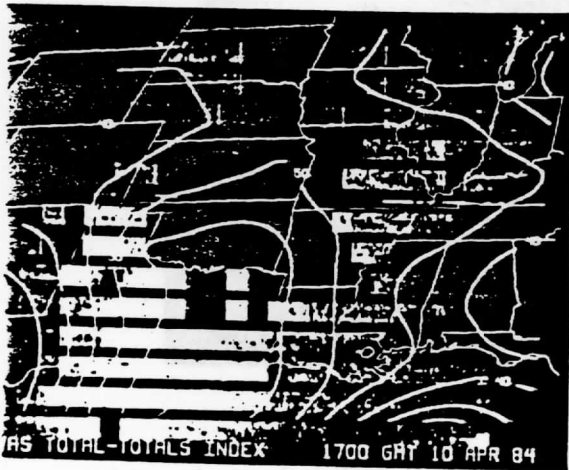


Fig. 8: Image of VAS derived atmospheric stability (total-totals) for 1700 GMT, 10 April 1984 portrayed at 7 km resolution with contours of horizontally averaged values superimposed.

ever probability estimate indicated a very high probability that severe weather would occur along the Texas-Louisiana border. Figure 10 shows that numerous tornadoes and hail storms did occur after 1000 GMT in this area. This is a typical demonstration of how McIDAS III is used to portray quantitative information for nowcasting severe weather. McIDAS III is also used to display satellite and radar imagery in animation or severe weather warning purposes.

#### 4. MESOSCALE NUMERICAL WEATHER PREDICTION

Mesoscale numerical weather prediction (NWP) models will soon play a key role in the short term (3-24 hours) forecasting of the subsynoptic scale

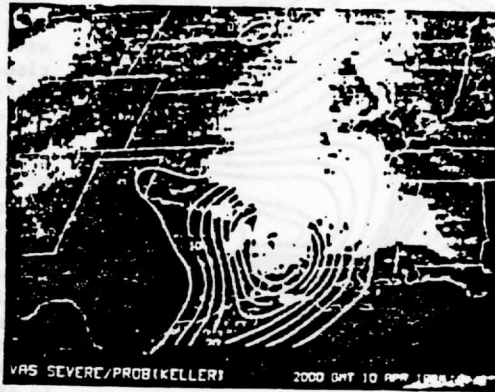


Fig. 9: Statistical probability of severe weather for 2100 GMT on 10 April 1984.

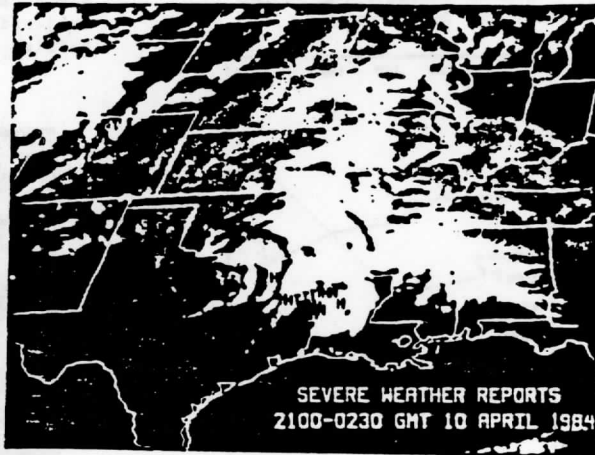


Fig. 10: Location of severe weather reports in the period 2100-0230 GMT overlaying a 0100 GMT GOES infrared cloud image.

mechanisms for severe convective weather. A ten level primitive equation model (Table I) has been implemented on McIDAS III in order to achieve experimental numerical forecasts of the intense weather forcing variables (e.g., vertical motion, stability, temperature, moisture, and horizontal wind) from time independent (one to three hourly) surface and upper air observations (Mills and Hayden, 1983). The upper air data consists primarily of VAS vertical temperature and moisture soundings and cloud and water vapor tracer winds. As shown by Le Marshall et al. (1984a), VAS soundings and winds complement each other in the NWP initial analysis; the soundings are restricted to cloud free air and the winds are specified in cloudy regions. The NWP model is used in a nowcasting mode so that several initial data independent objective forecasts can be made, all valid at the same prognosis time. The independence of the forecasts results from the time independence of the initial data. Given several initial condition independent forecasts, it is reasonable to expect that the mean forecast is most reliable in those geographical regions where the individual forecasts are repetitive. In regions where there

tions  
four  
and  
el

n of  
n  
t  
the  
ons  
ng  
tion

hese  
e  
ts  
ld.)

ere

rd

otion  
re 12  
the  
tical

ngs  
tive

across southern Alabama and over Georgia. It should be noted that the largest area of upward vertical motion in this region corresponds to the region where the most intense convection and severe weather occurred. The largest scale upward vertical motion occurs off the east coast and this appears to correspond with the precipitation shown in the radar summary along the northeast coast. This case study, along with several others which have been conducted on McIDAS III, indicate that the nowcasting application of mesoscale NWP models will improve the reliability of intense convective weather forecasts on a local basis. However, further development is needed before such a procedure can be put into operational practice. In particular, a dynamic initialization procedure must be implemented to preserve the observed and forecast divergence in the initial analyses so as to achieve more accurate short term (0-3 hour) numerical predictions.

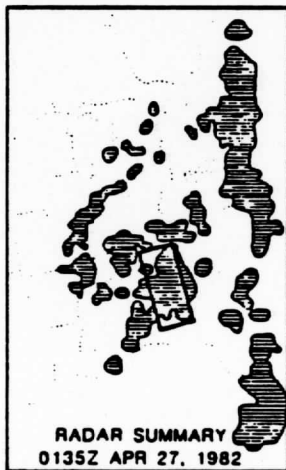


Fig. 12: Comparison between the average forecast of vertical motion for 0000 GMT and a radar summary of precipitation occurring at 0135 GMT. Areas of consistent forecasts of upward vertical motion are cross-hatched.

##### 5. SUMMARY AND FURTHER REMARKS

McIDAS III has made several nowcasting developments possible ranging from image animation to applications of a mesoscale NWP model. An IBM 4381 CPU will soon to be implemented (July 1984) as a replacement for the present IBM 4341 CPU. The 4381 will provide a factor of three increase in both processing speed and available memory. Also, the transition to intelligent user terminals, which are to be constructed with the powerful Intel 286

microprocessor, will greatly increase the efficiency of the McIDAS III system by minimizing user contention for the mainframe CPU. The McIDAS III system is the prototype for NOAA's VAS Data Utilization Centers (VDUC's) which are expected to support operational nowcasting services during the latter part of this decade.

##### 6. REFERENCES

- Chan, J. C. L., and W. M. Gray, 1982: Tropical cyclone movement and surrounding flow relationships. Mon. Wea. Rev., 110, 1354-1374.
- Keller, D. L., and W. L. Smith, 1983: A statistical technique for forecasting severe weather from vertical soundings by satellite and radiosonde. NOAA Technical Report NESDIS 5, Department of Commerce, NOAA/NESDIS, Washington, D.C., 35 pp.
- Le Marshall, J. F., W. L. Smith, and G. M. Callan, 1984a: Hurricane Debby—Analysis and numerical forecasts using VAS soundings. Preprint volume, 15th Technical Conference on Hurricanes and Tropical Meteorology, January 9-13, 1984, Miami, Florida; Published by American Meteorological Society, Boston, Massachusetts.
- Le Marshall, J. F., W. L. Smith, C. R. Diak, and G. M. Callan, 1984b: The use of a mesoscale numerical weather prediction model for nowcasting. To be submitted to Mon. Wea. Rev.
- Mills, G. A., and C. M. Hayden, 1983: The use of high horizontal resolution satellite temperature and moisture profiles to initialize a mesoscale numerical weather prediction model—A severe weather event case study. J. Clim. Applied Meteor., 22, 649-663.
- Mosher, F. R., 1979: Cloud drift winds from geostationary satellites. Atmospheric Technology, 10, 53-60.
- Mosher, F. R., and T. R. Stewart, 1981: Characteristics of water vapor tracked winds. NAVENVPREDRSCHFAC Contract Report, CR 81-06, 51 pp.
- Neumann, C. J., and J. M. Pelissier, 1981: Models for the prediction of tropical cyclone motion over the North Atlantic: An operational evaluation. Mon. Wea. Rev., 109, 522-538.
- Smith, W. L., V. E. Suomi, F. X. Zhou, and W. P. Menzel, 1982: Nowcasting applications of geostationary satellite atmospheric sounding data. Nowcasting, K. A. Browning, Ed., Academic Press, 123-135.
- Suomi, V. E., R. Fox, S. S. Limaye, and W. L. Smith, 1983: McIDAS III: A modern interactive data access and analysis system. J. Clim. Applied Meteor., 22, 766-778.
- Velden, C. S., and W. L. Smith, 1983: Monitoring tropical cyclone evolution with NOAA satellite microwave observations. J. Clim. Applied Meteor., 22, 714-724.
- Velden, C. S., W. L. Smith, and M. Mayfield, 1984: Applications of VAS and TOVS to tropical cyclones. Accepted for publication in Bull. Amer. Meteor. Soc.

A procedure is developed for estimating sea surface temperature (SST) from multispectral image data acquired from the VISSR atmospheric sounder on the geostationary GOES satellites. Theoretical regression equations for two and three infrared window channels are experimentally tested using clear field of view satellite radiances matched with reports of SST from NOAA island environmental buoys. The empirical regression equations are then used to produce daily regional analyses of SST. The daily analyses are used to study the response of SST to the passage of baroclinic eddies (1970) and baroclinic doublets (1982), and are also used as a first guess surface temperature in the retrieval of atmospheric

**Sea Surface Temperature - Observations from Geostationary Satellites**

**J. J. Bates and W. L. Smith**

**Cooperative Institute for Meteorological Satellite Studies**

**University of Wisconsin, Madison, WI 53706**

a scatter of 0.2-1.0°C and a slight warm bias with respect to the other measurements of SST. The VAS SST shows no detectable bias in the region of the El Chichón volcanic aerosol cloud. Finally, a multi-angle approach for determining SST from two GOES VAS satellites or a combination of VAS and AVHRR data is examined.

**Abstract**

A procedure is developed for estimating sea surface temperatures (SST) from multispectral image data acquired from the VISSR atmospheric sounder on the geostationary GOES satellites. Theoretical regression equations for two and three infrared window channels are empirically tuned using clear field of view satellite radiances matched with reports of SST from NOAA fixed environmental buoys. The empirical regression equations are then used to produce daily regional analyses of SST. The daily analyses are used to study the response of SST's to the passage of Hurricane Alicia (1983) and Hurricane Debbie (1982), and are also used as a first guess surface temperature in the retrieval of atmospheric temperature and moisture profiles over the oceanic regions. Monthly mean SST's for the western North Atlantic and the eastern equatorial Pacific during March and July 1982 were produced for use in the SST Intercomparison Workshop Series. Workshop results showed VAS SST's have a scatter of 0.8-1.0°C and a slight warm bias with respect to the other measurements of SST. The VAS SST's show no discernable bias in the region of the El Chichón volcanic aerosol cloud. Finally, a multi-angle approach for determining SST from two GOES VAS satellites or a combination of VAS and AVHRR data is examined.

## 1. Introduction

Since September of 1980, the operational geostationary satellites have carried the VISSR Atmospheric Sounder (VAS) first proposed by Suomi et al. (1971). VAS is a filtered radiometer possessing eight visible channel detectors and six thermal infrared detectors that sense visible radiation in one spectral band and infrared radiation in twelve spectral bands. A filter wheel in front of the detector package is used to achieve the infrared spectral selection. The central wavelengths of the infrared spectral bands lie between 3.9 and 15  $\mu\text{m}$  (Smith, 1983; Smith et al., 1981). Housed in the GOES satellite, the instrument spins at 100 rpm scanning the earth in a west-to-east direction and achieving spatial coverage of 1 km in the visible and 7 or 14 km in the infrared (depending on the detector used). The north-south coverage is achieved by stepping a scan mirror.

The VAS instrument can be programmed to operate in one of two modes; the Dwell-Sound (DS) mode or the Multispectral Image (MSI) mode. In the DS mode, multiple samples of the upwelling radiance in a given spectral band are sensed by the same detector by holding the filter wheel and mirror fixed during multiple spins of the spacecraft. The DS mode was designed to achieve the improved signal-to-noise ratio (SNR) required to interpret the spectral radiance measurements in terms of vertical temperature and moisture structure. As a result, only a limited latitudinal swath is usually achieved in this mode on each scan. In contrast, the MSI mode is operated in the imaging full disc scan and achieves radiance data in the visible, the 11.0  $\mu\text{m}$  atmospheric window region, and any two other infrared channels. For SST determination, the



two additional channels selected are the 3.9  $\mu\text{m}$  window and the 12.6  $\mu\text{m}$  water vapor absorption channel referred to as a "dirty" window. The instrument characteristics for the VAS SST channels are summarized in Table 1. VAS infrared data are quantized to a ten bit precision, which gives a temperature sensitivity between 0.05 to 0.2°C. Spatial averaging of two to nine individual fields of view (FOV) is employed to further improve the signal-to-noise ratio (SNR). The VAS instrument is carefully calibrated pre-launch, post-launch, and at the beginning of each line of data. A more complete description of the VAS instrument and its operating modes is given by Menzel et al. (1981) Regular archiving of VAS data from GOES using the Man-computer Interactive Data Access System (McIDAS) at the Space Science and Engineering Center (SSEC) began in March 1982 (Suomi et al., 1983).

## 2. Role of the geostationary satellites

The geostationary satellite has several important advantages over the polar orbiter for viewing SST variability. Because of the satellites altitude (38,000 km), only small variations in view angle (i.e., atmospheric depth) are experienced when observing a large spatial domain. This feature tends to minimize horizontal variations in satellite observed brightness temperature due to atmospheric absorption variations. Also, because the satellite is geostationary, a given geographical area is observed from time to time with the same viewing geometry. This feature tends to minimize time variations in satellite

observed brightness temperature due to temporal variations in atmospheric absorption. Finally, since the satellite views the earth quasi-continuously, the probability of obtaining cloud-free views of the ocean surface, at least once per day, is greatly enhanced. Also, sunglint contamination of the shortwave infrared window brightness temperature observations can be avoided by sampling at times when the viewed spot does not lie within the principle plane of the sun.

Prior to VAS, geostationary satellite sensors contained a single infrared window channel centered at  $11.0 \mu\text{m}$ . Consequently, multi-spectral techniques for correcting observed brightness temperature for atmospheric attenuation could not be employed. Nevertheless these data were corrected using a simple parameterization of the atmospheric absorption as a function of water vapor concentration in order to obtain time series analyses of SST's (Maul et al., 1978). More sophisticated radiative transfer estimates of atmospheric attenuation have also been used to obtain mesoscale patterns of SST using both GOES visible and  $11.0 \mu\text{m}$  brightness temperature observations (Maul, 1981). Zandlo and Smith (1982) used multi-spectral polar orbiter data to obtain atmospheric correction fields for the GOES  $11.0 \mu\text{m}$  channel brightness temperatures. The correction fields were updated at the time of the polar orbiter satellite overpasses. The GOES data provided the temporal and spatial variations of the SST field during the period between polar satellite overpasses.

As discussed below, the VAS alleviates the requirement for using ancillary information to achieve accurate SST estimates. Unfortunately, the VAS multi-spectral SST observation capability only exists on the

United States geostationary satellites whose coverage is limited to the western hemisphere. It is hoped that the success of VAS and its planned operational implementation in 1986 will prompt Europe, Japan, and India to incorporate this multi-spectral capability on their future geostationary satellites so that complete global coverage is achieved.

### 3. Basis for multispectral method

The concept of using two or more simultaneous brightness temperature measurements in different spectral bands to correct for atmospheric water vapor attenuation of surface temperature was first proposed by Anding and Kauth (1970) and initially tested by Prabhakara et al. (1974) using Nimbus satellite 11  $\mu\text{m}$  and 12  $\mu\text{m}$  window data. The brightness temperature differs for each window channel because of different absorption efficiencies (coefficients) for the different spectral bands. Using the assumption of weak absorption and parameterizing the atmospheric radiance in terms of the surface radiance, the surface temperature can be expressed in terms of the brightness temperature observed at two (or more) window wavelengths;

$$\text{SST (2 channel)} = T_B(W_1) + a[T_B(W_1) - T_B(W_2)] \quad (1)$$

$$\text{SST (3 channel)} = T_B(W_1) + b[T_B(W_1) - T_B(W_2)] + c[T_B(W_2) - T_B(W_3)] \quad (2)$$

where,

$$a = k_1 / (k_2 - k_1)$$

$$b = k_1 / 2(k_2 - k_1)$$

$$c = k_1 / 2(k_3 - k_1)$$

and,

$T_B(W_1)$  brightness temperature in window channel 1 (K)

$T_B(W_2)$  brightness temperature in window channel 2 (K)

$T_B(W_3)$  brightness temperature in window channel 3 (K)

$k_1, k_2, k_3$  mass absorption coefficients for the window channels

The early success of the multispectral method provided the impetus for the development of multispectral radiometers sensing in the atmospheric window regions such as the AVHRR and VAS. Prior to the acquisition of data from these spacecraft, theoretical performance simulations of the instrument response to a variety of atmospheric and surface conditions are made to determine the coefficients for the multispectral algorithm (Deschamps and Phulpin, 1980; McClain, 1981). Due to difficulties in modeling the effects of water vapor attenuation, however, theoretical simulations usually produce estimates of SST that have a bias when compared to in situ measurements of SST. As a result, a diverse set of satellite brightness temperature measurements matched with precise in situ measurements of SST are used to fine tune the theoretical simulations (McClain and Strong, 1984).

This procedure was used to gather a set of matches of VAS brightness temperatures with NOAA moored environmental buoys located in the

Gulf of Mexico, the North Atlantic, and the Great Lakes. The results of a linear regression analysis of these matches are summarized in Table 2. It is important to note that the multichannel coefficients for VAS are lower than those for the AVHRR (McClain et al., 1983), especially the two window channel algorithm. Only daytime data were used in these matches in order to make use of VAS 1 km visible imagery to ensure that strictly cloud-free FOV's were selected. The daytime tests for cloud filtering are similar to those described for the AVHRR. The VAS tests include a visible albedo threshold, upper and lower bounds on the brightness temperature differences between the three window channels, and bounds on the difference between the the two and three channel algorithm SST's. In addition, the resultant multichannel SST is required to lie between  $-2^{\circ}\text{C}$  and  $35^{\circ}\text{C}$  and a high resolution topography grid is checked to ensure that no FOV is over land. The results for each three by three FOV array centered at the buoy location containing at least two clear FOV's are averaged to produce a SST value for that array (approximately a 50 by 50 km square). Figure 1 is a VAS-derived three channel SST analysis of the western North Atlantic using this procedure. The analysis clearly shows the warmer waters of the Gulf Stream in contrast to the cooler slope and shelf waters to the west and north.

Recently, testing has begun on a cloud filtering scheme so that SST's from VAS data during the night can be processed. The scheme uses the same infrared cloud checks as described above and in addition requires that the two or more FOV's that pass those tests also have standard deviations from the average brightness temperature of less than

some prescribed bound. While there are not yet a sufficient number of nighttime matches to generate statistics, a regional analysis of SST's in the eastern North Pacific for this past winter is encouraging (Figure 2). This analysis has been used as a first guess surface temperature in the retrieval of atmospheric temperature and moisture profiles which are then used as input to numerical models.

#### 4. Results

##### A. Analysis of tropical cyclone/sea surface temperature interaction

SST plays a critical role in the formation, evolution, and dissipation of tropical cyclones. A SST of  $26.5^{\circ}\text{C}$  or greater is required for tropical cyclone formation, and passage of a tropical cyclone over an area of anomalously warmer water has been linked to intensification of tropical cyclones (Anthes, 1982). Once a tropical cyclone has formed, upwelling and vertical mixing of water in the surface layers of the ocean produce decreases in SST of  $1-5^{\circ}\text{C}$  (Leipper, 1967). The high temporal and spatial frequency of the VAS instrument make it an excellent data source for analyzing SST fields before and after the passage of tropical cyclones.

Hurricane Alicia (1983) was the first hurricane to strike the continental United States in over three years. Although Alicia was a rather small hurricane and only a minimal category three storm, on the Saffir/Simpson scale, it was one of the costliest storms in Texas history (Case and Gerrish, 1984). VAS MSI data were processed on a daily basis to produce a three window channel estimate of SST before,

during, and after Alicia. These data were then interpolated and objectively analyzed on a one half degree latitude/longitude grid (figure 3). NOAA environmental buoy estimates of SST along latitude 26°N taken within an hour of the VAS data are included for comparison.

On August 15, just prior to Alicia becoming a named tropical storm, VAS data (figure 3a) shows SST's in the central Gulf of Mexico generally running from 30-31°C. Alicia slowly gained strength over the warm gulf waters on the 16th (figure 3b), and data from the 17th (figure 3c) show a pool of very warm water (greater than 32°C) just south and east of Galveston Bay. Hurricane Alicia gained strength rapidly later on the 17th and made landfall early on the 18th. VAS SST data for later on the 18th, show a dramatic cooling of the water just east of Galveston Bay (1-4°C) with a lobe of cooler water extending back to the southeast. Note that the major cooling of SST's occurred to the right of the hurricane track, which is consistent with the theory and observations of Martin (1982). Strong cooling is also evident on August 19, although the lobe of cooling extending to the southeast is no longer visible. While a cool pool of water is still evident near Galveston on August 20, SST's have warmed by several degrees from the minimum. These observations suggest that while SST's may decrease dramatically in the wake of a hurricane they also return rapidly to the pre-storm values.

Similar, but less dramatic, changes in SST were observed during the passage of Hurricane Debbie (1982) between September 13 and 15. The VAS SST observations were produced as before, and a mean analysis for the three day period was made. Then the SST observations for each day was objectively analyzed, using as a first guess the mean analysis. This

process helps to eliminate artifacts in the objective analysis for each day due to data voids resulting from large areas of cloud cover. The mean analysis and the daily SST fields for September 13 and 15 are shown in figures 4a, 4b, and 4c. The mean analysis (figure 4a) shows rather weak SST gradients over the western North Atlantic with the warm waters of the Gulf Stream evident extending off the coast of Cape Hatteras. The daily analysis for September 13th (figure 4b) shows a pool of warm water (greater than 30°C) in the central portion of the figure. During the next 48 hours, Debbie moved northeastward, over the warm SST's, increased rapidly in strength to hurricane intensity (maximum sustained wind speeds increased from 30 to 90 kts.), and then began to recurve to the east. The daily SST analysis for September 15th reveals that the warm pool of water is now gone, a drop in the SST of two degrees from September 13th. Again VAS SST data show a pattern of warm water evident prior to hurricane passage and intensification, and cool water evident in the wake of the hurricane.

#### 4b. SST Intercomparison Workshop

The results of the SST intercomparison workshop series (JPL, 1983) are the first examination of monthly mean SST's derived from MSI data provided by the VAS instrument on the GOES series satellites. Because the procedure to derive SST's from VAS data is still in the developmental stage, several changes in the procedure were made between the processing of data for March 1982 and processing the data for July 1982. The most significant change was the use of the three window channel algorithm (3.9, 11.0, and 12.6  $\mu\text{m}$ ) in the processing of the July



data as opposed to the use of only the two window channel (11.0/12.6  $\mu\text{m}$ ) algorithm for the March data. Initially only the two channel algorithm was used in order to extend the analysis of SST into areas of sunglint in the tropics. However, the analysis of the March data showed that little additional data was gained by doing this. In addition, further satellite/buoy matches indicated that the triple window channel algorithm showed a smaller standard deviation than the two window channel algorithm and was less sensitive to the effects of volcanic aerosol contamination and low level inversion conditions. This is due to the smaller brightness temperature attenuation by aerosols and water vapor at 3.9  $\mu\text{m}$  than at 11.0 and 12.6  $\mu\text{m}$ . Thus, the decision was made to use the best product (i.e., the three window channel algorithm) for processing the July data.

Two large regions were chosen for analysis of VAS data from GOES-East, one in the western North Atlantic and one in the eastern Tropical Pacific. Since ship observations of surface layer temperature provide the only long-term climatology of SST, Reynolds (1982) climatology has been used as a standard from which satellite SST monthly mean anomaly fields were produced. Data from all sensors were binned on a two by two degree latitude/longitude grid for each month. SMMR data were required to be more than 600 km from land in order to avoid contamination from land. Thematic contour charts of sensor anomaly fields from climatology for March are shown in figure 5. VAS, AVHRR, and ship data all show a pattern of cold to warm to cold to warm proceeding southeast off the U.S. east coast; however the VAS data have a warm bias of 0.5 to 1.0°C. In the South Pacific, the VAS data show only a slight

warm bias and again are highly correlated with the AVHRR, ships, and XBT's. In particular, the VAS and AVHRR thematic contour anomaly charts show similar patterns with warm water along the coast from 20° to 30°S and extending to the west along 30°S, a pool of cold water along the coast from 0 to 10°S, another cold anomaly offshore, and near normal conditions elsewhere. The HIRS data show generally weaker anomaly patterns and a warm bias near the coastlines due to problems in accurately specifying the land/water boundaries (Susskind, personal communication). The HIRS data do show a warm anomaly along 30°S in the eastern South Pacific and a large warm anomaly in the western North Atlantic. Little correlation in patterns is found between the VAS and the SMMR product.

Table 3 summarizes the cross correlation statistics for each satellite verses ship-of-opportunity measurements for March 1982. Matches with ships were limited to a time window of  $\pm 12$  hours and a space window of  $\pm 50$  km from the satellite observation. VAS estimates of SST show a warm bias relative to ships for all regions ranging from +0.35 to 1.73°C. The largest biases (1.73°C and 1.05°C) are found with the lowest numbers of matches (21 and 53) and also occur at the largest satellite zenith angles (North Pacific region 20-56°N and South Pacific region 20-56°S). This indicates that the magnitude of the warm bias for the two channel algorithm may increase with increasing satellite zenith angle but also suggests that noisy ship data may be partly responsible for some of the bias.

The uniform warm bias in all regions, however, indicates a diurnal sampling bias and a possible bias in the matches used to tune the

empirical algorithm. Satellite/buoy matches are continuing to be collected in order to ensure that a seasonally and geographically diverse set of matches is used to update the coefficients for the empirical algorithms. It does appear though that the diurnal sampling of VAS data is largely responsible for the warm bias. VAS data were generally processed at 1530 and 1830 GMT (1030 and 1330 LST at the GOES-East subpoint) and only cloud-free observations were used. Thus, VAS SST's might be expected to have a warm bias relative to estimates of SST that average day and night data. Diurnal heating of the ocean skin temperature as observed by satellite infrared data has also been reported by Strong (1984) and by Deschamps and Frouin (1984). Future intercomparisons must take into account possible diurnal sampling biases of each sensor.

Additional cross correlation statistics for March show VAS with a scatter relative to ships of 0.79-1.24°C. The statistics show VAS well correlated with ships, and shows regional correlations very similar to those of the AVHRR. The one exception is the far South Pacific region (20-56°S). This again is the region of fewest matches and thus should be given little weight.

In the thematic anomaly charts for July (figure 6), the effects of the El Chiclon volcanic aerosol are very evident in the AVHRR data as a zonal band of cold anomalies from 10-30°N. VAS data, however, do not show an analagous anomaly in those latitudes. This result is due to differences in the spectral channels of the VAS and AVHRR, differences in the processing algorithms, and differences in the average viewing

geometry. The VAS, SMMR, and ship data all show a warm anomaly in the eastern tropical Pacific.

In the North Atlantic VAS region, the VAS data appears to be slightly warmer than the ship data, but again shows similar patterns. The VAS and AVHRR data show some correlation near the coast of the U.S., but meaningful comparisons between the two are hampered by the volcanic aerosol contamination in the AVHRR data. The anomaly patterns are much the same in a comparison the the VAS/SMMR data, however the SMMR data is contaminated by "cold" instrument warmup noise in much of the North Atlantic (Milman, personal communication). In the VAS region of the Pacific, the VAS, SMMR, and ship data all show warming. Here, the VAS and SMMR data show a high correlation with a pattern of warm anomalies along the coast and extending westward along the equator. In contrast, the HIRS data, while not showing any consistent bias in the El Chicón region, does show a large cold anomaly in this region.

Cross correlation statistics for July 1982 are summarized in Table 4. VAS SST's again show a slight warm bias in all regions. The very large warm bias at large local zenith angles evident in the March 1982 data, however, has been eliminated by the use of the three window channel algorithm. Little bias is evident in the region of the El Chicón volcanic aerosol (approximately 10-30°N). In this region, the AVHRR data show a cold bias of 0.50-0.75°C relative to ships. The VAS standard deviations are also generally smaller in July than in March due to the use of the three window channel algorithm. The cross correlations of VAS data with ship data, however, are much weaker in July than March.

After SST Intercomparison Workshop III, additional cross correlation tables were generated to try to answer some of the questions raised during the workshop. Most important to the interpretation of VAS data was the stratification of AVHRR data into day and night so that the daytime only VAS data could be directly compared to daytime only AVHRR data. Although the new cross correlation tables are masked to include only data greater than 600 km from land (to normalize the comparison between SMMR and the other sensors, but greatly reducing the number of VAS/ship matches), some trends are clearly evident. In March 1982, AVHRR shows a global average day minus night difference relative to ships of  $+0.43^{\circ}\text{C}$ . This reduces the VAS minus AVHRR day bias to  $+0.23^{\circ}\text{C}$ . The VAS versus ship biases remain unchanged since ships measure SST at some depth beneath the surface and are relatively insensitive to diurnal heating of the ocean skin. In July, on a global basis, the AVHRR day product is  $0.43^{\circ}\text{C}$  warmer than ships while the AVHRR night product is  $0.72^{\circ}\text{C}$  colder than ships. There is no discernable bias between AVHRR day SST's and VAS SST's outside the El Chico zone (i.e., in the South Pacific and North Atlantic), while within the El Chico zone (the mid-Pacific) AVHRR day is  $0.69^{\circ}\text{C}$  colder than VAS and  $0.50^{\circ}\text{C}$  colder than ships. These data clearly show that the diurnal heating of the ocean skin is being detected by VAS and AVHRR, and demonstrates that most of the VAS warm bias relative to the other sensors is due to this diurnal variability.

##### 5. Dual Angle Measurement

The dual angle approach to the measurement of SST is based on the principle that having observations for differing optical depths as a result of differing view angles (Figure 7) enables extrapolation to the zero optical depth condition (i.e., the surface radiance value). This approach should yield more accurate estimates of SST since all forms of atmospheric attenuation, including aerosols, are accounted for in the calculation of surface radiance (McMillin, 1975 and Barton, 1983). Simultaneous observations of atmospheric attenuated surface radiances to space can be made in the region of overlap from the operational GOES East and West VAS satellites, from a combination of VAS and AVHRR data, or from a single satellite by an instrument such as the Along-Track Scanning Radiometer (ATSR) proposed for the European Space Agency's satellite ERS-1.

Assuming weak absorption and parameterizing the atmospheric radiation in terms of the surface radiation, the surface Plank radiance can be expressed as a linear combination of the earth outgoing radiance from the area observed at two differing local zenith angles as,

$$B(T_S) = \alpha (\theta_W, \theta_E) B[T_B(\theta_E)] + \beta (\theta_W, \theta_E) B[T_B(\theta_W)] \quad (3)$$

where,

$T_S$  surface skin temperature (K)

$T_B$  brightness temperature corresponding to the radiance value  $B[T_B(\theta)]$

and,

$$\alpha (\theta_W, \theta_E) = \sec \theta_W / (\sec \theta_W - \sec \theta_E)$$

$$\beta(\theta_W, \theta_E) = \sec \theta_E / (\sec \theta_e - \sec \theta_W)$$

where,

$\theta_W$  local zenith angle from west satellite

$\theta_E$  local zenith angle from east satellite

On 16 November 1983, VAS DS data were acquired from both GOES East and GOES West within a half hour time interval. Portions of the north-west Gulf of Mexico and the Gulf of California were viewed by both satellites and permit calculations of SST using the multi-angle method. The results from three points chosen (Table 5) for each pair of window channels agree well with one another. Although there were no in situ SST observations available to match with the VAS data, the VAS multi-angle values agree well with the weekly estimates of SST from the AVHRR in these regions. While the overlap region of the GOES-East and GOES-West satellites is limited, a multi-angle approach combining VAS and AVHRR data would provide coverage over a large portion of the globe. Such an approach is currently under development.

#### 6. Conclusions and Recommendations

A procedure has been developed to screen VAS visible and infrared data for cloud-free regions and to estimate SST from the clear infrared radiances. This procedure has been used to produce a data set of matches between the VAS radiances and high quality buoy estimates of SST. A linear regression analysis of these matches was performed to generate an empirical algorithm relating VAS window channel brightness

temperatures to buoy estimates of SST. Daily maps of SST during Hurricanes Alicia (1983) and Debbie (1982) demonstrated the ability of VAS to monitor air-sea interactions at high temporal and spatial scales. Monthly mean estimates of SST from VAS data were examined as part of the SST Intercomparison Workshop Series and showed typical standard deviations of 0.8-1.0°C with a diurnal warm bias of about 0.5°C compared to other estimates of SST. The VAS results for July 1982 emphasize the importance of using three infrared channels for the estimation of SST both day and night, because of the smaller brightness temperature attenuation by water vapor and aerosols at 3.9  $\mu\text{m}$  than at 11.0 and 12.6  $\mu\text{m}$ .

Operational processing of VAS data from both GOES-East and GOES-West will begin in 1986. Prior to that time, matches of VAS SST's with buoys will continue in order to obtain a second set of daytime matches and to establish appropriate cloud screening tests for nighttime data. In addition, McIDAS will soon have the capability to navigate and process AVHRR data. This will allow an intercalibration of the VAS and AVHRR instruments and will also permit the multi-angle method of determining SST to be evaluated over large regions. It is hoped that by taking advantage of the best qualities of each instrument, that an optimal satellite SST product with even higher accuracy than any single product evaluated in the SST Intercomparison Workshop Series can be produced. Such a product is required by the climate modeling community and may also provide a means for accurately estimating surface fluxes over the oceans from satellite data.



**Acknowledgements**

Portions of this research were supported by National Science Foundation Grant ATM-8205386.

## References

Anding, D., and R. Kauth, Estimation of sea surface temperature from space, *Remote Sens. Environ.*, 1, 217-220, 1970.

Anthes, R.A., Tropical cyclones: their evolution, structure, and effects. *Meteorological Monographs*, 19, February 1982, 208 pp.

Barton, I.J., Dual channel satellite measurements of sea surface temperature, *Quart. J. R. Met. Soc.*, 109, 365-378, 1983.

Case, R.A., and H.P. Gerrish, Atlantic Hurricane season of 1983. *Mon. Wea. Rev.*, 112, 1020-1027.

Clark, G.B., Atlantic Hurricane season of 1983. *Mon. Wea. Rev.*, 111, 1071-1079, 1983.

Deschamps, P.Y., and T. Phulpin, Atmospheric correction of infrared measurements of sea surface temperature using channels at 3.7, 11, and 12  $\mu\text{m}$ , *Boundary Layer Meteorol.*, 18, 131-143, 1980.

Deschamps, P.Y., and R. Fouin, Large diurnal heating of the sea surface observed by the HCMR experiment, *J. Phys. Oceano.*, 14, 177-184, 1984.

JPL, Satellite-derived sea surface temperature: Workshop I. JPL Publication 83-34, Jet Propulsion Laboratory, California Inst. of Technology, Pasadena, CA.

Leipper, D.F., Observed ocean conditions and Hurricane Hilda, 1964. J. Atmos. Sci., 24, 182-196, 1967.

Maul, J.A., P. Webb DeWitt, A. Yanaway, and S.R. Baig, Geostationary satellite observations of Gulf Stream Meanders: infrared measurements and time series analysis. J. Geophys. Res., 83, 6123-6131, 1978.

Maul, G.A., Application of GOES visible-infrared data to quantifying mesoscale ocean surface temperature, J. Geophys. Res., 86, 8007-8021, 1981.

Martin, P.J., Mixed-layer simulation of buoy observations taken during Hurricane Elouise. J. Geo. Res., 87, 409-427, 1982.

McClain, E.P., Multiple atmospheric-window techniques for satellite sea surface temperatures, in Oceanography from Space, edited by J.F.R. Gower, Plenum, New York, 73-85, 1981.

McClain, E.P., W.G. Pichel, C.C. Walton, Z. Ahmad, and J. Sutton, Multi-channel improvements to satellite-derived global sea surface temperatures, Adv. Space Res., 2, 43-47, 1983.

McClain, E.P., and A.E. Strong, Improved ocean surface temperatures from space-comparisons with drifting buoys, Bull. Amer. Meteor. Soc., 65, 138-142, 1984.

McMillin, L.M., Estimation of sea surface temperature from two infrared window measurements with different absorption, J. Geophys. Res., 80, 5113-5117, 1975.

Menzel, W.P., W.L. Smith, and L.D. Herman, Visible infrared spin-scan radiometer atmospheric sounder radiometric calibration: An inflight evaluation from intercomparisons with HIRS and radiosonde measurements, Appl. Opt., 20, 3641-3644, 1981.

Prabhakara, C., G. Dalu, and V.G. Knudu, Estimation of sea surface temperature from remote sensing in the 11- to 13-micron window, J. Geophys. Res., 79, 5039-5044, 1974.

Reynolds, R.W., A monthly averaged climatology of sea surface temperatures, NOAA-TR-NWS-31, Washington, D.C., 35 pp., 1982.

Satellite-derived sea surface temperature: Workshop-3, February 22-25, 1984, Pasadena, California, xx pp.

Smith, W.L., V.E. Suomi, W.P. Menzel, H.M. Woolf, L.A. Sromovsky, H.E. Revercomb, C.M. Hayden, D.N. Erickson, and F.R. Mosher, First sounding results from VAS-D, Bull. Amer. Meteor. Soc., 62, 232-236, 1981.

Smith, W.L., The retrieval of atmospheric profiles from VAS geostationary radiance observations, J. Atmos. Sci., 40, 2025-2035, 1983.

Strong, A.E., Use of drifting buoys to improve accuracy of satellite sea surface temperature measurements, Tropical Ocean-Atmosphere Newsletter, No. 25, 16-18, 1984.

Suomi, V.E., T. Vonder Haar, R. Kraus, and A. Stamm, Possibilities for sounding the atmosphere from a geosynchronous spacecraft. Space Research, 11, COSPAR, 609-617, 1971.

Suomi, V.E., R. Fox, S.S. Limaye, and W.L. Smith, McIDAS-III: A modern interactive data access and analysis system. J. Clim. Applied Meteor., 22, 766-778, 1983.

Zandlo, J.A., W.L. Smith, W. P. Menzel, and C.M. Hayden, Surface temperature determination from an amalgamation of GOES and TIROS-N measurements. J. Applied Meteor., 21, 44-50, 1982.

## Figures

Figure 1. Daytime VAS three window channel SST( $^{\circ}$ C) for December 18, 1983, objectively analyzed on a 0.2 degree latitude/longitude grid.

Figure 2. Nighttime VAS three window channel SST( $^{\circ}$ C) for February 7, 1984, objectively analyzed on a 1.0 degree latitude/longitude grid.

Figure 3. Daytime VAS three window channel SST( $^{\circ}$ C) objectively analyzed on a 0.5 degree latitude/longitude grid for a) August 15, b) August 16, c) August 17, d) August 18, e) August 19, f) August 20, 1983.

Figure 4. Daytime VAS three window channel SST( $^{\circ}$ C) objectively analyzed on a 0.5 degree latitude/longitude grid for a) September 13, 14, and 15 mean, b) September 13, and c) September 15, 1982.

Figure 5. Thematic contour maps of SST anomalies( $^{\circ}$ C) for March 1982 for a) SMMR, b) AVHRR, c) VAS, d) ships, and e) HIRS/MSU.

Figure 6. Thematic contour maps of SST anomalies( $^{\circ}$ C) for July 1982 for a) SMMR, b) AVHRR, c) VAS, d) ships, and e) HIRS/MSU.

Figure 7. Geometric interpretation of the multi-angle surface temperature estimation technique.

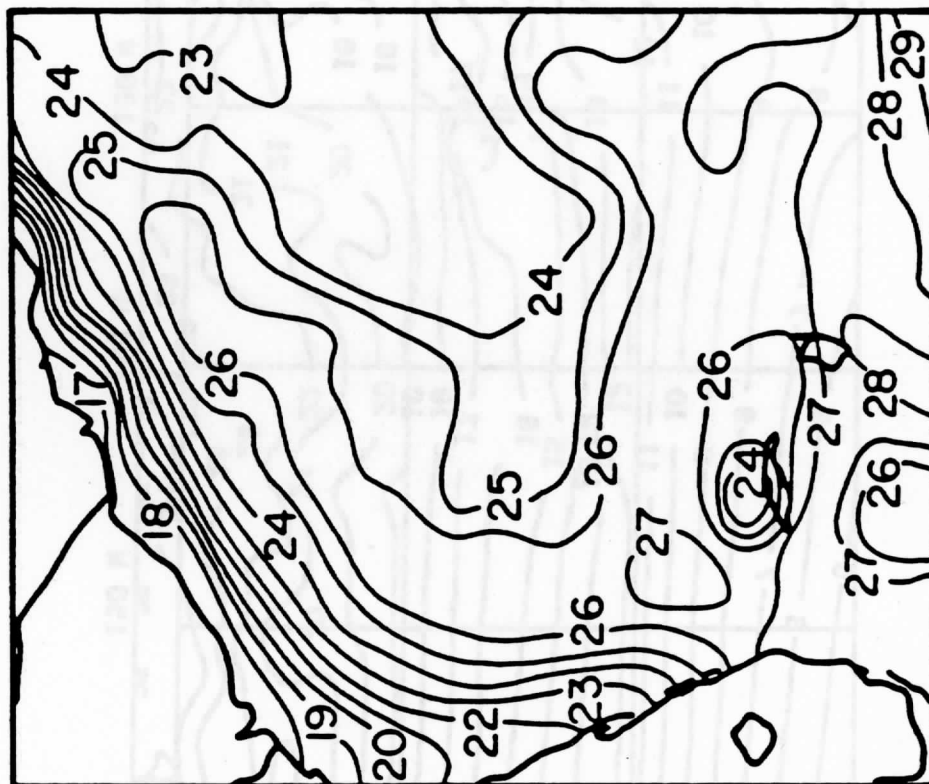


Figure 1.

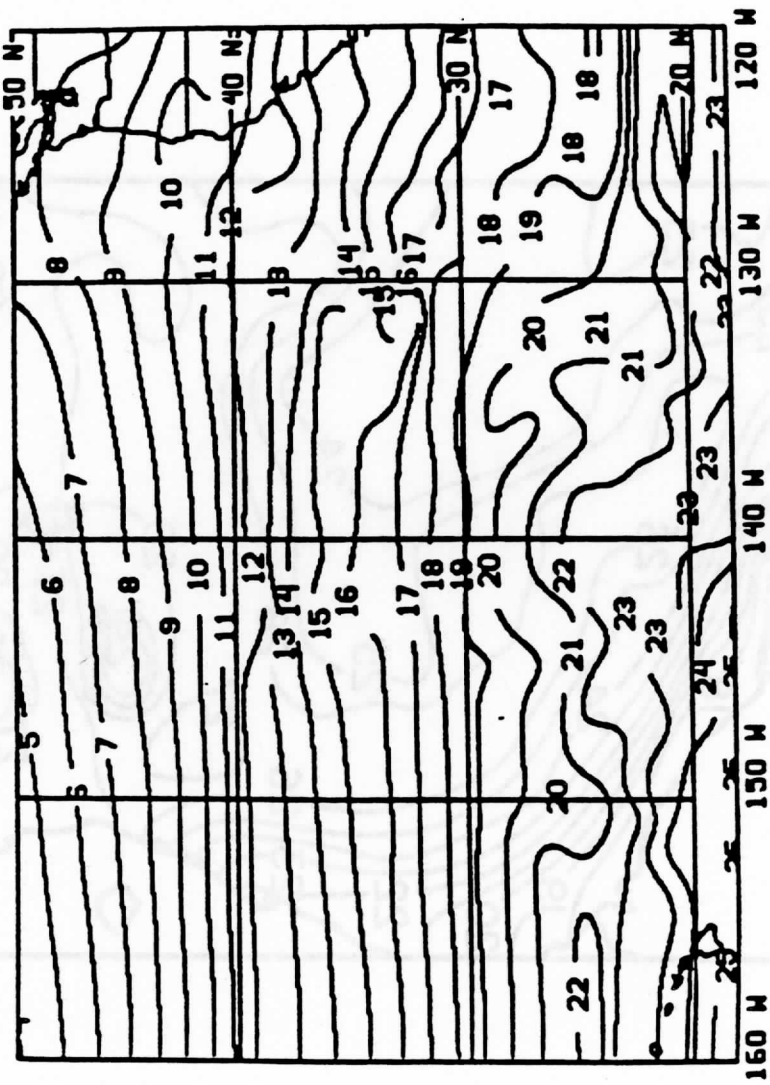


Figure 2.



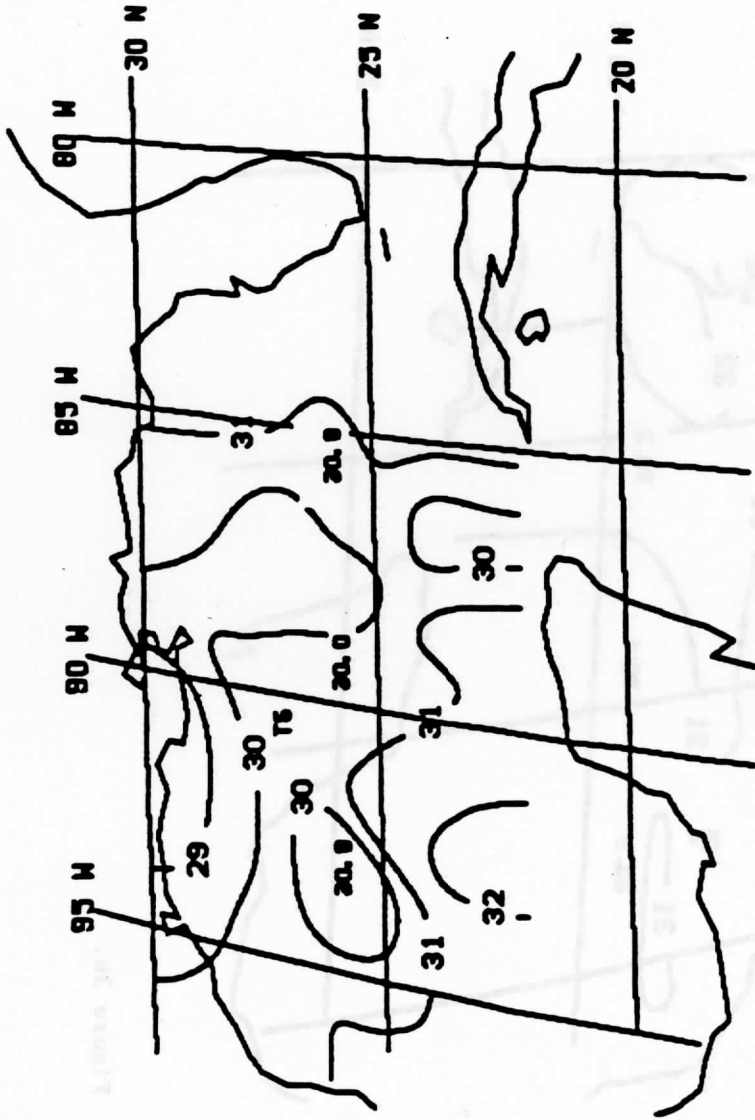


Figure 3a.

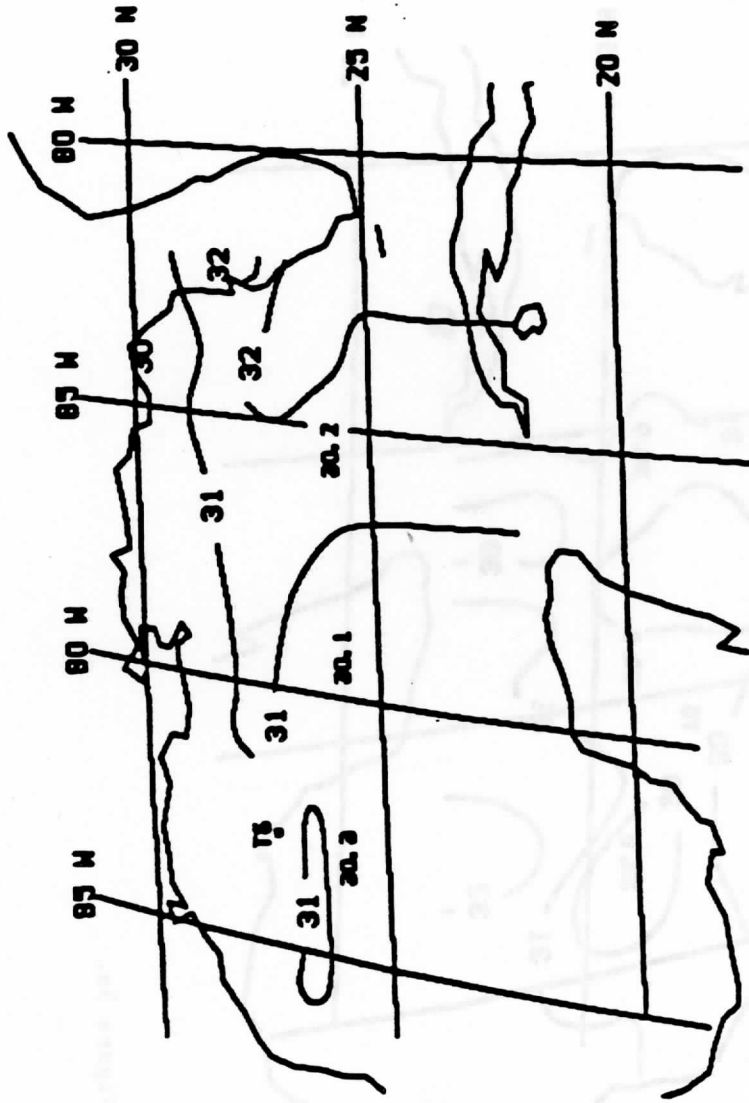


Figure 3b.

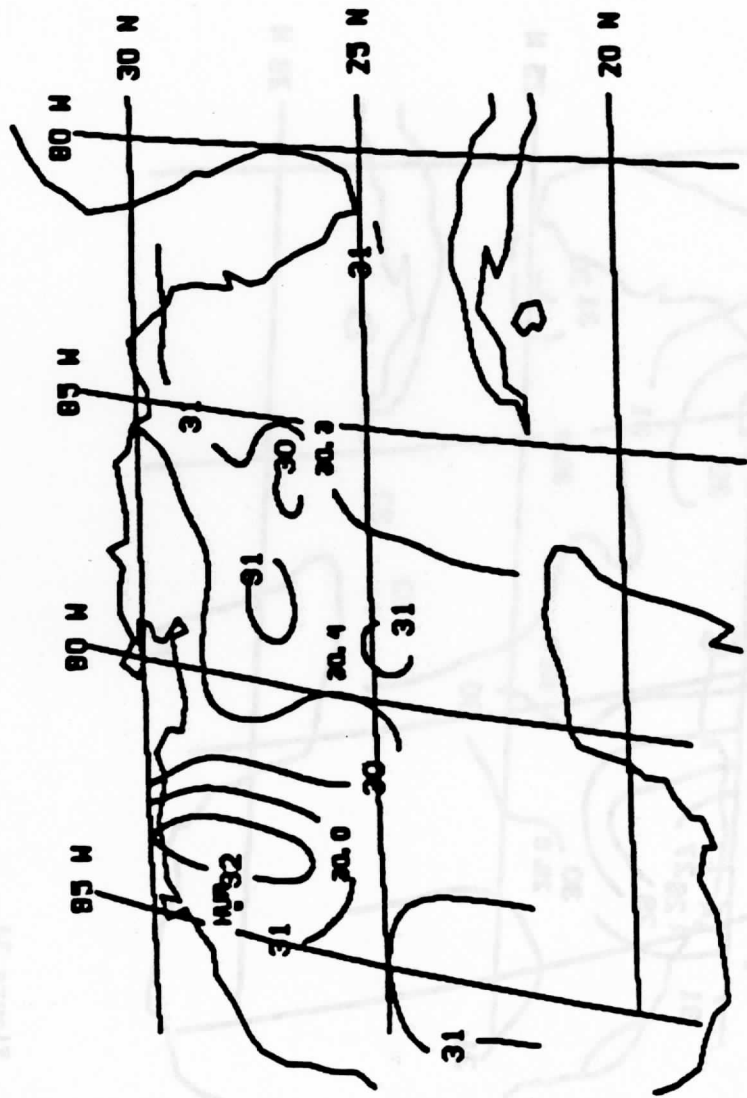


Figure 3c.

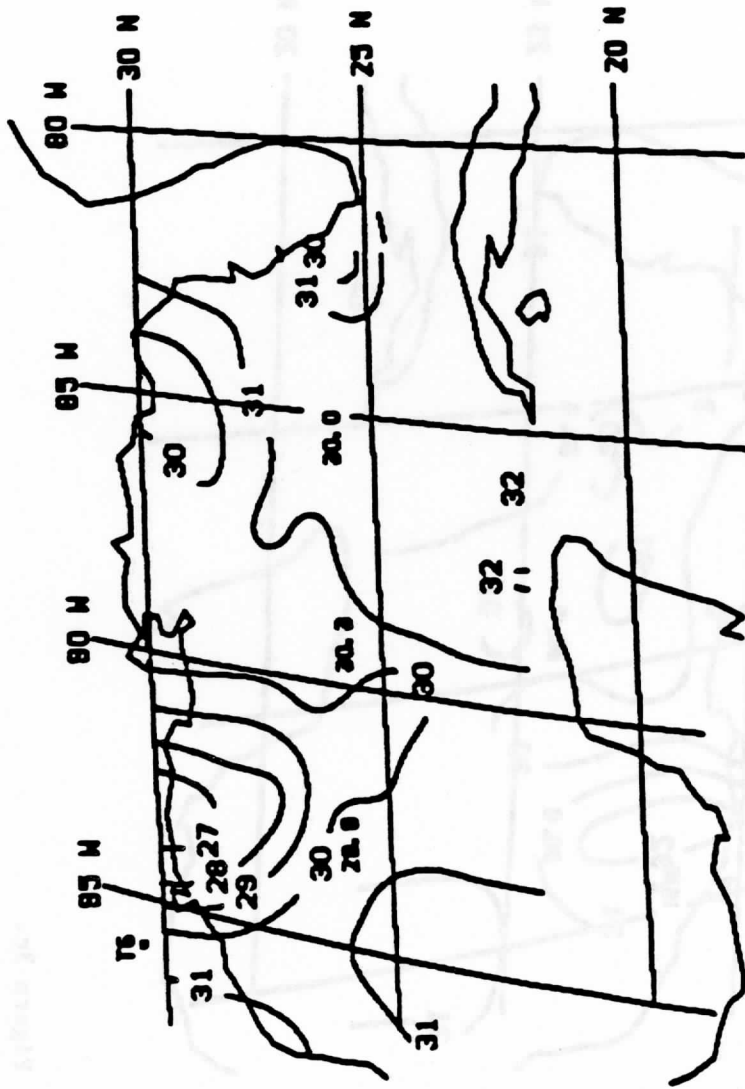


Figure 3d.

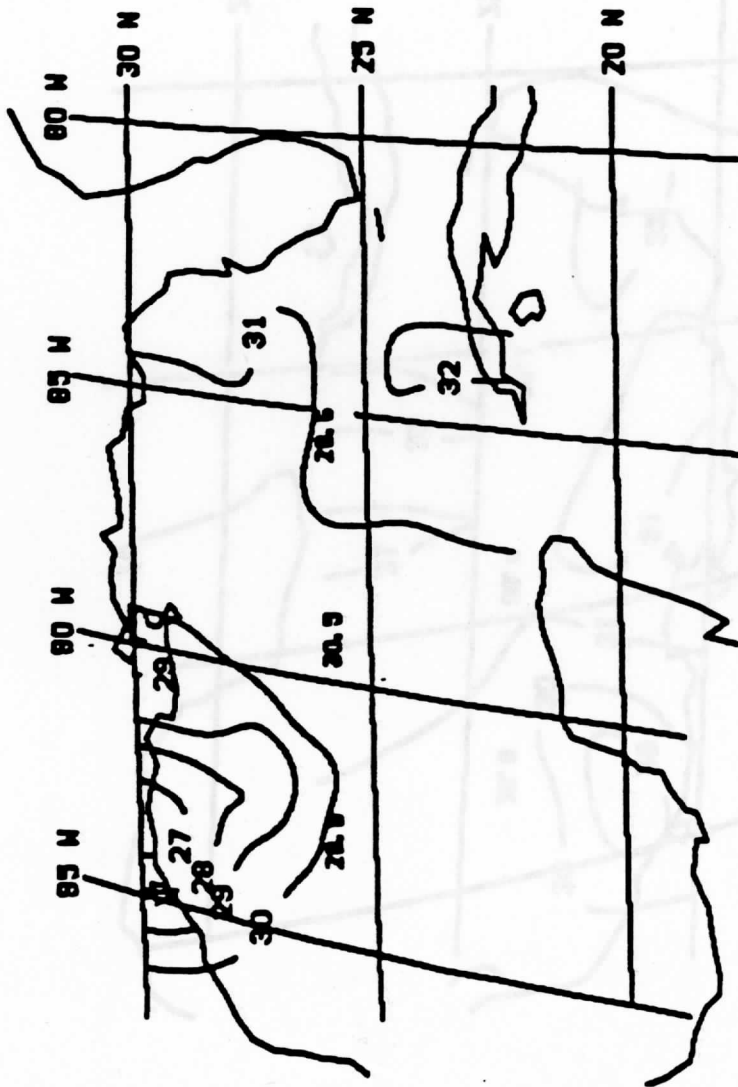


Figure 3e.

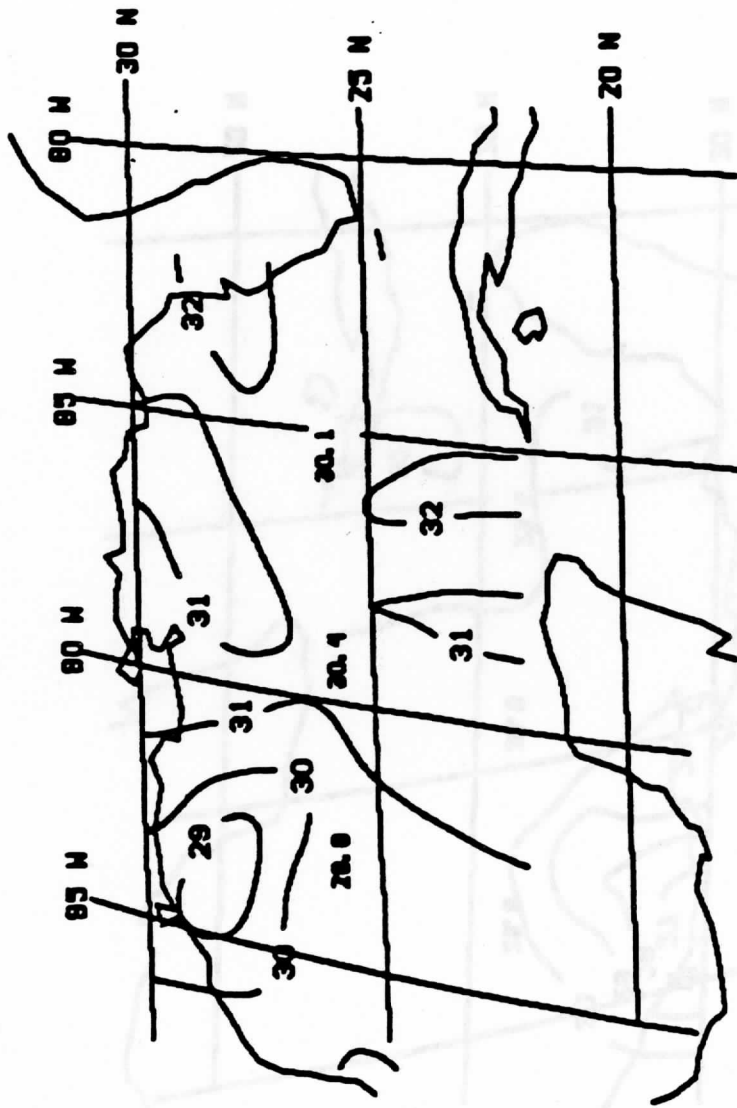


Figure 3f.

FIGURE 4a

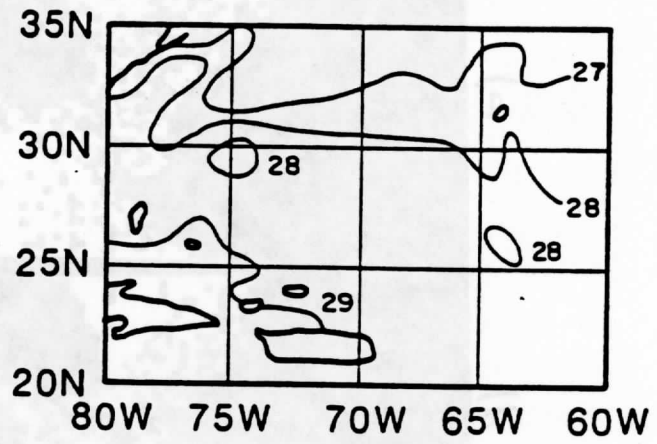


FIGURE 4b

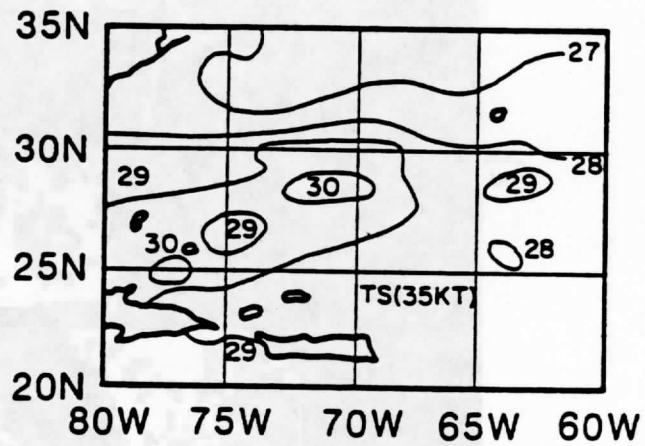


FIGURE 4c

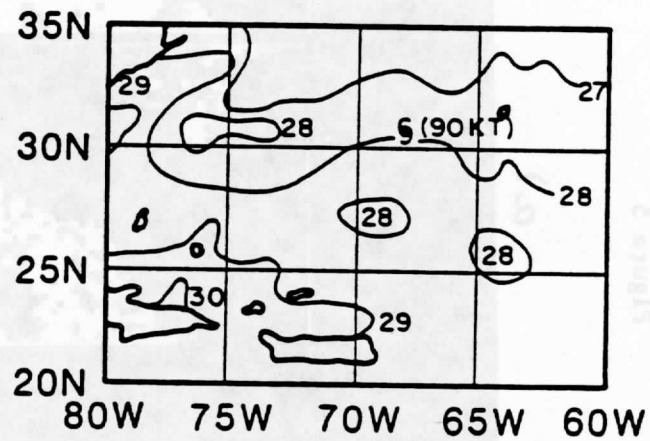


Figure 5

a)

b)

c)

d)

e)



Degrees Celsius

-3.5 -2.5 -1.5 -0.5 0.5 1.5 2.5 3.5



Figure 6

a.)                    b.)                    c.)                    d.)                    e.)



Degrees Celsius



-3.5 -2.5 -1.5 -0.5 0.5 1.5 2.5 3.5

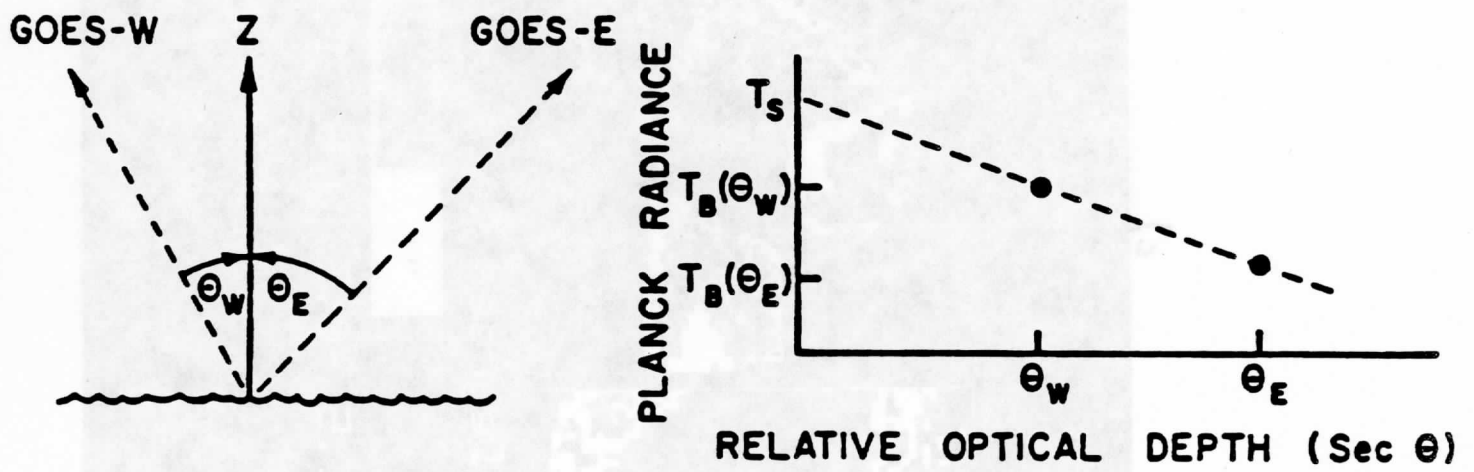


Figure 7.

Tables

Table 1. VAS SST channel instrument characteristics (GOES-5)

Spectral Channel	Central wavenumber (cm <sup>-1</sup> )	Single sample NEAT* (°C)	Nine sample NEAT* (°C)
7	789.39	0.37	0.12
8	889.52	0.10	0.03
12	2538.07	0.14	0.04

\*Noise Equivalent Temperature Difference

Table 2. VAS SST regression relations (SST in K)

	<u>Correlation</u> <u>Coefficient</u>	<u>Explained</u> <u>Variance (°C)</u>	<u>Standard</u> <u>Error (°C)</u>
2 Channel	0.83	0.68	1.12
3 Channel	0.87	0.76	0.98

$$\text{SST (2 channel)} = T_{11} + 1.2956(T_{11} - T_{12}) - 0.2846$$

$$\text{SST (3 channel)} = T_{11} + 0.7987(T_{3.9} - T_{12}) + 0.6316$$

TABLE 3

CROSS CORRELATIONS OF SATELLITE SST ESTIMATES VERSUS SHIP SST ESTIMATES FOR MARCH 1982

	Number of Matches			Bias			Standard Deviation			Cross Correlation						
	AVHRR	SMRR	HIRS	VAS	AVHRR	SMRR	HIRS	VAS	AVHRR	SMRR	HIRS	VAS				
Global	4322	1972	-	425	-0.06	-0.01	-	+0.63	0.81	1.20	-	0.96	0.58	0.25	-	0.59
North Pacific (0-56°N)	1563	815	-	127	-0.26	-0.05	-	+0.52	0.67	0.99	-	0.92	0.64	0.29	-	0.61
North Pacific (20-56°N)	1033	529	1054	53	-0.39	-0.01	+0.54	+1.05	0.65	1.03	1.07	0.89	0.60	0.36	0.28	0.63
Tropical Pacific (20°N-20°S)	837	412	858	165	+0.10	-0.22	+0.23	+0.20	0.73	0.87	0.93	0.90	0.13	0.08	0.03	0.10
South Pacific (20-56°S)	535	202	541	21	+0.24	+0.55	+0.05	+1.73	0.78	1.19	1.11	1.24	0.42	0.08	0.28	-0.39
South Pacific (0-56°S)	984	328	-	112	+0.26	+0.17	-	+0.52	0.80	1.14	-	1.20	0.29	0.11	-	0.23
VAS Pacific Region (14°N-30°S)	178	81	-	181	+0.06	-0.16	-	+0.35	0.89	0.91	-	1.06	0.23	-0.08	-	0.03
Global AVHRR	2214	1088	2229	211	+0.03	+0.12	+0.20	+0.55	0.86	1.11	1.04	1.12	0.48	0.29	0.20	0.41
E1 Chichon Mask	715	315	-	186	-0.33	-0.92	-	+0.76	0.61	1.18	-	0.79	0.58	-0.02	-	0.65

TABLE 4

CROSS CORRELATIONS OF SATELLITE SST ESTIMATES VERSUS SHIP SST ESTIMATES FOR JULY 1982

	Number of Matches			Bias			Standard Deviation			Cross Correlation						
	AVHRR	SMRR	HIRS	AVHRR	SMRR	HIRS	AVHRR	SMRR	HIRS	AVHRR	SMRR	HIRS				
Global	3962	1826	-	437	-0.54	-0.18	-	+0.60	0.90	1.08	-	0.85	0.44	0.38	-	0.26
North Pacific (0-56°N)	1368	708	-	116	-0.69	+0.26	-	+0.91	0.95	0.89	-	0.80	0.41	0.46	-	0.17
North Pacific (20-56°N)	514	221	-	26	-0.18	+0.11	-	+0.40	0.64	1.13	-	1.25	0.50	0.24	-	-0.10
Tropical Pacific (20°N-20°S)	779	366	-	165	-0.69	+0.10	-	+0.77	0.83	0.83	-	1.00	0.30	0.27	-	0.07
South Pacific (20-56°S)	958	480	-	51	-0.54	-0.31	-	+0.61	0.98	0.92	-	0.50	0.46	0.44	-	0.11
South Pacific (0-56°S)	883	359	-	126	-0.23	+0.06	-	+0.50	0.67	1.03	-	1.05	0.41	0.26	-	0.00
VAS Pacific Region (14°N-30°S)	162	104	-	174	-0.38	+0.16	-	+0.68	0.81	1.10	-	1.08	0.25	0.05	-	0.01
Global AVHRR	2305	1112	-	216	-0.20	+0.02	-	+0.49	0.77	1.08	-	0.90	0.49	0.41	-	0.26
EI Chichon Mask (0-56°N)	695	324	-	195	-0.81	-1.06	-	+0.49	0.87	1.06	-	0.67	0.38	0.21	-	0.40

# Total Ozone from NOAA Satellites—A Physical Model for Obtaining Measurements with High Spatial Resolution

XIA-LIN MA<sup>1</sup>

Cooperative Institute for Meteorological Satellite Studies, 1225 West Dayton Street, Madison, WI 53706

WILLIAM L. SMITH AND HAROLD M. WOOLF

NOAA/NESDIS Development Laboratory, 1225 West Dayton Street, Madison, WI 53706

(Manuscript received 11 June 1983, in final form 6 June 1984)

## ABSTRACT

A physical model is presented for calculating the total ozone amount from HIRS radiance measurements from TIROS-N/NOAA satellites. Simulations and retrievals indicate that the total ozone amount can be retrieved with an accuracy better than 5%. Comparisons are presented of analyses of real data physical ozone retrievals from HIRS observations with analyses of regression ozone retrievals from HIRS observations obtained operationally by NOAA/NESDIS, and with analyses of ozone measurements from the Nimbus-G satellite by the Total Ozone Mapping Spectrometer (TOMS). Comparisons of these analyses show that small scale ozone features not resolved by operational regression retrievals are resolved quite well by the higher spatial resolution HIRS retrievals using the physical algorithm.

## 1. Introduction

Ozone is an important atmospheric constituent between 10 and 50 km above the earth's surface. Because it absorbs ultraviolet radiation from the sun, ozone protects the biosphere from harmful effects of ultraviolet radiation. Also, ozone is a prime source of thermal energy in the low stratosphere and has been shown to be a useful tracer for stratospheric circulation (Dütsch, 1981). Prabhakara *et al.* (1970, 1973, 1976) and Lovill *et al.* (1982) had previously exploited remote sensing of the total ozone using satellite infrared emission measurements. Their studies reveal a strong correlation between the meridional gradient of total ozone and the wind velocity at tropopause levels (Lovill, 1972; Prabhakara *et al.*, 1973). Recently, Shapiro *et al.* (1982) have suggested the possibility of predicting the position and intensity of jet streams using total ozone measured by a satellite.

The main purpose of this paper is to present a method for obtaining total ozone with high spatial resolution from the TIROS-N/NOAA series of satellites. The ozone amount is derived from the 9.6  $\mu\text{m}$  ozone radiance observations made by the High-Resolution Infrared Radiation Sounder (HIRS). At the University of Wisconsin Space Science and Engineer-

ing Center (SSEC), HIRS and Microwave Sounding Unit (MSU) radiances observed from TIROS-N/NOAA satellites can be received and processed in real time. Temperature and water vapor profiles, as well as the total ozone distribution, are obtained (Smith *et al.*, 1979). The meteorological inferences possess a resolution of 75 km. Through use of a physical algorithm for processing the data, the influence of clouds on the ozone determinations is alleviated.

## 2. Algorithm

For a nonscattering atmosphere in local thermodynamic equilibrium, the radiative transfer equation may be expressed as

$$R(\nu, \theta) = B(\nu, T_s)\tau(\nu, \theta, p_s) - \int_0^{p_s} B(\nu, T) \left( \frac{\partial \tau(\nu, \theta, p)}{\partial p} \right) dp, \quad (1)$$

where  $R(\nu, \theta)$  is the radiance at a particular wavenumber  $\nu$  for a zenith angle of observation  $\theta$ ,  $B(\nu, T)$  is the Planck function of temperature, and  $\tau(\nu, \theta, p)$  is the transmittance from the pressure level  $p$  to the top of the atmosphere along the observation angle  $\theta$ . The subscript  $s$  denotes surface values, either ground or cloud. Equation (1) is used to estimate the total ozone in the atmosphere from HIRS radiance measurements in the 9.6  $\mu\text{m}$  spectral channel.

Ozone concentration is related to radiance to space

<sup>1</sup> Present affiliation: National Meteorological Bureau, Beijing, People's Republic of China.

through the transmittance  $\tau(\nu, \theta, p)$ . Using a first-order Taylor expansion of the Planck function in terms of temperature, and integrating Eq. (1) by parts, the radiative transfer equation can be expressed as

$$T_B(\nu, \theta) - T_B^n(\nu, \theta) = \int_0^{p_s} [\tau(\nu, \theta, p) - \tau^n(\nu, \theta, p)] Q(\nu, \theta, p) \frac{dp}{p},$$

where  $T_B(\nu, \theta)$  is the measured brightness temperature,  $T_B^n(\nu, \theta)$  is the brightness temperature calculated for the  $n$ th estimate of the ozone profile whose corresponding transmittance profile is  $\tau^n(\nu, \theta, p)$ , and

$$Q(\nu, \theta, p) = \frac{\partial B(\nu, \theta, T)/\partial T}{\partial B(\nu, \theta, T_B)/\partial T} \left( \frac{\partial T}{\partial \ln p} \right).$$

Using the mathematical derivation of Smith (1970, 1983) for water vapor retrieval, the brightness temperature measured by HIRS in the 9.6  $\mu\text{m}$  ozone band can be related to the ozone concentration  $u(p)$ :

$$T_B(\nu, \theta) - T_B^n(\nu, \theta) = \int_0^{p_s} \ln \frac{u(p)}{u^n(p)} W^n(\nu, \theta, p) \frac{dp}{p}, \quad (2)$$

where

$$W^n(\nu, \theta, p) = \left( \frac{\partial B(\nu, \theta, T)/\partial T}{\partial B(\nu, \theta, T_B)/\partial T} \right) \left( \frac{\partial T}{\partial \ln p} \right) \left( \frac{\partial \tau(\nu, \theta, p)}{\partial \ln u^n(p)} \right),$$

and the superscript  $n$  denotes an  $n$ th estimate. For every pressure level (0.1, 0.2, 0.5, 1.0, 1.5, 2.0, 3.0, 4.0, 5.0, 7.0, 10.0, 15.0, 20.0, 25.0, 30.0, 50.0, 60.0, 70.0, 85.0, 100.0, 115.0, 135.0, 150.0, 200.0, 250.0, 300.0, 350.0, 400.0, 430.0, 475.0, 500.0, 570.0, 620.0, 670.0, 700.0, 780.0, 850.0, 920.0, 950.0 and 1000.0 mb) an estimate of the true ozone concentration profile is obtained using

$$u^{n+1}(p) = u^n(p) \gamma^n(\nu), \quad j = 1, 2, \dots, 40.$$

Thus, according to (2), assuming that the true ozone profile is proportional to the  $n$ th estimate by the scalar  $\gamma^n(\nu)$ ,

$$\begin{aligned} \gamma^n(\nu) &= \frac{u(p)}{u^n(p)} \\ &= \exp \left\{ [T_B(\nu) - T_B^n(\nu)] \left[ \int_0^{p_s} W^n(\nu, p) \frac{dp}{p} \right]^{-1} \right\}. \end{aligned} \quad (3)$$

In summary, (3) is iterated until  $\gamma^n(\nu) \cong 1.0$ , and thus  $u(p) \cong u^n(p)$ . The total ozone amount is obtained by vertical integration of the mixing ratio profile.

The iteration is terminated as soon as the difference between the measured ozone brightness temperature and that calculated is less than the measurement noise level (approximately 0.2°C). The first guess ozone profile is constructed using regression relations between the ozone concentration and the infrared

brightness temperature observations of stratospheric carbon dioxide emission. There is excellent correlation between the ozone concentration and the brightness temperatures observed in the HIRS carbon dioxide channels (HIRS channels 1-4) because the dynamic processes which cause warm and cold stratospheric air also cause maxima and minima of total ozone. The regression coefficients are derived from a set of conventional ozone and temperature profiles (452 samples), and radiances synthesized from them, covering all seasons of the year over the Northern Hemisphere. Since the total ozone distribution changes rapidly with latitude across a transition zone around 30°N (Prabhakara *et al.*, 1973), two sets of regression coefficients are generated to separate midlatitude structures from low latitude structures. Furthermore, because ozone and temperature sounding data yield good statistics only up to 10 mb (~30 km), the ozone and temperature profiles are extrapolated using standard-atmosphere lapse rates between 10 and 1.0 mb (up to ~50 km). The contribution to the outgoing radiation by ozone above the 10 mb level is only a few percent of the total radiance measured. Above 50 km, the ozone contribution to the outgoing radiation is negligible.

The profile shape and the vertical position of the peak ozone mixing ratio corresponding to the ozone guess profile are crucial to obtaining a satisfactory retrieval, since only one ozone channel radiance in the 9.6  $\mu\text{m}$  band is available. This is because the true ozone profile is assumed to have the same shape as the first guess. If the position of the ozone peak mixing ratio is higher or lower than the true situation in the atmosphere, a large error will result in the total ozone calculation. Therefore, in order to make the ozone guess profile sufficiently accurate in both shape and the position of the ozone peak mixing ratio, it was found necessary to make an adjustment to the vertical position of the first guess ozone peak mixing ratio. Specifically, the ozone mixing ratio profile is moved up or down  $\delta N$  levels calculated by

$$\delta N = 0.5 + 1.4^*(T^{\text{cal}} - T^{\text{obs}}) \quad (4)$$

for low latitudes,

$$\delta N = -0.2 + 1.8^*(T^{\text{cal}} - T^{\text{obs}}) \quad (5)$$

for middle latitudes, where  $T^{\text{cal}}$  and  $T^{\text{obs}}$  are the brightness temperatures calculated from the ozone guess profile and observed in the ozone 9.6  $\mu\text{m}$  band, respectively. The coefficients of Eqs. (4) and (5) are obtained by linear regression between  $\delta N$  and  $(T^{\text{cal}} - T^{\text{obs}})$  obtained from an independent set of conventional sounding data (382 samples). For the regression analysis,  $\delta N$  was specified as that value which yielded the best retrieval of total ozone concentration. Generally, the  $\delta N$  adjusted profile will satisfy the radiance observation to within 5% of the measured value.



As already indicated, since the advent of the NOAA satellites, the temperature and water vapor distributions which are measured by HIRS carbon dioxide and water vapor channels and MSU oxygen channels can be retrieved. Furthermore, the pressure altitude and temperature of any cloud within the instrument's field of view can be estimated from CO<sub>2</sub> and window infrared radiance observations (Smith and Platt, 1978). From the ozone-CO<sub>2</sub>-O<sub>2</sub> radiance regression relations, a guess ozone profile can be established. Using the ozone transmittance calculated from the guess ozone profiles and the retrieved temperature, moisture and cloud conditions, the ozone brightness temperature corresponding to the guess is calculated using Eq. (1). Given the guess and the observed ozone brightness temperatures in the 9.6 μm region, δN is determined by Eq. (4) or (5). After modifying the ozone guess profile with δN pressure levels, the measured ozone radiance is used in the iterative solution (3) to achieve a final estimate of the ozone amount which satisfies the observed radiance value to well within measurement noise (i.e., less than 0.1 mW m<sup>-2</sup> sr cm<sup>-1</sup>).

### 3. Results and discussion

In order to assess the accuracy of HIRS total ozone measurements, the model for calculating ozone was applied to HIRS radiances synthesized from a temperature, water vapor and ozone sounding data set. The soundings, provided by Dr. Norman Phillips (NMC), were prepared as a dependent set for scientists to develop and test new instrument concepts or retrieval algorithms. The data set has 1600 soundings and is grouped into four categories corresponding to two seasons (summer and winter) and two latitude zones (tropical and middle). The ozone profile corresponding to each temperature and moisture profile was synthesized using a climatological height-latitude cross section of ozone mixing ratio and a climatological latitude profile of 500 mb temperature for summer and winter conditions (N. Phillips, personal communication, 1983). The ozone profile for a specific radiosonde observation was then merely assigned on the basis of the observed 500 mb temperature, with some small random error added to reduce the "built-

TABLE 1. Total ozone accuracy comparison. (Units: Dobson, where 1000 Dobson = 1 cm STP km<sup>-1</sup>; guess ozone profile fixed.)

Season	Latitudinal zone	Error* (guess, %)	Error (retrieval, %)
Summer	Low	12.6	4.0
Summer	Middle	6.4	5.5
Winter	Low	13.8	3.9
Winter	Middle	7.6	4.1

\* Error (%) is the sum of absolute differences between the guess total ozone (or retrieved) and the "true" total ozone divided by the sum of "true" total ozone values.

TABLE 2. Total ozone accuracy comparison (guess ozone profile adjusted).

Season	Latitudinal zone	Error (adjusted guess, %)	Error (retrieval, %)
Summer	Low	7.4	3.7
Summer	Middle	6.7	3.8
Winter	Low	8.1	4.0
Winter	Middle	8.9	3.3

in" 500 mb temperature versus ozone profile correlation in the final profile data set. HIRS radiances were synthesized for each sounding using the radiative transfer equation (1). The retrieval techniques described in Section 2 were then applied to obtain total ozone measurements.

Tables 1 and 2 present the accuracy of the guess total ozone that is predicted by the regression method and the total ozone obtained from the iterative technique. From Tables 1 and 2 it can be seen that the iterative technique is successful in producing a total ozone estimate which is more accurate than the regression guess even though there is a "built-in" temperature-ozone correlation in the data set as a result of the manner in which the ozone profile was prescribed. Furthermore, correcting the ozone guess profile using the HIRS ozone channel radiance improves both the guess estimate of total ozone and the iterative solution, the resulting average error being less than 4% of the mean total ozone of the data set.

A real data test of the retrieval procedure was conducted using a set of measurements by the HIRS flown on NOAA-6. The HIRS sounding data are received and processed in quasi-real time on the Man-computer Interactive Data Access System (McIDAS) at the University of Wisconsin (Smith *et al.*, 1979). Sounding radiances are generated from 3 × 3 arrays of HIRS fields of view yielding a spatial resolution of 75 km for the retrieved profiles. Cloud-top pressures and temperatures are specified (Smith and Platt, 1978), enabling the cloud contribution to the ozone channel radiance to be accounted for explicitly in (1).

TOMS (Total Ozone Mapping Spectrometer) estimates of total ozone kindly provided by A. J. Krueger (NASA, GLAS) were used to verify the NOAA-6 ozone retrievals. The TOMS estimates exhibit a precision of 2% relative to ground truth stations (Shapiro *et al.*, 1982). Two HIRS orbits were used for the comparison, one each on 24 and 30 April 1982. Also, total ozone estimates produced operationally from NOAA HIRS data by NESDIS and analyzed by the National Meteorological Center were obtained from X. Miller (personal communication, 1983) for comparison with the TOMS data for the same two days.

Figures 1 and 2 show analyses of HIRS physical, HIRS operational and TOMS total ozone estimates.

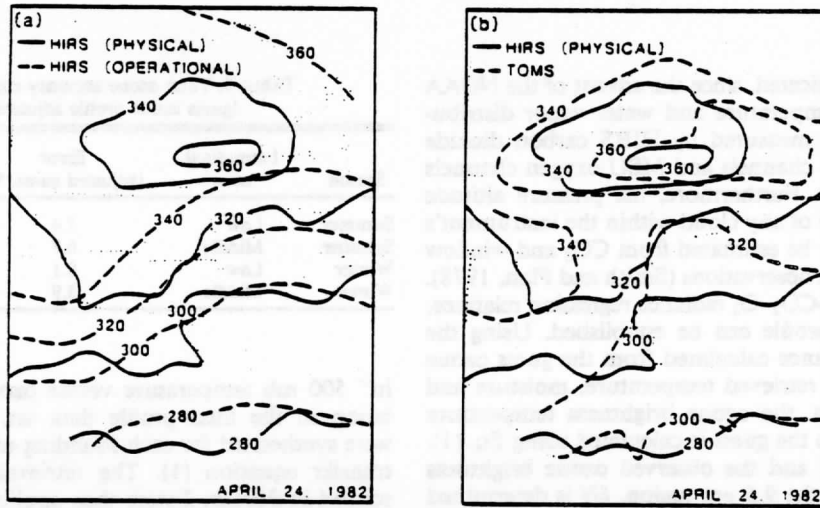


FIG. 1. Analyses of total ozone for 24 April 1982 retrieved from HIRS radiances using the physical algorithm with (a) operational pure regression retrievals and (b) ozone retrievals from TOMS measurements of the absorption of backscattered ultraviolet radiation.

Comparisons of the physical retrievals with the pure regression retrievals produced operationally (Figs. 1a and 2a) reveal that features can be resolved with much higher spatial resolution by the physical retrievals. This result is due to the fact that the physical retrievals are obtained with a spatial resolution of 75 km and for all cloud conditions, whereas the operational retrievals are spaced at a distance of 250 km and are not produced for overcast cloud conditions. Also, regression retrievals will always tend to underestimate the variance of the predicted variable if less than a perfect correlation exists with the predictor variable. Figures 1b and 2b, which compare analyses of HIRS physical ozone retrievals with TOMS obser-

vations, imply that the higher spatial resolution features are indeed real. For example, the high ozone concentration area estimated over Wisconsin on 24 April is in excellent agreement with the TOMS observations, as is the axis of high ozone concentration along the east coast on 30 April. Table 3 provides a comparison of the discrepancy between TOMS measurements and total ozone estimates using the physical model, as well as from the NESDIS operational regression model, for 30 common measurement locations. Figures 3 and 4 show the scatter plots of the three total ozone measurements. From Table 3 and the scatter plots, it can be seen that the discrepancy between the TOMS total ozone estimates and those

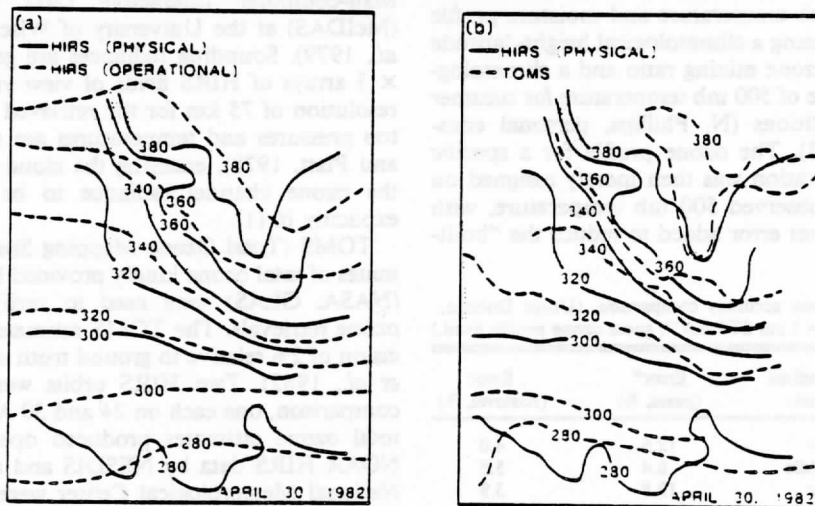


FIG. 2. As in Fig. 1 but for 30 April 1982.

B0555

T 20.18

4.3

4  
Paper 11  
6.0

TABLE 3. Discrepancy (%) of TOMS ozone measurements with HIRS retrievals obtained by the physical model and with the NESDIS operational regression model.

Time (GMT)	Physical model	Operational model
1411-1419		
24 April 1982	2.9	3.5
1330-1340		
30 April 1982	2.0	5.4

calculated from HIRS radiances by the physical retrieval model is much smaller than for the operational HIRS results. In most cases, the operational values of total ozone are smaller than those of the TOMS. It is apparent that the absolute and relative agreement of the total ozone estimates from HIRS with those from TOMS is significantly improved if the physical retrieval algorithm is used instead of a pure regression model. The average error (i.e., deviation from TOMS) of the physical retrieval estimates of total ozone is less than 3%, compared to 6% for the statistical regression (operational) results.

#### 4. Conclusion

In summary, a physical method for obtaining total ozone estimates from HIRS radiances has been presented. Both simulations and the results of real data retrievals indicate that an average accuracy of 4% can be achieved for total ozone estimates. Also, comparisons with TOMS retrievals indicate that the high resolution physical retrieval estimates more accurately represent the true total ozone distribution than those produced operationally using a pure regression algorithm. The method of ozone retrieval presented here

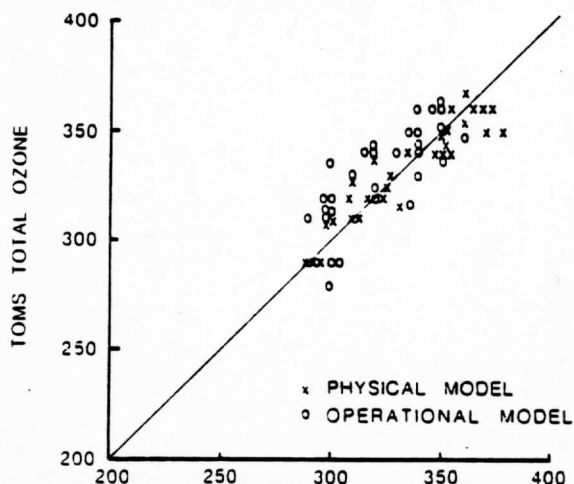


FIG. 3. Scatter diagrams of point comparisons of TOMS total ozone and HIRS physical and pure regression (operational) total ozone retrievals for 24 April 1982.

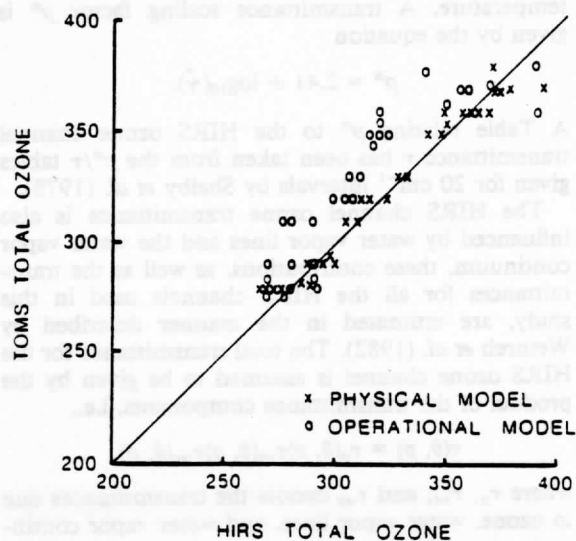


FIG. 4. As in Fig. 3 but for 30 April 1982.

has been included in the TOVS "Export Package" (Smith *et al.*, 1983) developed by the Cooperative Institute for Meteorological Satellite Studies (CIMSS) for processing direct readout TIROS-N/NOAA satellite sounding data.

*Acknowledgments.* We appreciate the assistance of Dr. Michael Weinreb (NOAA/NESDIS) in formulating the ozone transmittance model. Our appreciation is extended to Mrs. Gail Turluck and Mr. Tony Wendricks for their assistance in preparing the manuscript for publication. The support of Professor V. E. Suomi and his staff of the Space Science and Engineering Center at the University of Wisconsin is gratefully acknowledged.

#### APPENDIX

##### Ozone Transmittance Function

Transmittance accuracy is essential for the success of the ozone concentration retrieval process. Slight errors in transmittance calculations can result in significant errors in the retrieved ozone. The ozone transmittance function used in this study is based on the study of Gruenzel (1978) and the data of Selby *et al.* (1978) applied to a spectral response function approximating that for the HIRS ozone channel. The ozone transmittance for that channel has been represented as follows. The ozone equivalent path length  $\bar{\gamma}$  in units of  $\text{g kg}^{-1}$  is expressed as

$$\bar{\gamma} = \sec\theta \int_0^p q^* \left(\frac{p}{p_0}\right)^{2/5} \left(\frac{T_0}{T}\right)^{1/5} dp,$$

where  $q^*$  is the ozone mixing ratio,  $p$  and  $T$  are the atmospheric pressure and temperature, respectively,

and  $p_0$  and  $T_0$  are standard atmospheric pressure and temperature. A transmittance scaling factor  $p^*$  is given by the equation

$$p^* = 2.41 + \log_{10}(\bar{\gamma}).$$

A Table relating  $p^*$  to the HIRS ozone channel transmittance  $\tau$  has been taken from the  $p^*/\tau$  tables given for 20  $\text{cm}^{-1}$  intervals by Shelby *et al.* (1978).

The HIRS channel ozone transmittance is also influenced by water vapor lines and the water vapor continuum, these contributions, as well as the transmittances for all the HIRS channels used in this study, are estimated in the manner described by Weinreb *et al.* (1982). The total transmittance for the HIRS ozone channel is assumed to be given by the product of the transmittance components, i.e.,

$$\tau(\theta, p) = \tau_o(\theta, p)\tau_{wl}(\theta, p)\tau_{wc}(\theta, p),$$

where  $\tau_o$ ,  $\tau_{wl}$ , and  $\tau_{wc}$  denote the transmittances due to ozone, water vapor lines, and water vapor continuum, respectively.

#### REFERENCES

- Dütsch, H. U., 1981: Ozone research—Past—present—future. *Bull. Amer. Meteor. Soc.*, 62, 213–217.
- Gruenzel, R. R., 1978: Mathematical expressions for molecular absorption in Lowtran 3B. *Appl. Opt.*, 17, 2591–2593.
- Lovill, J. E., 1972: Characteristics of the general circulation of the atmosphere and the global distribution of total ozone as determined by the Nimbus III satellite infrared interferometer spectrometer. *Atmos. Sci. Pap. No. 180*, Dept. Atmos. Sci., Colorado State University, Fort Collins, XXX pp.
- , J. S. Ellis, F. M. Luther, T. J. Sullivan and R. L. Weichel, 1982: Defense meteorological satellite measurements of total ozone. *Geophys. Res. Lett.*, 9, 105–108.
- Prabhakara, C., B. J. Conrath and R. A. Hanel, 1970: Remote sensing of atmospheric ozone using the 9.6  $\mu\text{m}$  band. *J. Atmos. Sci.*, 26, 689–697.
- , E. B. Rodgers and V. V. Salomonson, 1973: Remote sensing of the global distribution of total ozone and the inferred upper-tropospheric circulation from Nimbus IRIS experiments. *Pure Appl. Geophys.*, 106–108, 1226–1237.
- , B. J. Conrath, R. A. Hanel and V. G. Kunde, 1976: The Nimbus 4 infrared spectroscopy experiment 3. Observations of the lower stratosphere thermal structure and total ozone. *J. Geophys. Res.*, 81, 6391–6399.
- Shapiro, M. A., A. J. Krueger and P. J. Kennedy, 1982: Nowcasting the position and intensity of jet streams using a satellite-borne total ozone mapping spectrometer. *Nowcasting*, K. A. Browning, Ed., Academic Press, 137–145.
- Selby *et al.* (1978)
- Smith, W. L., 1970: Iterative solution of the radiative transfer equation for temperature and absorbing gas profiles of an atmosphere. *Appl. Opt.*, 9, 1993–1999.
- , 1983: The retrieval of atmospheric profiles from VAS geostationary radiance observations. *J. Atmos. Sci.*, 40, 2025–2035.
- , and C. M. R. Platt, 1978: Comparison of satellite-deduced cloud heights with indications from radiosonde and ground-based laser measurements. *J. Appl. Meteor.*, 17, 1796–1802.
- , H. B. Howell and H. M. Woolf, 1979: The use of interferometric radiance measurements for sounding the atmosphere. *J. Atmos. Sci.*, 36, 566–575.
- , H. M. Woolf, C. M. Hayden, A. J. Schreiner and J. M. LeMarshall, 1983: The physical retrieval TOVS export package. *Tech. Proc. First Int. TOVS Study Conf.*, Iglu, Austria. [Available from Cooperative Institute for Meteorological Satellite Studies, University of Wisconsin, 1225 West Dayton Street, Madison, WI 53706.]
- Weinreb, M. P., H. E. Fleming, L. M. McMillin and A. C. Neuendorffer, 1981: Transmittances for the TIROS Operational Vertical Sounder. NOAA Tech. Rep. NESS 85, U.S. Dept. Commerce, Washington, DC, 59 pp.

AUGUST 1984	MA, SMITH AND WOOLF	000
AUGUST 1984	MA, SMITH AND WOOLF	000
AUGUST 1984	MA, SMITH AND WOOLF	000
AUGUST 1984	MA, SMITH AND WOOLF	000
AUGUST 1984	MA, SMITH AND WOOLF	000
AUGUST 1984	MA, SMITH AND WOOLF	000
AUGUST 1984	MA, SMITH AND WOOLF	000
AUGUST 1984	MA, SMITH AND WOOLF	000

B6555

T18

8.3

Paper 11

In this study, operational satellite temperature retrievals from the TIROS-N/NOAA 4-6 series of satellites and a large percentage of those produced for research purposes have used statistical techniques to remove limb effects in satellite observed radiances. In this study, temperature profiles have been derived using the radiative transfer equation in a form which properly takes into account the angle of observation. These profiles have been compared to those derived using the radiative transfer equation with "radial radiances" produced by a statistical limb correction technique similar to those now used operationally. This comparison has shown significant differences in the derived temperature profiles at large viewing angles, particularly in the case of strong vertical temperature gradients. Overall, the results suggest that for the calculation of temperature profiles from non-solar observations, the more proper

**LIMB EFFECTS IN SATELLITE TEMPERATURE SOUNDING**

**John F. Le Marshall**  
Cooperative Institute for Meteorological Satellite Studies  
Space Science and Engineering Center  
University of Wisconsin  
1225 West Dayton Street, 2nd Floor  
Madison, Wisconsin 53706

**Anthony J. Schreiner**  
Space Science and Engineering Center  
University of Wisconsin  
1225 West Dayton Street, 2nd Floor  
Madison, Wisconsin 53706

Submitted to Journal of Climate and Applied Meteorology

MAY 1984

2/JFL1/12

Abstract

To date, operational satellite temperature retrievals from the TIROS-N/NOAA A-G series of satellites and a large percentage of those produced for research purposes have used statistical techniques to estimate limb effects in satellite observed radiances. In this study temperature profiles have been derived using the radiative transfer equation in a form which properly takes into account the angle of observation. These temperature profiles have then been compared to those derived using the radiative transfer equation with "nadir radiances" produced by a statistical limb correction technique similar to those now used operationally. This comparison has shown significant differences in the derived temperature profiles at large viewing angles, particularly in the case of strong meridional temperature gradients. Overall, the results suggest that for the calculation of temperature profiles from non-nadir observations, the more proper physical solution is the preferred procedure for deriving temperature fields.

## 1. Introduction

During the "First International TOVS Study Conference" at Igls, Austria in 1983, stress was put on the use of physically based rather than empirical algorithms in future temperature retrieval procedures (Menzel and Lynch, 1983). In this spirit and also because of the widespread operational use of statistically limb corrected data, a study was undertaken to gauge the differences between temperature soundings generated from a full physical solution of the radiative transfer equation taking into account slant path, as opposed to those derived using a statistical correction to the slant path radiances followed by a physical solution of a nadir form of the radiative transfer equation.

Two adjacent orbits starting at 1200 GMT and 1340 GMT on 4 March 1982 were used for the study. These were chosen as they had been extensively studied at the "First International TOVS Study Conference," overlaid an area with a good conventional data base and, most importantly, exhibited a strong meridional temperature gradient. This strong gradient provided a means of examining any loss of information as a result of the limb modelling procedures.

## 2. The Retrieval Technique

The retrieval technique used produces temperature, moisture and ozone profiles which are a full solution of the radiative transfer equation. The solution methodology is described in detail in Smith et al. (1983). Briefly, the physical retrieval algorithm solves for a departure of the true atmospheric temperature, moisture, and ozone profile from a "guess" condition, as a function of the departure of observed radiances from those calculated for the "guess" profile. In this study a climatological first guess was used, tied to a surface air temperature and surface pressure derived from conventional surface data, to constrain the lowest levels of the soundings.



### 3. The Limb Correction Techniques

#### 3.1 Statistical

The statistical limb correction technique is similar to that used operationally (Werbowski, 1981) and was of the form used in the "First TOVS Export Package." The statistical limb correction coefficients, which are applied to non-nadir radiance observations to give nadir radiances, were generated using synthetic radiance data in a manner described by Smith et al. (1974). A global representation of 100 temperature and water vapor mixing ratio profiles was used to generate synthetic radiances and brightness temperatures at nadir and non-nadir angles. In the case of High-resolution Infra-Red Sounder (HIRS) observations, each profile was used with a variety of cloud heights and amounts to produce the radiances. For the Microwave Sounding Unit (MSU) data, although land and water surfaces are treated separately, hybrid samples were used for every fifth profile and one in ten soundings over land had randomly introduced precipitating clouds. In addition, the effect of sidelobes and emissivity was removed from the nadir MSU radiances. Limb brightness temperature correction coefficients were then computed using stepwise multiple linear regression, with the differences between the vertical path and slant path synthetic data being predictands and the product of the synthetic non-nadir channel brightness temperature and secant of the local zenith angle as well as the secant itself being predictors.

#### 3.2 Physical

The radiative transfer equation was used with non-limb corrected data to generate temperature profiles by utilizing a computationally efficient transmittance model which provided transmittances appropriate for the atmospheric path at the angle of observation. The model algorithm is similar to that described by McMillin and Fleming (1976). For the MSU transmittances, the

effects of side lobes on the transmittances has been computed by a regression technique rather than using the computationally costly process of convolving the antenna gain pattern with transmittances for a number of angles (Smith et al., 1983).

#### 4. The Retrievals

As previously described, the test orbits were processed using statistically limb corrected radiances and non-nadir radiances in conjunction with transmittances appropriate to a slant path. The temperatures were then analyzed at standard levels using the Barnes analysis scheme (Barnes, 1973). Figure 1 shows the analyzed 500 mb temperature fields, their differences, and the corresponding archived field from ECMWF. It can be seen the thermal gradients in the satellite only and ECMWF analyses show good agreement, although a bias of 1.5 degrees at 500 mb is evident for these orbits (Smith et al., 1983). An examination of the western edge of the 1340 GMT orbit shows the strong thermal gradient region has been best depicted by the full physical scheme. The differences between the two satellite analyses show little deviation in the center and become quite significant at larger angles. The differences at 700 mb and 250 mb are shown in Figure 2. Again, the differences increase at the edge and the large differences appear more frequently as one moves from 250 mb to 700 mb. The satellite analyses also show a difference over northern Africa where we believe the statistical limb correction to be less reliable because of extreme surface conditions. The distribution of differences was found to be similar for the eastern orbit.

The analyzed temperature fields were compared to the 1200 GMT radiosonde data. The differences in the root mean square error and the standard error

between the limb corrected (LC) and statistically non-limb corrected (NLC) fields (LC-NLC) are shown in Figure 3. In general, both the root mean square error and standard error are reduced by using the full physical scheme. At the lowest levels the differences are small, partially as a result of surface temperature and pressure constraints on the at those levels, while for the rest of the levels a positive impact is seen as a result of the full physical retrieval scheme.

## 5. Conclusions

It has been shown in this study that there appear to be systematic differences between soundings generated from statistically limb corrected data using a scheme similar to that now used operationally and those generated using transmittance functions appropriate to the angle of view. These differences can be significant at larger viewing angles. It appears from the sample examined, physical retrievals which account for the angle of view explicitly are more realistic and appear to better maintain temperature gradients in the limb. Overall, it would appear that the physical modelling of limb effects in the transmittance terms of the radiative transfer equation is the preferred method for temperature retrieval.

**Acknowledgments**

The authors wish to express their thanks to W. L. Smith, H. M. Woolf and C. M. Hayden for their help and encouragement.

... and W. L. Smith (Editors), 1963: A Report on the First International TOVS Study Conference. A report from the Cooperative Institute for Meteorological Satellite Studies, 1215 West Dayton Street, Madison, Wisconsin, 32708.

Smith, W. L., E. M. Woolf, F. G. Abel, C. E. Roper, W. Chaffin, and H. Hayden: 1974: Nimbus-2 sounder data processing system Part I: Measurement characteristics and data reduction procedures. Final Report for WPA Project Office, NASA Contract 8-70249-02, Goddard Space Flight Center, NASA, Washington, D.C., 10337, 99 pp.

Smith, W. L., E. M. Woolf, C. E. Roper, A. J. Schmitz, and J. E. Marshall: 1974: The physical retrieval TOVS expert package. Technical Proceedings of the First International TOVS Study Conference, Igfa. Institute for Cooperative Studies for Meteorological Satellite Studies, 1215 West Dayton Street, Madison, Wisconsin, 53706.

Woolf, H. M. (Editor), 1971: Atmospheric sounding from Nimbus. Technical Report 822-81, National Oceanic and Atmospheric Administration, National Earth Satellite Service, Washington, D.C., 20541.

## References

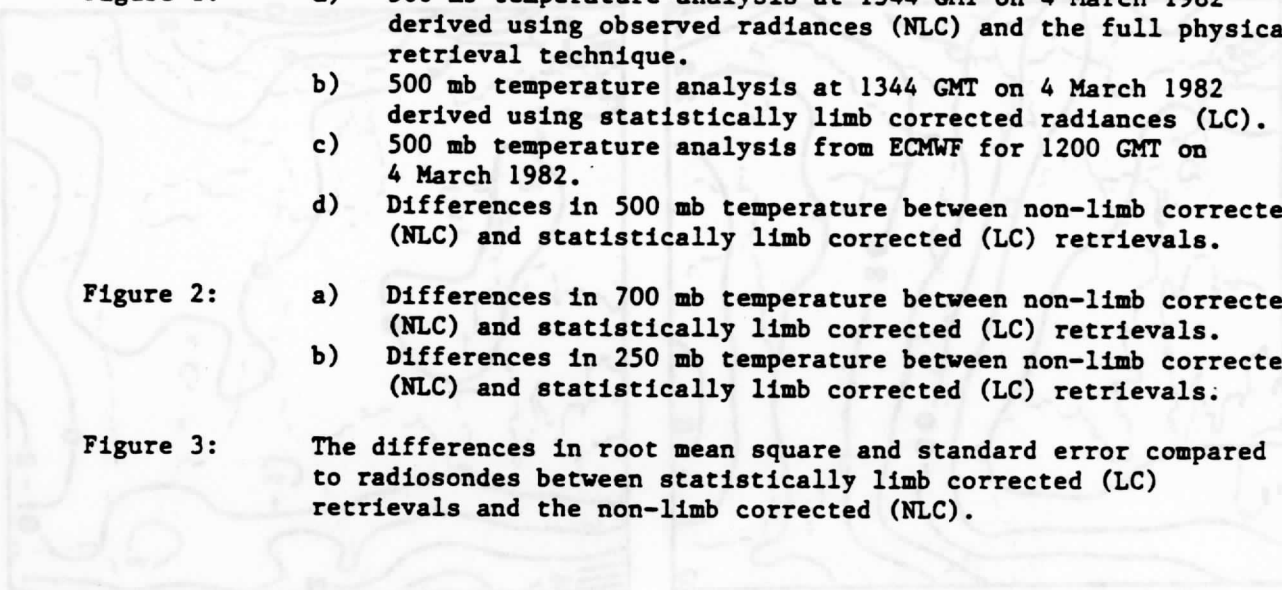
- Barnes, S. L., 1973: Mesoscale objective analysis using weighted time series observations. NOAA Technical Memorandum ERL NSSL-62, National Severe Storms Laboratory, 1313 Halley Circle, Norman, Oklahoma, 73069, 60 pp.
- McMillin, L. M., and H. E. Fleming, 1976: Atmospheric transmittance of an absorbing gas: A computationally fast and accurate transmittance model for gases with constant mixing ratios in homogeneous atmospheres. Applied Optics, 15, 358.
- Menzel, W. P. and M. J. Lynch (editors), 1983: A Report on The First International TOVS Study Conference. A report from the Cooperative Institute for Meteorological Satellite Studies, 1225 West Dayton Street, Madison, Wisconsin, 53706.
- Smith, W. L., H. M. Woolf, P. G. Abel, C. M. Hayden, M. Chalfant, and N. Grody, 1974: Nimbus-5 sounder data processing system Part I: Measurement characteristics and data reduction procedures. Final Report for GARP Project Office, NASA Contract S-70249-AG, NOAA Technical Memorandum NESS 57, National Oceanic and Atmospheric Administration, National Environmental Satellite Service, Washington, D.C., 20233, 99 pp.
- Smith, W. L., H. M. Woolf, C. M. Hayden, A. J. Schreiner, and J. F. Le Marshall, 1983: The physical retrieval TOVS export package. Technical Proceedings of The First International TOVS Study Conference, Igls, Austria. A report from the Cooperative Institute for Meteorological Satellite Studies, 1225 West Dayton Street, Madison, Wisconsin, 53706.
- Werbowski, A. (editor), 1981: Atmospheric Sounding Users Guide. NOAA Technical Report NESS 83. National Oceanic and Atmospheric Administration, National Earth Satellite Service, Washington, D.C., 20233.

### Figure Captions

- Figure 1:
- a) 500 mb temperature analysis at 1344 GMT on 4 March 1982 derived using observed radiances (NLC) and the full physical retrieval technique.
  - b) 500 mb temperature analysis at 1344 GMT on 4 March 1982 derived using statistically limb corrected radiances (LC).
  - c) 500 mb temperature analysis from ECMWF for 1200 GMT on 4 March 1982.
  - d) Differences in 500 mb temperature between non-limb corrected (NLC) and statistically limb corrected (LC) retrievals.

- Figure 2:
- a) Differences in 700 mb temperature between non-limb corrected (NLC) and statistically limb corrected (LC) retrievals.
  - b) Differences in 250 mb temperature between non-limb corrected (NLC) and statistically limb corrected (LC) retrievals.

- Figure 3: The differences in root mean square and standard error compared to radiosondes between statistically limb corrected (LC) retrievals and the non-limb corrected (NLC).



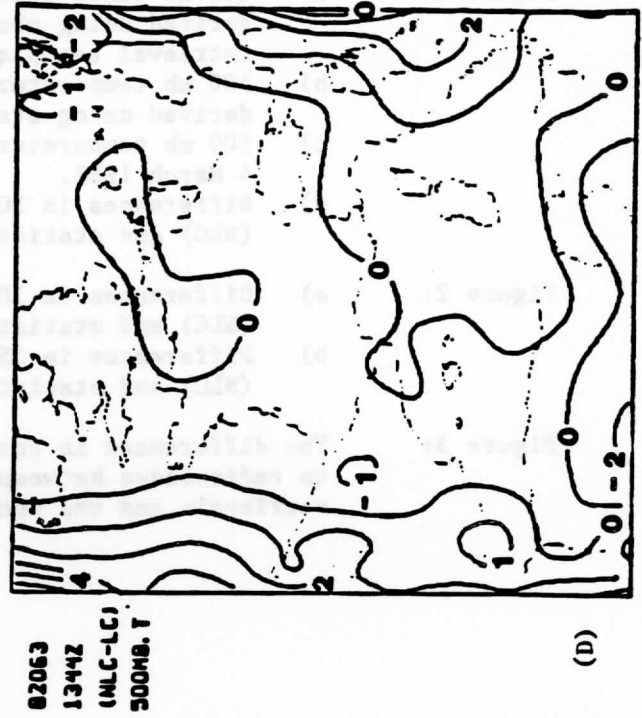
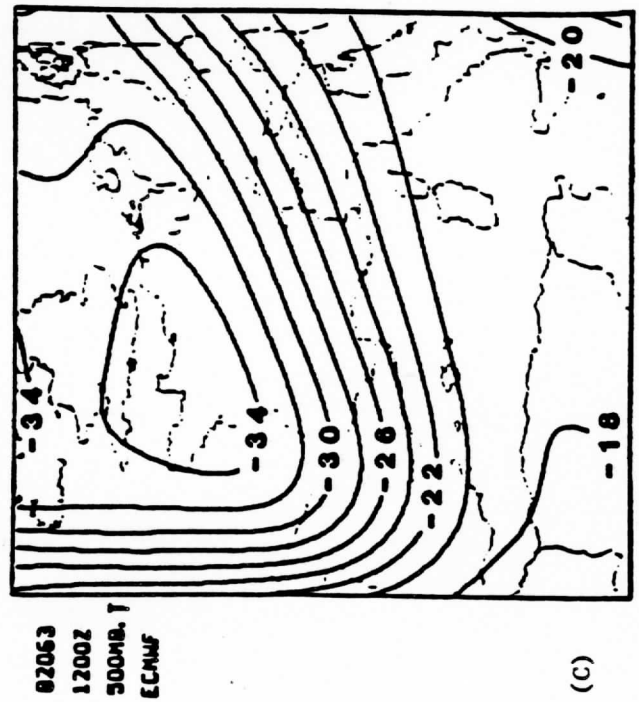
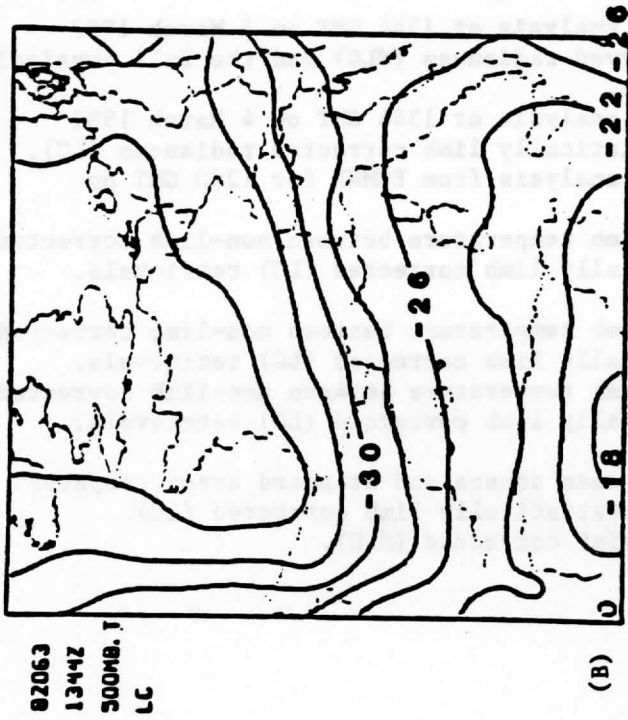
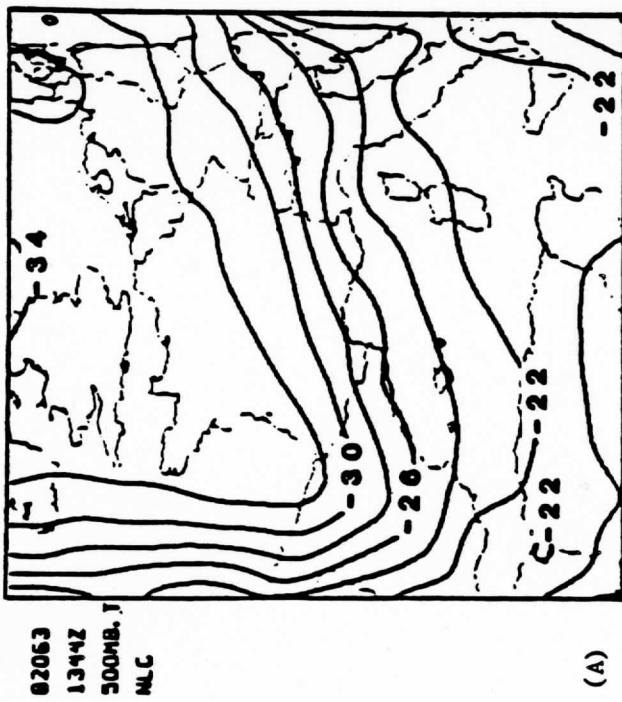
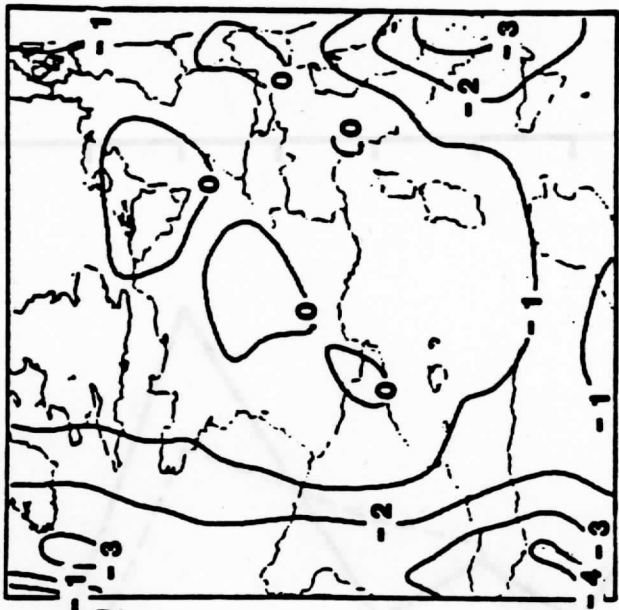
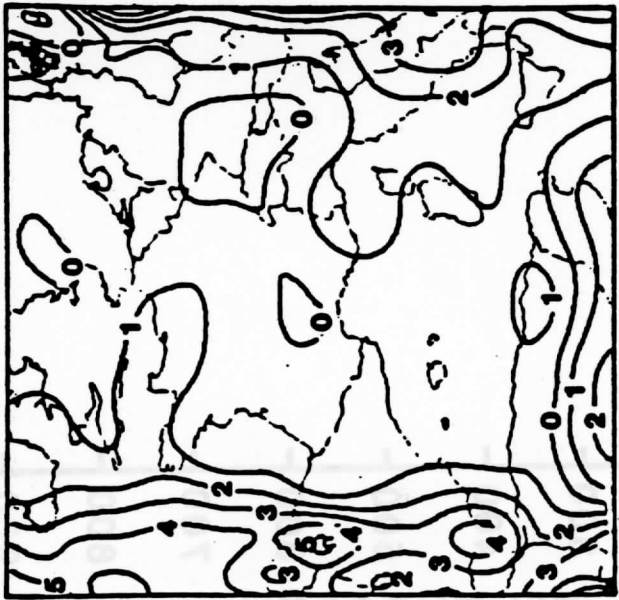


FIGURE 1



02063  
1344Z  
(NLC-LC)  
700MB. T

(A)



02063  
1344Z  
(NLC-LC)  
250MB. T

(B)

FIGURE 2



# RAOB VERIFICATION

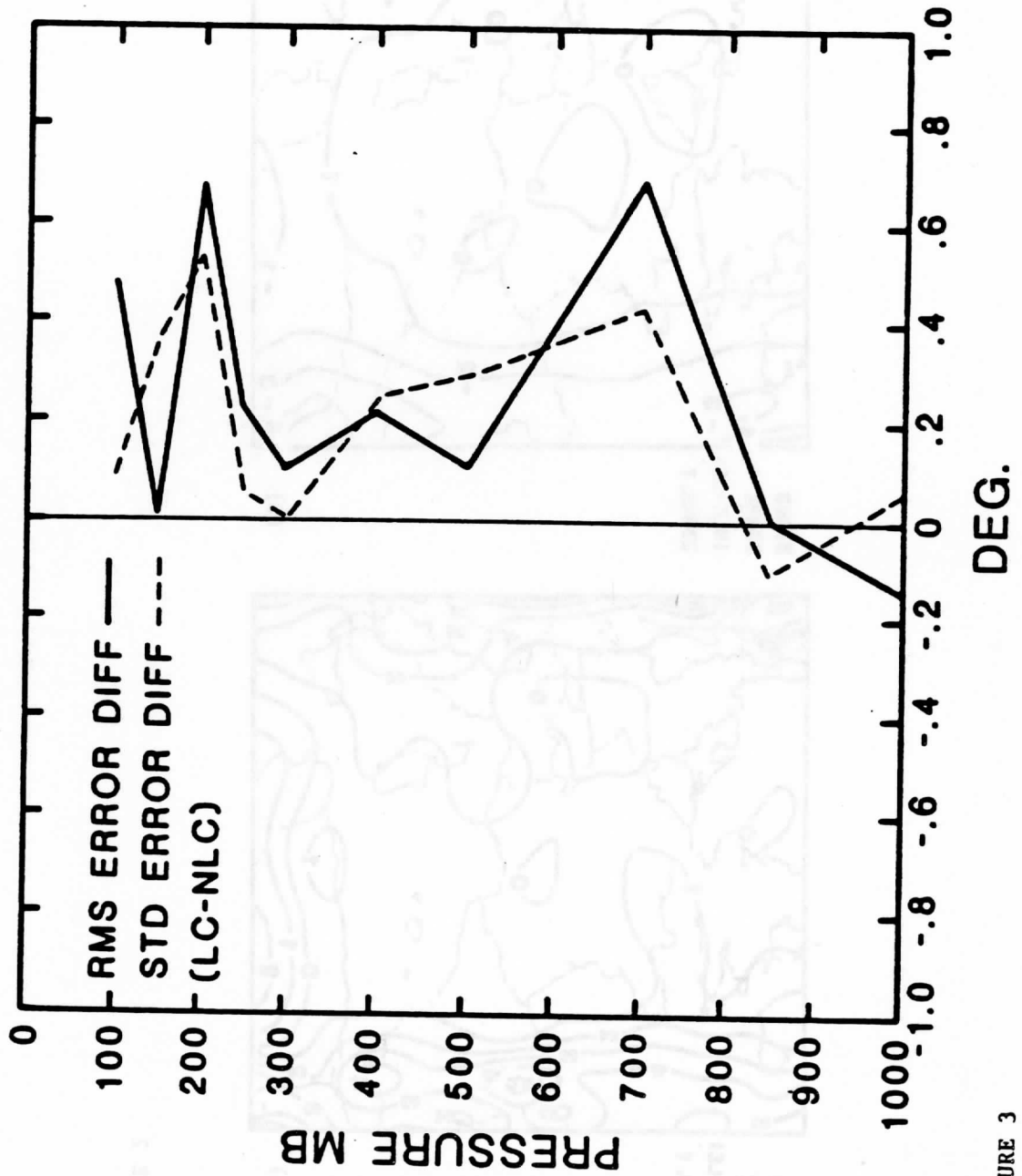


FIGURE 3

# GEOSTATIONARY SATELLITE SOUNDER (VAS) OBSERVATIONS OF LONGWAVE RADIATION FLUX

W.L. Smith and H.M. Woolf

NOAA/NESDIS Development Laboratory  
1225 W. Dayton St.  
Madison, WI 53706

## 1. Introduction

The VISSR Atmospheric Sounder (VAS) on the United States geostationary satellites measures the earth-atmosphere outgoing radiance in twelve spectral channels between 4.0 and 15  $\mu\text{m}$ . Since the radiance from the earth's surface and clouds, tropospheric water vapor, and tropospheric and stratospheric carbon dioxide are sampled, the spectrally integrated longwave radiation flux to space can be accurately measured from the VAS radiance observations. Furthermore, since the VAS radiances are highly dependent upon the temperature and moisture profile of the atmosphere, the vertical flux divergence of infrared radiation (i.e., the cooling rate profile) can be estimated. Most important, VAS can sample the radiation flux at hourly intervals; thus, the diurnal variation is observed and a correct daily average can be determined. Unfortunately, VAS data is limited to sub-polar regions of the western hemisphere. However, diurnal variation models can be formulated from the VAS observations and these can be used to time interpolate geographically complete "top of the atmosphere" radiation budget observations to be obtained from the forthcoming ERBE satellites in sun synchronous and low inclination orbits.

In this paper a global climatological sample of 1200 soundings are used to synthesize, by radiative transfer calculation, VAS multi-spectral radiance observations and spectrally integrated upward and downward infrared flux profiles for a variety of cloud conditions. Statistical linear regression analysis is performed to obtain relations between the upward and downward fluxes at fifteen pressure levels and spectral radiances from the nine long wavelength (6-15  $\mu\text{m}$ ) channels of the VAS.

The linear regression predictors and the standard errors of estimate of the regression relations are given. Furthermore, an algorithm is formulated for applying these regression relations to actual VAS observations. Comparisons are made between infrared flux profiles observed by the Suomi-Kuhn radiometer sonde (Suomi-Kuhn, 1958) and flux profiles estimated from simultaneous VAS observations. Finally, the algorithm is applied to VAS observations of the North Atlantic during 15-16 September 1982 to portray the vertical, horizontal, and temporal variation of the infrared cooling of the lower, middle, and upper tropospheric layers in a hurricane environment.

## 2. VAS Measurement Characteristics

The operational geostationary meteorological satellites--GOES--currently carry the VISSR Atmospheric Sounder (VAS). The GOES is spin stabilized in order to achieve the extremely high attitude control required for cloud motion vector determinations and mesometeorological applications of the imaging and sounding data. GOES-EAST is stationed over the equatorial Atlantic Ocean at 75°W while GOES-WEST is stationed over the equatorial Pacific at 135°W.

The VAS performs both the imaging and sounding functions of GOES, but not simultaneously, because different duty cycles are required for each function, and both the imaging and sounding detector arrays share a common optical system. The VAS possesses six infrared detectors; two are used primarily for imaging (7 km resolution) and four are used for sounding (14 km resolution). An onboard processor controls the VAS filter wheel to position one of twelve spectral band filters into the optical path of the detectors. For cloud imaging, VAS also possesses eight 1 km resolution visible detectors. All IR and visible channel detector arrays are aligned so that they trace out two 7 km or two 14 km west-east swaths across the earth (depending upon whether imaging or sounding) during each rotation of the spacecraft. The north south coverage is achieved by moving a mirror whose scan angle is also controlled by the on-board processor. For multi-spectral imaging (MSI) of clouds, atmospheric water vapor, and surface temperature patterns, one spin achieves eight 1 km resolution visible swaths, and either two 7 km resolution infrared swaths, or two 14 km resolution infrared swaths. During the current operational schedule, multi-spectral images of the earth's disc in the visible and three infrared spectral bands are usually achieved during eighteen minutes of each half hour cycle. The remaining time is devoted to sounding a pre-selected portion of the earth's disc. In order to achieve the higher radiometric accuracy required for sounding in the infrared bands, the scan mirror and filter wheel position are fixed in their positions for several spins of the spacecraft to dwell on a single swath longer and thereby improve the signal strength. For this dwell sounding (DS) mode of operation, typically 30-50 spins of the spacecraft are required to sample all spectral bands with the signal to noise ratio required for sounding. The number of spins (spin-budget) depends upon spatial resolution, the spatial coverage and temporal resolution requirements. The on-board processor allows these tradeoffs to be realized for various applications (e.g., twelve hour interval synoptic time large area sounding with coarse spatial resolution for initializing large scale numerical prediction models as opposed to hourly interval mesoscale (50 km) resolution sounding over a limited area for monitoring the rapid destabilization of the atmosphere prior to the development of intense convective storms). Typically, ten minutes each half hour cycle is devoted to sounding either a 15 degree north-south latitude swath with high spin budget (signal to noise) or a broader 25 degree latitude swath with a somewhat lower spin budget (lower signal to noise). Successive half-hour interval sounding sequences can be amalgamated to double the earth coverage on an hourly basis.

A summary of the VAS instrument characteristics associated with the DS mode is provided in Table 1. Note that the channels with higher noise are accorded the larger spin budgets, except for stratospheric channels (i.e., channels 1 and 2) for which spatial averaging is used to reduce the measurement noise level. For estimating the infrared flux distribution, the spectral radiances observed in the longwave channels (1-5, 7-10) achieved during the DS mode of operation are utilized. The shortwave channels (6,11,12) are not used because of the difficulty of accounting for cloud reflected solar contributions to the observed radiances.

TABLE 1  
VAS INSTRUMENT CHARACTERISTICS (GOES-5)

Spectral Channel	Central Wavenumber (cm <sup>-1</sup> )	Pressure of Peak Energy Contribution(mb)	Absorbing Constituent	Inflight Single Sample Noise (mw/m <sup>2</sup> -ster-cm <sup>-1</sup> )	Typical Spin Budget	Single Spatial Sample Noise (mw/m <sup>2</sup> -ster-cm <sup>-1</sup> )	Typical Sounding Brightness Temperature Noise <sup>1</sup> (°C)
1	679.95	40	CO <sub>2</sub>	2.740	1	2.740	0.6
2	691.20	70	CO <sub>2</sub>	1.360	4	0.680	0.2
3	702.89	150	CO <sub>2</sub>	1.020	4	0.510	0.2
4	714.85	450	CO <sub>2</sub>	0.940	2	0.660	0.2
5	751.37	950	CO <sub>2</sub>	0.760	2	0.540	0.2
6	2214.35	850	CO <sub>2</sub>	0.028	4	0.011	0.2
7	789.39	surface	H <sub>2</sub> O	0.640	2	0.450	0.2
8	889.52	surface	window	0.100	1	0.100	0.1
9	1379.69	600	H <sub>2</sub> O	0.650	4	0.330	0.2
10	1486.33	400	H <sub>2</sub> O	0.150	1	0.150	0.2
11	2254.28	500	CO <sub>2</sub>	0.029	4	0.015	0.2
12	2538.07	surface	window	0.009	1	0.009	0.1
				SPIN BUDGET	(30)		

<sup>1</sup>After averaging 25 radiance samples in one sounding area

### 3. Radiation Simulations

The radiation fluxes (upward and downward) were calculated for each atmospheric condition using the radiative flux transfer program kindly provided by Drs. M.D. Chou and A. Arking of NASA, GSFC. The method of computation of the infrared radiative terms due to H<sub>2</sub>O, CO<sub>2</sub>, and Ozone is based upon an accurate representation of the absorption coefficient as a function of temperature, pressure, and wavelength. Separation of these variables permits absorption coefficients calculated by exact line-by-line methods to be tabulated with temperature and absorbed amount as independent variables, thus enabling very rapid radiative flux computations to be performed for specific atmospheric conditions. Details of the method and computer program are given by Chou and Arking (1980, 1981).

The radiance-to-space for the VAS spectral channels (Table I) is computed using the radiative transfer equation and transmittance models formulated by McMillin and Fleming (1976), Fleming and McMillin (1977), and McMillin et al. (1979) to permit rapid calculations of temperature and moisture profiles from operational satellite sounding radiance observations. For the profile retrieval application the transmittance calculations must be very accurate. Specification of the fast transmittance model coefficients using exact line-by-line calculations for a small statistical sample of atmospheres allows high accuracy to be achieved. Details of the radiative transfer calculations for VAS are given by Smith (1983).

The temperature and moisture profiles used for the radiative flux and VAS spectral radiance simulations are the NESS 1200 radiosonde-rocketsonde set which covers all seasons, and latitudes (Smith et al., 1974). Two sets of radiative computations were performed for each of the 1200 soundings; (a) one assuming clear sky conditions, and (b) one assuming cloudy sky conditions. For the assumed "Clear Sky" conditions the observed temperature and moisture profile was used. For the cloudy condition a random number generator was used to select, with equal probability, either a high, middle, or low cloud condition and a fractional cloud cover of either 100%, 75%, 50%, or 25%. The three cloud types assumed were stratus (700-950 mb), altocumulus (300-700mb), and cirrus (tropopause-300mb). Once the cloud type and fractional coverage were selected, the moisture profile was modified within the cloud layer by combining the saturation mixing ratio with the "clear sky" mixing ratio using the fractional cloud cover as a weight in the combination. As a consequence, two sets of 1200 samples of upward and downward radiative fluxes and VAS spectral radiances to space were obtained, one for clear sky conditions, and one for cloudy sky conditions. Statistical regression analysis was applied to each set separately. Measurement errors for the VAS radiances were also synthesized using a Gaussian random number generator and the standard errors given in Table I.

### 4. Statistical Regression Results

Table II provides the statistical results of the step-wise multiple linear regression analysis performed on the simulated radiation flux and VAS multi-spectral radiance observations. Tables II(a) and (b) list the five most important VAS channels selected for estimating the upward and downward flux. The net flux (difference between the upward and downward flux) and the cooling

Table II: (a) Upward Flux Statistics

Pressure (MB)	Clear			Cloudy		
	Explained Variance (%)	Standard Error ( $w/m^2$ )	Predictors (VAS channel)	Explained Variance (%)	Standard Error ( $w/m^2$ )	Predictors (VAS channel)
3	99.9	1.2	7,10,4,8,9	99.8	2.2	5,8,10,2
7	99.9	1.2	7,10,8,4,9	99.8	2.2	5,8,10,2
16	99.9	1.2	7,10,8,4,9	99.8	2.3	5,7,10,3,8
38	99.9	1.4	7,10,8,4,9	99.8	2.4	5,7,10,3,8
87	99.9	1.5	7,10,8,4,9	99.8	2.6	5,7,10,3,8
200	99.9	1.2	8,9,7,4,1	99.7	4.6	8,9,7,10,1
300	99.9	1.3	8,9,7,5,1	99.2	27.1	8,5,9,10,1
400	99.9	1.6	8,9,7,5,2	77.9	25.6	8,5,9,10,1
500	99.9	2.1	5,2,4,8,9	79.8	25.5	8,7,9,10,1
600	99.8	2.5	5,2,4,8,7	80.1	26.7	8,7,9,10,1
700	99.7	3.4	5,2,4,8,7	79.3	32.0	8,7,4,3,5
800	99.6	4.6	8,4,3,9,7	73.5	35.0	8,7,4,3,5
900	99.7	4.0	8,7,5,4	72.7	38.7	8,7,4,3,5
1000	99.9	2.8	8,7,5	72.6	43.3	8,7,4,3,5

Table II: (b) Downward Flux Statistics

Pressure (MB)	Clear			Cloudy		
	Explained Variance (%)	Standard Error ( $w/m^2$ )	Predictors (VAS channel)	Explained Variance (%)	Standard Error ( $w/m^2$ )	Predictors (VAS channel)
3	59.5	0.4	3,4,1,9,10	57.5	0.4	1,2,8,7,4
7	73.2	0.5	3,4,1,5,7	72.8	0.5	1,2,4,10,3
16	87.4	0.4	3,4,1,5,7	86.1	0.4	1,2,10,4,3
38	93.8	0.4	1,4,5,8,9	92.9	0.4	1,8,7,9,10
87	95.2	0.5	2,4,1,5,7	95.0	0.5	2,4,1,5,7
200	84.8	1.2	3,10,1,9,4	67.1	13.7	3,1,8,7,9
300	91.3	3.0	4,10,2,3,9	70.1	20.9	10,9,4,1,2
400	95.9	4.3	4,2,10,5,3	73.6	24.8	10,4,2,1,5
500	96.7	5.4	4,2,9,8,10	69.7	28.4	10,4,2,1,5
600	98.0	5.2	5,9,7,8,2	64.5	31.4	10,4,2,1,5
700	97.3	7.1	5,9,7,8,2	64.2	34.7	10,8,7,5,9
800	97.5	8.2	5,9,7,8,3	57.6	39.0	8,7,5,2,1
900	97.5	9.8	8,7,5,4,9	59.5	42.2	8,7,5,3,4
1000	98.1	10.3	8,7,5,4,9	62.1	46.3	8,7,5,9,10

Table II: (c) Net Flux Statistics

Pressure (MB)	CLEAR		CLOUDY	
	Explained Variance (%)	Standard Error ( $w/m^2$ )	Explained Variance (%)	Standard Error ( $w/m^2$ )
3	99.9	1.2	99.8	2.3
7	99.9	1.3	99.8	2.3
16	99.9	1.3	99.8	2.4
18	99.9	1.4	99.8	2.5
87	99.9	1.6	99.8	2.6
200	99.9	1.7	96.6	11.6
300	99.6	2.5	96.1	9.7
400	99.0	3.6	82.9	27.6
500	98.3	4.4	81.7	26.1
600	97.9	4.5	80.6	26.2
700	95.9	6.0	80.9	18.9
800	94.1	6.5	64.0	26.2
900	89.4	7.8	63.3	23.9
1000	76.8	9.7	60.9	21.4

Table II: (d) Cooling Rate Statistics

Pressure (MB)	CLEAR		CLOUDY	
	Explained Variance (%)	Standard Error ( $^{\circ}C/day$ )	Explained Variance (%)	Standard Error ( $^{\circ}C/day$ )
3-7	42.2	1.1	49.7	1.0
7-16	54.8	0.5	32.3	0.6
16-18	61.3	0.3	52.4	0.3
18-87	83.2	0.2	81.2	0.1
87-200	69.9	0.1	60.5	0.8
200-300	83.8	0.2	74.7	1.5
300-400	80.4	0.3	50.7	1.8
400-500	61.7	0.4	47.9	0.6
500-600	56.7	0.3	70.7	0.4
600-700	46.2	0.3	56.2	0.9
700-800	61.7	0.3	58.5	2.0
800-900	49.3	0.4	43.0	0.4
900-1000	54.0	0.5	34.9	0.6

rate (proportional to the difference between the net fluxes at the top and bottom of an atmospheric layer) are computed from the upward and downward flux estimates.

As may be seen from Table II, the upward flux at the top of the atmosphere (i.e., 3 mb) is predicted exceedingly well for both clear and cloudy conditions. For clear conditions the most important VAS channel radiance predictors are the three water vapor radiance channels (7, 9, and 10), the water vapor "window" radiance channel (8), and mid-tropospheric CO<sub>2</sub> radiance channel (4). For cloudy conditions, the lower tropospheric CO<sub>2</sub> channel (5) is the most important predictor because of its dependence upon cloud and atmospheric temperature, and water vapor emission (Smith and Platt, 1979).

For clear sky conditions, the upward, downward, and net flux (and cooling rate) estimates from VAS radiance observations are excellent. This is because for clear sky conditions the VAS spectral radiances sample all of the major contributors to the upward and downward flux profiles (i.e., surface temperature and atmospheric temperature and water vapor profiles). However, for cloudy conditions the tropospheric accuracies are degraded because of the lack of sensitivity of VAS radiance observations to cloud thickness or the atmosphere beneath the cloud and the difficulty in differentiating between different cloud types of varying fractional amounts. Improved flux profile results for cloudy conditions would undoubtedly be achieved if the cloud pressure amount were held constant and if the "clear sky" radiances were also used as predictors of the cloud condition fluxes. In the application of such an algorithm, the clear sky radiance, cloud height, and fractional cloud coverage would have to be determined, thus complicating the application software. However, since the techniques for calculating clear-column radiance, cloud height, and cloud amount in partly cloudy sky conditions have been developed for sounding retrieval applications (Smith and Woolf, 1976), this approach for improving the cloud flux profile results will be investigated in a subsequent study.

##### 5. Application Algorithm

In the application of the clear sky and cloudy sky regression equations to actual VAS radiance observations, it is necessary to determine the cloud condition for each field-of-view within the area for which the flux is to be estimated. Arbitrarily choosing a sampling area of 125 km, there exist 81 (a 9x9 array) VAS fields-of-view (spectral radiance observations) to estimate the infrared flux profile. In order to separate the clear from cloud contaminated fields-of-view, a cumulative frequency distribution analysis of the 11 μm window brightness temperatures is used. Beginning with the maximum brightness temperature, the cumulative frequency of occurrence of observations less than the maximum is defined in one degree intervals. The mode value (i.e., presumed mean of the cloudfree observations) is defined for a Gaussian distribution as that brightness temperature where the increase in the frequency of occurrence from one step to the next is less than the increase observed at the previous step. That is

$$\bar{T}_B = T_B \text{ for which } f(T_B - 1) - f(T_B) < f(T_B) - f(T_B + 1)$$



where  $f$  is the cumulative frequency of occurrence of brightness temperature values less than the maximum.  $T_B$  is accepted as being due to cloudfree observations if it is not less than  $10^\circ\text{K}$  below the maximum and if its magnitude is greater than  $275^\circ\text{K}$ , an extreme minimum surface temperature,  $T_{\min}$  (e.g.,  $275^\circ\text{K}$  for oceans). If  $T_B$  is accepted as being clear, then all fields-of-view satisfying the condition

$$T_B \geq \text{MAX}(T_{\text{MIN}}, 2\bar{T}_B - T_{\text{MAX}})$$

are presumed to be clear. If  $T_B$  is not accepted as being due to clear observations, then clear fields-of-view are defined, if  $T_{\text{max}} \geq T_{\text{MIN}} + 10^\circ\text{K}$ , as those satisfying the condition

$$T_B \geq T_{\text{max}} - 5^\circ\text{K} \quad (T_{\text{max}} \geq T_{\text{MIN}} + 10^\circ\text{K})$$

All remaining fields-of-view are presumed to contain cloud.

Once the cloud-free observations are separated from the cloud-contaminated observations, average clear and cloud radiances are computed and the corresponding radiative flux values derived using the clear and cloudy regression relations, respectively. The area average flux values are then given by the weighted average,

$$\bar{F} = \frac{n}{n+m} \bar{F}_{\text{cld}} + \frac{m}{n+m} \bar{F}_{\text{cld}}$$

where  $n$  is the number of cloudy fields-of-view and  $m$  is the number of clear fields-of-view.

## 6. Sample Results

Figure 1 shows two comparisons of VAS derived radiation flux and that observed by the Suomi-Kuhn radiometersonde. Both satellite (VAS) and in-situ (radiometersonde) observations are for Madison, Wisconsin within the same hour of the day. Because of differing atmospheric conditions (particularly clouds), there are large differences in the upward and downward flux observations for these days but these differences are inferred quite well from the VAS spectral radiance measurements. As an example, at the 500 mb level the difference in the net flux between the two days is observed to be  $105 \text{ w/m}^2$  whereas the VAS estimate is  $90 \text{ w/m}^2$ . The agreement between the observed fluxes and the VAS estimates is generally within  $25 \text{ w/m}^2$ . This agreement is very good considering the expected errors of the radiometersonde measurements and the Chou-Arking radiative flux model upon which the VAS estimates are based. The skill in the inference of upward, downward, and net flux below cloud level is also noteworthy.

Figures 2, 3, and 4 show results for a VAS analysis of the outgoing longwave radiation flux, and the infrared cooling rates of three layers of the atmosphere over the subtropical Atlantic Ocean during September, 1982 when hurricane Debbie was moving Northeastward off the east coast of the United States. These radiative flux computations were performed using the method outlined in section 5 for a resolution of  $125 \text{ km}$  linear resolution. The "eye" of the storm is located at the low center of  $125 \text{ w/m}^2$  shown on the upward

longwave flux analyses. One can see very strong horizontal gradients of outgoing longwave flux between the storm environment, where the values are in excess of  $300 \text{ w/m}^2$ , and the storm center, where the values are as low as  $125 \text{ w/m}^2$ . The axis of low values of outgoing flux produced by the deep convective clouds and cirrus "blowoff" is oriented from the Southwest to Northeast, the approximate direction of storm motion (compare figure 2a, 3a, and 4a). Comparing the cooling rate charts for the three atmospheric layers and three twelve hour interval time periods, one can see that the strongest infrared cooling ( $>3^\circ\text{C/day}$ ) exists in the upper tropospheric layer ahead of the storm, probably the result of the very dense middle level cloudiness in this region. The changes in the intensity of this cooling maximum is correlated well with the changes in the intensity of the storm, which increased between 15 and 16 September. The infrared radiative warming associated with the storm was confined to the middle tropospheric layer (400-700 mb) in close proximity to the storm center. The spatial distribution of the cooling (or warming) distribution for this layer is very similar to the outgoing flux distribution, the warming centers existing at the locations of minimum flux associated with high dense clouds. In the near surface layer, cooling is observed everywhere with a minimum beneath the dense storm cloudiness and maximums in the clear environment. The time continuity of all the derived quantities is excellent, indicating good relative accuracy for the performance of radiation budget studies using VAS observations during the life cycle of meteorological events.

#### 7. Summary

An algorithm was developed for estimating radiation flux distributions from multi-spectral VAS observations. Intercomparisons with radiometer sonde observations indicate useful accuracies can be achieved. An example application to three twelve hour interval VAS observations of the hurricane Debbie environment show that meaningful horizontal and vertical distributions of infrared radiation cooling can be derived. The relative consistency and time continuity of the results imply their utility for the performance of radiation budget studies from VAS observations during the life cycle of various meteorological phenomena. Furthermore, it is planned to use multi-spectral VAS radiation flux determinations to define diurnal variation models to convert actual "Top of the Atmosphere" flux measurements from the forthcoming ERBE instruments into daily average values. The amalgamation of VAS and ERBE measurements could provide a highly accurate depiction of the four dimensional infrared radiative cooling distribution on a regional basis.

## References:

- Suomi, V.E., and P.M. Kuhn, 1958: An economical net radiometer sonde, Tellus, Vol. 10, No 1.
- Chou, M.D., and A. Arking, 1980: Computations of infrared cooling rates in the water vapor bands, J. Atmos. Sci., 37, 855-867.
- Fleming, H.E., McMillin, L.M., Atmospheric transmittance of an absorbing gas 2: A computationally fast and accurate transmittance model for slant paths at different zenith angles. Applied Optics, Vol. 16, No. 5, May 1977.
- McMillin, L.M., Fleming, H.E., Atmospheric transmittance of an absorbing gas: a computationally fast and accurate transmittance model for absorbing gasses with constant mixing ratios in homogeneous atmospheres, Applied Optics, Vol. 15, no. 2, p. 358, February 1976.
- Smith, W.L., Woolf, H.M., Able, P.G., Hayden, C.M., Chalfant, M., and Grody, N., 1974: Nimbus 5 sounder data processing system, Part I; Measurement characteristics and data reduction procedures. NOAA Tech. Mem. 57, 99 pp.
- Smith, W.L., and H.M. Woolf, 1976: The use of eigenvectors of statistical covariance matrices for interpreting satellite radiometer observations. J. Atmos. Sci., 33, 1127-1140.
- Smith, W.L., and C.M.R. Platt, 1979: Comparison of satellite-deduced cloud heights with indications from radiosonde and ground-based laser measurements. J. Applied Meteor., pp. 1796-1802.
- Smith, W.L., 1983: The retrieval of atmospheric profiles from VAS geostationary radiance observations. J. Atmos. Sci., (to be published).

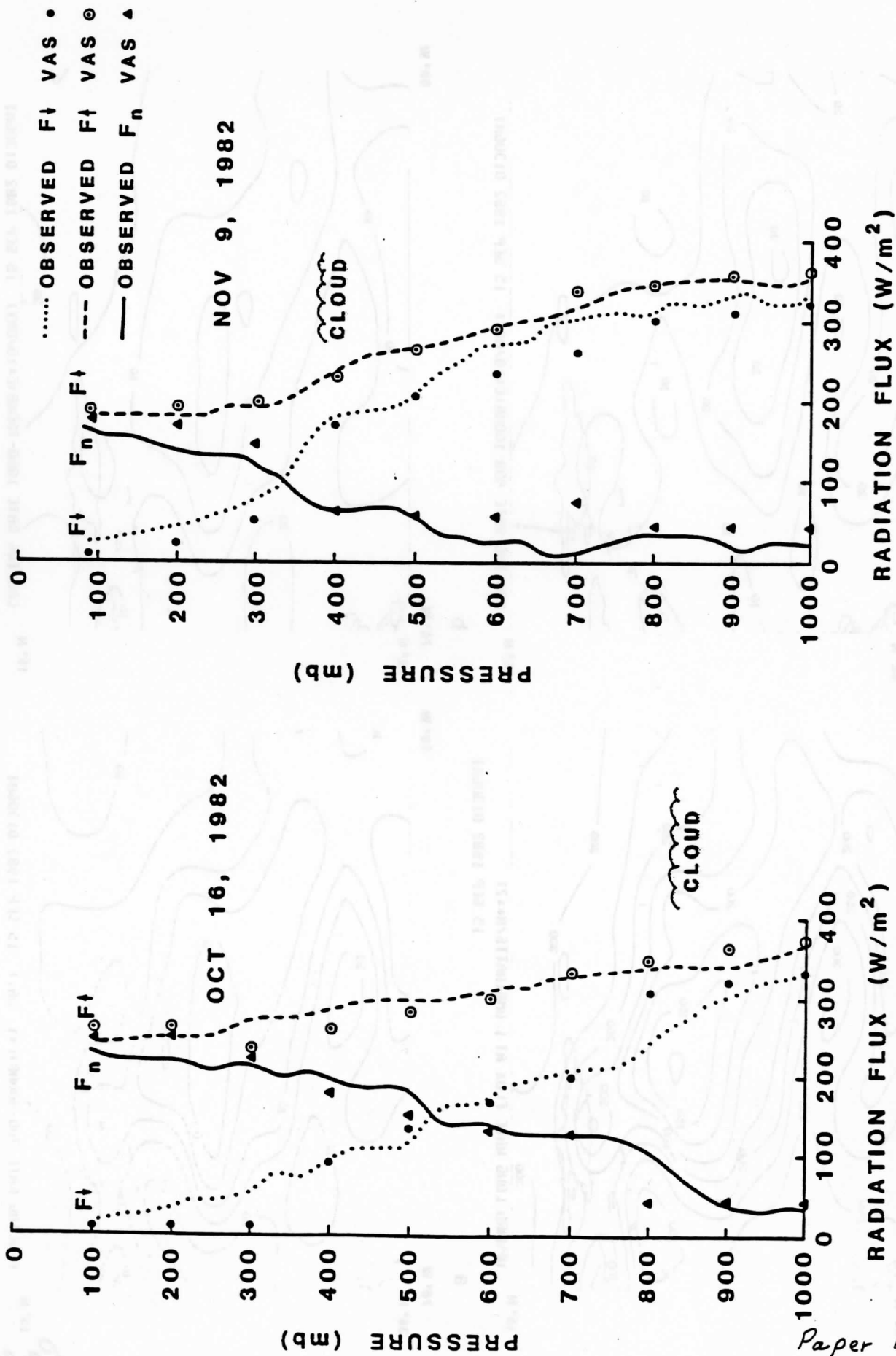


Figure 1: Comparison of upward, downward, and net radiation flux observed by radiometersonde (curves) and estimated from simultaneous VAS measurements (points) for Madison, Wisconsin, on a) 16 October 1982, and b) 9 November 1982.

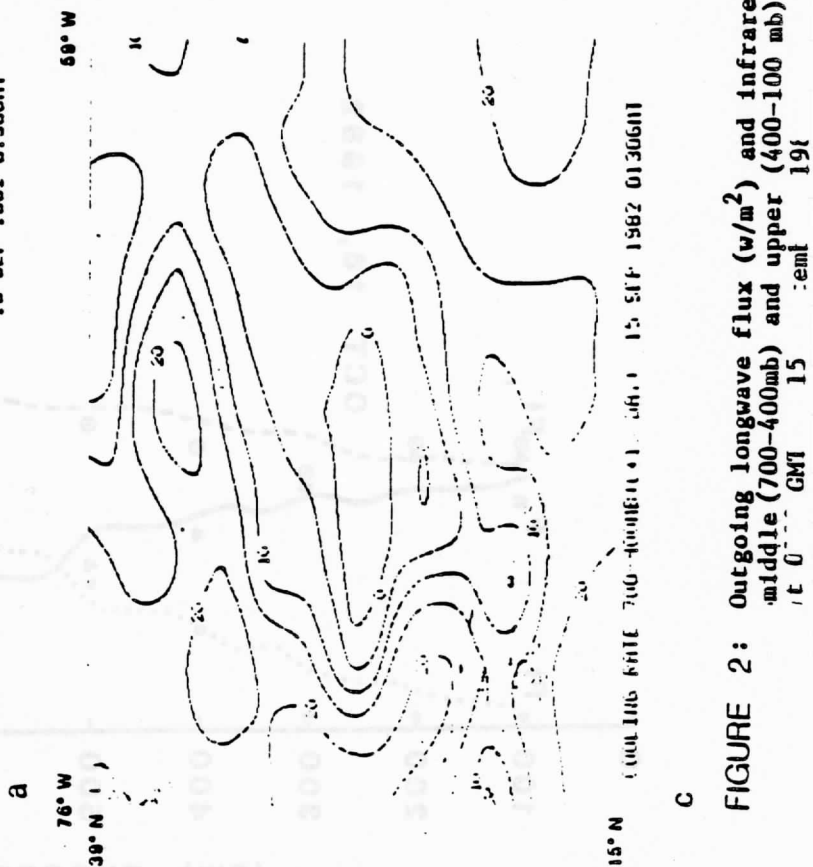
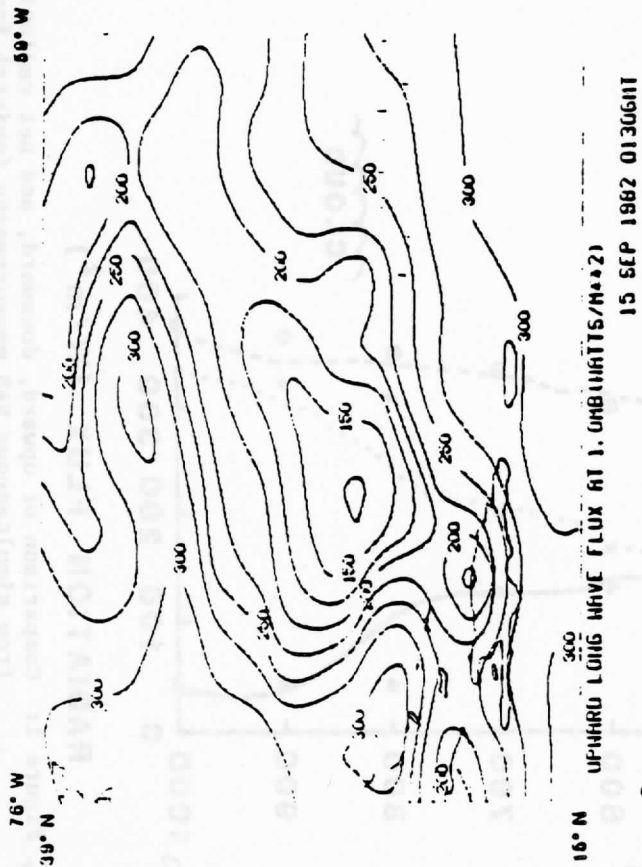
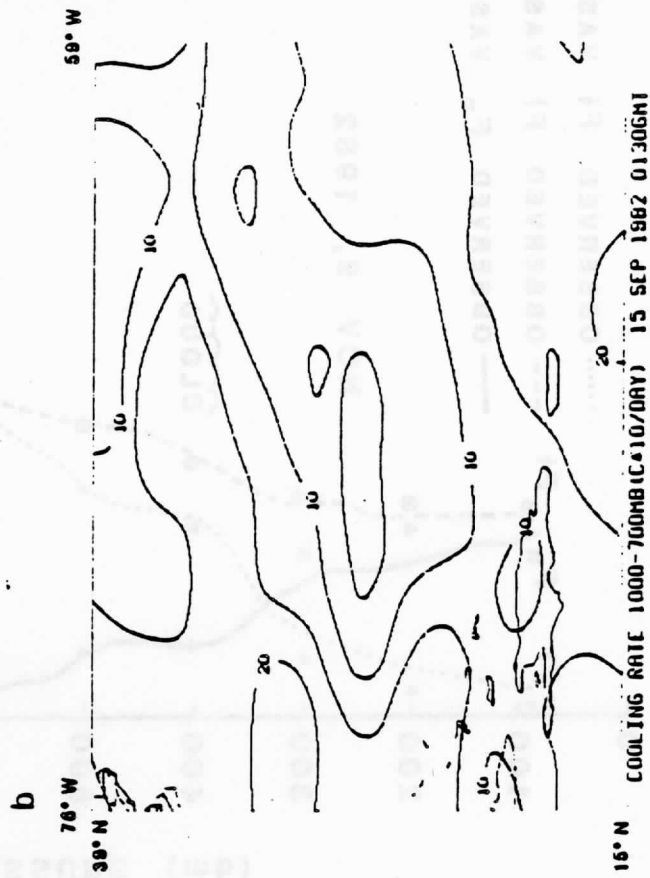
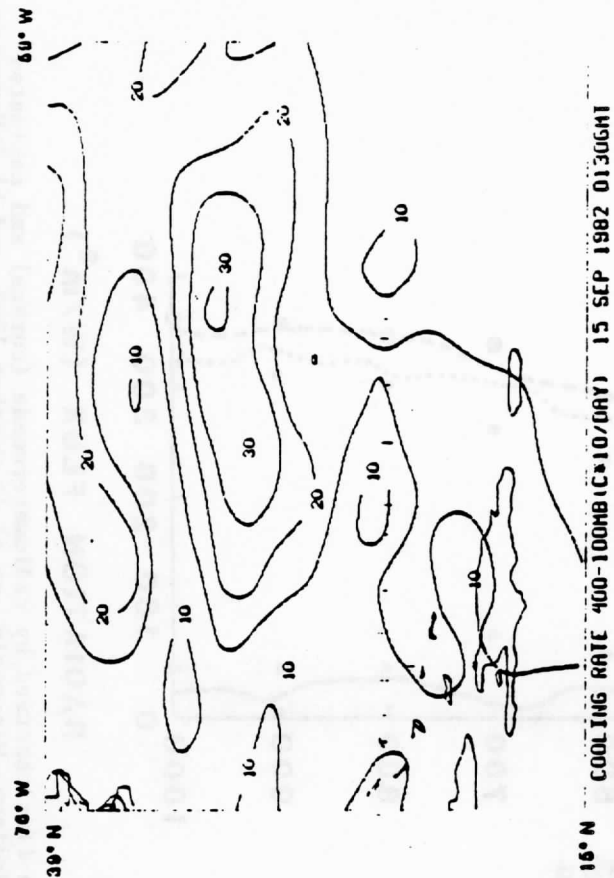
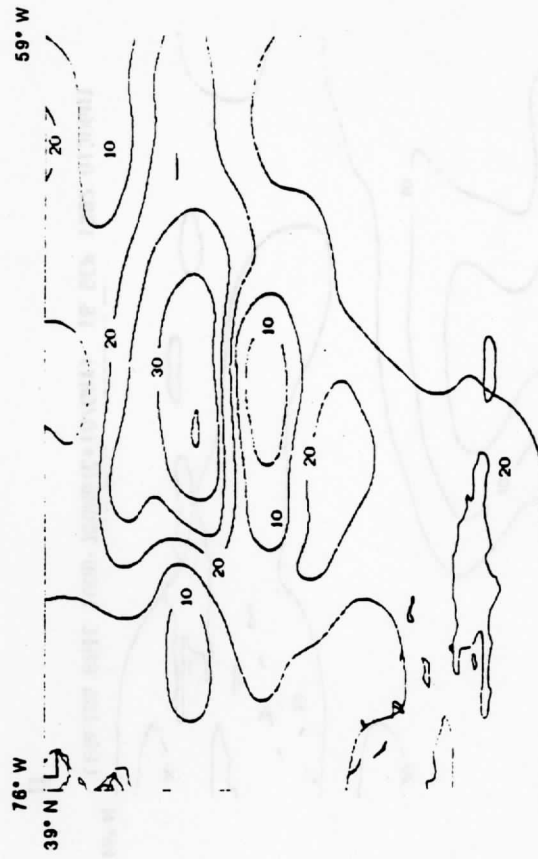
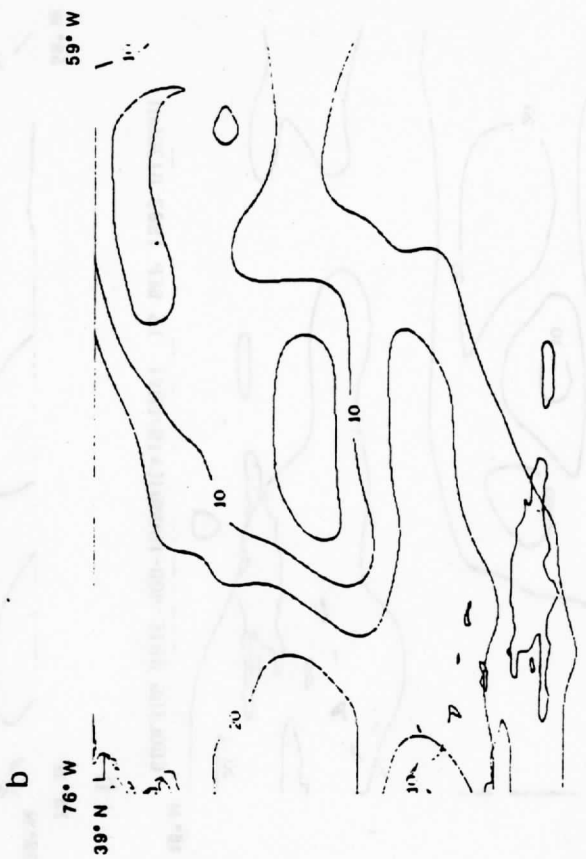


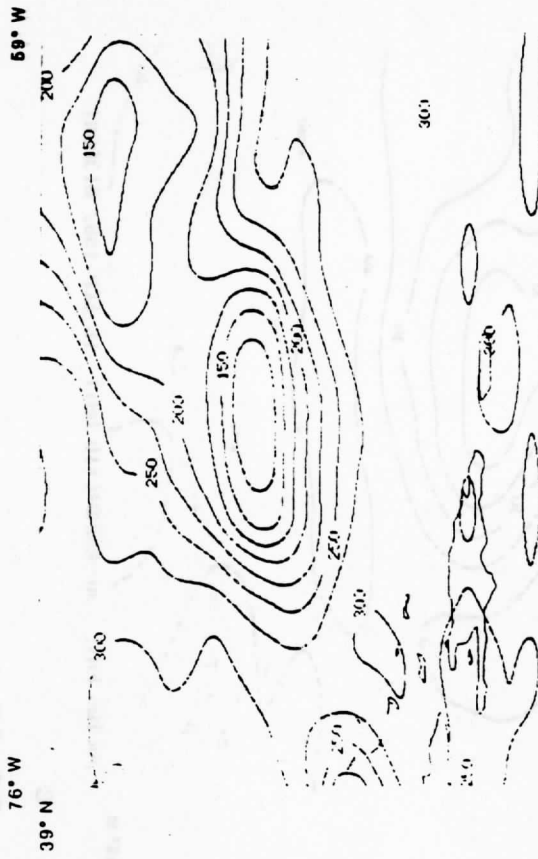
FIGURE 2: Outgoing longwave flux ( $W/m^2$ ) and infrared cooling ( $^{\circ}C \times 10/day$ ) for the lower (1000-700 mb), middle (700-400mb) and upper (400-100 mb), tropospheric layers as inferred from VAS radiances at 0 GMT 15 SEP 1982



15° N UPWARD LONG WAVE FLUX AT 1.0MB(WATTS/M²) 15 SEP 1982 1330GMT



15° N COOLING RATE 400-1000MB(C\*10/DAY) 15 SEP 1982 1330GMT

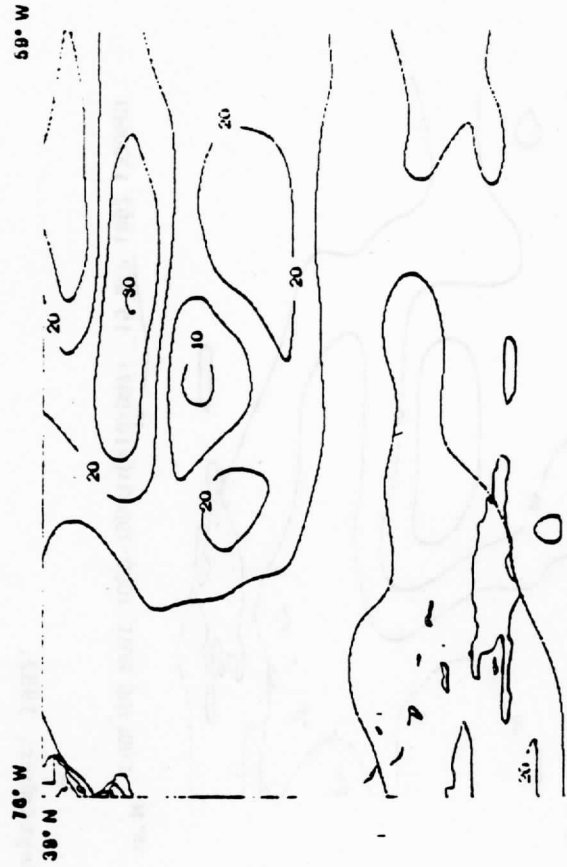


15° N COOLING RATE 1000-700MB(C\*10/DAY) 15 SEP 1982 1330GMT



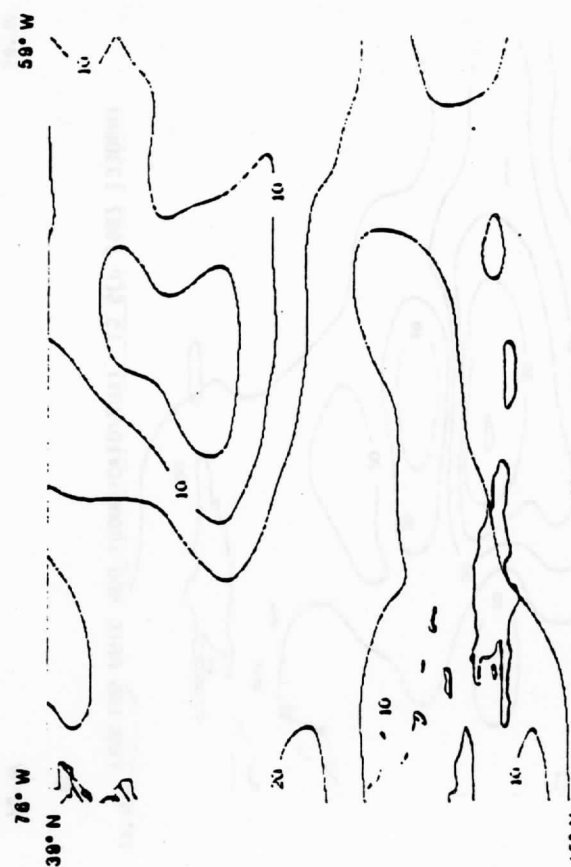
15° N UPWARD LONG WAVE FLUX AT 1.0MB(WATTS/M²) 15 SEP 1982 1330GMT

FIGURE 3: Same as figure 2, but for 1330 GMT on 15 September, 1982.



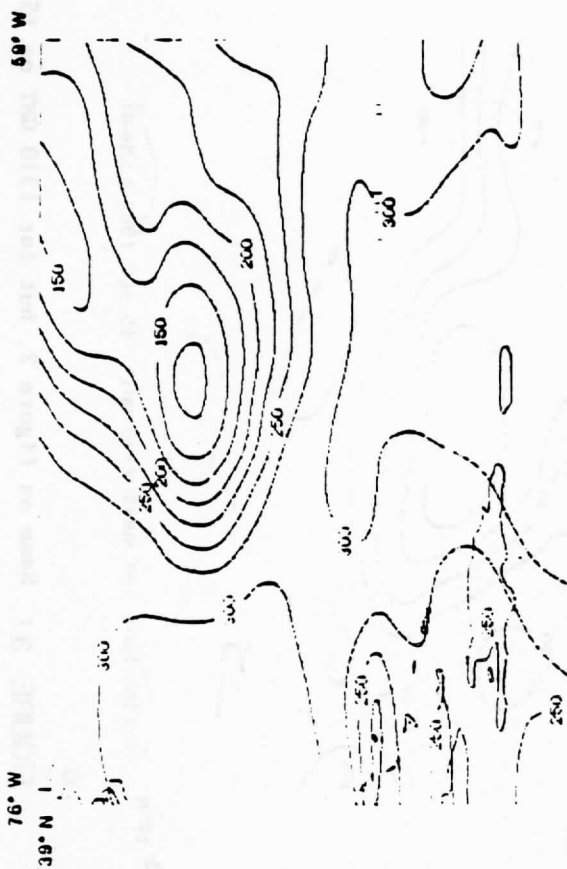
15° N UPWARD LONG WAVE FLUX AT 1.0MB (WATTS/M<sup>2</sup>) 16 SEP 1982 0130GMT

a



16° N COOLING RATE 400-1000MB (C\*10/DAY) 16 SEP 1982 0130GMT

b



15° N UPWARD LONG WAVE FLUX AT 1.0MB (WATTS/M<sup>2</sup>) 16 SEP 1982 0130GMT

c



16° N COOLING RATE 1000-700MB (C\*10/DAY) 16 SEP 1982 0130GMT

d

FIGURE 4: Same as figure 2, but for 0130 GMT on 16 September, 1982.

The Interactive Videographic Computer--  
A Revolutionary Tool for Meteorological Research

William L. Smith  
Cooperative Institute for Meteorological Satellite Studies  
University of Wisconsin  
1225 West Dayton Street, 2nd Floor  
Madison, Wisconsin 53706

ABSTRACT

Meteorological research has been greatly accelerated through the use of interactive videographic computer systems. These systems enable results of experiments to be displayed, almost instantaneously, in the form of horizontal contour analyses, vertical cross-sections or false color imagery. Experimental results and satellite and radar imagery can be displayed in three or four dimensional (animated) fields. The interactive videographic capability has been particularly valuable at the CIMSS for (1) intercomparing new remote sensing results with conventional observations (e.g., satellite soundings versus radiosondes) to enable rapid development of new satellite sounding software, (2) intercomparing multi-spectral satellite imagery with contour analyses of atmospheric state parameters (e.g., 6.3  $\mu\text{m}$  water vapor imagery with 300 mb wind analyses), (3) blending different meteorological observations for achieving optimal composite analyses (e.g., blending geopotentials from satellite and radiosonde soundings with winds achieved by cloud or moisture motion tracing from animated geostationary imagery), and (4) viewing the results produced by numerical weather prediction models due to changes in the initial conditions and/or model physics thereby enabling interactive modification of the initial conditions and/or "tuning" of the physics.

Software developed at the CIMSS for the conduct of research with the University of Wisconsin's Man-computer Interactive Data Access System (McIDAS) is reviewed. A videotape presentation of example research applications of McIDAS is to be shown during the presentation.



PASSIVE REMOTE SOUNDING FROM METEOROLOGICAL SATELLITES

William L. Smith  
NOAA/NESDIS Development Laboratory  
1225 West Dayton Street, 2nd Floor  
Madison, Wisconsin 53706

1. Instrumentation Overview

During the past two decades passive infrared and microwave radiometers have been used to provide vertical temperature and moisture profiles from meteorological satellites. The infrared instruments have evolved from the moderate spectral and low spatial resolution interferometers and grating spectrometers flown on the early Nimbus satellites to the high spatial and low spectral resolution filter radiometers currently flying on the operational polar orbiting (NOAA) and geostationary (GOES) satellites. The evolution of the infrared instruments has been driven by the need for high spatial resolution to probe the clear air interstices of the earth's broken cloud cover. Microwave sounders, which penetrate clouds, were initially much larger and more power consuming than infrared radiometers, but advances in technology have permitted the number of spectral channels to be increased and the field of view to be reduced without a corresponding increase in the weight, volume, and power requirements. Advanced microwave radiometers possessing twenty channels in the frequency range from 18-190 GHz to observe water vapor profiles with 15 km horizontal resolution as well as temperature profiles are planned to be carried by polar orbiting satellites before the end of this decade. Passive radiometry proposed for future geostationary satellites consists of a high spectral resolution interferometer which utilizes nonlinear delay scanning to optimize the signal to noise ratio of the fine scale vertical structure signatures of the temperature and moisture profile. A grating spectrometer which utilizes detector arrays to achieve both high spatial and spectral resolution is also proposed for implementation on future polar satellites.

2. Current Techniques

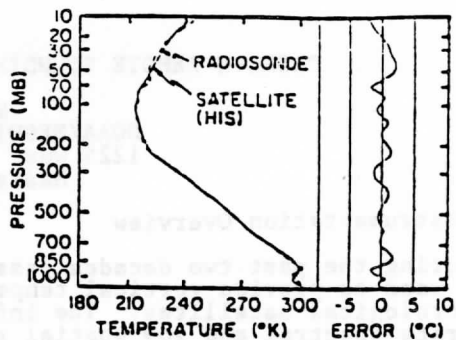
Polar orbiting meteorological satellites (the TIROS-N/NOAA-6 series) carry the TIROS Operational Vertical Sounder (TOVS) which consists of three instruments: 1) the High-resolution InfraRed Sounder (HIRS), 2) the Microwave Sounding Unit (MSU), and 3) the Stratospheric Sounding Unit (SSU). The HIRS consists of a visible channel and 19 low spectral resolution (approximately  $15 \text{ cm}^{-1}$ ) infrared channels within the  $3.7\text{-}15 \mu\text{m}$   $\text{CO}_2$  and  $\text{H}_2\text{O}$  absorbing region. Its nominal spatial resolution of 30 km and contiguous scan geometry permit clear air soundings to be achieved over 80% of the earth with a resolution of 250 km. The MSU consists of four spectral channels operating in the 60 GHz complex of oxygen absorption lines. Its spatial resolution is 140 km and it has the advantage of sensing through most cloud. The SSU consists of three channels at  $15 \mu\text{m}$  which uses pressure modulation to monitor the temperature profile of the stratosphere with a 200 km spatial resolution.

The TOVS data is processed globally by NOAA in Washington with a spatial resolution of 250 km. The retrieval technique used consists of 1) amalgamating data from the three instruments to provide a single set at the locations of the HIRS footprint, 2) estimating clear air radiances for the infrared channels by selection and/or application of a cloud elimination processing technique, and 3) applying a statistical regression algorithm, based upon a set of quasi-coincident radiance observations and radiosondes gathered over prior days, to estimate the temperature and water vapor profile of the atmosphere.

The NOAA/NESDIS Development Laboratory at the University of Wisconsin has developed a high spatial resolution (i.e., 75 km) TOVS sounding data processing system which has been adopted by numerous direct readout data users. The latest version of the "TOVS Direct Readout User Package" from the laboratory converts the radiance data into meteorological profiles using a physical solution of the radiative transfer equation rather than empirical regression in order to account for the influence of surface variables (i.e., terrain elevation, emissivity, and temperature) in the profile solutions and to permit the infrared data to be utilized for overcast as well as clear and partly cloudy sky conditions. These attributes are particularly important for the real time use of the data in regional mesoscale weather analysis and forecast models.

As an example of the quality of high resolution TOVS physical sounding retrievals, Figure 1 shows a comparison of analyses of soundings obtained from consecutive orbits of the NOAA-7 satellite over Europe and operational analyses from the European Center for Medium-range Weather Forecast (ECMWF). Both sets of geopotential thickness analyses (proportional to the layer mean temperature) of the 1000-700 mb layer are similar and one can see good time continuity in these analyses for this geographical region of complex terrain conditions (i.e.,

instrumental noise for a diverse sample of radiosonde profiles. Shown in Figure 3a are the RMS errors of the retrieval temperatures averaged over the standard layers used in meteorological practice. As can be seen, the accuracy improves with spectral resolution, the errors being less than 1°C for the mesoscale sounding mode. Figure 3b shows two examples of profiles which clearly illustrate the ability to retrieve fine scale vertical structure from the HIS mesoscale mode interferogram radiance observations. This result represents a major improvement over our current sounding capability.



Another method of improving the vertical resolution of remotely sensed soundings over land is to combine satellite radiance observations with ground based radiometric data from an upward looking microwave radiometer. Although a network of ground based remote sensors does not yet exist, an experimental zenith sounding microwave Profiler instrument is located at Denver, Colorado. GOES VAS radiances have been combined with simultaneous measurements from the four microwave channels of the Profiler to test the concept of combining "Topside" and "Bottomside" remote sounding radiances to achieve improved results.

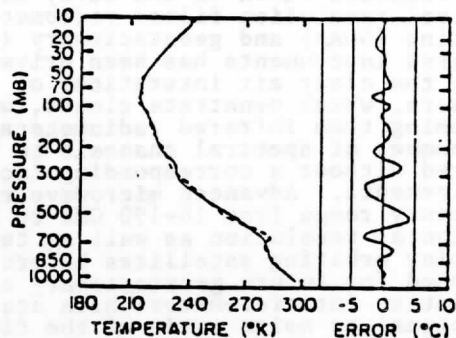


Figure 4a shows the temperature profile weighting functions for the VAS and Profiler radiance observations for Denver, Colorado.

Fig. 3b.

As can be seen, the Profiler temperature observation is strong and complements the VAS sensitivity to lower atmospheric temperature. The Profiler temperature sensitivity is strong and complements the VAS temperature sensitivity at upper tropospheric levels which dominates that of the Profiler.

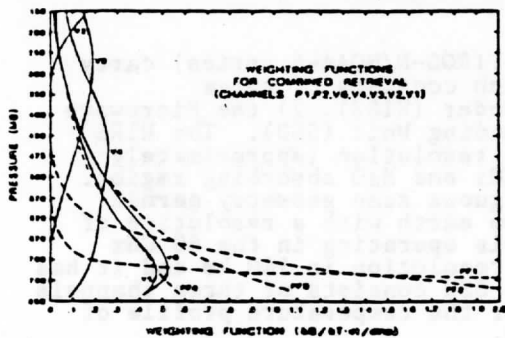


Fig. 4a: Profiler and VAS weighting functions derived from retrieval at 1322 GMT 10 November 1982.

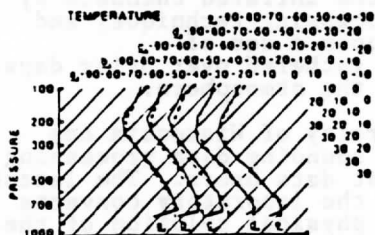


Fig. 4b: Time sequence of VAS temperature profiles initialized with the climatological guess (dashed lines) vs. those initialized with the simultaneous Profiler data (solid lines) for the times: a, 1348; b, 1548; c, 1648; d, 2048, e, 2248 GMT on 10 November 1982 at Denver, Colorado. Temperature scales have been displaced to allow easier viewing of the five separate times.

Figure 4b demonstrates the improvement in lower tropospheric resolution achieved by incorporating Profiler data with the VAS data in the sounding retrieval process. Shown is the time variation of soundings retrieved from VAS radiances alone (dashed) and from VAS plus Profiler radiance data. The ability to retrieve the time variation of the boundary layer temperature structure using the combined system is apparent.

#### 4. Summary

Passive remote sounding from satellites has evolved rapidly over the past fifteen years. Current systems are capable of achieving both high spatial and temporal resolutions but the vertical resolution is limited. Improved vertical resolution can be achieved in the future by measuring the fine scale spectral features of the atmosphere's radiance to space and by combining the satellite data with observations from a network of ground based zenith viewing microwave radiometers.

mountains, deserts, and land/sea transitions). The greater horizontal detail of the TOVS analyses of lower tropospheric thickness is presumably due in part to the relatively high density of satellite soundings.

United States geostationary meteorological satellites (GOES) carry the VISSR Atmospheric Sounder (VAS). The VAS possesses 7 km resolution and 14 km resolution detectors which can sound the atmosphere in twelve spectral bands of the infrared spectrum; there are two window channels (4.0 and 11.0  $\mu\text{m}$ ), three water vapor channels (6.7, 7.2, and 12.7  $\mu\text{m}$ ), and seven carbon dioxide channels (4.4, 4.5, 13.3, 14.0, 14.2, 14.5, and 14.7  $\mu\text{m}$ ). VAS temperature and water vapor profiles are obtained from VAS radiance

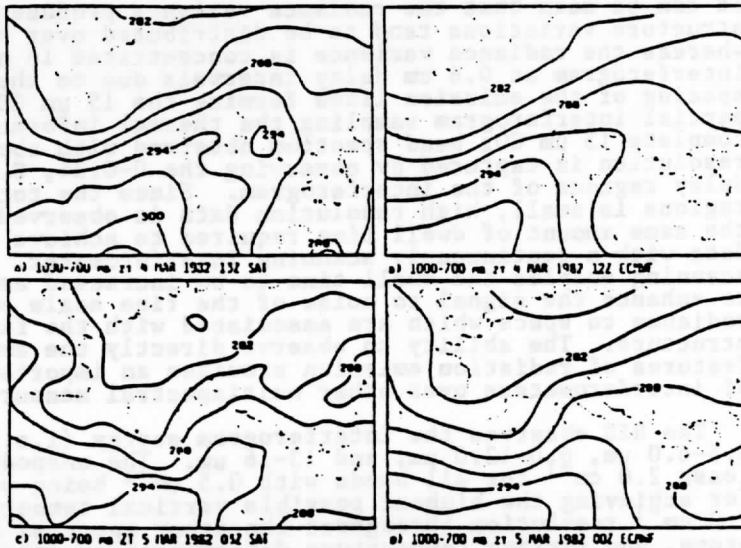


Fig. 1: Analysis of TOVS (SAT) and Radiosonde (ECMWF) 1000-700 mb geopotential thickness (decameters).

data by a physical solution similar to that developed for processing TOVS data. VAS does not possess microwave channels so sounding information is limited to the atmosphere above cloud-top level in areas of extensive cloud cover. However, a dramatic resolution advantage of VAS over TOVS and radiosondes exists in both the spatial and temporal domains. Soundings with a resolution better than 75 km can be provided with a temporal frequency of one hour to improve local weather services and the forecasting of rapidly developing storms. As with the TOVS soundings, however, the VAS soundings have a poor vertical resolution (4-5 km).

### 3. Improving the Vertical Resolution

To approach the vertical resolution required for mesometeorological applications, a satellite sounding instrument must achieve a spectral resolution ( $\Delta\nu/\nu$ ) of 0.1%. For example a spectral resolution of  $0.7 \text{ cm}^{-1}$  is needed in the  $600-800 \text{ cm}^{-1}$  ( $15 \mu\text{m}$ ) band and  $2 \text{ cm}^{-1}$  in the  $2300-2400 \text{ cm}^{-1}$  ( $4.3 \mu\text{m}$ ) thermal emission bands of  $\text{CO}_2$ . Although this spectral resolution is beyond the capabilities of filter radiometers, it can be achieved from an earth-oriented geostationary platform using a Michelson interferometer called HIS (High-resolution Interferometer Sounder). In the HIS design, the Michelson interferometer provides data of variable spectral resolution, dependent upon the delay limit of the interferogram scan. This allows a balance to be achieved between vertical resolution and horizontal coverage as needed to optimize the use of geostationary satellite soundings for resolving various scales of atmospheric motion. For the longest wavelengths of the thermal radiation measured ( $13-16 \mu\text{m}$ ), partial interferogram sampling is used to achieve the required spectral resolution with acceptable dwell times. This is possible because nearly all the spectral information is confined to several narrow delay regions as a result of the relatively uniform spacing of the  $\text{CO}_2$  emission lines.

Figure 2 illustrates the concentration of the thermal profile information in the narrow resonance regions of the interferogram of the  $15 \mu\text{m}$   $\text{CO}_2$  band radiant emission to space. (The radiance spectrum is the Fourier transform of the interferogram.) The variance of radiance in the interferogram domain for a statistical sample of mid-latitude soundings is compared to the variance of radiance in the spectral domain.

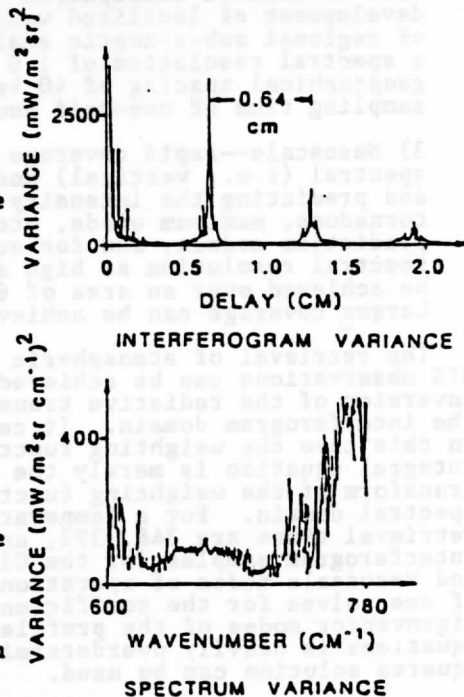


Fig. 2.

It can be seen that the radiance variance produced by temperature profile structure variations tend to be distributed over the entire spectral domain, whereas the radiance variance is concentrated in narrow resonances of the interferogram at 0.6 cm delay intervals due to the nearly uniform  $1.6 \text{ cm}^{-1}$  spacing of the emission lines forming the  $15 \text{ }\mu\text{m}$   $\text{CO}_2$  absorption band. Using partial interferogram sampling the thermal information content contained in a complete  $15 \text{ }\mu\text{m}$   $\text{CO}_2$  band spectrum observed with about  $0.5 \text{ cm}^{-1}$  spectral resolution is captured by observing the 0-0.24, 0.59-0.70, and 1.26-1.33 cm delay regions of the interferogram. Since the total delay span of the three regions is small, high resolution data is observed through partial scanning in the same amount of dwell time required to achieve much lower spectral resolution data with a continuously scanning interferometer. Most important, partial scanning enables the dwell time to be increased as a function of delay in order to enhance the signal to noise of the fine scale spectral features of the radiance to space which are associated with the fine scale vertical temperature structure. The ability to observe directly the amplitude of fine scale spectral features of radiation emission provides an important signal to noise advantage of interferometers over other multispectral measurement approaches.

The HIS observes the interferogram energy (i.e., spectrum) in three bands: 3.5-6.0  $\mu\text{m}$ , 6.0-13.0  $\mu\text{m}$ , and 13-16  $\mu\text{m}$ . The unapodized spectral resolution is at least  $2.0 \text{ cm}^{-1}$  for all bands with  $0.5 \text{ cm}^{-1}$  being possible in the 13-16  $\mu\text{m}$  band for achieving the highest possible vertical temperature profile resolution. The  $2.0 \text{ cm}^{-1}$  resolution throughout the other spectral bands enables water vapor, ozone, and surface temperature determinations from radiance observations which are spectrally pure in the sense that they are primarily due to a single emitting constituent. In practice, however, the complete set of radiance data influences the definition of all meteorological quantities because of their interdependences (e.g., water vapor profile determinations depend upon temperature structure). With the HIS spectral bands of observation and resolution, there are about 500 spectral channels observed for the determination of the desired surface and atmospheric properties.

The HIS, on a geostationary satellite, will be capable of performing in three different operational modes:

- 1) Global--sampling from the entire earth's disk within view of the spacecraft to satisfy the data demands of synoptic scale numerical weather prediction models. In this mode of operation the 10 km resolution radiometric data collected would have a spectral resolution of  $2 \text{ cm}^{-1}$  and a geographical spacing of 80 km. The entire earth's disk would be sampled within one-half hour.
- 2) Regional--quasi-continuous monitoring of a region of 2,000-3,000 km on a side to observe atmospheric stability variations associated with the development of localized weather and to provide data for the initialization of regional sub-synoptic scale numerical prediction models. For this purpose a spectral resolution of  $1.0 \text{ cm}^{-1}$  (for the  $15 \text{ }\mu\text{m}$  sounding channels) and a geographical spacing of 40 km will be achieved over the region within a total sampling time of one-half hour.
- 3) Mesoscale--rapid coverage of a local region with the highest achievable spectral (i.e., vertical) and spatial resolution, for isolating the location and predicting the intensity of severe weather (e.g., flash floods, tornadoes, maximum winds, etc.), for initializing storm scale numerical prediction models, and for subjective point forecasting. For this purpose a spectral resolution as high as  $0.5 \text{ cm}^{-1}$  and a spacing as small as 10 km can be achieved over an area of 600 km linear dimension every one-half hour. Larger coverage can be achieved by decreasing the repetition rate.

The retrieval of atmospheric profiles from HIS observations can be achieved by direct inversion of the radiative transfer equation in the interferogram domain. It can be shown that in this case the weighting function of the integral equation is merely the Fourier transform of the weighting function in the spectral domain. For a temperature profile retrieval there are 348, 392, and 420 interferogram samples for the Global, Regional and Mesoscale modes of operation respectively. If one solves for the coefficients of twenty eigenvector modes of the profile, the system of equations is heavily overdetermined and a least squares solution can be used.

Figure 3 shows the result achieved from HIS observations simulated with realistic

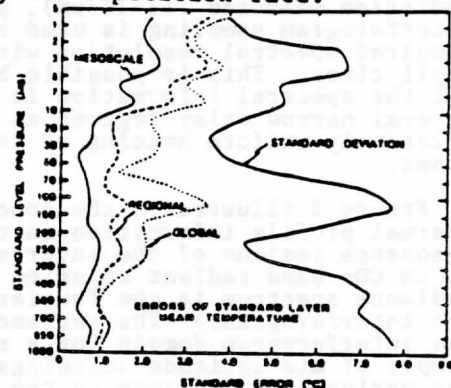


Fig. 3a.

## RECENT ADVANCES IN SATELLITE REMOTE SOUNDING

William L. Smith and Henry E. Revercomb  
Cooperative Institute for Meteorological Satellite Studies  
Space Science and Engineering Center  
University of Wisconsin

H. Benton Howell and Harold M. Woolf  
NOAA/NESDIS Development Laboratory

1225 West Dayton Street  
Madison, Wisconsin, 53706, USA

### Abstract

Recent advances in the science and technology of passive remote sounding from satellites are discussed. A new algorithm is described which permits direct simultaneous solution of the radiative transfer equation for temperature and water vapor profiles as well as surface skin temperature. Comparisons between results using the new simultaneous retrieval method and those from established iterative methods for polar orbiting TIROS Operational Vertical Sounder (TOVS) data are presented. Finally, the status of the 1000 spectral channel High-resolution Interferometer Sounder (HIS) being developed for future geostationary satellites is discussed. Results achieved from a balloon test are presented to demonstrate the vertical resolution achievable by the HIS sounding technique.

### 1. Overview

The science and technology of passive remote sounding of atmospheric temperature and moisture have evolved rapidly during the past two decades. Infrared instruments have evolved from the moderate spectral and low spatial resolution interferometers and grating spectrometers flown on the early Nimbus satellites to the high spatial resolution filter radiometers currently flying on the operational polar orbiting (NOAA) and geostationary (GOES) satellites. The evolution of the infrared instruments has been driven by the need for high spatial resolution to probe the clear air interstices of the earth's broken cloud cover. Passive infrared radiometry proposed for future geostationary satellites consists of a high spectral resolution interferometer which utilizes nonlinear delay scanning to optimize the signal to noise ratio of the fine scale vertical structure signatures of the temperature and moisture profiles. A grating spectrometer which utilizes detector arrays to achieve both high spatial and spectral resolution is also proposed for implementation on future polar satellites. Microwave sounders, which penetrate clouds, have steadily improved due to advances in technology that have permitted the number of

spectral channels to be increased and the field of view to be reduced without a corresponding increase in the weight, volume, and power requirements. Advanced microwave radiometers possessing twenty channels in the frequency range from 18-190 GHz to observe water vapor profiles with 15 km horizontal resolution as well as temperature profiles are planned to be carried by polar orbiting satellites before the end of this decade. The most pressing technological challenge is the development of a practical microwave sounding instrument for operation from geostationary orbit.

Methods of transforming the satellite spectral radiance observations into vertical temperature and moisture profiles have also been improved. Empirical regression solutions which rely on radiosonde data are now being replaced by direct physical solutions of the radiative transfer equation. Unlike empirical regression, physical solutions permit the influences of surface variables (i.e., terrain elevation, emissivity, and temperature) to be accounted for accurately in the profile determinations and allow the infrared data to be utilized in overcast as well as clear and partly cloudy sky conditions.

### 2. Direct Physical Solution

An important advance in the profile retrieval methodology is the simultaneous temperature/water vapor solution developed by Smith and Woolf (1984). They solve the radiative transfer equation in the perturbation form:

$$\delta T^* = \int_0^P \delta U \left[ \frac{\partial T}{\partial p} \frac{\partial \tau}{\partial U} \frac{(\partial B / \partial T)}{(\partial B / \partial T^*)} \right] dp$$
$$- \int_0^P \delta T \left[ \frac{\partial \tau}{\partial p} \frac{(\partial B / \partial T)}{(\partial B / \partial T^*)} \right] dp + \delta T_S \left[ \frac{(\partial B_S / \partial T_S)}{(\partial B / \partial T^*)} \right] \tau_s \quad (1)$$

where  $T^*$  is brightness temperature,  $U$  is precipitable water vapor,  $B$  is Planck radiance,  $T$  is temperature,  $T_S$  is surface-skin temperature,  $\tau$  is transmittance, and  $p$  is

pressure. The perturbation,  $\delta$ , is with respect to an a priori estimated or mean condition. The pressure dependence of all integrand variables is to be understood. In order to solve (1) for  $\delta U$ ,  $\delta T$ , and  $\delta T_s$  from a set of spectrally independent radiance observations, we make the following profile representations in terms of arbitrary pressure functions,  $\phi(p)$ :

$$\delta q(p) = g \sum_{i=1}^N \alpha_i q_0(p) \phi_i(p) \quad (2a)$$

$$\delta T(p) = - \sum_{i=N+1}^N \alpha_i \phi_i(p) \quad (2b)$$

where  $q(p)$  is the water vapor mixing ratio and  $g$  is gravity. The zero subscript indicates the a priori condition. Equation 2a implies from the gas law and hydrostatic equation that

$$\delta U(p) = \sum_{i=1}^N \alpha_i \int_0^p q_0(p) \phi_i(p) dp \quad (2c)$$

Substituting representations (2b) and (2c) into (2) and letting  $\alpha_i = \delta T_{i,j}$  yields for each spectral radiance observation,  $S_{i,j}^*$ , for a set of  $K$  spectral channels:

$$\delta T_{j,j}^* = \sum_{i=0}^M \alpha_i \phi_{i,j} \quad j=1,2,\dots,K \quad (3)$$

where

$$\phi_{0,j} = \frac{\partial B_{i,j} / \partial T_s}{\partial B_{i,j} / \partial T_j} S_{i,j}$$

$$\phi_{1,j} = \int_0^p \int_0^p q_0 \phi_i dp \left[ \frac{\partial T}{\partial p} \frac{\partial \tau}{\partial U} \frac{\partial B_{i,j} / \partial T}{\partial B_{i,j} / \partial T_j} \right] dp \quad i \leq N \quad (4)$$

$$\phi_{1,j} = \int_0^p \int_0^p \frac{\partial \tau}{\partial p} \frac{\partial B_{i,j} / \partial T}{\partial B_{i,j} / \partial T_j} dp \quad N < i \leq M$$

The  $\phi_{i,j}$  quantities are calculated from the a priori estimated or mean profile conditions. Written in matrix form

$$t^* = \phi \alpha \quad (5)$$

where  $t^*$  is a row vector of  $K$  radiance observations,  $\alpha$  is a row vector of  $M+1$  coefficients, and  $\phi$  is a matrix having dimensions  $(K \times M+1)$ . Assuming that  $K \geq M+1$ , then the least squares solution of (5) is employed to give

$$\alpha = (\phi^T \phi)^{-1} \phi^T t^* \approx (\phi^T \phi + \gamma I)^{-1} \phi^T t^* \quad (6)$$

where  $( )^T$  indicates matrix transposition and  $( )^{-1}$  indicates matrix inverse. The  $\gamma I$  term, where  $\gamma$  (nominally 0.1) is a scalar and  $I$  is the identity matrix, is incorporated to stabilize the matrix inverse. Once the  $\alpha_i$ 's are

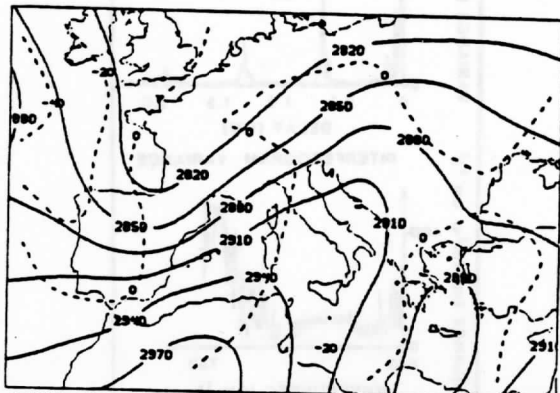
determined,  $\delta T_s$ ,  $\delta q$ , and  $\delta T$  are specified from (2) and added to the a priori estimates to yield the final solutions for surface-skin temperature and the water vapor mixing ratio and temperature profiles.

The choice of pressure functions  $\phi(p)$  is arbitrary. For example, empirical orthogonal functions (i.e., eigenvectors of the water vapor and temperature profile covariance matrices) are used here in the application of the algorithm to high spectral resolution interferometric data. For its application to the TIROS Operational Vertical Sounder (TOVS) data and the VISSR Atmospheric Sounder (VAS) observations, natural functions, the profile weighting functions ( $d\tau/d\ln p$ ) of the radiative transfer equation, are used.

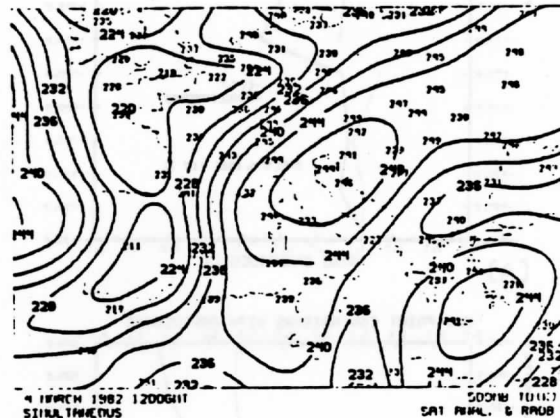
The main advantage of this new retrieval method is that it enables the temperature and water vapor profiles and the surface skin temperature to be determined simultaneously using all the radiance information available. This solution alleviates the problem associated with water vapor radiance dependence upon temperature and the dependence of several of the carbon dioxide channel radiance observations used for temperature profiling, on the water vapor concentration. The dependence of the radiance observations on surface emissions is accounted for in the simultaneous solution by the inclusion of surface temperature as an unknown. Also, since only a single matrix inversion is required for the specification of all parameters, the solution is computationally efficient. Finally, ancillary observations of temperature and/or moisture from surface sensors or aircraft, for example, can be readily incorporated in the solution through the use of (2) in addition to (3) assuming that the left hand side is known for certain pressures.

The simultaneous retrieval method is used at CIMSS for their routine processing of geostationary satellite VAS and polar orbiting satellite TOVS sounding data. The improvement of the simultaneous and direct retrieval method over the prior iterative method used at CIMSS (Smith et al., 1983) and similar to that of Susskind (1984), is demonstrated from TOVS orbits over Europe obtained during the ALPine EXperiment (ALPEX). (These orbits are part of a standard set selected by the International Radiation Commission's TOVS Working Group for the intercomparison of retrieval methods.) The physics for tracing clouds, surface emissivity, terrain elevation and reflected sunlight is identical for both approaches and described by Smith et al. (1983). The initial guess profile was obtained by regression in both cases.

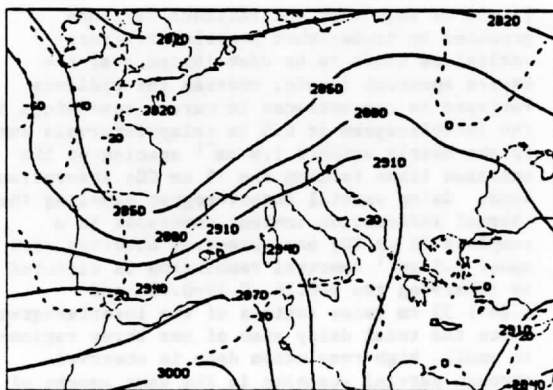
Figure 1a shows the 1000-700 mb geopotential thickness field from TOVS using the simultaneous method and its deviation from the European Centre for Medium-range Weather Forecasting (ECMWF) analysis of radiosonde data. Figure 1b shows a similar result for the iterative algorithm. As can be seen the



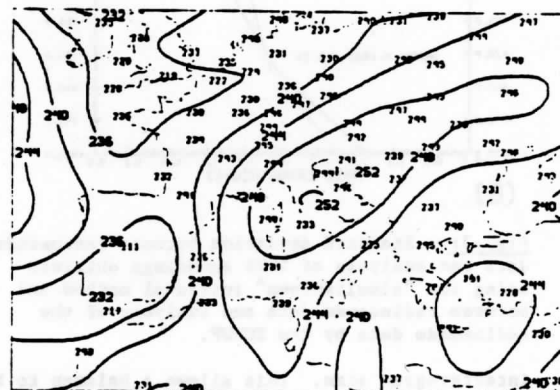
(A)



(A)



(B)



(B)

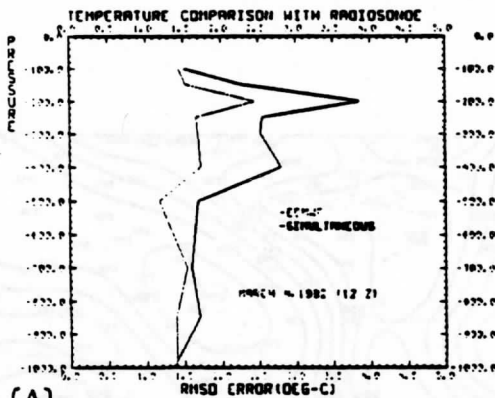
**Fig. 1:** Analysis of 1000-700 mb thickness values obtained by the "simultaneous" (1a) and "iterative" (1b) retrieval methods. The dashed lines display their deviations from an ECMWF analysis of radiosonde data.

geopotential height patterns resulting from the two retrieval algorithms are very similar but the deviations from radiosonde data are smaller for the simultaneous method in both the trough and ridge areas. Figure 2 shows a similar result for 500 mb dewpoint temperature field. Finally, Figure 3 provides comparisons of standard error estimates of the simultaneous method using the radiosonde values as "truth." As may be seen, the temperature and dewpoint errors for the simultaneous method are only slightly larger than those associated with the ECMWF analysis. As a result of the improvements shown here a new "Physical Retrieval TOVS Export Package" for processing direct readout TOVS data is being produced for the international direct broadcast satellite data user community.

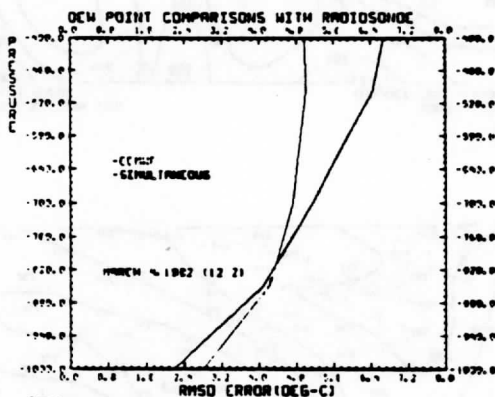
**Fig. 2:** Analysis of 500 mb dewpoint temperatures obtained by the "simultaneous" (2a) and "iterative" retrieval methods. Radiosonde values are plotted.

### 3. Improving the Vertical Resolution

To significantly improve the vertical resolution over that achieved by current operational radiometers, a satellite sounding instrument must achieve a spectral resolution ( $\Delta\nu/\nu$ ) of 0.1%. For example a spectral resolution of  $0.7 \text{ cm}^{-1}$  is needed in the  $600\text{--}800 \text{ cm}^{-1}$  ( $15 \mu\text{m}$ ) band and  $2 \text{ cm}^{-1}$  in the  $2300\text{--}2400 \text{ cm}^{-1}$  ( $4.3 \mu\text{m}$ ) thermal emission bands of  $\text{CO}_2$ . Although this spectral resolution is beyond the capabilities of filter radiometers, it can be achieved from an earth-oriented geostationary platform using a Michelson interferometer called HIS (High-resolution Interferometer Sounder) (Smith et al., 1983). In the HIS design, the Michelson interferometer provides data of variable spectral resolution, dependent upon the delay limit of the



(A)



(B)

Fig. 3: Standard deviation between radiosonde data and analyses of TOVS soundings obtained using the "simultaneous" retrieval method and between radiosonde data and analyses of the radiosonde data by the ECMWF.

interferogram scan. This allows a balance to be achieved between vertical resolution and horizontal coverage as needed to optimize the use of geostationary satellite soundings for resolving various scales of atmospheric motion. The delay scan mirror is laser controlled to achieve the precision needed to resolve fine spectral signatures. For the longest wavelengths of the thermal radiation measured (13-16  $\mu\text{m}$ ), partial interferogram sampling is used to achieve the required spectral resolution with acceptable dwell times. This is possible because nearly all the spectral information is confined to several narrow delay regions as a result of the relatively uniform spacing of the  $\text{CO}_2$  emission lines.

Figure 4 illustrates the concentration of the thermal profile information in the narrow resonance regions of the interferogram of the 15  $\mu\text{m}$   $\text{CO}_2$  band radiant emission to space. (The radiance spectrum is the Fourier transform of the interferogram.) The variance of radiance in the interferogram domain for a statistical sample of mid-latitude soundings is compared to the variance of radiance in the spectral domain.

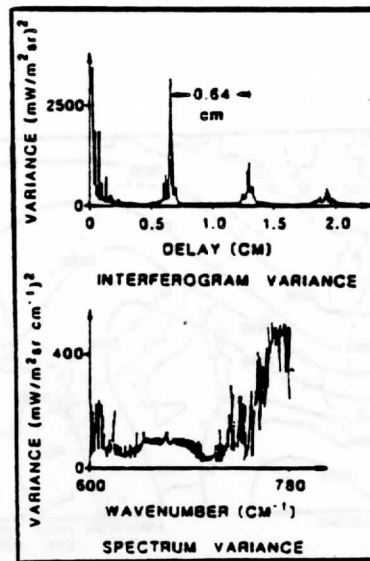


Fig. 4: Variance of interferogram and spectrum radiances.

It can be seen that the radiance variance produced by temperature profile structure variations tends to be distributed over the entire spectral domain, whereas the radiance variance is concentrated in narrow resonances of the interferogram at 0.6 cm delay intervals due to the nearly uniform 1.6  $\text{cm}^{-1}$  spacing of the emission lines forming the 15  $\mu\text{m}$   $\text{CO}_2$  absorption band. Using partial interferogram sampling the thermal information content contained in a complete 15  $\mu\text{m}$   $\text{CO}_2$  band spectrum observed with about 0.5  $\text{cm}^{-1}$  spectral resolution is captured by observing the 0-0.24, 0.59-0.70, and 1.26-1.33 cm delay regions of the interferogram. Since the total delay span of the three regions is small, high resolution data is observed through partial scanning in the same amount of dwell time required to achieve much lower spectral resolution data with a continuously scanning interferometer. Most important, partial scanning enables the dwell time to be increased as a function of delay in order to enhance the signal to noise of the fine scale spectral features of the radiance to space which are associated with the fine scale vertical temperature structure. The ability to observe directly the amplitude of fine scale spectral features of radiation emission provides an important signal to noise advantage of interferometers over other multispectral measurement approaches.

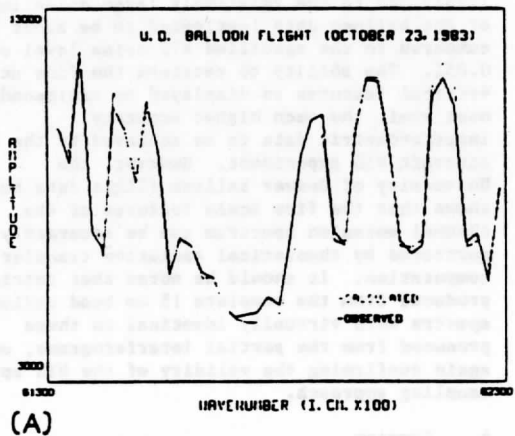
The HIS observes the interferogram energy (i.e., spectrum) in three bands: 3.5-6.0  $\mu\text{m}$ , 6.0-13.0  $\mu\text{m}$ , and 13-16  $\mu\text{m}$ . The unapodized spectral resolution is at least 2.0  $\text{cm}^{-1}$  for all bands with 0.5  $\text{cm}^{-1}$  being possible in the 13-16  $\mu\text{m}$  band for achieving the highest possible vertical temperature profile resolution. The 2.0  $\text{cm}^{-1}$  resolution throughout the other spectral bands enables water vapor, ozone, and surface temperature determinations from radiance



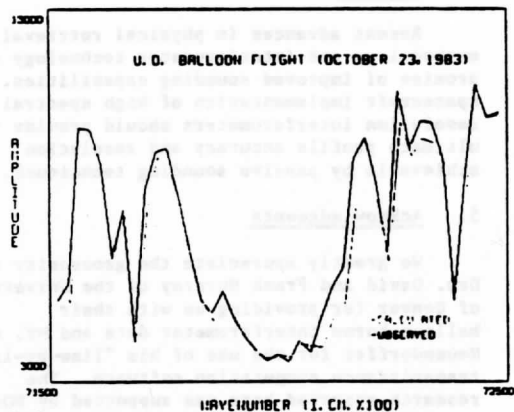
observations which are spectrally pure in the sense that they are primarily due to a single emitting constituent. In practice, however, the complete set of radiance data influences the definition of all meteorological quantities because of their interdependences (e.g., water vapor profile determinations depend upon temperature structure). With the HIS spectral bands of observation and resolution, there are about 500 spectral channels observed for the determination of the desired surface and atmospheric properties.

Theoretical studies indicate that temperature accuracies close to 1°C should be achieved by HIS from the surface to the 10 mb level (Smith et al., 1979, 1983). A U-2 aircraft demonstration of the HIS sounding capability is to be conducted early next year.

A preliminary empirical study of the feasibility of the HIS concept has just been conducted using interferometric data gathered by



(A)



(B)

Fig. 5: Comparison between observed and calculated upwelling radiance at 93,000 ft over White Sands Missile Range, New Mexico on October 23, 1983, 1500 GMT: (a) 613-623  $\text{cm}^{-1}$  and (b) 715-725  $\text{cm}^{-1}$ . The radiance amplitude is in units of  $\text{mW/m}^2 \text{str cm}^{-1}$ .

a Michelson interferometer built by a team of scientists and engineers at the University of Denver under the guidance of Drs. David and Frank Murcray. The spectral radiance observations were obtained from a high altitude balloon (at 93,000 feet) hovering over White Sands Missile Range, New Mexico. Although a spectral range of 8-17  $\mu\text{m}$  was achieved, only the 13-16  $\mu\text{m}$  region is analyzed here since it coincides with the primary HIS spectral band for temperature profiling.

Figure 5 shows comparisons for two narrow Q-branch regions between the observed spectrum (obtained by Fourier transformation of the interferogram) at 0.24  $\text{cm}^{-1}$  resolution and one calculated using the NESDIS line by line program (Neuendorffer et al., 1977) and the White Sands radiosonde. The agreement of the calculated spectral features with those observed is remarkable and as such establishes the credibility of both the spectral observations and the theoretical representation of atmospheric transmittance for this spectral region. The accuracy of the atmospheric transmittance computation is critical to the success of the inverse solution. Differences in the magnitude of the radiances are expected because of instrument calibration uncertainties and errors in the assumed atmospheric and surface temperature conditions. However, there are some very large discrepancies, as large as 10%, which are not understood at this time. The cause of these discrepancies will hopefully be uncovered using an extensive set of comparisons based on the forthcoming and much more precise U-2 aircraft interferometric measurements.

Figure 6 shows an intercomparison of the observed and theoretical (calculated from radiosonde) interferograms for the 600-780  $\text{cm}^{-1}$  spectrum. There is excellent agreement in the location and amplitudes of the main regions of resonance produced by uniform  $\text{CO}_2$  line spacing. This agreement confirms the clustering of

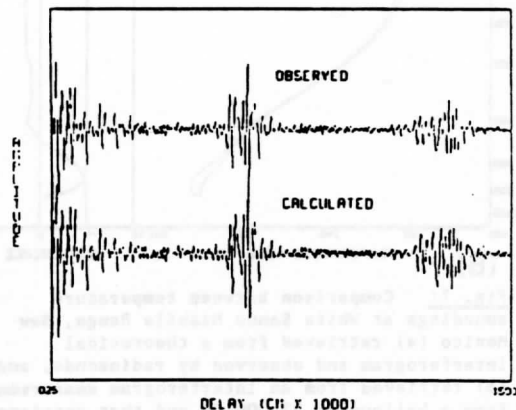


Fig. 6: Comparison between "observed" and "calculated" interferograms for 600-780  $\text{cm}^{-1}$ .

thermal structure information in narrow delay regions of the 15  $\mu$ m band interferogram and therefore establishes credibility to the proposed HIS optimal sampling technique.

Finally, temperature profile retrievals are produced from both the "observed" and "theoretical" interferograms. In order to simulate the HIS optimal (partial) scan result, only data in the 0-0.24, 0.59-0.70, and 1.26-1.33 cm delay regions were considered. The retrieval solution is that given by (6) with

$$t_i^* = \delta I(x_i) = \sum_{j=1}^{15} a_j \int_0^p W_o(x_i, p) \phi_j(p) dp$$

$i=1,2,\dots,1025$

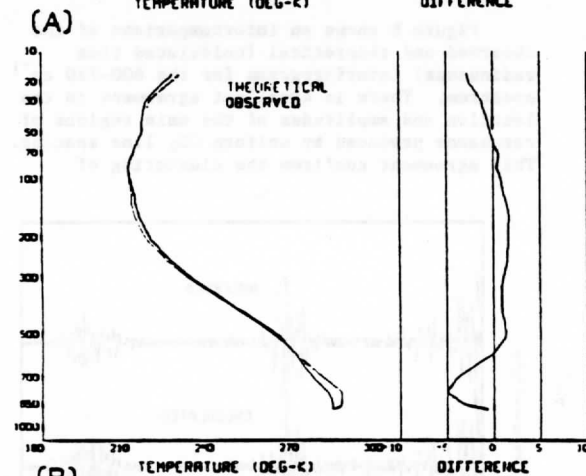
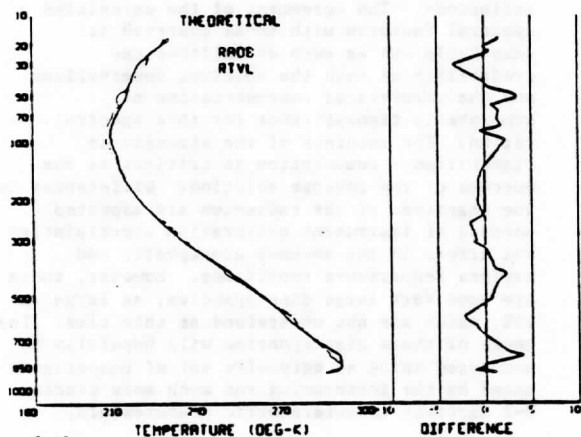


Fig. 7: Comparison between temperature soundings at White Sands Missile Range, New Mexico (a) retrieved from a theoretical interferogram and observed by radiosonde, and (b) retrieved from an interferogram measurement from a balloon at 93,000 ft and that retrieved from the theoretical interferogram.

where  $I(x_i)$  is the interferogram signal ( $x$  being delay),  $\phi_j(p)$  are empirical orthogonal functions of temperature (the water vapor part is excluded here), and the weighting function

$$W_o(x_i, p) = - \int \frac{780 \frac{\partial B_v[T_o(p)]}{\partial T} \frac{\partial \tau_v(p)}{\partial p} \cos(2\pi vx) dv}{600}$$

The temperature profile is given by (2b) once  $a$  is determined from (6). It is obvious that the solution is greatly overdetermined, having 1025 measurements to determine 15 unknowns.

Figure 7 shows (a) the comparison between the retrieval from the theoretical interferogram and the White Sands radiosonde and (b) the comparison between the retrieval from the observed interferogram and the retrieval from the theoretical interferogram. The agreement between the two retrievals is good except near the surface where the retrieval from the "observed" interferogram fails to resolve the low level inversion. This deficiency is most likely due to the relatively large noise level of the balloon data (estimated to be about 1%) compared to the specified HIS noise level of 0.05%. The ability to retrieve the fine scale vertical features as displayed by radiosondes must await the much higher accuracy interferometric data to be achieved by the U-2 aircraft HIS experiment. However, the University of Denver balloon flight data have shown that the fine scale features of the thermal emission spectrum can be accurately portrayed by theoretical radiative transfer computation. It should be noted that retrievals produced from the complete 15  $\mu$ m band radiance spectra were virtually identical to those produced from the partial interferograms, once again confirming the validity of the HIS optimal sampling approach.

#### 4. Summary

Recent advances in physical retrieval methodology and interferometer technology show promise of improved sounding capabilities. The spacecraft implementation of high spectral resolution interferometers should provide the ultimate profile accuracy and resolution achievable by passive sounding techniques.

#### 5. Acknowledgments

We greatly appreciate the generosity of Drs. David and Frank Murcray of the University of Denver for providing us with their balloon-borne interferometer data and Mr. Arthur Neuendorffer for the use of his "line-by-line" transmittance computation software. The research reported here was supported by NOAA contract NA81-AA-H-00024 and NASA contracts NASS-27608 and NAG5-274.

## 6. References

- Neuendorffer, A. C., 1977: Rapid atmospheric transmittance through fast Fourier convolution. Journal of the Optical Society of America, 67, 1376.
- Smith, W. L., H. B. Howell, and H. M. Woolf, 1979: The use of interferometric radiance measurements for sounding the atmosphere. Journal of the Atmospheric Sciences, 36, 566-575.
- Smith, W. L., H. M. Woolf, C. M. Hayden, A. J. Schreiner, and J. F. Le Marshall, 1983: The physical retrieval TOVS Export Package. The Technical Proceedings of the First International TOVS Study Conference (W. Paul Menzel, ed.), August 29-September 2, 1983, Igls, Austria. Published by the Cooperative Institute for Meteorological Satellite Studies, 1225 West Dayton Street, Madison, Wisconsin, 53706.
- Smith, W. L., H. E. Revercomb, H. B. Howell, and H. M. Woolf, 1983: HIS--A satellite instrument to observe temperature and moisture profiles with high vertical resolution. Preprint Volume: Fifth Conference on Atmospheric Radiation, October 31-November 4, 1983, Baltimore, Maryland. Published by the American Meteorological Society, Boston, Massachusetts.
- Smith, W. L., and H. M. Woolf, 1984: Improved vertical soundings from an amalgamation of polar and geostationary radiance observations. Preprint Volume: Conference on Satellite Meteorology/Remote Sensing and Applications, June 25-29, 1984, Clearwater Beach, Florida. Published by the American Meteorological Society, Boston, Massachusetts.
- Susskind, J. and M. T. Chahine, 1983: The GLAS physical numerical algorithm for analysis of HIRS-2/MSU data. The Technical Proceedings of the First International TOVS Study Conference (W. Paul Menzel, ed.), August 29-September 2, 1983, Igls, Austria. Published by the Cooperative Institute for Meteorological Satellite Studies, 1225 West Dayton Street, Madison, Wisconsin, 53706.

VAS Data Acquisition and Processing System  
for a Personal Computer

Ralph G. Dedecker  
Space Science and Engineering Center  
University of Wisconsin  
1225 West Dayton Street, 4th Floor  
Madison, Wisconsin 53706

Robert N. Green  
NOAA/NESDIS Regional and Mesoscale Meteorology Branch  
c/o Department of Atmospheric Science  
Colorado State University, Foothills Campus  
Fort Collins, Colorado 80523

H. Benton Howell  
NOAA/NESDIS Development Laboratory  
1225 West Dayton Street, 2nd Floor  
Madison, Wisconsin 53706

ABSTRACT

A user-friendly, menu-driven operating system for a hard disk based personal computer has been developed for the acquisition of VAS data products generated on the University of Wisconsin-Space Science and Engineering Center's Man-computer Interactive Data Access System (McIDAS) mainframe computer for subsequent processing and display on the personal computer. A number of VAS products, such as observed brightness temperatures, temperature and moisture fields derived from observations, height fields, etc., can be acquired with a minimum of keystrokes and without user knowledge of command formats, parameters, etc. The details of the communications parameters (phone numbers, identification codes for logging on), McIDAS commands and parameters, as well as the names of receiving files for the personal computer are prepared (and stored) by programmers and need not be the concern of the user. The software was developed using assembly language, FORTRAN and Pascal.

The VAS operating system is entered upon either power-up or restart, presenting the main menu with three options, as illustrated in Fig. 1.

Upon selection of any of the stated special function keys, the appropriate menu will be displayed. For example, the communications menu is shown in Fig. 2.

Other options presented by the main menu (retrieval analysis and image analysis) display similar menus listing the available options. Thus the implementation of any option for the acquisition or display of any of a number of VAS data products can be achieved by simply selecting the desired option and pressing a single special function key.

## VAS DATA ACQUISITION AND PROCESSING SYSTEM FOR A PERSONAL COMPUTER

Ralph G. Dedecker  
Space Science and Engineering Center  
1225 West Dayton Street  
Madison, Wisconsin 53706 USA

Robert N. Green  
NOAA/NESDIS Regional and Mesoscale Meteorology Branch  
Colorado State University, Foothills Campus/CIRA  
Fort Collins, Colorado 80523 USA

H. Benton Howell  
NOAA/NESDIS Development Laboratory  
1225 West Dayton Street  
Madison, Wisconsin 53706 USA

### 1.0 MOTIVATION

The microcomputer is the basis for a low-cost interactive video-graphic workstation for meteorological research and operational weather forecasting. A workstation with video-graphic capability is needed for the display of satellite and radar imagery and contour analyses of conventional and satellite surface and vertical sounding observations. The imagery and quantitative data can be accessed from a central computer (e.g., the UW McIDAS, the National Weather Service facility, or a commercial service) using a telephone and modem.

In order to exploit the opportunity for meteorological research and forecast applications of the microcomputer, a menu-driven software system has been developed for the IBM personal computer series. The software, described in this paper, provides three general capabilities:

- remote access to a satellite data base via automatic communication,
- display and analysis of satellite image products prepared on the main frame, and,
- display of temperature and moisture information derived from the VISSR Atmospheric Sounder (VAS).

Future work will generate a software package which will produce a wide variety of meteorological products (e.g., vorticity analyses, vertical cross-sections, isentropic analyses). This is underdevelopment for use in weather service forecast offices and research and educational institutions. Particular emphasis is being given to production of meteorological products from geostationary satellite VAS imaging and sounding system, since it provides high spatial resolution and half-hour interval data useful for local weather analysis and forecasting.

### 2.0 HARDWARE

In order to minimize the cost, the VAS PC work station was designed to use standard off-the-shelf hardware. The required components

are based on the IBM personal computer family. Figure 1 shows a block diagram of the required hardware.

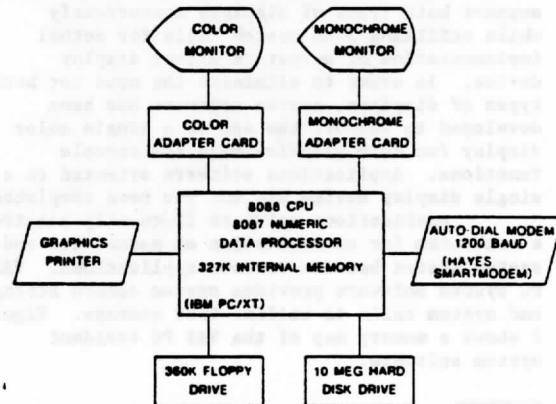


FIGURE 1. HARDWARE REQUIRED FOR THE VAS PC TERMINAL

The IBM PC/XT with a minimum of 328k bytes of memory and a numeric coprocessor (INTEL 8087) is used as the base unit. Current VAS PC software and data bases require approximately 2MB of disk storage space therefore requiring the use of a hard disk. Additional options include the IBM monochrome display card and a monochrome monitor (used as the system console), the IBM color graphics adaptor card and an RGB monitor (used to display graphics and images), an IBM, EPSON, NEC, C.ITOH, or PROWRITER dot matrix printer (used for hard copy of both graphics and text), and a 1200 BAUD Hayes Smartmodem (used to asynchronously acquire data).

Some IBM-compatible computers have been tested in part (such as the COMPAQ) and have been found compatible with the PC VAS software. However, since the software makes extensive use of the IBM PC graphics hardware, care should be taken when selecting an alternate main unit and graphics adapter.

### 3.0 OPERATING SYSTEM SOFTWARE -- GENERAL

The VAS PC software operates under the standard PC DOS or MS DOS operating system. In addition, resident software has been developed to supplement MS DOS control functions and hardware device drivers where necessary. Of the minimum 328k bytes of memory required for the VAS PC work station, MS DOS and VAS PC terminal resident software utilizes approximately 132k bytes thus making approximately 196k available of applications software. All resident software has been developed using the 8086 assembly language of the native INTEL 8088 microprocessor.

The system software design philosophy has been to use as many of the MS DOS system interfaces as possible so as to help facilitate future software compatibility. The system software implements system calls to MS DOS for system services when possible. When calls to MS DOS are not possible, calls are made to the BIOS (basic input output system ROM). When services cannot be provided via BIOS calls, the system software operates directly on the system hardware.

Standard IBM PC system software does not provide support for more than one display (console device) operation at one time. The VAS PC work station utilizes both a monochrome display for operator console text and menus and a color RGB display for graphics and images. Resident system software has been developed to support both types of displays concurrently while utilizing BIOS system calls for actual implementation of output to either display device. In order to eliminate the need for both types of displays, system software has been developed to support the use of a single color display for both graphic-image and console functions. Applications software oriented to a single display device has not yet been completed.

Applications software frequently requires a mechanism for communication of parameters and system states between various applications. VAS PC system software provides system common storage and system calls to utilize that storage. Figure 2 shows a memory map of the VAS PC resident system software.

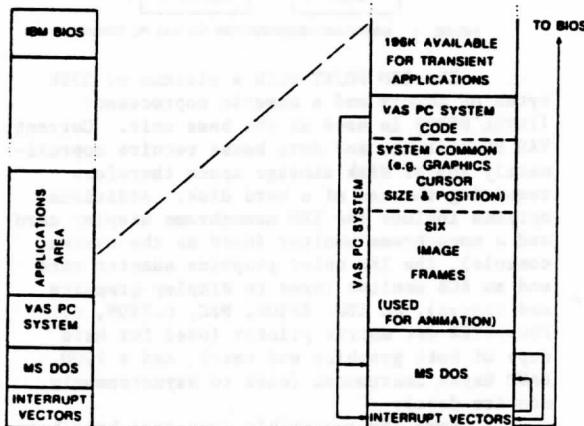


FIGURE 2. MEMORY MAP SHOWING VAS PC RESIDENT SYSTEM SOFTWARE.

### 3.1 Operating System Software -- Image and Graphic Controls

The VAS PC applications software makes extensive use of graphics and images, and provides mechanisms for saving and restoring graphic and image frames between system common memory and the color display. Three different display resolutions are supported, as well as frame animation and annotation.

The standard IBM graphics display adapter board employs 16k bytes of memory to hold a graphic or image frame. IBM BIOS software provides support for two different display resolutions. When the color display is in the high resolution mode, the 16k bytes of memory allow a 200 rows by 640 columns by 1 bit (black and white) frame. Graphic frames as well as some satellite images are displayed in the high resolution mode (via half toning techniques using a "dither" matrix). When the color display is in the medium resolution mode, the 16k bytes of memory allow a 200 rows by 320 columns by 2 bits frame. Two color palettes are available in this mode, a red, green, yellow palette, and a cyan, magenta, white palette. Graphic frames are displayed in the medium resolution mode. VAS PC system software provides controls for an additional resolution format. When using this low resolution format, a frame can contain 100 rows by 160 columns by 4 bits (16 colors). The 16 colors can be any from the following: black, dark grey, blue, bright blue, green, bright green, cyan, bright cyan, red, bright red, yellow, bright yellow, magenta, bright magenta, light grey, white. Since grey scales are not possible with the standard IBM color graphics adapter, color-coded satellite images are displayed in the low resolution mode. Figure 3 summarizes the three graphics modes available.

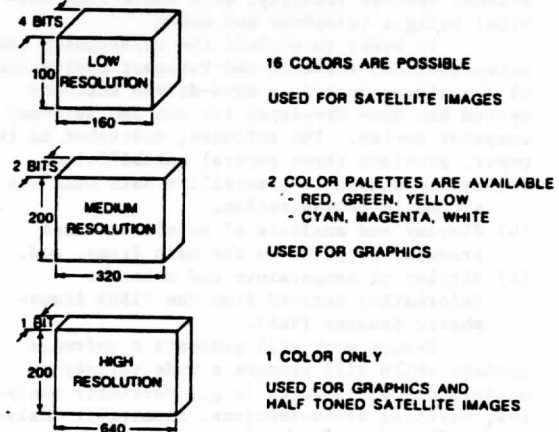


FIGURE 3. THE STANDARD IBM COLOR GRAPHICS ADAPTER GRAPHIC MODES.

Graphic or image frames can be animated via VAS PC system software calls. Storage is provided for up to 6 frames (see figure 2) in any of the three resolutions described above. Each frame requires approximately 16k bytes of resident memory, and more than 6 frames could be allocated at system configuration time. A trade off must be made between total system memory requirements and the number of frames desired.

Animation rates of up to approximately 15 frames per second are achieved by actually moving an image frame (16k bytes) from system common memory to the color adapter display memory.

### 3.2 Operating System Software -- Non Resident System Utilities

Most of the VAS PC applications software is written in Pascal and FORTRAN. In addition to the resident system services, a number of non-resident utility system routines have been developed to provide system interfaces to the resident system software and system hardware resources.

A group of routines provide a set of low level graphics commands to select the various graphics modes and to provide a set of calls for generating line graphics. A scheme for providing a graphics cursor has been implemented using an exclusive-or function with the color display adapter memory.

Console character display routines provide an ability to generate formatted displays (frequently used with menus) and routines allow keyboard extended character input (function keys) along with character filtering and user feedback.

### 3.3 Operating System Software -- Program Linkage

The VAS PC work station software includes many more application routines than can be fit into the 196k bytes of memory available for applications. System software has been developed that provide means to invoke, by chaining, various applications from menus or from other applications.

## 4.0 COMMUNICATIONS

All real time data that is required by the applications programs that are part of the VAS PC software are acquired via a 1200 BAUD asynchronous modem and dial up telephone link. Currently, all real time data are acquired from the IBM 4381 based McIDAS main frame located at the University of Wisconsin Space Science and Engineering Center. Software has been developed on the McIDAS to compress the data sent to the VAS PC system thus reducing transmission time required to transmit such products as satellite images. A number of utility routines have been developed on the VAS PC terminal to allow automated data acquisition.

The VAS PC communications software expects a Hayes Smartmodem to be used as an interface to the McIDAS system, and as such, routines have been developed to use the automatic dialing capabilities of the Hayes modem. Routines are also available to automatically detect key character strings sent from the McIDAS system and to respond to the character strings so that automatic logon and data requests are possible. The VAS PC communications utility routines actually emulate operator keyin requests that are sent to the McIDAS main frame. Utilities also allow local disk file storage of incoming data.

## 5.0 APPLICATIONS SOFTWARE -- THE MENU SYSTEM

All VAS PC applications software is designed to be invoked from menus. The user generally chooses a menu item (invokes a process) by pressing one of the function keys that are part of the standard IBM PC keyboard. Initially, the user is presented with a main menu. Choosing an item from the main menu, results in the display of another menu providing more specific choices than those available from the main menu. Each menu item, in turn, results in the end process desired being invoked or in the display of a sub menu. Inversely, repetitively pressing the "Esc" key results in returning to the next higher level menu until the main menu is displayed. Current development of the VAS PC terminal applications software provides for three options from the main menu (see Figure 4):

```

VAS
DATA ACCESS AND PROCESSING SYSTEM

MAIN MENU

KEY          ACTION

F1.         GENERAL McIDAS COMMUNICATIONS
F2.         RETRIEVAL ANALYSIS
F3.         SATELLITE IMAGE ACQUISITION AND ANALYSIS

PLEASE PRESS THE FUNCTION KEY (F1..F3) OF YOUR
CHOICE. OR PRESS 'ESC' TO RETURN TO DOS.

```

FIGURE 4. THE MAIN MENU.

- 1) General McIDAS communications -- provides a means of a simple general purpose communications with McIDAS and a means for defining and changing the telephone number, user, and project numbers used for communications (see Figure 5).

```

COMMUNICATIONS CONTROL MENU

KEY          ACTION

F1.         ACQUIRE DATA FROM McIDAS
F2.         CONNECT TO McIDAS AS A SIMPLE TERMINAL
F3.         SEND A TEXT FILE TO McIDAS
F4.         CHANGE THE TELEPHONE NUMBER, USER
            ID. AND PROJECT NUMBER FOR
            COMMUNICATIONS WITH McIDAS

PLEASE PRESS THE FUNCTION KEY (F1..F4) OF YOUR
CHOICE. OR PRESS 'ESC' TO EXIT

```

FIGURE 5. THE GENERAL McIDAS COMMUNICATION MENU.

- 2) Retrieval analysis -- provides a menu of analysis and display routines which are

specifically designed for VAS retrievals processed on the McIDAS. At present, the data used by these routines are collected as ASCII text files and contain temperature, dew point and wind data for standard VAS levels and brightness temperatures for each VAS channel (see Figure 6).

VAS RETRIEVAL ANALYSIS MENU	
KEY	ACTION
F1.	INITIALIZE VAS BACKGROUNDS
F2.	CONVERT TEXT TO BINARY FILE
F3.	LOCATE VAS RETRIEVALS
F4.	PLOT RETRIEVAL PARAMETER
F5.	PRINT RETRIEVAL
F6.	ANALYZE RETRIEVALS (BARNES)
F7.	CONTOUR ANALYZED FIELD
F8.	PLOT RETRIEVAL PROFILE
F9.	REVIEW RETRIEVAL FILE

PLEASE PRESS THE FUNCTION KEY (F1..F9) OF YOUR CHOICE. OR PRESS "ESC" TO EXIT.

FIGURE 6. RETRIEVAL ANALYSIS MENU.

- 3) Satellite image acquisition/display/analysis — provides communications mechanisms to acquire and display GOES images (VAS and VISSR) in either high resolution (halftone) or low resolution (color coded) graphics modes, and to display a contour analysis of selected VAS brightness temperatures (see Figure 7).

SATELLITE IMAGE ACQUISITION/DISPLAY/ANALYSIS MENU

KEY	ACTION
F1.	DISPLAY CURRENT FILE OF VAS BRIGHTNESS TEMPERATURES
F2.	ACQUIRE AND DISPLAY VISSR HALFTONE (HI RES) IMAGE
F3.	ACQUIRE AND DISPLAY VISSR COLOR-CODED (LO RES) IMAGE
F4.	DISPLAY CONTOUR ANALYSIS OF CURRENT FILE OF VAS BR. TEMPS.
F5.	ANIMATE/SAVE/RESTORE IMAGES

PLEASE PRESS THE FUNCTION KEY (F1..F5) OF YOUR CHOICE. OR PRESS "ESC" TO EXIT

FIGURE 7. THE SATELLITE IMAGE ACQUISITION DISPLAY AND ANALYSIS MENU.

5.1 Applications Software - General McIDAS Communications

"Acquire data from McIDAS" — Upon selection of this option, the contents of a text file are displayed, including: a McIDAS command, file names of locally generated disk files, names of programs to be subsequently invoked, the end-of-data message expected as termination of the data stream and

an indicator of display option (e.g., halftone or 16-level image). Prompts are then displayed, allowing each item to be left as is or changed. After the last item is either changed or skipped, the general data acquisition program is initiated. This program automatically dials, logs onto McIDAS, issues the specified command, opens a receive file, receives and stores the incoming data until the end-of-data message is received, logs off McIDAS, closes the receive file and turns control over to the next program to be executed. The next program may be an applications program, e.g., to decode and/or display the data received, or the communications menu program from which this action originated. If communications with McIDAS cannot be established, or if the link is disconnected before the terminating message is received, a message to that effect is displayed, and upon the entry of an "ESC" key, control is returned to the communications menu program.

"Connect to McIDAS as a simple terminal" — This option automatically dials the McIDAS main frame, logs onto McIDAS and then allows the user to communicate with the McIDAS system in the same manner as any other ASCII McIDAS terminal.

"Send a text file to McIDAS" — This option allows automatic transmission of a text file to the McIDAS main frame in a manner consistent with McIDAS system software.

"Change the communications parameters" — This option allows specifying the telephone number, user ID, and project number that are stored in a file and are used for automatic dialup and logon parameters with the McIDAS main frame.

5.2 Applications Software -- Retrieval Analysis

"Initialize VAS Backgrounds" — This program is executed to load graphic images into the six frames of RAM memory which are used by the other programs in this menu. The use of the retrieval analysis programs has concentrated on case study analysis in one geographic area. By generating the geographic background once for the case study region, one increases the speed of the applications routines.

"Convert text to binary file" — The ASCII text file of VAS data from McIDAS is processed by this routine to filter out possible transmission errors and to create a binary file to be read by the application programs. It is more efficient to read binary files and, thus an increase in execution speed is realized. The resultant file contains all VAS retrievals for a given time period and geographic area formatted one retrieval per record.

"Locate VAS retrievals" — All retrievals for a given time period are plotted on a background map with a sequence number placed at its latitude-longitude position. The sequence number may be used to access a specific retrieval in other programs. Figure 8



shows an example of the graphics output of this routine.

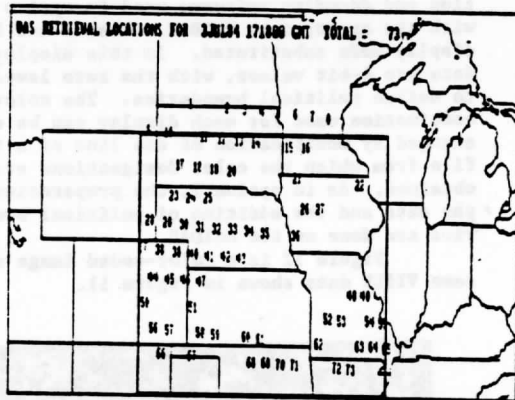


FIGURE 8. EXAMPLE OF "LOCATE VAS RETRIEVALS"

"Plot retrieval parameter" --

A graphic display similar to the previous program's output is generated with the sequence number being replaced by a VAS retrieval parameter chosen by the user from a menu table. A hardcopy of this display may be hand-analyzed.

"Print retrieval" --

The data for the complete retrieval may be displayed in a text format on the monochrome monitor with this program. The retrievals to be displayed are selected by either sequence number or by latitude-longitude box coordinates. A hardcopy of the text is available if the printer is activated by the "Control-Print Screen" command.

"Analyze retrievals (Barnes)" --

A retrieval file can be objectively analyzed with a two-pass Barnes technique. Due to program size limitations, the routine is limited to a file size of 125 observations and an output grid dimension of 16 x 11 one degree longitude-latitude points. The execution time is about two minutes for a typical 60 observation file. The output of this routine is a gridded file which can be used by other programs.

"Contour analyzed field" --

The output file from the analysis program can be displayed in a contoured format in the medium resolution graphic mode. Up to three different fields may be displayed at once with the three different colors available. The contoured field is displayed on a geographic background. Figure 9 presents an example of the contoured product.

"Plot retrieval profile" --

A retrieval can be plotted on a Skew T/log P background. The temperature data is plotted with a solid line, and a dashed line is used for the dew point data. The user has the option of plotting a second retrieval on the same graphic in a contrasting color for comparison analysis. This program also displays information on the monochrome screen showing various computed indices and parameters derived

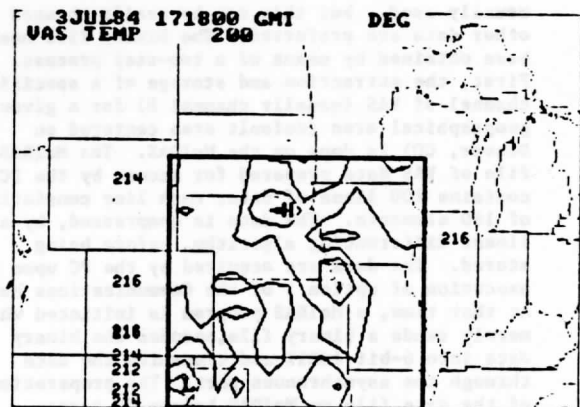


FIGURE 9.

EXAMPLE OF "CONTOUR ANALYZED FIELD"

from the retrieval. Because of sparse availability of wind data for the VAS retrievals, some of the wind-dependent parameters are not useable. Figure 10 gives an example of this routine's graphic output.

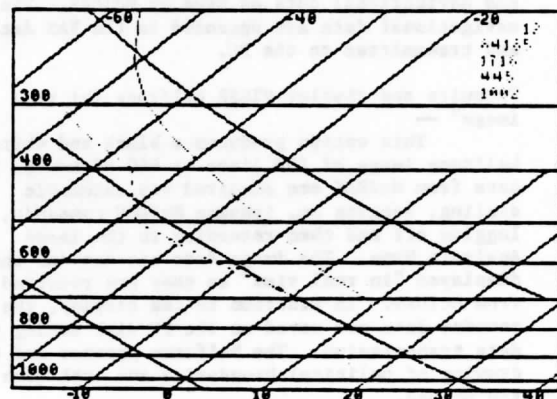


FIGURE 10.

EXAMPLE OF "PLOT RETRIEVAL PROFILE"

"Review retrieval file" --

This program is available to the analyst to quickly scan a given VAS retrieval file. Each retrieval is plotted on the Skew T/log P background, erased and the next plotted as rapidly as possible. The intent of the process is to quickly do a quality control check of a complete file, and to obtain an idea of the makeup of the VAS retrievals.

5.3 Applications Software -- Satellite Image Acquisition, Display and Analysis

"Display current file of VAS brightness temperatures" --

The immediate data source for this display is a binary disk file specified by a "VAS parameter" text file. The name of the file of the latest VAS data acquired from the McIDAS is

usually used, but this can be easily changed if other data are preferred. The binary file has been obtained by means of a two-step process. First, the extraction and storage of a specified channel of VAS (usually channel 8) for a given geographical area (default area centered on Denver, CO) is done on the McIDAS. The McIDAS - file of VAS data prepared for access by the PC contains 100 lines of data, each line consisting of 160 elements. The data is compressed, by a linear differencing algorithm, before being stored. The data are acquired by the PC upon the execution of option 1 of the Communications Menu. At that time, a McIDAS program is initiated which merely reads a binary file, encodes the binary data into 6-bit ASCII and transmits the data through the asynchronous port. The preparation of the data file on McIDAS before PC access minimizes the access time, which is approximately five minutes. After being stored on the PC, in encoded and compressed form, the data are decoded and expanded to its original form. The display program uses the minimum and maximum values of the data to establish the color coding. Ten of 16 available colors are used. The data are plotted line by line in the low resolution mode, after which the political boundaries are plotted. The navigation of the image, i.e. the transformation from earth coordinates to screen coordinates, is accomplished using the same algorithms and navigational data as used by McIDAS. The navigational data are appended to the VAS data and transmitted to the PC.

"Acquire and display VISSR halftone (hi res) image" --

This option produces a black and white halftone image of 200 lines by 640 elements. The data from McIDAS are acquired via automatic dialing, logging on, issuing McIDAS commands, logging off and then returning to the Image Analysis Menu. The image data are decoded and displayed "in real time" as they are received from McIDAS. In addition to the display, the encoded data are saved on the PC disk during the data transmission. The halftone process and the drawing of political boundaries are both done on the McIDAS.

Figure 11 is an example of a halftone image display. The image is a GOES-6 VISSR visible image of hurricane "Josephine" on 12 Oct 1984.

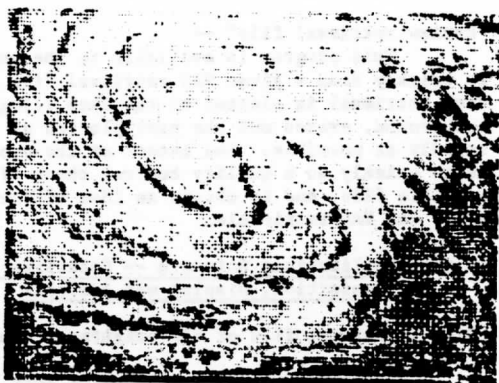


FIGURE 11. VISSR VISIBLE HALFTONE IMAGE OF HURRICANE "JOSEPHINE" (12 OCT 84, 13Z) (IMAGE CENTER 33° N, 71° W)

"Acquire and display VISSR color-coded (low res) image" --

This option uses the same data acquisition and decoding software used in option 2, with the appropriate McIDAS commands and PC display mode substituted. In this display, the data are 4-bit values, with the zero level used to define political boundaries. The color combination used for each display can be easily changed by modification of one line of a text file from which the color designations are obtained. As in option 2, the preparation of the data and the addition of political boundaries are done on the McIDAS.

Figure 12 is a color-coded image of the same VISSR data shown in Figure 11.

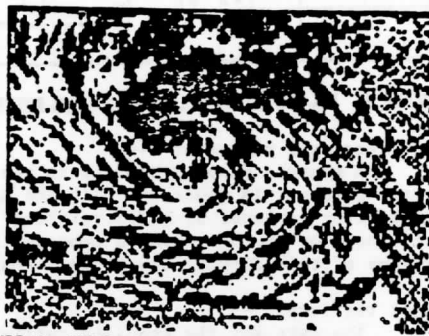


FIGURE 12. VISSR VISIBLE COLOR-CODED IMAGE OF HURRICANE "JOSEPHINE" (12 OCT 84, 13Z) (IMAGE CENTER 33° N, 71° W)

"Display contour analysis of current file of VAS br. temps." --

This option plots a contour analysis of a 20 by 20 grid of values extracted from the same binary file of 100 by 160 points displayed in option 1. The contour interval and smoothing parameters are specified in a text file for easy access and modification. This plot is an example of the medium resolution graphics which can plot in either of two sets (palettes) of 3 colors each. When the plot is completed, control is returned to the Image Analysis Menu.

Figure 13 is an example of a medium-resolution graphics contour analysis of VAS channel 8 (11 μm) brightness temperatures.

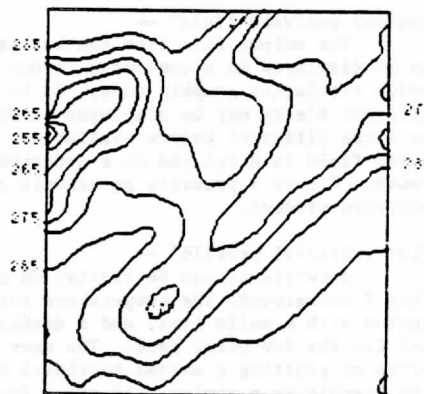


FIGURE 13. CONTOUR ANALYSIS OF VAS CHANNEL 8 (11 μm) BRIGHTNESS TEMPERATURES USING MEDIUM RESOLUTION GRAPHICS.

"Animate/save/restore images" --

This option executes a multi-purpose program which is used primarily to prepare and display "movie loops" of satellite images. The most effective display is obtained when all frames are in the same graphics mode (resolution). Of the three modes, the high and medium resolutions are best, because of the longer delay between frames in the low resolution mode. While the animation is in progress, the sequence and dwell times of the frames can be changed. All command definitions are well described, and invalid entries produce only an audible signal, and are subsequently ignored. Upon entry of the "exit" option, control is returned to the Image Analysis Menu.

6.0 SUMMARY

This paper has presented a VAS data acquisition and processing system based on a microcomputer system. The hardware consists of relatively inexpensive, off-the-shelf components which are readily available. Custom designed system software enhances the basic microcomputer operating system to take advantage of special hardware features. An easy-to-use user interface utilizing menus minimizes the computer knowledge required for the operator. The major components of the applications software allow for communications with the McIDAS mainframe computer for VAS data acquisition, analysis of VAS retrieval data, and display and animation of satellite imagery.

7.0 ACKNOWLEDGEMENTS

The work presented in this paper has been funded in part by the NOAA Operational VAS Assessment Program through grants to the NOAA cooperative institutes at the University of Wisconsin at Madison and Colorado State University.

We wish to express our gratitude to the following people for their contributions to the present VAS PC System: Tom Whittaker, UW/SSEC, Fred Nagle, NOAA/NESDIS/Development Laboratory, and to Tony Schreiner, Chris Velden, Gary Wade, and Ray Zehr for helping with preparations for this presentation. Many thanks to Jan Waite for her accurate and expeditious production of the manuscript and to Tony Wendricks for the graphics.

REAL TIME METEOROLOGICAL APPLICATIONS OF THE GEOSTATIONARY SATELLITE SOUNDER ON GOES-6:  
BATTLING THE COMPUTER, CODE AND CLOCK

<sup>1</sup>C. M. Hayden<sup>1</sup> and A. J. Schreiner<sup>2</sup>

<sup>1</sup>NOAA/NESDIS Development Laboratory  
1225 West Dayton Street, 2nd Floor, Madison, Wisconsin, 53706

<sup>2</sup>Space Science & Engineering Center  
1225 West Dayton Street, 2nd Floor, Madison, Wisconsin, 53706

Abstract

From the beginning of December 1983 through mid-February 1984 the Cooperative Institute for Meteorological Satellite Studies (CIMSS) carried out an exercise to deliver temperature and moisture profiles, derived from the GOES-6 VISSR Atmospheric Sounder (VAS), to the National Meteorological Center (NMC) in time for input to the operational forecast at 1330 GMT. The purpose was to provide meteorological data coverage over the data sparse eastern Pacific (EPAC) where timely polar orbiting satellite data are not available. Although a product was delivered only 40 percent of the time, the experiment successfully demonstrated the feasibility of a totally automated VAS retrieval procedure. Data reliability achieved at the EPAC scale appears to be good, though lack of independent verification data requires that forecast impact studies delineate their ultimate value.

Introduction

The NESDIS Development Laboratory (NESDIS/DL) as part of the Cooperative Institute for Meteorological Satellite Studies (CIMSS) at the University of Wisconsin (UW) in Madison, Wisconsin is charged with the responsibility of developing techniques for applying space borne measurements of outgoing radiation to the problem of weather analysis and forecast. Particular attention is focused on the application of the VISSR Atmospheric Sounder (VAS), which is carried on the geostationary meteorological satellites as a research tool pending operational implementation with the GOES satellites circa 1986. The primary function of the VAS is the description of atmospheric temperature and moisture profiles with a spatial separation of as little as 90 km and a temporal resolution of as little as one hour. This function requires development of an integrated system for the acquisition of raw data from the satellite, reduction of the radiances into the meteorological parameters, quality control in terms of other meteorological observations, and, finally, delivery to the user. The NESDIS/DL has the responsibility of designing and implementing the processing system and the NESDIS Advanced Satellite Products Project (NESDIS/ASPP) (also at the UW in Madison, Wisconsin) the responsibility of exercising the system in a quasi-operational mode. A powerful constraint on the system is a requirement of operational feasibility. Data reduction and product dissemination must be accomplished within a limited time, or they become, quite literally, as useless as yesterday's weather. Furthermore, it is necessary that the processing system be reasonably failsafe in delivering a routine dependable product of uniform quality. The denizens of operations have little patience for otherwise.

Life with VAS is complicated by the fact that emphasis is seasonally adjusted to accommodate the more pressing needs of the National Weather Service (NWS). In spring/summer the focus is centered on the genesis of severe storms and a cooperative application of VAS is carried out with the NWS/Satellite Field Services Station (SFSS) and NWS/National Severe Storm Forecast Center (NSSFC) at Kansas City, Missouri. A description of this effort and the types of products generated can be found in Anthony and Wade (1983)<sup>1</sup>. In essence, special emphasis is directed to the rapid, small scale evolution of atmospheric stability as measured by cooler, drier air overlaying warmer moister air. In summer/fall, attention turns to a joint program with the NWS/National Hurricane Center (NHC) in Miami, Florida for the monitoring and prediction of tropical storms. In this application emphasis is on a larger scale, steering environment. Details can be found in Velden et al. (1983)<sup>2</sup>. Finally, in winter the VAS is applied to data collection over the eastern Pacific in cooperation with the NWS/National Meteorological Center (NMC) in Suitland, Maryland. Emphasis here is on the synoptic scale for the initialization of 12 to 72 hour forecasts over the continental United States. It is this last system which will be treated in this paper.

The eastern Pacific (EPAC) exercise differed in one important respect from other season's applications of VAS. For both severe storm and hurricane processing, strong emphasis has been placed on man/computer interactive techniques using the McIDAS (Man-computer Interactive Data Access System) (Suomi et al., 1983)<sup>3</sup>. These techniques include: the imaging of radiometric data for qualitative interpretation, manual (cursor) selection of target tracers for the derivation of winds from cloud motion, location selection for atmospheric temperature/moisture profiling with operator determined horizontal density, and manual editing based on qualitative decision. In EPAC processing the emphasis has been to remove the man from the loop (motivated in part by the 6:30 a.m. (local) deadline for delivery to the NMC). The extent of success in this endeavor is documented in the following.

### The EPAC System

The processing of the EPAC data involved three separate entities: raw data acquisition at the NESDIS Command and Data Acquisition Station (CDAS) at Wallops Island, Virginia; data processing at the CIMSS; and data utilization at the NMC. The first two are linked via telephone whereas the latter two are joined via a Wisconsin data link to the Suitland IBM 360-195 and an NMC terminal (graphics and video display) to the Wisconsin McIDAS. Raw data retransmitted from the CDAS is received directly at the CIMSS from a transponder satellite and processed meteorological data is sent over the landline to NMC at Suitland, Maryland. The McIDAS terminal at NMC was used to monitor the data and, on occasion, edit individual reports in the McIDAS data base before transmission to the NMC (see Figure 2).

It was agreed between CIMSS and the NMC that the EPAC exercise would begin on 28 November 1983 and extend for a nine week period. The goal was to obtain VAS retrievals over the eastern Pacific in time for operational use with the Limited-area Forecast Model (LFM) which has a data cut-off of 1330 GMT for observations nominally representative of 1200 GMT. This was to be attempted twice per week. December was to serve as a shakedown phase for the processing system at CIMSS and as a learning period at NMC where the data would be viewed, evaluated, and used in an off-line (non-operational) analysis/forecast mode. At the end of December a decision was to be made as to whether the quality was good enough for operational use, and if favorable, the data were to be so used during January, 1984. As it turned out, the test period was extended, and a decision was made on 25 January 1984 not to use the data operationally.

An important restriction (which shadows all VAS assessment exercises) was that the VAS operation not unduly disrupt normal operational activities of the GOES satellite. For this reason, data acquisition had to be split into three latitudinal segments acquired in the time slots 1103-1113 GMT, 1133-1143 GMT, and 1203-1213 GMT. An example of these separate swaths for one of the EPAC cases is shown as Figure 1. These data were to be processed as they were received with the condition that all segments be complete by 1230 GMT so that they could be viewed by NMC before final transmission at 1300 GMT.



*Fig. 1: EPAC 3 time slot image of the 11 micrometer measurement for 6 February 1984.*

A flow diagram of the CIMSS processing system on McIDAS is shown in Figure 2. The system was not in place on 1 December 1983 but evolved through experience and frustration throughout the exercise, albeit at a decreasingly frenetic pace. It is important to emphasize, however, that none of the changes involved the scientific algorithms associated with deriving meteorological parameters from space observed radiance. They all involved the logistics of the processing and fine tuning of the procedures in the hostile climate of an unattended system. The science is the easy part.

An understanding of the system shown in Figure 2 requires a familiarity with the temperature retrieval algorithm. Basically, one begins with an initial estimate of the atmospheric temperature and moisture profile (in the vertical) and perturbs this estimate until the calculated outgoing radiances which would be observed from such conditions match those which are observed in all the spectral measurements. For the VAS instrument there are 11 such measurements which sense at different layers of the atmosphere. The assignment of the first estimate profile is important because of the limited vertical resolution of the radiometer (the radiative signal for each channel arises from a layer several kilometers in extent). Consequently, the final result achieved by perturbing the initial profile is not independent of the guess. Other things being equal, the better the guess the better the retrieval with the corollary that the residual error is correlated with the error of the guess. The last feature is especially vexing to users of satellite data who assemble gridpoint estimates of meteorological fields using statistically optimized algorithms. With such algorithms it is difficult to account for correlated error, and it was strongly recommended by the NMC that the retrieval processing not include any forecast products as first estimates (as has been traditional in other exercises including a previous Pacific test with GOES-4 (O'Lenic, 1982)<sup>4</sup>). The considerable increase in system complexity engendered by this recommendation was cheerfully accepted.

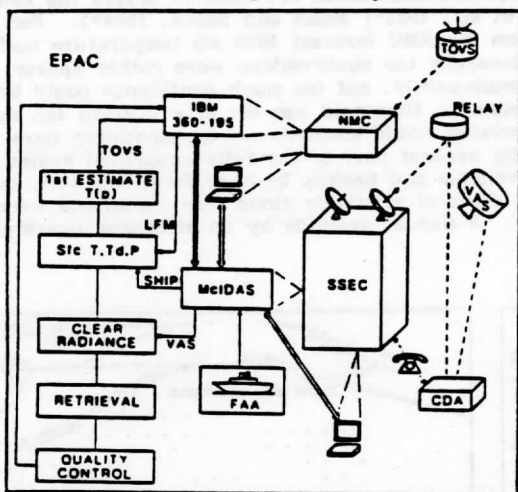


Fig. 2: The EPAC system. The three institutions involved are indicated. Solid double arrows represent communication lines between computers and terminals. The five retrieval processing entities are shown at the left.

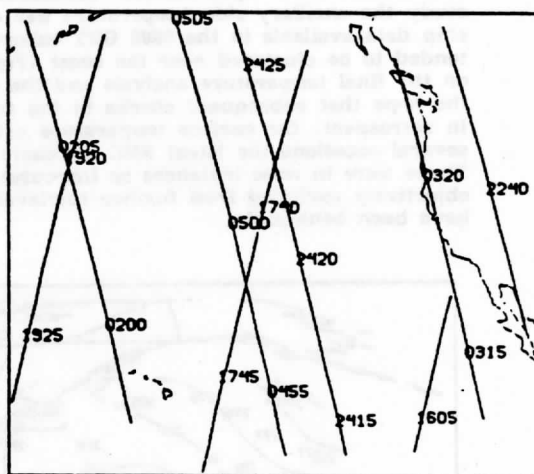


Fig. 3(a).

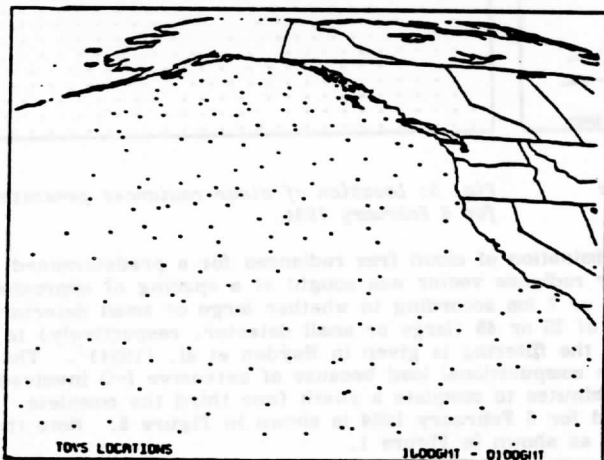


Fig. 3(b).

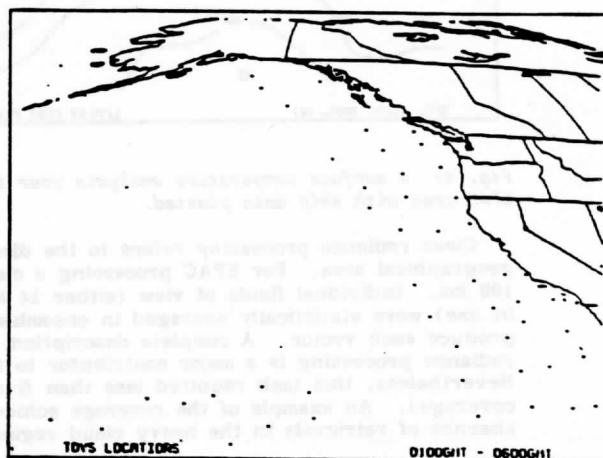


Fig. 3(c).

Fig. 3: TOVS orbits covering the EPAC area (a) and an example of data coverage for early (b) and late (c) cut-off times.

Figure 3 shows the source for acquiring first estimate atmospheric temperature profiles (the retrieval algorithm for moisture does not require a first estimate). Figure 3(a) shows an example of suborbital paths for the polar orbiting NOAA-7 and NOAA-8 (trailing by approximately four hours) satellites over the eastern Pacific. Typically, rather complete geographical coverage is available from 1600-0100 GMT

(Figure 3(b)), and a drop on these data from Suitland was scheduled daily at 0500 GMT. The temperatures from the retrievals were objectively analyzed at a mesh of two degrees latitude and longitude for 15 pressure levels from 1000 to 10 mb to serve as a backup first guess file. A final first guess file was derived from TOVS data collected between 0100-0600 GMT with a data drop scheduled at 0900 GMT. The second drop provides fairly good coverage over the eastern Pacific from NOAA-8 with the exception that a key orbit readout at Laignon is usually unavailable. An example of this coverage, with the Laignon orbit missing is shown in Figure 3(c). Thus the first guess used in the EPAC processing of 1200 GMT data was always at least six hours off time and therefore could contain a relatively large error in rapidly evolving systems. However, there is no danger of error correlated with the NMC forecast products since the NOAA retrievals are based on statistical regression using a radiosonde derived dependent sample.

A second critical source of ancillary data is an estimate of the surface skin temperature. This value is used to exclude or correct cloud contaminated measurements, based on its discrepancy from a VAS-derived skin temperature. The VAS measurements include three channels which are used to derive the skin temperature by a "split window" technique (Chesters et al., 1983<sup>5</sup>; Bates and Smith, 1984<sup>6</sup>). For the EPAC study the ancillary skin temperature was estimated from the NMC forecast 1000 mb temperature updated with ship data available in the 0600 GMT collection bin. Generally the observations were rather sparse, and tended to be clustered near the coast (Figure 4). Consequently, not too much confidence could be placed on the final temperature analysis and the cloud contamination threshold was set at a tolerant ten degrees in the hope that subsequent checks in the retrieval processing would eliminate unrepresentative measurements. In retrospect, the surface temperature estimate was the weakest part of the fully automated system. On several occasions the latest NMC forecasts were not available and backup 24 hour forecasts were used. These were in some instances so inaccurate that large areas of relatively cloud free conditions were objectively excluded from further retrieval processing. A manual override by an attending operator would have been beneficial.

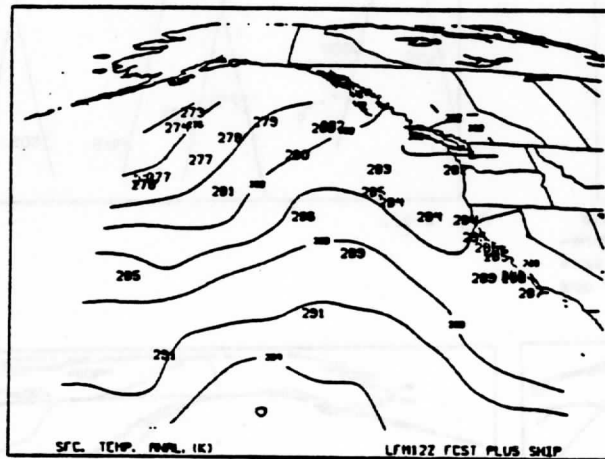


Fig. 4: A surface temperature analysis over the EPAC area with ship data plotted.

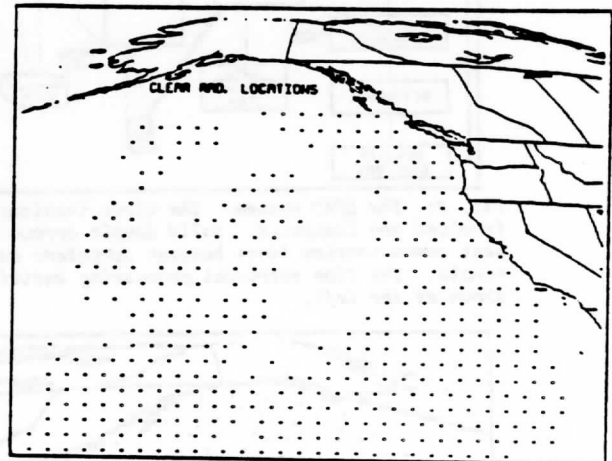


Fig. 5: Location of clear radiances generated for 6 February 1984.

Clear radiance processing refers to the discrimination of cloud free radiances for a predetermined geographical area. For EPAC processing a clear radiance vector was sought at a spacing of approximately 100 km. Individual fields of view (either 14 km or 7 km according to whether large or small detector was in use) were statistically averaged in ensembles of 25 or 45 (large or small detector, respectively) to produce each vector. A complete description of the filtering is given in Hayden et al. (1984)<sup>7</sup>. The clear radiance processing is a major contributor to the computational load because of extensive I-O involved. Nevertheless, this task required less than five minutes to complete a swath (one third the complete coverage). An example of the coverage achieved for 6 February 1984 is shown in Figure 5. Note the absence of retrievals in the heavy cloud regions as shown in Figure 1.

The fourth step, the retrieval, is accomplished using the products of the previous three steps. The algorithm is as described by Smith (1983)<sup>8</sup> except that an "enhancement" procedure designed to more closely fit the observed radiances was not invoked. This cowardly choice was made without extensive investigation because the enhancement procedure is known to produce occasionally bizarre results given incorrect radiances. Lacking local human control over the output, conservatism seemed the best choice. A display of the retrievals obtained for 6 February 1984 is given in Figure 6. Note that in many instances the purportedly clear radiances did not yield a retrieval. The retrieval algorithm processing was the second major computational load, requiring approximately four minutes.

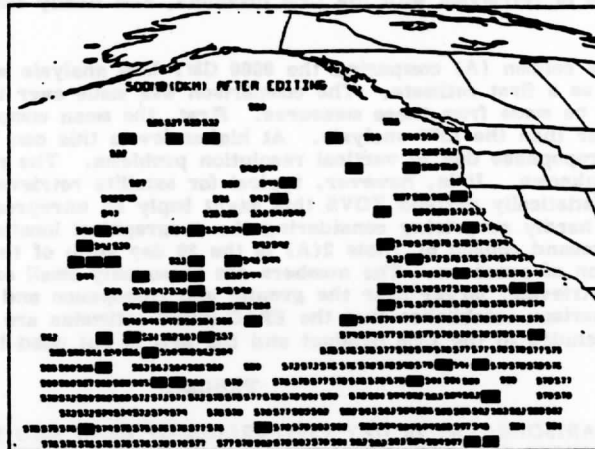


Fig. 6: Retrievals obtained for 6 February 1984 with objectively edited values blocked out.

The final step, quality control, included both objective and man-interactive editing. The objective procedure is in essence a comparison of each retrieval with its neighbors. Two parameters were investigated: the change to the first guess temperature at 500 mb and the derived 500 mb geopotential. In both instances the parameter field is objectively analyzed using all reports and those which are not well "fit" are flagged for rejection. In the man-interactive editing by the NMC, all reports are displayed for any chosen parameter on videographics over a TV display of the cloud field. Objectively edited reports are plotted in a distinctive color. (The objectively edited reports for 6 February 1984 are indicated by solid rectangles in Figure 6.) The operator has the option of deleting more reports or of restoring the objectively edited ones. At the completion of editing the McIDAS file was transmitted to the IBM-360 where it could be accessed by NMC analysis routines. Objective editing is very quick. Man interactive editing is very slow.

#### Performance

The system did not work perfectly. In fact, its complexity made it quickly obvious that shakedown was more than a two day per week operation. In early December CIMSS changed to a five day and in January to a seven days per week schedule. By mid-January the software reliability was excellent, but difficulties in data reception both from the CDAS and from the IBM-360 were never completely solved. The latter was usually caused by down time on the unattended McIDAS. The overall record shows that from 29 November 1983 through 18 February 1984 CIMSS collected VAS data and transmitted retrievals on 51 days. On 24 of these days the data was delivered by 1330 GMT. Of the latter not all were usable to the NMC because they frequently had difficulty with the McIDAS monitoring terminal and were unable to evaluate the product. A diagnostic listing of the system weakness is given in Table 1.

TABLE 1  
EPAC SCORECARD FOR SUCCESS AND FAILURE IN TRANSMISSION  
OF REAL TIME VAS FOR 61 DAYS ATTEMPTED  
BETWEEN 1 DECEMBER 1983 AND 17 FEBRUARY 1984

CDAS problem	9 days
McIDAS disabled	15 days
IBM-360 disabled	5 days
Programmer/operator error	8 days
Success	24 days

It should be mentioned that the IBM 360-195 failures are presumed rather than proven. On these days (four of which were on the weekend), data were transmitted from McIDAS but not acknowledged. The record is somewhat worse than it might have been since two of the programmer failures occurred after the 25 January "no go" decision opened the gateway to system "improvements."

Success must be judged not simply by system throughput but also by product quality. Certainly this is a more difficult measure because of the absence of other data in the Pacific, and the ultimate value must be shown by weather forecast impact studies. Nevertheless, some estimate of quality is possible by considering different components of the system. Those which shall be addressed here are first estimate



quality, a comparison of retrievals with the LFM products, and finally temporal stability of the radiance measurements.

Table 2 contains a column (A) comparing the 0000 GMT LFM analysis with the analyses derived from the TOVS data to serve as a first estimate. The comparison was made over the area 20-55°N and 130-155°W. Two conclusions can be made from these measures. First, the mean comparison shows that the EPAC guess is consistently warmer than the LFM analysis. At higher levels this can be attributed to a failure to capture the colder tropopause due to vertical resolution problems. The reason for the rather large bias at 700 and 500 mb is unknown. It is, however, typical for satellite retrievals to show bias errors in vertical profiles. For the statistically derived TOVS this might imply an unrepresentative dependent sample of radiosonde profiles; hardly surprising considering the geographical location of this comparison. Second, the more important second column of Table 2(A) is the 20 day mean of the standard deviation between EPAC and LFM as a function of pressure. The numbers are reasonably small and have a variation which is typical of satellite retrievals; larger near the ground and tropopause and best at mid-levels near 500 mb. Presumably the comparison establishes that the EPAC initial estimates are fairly accurate, since the TOVS retrievals are not included in the LFM product and the LFM is not used in generating the TOVS.

TABLE 2

STATISTICAL COMPARISONS: A) 20 DAY COMPARISON OF MEAN AND STANDARD DEVIATION DIFFERENCE BETWEEN EPAC GUESS AND LFM ANALYSIS AT 0000 GMT (EPAC-LFM), B) 8 DAY COMPARISON OF RETRIEVALS--LFM+12 FORECAST (VALID 1200 GMT) C) 8 DAY COMPARISON OF RETRIEVALS--LFM ANALYSIS (VALID 1200 GMT)

Level	-----A-----		-----B-----		-----C-----	
	Mean	Mean Sigma	Mean	Mean Sigma	Mean	Mean Sigma
1000	0.8	2.5	-	-	-	-
850	0.4	2.4	1.2	2.6	1.4	2.3
700	1.1	2.2	1.8	2.1	1.9	1.7
500	1.1	1.8	1.4	2.0	1.6	1.8
400	0.7	1.8	0.5	1.9	1.1	1.9
300	0.7	2.0	-0.7	2.0	0.2	1.9
250	1.2	2.4	-0.1	2.3	-0.0	2.2
200	1.8	2.6	0.2	2.1	0.0	2.2
150	1.0	1.5	-0.5	1.4	-1.0	1.3
100	0.6	1.7	-1.5	1.6	-1.7	1.5

Columns (B) and (C) of Table 2 compare the EPAC retrievals to the LFM 12 hour forecast and the final LFM analysis respectively, all valid at 1200 GMT. It is interesting to see that rather than alleviating the low level bias of the first estimate profile, the retrievals have increased it. Such a bias can be adjusted by applying a "correction" to the measured radiances (Weinreb and Fleming, 1974)<sup>2</sup>, but we were reluctant to do this to the transparent channels for three reasons. First, the eastern GOES, with approximately the same instrument, shows no bias problem over data rich areas and, for the one day of VAS coverage from both satellites (16 November 1983) the measured radiances of east and west agreed well in areas of overlap. Second, a bias in the most transparent CO<sub>2</sub> channel should affect the moisture retrieval such that too high a radiance gives too dry (and warm) an atmosphere. Visual daily inspection of the low level moisture field revealed no obvious bias. Finally, there is no compelling reason to believe that the bias of the TOVS retrievals, carried over to the VAS, is incorrect. Consequently, to make no correction seemed the better course. Perhaps the forecast impact studies will shed some light on this question. Columns (B) and (C) of Table 2 show that the tropopause bias has been corrected. Some radiance "tuning" (to be described below) was applied to the more opaque VAS channels which may have produced this result.

Comparison of the EPAC retrievals with the LFM analysis (column (C)) gives slightly lower discrepancies than comparison with the forecast (column (B)), especially at low levels. Assuming that the analysis is more accurate than the forecast this result implies that the VAS has the capability of improving on the forecast over the eastern Pacific. Whether the VAS can also improve the analysis cannot be answered. The fact that the absolute values of the comparison are quite small is either good or bad according to point of view. If one believes the LFM product to be good, he would wish for small discrepancies. If, on the other hand, one wishes to have impact on the analysis, he would wish for large discrepancies. It was our qualitative opinion that the LFM analyses were generally good during the EPAC experiment.

Columns (A) and (C) of Table 2 afford a comparison of the TOVS vs. VAS retrievals insofar as each compare to the LFM analysis. It appears that the VAS compare slightly better. This may result, however, from the fact that the time discrepancy is less for the VAS. At the least VAS seems competitive with TOVS.

It was mentioned above that the VAS measurements were monitored to determine their bias properties. One of the ancillary programs included in the EPAC system used the LFM 12 hour forecast to calculate outgoing radiances at each clear radiance location and calculate a mean difference over the sample for each channel. A 23 day average of these means and their standard deviation are shown as Table 3. Also shown are adjustments actually assigned on 8, 10, 14, and 19 January.

TABLE 3

A) 23 DAY AVERAGE AND STANDARD DEVIATION OF RADIANCE ADJUSTMENTS  
CALCULATED FROM THE LFM+12 FORECAST VALID AT VAS OBSERVATION TIME AND  
B-E) ADJUSTMENT VECTOR APPLIED FOR EPAC RETRIEVALS--UNITS ARE MW/(m<sup>2</sup>-sr-cm<sup>-1</sup>)

Channel	-----A-----		--B--	--C---	--D---	--E---
	Mean	Sigma	8 Jan	10 Jan	14 Jan	19 Jan
1	-0.73	0.98	-1.2	-1.2	-1.2	-1.2
2	-1.28	0.72	-0.9	-0.8	-0.8	-0.8
3	-0.41	0.19	-0.6	-0.7	0.0	0.0
4	-0.27	0.54	-0.4	-0.6	0.0	0.0
5	1.20	0.96	0.0	0.0	0.0	1.0
6	-0.002	0.019	-0.02	-0.02	0.0	0.0

Column (A) of Table 3 indicates that some negative adjustment is required for the more opaque (channels 1 and 2) measurements if the retrievals are to agree, in the mean with the forecast. Such an adjustment was consistently applied (B-D), and served to alleviate the upper level bias as shown in Table 2. The more transparent (and cloud contaminated) channels are not so readily assessed. Columns (B) and (C) show that there was an initial attempt to fine tune the corrections. However, on 14 January all of the biases became positive (a unique occurrence during the 21 days) and we decided with exasperation that the stability of the comparison hardly justified fine tuning of the transparent channels. On that day the bias for all transparent channels was removed. However, in the course of the next few days we noticed that we were losing, based on internal quality checks, too many soundings because of channel 5 and a bias was restored to that measurement. This brief scenario of frustration serves to emphasize once again that it is very difficult to determine a true bias for a satellite channel. The accuracy of a calculated radiance is almost certainly situation dependent and will vary from one atmosphere to another. This reinforces our long held, but usually ignored, plea that satellite retrievals be used according to the gradient pattern they describe rather than absolute measurements of the mass field.

Another comment on system performance concerns the automatic editing of the retrievals. There are a myriad of parameters to choose for editing; ways of analyzing the fields, and criteria for acceptance/rejection. Myriad cubed is a huge number. Our final procedure naturally involved much trial and error, but the choice seemed to perform satisfactorily over the month or more it was in place. Nevertheless, in any individual situation, a person looking at the cloud pattern, the analyzed fields, and the plotted reports would (and NMC did) take umbrage at one or two of the choices, or oversights, of the objective editor. We found, however, that if the human were allowed to prevail, the ultimate analysis was little affected. Equivalently, we found that attempts to enhance the fields by adding soundings were of little use. This result may be a consequence of the McIDAS objective analysis method, but for the scale of phenomenon sought in the EPAC experiment such seems unlikely. We conclude that prospects are bright for a totally automatic application of VAS in the EPAC scenario.

#### Summary

The foregoing has described an experiment at the CIMSS to produce a real time set of retrievals from the VAS for use by the NMC. A number of complicating factors such as a different raw data acquisition on Wednesdays and a switch from large to small detectors in January have not been discussed. They do not alter the primary conclusion that the effort was reasonably successful, even though the product was delivered for only 40 percent of the attempts. A great deal was learned about automatic processing of VAS data, and apart from repeated reaffirmation of Murphy's Law we reached three important conclusions. Objective processing of VAS on the EPAC scale is feasible. Man-interactive editing and enhancing at this scale is of little advantage (and very difficult because of time constraints). Finally, adjustment of radiance bias vectors to improve the absolute values of the retrievals is uncertain and unrewarding. The data user must again be beseeched to consider the gradient rather than absolute value represented by the data.

#### References

1. Anthony, R. W., and G. S. Wade, 1983: VAS operational assessment findings for spring 1982/83. Preprint Volume, 13th Conference on Severe Local Storms, October 17-20, 1983, Tulsa, Oklahoma, pp. J23-J28, Published by American Meteorological Society, Boston, Massachusetts.
2. Velden, C. S., W. L. Smith, and M. Mayfield, 1984: Applications of VAS and TOVS to tropical cyclones. Submitted to the Bull. Amer. Meteor. Soc.
3. Suomi, V. E., R. Fox, S. S. Limaye, W. L. Smith, 1983: McIDAS III: A modern interactive data access and analysis system. J. Clim. Appl. Meteor., 22, 766-778.
4. O'Lenic, E., 1982: Evaluation of the effect of VAS data on some NMC analyses and forecasts. NMC Office Note 253, April, 1982.

5. Chesters, D., L. W. Uccellini, and W. D. Robinson, 1983: Low level water vapor fields from the VISSR Atmospheric Sounder (VAS) "split window" channels. J. Clim. Appl. Meteor., 22, 725-743.
6. Bates, J. J., and W. L. Smith, 1984: Sea surface temperatures--observations from geostationary satellites. To be submitted to J. Geophys. Res.
7. Hayden, C. M., W. P. Menzel, and A. J. Schreiner, 1984: The clouds and VAS. Preprint Volume, Conference on Satellite Meteorology/Remote Sensing and Applications, June 25-29, 1984, Clearwater Beach, Florida, published by American Meteorological Society, Boston, Massachusetts.
8. Smith, W. L., 1983: The retrieval of atmospheric profiles from VAS geostationary radiance observations. J. Atmos. Sci. 40, 2025-2035.
9. Weinreb, M. P. and H. E. Fleming, 1974: Empirical radiance corrections: A technique to improve satellite soundings of atmospheric temperature. Geophysical Research Letters, 1, 298-300.

2/CMH3/21

## ACARS Wind Measurements: An Intercomparison with Radiosonde, Cloud Motion and VAS Thermally Derived Winds

RAYMOND J. LORD, W. PAUL MENZEL<sup>1</sup> AND LORI E. PECHT<sup>2</sup>

*Space Science and Engineering Center, University of Wisconsin, Madison, WI 53706*

(Manuscript received 7 June 1983, in final form 22 March 1984)

### ABSTRACT

Statistical comparisons between winds measured by ACARS and winds obtained from radiosondes, geostationary satellite image cloud motions, and VAS are presented. Observations from three separate comparisons reveal over 60% of wind vector magnitude differences are within  $9 \text{ m s}^{-1}$ , and 70% of the directional differences are within  $15^\circ$ . The comparisons indicate that the ACARS system provides an independent source of wind data that complements other sources of wind data for constructing composite wind field analyses.

### 1. Introduction

A study was conducted to explore the utility of meteorological data obtained from the ARINC (Aeronautical Radio, Inc.) Communications, Addressing and Reporting System (ACARS). Comparisons between ACARS and several other methods of determining wind values were made. One method of obtaining winds is to track the motion of clouds seen on time sequences of geostationary satellite images (Mosher, 1979). Another method involves the application of the gradient and thermal wind equations to geopotential fields derived from radiance measurements by the VISSR (Visible Infrared Spin Scan Radiometer) Atmospheric Sounder (VAS) (Montgomery, 1984). The third method included in this study is the conventional radiosonde balloon tracking.

All data processing was done on the Man-computer Interactive Data Access System (McIDAS) at the University of Wisconsin-Madison (Suomi *et al.*, 1983). Acquisition of ACARS data was from the National Meteorological Center (NMC) data base in Suitland.

### 2. ACARS description

ACARS provides meteorological reports from units installed aboard commercial aircraft. The units or MOATs (Meteorological Optional Auxiliary Terminal) are now operational on eleven American Airlines B-747's. Reports from these aircraft are sent to ground-based radio receiving stations from which they are transferred by telephone lines through ARINC to NMC.

<sup>1</sup> Present Affiliation: NOAA/NESDIS, Madison, WI 53706.

<sup>2</sup> Present Affiliation: Analytic Services, Inc., Arlington, VA 22210.

Parameters measured by ACARS units include latitude, longitude, time, altitude, temperature, wind direction and wind speed. The wind measurements are obtained via the aircraft's Inertial Navigation System (INS) which measures aircraft acceleration, velocity, position and angles of altitude. Measurements taken by the aircraft pitot-static system and outside air temperature measurement systems are combined to determine a true airspeed vector. This vector is then fed to the INS computer where it is subtracted from the ground speed vector to obtain the wind velocity (Rhyne, 1980). This information is recorded every 7.5 min. Data originates from over the United States and the Caribbean, thus providing useful information for various forecasts and comparisons. ACARS is similar in many respects to the ASDAR (Aircraft to Satellite Data Relay) program (Sparkman and Giraytys, 1981). The major difference, however, is ASDAR data are transferred to earth via the GOES (Geostationary Operational Environmental Satellite) Data Collection System, while ACARS data transfer is directly to the ground.

### 3. Wind derivation techniques

#### a. Gradient-thermal winds

Gradient winds represent motion parallel to isobars subject to Coriolis and centripetal forces balanced against pressure gradient forces. The geopotential height fields derived from the VAS data are used to evaluate the gradient wind (Montgomery, 1984). In addition the vertical wind shear is calculated from the horizontal gradient of the geopotential thickness between two pressure levels. This is often referred to as the thermal wind. The combined gradient thermal wind (or VAS wind) is derived completely from the

TABLE 1. Comparison of ACARS and radiosonde winds. Latitude and longitude are given in degrees and minutes (DDMM); direction as degrees from north.

Date of observation	Time (GMT)	ACARS				RAOB				Distance between RAOB and ACARS (km)			
		Latitude (DDMM)	Longitude (DDMM)	pressure (mb)	Direction (deg)	Speed (m s <sup>-1</sup> )	Time (GMT)	Latitude (DDMM)	Longitude (DDMM)		pressure (mb)	Direction (deg)	Speed (m s <sup>-1</sup> )
27 Aug 1982	1000	3826	8143	238	281	26	1200	3822	8233	238	268	25	72
27 Aug 1982	1008	3807	8250	238	270	23	1200	3822	8233	238	268	25	39
27 Aug 1982	1038	3629	8702	215	280	15	1200	3615	8634	215	285	18	49
27 Aug 1982	1225	3916	8956	208	257	38	1200	3839	8858	208	266	35	106
27 Aug 1982	1255	3654	9313	194	239	21	1200	3653	9354	194	231	13	60
7 Oct 1982	1050	3326	11723	218	285	19	1200	3249	11708	218	287	22	70
7 Oct 1982	1127	3407	11119	218	275	19	1200	3501	11044	218	262	22	111
7 Oct 1982	1157	3414	10603	218	233	20	1200	3503	10637	218	240	25	107
13 Oct 1982	1136	3909	7756	237	255	48	1200	3857	7727	237	259	46	44
13 Oct 1982	1214	3743	8243	237	247	56	1200	3822	8233	237	246	48	71
13 Oct 1982	1244	3628	8621	237	244	54	1200	3615	8634	237	237	56	34
13 Oct 1982	1323	3622	9358	195	233	42	1200	3653	9354	195	235	34	54
13 Oct 1982	1329	3445	9157	237	229	54	1200	3450	9215	237	236	48	33
14 Oct 1982	1012	3836	10804	195	066	29	1200	3907	10832	195	080	33	72
14 Oct 1982	1020	3202	10148	214	261	35	1200	3157	10211	214	257	30	35
14 Oct 1982	1032	3806	8248	237	261	60	1200	3822	8233	237	258	56	30
14 Oct 1982	1043	3225	9750	454	257	17	1200	3213	9811	454	257	21	41
14 Oct 1982	1102	3658	8633	237	257	54	1200	3615	8634	237	255	59	78
14 Oct 1982	1147	3458	9213	257	250	42	1200	3450	9215	257	250	41	16
15 Oct 1982	1001	4104	9025	261	309	29	1200	4040	8941	261	301	30	76
15 Oct 1982	1022	3801	8217	237	286	19	1200	3822	8233	237	279	22	50
15 Oct 1982	1045	3700	8619	237	276	7	1200	3615	8634	237	272	15	80
15 Oct 1982	1122	3504	9155	237	266	16	1200	3450	9215	237	256	21	39
15 Oct 1982	1333	4009	7503	431	269	48	1200	3927	7434	431	269	39	91
15 Oct 1982	1356	3957	7745	334	259	45	1200	3857	7727	334	275	33	111
											Average	33.44	32.68
											Standard Deviation	15.76	13.33

TABLE 2. Comparison of ACARS and cloud-tracked winds. See Table 1.

Date of observation	Time (GMT)	Latitude (DDMM)	Longitude (DDMM)	ACAR			Time (GMT)	Latitude (DDMM)	Longitude (DDMM)	WINDCO			Distance between WINDCO and ACARS (km)
				Pressure (mb)	Direction (deg)	Speed (m s <sup>-1</sup> )				Pressure (mb)	Direction (deg)	Speed (m s <sup>-1</sup> )	
27 Aug 1982	902	3926	7944	217	278	33	1030-1100	3935	8011	243	264	29	37
27 Aug 1982	907	3902	8927	214	254	29	1000-1030	3853	8908	248	276	27	28
27 Aug 1982	914	3857	8800	214	252	25	1030-1100	3850	8834	257	277	27	48
27 Aug 1982	937	3936	8348	215	264	42	1000-1030	3937	8405	188	254	44	22
27 Aug 1982	952	3938	8042	215	278	37	1000-1030	3931	8047	234	262	29	23
27 Aug 1982	953	3843	8036	238	281	27	1000-1030	3831	8037	309	268	26	20
27 Aug 1982	959	3937	7913	214	282	32	1000-1030	4032	7958	221	269	38	106
27 Aug 1982	1000	3826	8143	238	281	26	1000-1030	3851	8153	206	262	27	43
27 Aug 1982	1008	3807	8250	238	270	23	1000-1030	3740	8140	232	267	19	111
27 Aug 1982	1015	3737	8349	238	282	22	1030-1100	3656	8335	172	283	23	77
27 Aug 1982	1023	3707	8449	238	294	18	1000-1030	3700	8401	172	282	22	69
27 Aug 1982	1053	3550	8910	237	323	10	1030-1100	3557	8928	244	315	15	39
27 Aug 1982	1100	3528	9019	237	325	12	1030-1100	3517	9031	296	320	10	28
7 Oct 1982	1228	4158	8319	262	238	49	1300-1330	4121	8310	231	244	41	66
7 Oct 1982	1235	4207	8148	237	240	51	1330-1400	4139	8223	238	238	43	72
7 Oct 1982	1250	4155	7845	237	271	29	1300-1330	4235	7836	296	276	23	78
7 Oct 1982	1258	4146	7716	237	282	32	1300-1330	4150	7649	257	278	17	42
7 Oct 1982	1305	4125	7554	294	266	15	1330-1400	4148	7625	252	281	18	58
7 Oct 1982	1356	4009	7733	299	269	18	1330-1400	3950	7736	290	271	14	31
7 Oct 1982	1411	4012	7957	239	264	33	1330-1400	3929	8021	289	248	22	85
7 Oct 1982	1418	4011	8106	240	259	38	1300-1330	3950	8103	278	251	25	37
7 Oct 1982	1433	4009	8322	240	238	39	1330-1400	4019	8309	269	234	38	29
7 Oct 1982	1441	4007	8430	239	244	45	1300-1330	4057	8442	260	235	46	91
												Average 27.09	
												Standard Deviation 10.19	
												Average 29.78	
												Standard Deviation 11.27	

TABLE 3. Comparison of ACARS and VAS winds. See Table 1.

Date of observation	Time (GMT)	Latitude (DDMM)	Longitude (DDMM)	ACARS Pressure (mb)	Direction (deg)	Speed (m s <sup>-1</sup> )	Time (GMT)	Latitude (DDMM)	Longitude (DDMM)	VAS Pressure (mb)	Direction (deg)	Speed (m s <sup>-1</sup> )	Distance between VAS and ACARS (km)
13 Oct 1982	1251	3613	8718	237	242	54	1300	3635	8721	250	254	46	39
13 Oct 1982	1259	3556	8814	237	240	54	1300	3553	8826	250	256	44	17
13 Oct 1982	1306	3540	8909	237	235	53	1300	3531	8911	250	256	40	15
13 Oct 1982	1308	3737	9229	195	235	38	1300	3721	9149	200	249	49	68
13 Oct 1982	1314	3322	9004	237	232	51	1300	3517	8943	250	256	43	36
13 Oct 1982	1315	3659	9315	195	235	43	1300	3725	9320	200	249	50	45
13 Oct 1982	1321	3504	9101	237	231	53	1300	3520	9114	250	253	46	34
13 Oct 1982	1323	3622	9358	195	233	42	1300	3541	9337	200	250	52	85
13 Oct 1982	1329	3445	9157	237	229	54	1300	3449	9156	250	250	50	5
13 Oct 1982	1330	3541	9438	195	238	41	1300	3545	9507	200	251	50	46
13 Oct 1982	1336	3427	9254	237	232	53	1300	3437	9316	250	251	53	36
13 Oct 1982	1338	3457	9511	195	240	45	1300	3455	9542	200	252	56	47
13 Oct 1982	1344	3408	9350	237	233	52	1300	3353	9346	250	254	53	29
13 Oct 1982	1345	3413	9543	233	233	53	1300	3404	9605	250	253	64	37
13 Oct 1982	1359	3328	9351	463	243	36	1300	3259	9347	450	255	49	55
14 Oct 1982	1002	3908	7904	237	256	62	1200	3859	7845	250	267	51	33
14 Oct 1982	1004	3907	10646	195	074	29	1200	3937	10611	200	070	30	75
14 Oct 1982	1005	3143	10431	213	264	30	1200	3232	10421	200	275	32	94
14 Oct 1982	1009	3851	7959	237	255	63	1200	3832	7936	250	269	57	49
14 Oct 1982	1024	3822	8152	237	259	60	1200	3821	8144	250	262	48	9
14 Oct 1982	1028	3211	10028	214	264	31	1200	3222	10110	200	264	21	71
14 Oct 1982	1032	3806	8248	237	261	60	1200	3750	8254	250	267	45	31
14 Oct 1982	1039	3750	8345	237	261	59	1200	3730	8339	250	271	52	36
14 Oct 1982	1047	3733	8441	237	258	59	1200	3643	8416	250	271	52	102
14 Oct 1982	1054	3716	8551	238	260	59	1200	3645	8542	250	271	52	59
14 Oct 1982	1102	3659	8633	237	257	55	1200	3729	8636	250	270	46	54
14 Oct 1982	1109	3640	8729	237	255	55	1200	3648	8706	250	270	47	46
14 Oct 1982	1117	3622	8825	237	257	51	1200	3602	8834	250	270	44	51
14 Oct 1982	1124	3602	8922	237	254	49	1200	3602	8856	250	267	46	33
14 Oct 1982	1132	3541	9019	237	255	46	1200	3518	9013	250	262	48	44
14 Oct 1982	1139	3520	9117	237	253	44	1200	3521	9140	250	255	42	36
14 Oct 1982	1147	3459	9213	237	250	42	1200	3437	9211	250	255	43	43
14 Oct 1982	1154	3437	9310	237	248	40	1200	3422	9330	250	248	31	41
14 Oct 1982	1202	3414	9407	237	248	38	1200	3344	9408	250	250	28	55
14 Oct 1982	1209	3352	9501	294	257	32	1200	3426	9500	300	255	26	65
												Average	48.17
												Standard Deviation	9.74
												Average	45.31
												Standard Deviation	9.35

VAS determinations of geopotential thickness. These winds are determined from radiances emanating from a square area with 75 km on a side and thus represent an average wind, in contrast to the single point observations from the aircraft and radiosonde.

#### b. Radiosonde winds

The radiosonde winds are determined as functions of height by tracking the ascent curve of a balloon filled with buoyant gas. This conventional method of wind measurement is well documented in the literature (Reiter, 1967).

#### c. Cloud-tracked winds

Another method of establishing winds is to trace the motion of cloud elements viewed on time sequences of geostationary satellite images. This process is based on the assumption that the cloud elements follow the motion of the air in their vicinity. By tracking the movement of a cloud element through a sequence of navigated VISSR images, wind speed and direction are determined. These winds represent average motion over the satellite field of view size (1 km resolution for the visible images). Cloud heights are assigned by using the infrared data in conjunction with a nearby atmospheric sounding (Mosher, 1979).

#### 4. Comparisons

Several comparisons were made between wind measurements obtained from ACARS data and those determined by the radiosonde, cloud tracking and VAS thermal wind calculations. Aircraft reports close in time, within 2 h, and horizontal distance, within 111 km, with respect to the radiosonde and satellite derived winds were found on several days. Radiosonde winds were interpolated from significant level data to correspond directly with the ACARS altitude; VAS derived winds within 20 mb of the ACARS altitude were accepted for comparison while cloud drift winds within 70 mb were included (the height assignment for the clouds is usually not known to better than 50 mb (Menzel *et al.*, 1983)).

The radiosonde comparisons from five different days are listed in Table 1. The agreement between the two methods of wind measurements is fairly good; in Table 4 radiosonde winds are offset by  $-0.76 \text{ m s}^{-1}$  in the mean and have a relative root mean square deviation of  $5.33 \text{ m s}^{-1}$  with respect to ACARS winds. Wind directions compare typically within  $8^\circ$ . While some comparisons are made with measurements as much as 2 h apart, these are of upper level winds (around 250 mb) and are not expected to vary rapidly. These comparisons fall within the accuracy of upper level wind measurements by radiosondes; for 41 paired, simultaneous radiosonde flights for launch sites 16.25 km apart, Lenhard (1973) found

observed wind vector magnitude variability between 2 and  $10 \text{ m s}^{-1}$  within a height range of 5–10 km.

In order to find suitable comparisons of cloud tracked winds to ACARS winds, it was necessary to find an airplane flight path through trackable clouds. The aircraft flights near the jet and cirrus streaks were found to be most usable for the cloud track wind comparisons. The comparisons for two days are listed in Table 2. Again the results are fairly good; in Table 4 cloud tracked (denoted by WINDCO) less ACARS winds are offset by  $-2.70 \text{ m s}^{-1}$  and have a relative root mean square deviation of  $5.64 \text{ m s}^{-1}$ . Wind directions compare typically within  $12^\circ$ . Cloud wind speeds were found to have rms differences of 6–10  $\text{m s}^{-1}$  during the First GARP Global Experiment when determined at the same location and time by different data producers (Mosher, 1981); thus the ACARS and cloud drift wind measurements intercompare within the accuracy of the cloud tracked wind measurements.

The comparisons with VAS derived gradient thermal winds were accomplished on two separate days, when the airplane flew through clear air at times when VAS sounding data were available. Table 3 shows these comparisons. The results in Table 4 show the VAS wind speeds to be offset by  $-2.86 \text{ m s}^{-1}$  and to have a relative root mean square deviation of  $7.83 \text{ m s}^{-1}$ . Wind directions are within  $8^\circ$ . The VAS gradient-thermal wind calculation is based upon the assumption of steady state conditions in the atmosphere. Since a majority of ACARS observations are at relatively high altitudes (200 mb) with wind speeds approaching  $50 \text{ m s}^{-1}$ , obviously there is a departure from the gradient wind assumption. However, while the VAS/ACARS rms difference ( $7.83 \text{ m s}^{-1}$ ), is greater than the RAOB/ACARS rms difference ( $5.33 \text{ m s}^{-1}$ ), it is clear that the VAS thermal winds at higher altitudes provide wind information that complements other observation methods. In addition, VAS winds are often available when and where other observations are not: cloud motion vectors are unavailable in clear areas; radiosondes are launched only at synoptic times at only selected sites; ACARS data is by definition only following a flight path.

Figure 1 shows the cumulative frequency of the

TABLE 4. Summary of ACARS comparisons.

Comparison	Magnitude		Direction	
	Average offset ( $\text{m s}^{-1}$ )	Relative rms deviation ( $\text{m s}^{-1}$ )	Average offset (deg)	Relative rms deviation (deg)
RAOB vs ACARS	-0.76	5.33	0.64	7.43
WINDCO vs ACARS	-2.70	5.64	-3.48	11.51
VAS vs ACARS	-2.86	7.83	11.37	7.12



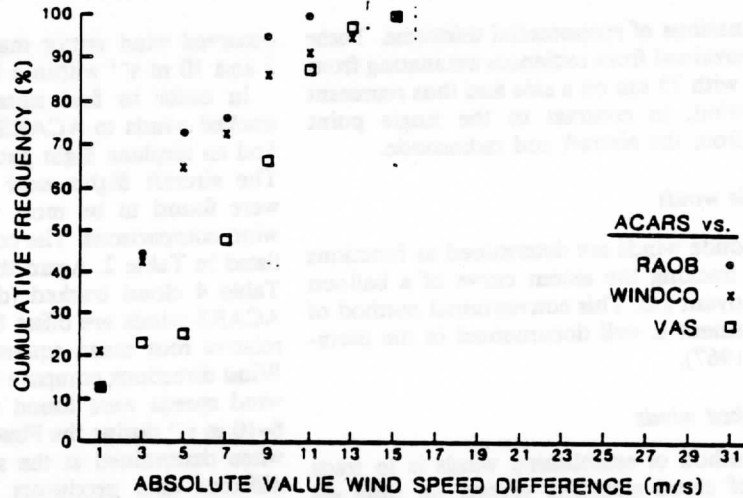


FIG. 1. Cumulative frequency of wind vector magnitude differences for three separate ACARS comparisons.

vector magnitude differences for the comparisons discussed above; Fig. 2 shows the cumulative frequency of the vector direction differences. In Fig. 1, over 60% of all the comparisons have vector magnitude differences within  $9 \text{ m s}^{-1}$ . Over 70% of the radiosonde comparisons have differences within  $5 \text{ m s}^{-1}$ . In Fig. 2, the wind directions compare quite favorably with over 70% of all directional differences within  $15^\circ$ ; 70% of the directions for the radiosonde comparisons are within  $7^\circ$ . The difference in observing techniques (spot versus average wind) and the atmospheric variability (due to unavoidable space-time differences in the observations) are responsible for some of the differences in these ACARS comparisons, so the true differences are somewhat less than reported

here. The different wind measuring methods have comparable accuracies and can be used to form composite wind field descriptions.

##### 5. Conclusion

Comparisons presented here indicate that the ACARS data compares to other observing methods within the accuracy associated with those other observing methods. The ACARS system provides an independent data source that can complement other wind data for constructing wind field analyses.

The major difficulty of the ACARS system as it exists today lies in the poor availability of the data. Acquisition of the data for these comparisons was very cumbersome (by remote job entry interrogation

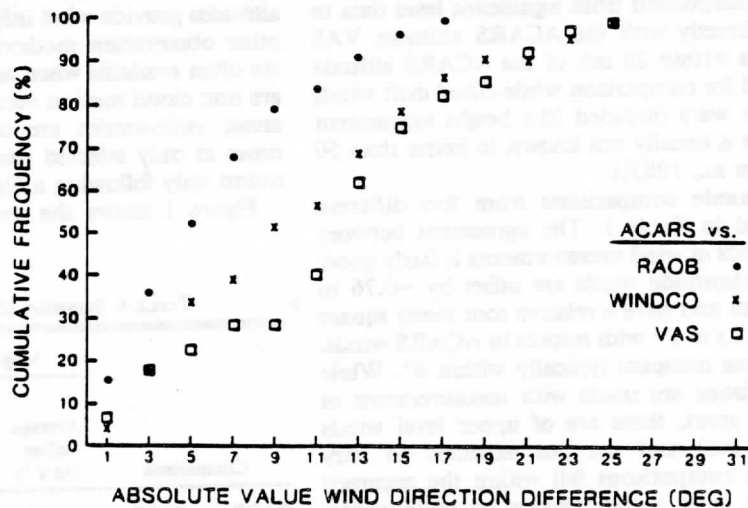


FIG. 2. Cumulative frequency of wind vector directional differences for three separate ACARS comparisons.

of the NESS/Suitland data base) and resulted in untimely data. Because of the apparent accuracy and usefulness of these data, we believe that they would be beneficial for improved weather analyses if they were made available to the general public in real time through the FAA (Federal Aviation Administration) wire service.

*Acknowledgments.* This research was supported by the National Aeronautics and Space Administration under Grant NAS5-21965. The authors benefitted from several discussions with Dr. William L. Smith, Director of the NOAA/NESDIS Development Laboratory. In addition, Dr. Christopher M. Hayden and Mr. Harold Woolf of NOAA/NESDIS Development Laboratory counselled on VAS system operations and assisted in ACARS software development. From the staff of the Space Science and Engineering Center, University of Wisconsin-Madison, Mr. Chris Velden analyzed the VAS retrievals and Mr. Dave Santek provided McIDAS programming support.

## REFERENCES

- Lenhard, R. W., 1973: Variability of wind over a distance of 16.25 km. *J. Appl. Meteor.*, 12, 1075-1078.
- Menzel, W. P., W. L. Smith and R. R. Stewart, 1983: Improved cloud motion wind vector and altitude assignment using VAS. *J. Climate Appl. Meteor.*, 22, 377-384.
- Montgomery, H., 1984: VAS demonstration description, summary, and final report. NASA. Publication (in press).
- Mosher, F. R., 1979: Cloud drift winds from geostationary satellites. *Atmos. Tech.*, 10, 53-60.
- , 1981: The compatibility of cloud tracked winds from the United States, European, and Japanese geostationary satellites. *Adv. Space Res.*, COSPAR, 1, 139-146.
- Reiter, E. R., 1967: *Jet Streams*. Doubleday, 189 pp.
- Rhyne, R. H., 1980: Accuracy of aircraft velocities obtained from inertial navigation systems for application to airborne wind measurements. *NASA Tech. Memo.*, 81826, 15 pp.
- Sparkman, J. K., and J. Giraytys, 1981: ASDAR: A FGGE real-time data collection system. *Bull. Amer. Meteor. Soc.*, 62, 394-400.
- Suomi, V. E., R. Fox, S. S. Limaye, and W. L. Smith, 1983: McIDAS III: A modern interactive data access and analysis system. *J. Climate Appl. Meteor.*, 22, 766-778.

Routine Generation of VAS Products  
for National Center Evaluation

Anthony L. Siebers  
NOAA/NWS Systems Requirements Branch

W. Paul Menzel  
NOAA/NESDIS Satellite Applications Laboratory

Rodney L. Sorensen  
NOAA/NESDIS Product Systems Branch

Advanced Satellite Products Project  
1225 West Dayton Street, 2nd Floor  
Madison, Wisconsin 53706

Over the past seven years, a real time VISSR Atmospheric Sounder (VAS) processing capability has been developed at the University of Wisconsin's Space Science and Engineering Center. At present, the VAS data are processed in a quasi-operational mode in order to assess the operational utility of the data. The data are processed interactively on the McIDAS, and are available in real time at the three national centers of the National Weather Service (National Hurricane Center, National Meteorological Center, National Severe Storms Forecast Center) via remote computer terminals. The procedures for generating VAS retrievals are presented, along with some of the VAS derived products.

Sea surface temperatures from VAS MSI data

Space Science and Engineering Center  
University of Wisconsin-Madison  
1225 W. Dayton Street  
Madison, WI 53706

Final Report

by

John J. Bates

May 31, 1984

JPL contract number - 956477

This work was performed for the Jet Propulsion Laboratory, California Institute of Technology, and was sponsored by the National Science Foundation Grant #ATM-8205386.

Reference herein to any specific commercial product, process, or service by trade name, trademark, manufacturer, or otherwise, does not constitute or imply its endorsement by the United States Government, the Space Science and Engineering Center, the National Science Foundation, or the Jet Propulsion Laboratory, California Institute of Technology.

This report contains no new technology.

*Paper 21*

Abstract

A procedure is developed for estimating sea surface temperatures (SST) from multispectral image data acquired from the VISSR atmospheric sounder on the geostationary GOES satellites. Theoretical regression equations for two and three infrared window channels are empirically tuned using clear field of view satellite radiances matched with reports of SST from NOAA fixed environmental buoys. The empirical regression equations are then used to produce daily regional analyses of SST. Monthly mean SST's for the western North Atlantic and the eastern equatorial Pacific during March and July 1982 were produced for use in the SST Intercomparison Workshop Series. Workshop results showed VAS SST's have a scatter of 0.8-1.0°C and a slight warm bias with respect to the other measurements of SST. The VAS SST's show no discernible bias in the region of El Chichón volcanic aerosol cloud.

## 1. Introduction

The results of the SST intercomparison workshop series (JPL, 1983) are the first examination of monthly mean SST's derived from MSI data provided by the VAS instrument on the GOES series satellites. While VAS instruments are currently only on the U.S. geostationary satellites, limiting coverage to the western hemisphere, it is hoped that the success of VAS will encourage the European Space Agency, Japan, and India to consider installing a VAS instrument on their future geostationary satellites.

Because the procedure to derive SST's from VAS data is still in the developmental stage, several changes in the procedure were made between the processing of data for March 1982 and processing the data for July 1982. The most significant change was the use of the three window channel algorithm (3.9, 11.0, and 12.6  $\mu\text{m}$ ) in the processing of the July data as opposed to the use of only the two window channel (11.0/12.6  $\mu\text{m}$ ) algorithm for the March data. Initially only the two channel algorithm was used in order to extend the analysis of SST into areas of sunglint in the tropics. However, the analysis of the March data showed that little additional data was gained by doing this. In addition, further satellite/buoy matches indicated that the triple window channel algorithm showed a smaller standard deviation than the two window channel algorithm and was less sensitive to the effects of volcanic aerosol contamination and low level inversion conditions. This is due to the smaller brightness temperature attenuation by aerosols and water vapor at 3.9  $\mu\text{m}$  than at 11.0 and 12.6  $\mu\text{m}$ . Thus, the decision was made to use the best product (i.e., the three window channel algorithm) for processing the July data.

## 2. March 1982 Results

Two large regions were chosen for analysis of VAS data from GOES-East, one in the western North Atlantic and one in the eastern Tropical Pacific. Since ship observations of surface layer temperature provide the only long-term climatology of SST, Reynolds (1982) climatology has been used as a standard from which satellite SST monthly mean anomaly fields were produced. Data from all sensors were binned on a two by two degree latitude/longitude grid for each month. SMMR data were required to be more than 600 km from land in order to avoid contamination from land. Thematic contour charts of sensor anomaly fields from climatology for March are shown in Figure 1. VAS, AVHRR, and ship data all show a pattern of cold to warm to cold to warm proceeding southeast off the U.S. east coast; however the VAS data have a warm bias of 0.5 to 1.0°C. In the South Pacific, the VAS data show only a slight warm bias and again are highly correlated with the AVHRR, ships, and XBT's. In particular, the VAS and AVHRR thematic contour anomaly charts show similar patterns with warm water along the coast from 20° to 30°S and extending to the west along 30°S, a pool of cold water along the coast from 0 to 10°S, another cold anomaly offshore, and near normal conditions elsewhere. The HIRS data show generally weaker anomaly patterns and a warm bias near the coastlines due to problems in accurately specifying the land/water boundaries (Susskind, personal communication). The HIRS data do show a warm anomaly along 30°S in the eastern South Pacific and a large warm anomaly in the western North Atlantic. Little correlation in patterns is found between the VAS and the SMMR product.

Table 1 summarizes the cross correlation statistics for each satellite verses ship-of-opportunity measurements for March 1982. Matches with ships were limited to a time window of  $\pm 12$  hours and a space window of  $\pm 50$  km from the satellite observation. VAS estimates of SST show a warm bias relative to ships for all regions ranging from  $+0.35$  to  $1.73^{\circ}\text{C}$ . The largest biases ( $1.73^{\circ}\text{C}$  and  $1.05^{\circ}\text{C}$ ) are found with the lowest numbers of matches (21 and 53) and also occur at the largest satellite zenith angles (North Pacific region  $20-56^{\circ}\text{N}$  and South Pacific region  $20-56^{\circ}\text{S}$ ). This indicates that the magnitude of the warm bias for the two channel algorithm may increase with increasing satellite zenith angle but also suggests that noisy ship data may be partly responsible for some of the bias.

The uniform warm bias in all regions, however, indicates a diurnal sampling bias and a possible bias in the matches used to tune the empirical algorithm. Satellite/buoy matches are continuing to be collected in order to ensure that a seasonally and geographically diverse set of matches is used to update the coefficients for the empirical algorithms. It does appear though that the diurnal sampling of VAS data is largely responsible for the warm bias. VAS data were generally processed at 1530 and 1830 GMT (1030 and 1330 LST at the GOES-East subpoint) and only cloud-free observations were used. Thus, VAS SST's might be expected to have a warm bias relative to estimates of SST that average day and night data. Diurnal heating of the ocean skin temperature as observed by satellite infrared data has also been reported by Strong (1984) and by Deschamps and Frouin (1984). Future intercomparisons must take into account possible diurnal sampling biases of each sensor.

Additional cross correlation statistics for March show VAS with a scatter relative to ships of  $0.79-1.24^{\circ}\text{C}$ . The statistics show VAS well correlated with ships, and shows regional correlations very similar to those of the AVHRR. The one exception is the far South Pacific region ( $20-56^{\circ}\text{S}$ ). This again is the region of fewest matches and thus should be given little weight.

### 3. July 1982 Results

In the thematic anomaly charts for July (Figure 2), the effects of the El Chicón volcanic aerosol are very evident in the AVHRR data as a zonal band of cold anomalies from  $10-30^{\circ}\text{N}$ . VAS data, however, do not show an analogous anomaly in those latitudes. This result is due to differences in the spectral channels of the VAS and AVHRR, differences in the processing algorithms, and differences in the average viewing geometry. The VAS, SMMR, and ship data all show a warm anomaly in the eastern tropical Pacific.

In the North Atlantic VAS region, the VAS data appears to be slightly warmer than the ship data, but again shows similar patterns. The VAS and AVHRR data show some correlation near the coast of the U.S., but meaningful comparisons between the two are hampered by the volcanic aerosol contamination in the AVHRR data. The anomaly patterns are much the same in a comparison the the VAS/SMMR data, however the SMMR data is contaminated by "cold" instrument warmup noise in much of the North Atlantic (Milman, personal communication). In the VAS region of the Pacific, the VAS, SMMR, and ship data all show warming. Here, the VAS and SMMR data show a high correlation with a pattern of warm anomalies along the coast and extending westward along the equator. In contrast, the HIRS data, while not showing any consistent bias in the El Chicón region, does show a large cold anomaly in this region.

Cross correlation statistics for July 1982 are summarized in Table 2. VAS SST's again show a slight warm bias in all regions. The very large warm bias at large local zenith angles evident in the March 1982 data, however, has been eliminated by the use of the three window channel algorithm. Little bias is evident in the region of the El Chichón volcanic aerosol (approximately 10-30°N). In this region, the AVHRR data show a cold bias of 0.50-0.75°C relative to ships. The VAS standard deviations are also generally smaller in July than in March due to the use of the three window channel algorithm. The cross correlations of VAS data with ship data, however, are much weaker in July than March.

After SST Intercomparison Workshop III, additional cross correlation tables were generated to try to answer some of the questions raised during the workshop. Most important to the interpretation of VAS data was the stratification of AVHRR data into day and night so that the daytime only VAS data could be directly compared to daytime only AVHRR data. Although the new cross correlation tables are masked to include only data greater than 600 km from land (to normalize the comparison between SMMR and the other sensors, but greatly reducing the number of VAS/ship matches), some trends are clearly evident. In March 1982, AVHRR shows a global average day minus night difference relative to ships of +0.43°C. This reduces the VAS minus AVHRR day bias to +0.23°C. The VAS versus ship biases remain unchanged since ships measure SST at some depth beneath the surface and are relatively insensitive to diurnal heating of the ocean skin. In July, on a global basis, the AVHRR day product is 0.43°C warmer than ships while the AVHRR night product is 0.72°C colder than ships. There is no discernable bias between AVHRR day SST's and VAS SST's outside the El Chichón zone (i.e., in the South Pacific and North Atlantic), while within the El Chichón zone (the mid-Pacific) AVHRR day is 0.69°C colder than VAS and 0.50°C colder than ships. These data clearly show that the diurnal heating of the ocean skin is being detected by VAS and AVHRR, and demonstrates that most of the VAS warm bias relative to the other sensors is due to this diurnal variability.

#### 4. Evaluation of Other Products

##### 4a. AVHRR

The AVHRR MCSST is the only operational satellite SST analysis currently and is the most accurate and consistent product evaluated at the workshop series. As with all SST data sources, care and understanding must be used when evaluating and applying this data. Studies such as that by Legeckis and Pichel (1984) are particularly useful in interpreting the weekly MCSST analyses. Users must also understand the nature and variability of ocean surface skin temperature measurements as opposed to ship bulk surface layer measurements. For example, the MCSST analysis for March 1982 has been criticized for showing a warm anomaly along the equator from the western Pacific into the western Indian Ocean; an area where ship climatology shows little monthly variability. The AVHRR day-night thematic contour analysis (not shown), however, shows that this warm anomaly may be the result of diurnal warming of the ocean surface. In fact, the AVHRR day-night analyses show a distinct diurnal pattern of solar heating from December 1981 to March 1982 to July 1982. In December 1981, a consistent zonal band of warm daytime SST anomalies is found from about 30-50°S, in the southern (summer) hemisphere. In March 1982, the warm anomaly has become more diffuse and shows the largest anomalies on the equator. By July 1982, the



warm anomaly evident as a zonal band in the northern (summer) hemisphere. Diurnal variability of the oceans skin is being measured by satellite sensors, as is evident from the analysis of AVHRR day-night measurements.

#### 4b. SMMR

The problems with the SMMR SST product are largely due to instrumental difficulties. The SMMR antenna biases are large and vary in time and space, and side-lobe interference requires observations to be greater than 600 km from land. In spite of these difficulties, SMMR analyses of the Pacific and Indian Oceans appear reasonable. Unfortunately, the antenna problem makes it difficult to evaluate the problem of microwave emissivity changes of the ocean surface with wind speed, while the land mask restricts analysis of the important boundary currents. The SMMR/ship product is an improvement on SMMR alone, but it does not take full advantage of all the different sensors for measuring SST.

#### 4c. HIRS/MSU

Evaluation of the HIRS/MSU product is difficult because of changes in the product from one time to the next and because the data were presented late. The HIRS/MSU anomaly patterns generally look noisy and weaker than the anomaly patterns of the other sensors. In March 1982, the HIRS/MSU shows no correlation with any of the other products and a standard deviation from climatology of about 1°C. The July 1982 statistics are better, but the anomaly patterns are inconsistent, showing an overall cool bias. Particularly troublesome is a cool anomaly in the eastern Equatorial Pacific where all the other sensors show a warm anomaly.

### 5. Recommendations

#### 5a. Improvements in infrared sensors

Recent theoretical and empirical studies of the infrared portion of the earth's spectrum have revealed that neither VAS nor AVHRR have the optimal channel selection for SST detection. Studies are now underway to determine which window regions using a filtered radiometer would yield the most accurate SST's. In the long term, though, an infrared spectrometer interferometer instead of a filtered radiometer will be a much better instrument since it would permit use of all portions of the infrared window regions to be utilized.

#### 5b. A combined product

Efforts should begin on a combined satellite SST product that takes advantage of the benefits of each sensing system discussed in the workshop series. Such an approach should use the raw data from each instrument, not just the finished products such as the SMMR/Ship composite. The McIDAS system has the capability of processing raw data from all sensors used in the workshop series. It is time to begin a program to produce an operational SST analysis.

5c. Research panel on SST sensing

A research panel to set research program goals, evaluate present systems, and recommend areas for further study should be set up under the direction of NSF or other appropriate agency. This panel should coordinate efforts between ongoing ocean research programs and the remote sensing community. This panel could also serve as the focus for the development of a combined SST product.

## References

- Deschamps, P.Y., and R. Fouin, Large diurnal heating of the sea surface observed by the HCMR experiment, *J. Phys. Oceano.*, 14, 177-184, 1984.
- JPL, Satellite-derived sea surface temperature: Workshop I. JPL Publication 83-34, Jet Propulsion Laboratory, California Inst. of Technology, Pasadena, CA.
- Legeckis R., and W. Pichel, Monitoring of long waves on the eastern Equatorial Pacific 1981-83 using satellite multi-channel sea surface temperature charts. NOAA Technical Report NESDIS 8, Washington, D.C., 1984.
- Reynolds, R.W., A monthly averaged climatology of sea surface temperatures, NOAA-TR-NWS-31, Washington, D.C., 35 pp., 1982.
- Strong, A.E., Use of drifting buoys to improve accuracy of satellite sea surface temperature measurements, *Tropical Ocean-Atmosphere Newsletter*, No. 25, 16-18, 1984.

TABLE 1

CROSS CORRELATIONS OF SATELLITE SST ESTIMATES VERSUS SHIP SST ESTIMATES FOR MARCH 1982

	Number of Matches			Bias			Standard Deviation			Cross Correlation						
	AVHRR	SMMR	HIRS	VAS	AVHRR	SMMR	HIRS	VAS	AVHRR	SMMR	HIRS	VAS				
Global	4322	1972	-	425	-0.06	-0.01	-	+0.63	0.81	1.20	-	0.96	0.58	0.25	-	0.59
North Pacific (0-56°N)	1563	815	-	127	-0.26	-0.05	-	+0.52	0.67	0.99	-	0.92	0.64	0.29	-	0.61
North Pacific (20-56°N)	1033	529	1054	53	-0.39	-0.01	+0.54	+1.05	0.65	1.03	1.07	0.89	0.60	0.36	0.28	0.63
Tropical Pacific (20°N-20°S)	837	412	858	165	+0.10	-0.22	+0.23	+0.20	0.73	0.87	0.93	0.90	0.13	0.08	0.03	0.10
South Pacific (20-56°S)	535	202	541	21	+0.24	+0.55	+0.05	+1.73	0.78	1.19	1.11	1.24	0.42	0.08	0.28	-0.39
South Pacific (0-56°S)	984	328	-	112	+0.26	+0.17	-	+0.52	0.80	1.14	-	1.20	0.29	0.11	-	0.23
VAS Pacific Region (14°N-30°S)	178	81	-	181	+0.06	-0.16	-	+0.35	0.89	0.91	-	1.06	0.23	-0.08	-	0.03
Global AVHRR	2214	1088	2229	211	+0.03	+0.12	+0.20	+0.55	0.86	1.11	1.04	1.12	0.48	0.29	0.20	0.41
El Chichon Mask North Atlantic (0-56°N)	715	315	-	186	-0.33	-0.92	-	+0.76	0.61	1.18	-	0.79	0.58	-0.02	-	0.65

TABLE 2

CROSS CORRELATIONS OF SATELLITE SST ESTIMATES VERSUS  
SHIP SST ESTIMATES FOR JULY 1982

	Number of Matches				Bias				Standard Deviation				Cross Correlation			
	AVHRR	SMMR	HIRS	VAS	AVHRR	SMMR	HIRS	VAS	AVHRR	SMMR	HIRS	VAS	AVHRR	SMMR	HIRS	VAS
Global	3962	1826	-	437	-0.54	-0.18	-	+0.60	0.90	1.08	-	0.85	0.44	0.38	-	0.26
North Pacific (0-56°N)	1368	708	-	116	-0.69	+0.26	-	+0.91	0.95	0.89	-	0.80	0.41	0.46	-	0.17
North Pacific (20-56°N)	514	221	-	26	-0.18	+0.11	-	+0.40	0.64	1.13	-	1.25	0.50	0.24	-	-0.10
Tropical Pacific (20°N-20°S)	779	366	-	165	-0.69	+0.10	-	+0.77	0.83	0.83	-	1.00	0.30	0.27	-	0.07
South Pacific (20-56°S)	958	480	-	51	-0.54	-0.31	-	+0.61	0.98	0.92	-	0.50	0.46	0.44	-	0.11
South Pacific (0-56°S)	883	359	-	126	-0.23	+0.06	-	+0.50	0.67	1.03	-	1.05	0.41	0.26	-	0.00
VAS Pacific Region (14°N-30°S)	162	104	-	174	-0.38	+0.16	-	+0.68	0.81	1.10	-	1.08	0.25	0.05	-	0.01
Global AVHRR	2305	1112	-	216	-0.20	+0.02	-	+0.49	0.77	1.08	-	0.90	0.49	0.41	-	0.26
El Chichon Mask North Atlantic (0-56°N)	695	324	-	195	-0.81	-1.06	-	+0.49	0.87	1.06	-	0.67	0.38	0.21	-	0.40

Figure 1. Thematic contour SST anomaly charts for March, 1982, for a) SMMR, b) AVHRR, c) VAS, d) Ships, and e) HIRS-MSU. (Original figures can be found in JPL publication Satellite-derived Sea Surface Temperature Intercomparison: Workshop III.)

a)                      b)                      c)                      d)                      e)

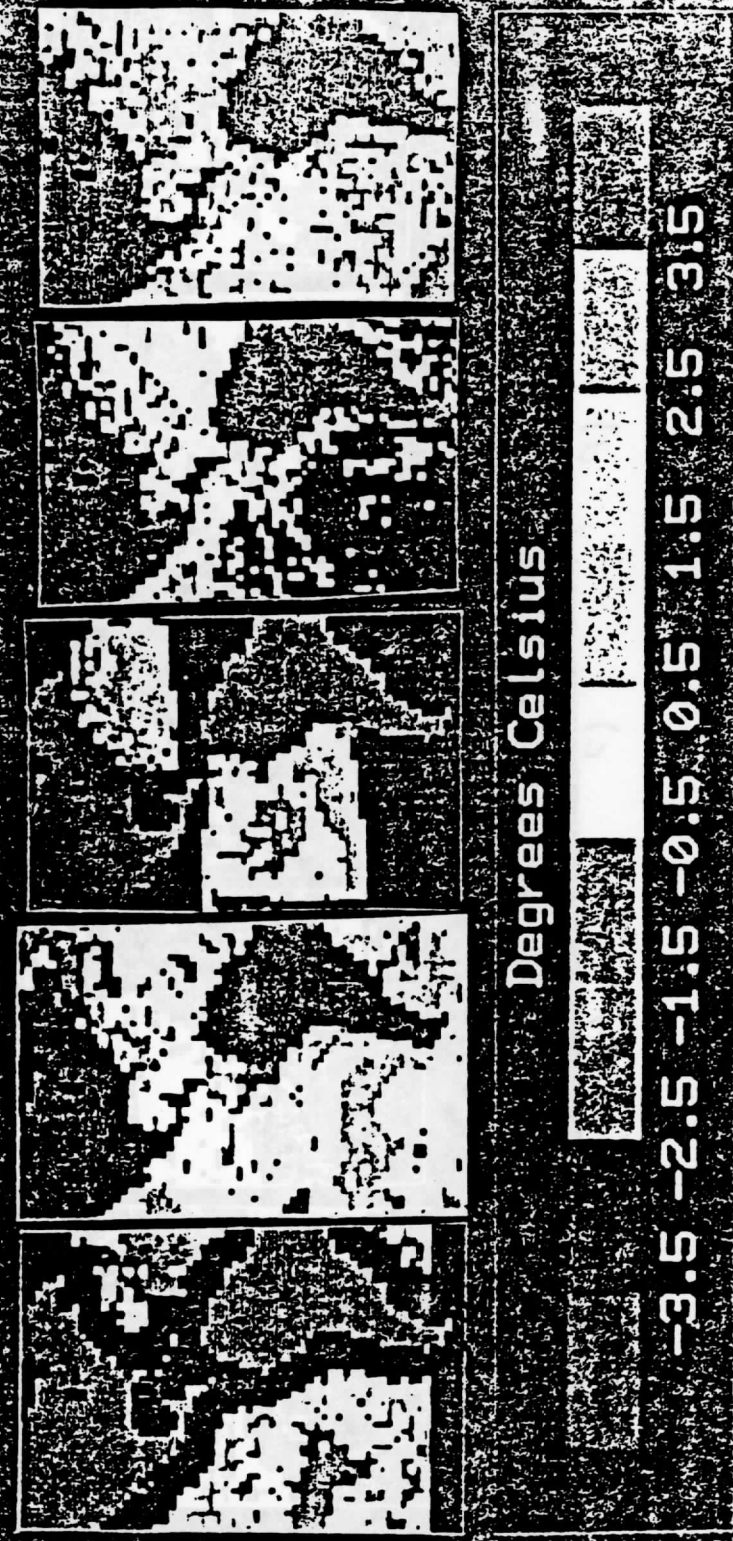
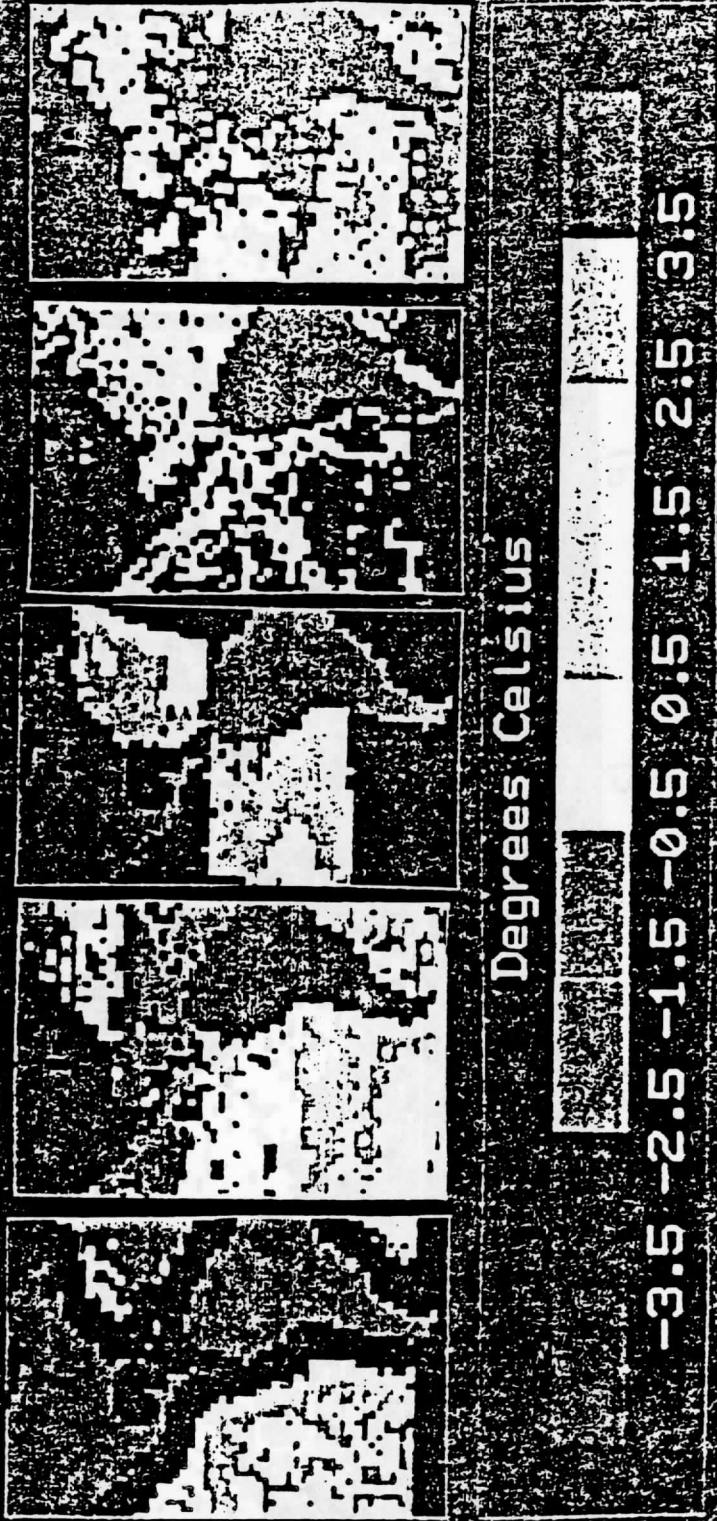


Figure 2. Thematic contour SST anomaly charts for July, 1982, for a) SMMR, b) AVHRR, c) VAS, d) Ships, and e) HIRS-MSU. (Original figures can be found in JPL publication Satellite-derived Sea Surface Temperature Intercomparison: Workshop III.)

a)                      b)                      c)                      d)                      e)



THE USE OF ADJOINT EQUATIONS TO SOLVE A  
VARIATIONAL ADJUSTMENT PROBLEM WITH ADVECTIVE CONSTRAINTS

by

John M. Lewis  
NOAA/NESDIS Development Laboratory  
Systems Design and Applications Branch  
1225 West Dayton Street  
Madison, Wisconsin 53706, U.S.A.

and

John C. Derber  
Space Science and Engineering Center  
1225 West Dayton Street  
Madison, Wisconsin 53706, U.S.A.

Submitted to Tellus

AUGUST 1984

2/JML2/05



## Abstract

A methodology is developed to guarantee time continuity in a sequence of analyses. Coupling is accomplished by requiring the least squares minimization of adjustments to the analyses subject to dynamic constraints. In this paper the analyses are assumed to be governed by advective constraints such as those used in vorticity conservation models, however the method can easily be applied to other constraints. The results correspond to the application of a strong constraint as introduced by Sasaki (1970), but the procedure used to accomplish the minimization is an alternative to the traditional methods for solution of the Euler-Lagrange equation. The method allows easier inclusion of more time levels in the analysis sequence as well as accommodation of more complicated constraints.

The method is tested using both simulated and real data. The simulated data studies use a one dimensional advection equation with progressively more complicated dynamics: constant advection velocity, spatially varying advection velocity, and nonlinear advection. The real data case study uses an advection of quasi-geostrophic potential vorticity constraint to examine the height adjustment process for three time periods on 6 March 1982. Separate studies are made for analyses derived from VAS and RAOB data. The results of this study indicate the method has excellent potential to reduce the random component of the analysis errors.

## 1. Introduction

Past data are routinely incorporated into the present analysis at operational prediction centers by using a background or guess field to initiate the analysis. The background field has traditionally been the 12 h forecast from a previous analysis. Thus, the past data are indirectly combined with the current data and the time coupling is pragmatically accomplished. With the advent of new atmospheric profiling systems such as the Profiler and the VISSR Atmospheric Sounder (VAS) (Hovermale, 1983), the coupling of successive analyses is complicated by the fact that observations are becoming quasi-continuous in time. Various methods for using this data have been proposed and referred to as four-dimensional data assimilation techniques. These methods have been thoroughly reviewed by Bengtsson (1975) with more recent work found in Bengtsson et al. (1981). The focus of this research is on developing a new methodology for dynamically coupling many analyses closely spaced in time.

Miyakoda and Talagrand (1971) attempted to use a sequence of simulated analyses for a period of several days in order to improve the initial conditions for a barotropic model. In their approach, the synthesized initial condition was a weighted average of the current analysis (initial condition) and predictions to the current time using the past analyses. They found that for a linear model with constant advecting velocity, the observational error can be curtailed by averaging the prediction results and analysis with equal weight. This is a special case of the method developed in this paper. However, for the nonlinear equation, a simple averaging did not improve the results. Instead, to account for the error growth with time, a weighted average was used by Miyakoda and Talagrand with the weights determined from the error covariances of the forecast model. Because of the statistical

nature of the covariances, the optimal weights are difficult to find and generally vary from case to case.

Instead, if the emphasis is placed on the temporal continuity in the sequence of data sets, the adjustments are best handled by minimizing the sum of squared discrepancies between the solution from a forecast model and the observations at the various times. Because the forecast model fits the data at the analysis times it is unnecessary to ascribe weights according to the data's age. The primary advantage of this approach is the mutual adjustment of the analyses which effectively increases the data base at each time by using information at other analysis times through the forecast equations. This is the traditional variational approach formulated by Sasaki (1958, 1970).

Although attractive in principle, the multiple time level variational problem is cumbersome for even simple advective constraints when traditional methods are used (Lewis and Panetta, 1983). The governing Euler-Lagrange (E-L) equations are typically a coupled set of high order differential equations that are difficult to solve under ideal circumstances, namely linear dynamics and equal separation between analyses. When more realistic circumstances prevail, approximations are generally necessary to make the problem tractable (Bloom, 1983).

An attractive alternative to solving the E-L equations associated with the variational analysis problem has appeared in optimal control theory. LeDimet and Talagrand (1984, personal communication) are developing a general formalism for meteorological variational analysis as an application of optimal control theory that builds on the ideas of Lions (1971). Rather than finding the solution through the E-L equations, the functional is minimized by finding its gradient with respect to one of the analysis states (e.g., the initial

state) and then using methods such as steepest descent or conjugate gradient to iterate toward the optimal state. The process of finding the gradient of the functional makes use of adjoint equations (e.g., Courant and Hilbert, 1962, p. 770) which are used for integrating difference fields in time. Unlike the more traditional variational approach, the adjoint approach remains tractable even with quite complicated constraints.

The multi-time level variational adjustment problem is addressed here using these optimization strategies. Following the development of basic theory, some conceptual examples and numerical experiments will be presented using advection equations. Finally, the application of the method to a case study involving VAS data will be presented. The models used in this study are fairly simple, however the strategy can be extended to more complicated problems without much difficulty.

## 2. The method

In this section an iterative method is described which minimizes the weighted squared difference between the original analyses at several times and the coincident solutions to the constraint for a given variable ( $q$ ). This problem is solved using standard nonlinear minimization algorithms utilizing a gradient calculated from adjoint equations. The constraint is some forecast model providing estimates  $q(t_p)$ , where  $t_p$  refers to the analysis times. The final analyses are constrained to satisfy the model forecast ( $q(t_p)$ ) from a set of initial conditions ( $q(t_1)$ ). Mathematically, an equivalent problem is to find the initial conditions to the forecast model which produces a solution minimizing

$$J(q(t_1)) = \frac{1}{2} \sum_{p=1}^P \langle W(t_p) \cdot (q(t_p) - \bar{q}(t_p)), q(t_p) - \bar{q}(t_p) \rangle \quad (1)$$

where  $J(q(t_1))$  is the functional dependent on the initial conditions  $(q(t_1))$ ,  $\langle, \rangle$  is the inner product over space,  $\bar{q}(t_p)$  is a vector of length  $M$  containing the original analyzed gridpoint values of the variable  $q$  at time levels  $t_p$ , and  $W(t_p)$  is a  $M \times M$  diagonal weighting matrix, which can be used to discriminate confidence levels at the various analysis times. Here we have decided to minimize the functional with respect to  $q(t_1)$  and accordingly express the functional as  $J(q(t_1))$ . The functional could be minimized with respect to  $q$  at any time (e.g.,  $J(q(t_p))$ ). The result will be the same for any  $t_p$  when the constraint is linear. This can be seen intuitively by realizing that the model is considered perfect and once an optimal state is found at an arbitrary time, the associated optimal states are found by forecasting and/or hindcasting to the various times using the adjusted state as initial conditions. In the nonlinear case, more than one solution to the algorithm is possible. Thus, it is uncertain whether or not the algorithm will converge to the same solution. However, it can be shown that for the implicit time differencing used in this paper any solution found by minimizing with respect to one time level is also a solution with respect to another time level.

$J$  is minimized by finding the gradient of  $J$  with respect to the initial conditions,  $\text{Grad}\{J(q(t_1))\}$ , followed by the use of a standard nonlinear programming algorithm. In this study, the steepest descent algorithm was initially tested (e.g., Polak, 1971, pp. 28-40) and it worked well with uniform weighting. However, when nonuniform weighting was used, we found the conjugate gradient method (e.g., Polak, 1971, pp. 53-54) to be more satisfactory. For simplicity only the application to steepest descent will be described. The generalization to conjugate gradient is straightforward.

The steepest descent algorithm is outlined as follows:

Step 1. Find the gradient of  $J$ ,  $\text{Grad } J$ , with respect to some initial conditions  $q^v(t_1)$ .  $v$  specifies the iteration.

Step 2. Find the optimal stepsize,  $\rho^v$ , such that  $J$  is minimized along the line of possible initial conditions  $q(t_1) = q^v(t_1) - \rho^v \text{Grad } J^v$  ( $\rho > 0$ ). For a linear model  $\rho^v$  can be calculated explicitly. However, for a nonlinear model the stepsize usually cannot be determined analytically. For the nonlinear constraint in this paper a quadratic line search algorithm (e.g., Avriel, 1976) is used to estimate  $\rho^v$ .

Step 3. Update the initial conditions  $q^{v+1}(t_1) = q^v(t_1) - \rho^v \text{Grad } J^v$ .

Step 4. Check to see if some convergence criterion is met ( $|\text{Grad } J^v| < \epsilon$ ). If not, go to step 1. Note that if  $\text{Grad } J = 0$ , the functional is at a minimum for the linear constraint. If the constraint is nonlinear, the functional can be at any stationary point, i.e., a local minimum, local maximum, or saddle point. However, the functional value must be less than or equal to the original functional value.

In the next subsection (2.1) the procedure for finding  $\text{Grad } J^v$  and  $\rho^v$  is outlined. Subsection 2.2 describes a special case where the optimal initial field is a simple average of the analysis and hindcasts to the initial time. In subsection 2.3, the relationship between this method and the one suggested by Thompson (1969) is described.

## 2.1 Determination of $\text{Grad } J$

$\text{Grad } J^v$  is determined using a method based upon a general formalism being developed by Talagrand and Le Dimet (1984, personal communication). If  $J'$  is defined as the first order change in the functional resulting from a small perturbation  $q'(t_1)$  about the initial condition  $q(t_1)$ , then  $J'$  is the directional derivative in the  $q'(t_1)$  direction and is given by

where we have simplified the notation by introducing the adjoint variable  $\hat{q}_p(t_p) \equiv W(t_p)(q(t_p) - \tilde{q}(t_p))$ . Since the adjoint variable will be integrated back to the initial time  $t_1$ , the subscript  $p$  on  $\hat{q}_p(t)$  is introduced to keep track of the time level where the adjoint variable was initialized. To isolate  $q'(t_1)$  on the right hand side of the inner product the identity for a real matrix  $A$

$$\langle x, Ay \rangle = \langle A^T x, y \rangle$$

is applied repeatedly where  $A^T$  is the transpose of  $A$ , resulting in

$$\langle \text{Grad } J, q'(t_1) \rangle = \sum_{p=1}^P \langle [ \prod_{k=1}^K D^T(t_1 + k\Delta t) ] \hat{q}_p(t_p), q'(t_1) \rangle. \quad (7)$$

Thus implying that

$$\text{Grad } J = \sum_{p=1}^P [ \prod_{k=1}^K D^T(t_1 + k\Delta t) ] \hat{q}_p^v(t_p) \quad (8)$$

This form of  $\text{Grad } J$  is not very practical, with the  $D^T(t_1 + k\Delta t)$  matrices being very difficult to evaluate. Therefore, (8) will be rewritten in a form similar to the basic constraint.

This is done by defining

$$\hat{q}_p(t - \Delta t) = D^T(t) \hat{q}_p(t), \quad (9)$$

and repeatedly substituting into (8) yielding

$$\text{Grad } J = \sum_{p=1}^P \hat{q}_p(t_1). \quad (10)$$

Note that (9) expanded as in (4) gives

$$\hat{q}_p(t) - \hat{q}_p(t - \Delta t) = -A^T(t) \cdot (\hat{q}_p(t) + \hat{q}_p(t - \Delta t)), \quad (11)$$

which is referred to as the adjoint equation. Thus,  $\text{Grad } J^v$  can be found by integrating  $\hat{q}_p(t_p) = W(t_p)(q(t_p) - \tilde{q}(t_p))$ , the weighted difference between the

model forecasts and the analyses, from  $t=t_p$  to  $t=t_1$  using the adjoint equation (11) for each  $t_p$  and summing the results. However, since (11) is linear, (10) can be evaluated with a single integration of the adjoint equation from the last analysis time to the initial time by inserting the weighted differences,  $W(t_p)(q(t_p) - \tilde{q}(t_p))$ , whenever one of the analysis times ( $t_p$ ) is reached. Thus, Grad J is found with a single integration of the adjoint model.

## 2.2 Unitary system

A special case of this problem exists when  $A(t) = -A^T(t)$ , thus implying that  $D^T = D^{-1}$ . When  $D^T = D^{-1}$ ,  $D$  is referred to as a unitary matrix (Kreyszig, 1978, see pages 195-206). Then the adjoint integration of the weighted forecast differences becomes equivalent to integrating the weighted differences backwards in the model equations. The optimal stepsize can be shown to be  $1/P$  and the method will converge in one iteration if all points are weighted equally ( $W_p = I$ ). Thus, at the minimum

$$q(t_1) = - \frac{1}{P} \sum_{p=1}^P \left[ \prod_{k=1}^K D^{-1}(t_1 + k\Delta t) \right] \tilde{q}(t_p) \quad (12)$$

A unitary system with equal weights has optimal initial conditions given by the average of the initial analyses integrated to  $t=t_1$ . This result implies that the optimal forecast is the average of the forecasts. The linear vorticity equation with constant advection velocity studied by Miyakoda and Talagrand (1971) is an example of a unitary system.

## 2.3 Relationship to Thompson's scheme

When the integration of the linear advection equation from one analysis time to the other is done in one step, the results from this method can be



shown to be equivalent to the Thompson (1969) approach as applied by Lewis (1982) or for multiple time levels as developed by Lewis and Panetta (1983). This intuitively follows since both methods are minimizing the same functional under the same constraint.

The minimization technique discussed in this paper has three major advantages over the Thompson method. First, the method allows multiple timesteps between analysis times thus eliminating the truncation problem associated with large separation between analysis times as discussed in Lewis (1982). Because of this, limitations on the maximum time separation between analysis times are eliminated. Also, the inclusion of many analysis times becomes almost trivial with this method, while as shown by Lewis and Panetta (1983) the inclusion of many times in the Thompson method is cumbersome. Finally, this method is easier to implement on more complicated model equation sets. A potential disadvantage of this method is the required amount of computer time. Since the method is iterative with each iteration requiring at least one forward model integration and one adjoint model integration, complex models could be very time consuming. However, as will be seen in the next section, the method appears to converge in only a few iterations.

### 3. Simulated data study: the one dimensional advection equation

In order to assess the degree of error reduction that can be accomplished through temporal coupling of analyses, data sets are constructed from analytic solutions of the one-dimensional advection equation. This dynamical constraint is examined in progressively more complicated formulations starting from advection with constant velocity, followed by advection with spatially varying velocity, and finally nonlinear advection governed by Burgers' equation (Burgers, 1939; Platzman, 1964).

The initial state is taken to be

$$q = \sin x \quad 0 \leq x < 2\pi .$$

The governing constraints are:

$$a) \quad \frac{\partial q}{\partial t} + c \frac{\partial q}{\partial x} = 0 , \quad c = \text{constant} \quad (13a)$$

$$b) \quad \frac{\partial q}{\partial t} + v(x) \frac{\partial q}{\partial x} = 0 , \quad v(x) = \frac{6}{(2\pi)^2} \cdot x(2\pi - x) \quad (13b)$$

$$c) \quad \frac{\partial q}{\partial t} + q \frac{\partial q}{\partial x} = 0 \quad (13c)$$

where the coefficient used in the definition of the parabolic profile,  $v(x)$ , in (13b) is chosen so that the average velocity over the interval is 1. The analytical solutions to these advection equations are:

$$q = \sin (x - ct)$$

$$q = \sin (2\pi x / [x + (2\pi - x)\exp([3/\pi]t)])$$

$$q = \sin (x - qt)$$

The finite difference form of the linear advection model (13a,b) is given in (14).

$$\frac{q_i(t + \Delta t) - q_i(t)}{\Delta t} + v_i \cdot \left( \frac{\bar{q}_{i+1} - \bar{q}_{i-1}}{2\Delta x} \right) = 0 \quad (14)$$

where

$$\bar{q}_i = \frac{q_i(t + \Delta t) + q_i(t)}{2}$$

and  $v$  is a prescribed velocity field. The adjoint equations are given in (15)

$$\frac{\hat{q}_i(t + \Delta t) - \hat{q}_i(t)}{\Delta t} + \frac{(v_{i+1} \bar{q}_{i+1} - v_{i-1} \bar{q}_{i-1})}{2\Delta x} = 0 \quad (15)$$

where

$$\bar{q}_i = \frac{\hat{q}_i(t + \Delta t) + \hat{q}_i(t)}{2}$$

Note that if the advecting speed is constant as in (13a), the system is unitary.

The nonlinear advection equation (13c), is presented in (16) in finite difference form with the associated adjoint equation given in (17).

$$\frac{q_i(t + \Delta t) - q_i(t)}{\Delta t} + \bar{q}_i \cdot \left( \frac{\bar{q}_{i+1} - \bar{q}_{i-1}}{2\Delta x} \right) = 0 \quad (16)$$

$$\frac{\hat{q}_i(t + \Delta t) - \hat{q}_i(t)}{\Delta t} + \frac{\bar{q}_{i+1} \bar{q}_{i+1} - \bar{q}_{i-1} \bar{q}_{i-1}}{2\Delta x} - \bar{q}_i \frac{\bar{q}_{i+1} - \bar{q}_{i-1}}{2\Delta x} = 0 \quad (17)$$

Both (16) and (17) are solved iteratively with periodic boundary conditions. Note that in all cases, the finite differencing of the adjoint equations are derived such that they are consistent with the finite differencing of the constraint.

The functional for all experiments in this paper is given by (1). The weighting matrix  $W(t_p)$  is the identity matrix for the simulated data study. However, for the real data case study, the weighting matrix is defined from the objective analysis routine, thus incorporating some information on the expected spatial distribution of analysis quality.

Temporally correlated error has been treated by Thompson (1969) and Lewis (1982) and these studies have shown that the correlated error cannot be reduced to the same degree as random error. For perfectly correlated error in time (e.g., identical phase errors in the case of linear advection), no reduction in error is possible. The reduction in error after adjustment will

be bounded by zero and the maximum limit that occurs in the case of an uncorrelated error in time. In this exercise, the analyses will be generated by adding a normally distributed uncorrelated error in space and time to the analytic solutions. The amplitude of the error is 10% of the amplitude of the basic solution.

In the case of linear advection with constant velocity the equation is unitary, thus only one iteration is necessary. An iteration is defined as a forward integration using the constraint followed by a backward integration to the initial time using the adjoint equation. As stated in the previous chapter, for a unitary system the solution to the minimization is the average of the forecast and hindcasts from each of the analysis times. For two time levels, the adjusted analysis at the second time level is the average of a forecast from the initial time and the analysis, while the adjusted analysis at the initial time is the average of the hindcast from the second time and the initial analysis. Therefore, the error in the adjusted analyses is the average of the forecast error and the analysis error. Note that the forecast error is composed of two components, the error resulting from the initial conditions and the modelling errors. For these simple test cases, the modelling error results only from the finite differencing. Therefore, as the time step in the model decreases, the model error decreases and the forecast error approaches the error resulting from errors in the initial condition. For the linear problem, this initial error is merely advected from one location to another location. Thus, when this error is averaged with the random error at the analysis time, the result should approach a 50% reduction in mean square error as the time step becomes small.

The reduction in mean square error for an ensemble of 300 experiments are displayed in Fig. 1 for various numbers of time steps used to integrate between the analyses. The reduction is plotted as a function of the time

separation constant (=propagation speed  $\times$  time between analyses/spatial increment) since the model truncation error is a function of this constant, the number of timesteps between analyses and the wavelength. Note that the time separation constant is equivalent to the Courant number in Lewis (1982) when one timestep is used between analyses. As expected, the reduction in mean square error approaches the theoretical limit of 50% as the number of time steps increases. The curve labeled "1" is equivalent to the adjustment by Thompson's (1969) method which makes the forecast from one analysis time to the other in a single step. The discrepancy between this curve and the corresponding curve in Lewis (1982,  $16\Delta s$  curve in Fig. 2) which used Thompson's method, resulted from Lewis' use of a finite difference form of the Euler-Lagrange equation that was inconsistent with the differencing used in the constraint.

For the case of linear advection with spatially varying velocity, the system is no longer unitary so several iterations were generally necessary to reach the minimum. The associated reduction in mean square error is displayed by the solid curves in Fig. 2. When compared with Fig. 1 it is noted that the reduction is generally less than the constant velocity case, although the profiles are similar. The truncation error in the forecast with variable speed is greater than the constant velocity case, yet the approach to the 50% limit is not much different. Since the variable velocity case is not unitary, it is interesting to compare these optimal results with those obtained by the averaging process of Miyakoda-Talagrand. The results associated with averaging are displayed by the dashed lines in Fig. 2 and can be seen to give good results but definitely inferior to the optimal results.

For the nonlinear advection equation, a time step of  $\Delta t=0.1$  is chosen to integrate between the analysis times of  $t=0$  and  $t=0.9$ , the latter value chosen

so that multiple valued analytic solutions can be avoided in the case of Burgers' equation. The spatial increment is  $2\pi/8$  and thus  $q_{\max} \Delta t / \Delta x \approx 0.1$ , which is sufficiently accurate for the implicit scheme. A quadratic line search is used to find the optimum step size on each iteration. The rate of convergence can be measured in terms of  $|\text{Grad } J|$  as shown in Fig. 3a as a function of the number of iterations. The convergence is especially rapid within the first few iterations. The decrease in the value of the functional is shown in Fig. 3b and the reduction in rms error is shown in Fig. 3c. Unlike the linear advection, the functional reduction is greater than 50% and the mean square error reduction is less than 50%. The functional reduction is given as a percentage of the original functional value (iteration 0) calculated using  $q(t_1)$  to initialize the forecast model. From Figs. 3b and 3c, the functional reduction is seen to be nearly 70% whereas the average rms error reduction is about 20% (from 0.10 to 0.08) which translates into a 36% reduction in mean square error. Since a change in  $q$  alters both the quantity being advected and the advecting velocity, a small change in the initial condition can result in a larger change in the final solution than for the linear case. Because of this, a solution closer to the observations can be found with an associated functional reduction greater than 50%. However, since the adjustments are smaller than those in the linear case, the error reduction is less than 50%.

#### 4. Case study

##### 4.1 Synoptic situation and data distribution

Upper air data collected on March 6-7, 1982 over the central United States of America are used to test the adjustment process. This day was especially attractive for the evaluation since a special network of rawinsonde

observations (RAOB) was operated by the National Aeronautics and Space Administration. These data were collected at three hour intervals as part of the Atmospheric Variability Experiment. Temperature retrievals from the VISSR Atmospheric Sounder (VAS) (Smith, 1983) aboard the geostationary satellite GOES-5, were valid 30 minutes before the RAOB data. The test is made on a sequence of three rawinsonde (satellite) data collection periods: 2100 (2030), 0000 (2330), and 0300 (0230) GMT on March 6-7.

The synoptic pattern during this time period was characterized by a strong baroclinic zone extending from Mexico up through the northeastern United States. A cloud band paralleled the baroclinic zone with imbedded convective activity along the Texas and Louisiana coasts.

The distribution of RAOB and VAS data at 0000 GMT are shown in Figs. 4b and 5b, respectively. These distributions are typical of the other time periods where the number of observations are approximately 35 and 180 for RAOB and VAS, respectively. The average spatial separation between VAS (RAOB) sites is approximately 100 (250) km. Both sets exhibit a concentration of observations in north central Texas. The retrieval free corridor in the VAS data, extending northeastward from the Texas coast, corresponds to the cloud band where the VAS is unable to detect the temperature structure below cloud top level. The cloud band can be seen in the infrared imagery that is used as background for the vertical motion patterns displayed in Fig. 7.

#### 4.2 Interpolation and weighting of observations

The analyses shown in this research were generated by the Barnes' method (Barnes, 1973) on a 111 km (1 degree of latitude) grid. This is roughly the average spacing for VAS observations and half the average spacing for rawinsonde observations. In addition to generating the heights at grid points, a

by-product of the method is a field depicting the "density of observations" surrounding each grid point. This distribution is an accumulation of the weights accorded each observation used in defining the grid point value. These weighting distributions are shown in Figs. 4a and 5a for the observations of height at 700 mb for RAOB and VAS, respectively. The grid point values of the density distributions are used as the diagonal elements of the weighting matrix in the functional J (Eq. 1).

#### 4.3 Dynamical model and solution of the adjustment equations

The dynamical constraint used in the case study is the conservation of geostrophic potential vorticity. The two parameter model described by Lewis (1982) was used. The finite difference form of the constraint is given by (15) in section 3.

Boundary conditions for the prediction have been assumed known from the analyses at the three times with values at intermediate times found by linear interpolation. A timestep,  $\Delta t$ , of 30 minutes is used for the prediction which produces values of approximately 0.20 and 0.10 for  $V_{\max} \Delta t / \Delta s$  at 250 and 700 mb, respectively. The iteration process for finding the minimum of functional J was considerably improved when the conjugate gradient method (e.g., Polak, 1971, pp. 53-54) was used instead of the steepest descent method.

#### 4.4 Height adjustments and vertical motion fields

Our discussion will focus on the height adjustments at 700 mb since the results at 250 mb were very similar. Fig. 6 shows both the input (solid) and output (dashed) heights for RAOB and VAS. The most obvious differences between the VAS and RAOB inputs are:



(i) the VAS analyses of the 297 and 300 dm contours over the Oklahoma-Texas area extend substantially further to the west than the RAOB analyses at the first two times;

(ii) the appearance of some ridging over the Gulf of Mexico on the VAS analyses; and

(iii) the last VAS analysis is disorganized and inconsistent with the first two VAS analyses.

Examination of the adjustment pattern makes it evident that the RAOB heights are altered less, or stated alternatively, they are more consistent with the constraint. RMS adjustments for RAOB and VAS are 3.7 and 7.9 m (13.5 and 22.0 m at 250 mb), respectively. The larger figure for the VAS is contributed chiefly by the last time period where the input analysis is very inconsistent with the other analyses. The adjustments are reasonable considering the observational and analysis errors. A comparison of the raob and satellite analyses indicated standard deviations of 14 and 42 m at 700 and 250 mb for the input, and 12 and 53 m for the output. Thus, the 700 mb fields were statistically closer after adjustment whereas the 250 mb analyses were further apart. A positive bias of about 6 m (VAS higher than RAOB) existed at 250 mb before and after adjustment.

While the adjustment procedure appears to have improved the orientation and position of the Oklahoma-Texas trough in the VAS depiction, the 300 dm contour still extends substantially further to the west than the RAOB analysis indicates. Since this condition existed on two of the input analyses, it can be inferred that the error was correlated in time and could not be removed. A perfectly correlated error in time implies that the solution to the governing constraints initialized with the various input analyses will produce the same error pattern at a fixed point in time. The spurious ridging over the Gulf of

Mexico is removed by the adjustment process and reveals an advantage of the method, namely that the dynamical time continuity required by the adjustment can remove spurious features present in the input data.

The vertical motion fields at 500 mb were calculated from an omega equation consistent with the two parameter prediction model. These fields are shown in Fig. 7. Only the input is shown for the RAOB since the input and output omegas were very similar. The most obvious feature is the small scale structure evident in the VAS. The strong lifting in east Texas at 2330 and 0230 GMT is suspicious; this lifting is well behind the cloud band as depicted by the infrared imagery. Also, the lifting pattern in Mexico is questionable, well to the rear of the advancing baroclinic zone. The adjusted omegas are much better correlated with the ascent-descent regions as inferred from the infrared imagery. They also bear a strong resemblance to the omega pattern derived from the RAOB data. It appears from these results that the VAS data are noisy and the noise is quite successfully eliminated by the adjustment procedure.

In this case, the cloud cover was nearly fixed relative to the translating synoptic system. Accordingly, the Lagrangian advection of information from the data rich to data sparse regions was small relative to the situation where data sparse regions exhibit a more random distribution in space and time. Ideally, the adjustment scheme extrapolates information both forward and backward in time by using the model constraints in much the same way that forecast models are used to generate guess fields for analysis in data sparse regions.

##### 5. Summary and discussion of extensions to more complicated models

Our purpose in this paper has been to develop a methodology for coupling successive analyses subject to forecast model constraints. We have used an

example of simple advection. The problem is cast as a minimization of weighted discrepancies in the analyses at the various times, subject to the model constraints. Traditionally, the solution to this variational problem has been obtained via direct solution of the Euler-Lagrange (E-L) equations to minimize the functional. The governing differential equations are higher order than the constraints and the number of equations in the coupled set increase with the number of time levels, making the solution to the coupled set difficult for even the simplest constraints. The key to the simplification obtained here comes through the minimization of the functional (sum of weighted squared discrepancies) by finding its gradient with respect to the dependent variable at one of the time levels, e.g., the initial state. The gradient is shown to be given by solutions to a set of adjoint equations which are used to integrate backward in time to the initial state. Unlike the traditional variational approach, the adjoint equations are tractable even with complicated constraints. Knowledge of the gradient, coupled with standard algorithms such as steepest descent or conjugate gradients, permits the minimization.

The principal deficiency in the method is the limitation imposed by assuming a perfect model. That is, all inconsistency between successive analyses are attributable to errors in the observations and/or objective methods used to interpolate observations to mesh points. Unfortunately, a straightforward procedure to generalize this method to incorporate the model as a weak constraint is not available. Nevertheless, the benefits accrued by amalgamating the analyses using an imperfect model as the constraint can partially offset the errors normally made in a static analysis.

When the advective constraint is linear with constant velocity and the weighting is uniform, the result of the adjustment process is identical to

simple averaging of the forecasts. Miyakoda and Talagrand (1971) have demonstrated the utility of this approach with linear dynamics. Thompson's (1969) approach handles the case of varying advection velocities through the solution to the E-L equations associated with minimizing squared discrepancies subject to the advective constraint. Thompson's method results in solutions identical to the algorithm described here when the forecast and hindcast are made in a single timestep. The principal advantages of this method over Thompson's is the ease with which multiple timesteps are accommodated to reduce truncation error and the simplicity of including many analysis times. It should be noted that this method (or probably any dynamical method) cannot eliminate errors correlated in time through the dynamics of the model. It is unlikely that errors correlated to synoptic patterns, such as those that may be found from satellite soundings, can be substantially reduced since the errors will move with the system.

For nonlinear dynamics, the methodology is especially attractive because it avoids the drastic assumptions that are generally invoked to make the E-L equations tractable. Simulations with Burgers' equation indicates a robust algorithm that can significantly reduce mean square error.

The practicality of this technique has been demonstrated for the simple models in this paper. The analysis of heights for a sequence of three time periods during the winter of 1982 have shown that the method has potential to reduce the random error in the VAS height fields and make the analysis more compatible with the synoptic features depicted by the rawinsonde data. Vertical motions at 500 mb derived from the adjusted heights also show better correlation with cloud cover than the unadjusted fields.

Perhaps the greatest potential for this assimilation method lies not in the simple applications used in this paper, but rather in its extensions to

more complex models. Currently, the method is being tested on a multilevel quasigeostrophic model with good results. The convergence rate for this model is still quite rapid. Results from this work will appear in a future paper.

The assimilation method can be used on a wide variety of forecast models with the restriction that the model must be continuously differentiable with respect to the initial conditions. Thus, models containing frictional dissipation and diabatic effects can be used if the parameterizations are properly formulated. Unfortunately, many parameterization schemes are written with inequalities dependent on forecast variables and accordingly are not differentiable.

The extension to a primitive equation model appears to be relatively straightforward assuming the parameterization schemes are differentiable. The major difficulty in using a primitive equation model is the large increase in computing time. The method relies on an iterative method to find the minimum with at least one integration of the forecast model and the adjoint model required per iteration. Also, at least one additional integration of the forecast model is required to determine the stepsize. In the multilevel quasigeostrophic model and the simple models used in this paper, it has been possible to determine the stepsize with a single model integration. With a primitive equation model, the functional may not change as smoothly in the search direction and several integrations of the forecast model may be necessary to determine the stepsize. However, even if some increase in the computing time occurs due to a decrease in the convergence rate or an increase in the number of integrations necessary to determine the stepsize, the method should at least be practical for research purposes.

Another potential difficulty in applying the method to a primitive equation model may be amplification of nonphysical modes in order to better fit the data. However, these nonphysical modes can be suppressed with little

additional computation by introducing terms in the functional penalizing large amplitudes of the undesirable modes. This change to the functional would not entail any additional integrations of the adjoint or forecast model.

## Acknowledgments

It was during the 14th Stanstead Seminar at Bishop's University in Quebec that Olivier Talagrand first mentioned the ideas of the "adjoint" method to us. We are grateful for the continued dialogue with both Olivier Talagrand and Francois Le Dimet. We appreciate the constructive comments on the manuscript made by Christopher Hayden and Thomas Koehler and the three referees. Jim Purser's suggestions on the simulated data study were helpful and Gary Wade assisted us in producing displays of data.

## References

- Avriel, M., 1976: Nonlinear Programming: Analysis and Methods. Prentice-Hall, Inc., Englewood Cliffs, New Jersey, 512 pp.
- Barnes, S. L., 1973: Mesoscale objective analysis using weighted time-series observations. NOAA Technical Memorandum ERL NSSL-62, National Severe Storms Laboratory, 1313 Halley Circle, Norman, Oklahoma, 73069, 60 pp., [NTIS COM-73-10781].
- Bengtsson, L., 1975: Four-dimensional assimilation of meteorological observations. Geneva, World Meteorological Organization, International Council of Scientific Unions. Joint Organizing Committee. 75 pp. (GARP Publications Series No. 15)
- Bengtsson, L., M. Ghil and E. Kallén (eds.), 1981: Dynamic Meteorology: Data Assimilation Methods. Springer-Verlag, Berlin, 330 pp.
- Bloom, S. C., 1983: The use of dynamical constraints in the analysis of mesoscale rawinsonde data. Tellus, 35A, 363-378.
- Burgers, J. M., 1939: Mathematical examples illustrating relations occurring in the theory of turbulent fluid motion. Verhandelingen der Koninklijke Nederlandsche Akademie van Wetenschappen (Erste Sectie), 17, 53 pp.
- Courant, R., and D. Hilbert, 1962: Methods of Mathematical Physics, Vol. II. Interscience Publ., 830 pp.
- Hovermale, J., 1983: Summary of a workshop on atmospheric profiling. Bull. Amer. Meteor. Soc., 64, 1062-1066.
- Kreyszig, E., 1978: Introductory Functional Analysis with Applications. John Wiley and Sons, 688 pp. (see pages 195-206).
- Lewis, J. M., 1982: Adaptation of P. D. Thompson's scheme to the constraint of potential vorticity conservation. Mon. Wea. Rev., 110, 1618-1634.
- Lewis, J. M., and L. Panetta, 1983: The extension of P. D. Thompson's scheme to multiple time levels. J. Clim. and Applied Meteor., 22, 1649-1653.
- Lions, J. L., 1971: Optimal Control of Systems Governed by Partial Differential Equations. Translated by S. K. Mitter, Springer-Verlag, Berlin-Heidelberg.
- Miyakoda, K., and O. Talagrand, 1971: The assimilation of past data in dynamical analysis, I. Tellus, 23, 310-317.
- Platzman, G. W., 1964: An exact integral of complete spectral equations for unsteady one-dimensional flow. Tellus, 16, 422-431.
- Polak, E., 1971: Computational Methods in Optimization, A Unified Approach. Academic Press, New York, 329 pp.



Sasaki, Y., 1958: An objective analysis based on the variational method. J. Meteor. Soc. Japan, 11, 36, 77-88.

Sasaki, Y., 1970: Some basic formalisms in numerical variational analysis. Mon. Wea. Rev., 98, 875-883.

Smith, W. L., 1983: The retrieval of atmospheric profiles from VAS geostationary radiance observations. J. Atmos. Sci., 40, 2025-2035.

Thompson, P. D., 1969: Reduction of analysis error through constraints of dynamical consistency. J. Applied Meteor., 8, 738-742.

Figure legends

- Figure 1: Reduction in the mean square error as a function of the time separation constant (=propagation speed x time between analyses/spatial increment) for two time-level adjustment. The curve labeled "1" used one time step in the integration process whereas the curve labeled "2" used two time steps to integrate from one analysis to the other, etc.
- Figure 2: Same as Fig. 1 except that the results pertain to the advection constraint with variable velocity rather than constant velocity. The dashed curve shows the error reduction resulting from the two time step case when the final fields are found by averaging the analysis with the forecast (hindcast).
- Figure 3: Adjustment in the nonlinear case as a function of the number of iterations: (a) convergence of the scheme, (b) reduction in the functional value, and (c) error at each time. Term 1 and term 2 in (b) represent the squared deviations at the early and late time, respectively.
- Figure 4: Rawinsonde observations at each of the three analysis times on March 6, 1982. (a) The relative weighting distribution that is objectively determined from the density of observations and (b) the location of rawinsonde stations.
- Figure 5: Same as Fig. 4 except that these observations are from VAS.
- Figure 6: Height analyses at 700 mb on March 6, 1982. Solid lines are contours of the input analysis whereas dashed lines are output that result from adjustment procedure. (a), (b), and (c) are obtained from rawinsonde observations alone, while (d), (e), and (f) use only VAS observations.
- Figure 7: Vertical motion fields at 500 mb in  $\mu\text{bar s}^{-1}$ , superimposed over infrared imagery that is valid at the corresponding times.

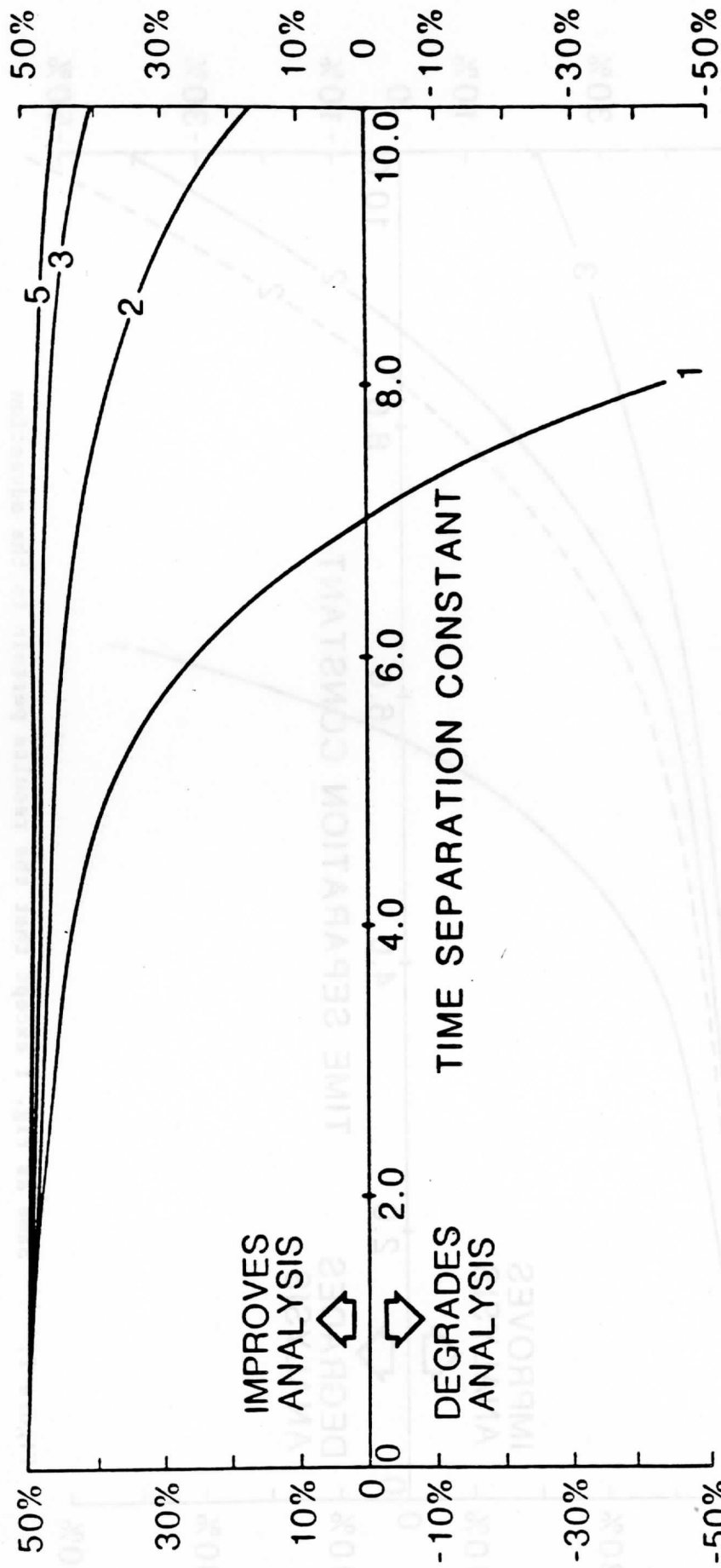


Figure 1: Reduction in the mean square error as a function of the time

separation constant (=propagation speed x time between

analyses/spatial increment) for two time-level adjustment. The

curve labeled "1" used one time step in the integration process

whereas the curve labeled "2" used two time steps to integrate

from one analysis to the other, etc.

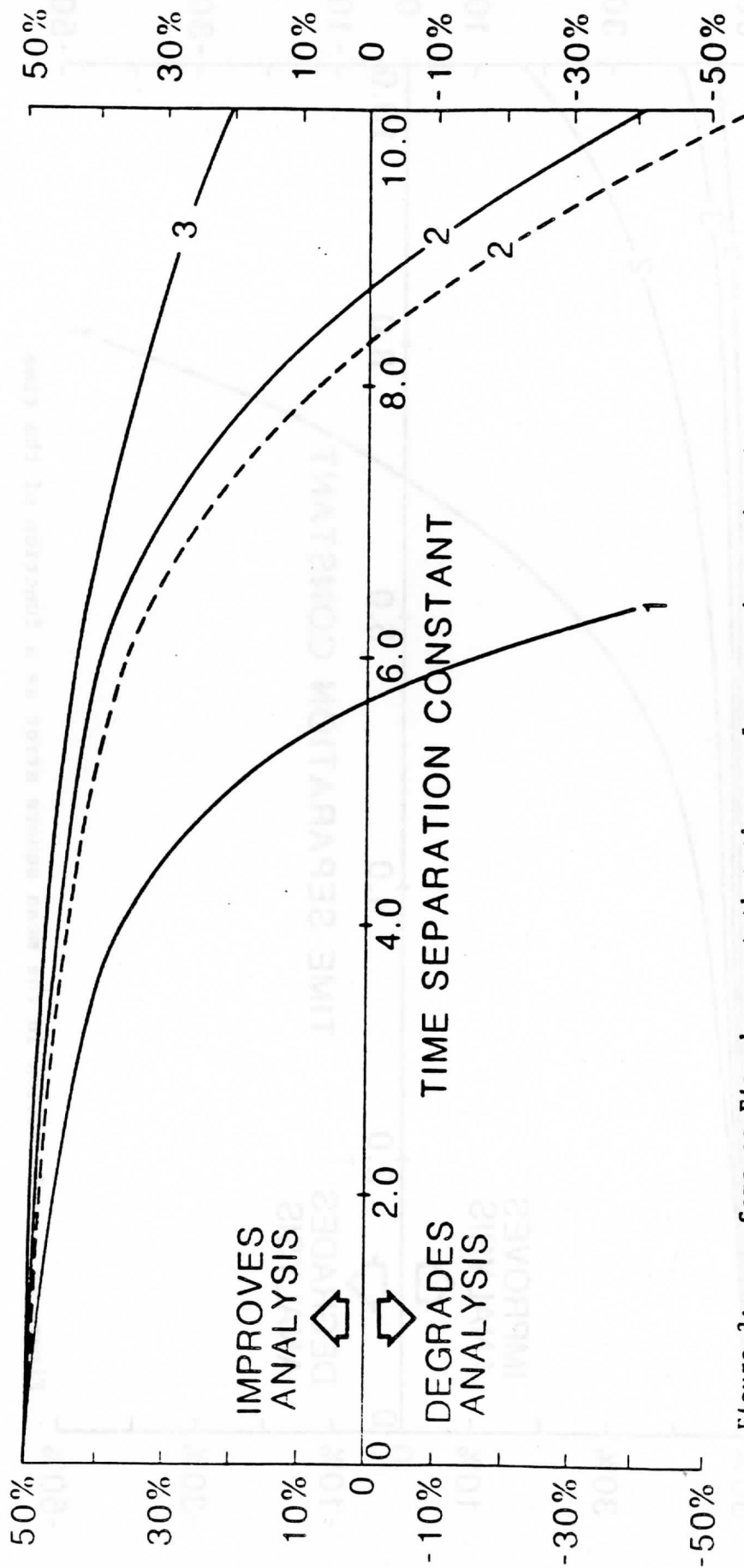


Figure 2: Same as Fig. 1 except that the results pertain to the advection constraint with variable velocity rather than constant velocity. The dashed curve shows the error reduction resulting from the two time step case when the final fields are found by averaging the analysis with the forecast (hindcast).

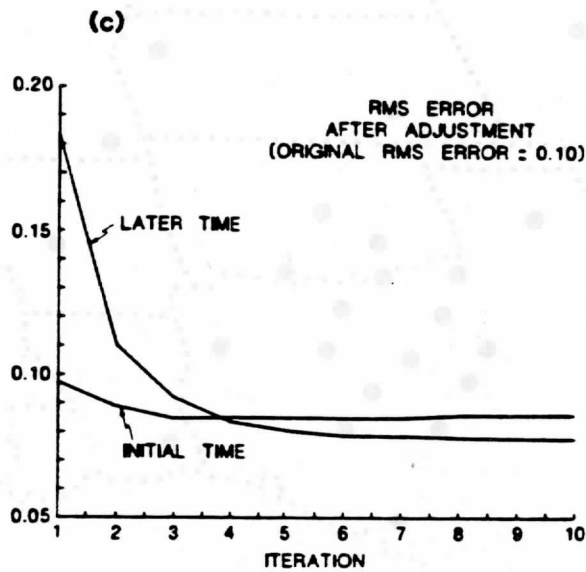
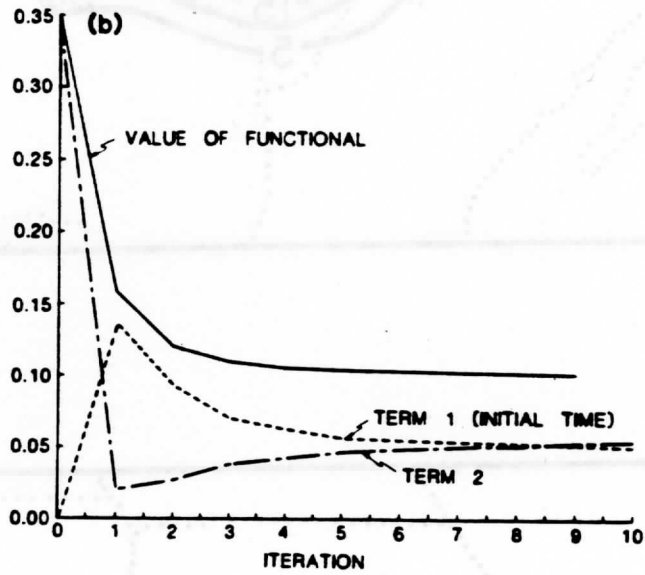
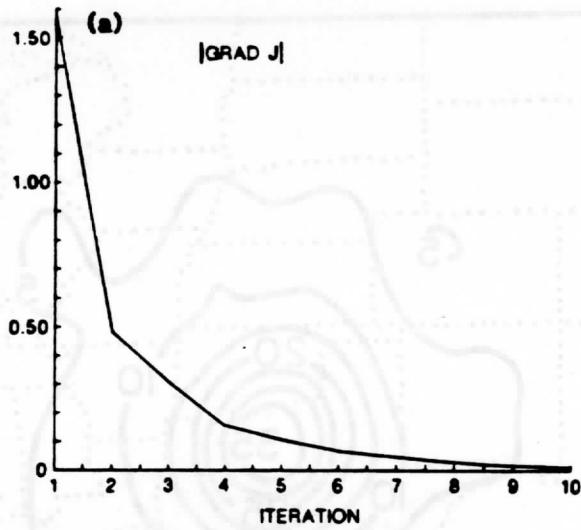
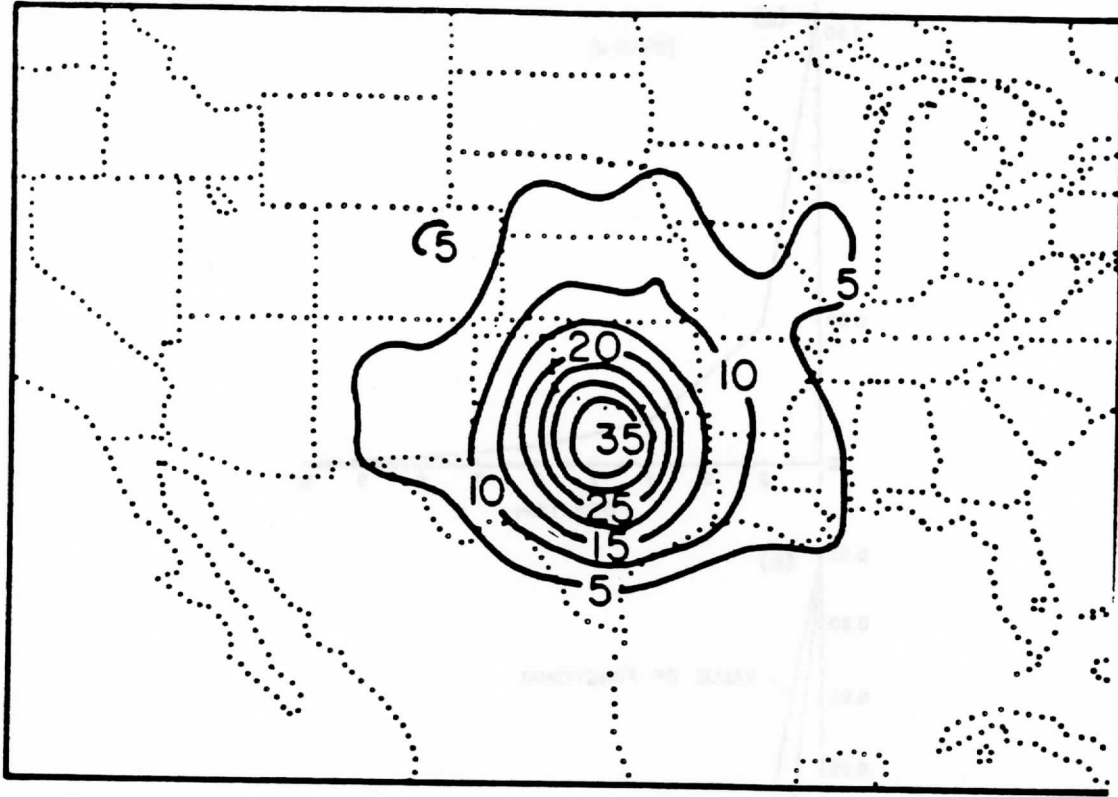


Figure 3

(a)



(b)

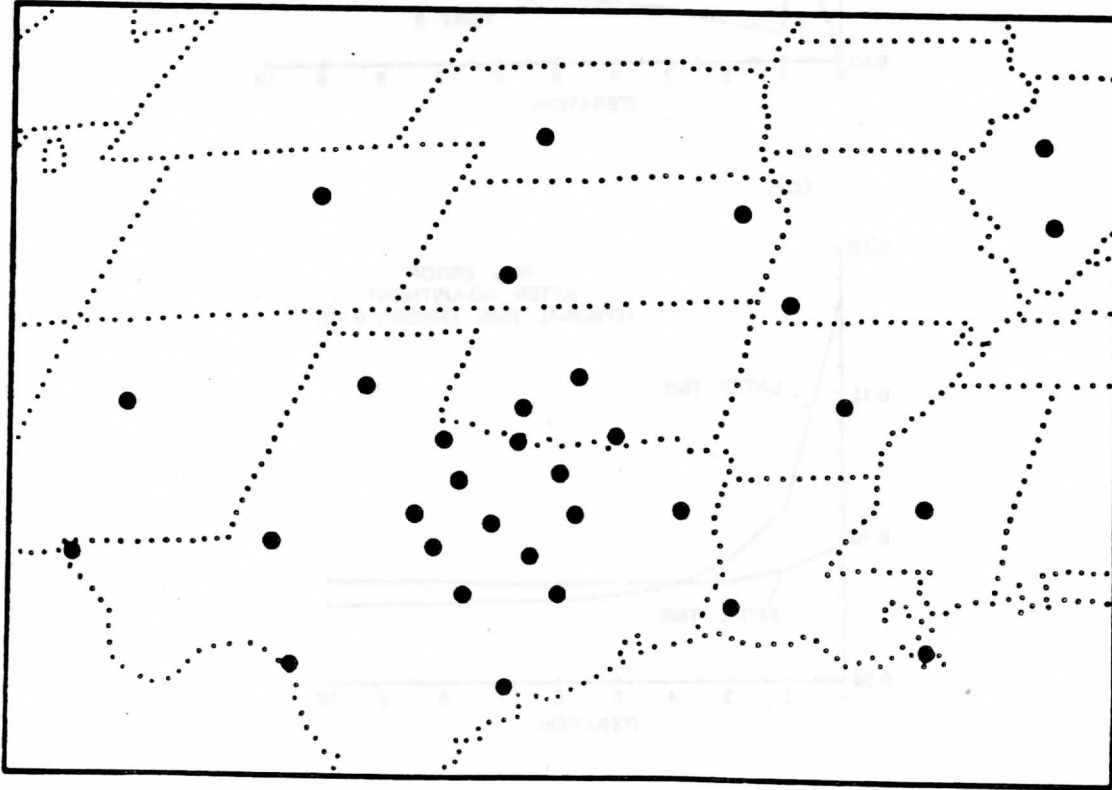
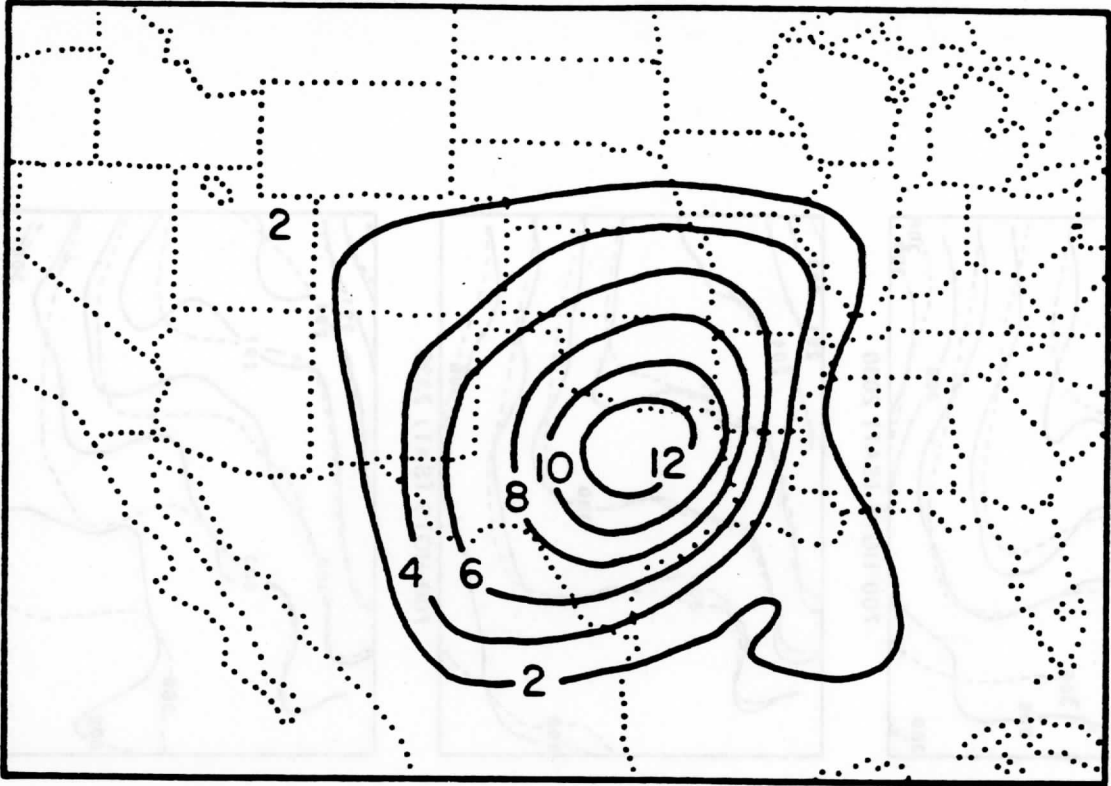


Figure 4: Rawinsonde observations at each of the three analysis times on March 6, 1982. (a) The relative weighting distribution that is objectively determined from the density of observations and

(a)



(b)

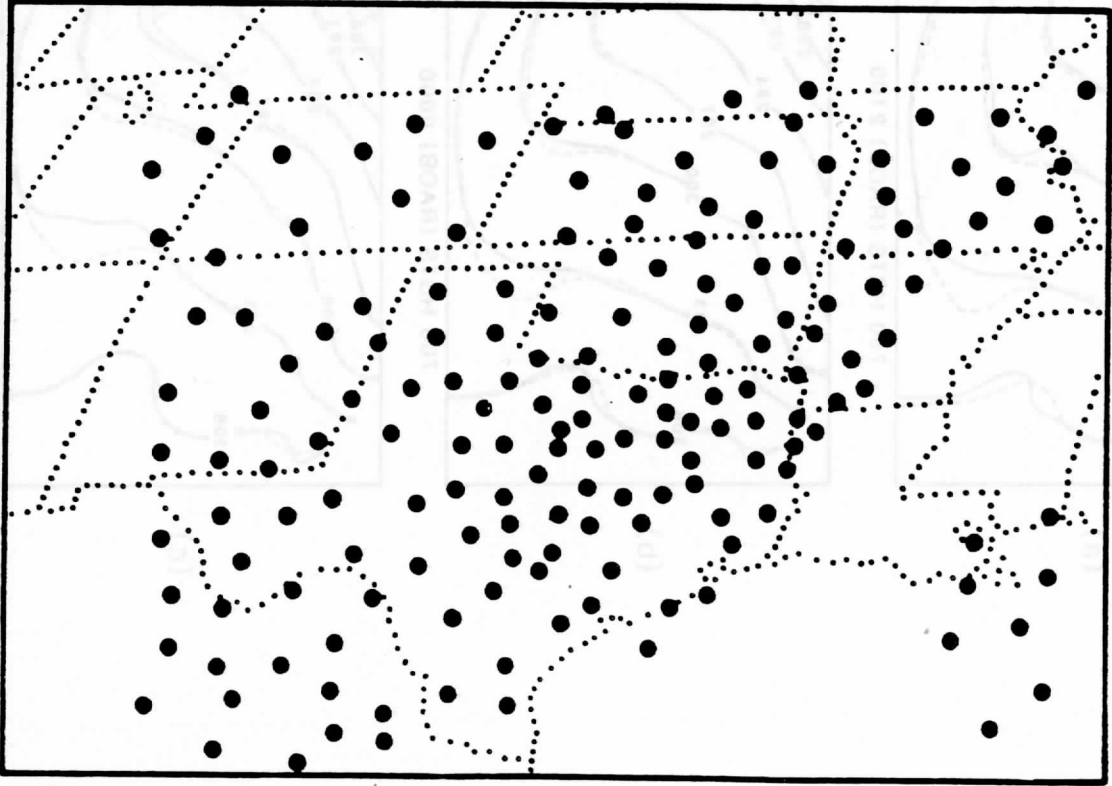


Figure 5: Same as Fig. 4 except that these observations are from VAS.

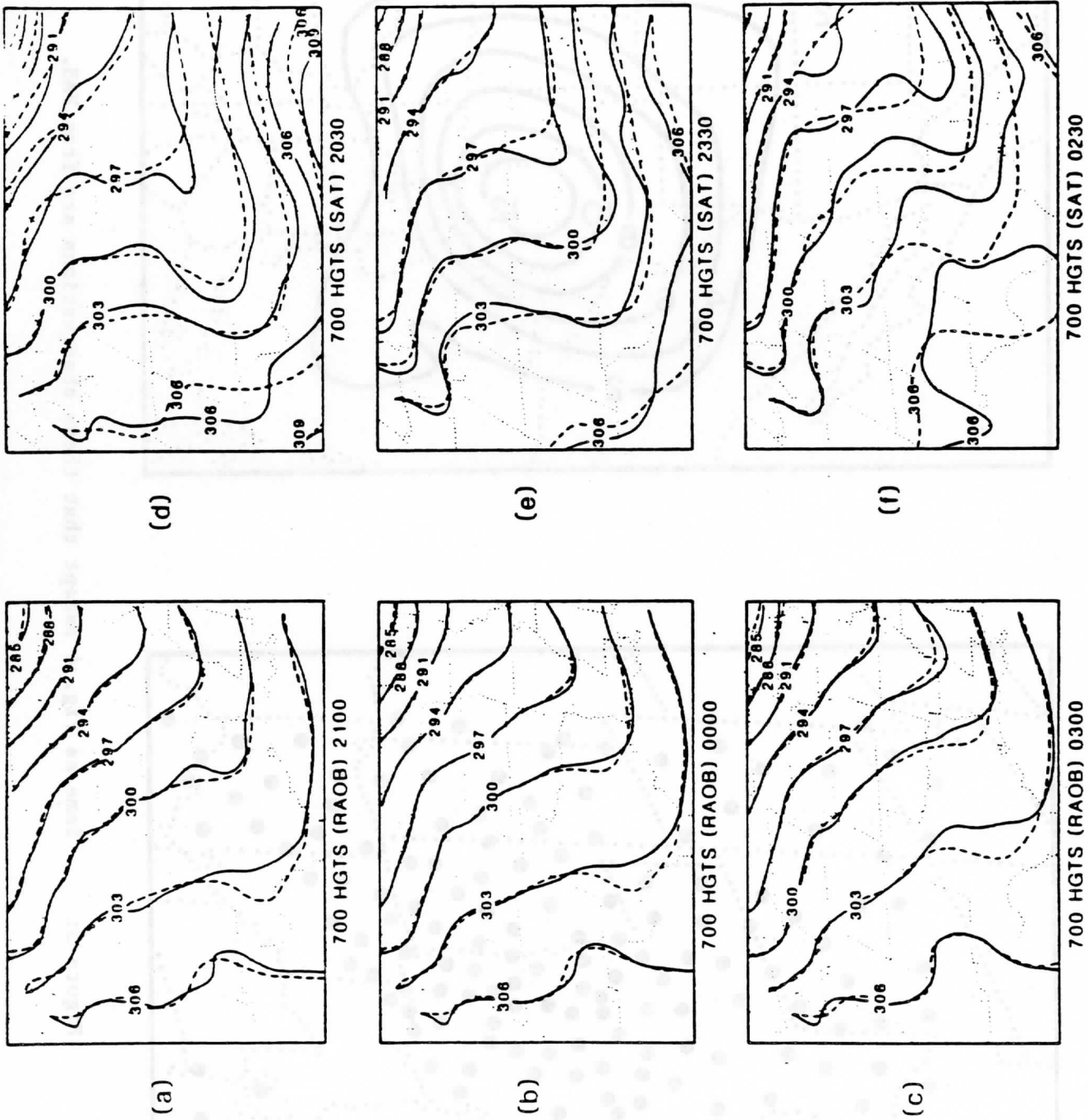


Figure 6: Height analyses at 700 mb on March 6, 1982. Solid lines are contours of the input analysis whereas dashed lines are output that result from adjustment procedure. (a), (b), and (c) are obtained from rawinsonde observations alone, while (d), (e), and (f) use only WAS observations.



VAS (INPUT)



2030

VAS (OUTPUT)



2030

RAOB



2100



2330



2330



0000



0230



0230



0300

Figure 7

## An Extended Lagrangian Theory of Semi-Geostrophic Frontogenesis

M. J. P. CULLEN AND R. J. PURSER

*Meteorological Office, Bracknell, Berkshire RG12 2SZ U.K.*

(Manuscript received 9 August 1983, in final form 8 February 1984)

### ABSTRACT

The Lagrangian conservation law form of the semi-geostrophic equations used by Hoskins and others is studied further in two and three dimensions. A solution of the inviscid equations containing discontinuities corresponding to atmospheric fronts is shown to exist for all time under fairly general conditions, and to be unique if the potential vorticity is required to be nonnegative. Computational results show that this solution agrees with high resolution solutions of the viscous semi-geostrophic equations. The solution, however, disagrees with that obtained from the two-dimensional viscous primitive equations. An important aspect of the difference is that the semi-geostrophic solutions allow the front to propagate into the interior of the fluid while the primitive equation solutions do not. This is discussed. If correct, it may indicate a tendency for a separation effect in the atmosphere where frictional effects are present.

### 1. Introduction

This paper considers an attempt to model mature atmospheric fronts by extending the frontogenesis model originally developed by Hoskins and Bretherton (1972). Their model uses the semi-geostrophic equations, in particular a Lagrangian conservation form of them. In a previous paper (Cullen, 1983, referred to hereafter as C), one of the authors proposed an extension to this model by continuing to solve the Lagrangian conservation laws after the initial formation of the front. In this paper we develop and examine these ideas further.

The theory of Hoskins and Bretherton is now widely accepted as a mechanism for producing atmospheric fronts. However, comparison of their predictions with observation is difficult because their solutions continue only up to the initial formation of a discontinuity. At this stage frontogenetic effects dominate frontolytic effects. Observations of mature fronts, for instance those described by Sanders (1955), show a balance between the effects. Thus, authors who have attempted to compare the Hoskins and Bretherton model with the atmosphere, such as Blumen (1980) and Ogura and Portis (1982), have found disagreements. Despite this a number of qualitative features of observed fronts were successfully predicted. Attempts to resolve the disagreements by adding frictional effects to the model were not very successful. In particular, it was still found to be impossible to reproduce an observed vertical velocity maximum near the ground. There is thus a strong incentive to try to extend the theory to cover mature fronts.

The difficulty in using semi-geostrophic theory to describe fronts beyond their initial formation is that

it is clear that the scale analysis used to derive the equations is no longer valid everywhere. In C it was suggested that the Lagrangian conservation laws derived from the equations might still be valid for most fluid particles. This is plausible because no fluid crosses a front, by definition, and thus only a small proportion of the fluid is likely to come close to the frontal surface. The solution is constructed geometrically, assuming that certain volumes of fluid have specified values of absolute momentum and potential temperature. Thus changes to the values of these quantities for a small proportion of the fluid particles caused by local breakdown of the conservation laws may have only a small effect on the solution. If organized convection were present, however, the conservation laws could be violated for a large proportion of the fluid and the solution would not be expected to be very useful.

The likely validity of the model proposed in C thus depends on the proportion of the fluid volume in which the scale analysis leading to semi-geostrophic theory breaks down and the ageostrophic accelerations are large. According to Hoskins and Bretherton, this should happen only when the frontal vorticities  $\zeta$  reach about  $25f$ . They also suggest that three-dimensional turbulence would have set in before then, because the local Richardson number is of the order  $f/\zeta$ . However, computations by Orlanski and Ross (1977) and Ross and Orlanski (1982) using the primitive equations suggest that the scale analysis is not valid for vorticities larger than about  $2f$ . After this stage the ageostrophic wind parallel to the front became significant. A possible explanation for this disagreement is the different method of determining the cross-frontal circulation. In the semi-geostrophic model the cross-frontal flow is determined implicitly by an omega equation. The implied

accelerations can be estimated from the rate of change of the forcing terms in the omega equation, as was done by Hoskins. In a primitive equation model the circulation can only be changed explicitly by an ageostrophic wind parallel to the front. Orlanski and Ross found that the resulting circulation was similar to that obtained using the omega equation method with the addition of an inertio-gravity oscillation. It is possible that the larger accelerations were associated with this oscillation. The calculated pattern of the ageostrophic wind and the separation they obtained between the line of maximum wind shear and temperature gradient are on scales close to their model grid length and will require further investigations using higher resolution models. At the present time, therefore, there must be uncertainty about the range of validity of semi-geostrophic models.

Though the method described in C of extending the solution to cover mature fronts seems plausible, it may not be the only way of doing so. In particular, the results reported in C suggest that a different type of solution is obtained by solving the primitive equations with artificial viscosity. It is only possible to choose between such solutions by incorporating the assumptions into realistic three-dimensional models and testing against real data.

This paper continues the work started in C and is divided into two parts. The first shows how the geometrical method which was applied in an *ad hoc* manner in C can be shown rigorously to give a unique solution for data with nonnegative potential vorticity under certain conditions on the physical domain. The method is also shown to be applicable to the three-dimensional equations derived by Hoskins and Draghici (1977) using the geostrophic momentum approximation. The method allows a number of additional properties of fronts to be deduced, for instance, that a discontinuity in temperature and velocity cannot be formed even at a finite discontinuity of potential vorticity. This is a stronger result than that obtained by Hoskins and Bretherton. The results also mean that such flows are predictable of type 1 or 2 in the sense of Lorenz (1969). This means that the solutions are determined for all time by the initial and boundary conditions and are continuously dependent on the data. The latter requirement is essential if the neglected ageostrophic accelerations are to be small.

The second part presents further computational results. A model in which the two-dimensional semi-geostrophic equations are solved using finite differences is described. In this model the ageostrophic winds have to be determined iteratively. This has two purposes. It allows a direct comparison with finite difference integrations of the primitive equations. Some of the differences reported in C may have simply represented the difference between two types of computational method, despite the use of very high resolution. Secondly, since artificial viscosity has to be added to the

semi-geostrophic equations when solved by finite differences, we can check the agreement between the inviscid Lagrangian solution described in C and a slightly viscous solution. This is important because an inviscid solution can only be regarded as physically useful if it is the limit as the viscosity tends to zero of a viscous solution.

Comparisons between solutions obtained by the Lagrangian construction and the two finite difference models are presented. The same values for the artificial viscosity are used in both cases. The results show closer agreement between the finite difference semi-geostrophic solution and the Lagrangian solution than between the two finite difference solutions. The largest vertical velocities are concentrated nearer the boundary in the semi-geostrophic solution.

The most important qualitative difference between the semi-geostrophic and primitive equation solutions is in the handling of the upper and lower boundary conditions. The Lagrangian theory gives a unique solution if the rigid wall boundary conditions are interpreted as meaning only that no fluid can cross the boundary. If the requirement is that fluid initially in contact with the boundary remains there, then no solution exists. Therefore fluid has to be squeezed away from the boundaries by lateral motions: in effect, the boundary is drawn into the fluid. In the primitive equation model the vertical velocity is zero at the boundary and so fluid cannot move away from it. Therefore, at least one of the Lagrangian conservation properties cannot be satisfied.

In reality, this need not be such a contradiction. A real fluid would not contain an actual discontinuity and the conservation laws would not be valid for every fluid particle. If the discontinuity is replaced by a shear layer, the kinematic boundary condition can be satisfied. The semi-geostrophic results suggest a tendency for a separation effect at the boundary. The physical correctness of this prediction can only be checked by tests against real data. It is tempting but speculative to relate it to the occlusion process.

## 2. Basic theory for the two-dimensional deformation model

### a. Basic equations

Consider the dimensionless Lagrangian form of the equations used for the deformation model introduced by Hoskins and Bretherton (1972) and studied in C. These are

$$\left. \begin{aligned} \frac{DM}{Dt} + \alpha M &= 0 \\ \frac{D\theta}{Dt} &= 0 \\ \frac{DA}{Dt} + \alpha A &= 0 \end{aligned} \right\} \quad (2.1)$$

where

$$\frac{D}{Dt} = \frac{\partial}{\partial t} + u \frac{\partial}{\partial x} + w \frac{\partial}{\partial z}$$

$$M = v + x$$

and  $\alpha$  is a given deformation rate:  $M$  is called the potential momentum and  $A$  is the area of a fluid element in the  $(x, z)$  plane. The coordinate  $z$  is a function of pressure as defined in the preceding references. The equations for cross-front geostrophic balance and the hydrostatic equation give

$$\left. \begin{aligned} \frac{\partial \phi}{\partial x} &= v \\ \frac{\partial \phi}{\partial z} &= \theta \end{aligned} \right\} \quad (2.2)$$

The problem is to be solved in a closed convex region  $\Omega$  with rigid upper and lower boundaries at  $z = 0, 1$ . Since fluid elements shrink with the basic deformation rate, it is convenient to consider a domain in the  $(x, z)$  plane which also shrinks at this rate, so we suppose that the boundary conditions in  $x$  are rigid walls at

$$x = \pm e^{-\alpha t} \quad (2.3)$$

*b. Smooth solutions*

It is convenient to start by recalling some standard analysis of the solutions of (2.1) assuming that they are differentiable. In this case the potential vorticity

$$q = \frac{\partial(M, \theta)}{\partial(x, z)} \quad (2.4)$$

is conserved following the motion:

$$\frac{Dq}{Dt} = 0 \quad (2.5)$$

We introduce a modified pressure variable

$$P = \phi + \frac{1}{2} x^2 \quad (2.6)$$

Then

$$(M, \theta) = \left( \frac{\partial P}{\partial x}, \frac{\partial P}{\partial z} \right) \quad (2.7)$$

Defining the Hessian matrix as

$$Q = \begin{bmatrix} \frac{\partial^2 P}{\partial x^2} & \frac{\partial^2 P}{\partial x \partial z} \\ \frac{\partial^2 P}{\partial z \partial x} & \frac{\partial^2 P}{\partial z^2} \end{bmatrix} \quad (2.8)$$

then

$$q = \det(Q) \quad (2.9)$$

This matrix is of special importance in determining the ageostrophic circulation  $(u, w)$  and the pressure tendency  $\Gamma = \partial \phi / \partial t$ . For example, we have

$$\nabla \Gamma + Q \cdot u = b, \quad (2.10)$$

where  $\nabla = (\partial/\partial x, \partial/\partial z)$ ,  $u = (u, w)$ ,  $b = (-\alpha \partial P / \partial x, 0)$ . The continuity equation

$$\frac{\partial u}{\partial x} + \frac{\partial w}{\partial z} + \alpha = 0 \quad (2.11)$$

can be used to eliminate the velocity components to give

$$\nabla \cdot (Q^{-1} \cdot \nabla \Gamma) = \alpha + \nabla \cdot Q^{-1} \cdot b \quad (2.12)$$

This equation can be solved; i.e., subject to suitable boundary conditions, provided that it is elliptic, implying that  $Q$  is positive definite. In some circumstances (2.12) can be solved when  $Q$  is singular by using an integrated form of the continuity equation (integrated along the line of the characteristics between opposite boundaries), but the problem is ill-posed when  $Q$  has a negative eigenvalue. In the latter case, the physical system would be subject to convective, inertial or symmetric instability; it would not be properly describable by the semi-geostrophic equations because acceleration components then become of comparable magnitude to the corresponding pressure gradient forces.

The following geometric picture of this constraint is important. Regard  $P(x, z)$  as the elevation of a surface above the  $(x, z)$  plane. Then  $Q$  gives the curvature components of the surface, in the case where  $P$  varies slowly with  $x$  and  $z$ . Thus the potential vorticity  $q$  is essentially proportional to the Gaussian curvature of the surface. The condition that  $Q$  has no negative eigenvalues, assuming that  $P$  is twice differentiable, is equivalent to stating that the surface  $P(x, z)$  is convex when viewed from below. It will be shown that this geometrical interpretation can be used in cases where the solutions are not differentiable.

*c. Discontinuous solutions*

In C it was demonstrated that, for simple piecewise constant initial data, a solution of (2.1) and (2.2) could be constructed by geometry. The construction is illustrated in Fig. 1. The values of  $M$  and  $\theta$  are constant on each element, and the slope of the line separating the elements in the  $(x, z)$  plane is given by the geostrophic and hydrostatic relations by the formula first pointed out by Margules in 1906

$$\frac{[M]}{[\theta]} \quad (2.13)$$

The solution then appeared to be uniquely specified by the areas of the elements, the values of  $M$  and  $\theta$  within them, and the condition that the solution is statically stable.

The modified pressure  $P$  defined by (2.6) can be used for piecewise constant data also. The surface  $P(x, z)$  is now made up of flat faces on which  $\partial P / \partial x$  and  $\partial P / \partial z$  are constant. If  $P$  is continuous, the jump condition (2.13) is automatically satisfied for the edges

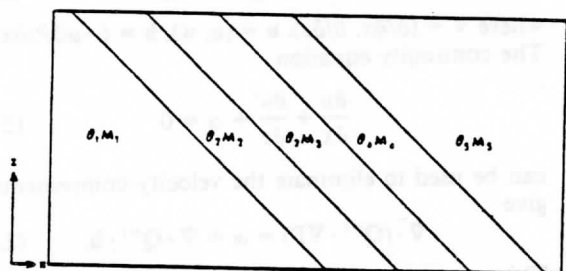


FIG. 1. Piecewise constant solution to the deformation problem.

where faces join. The surface corresponding to the solution in Fig. 1 is shown in Fig. 2. The condition that the solution in physical space is statically stable becomes a condition that the surface  $P(x, z)$  is convex viewed from below. This suggests that the convexity condition can be used as a condition for dynamical stability for solutions not differentiable everywhere, instead of the potential vorticity which is difficult to define. By using convexity to define dynamical stability we find it is then possible to prove a rigorous existence theorem for piecewise constant solutions of (2.1) and (2.2). In this paper a somewhat intuitive version of the proof is given; a more rigorous treatment will be given elsewhere [Purser and Cullen (in preparation)].

d. Definitions and consequences

A solution of the semi-geostrophic problem (2.1), (2.2) is called dynamically stable if the associated surface  $P(x, z)$  is convex (viewed from below), i.e., the region in  $R^3$  with coordinates  $(x, z, S)$  defined by

$$S \geq P(x, z), \tag{2.14}$$

is a convex subspace of  $R^3$ .

Write the convex subspace defined by (2.14) as  $V$ . Then  $V$  has the following properties (e.g., see Rockafellar, 1970):

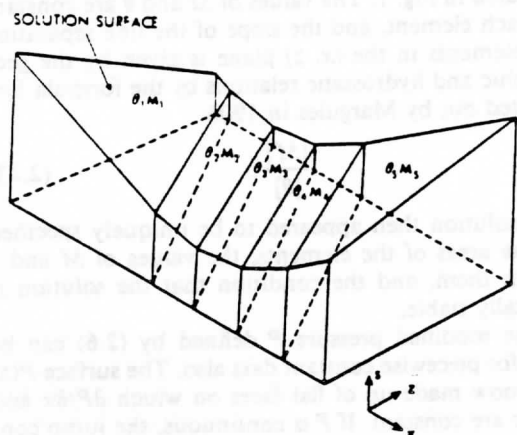


FIG. 2. Solution surface  $P(x, z)$  corresponding to solution in Fig. 1.

1)  $V$  can be represented as the intersection of half spaces

$$L(x) \geq 0, \tag{2.15}$$

where  $L$  is a linear function of  $x$ . The planes

$$L(x) = 0 \tag{2.16}$$

are called tangent planes of  $V$ .

2) Every point on the boundary of  $V$  has at least one tangent plane touching it.

e. Theorem 1

The problem (2.1), (2.2) in  $\Omega$  has a unique dynamically stable solution for all time given bounded piecewise constant initial data for  $M$  and  $\theta$  at  $t = 0$ . The solution is continuously dependent on the initial data.

Proof—basic construction

This theorem is proved by explicit construction of the surface  $P(x, z)$ . The essential step is shown in Fig. 3. Given the region  $\Omega$  in the  $(x, z)$  plane, consider an infinite extension of it in the  $S$  coordinate to a convex cylindrical surface  $V$  in  $R^3$  (Fig. 3a). Now construct a convex surface  $Y$  as the successive intersection of planes

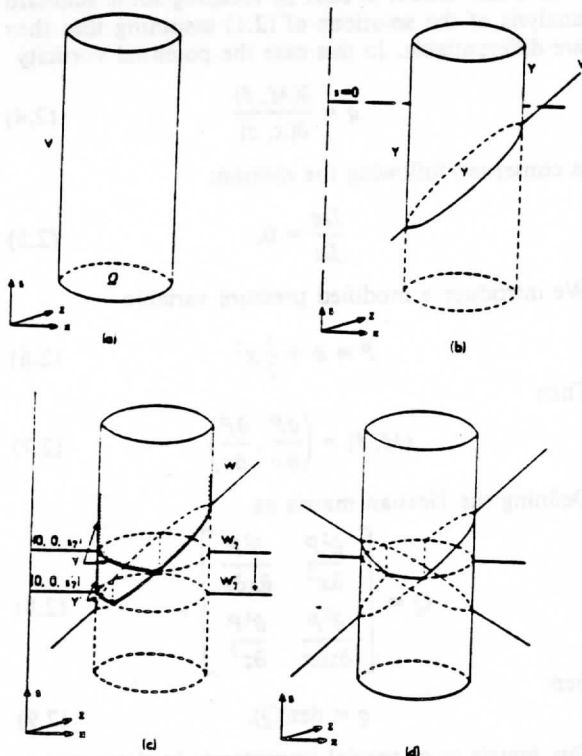


FIG. 3. Construction of surface  $P(x, z)$ : (a) infinite cylinder  $V$  with cross section  $\Omega$ . (b) intersection of plane  $W$ , of given slope with the cylinder  $V$ . (c) effect of changing the  $S$  coordinate of the plane  $W$  from  $S_1$  to  $S_2$ , giving convex surfaces  $Y$  and  $Y'$ . (d) final arrangement with several intersecting planes

$W_i$  with  $V$ , subject to the condition that the planes are not perpendicular to the plane  $S = 0$ . (Fig. 3b). The angle of each plane  $W_i$  with the  $S$  axis is specified. At each stage the lower boundary of  $Y$ , denoted  $Y_i$ , is a piecewise flat convex surface. If the planes  $W_i$  are moved up and down, the areas of those parts of  $Y_i$  which have a given tangent plane change (Fig. 3c).

Suppose the initial data are given in the form of a list  $(M_i, \theta_i, A_i)$  of values of  $M$  and  $\theta$  on finite elements with areas  $A_i$  in the  $(x, z)$  plane. Suppose that

$$\sum_{i=1}^n A_i = \text{area of } \Omega. \quad (2.17)$$

Then at any future time  $t$ , we seek to arrange the elements with values of  $(M, \theta)$  given by  $(M_i e^{-\alpha t}, \theta_i)$  by (2.1) and areas  $A_i e^{-\alpha t}$  so that the continuity equation is satisfied. This is done by associating the  $i$ th element with a plane  $W_i$  with gradient

$$\left. \begin{aligned} \frac{\partial P}{\partial x} &= v + x = M_i \\ \frac{\partial P}{\partial z} &= \theta = \theta_i \end{aligned} \right\} \quad (2.18)$$

and seeking to construct the surface  $Y$  in Fig. 3 such that the area of the face of  $Y$  formed by the plane  $W_i$  is  $A_i$ . Since the angle of each plane  $W_i$  with the  $S$ -axis is fixed by (2.13), the areas can be changed only by moving the  $W_i$  up and down. The remainder of the proof shows how this is done.

An arrangement of the planes  $W_i$  can be uniquely defined by specifying their  $S$  coordinates at  $x = z = 0$  (Fig. 4).

*f. Lemma*

Any increase in  $S_k$  with  $S_i$  ( $i \neq k$ ) and  $M_i, \theta_i$  all kept constant will result in an increase in the area  $A_k$  bal-

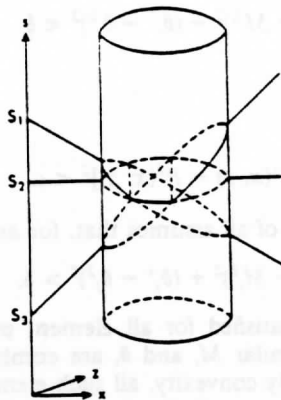


FIG. 4. Definition of intersection of planes with the cylinder  $V$  in terms of  $S$  coordinates of planes.

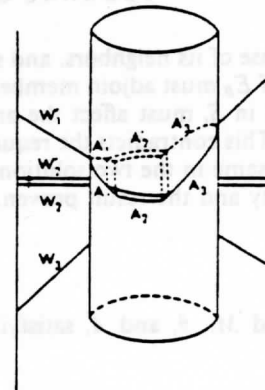


FIG. 5. Effect of a perturbation to the  $S$  coordinate of the plane  $W_2$ .

anced by a decrease in the areas of each of the neighboring faces.

*Proof*

This follows immediately from the convexity of the surface  $Y$ . The effect of a perturbation in  $S_2$  is shown in Fig. 5.

The area  $A_2$  changes monotonically with the same sign.

*g. Uniqueness*

Given the values of  $M_i, \theta_i$  and  $A_i$ , then if a solution characterized by the coordinates  $S_i$  exists, it is unique within a uniform change in all the  $S_i$ .

*Remark*

The fact that  $\Omega$  is convex is essential for this result.

*Proof*

Suppose two solutions, represented by surfaces  $Y_1$  and  $Y_2$ , exist. Suppose that the associated coordinates are  $S_i^1$  and  $S_i^2$ . Calculate the differences  $(S_i^2 - S_i^1)$ . Divide the planes  $W_i$  into two sets,  $E_A$  and  $E_B$ .  $E_A$  contains the planes for which  $S_i^2 - S_i^1$  attains its maximum value, say  $\delta$ .  $E_B$  contains the remainder. Because there are a finite number of planes,  $E_A$  contains at least one member. If the theorem is true, then  $E_B$  must be empty so that  $S_i^2$  can be obtained from  $S_i^1$  by the simple translation

$$S_i^2 = S_i^1 + \delta. \quad (2.19)$$

Suppose, conversely, that  $E_B$  is not empty. Then, after carrying out the translation (2.19), all the coordinates of members of  $E_A$  in the two solutions agree, and  $S_i^2 < S_i^1$  for all members of  $E_B$ . Conversion of  $Y_1$  to  $Y_2$  now requires negative changes to all the  $S_i$  associated with  $E_B$ , while preserving the areas of all the faces. Since the area of a face changes monotonically with

its  $S_i$  at the expense of its neighbors, and since at least some members of  $E_B$  must adjoin members of  $E_A$ , the required changes in  $S_i$  must affect the areas of these members of  $E_A$ . This contradicts the requirement that the areas are the same in the two solutions. Therefore  $E_B$  must be empty and the result proven.

*h. Existence*

Given bounded  $M_i$ ,  $\theta_i$ , and  $A_i$  satisfying (2.17), a solution exists.

*Proof*

We construct a first guess by assigning arbitrary coordinates to planes  $W_i$  with the correct slope and constructing the surface  $Y$ . The areas of the intersections of  $W_i$  with  $Y$  need not be correct and some planes may not intersect  $Y$  at all. We then adjust the coordinates  $S_i$  iteratively to obtain the correct areas. At some stage of the iteration, assume that we have a set of coordinates  $S = \{S_i\}$  yielding areas  $A' = \{A'_i\}$ . Some of the  $A'_i$  may be zero. We define the error norm

$$N_2(S) = \sum_{i=1}^n |A_i - A'_i|^2 \tag{2.20}$$

Because  $M_i$  and  $\theta_i$  are bounded, the planes  $W_i$  cannot be perpendicular to the plane  $S = 0$ . Since there are a finite number of planes, they must all intersect each other and the surface  $V$  at a finite angle. (If two planes are parallel, then  $M_i = M_j$ ,  $\theta_i = \theta_j$  and their associated areas can be combined). Therefore all possible intersections of the planes  $W_i$  with  $V$  can be obtained within a finite range of  $S$ , as can be seen from Fig. 4.

Therefore, for some  $S = S_0$ ,  $N_2(S)$  attains its minimum. Write the associated values of  $(A'_i - A_i)$  as  $\mathcal{E}_i$ .

We divide the elements into two sets,  $E_a$  and  $E_b$ :  $E_a$  contains elements for which  $\mathcal{E}$  is the maximum  $\mathcal{E}_a$ ;  $E_b$  contains the remainder. Then since  $N_2(S)$  has been minimized, if  $E_b$  is not empty, at least one member  $k$  of  $E_a$  adjoins members of  $E_b$ . Element  $k$  may also adjoin other elements of  $E_a$ . By reducing  $S_k$  we can reduce  $\mathcal{E}_k$  by an arbitrary amount: say  $(a + b)$ . By doing so we increase the combined areas of other elements by  $(a + b)$ . Suppose that the areas of elements in  $E_a$  are increased by a total amount  $a$  and in  $E_b$  by a total amount  $b$ . The resulting change  $\Delta N_2$  in  $N_2$  comprises three parts: 1)  $\Delta N_2^{(a)}$  due to changes in areas of elements in  $E_a$  excluding  $k$ , 2)  $\Delta N_2^{(k)}$  due to the change in the area of element  $k$  and 3)  $\Delta N_2^{(b)}$  due to changes in members of  $E_b$ . We let  $\mathcal{E}_a$  be the maximum error for members of  $E_b$ ; then, by definition,  $\mathcal{E}E_b < \mathcal{E}_a$ . Using the simple inequality, for positive  $a_i$ :

$$(\Sigma(A_i + a_i)^2 - \Sigma A_i^2) \leq (\text{Max} A_i + \Sigma a_i)^2 - (\text{Max} A_i)^2 \tag{2.21}$$

Then it follows that

$$\begin{aligned} \Delta N_2^{(a)} &\leq 2\mathcal{E}_a a + a^2 \\ \Delta N_2^{(k)} &\leq 2\mathcal{E}_k b + b^2 \\ \Delta N_2^{(b)} &= -2\mathcal{E}_a(a + b) + a^2 + b^2 + 2ab \end{aligned} \tag{2.22}$$

Hence

$$\Delta N_2 \leq -2(\mathcal{E}_a - \mathcal{E}_k)b + 2(a^2 + b^2 + ab) \tag{2.23}$$

Since the rate at which the area of an element changes with respect to its  $S$  coordinate is bounded, it is always possible to find a change in  $S$  and, hence,  $a$  and  $b$  which is sufficiently small such that

$$(\mathcal{E}_a - \mathcal{E}_k)b > (a^2 + b^2 + ab), \tag{2.24}$$

and so  $\Delta N_2 < 0$ . Therefore,  $E_b$  must be a null set and so the errors  $\mathcal{E}_i$  in the areas of all the segments are equal. Since they sum to zero, they must all vanish. Therefore the desired solution of the problem has been obtained.

*i. Continuity*

The solution, characterized by the set of coordinates  $\{S_i\}$ , depends continuously on  $M_i$ ,  $\theta_i$ , and  $A_i$ .

*Proof*

Only an intuitive proof is given here, since a rigorous proof requires considerable care. It is clear that, since  $M_i$  and  $\theta_i$  are represented in (2.18) by the components of the gradient of the solution  $P(x, z)$ , we can consider perturbations in  $M_i$  and  $\theta_i$  together and treat perturbations in  $A_i$  separately.

Given an arbitrarily small quantity  $\epsilon$ , which measures a change in the coordinates  $\{S_i\}$  of the planes making up  $P(x, z)$ , we seek to find a  $\delta$  such that, for any two sets of data satisfying

$$\sum_{i=1}^n (M_i^1 - M_i^2)^2 + (\theta_i^1 - \theta_i^2)^2 < \delta \tag{2.25}$$

$$A_i^1 = A_i^2$$

we have

$$\int [P^1(x, z) - P^2(x, z)]^2 < \epsilon \tag{2.26}$$

The proof first of all assumes that, for any  $i$  and  $j$ ,

$$(M_i^1 - M_j^2)^2 + (\theta_i^1 - \theta_j^2)^2 > \delta \tag{2.27}$$

If (2.27) is not satisfied for all element pairs, then elements with similar  $M_i$  and  $\theta_i$  are combined into larger elements. By convexity, all such elements with almost equal slopes must be contiguous on the solution surface. Once (2.27) is satisfied, then a perturbation to the slope of any one element will not change its position on the solution surface (Fig. 6). Thus the effect

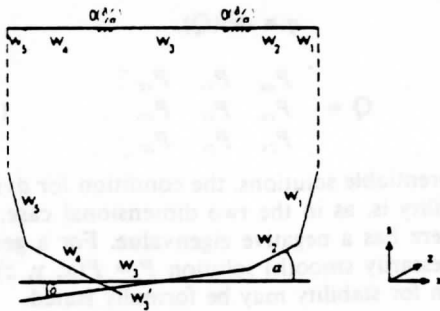


FIG. 6. Effect of a small change in the slope of  $w_3$ ; the slopes of all the planes are distinct.

on  $P(x, z)$  is localized and can be estimated in terms of the size of the perturbation  $\delta$  and the maximum linear dimension of the region. This is because  $P^1(x, z)$  and  $P^2(x, z)$  have gradients everywhere which either differ by less than  $\delta$  or differ by a larger amount  $\alpha$ , representing the difference in slope between adjoining elements, on a region of size  $\delta/\alpha$ , where the interelement boundaries have moved in  $(x, z)$  space (Fig. 7). A similar argument proves that combining elements with nearly equal slopes so that (2.26) is satisfied has a small effect on  $P(x, z)$ .

j. General initial data

The theorem that has been proved establishes the existence of a bounded solution to (2.1-2.3) for general piecewise constant initial data. If the initial data can be approximated to arbitrarily high accuracy by a piecewise constant field, then a corresponding sequence of approximate solutions can be generated. Provided that these can be bounded independently of the degree of approximation, they will converge to a limit which is the solution for general initial data. While it seems clear that any meteorologically relevant data satisfy this condition, provided turbulent regions are not resolved, the correct mathematical conditions are not obvious.

3. Three-dimensional semi-geostrophic theory

a. Basic equations

The three-dimensional equations are the natural generalization of the two-dimensional set studied in the previous section. The potential momentum now has two components  $M$  and  $N$ , closely associated with "geostrophic coordinates"  $X$  and  $Y$ , which change nontrivially in time. A detailed study of the equations is given in Hoskins and Draghici (1977). The essential dimensionless problem, where the  $f$ -plane and Bousinesq approximations have been made, is

$$\left. \begin{aligned} \frac{Du_x}{Dt} - v_{ax} &= 0 \\ \frac{Dv_x}{Dt} + u_{ax} &= 0 \\ \frac{D\theta}{Dt} &= 0 \end{aligned} \right\} \quad (3.1)$$

with

$$\frac{\partial u}{\partial x} + \frac{\partial v}{\partial y} + \frac{\partial w}{\partial z} = 0 \quad (3.2)$$

$$v_x = \frac{\partial \phi}{\partial x}, \quad -u_x = \frac{\partial \phi}{\partial y}, \quad \theta = \frac{\partial \phi}{\partial z}$$

where

$$\left. \begin{aligned} \frac{D}{Dt} &= \frac{\partial}{\partial t} + (u_x + u_{ax}) \frac{\partial}{\partial x} + (v_x + v_{ax}) \frac{\partial}{\partial y} + w \frac{\partial}{\partial z} \\ u &= u_x + u_{ax}, \quad v = v_x + v_{ax} \end{aligned} \right\} \quad (3.3)$$

We define

$$\left. \begin{aligned} M &= v_x + x \\ N &= -u_x + y \end{aligned} \right\} \quad (3.4)$$

Then

$$\left. \begin{aligned} \frac{DM}{Dt} &= u_x \\ \frac{DN}{Dt} &= v_x \end{aligned} \right\} \quad (3.5)$$

The set (3.5) can be rewritten in the form

$$\left. \begin{aligned} \frac{\partial M}{\partial t} + u_x \cdot \nabla M + u_{ax} \cdot \nabla M &= u_x \\ \frac{\partial N}{\partial t} + u_x \cdot \nabla N + u_{ax} \cdot \nabla N &= v_x \\ \frac{\partial \theta}{\partial t} + u_x \cdot \nabla \theta + u_{ax} \cdot \nabla \theta &= 0 \end{aligned} \right\} \quad (3.6)$$

where

$$\left. \begin{aligned} u_x &= (u_x, v_x, 0) \\ u_{ax} &= (u_{ax}, v_{ax}, w) \end{aligned} \right\} \quad (3.7)$$

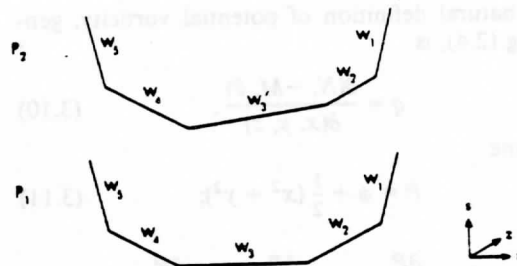


FIG. 7. Effect on the interelement boundaries of a change in slope of  $w_3$ .



and we have

$$\begin{aligned} \frac{\partial u_g}{\partial x} + \frac{\partial v_g}{\partial y} &= 0 \\ \frac{\partial u_{ag}}{\partial x} + \frac{\partial v_{ag}}{\partial y} + \frac{\partial w}{\partial z} &= 0 \end{aligned} \quad (3.8)$$

These equations can be solved by a splitting technique, as is often used in primitive equation models (e.g., Gadd, 1978). Suppose that at any given time, the value of  $\phi$  is known everywhere. Then  $\theta$ ,  $M$  and  $N$  are determined as the gradients of  $\phi$  by the geostrophic and hydrostatic relations (3.2) and the definitions (3.4). The ageostrophic wind is implicitly determined by the equations of motion (3.6) and the requirement that  $\partial M/\partial t$ ,  $\partial N/\partial t$  and  $\partial \theta/\partial t$  must be related by the geostrophic and hydrostatic relations. This can be achieved by regarding the fluid at the given time as made up of elements, each with a definite value of  $M$ ,  $N$  and  $\theta$ . In the first step of the solution, the values of  $M$  and  $N$  are updated by  $u_g \Delta t$  and  $v_g \Delta t$ , where  $\Delta t$  is the time-step; and the elements are then advected into new positions by the geostrophic wind. The behavior of this part of the equations can be analyzed by considering the associated ordinary differential equations following fluid elements:

$$\begin{aligned} \frac{dM}{dt} &= y - N \\ \frac{dN}{dt} &= M - x \end{aligned} \quad (3.9)$$

On a doubly periodic domain,  $x$  and  $y$  are bounded; and the part of the solution of (3.9) which depends on  $M$  and  $N$  is just an oscillation. Therefore there is unlikely to be any difficulty in this part of the solution to (3.6).

The remainder of (3.6) describes advection by an unknown wind  $u_{ag}$  satisfying the incompressibility condition (3.8), so that fluid elements are moved without change of volume or of their values of  $M$ ,  $N$  and  $\theta$  to new positions such that the geostrophic and hydrostatic relations are satisfied. We now prove the existence of such an incompressible ageostrophic wind field.

#### b. Existence of implied ageostrophic circulation

The natural definition of potential vorticity, generalizing (2.4), is

$$q = \frac{\partial(N, -M, \theta)}{\partial(x, y, z)} \quad (3.10)$$

We define

$$P = \phi + \frac{1}{2}(x^2 + y^2); \quad (3.11)$$

then

$$M = \frac{\partial P}{\partial x}, \quad N = \frac{\partial P}{\partial y}, \quad \theta = \frac{\partial P}{\partial z} \quad (3.12)$$

Hence

$$q = \det(Q),$$

where

$$Q = \begin{bmatrix} P_{xx} & P_{xy} & P_{xz} \\ P_{yx} & P_{yy} & P_{yz} \\ P_{zx} & P_{zy} & P_{zz} \end{bmatrix} \quad (3.13)$$

For differentiable solutions, the condition for dynamical stability is, as in the two dimensional case, that  $Q$  nowhere has a negative eigenvalue. For a general (not necessarily smooth) solution  $P = P(x, y, z)$ , the condition for stability may be formally stated.

#### Definition

A solution of the three-dimensional semi-geostrophic equations is called dynamically stable within the  $(x, y, z)$  domain  $D$ ; if the hypersurface in  $(x, y, z, S)$  space defined by  $S \geq P(x, y, z)$  is convex.

#### Theorem 2

Inside a convex three-dimensional domain  $D$ , there is a unique arrangement of a given finite collection of elements of the fluid, each with uniform prescribed values  $M_i$ ,  $N_i$  and  $\theta_i$ , and volumes  $\tau_i$ , that is dynamically stable provided that

$$\sum_i \tau_i = \tau_D,$$

where  $\tau_D$  is the volume of  $D$ .

#### Proof

This is identical to the proofs of existence and uniqueness for the two-dimensional problem in Section 2, since convexity is an  $n$ -dimensional property.

#### Remarks

The proofs of continuous dependence on the data and extensions to general initial data are also identical to the two-dimensional case.

#### 4. Further results

The theorems proved in the previous two sections show that a great deal can be inferred about the solution of the Lagrangian conservation law form for the semi-geostrophic equations from geometrical arguments, in particular the identification of dynamically stable solutions with convexity of the solution surface. These arguments can be used to establish a number of additional results, some of which are described in this section. They will be stated for the two-dimensional problem so that the arguments behind them can be easily illustrated by accompanying diagrams. Similar results hold in three dimensions.

a. Nonexistence of internal fronts

Theorem 3

If the potential vorticity is bounded, solutions to the semi-geostrophic equations cannot possess localized internal discontinuities in  $M$  and  $\theta$ . Any discontinuities must intersect the boundary of the domain.

Proof

The preceding results show that there is a unique convex solution surface  $P(x, z)$ . The gradients of this surface are  $M$  and  $\theta$ . Suppose that its gradient changes discontinuously at some isolated point. By changing coordinates, this can be treated as the origin. Thus suppose that at  $(0, 0)$   $\nabla P$  changes from  $(-g, 0)$  to  $(g, 0)$  and that  $P(0, 0) = 0$ . As  $x$  decreases from zero, the convexity of  $P$  means that  $\partial P/\partial x$  must decrease from  $-g$  and so  $P$  must satisfy

$$\begin{aligned} P(x, z) &\geq -gx, & x < 0 \\ P(x, z) &\geq gx, & x \geq 0 \end{aligned} \quad (4.1)$$

The magnitude of  $\nabla P$  must increase as  $x$  moves away from the origin and so

$$\nabla P(x) \cdot x \geq P(x) \quad \text{for all } x = (x, z). \quad (4.2)$$

Consider the rectangular circuit  $ABCD$  shown in Fig. 8a, whose dimension  $l$  is chosen such that on segment  $BC$

$$P(x) \geq g\delta. \quad (4.3)$$

It must be possible to satisfy this condition because the discontinuity at the origin is isolated. At each point on  $ABCD$ , inequality (4.2) defines a set of values which cannot be taken by the gradients of  $P$ . This is shown as a region in gradient space in Fig. 8b. Therefore, the potential circulation

$$C(\delta, l) = \int_{ABCD} q dx dz$$

around  $ABCD$  is greater than that defined by the region in Fig. 8; i.e.,

$$C(\delta, l) \geq g^2 \delta / l. \quad (4.4)$$

However, since the potential vorticity everywhere is bounded, say by  $q_{\max}$ , and the area of circuit  $ABCD$  is  $2l\delta$ , then

$$\begin{aligned} q &\leq q_{\max} \\ l^2 &\geq g^2 / q_{\max} \end{aligned} \quad (4.5)$$

Conversely, for any  $l$ , with  $|l| < gq_{\max}^{-1/2}$ ,  $q \leq q_{\max}$  implies that

$$P(x, z) \leq g\delta \quad (4.6)$$

somewhere on  $BC$  for all  $\delta$ . Hence,

$$P(0, l) = 0 \quad (4.7)$$

if  $|l| < gq_{\max}^{-1/2}$ . Eqs. (4.1) and (4.7) together imply that the discontinuity in gradient must extend from the

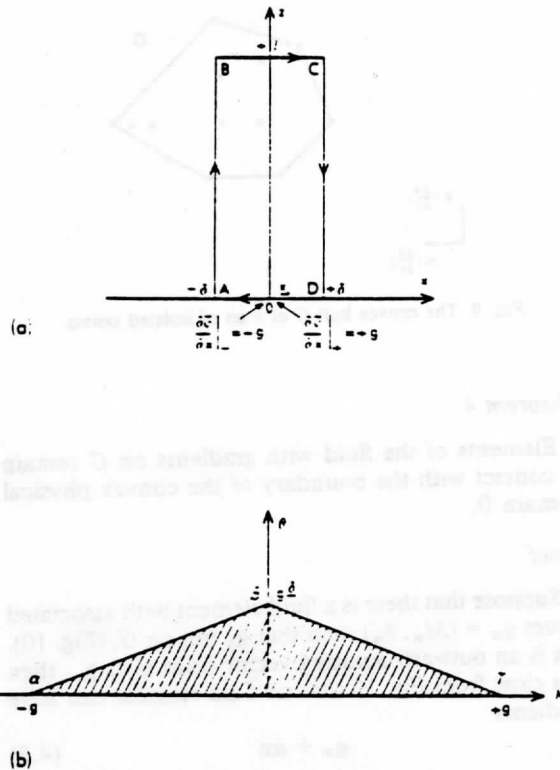


FIG. 8. (a) definition of the circuit  $ABCD$  in real space for Theorem 3. (b) associated region in gradient space from which values of gradients on the circuit  $ABCD$  referred to by Theorem 3 are excluded.

origin to  $\pm gq_{\max}^{-1/2}$  along the  $z$  axis. This argument can be repeated at the ends of this line segment to continue it as far as the boundary, thus completing the proof.

Analogous constructions may be made in the three-dimensional equations of Hoskins and Draghici (1977), initially by replacing circuit  $ABCD$  by the surface of a disc formed by rotating  $ABCD$  about  $AD$ . The corresponding excluded region of gradient space is the double-cone formed by rotating triangle  $\alpha\beta\gamma$  about  $\alpha\gamma$ .

This theorem is a stronger statement than that in Hoskins and Bretherton (1972, p. 16) as it prohibits fronts even at a finite discontinuity of potential vorticity.

b. Behavior of fluid elements on the boundary

Consider the case used to prove the theorem in Section 2, where the data are piecewise constant and defined by values  $M_i$  and  $\theta_i$  on elements of area  $A_i$ .

Definition

The "convex hull" of a set is the smallest convex set containing it. The convex hull of the set of points in gradient space with coordinates  $(M_i, \theta_i)$  is shown in Fig. 9, denote its boundary by  $G$ .

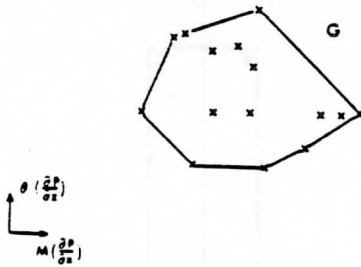


FIG. 9. The convex hull  $G$  of a set of isolated points.

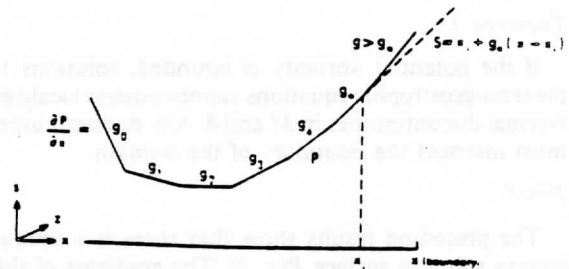


FIG. 11. Contradiction obtained if element with gradient on  $G$  is not in contact with the boundary in physical space.

**Theorem 4**

Elements of the fluid with gradients on  $G$  remain in contact with the boundary of the convex physical domain  $\Omega$ .

*Proof*

Suppose that there is a fluid element with associated values  $g_* = (M_*, \theta_*)$  such that  $g_*$  lies on  $G$ , (Fig. 10). If  $n$  is an outward pointing vector from  $G$  at  $g_*$ , then it is clear from Fig. 10 that no fluid element can have gradients

$$g_* + \alpha n \tag{4.8}$$

for any positive  $\alpha$ . Suppose that this fluid element is not in contact with the boundary of the physical domain. Let  $x_*$  be a point in the element. Then, the convexity of the solution surface means that

$$\frac{\nabla P(x) \cdot (x - x_*)}{|x - x_*|}$$

increases as  $|x - x_*|$  increases. Thus if  $(x - x_*)$  is chosen to be parallel to  $n$ ,  $\nabla P(x)$  must take on values of the form (4.8) with  $\alpha > 0$  (Fig. 11). This contradicts the hypothesis, and proves that the element must be in contact with the boundary.

Note that this does not mean that elements of the fluid originally on the boundary of the physical domain  $\Omega$  remain there.

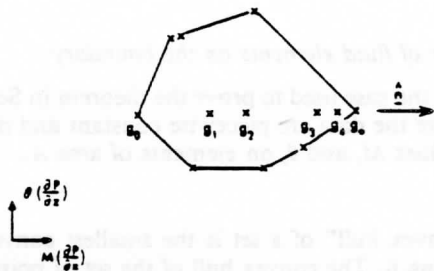


FIG. 10. The extreme values of the gradient  $(M, \theta)$  along a line parallel to  $n$  are obtained where that line intersects  $G$ .

*c. Characterization of data leading to frontogenesis*

The process of frontogenesis studied here involves the pinching together of boundary points of the fluid, usually followed by the intrusion of the resulting contact discontinuity into the interior of the domain. When the initial potential vorticity is bounded, the possible locations of frontogenesis are restricted by the following theorem:

**Theorem 5**

Given initial values of  $M$  and  $\theta$  which are continuous functions of  $(x, z)$  and bounded potential vorticity  $q$ . The values of  $(M, \theta)$  for all points in  $\Omega$  define a region  $\mathcal{R}$  in  $(M, \theta)$  space with boundary  $\Gamma$  (Fig. 12). Then frontogenesis can only occur at points  $(x, z)$ , where associated values of  $(M, \theta)$  are on a concave portion of  $\Gamma$ . If  $\Gamma$  is convex, then  $M$  and  $\theta$  remain continuous functions of  $(x, z)$ .

*Proof*

Because of the convexity of the solution surface  $P(x, z)$  and the continuity of the initial data, points not on the boundary of  $\Omega$  have gradients strictly inside the region  $\mathcal{R}$  in  $(M, \theta)$  space. This follows immediately from Theorem 4. If a discontinuity forms at a later time, this corresponds to a fold in the solution surface where the gradients necessary to smooth out the fold are not in  $\mathcal{R}$ . Suppose that the points either side of the intersection of the front with the boundary of  $\Omega$  are  $g_1$  and  $g_2$ ; these must both be on  $\Gamma$  in gradient space (Fig. 13). Then the missing gradients lie on the straight line connecting  $g_1$  and  $g_2$ ; since they are not in  $\mathcal{R}$ , they must correspond to a concave portion of  $\Gamma$ . If  $\Gamma$  is everywhere convex, no discontinuity can form and  $P(x, z)$  stays smooth for all time.

This theorem generalizes the observation of Hoskins (1971, p. 143) that, in studies using the  $\tan^{-1}(x)$  profile of potential temperature, the surface front forms in the warmer half of the fluid and the upper front forms in the colder half of the fluid, as seen schematically in Fig. 14.

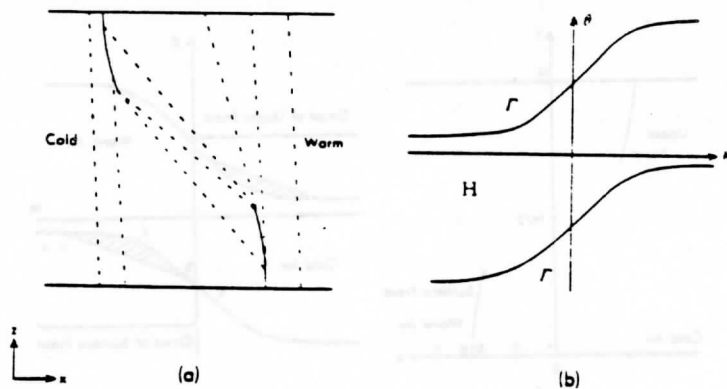


FIG. 12. (a) Typical isotherms in physical space associated with frontogenesis; (b) Associated region in gradient space, as required for Theorem 5.

#### d. Conservation of potential circulation

An important and rather paradoxical feature of these frontogenesis models concerns the total potential circulation  $C$  associated with a material cross section. Eqs. (2.1) suggest that  $C$  should obey the conservation law

$$\frac{D}{Dt} [C(t)e^{a\eta}] = 0, \quad (4.9)$$

where the circulation round any circuit can only be changed by the basic deformation field. This would certainly be the case if the circuit in  $(x, z)$  space associated with  $C$  were purely advected. However, if  $C$  is associated with a circuit at the domain boundary, (4.9) is no longer obeyed after a front forms because the injection of a new region of  $(M, \theta)$  space, the shaded area of Fig. 14b into the interior of the fluid acts like an impulsive line source of potential vorticity. Thus, while the potential vorticity is conserved following each fluid parcel, the Eulerian mean potential vorticity may change.

#### e. Nonconvex physical domains

The uniqueness of the solution to (2.1), (2.2) was proved only for convex physical domains  $\Omega$ . Since the  $z$  coordinate is a function of pressure, this corresponds to a convex domain in  $(x, p)$ . If the upper boundary is taken as  $p = 0$ , there is no problem there. The lower boundary will normally have concave portions where surface pressure is locally a maximum, e.g., in valleys. In these regions distinct fluid elements can be trapped and not interact with the rest of the solution. These correspond to trapped stable layers near the ground in mountain valleys, (Fig. 15). Any of these can be interchanged without affecting the rest of the solution.

The nonuniqueness only affects the rearrangement in Theorem 2. Uniqueness of the solution to the true physical problem is obtained by assuming that there is no sudden rearrangement of stable layers.

#### f. Dynamically unstable data

The theorems proved in Sections 2 and 3 give unique dynamically stable solutions. These can formally be found even from an initially given unstable configuration of the fluid. However, under these conditions, the assumptions implicit in the semi-geostrophic approximation are no longer valid, since large ageostrophic accelerations will be generated. The consequent rearrangement of fluid elements is thus unlikely to proceed realistically. Thus the theorems should not be used as a substitute for convective parameterizations.

### 5. Finite difference solutions of the slightly viscous semi-geostrophic equations

#### a. Basic requirement

The physical validity of the inviscid semi-geostrophic equations first breaks down because the Richardson number  $Ri$  falls below  $1/4$  and turbulent mixing with associated large accelerations sets in (Hoskins and Bretherton, 1972; Hoskins, 1982). If the effects of turbulence are, as usual in numerical models, represented by an eddy viscosity, then (2.1) becomes

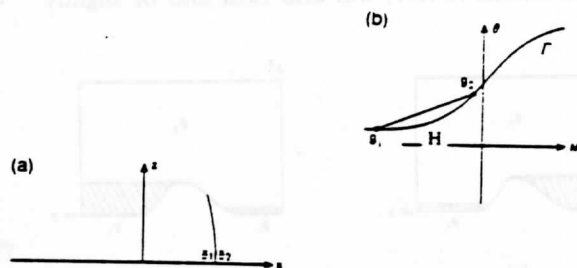


FIG. 13. Definitions of points associated with frontogenesis in the proof of Theorem 5 for (a) physical space and (b) gradient space.

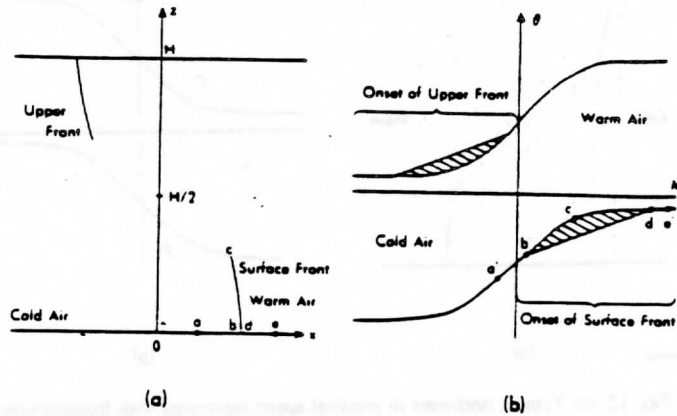


FIG. 14. (a) Schematic illustration of a stage in the growth of the frontal discontinuities for uniform potential vorticity. A  $\tan^{-1}(x)$  temperature profile is used in  $(x, z)$  space. (b) The same stage in gradient space. Points a, b, c, d, e correspond to points a, b, c, d, e in real space (Fig. 14a). The shaded regions correspond to the frontal discontinuities.

$$\left. \begin{aligned} \frac{DM}{Dt} + \alpha M &= \epsilon \nabla^2 M \\ \frac{D\theta}{Dt} &= \epsilon \nabla^2 \theta \\ \frac{DA}{Dt} + \alpha A &= 0 \end{aligned} \right\} \quad (5.1)$$

If  $\epsilon$  is chosen so that  $Ri > 1/4$  for all time, then scale analysis implies that the vorticity will remain less than  $10f$ , where  $f$  is the Coriolis parameter, and the neglect of the ageostrophic accelerations will remain valid for the "viscous" problem. In reality the neglected terms will be crucial in the detailed dynamics of the turbulent mixing. It is then hoped that the solution of (5.1), which will contain strong but smooth shear layers, will be a good "broad-brushed" approximation to the true solution of the primitive equations, which contain turbulent shear layers. Such approximations are routine in other areas of computational fluid dynamics, for instance, shock modeling.

It seems highly likely that, since the existence of solutions to the inviscid problem (2.1) has been proved, that solutions to (5.1) will also exist and be slightly

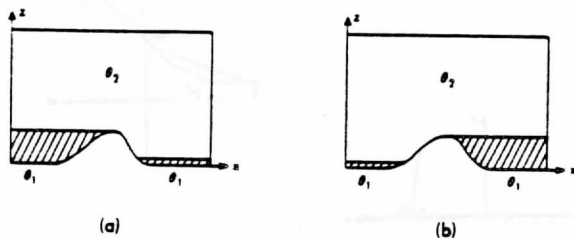


FIG. 15. A particular example of the nonuniqueness of solutions when the domain is not convex.  $M$  is uniform.  $\theta$  takes either of two values  $\theta_1$  (shaded) or  $\theta_2$  ( $>\theta_1$ ).

smoothed versions of the inviscid solution. However, a proof of this is not yet available. A finite difference solution of (2.1) on a fixed grid could only be obtained by solving (5.1), with  $\epsilon$  regarded as an artificial viscosity. Thus, it is interesting to study finite difference solutions of (5.1) to check their convergence to the solutions derived in C by explicit construction and the solutions obtained in C by finite difference approximations to the two-dimensional primitive equations with artificial viscosity.

b. Solutions for the cross-front circulation

Consider first how (2.1) could be solved by finite difference methods. We write these in the standard dimensionless Eulerian form:

$$\frac{\partial v}{\partial t} + u \frac{\partial v}{\partial x} + \alpha v + w \frac{\partial v}{\partial z} + \alpha x + u = 0 \quad (5.2)$$

$$\frac{\partial \theta}{\partial t} + u \frac{\partial \theta}{\partial x} + w \frac{\partial \theta}{\partial z} = 0$$

$$\frac{\partial u}{\partial x} + \alpha + \frac{\partial w}{\partial z} = 0$$

$$\frac{\partial \phi}{\partial x} = v$$

$$\frac{\partial \phi}{\partial z} = \theta$$

$$M = v + x$$

$$w = 0 \text{ at } z = 0, 1$$

This set contains explicit predictions for  $v$  and  $\theta$ , but  $u$  and  $w$  are determined implicitly by the diagnostic equations (5.3). The continuity equation implies that  $u$  and  $w$  can be represented in terms of a streamfunction  $\psi$  by

$$u = -\alpha x - \partial\psi/\partial z \tag{5.4}$$

$$w = \partial\psi/\partial x$$

Then (5.2) and (5.3) determine  $\psi$  implicitly by the equation

$$\frac{\partial}{\partial z} [(-\alpha x - \partial\psi/\partial z)\partial M/\partial x + (\partial\psi/\partial x)\partial M/\partial z + \alpha M]$$

$$= \frac{\partial}{\partial x} [(-\alpha x - \partial\psi/\partial z)\partial\theta/\partial x + (\partial\psi/\partial x)\partial\theta/\partial z]. \tag{5.5}$$

It is well-known that this equation changes type according to the sign of the potential vorticity  $q$  defined by (2.4), being elliptic, parabolic or hyperbolic according to whether  $q$  is positive, zero, or negative. The discriminant of (5.5) is, in fact,

$$\left(\frac{\partial\theta}{\partial x} + \frac{\partial M}{\partial z}\right)^2 - 4 \frac{\partial M}{\partial x} \frac{\partial\theta}{\partial z}. \tag{5.6}$$

When a discontinuity forms,  $\partial M/\partial x$ ,  $\partial M/\partial z$ ,  $\partial\theta/\partial x$  and  $\partial\theta/\partial z$  all tend to infinity in the fixed ratio

$$1:S:S^2,$$

where  $S$  is the slope of the discontinuity,  $[\theta]/[M]$ . If these ratios are taken for finite values of the gradients, (5.6) vanishes. This suggests that (5.5) will exhibit parabolic behavior near a discontinuity, and may thus be difficult to solve.

Now consider the problem of finding  $\psi$  after a discontinuity has formed and the solution is similar to those shown in C. The velocity normal to the frontal surface must remain continuous, but the tangential velocity may be discontinuous. In the special case solved in C, where lines of constant  $M$  and  $\theta$  coincide, it is possible to construct an equation for  $\psi$  along the isotherms. The geostrophic and hydrostatic relations (5.3) then show that the slope of an isotherm is  $d\theta/dM$  where the solution is smooth, and  $[\theta]/[M]$  at a frontal surface. Since values of  $\theta$  are conserved and  $M$  is proportional to  $e^{-\alpha z}$  following fluid particles, the slopes of isotherms are proportional to  $e^{\alpha z}$ . Thus the streamfunction  $\psi$  obeys the equation

$$\frac{\partial^2\psi}{\partial l^2} = \alpha S, \tag{5.7}$$

where  $l$  is a coordinate along an isotherm with slope  $S$ .

The difficulty of solving (5.7) is shown in Fig. 16. If an isotherm intersects both boundaries, (5.7) can be solved with the boundary conditions  $\psi = 0$  at  $z = 0, 1$ . Otherwise, the problem can only be solved by establishing the geometry of intersections of isotherms and requiring  $\psi$  to be continuous at them. The well-posedness of this is guaranteed by Theorem 1. However, it seems impossible to solve such a problem directly where the discontinuities are "smeared" over grid-lengths. The viscous problem (5.1) would become similarly difficult to solve as  $\epsilon$  is reduced. It therefore

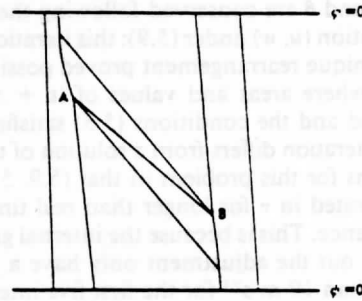


FIG. 16. Solution of Eq. (5.7) assuming zero potential vorticity, with potential isotherms shown.  $\psi$  is determined along  $AB$  by continuity of  $\psi$  at  $A, B$ .

seems necessary to use an iterative method to calculate  $\psi$ .

This behavior in the inviscid case suggests that the solution is not locally determined, even though the ageostrophic accelerations are small. The method of solution must therefore allow information to propagate a large distance at each timestep.

*c. Iterative method of solution*

Solve (5.2), (5.3) by splitting as follows:

*Step 1*

$$\frac{\partial}{\partial t} (v + x) - \alpha x \frac{\partial}{\partial x} (v + x) + \alpha(v + x) = 0$$

$$\frac{\partial\theta}{\partial t} - \alpha x \frac{\partial\theta}{\partial x} = 0 \tag{5.8}$$

At the end of this step  $v$  and  $\theta$  do not satisfy (5.3).

*Step 2*

Introduce an imaginary iteration time  $\tau$  and solve

$$\frac{\partial(v+x)}{\partial\tau} + u' \frac{\partial(v+x)}{\partial x} + w' \frac{\partial(v+x)}{\partial z} = \epsilon' \nabla^2 (v+x) \tag{5.9}$$

$$\frac{\partial\theta}{\partial\tau} + u' \frac{\partial\theta}{\partial x} + w' \frac{\partial\theta}{\partial z} = \epsilon' \nabla^2 \theta$$

where  $u'$  and  $w'$  evolve in  $\tau$  according to

$$\frac{\partial u'}{\partial\tau} + \frac{\partial\phi}{\partial x} - v = k \nabla^2 u'$$

$$\frac{\partial u'}{\partial x} + \frac{\partial w'}{\partial z} = 0, \quad w' = 0 \quad \text{at } z = 0, 1 \tag{5.10}$$

$$\frac{\partial\phi}{\partial z} = \theta$$

If we assume that (5.9), (5.10) have to be integrated for a time  $\tau = \eta t$  to obtain convergence, then the artificial viscosity  $\epsilon'$  must be set to  $\eta^{-1}\epsilon$ .

The viscous term in (5.10) ensures that the mag-

nitudes of  $u'$  and hence  $w'$  decrease with  $\tau$ . Since  $(\tau + x)$  and  $\theta$  are conserved following the incompressible motion  $(u, w)$  under (5.9); this iteration converges to the unique rearrangement proved possible in Theorem 1, where areas and values of  $(\tau + x)$  and  $\theta$  are preserved and the conditions (5.3) satisfied.

This iteration differs from a solution of the primitive equations for this problem in that (5.9, 5.10) have to be integrated in  $\tau$  for longer than real time to obtain convergence. This is because the internal gravity waves carrying out the adjustment only have a phase speed greater than  $10 \text{ m s}^{-1}$  for the first five internal modes. The solution of the semi-geostrophic equations requires information on detailed vertical structure to be transmitted equally fast for all internal modes. If the semi-geostrophic solution is to be physically valid, a fast mechanism must exist for transferring the information in the atmosphere.

A similar method can be used for the three dimensional semi-geostrophic equations. Though the direct proof of Theorem 2 only holds on an  $f$ -plane, the iteration can be written for variable  $f$  as follows, where a dimensional form is used.

Step 1

$$\begin{aligned} \frac{\partial u_g}{\partial t} + u_g \cdot \nabla u_g &= 0 \\ \frac{\partial v_g}{\partial t} + u_g \cdot \nabla v_g &= 0 \\ \frac{\partial \theta}{\partial t} + u_g \cdot \nabla \theta &= 0 \\ u_g &= \left( -f^{-1} \frac{\partial \phi}{\partial y}, f^{-1} \frac{\partial \phi}{\partial x} \right) \end{aligned} \tag{5.11}$$

such that

$$\frac{\partial u_g}{\partial x} + \frac{\partial v_g}{\partial y} + \frac{\partial w_g}{\partial z} = 0.$$

Step 2

$$\begin{aligned} \frac{\partial u_c}{\partial \tau} + u' \cdot \nabla u_c - f v' &= \epsilon' \nabla^2 u_c \\ \frac{\partial v_c}{\partial \tau} + u' \cdot \nabla v_c + f u' &= \epsilon' \nabla^2 v_c \\ \frac{\partial \theta}{\partial \tau} + u' \cdot \nabla \theta &= 0 \end{aligned} \tag{5.12}$$

where

$$\begin{aligned} \frac{\partial u'}{\partial \tau} + \frac{\partial \phi}{\partial x} - f v_g &= k \nabla^2 u' \\ \frac{\partial v'}{\partial \tau} + \frac{\partial \phi}{\partial y} + f u_g &= k \nabla^2 v' \\ \frac{\partial u'}{\partial x} + \frac{\partial v'}{\partial y} + \frac{\partial w'}{\partial z} &= 0 \\ \frac{\partial \phi}{\partial z} &= g \theta / \theta_0 \end{aligned} \tag{5.13}$$

On an  $f$ -plane, Theorem 2 shows that this scheme will converge to a solution where  $u_g, v_g$  satisfy the definitions

$$\frac{\partial \phi}{\partial x} = f v_g, \quad \frac{\partial \phi}{\partial y} = -f u_g.$$

If  $f$  is variable, convergence can be established only by experiment.

d. Lower boundary condition

The boundary condition  $w = 0$  at  $z = 0$  and 1 corresponds to assuming rigid boundaries at  $p = 0$  and  $p_0$ , where  $p_0$  is a fixed surface pressure. Heckley and Hoskins (1982) used more realistic boundary conditions. It is also desirable to be able to use (5.11) to (5.13) in sigma coordinates, to avoid the use of the Boussinesq approximation as in (5.1). The correct lower boundary condition at  $z = 0$  is

$$\frac{\partial p_*}{\partial t} + u \frac{\partial p_*}{\partial x} = -p_* w, \tag{5.14}$$

where

$$v = \frac{\partial \phi_*}{\partial x} \tag{5.15}$$

and  $p_*, \phi_*$  are values of  $p$  and  $\phi$  at  $z = 0$ . The condition (5.14) can be approximated by

$$\frac{\partial \phi_*}{\partial t} + u \frac{\partial \phi_*}{\partial x} = -w \tag{5.16}$$

and by the continuity equation

$$-w = -\alpha - \int_0^1 \frac{\partial u}{\partial x} dz. \tag{5.17}$$

The effect of using this condition instead of the rigid wall condition in Theorem 1 is that the areas of segments of constant  $M$  and  $\theta$  are not exactly conserved, since the geopotential at  $z = 0$  must adjust to satisfy (5.15). Since  $p_*$  only has to vary by about  $\pm 5\%$  of its mean value under normal conditions, this represents only a small relative change in areas of segments. It should therefore be possible to extend the explicit construction used in the proof of Theorem 1 iteratively. This involves the following procedure:

- 1) Solve with fixed areas, and obtain  $v$  at  $z = 0$ ,
- 2) Calculate  $\phi_*$  and hence  $p_*$  from (5.15),
- 3) Correct areas of segments in contact with lower boundary to allow for transfer of mass across  $z = 0$ ,
- 4) Solve again with new areas, and repeat to convergence.

The result of implementing this procedure in the case studied in C will be shown later. Convergence of this iteration requires the property from Theorem 1, that the solution depends continuously on the areas of the elements.

The condition (5.14) can be implemented in the iterative procedure (5.9), (5.10) by modifying (5.10) as follows:

$$\left. \begin{aligned} \frac{\partial u'}{\partial \tau} + \frac{\partial \phi}{\partial x} - v &= k \nabla^2 u' \\ \frac{\partial u'}{\partial x} + \frac{\partial w'}{\partial z} &= 0 \\ w' = 0 \text{ at } z = 1, \quad \phi = \phi_* \text{ at } z = 0 \\ w' &= - \left( \frac{\partial \phi_*}{\partial t} + u \frac{\partial \phi_*}{\partial x} \right) \text{ at } z = 0 \\ \frac{\partial \phi}{\partial z} &= \theta \end{aligned} \right\} \quad (5.18)$$

### c. Finite difference approximations, and horizontal boundary condition

The iterative methods (5.8)–(5.10) for the two dimensional deformation problem, (5.11)–(5.13) for the three dimensional semi-geostrophic model, and (5.18) with the correct lower boundary condition can all be solved by standard finite difference procedures. For the data used in C, it was found sufficient to use a forward timestep in (5.8) and a backward-implicit scheme in (5.9) and (5.10).

The horizontal boundary conditions must be precisely specified for the finite difference calculations. These have to be consistent with (2.3); and so the required conditions are

$$\left. \begin{aligned} u' &= 0 \\ \frac{\partial \theta}{\partial t} = \frac{\partial(v+x)}{\partial t} &= 0 \end{aligned} \right\} \text{ at } x = \pm e^{-\alpha t}. \quad (5.19)$$

The second condition ensures that spurious values of  $\theta$  and  $(v+x)$  are not generated at the boundary.

It is important to note the difference in the way in which artificial viscosity is used in (5.8)–(5.10). A large viscosity is used in (5.10) to accelerate convergence; it has no effect on the history carrying variables since the "velocities"  $u', w'$  are not physically realistic, but just iteration parameters. The artificial viscosity in (5.9) is used to capture the fronts, and since Theorem 1 proves the existence of a solution to the inviscid problem, this viscosity can be reduced as the mesh is refined, so  $\epsilon$  will be proportional to  $\Delta x^2$ . In a three-dimensional primitive equation integration there is a single set of velocity components, and there is no way of applying different diffusion coefficients to geostrophic and ageostrophic winds; the best that can be done is divergence damping (Dey, 1978). In two dimensions, as here, it is possible to use different diffusion coefficients for  $u$  and  $v$ .

## 6. Results

The first case for which results are presented uses the same data as in C. Plots of the data are given in Figs. 17 and 18. Though zero potential vorticity is not

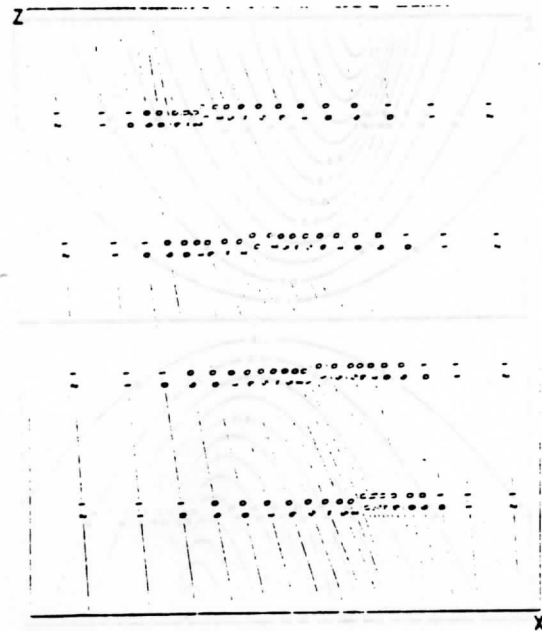


FIG. 17. Initial potential temperature data given by Eq. (6.1).

the most physically realistic case, it has not so far proved possible to implement the exact geometrical construction used to prove Theorem 1 as a practical computational tool in any other case. Therefore these data were used to allow a comparison of finite difference solutions with the exact construction. Using this data yields a discontinuity at the boundaries when  $\alpha t = 1.5$ . The initial data are derived from

$$\left. \begin{aligned} u &= -\alpha x \\ v &= X(x, z) - x \\ \theta &= 1 + \tan^{-1}[5X(x, z)] \end{aligned} \right\} \quad (6.1)$$

where  $X(x, z)$  is defined by

$$\frac{x - X(x, z)}{z - \frac{1}{2}} = \frac{-5}{1 + [5X(x, z)]^2} \quad (6.2)$$

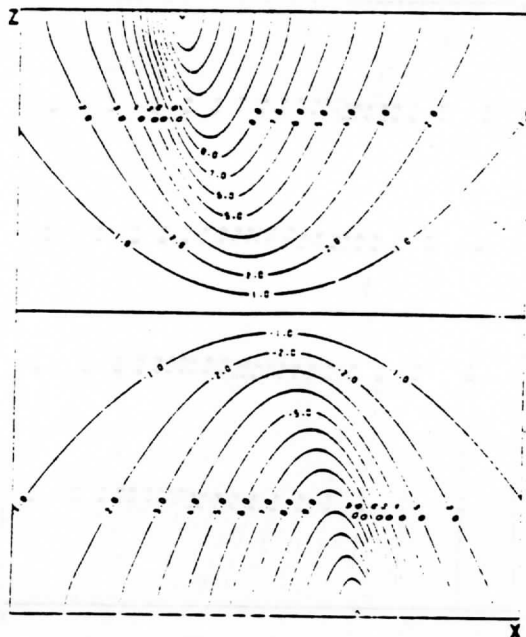
and boundary conditions (5.14) at  $z = 0$ ,  $w = 0$  at  $z = 1$  and (2.3) at  $x = \pm e^{-\alpha t}$ . The models compared are

1) Explicit construction as in Theorem 1 with iterative modification to treat the lower boundary condition (referred to as EC). This model will exactly reproduce the Hoskins and Bretherton solution up to when the front forms.

2) Finite difference solution to the primitive two-dimensional equations with artificial viscosity added (referred to as PE). Second-order central differencing is used throughout, as in C.

3) Finite difference semi-geostrophic solution of (5.8) and (5.18) (referred to as SG). The same finite



FIG. 18. Initial  $\beta$ -velocity field given by Eq. (6.1).

difference approximations are used as in 2), with a  $200 \times 20$  grid.

The results from EC are given in Figs. 19 and 20, which show the potential temperature and long-front component of velocity. The comparison between PE and SG is complicated by the fact that it proved possible to run SG with a much lower value for the artificial

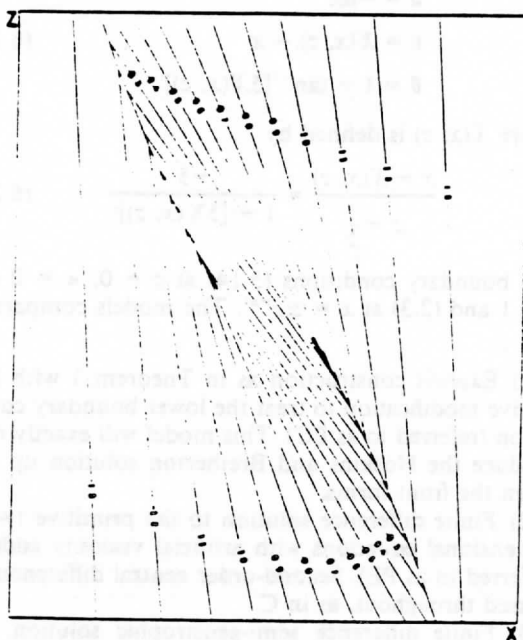


FIG. 19. Potential temperature after 13.9 h for data (6.1). EC.

viscosity ( $190 \text{ m}^2 \text{ s}^{-1}$ ) than PE ( $2.5 \times 10^4 \text{ m}^2 \text{ s}^{-1}$ ), if the same coefficient is used for all variables in PE. Since the frontal structure is sensitive to this coefficient, e.g., Williams (1974), two cases are presented.

In Figs. 21-23 the potential temperature, long-front velocity and vertical velocity are shown from an integration of PE using a coefficient of  $190 \text{ m}^2 \text{ s}^{-1}$  for  $v$  and  $\theta$  but an increased value for  $u$ . These can be compared directly with Figs. 24-26, obtained using SG. No vertical diffusion was used, so that there is no attempt to model atmospheric boundary layer effects in this work.

The results from PE look rather different to those presented in C because of the different diffusion coefficients used here. The overall width of the frontal zone is greater in PE than in EC and SG. The potential temperature comparison (Figs. 19, 21 and 24) shows that above and below the frontal surface the slopes of the isotherms in PE disagree with those in SG and EC. Near  $z = 1/2$ , the slopes are much shallower in EC than in either PE or SG, which are similar. In the case of PE, this difference remains as the resolution is further increased, in SG the slopes show slow convergence towards the EC results. This suggests that the errors at this level are caused by lack of resolution. The problem only becomes serious after the initial formation of the front. The dimensionless slope given by thermal wind balance is given by  $dM/d\theta$  which for the data (6.1) is proportional to  $\sec^2(X)$ . This has a sharp minimum near the  $\theta = 0^\circ\text{C}$  isotherm. Smearing of the profiles by truncation error could result in this minimum not being well resolved after a long integration period.

FIG. 20. The  $\beta$ -velocity after 13.9 h for data (6.1). EC.

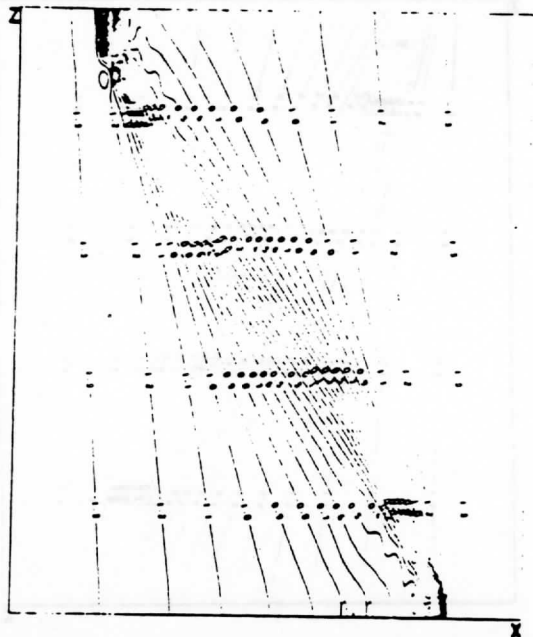


FIG. 21. Potential temperature after 13.9 h. PE.  $200 \times 20$  grid diffusion coefficient  $190 \text{ m}^2 \text{ s}^{-1}$  for  $v$  and  $\theta$ .  $3.75 \times 10^4 \text{ m}^2 \text{ s}^{-1}$  for  $u$ .

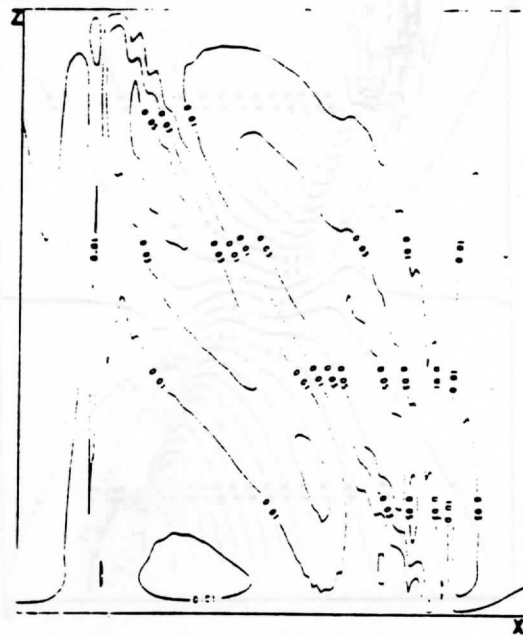


FIG. 23. Vertical velocity after 13.9 h. model as in Fig. 21.

The differences in the long-front velocity (Figs. 20, 22 and 25) are less obvious. The magnitude of  $v$  is consistently greater in PE than in SG and EC. The jump in  $v$  extending away from the frontal zone in EC is because of the use of data piecewise constant in

$M$  and the change in alignment of the segments because of the presence of the front. This indicates a lack of realism in the choice of initial data. The effect is lost in the finite difference integrations by numerical smoothing. The maximum vorticity in SG and PE is about  $12f$ , roughly the maximum amount allowed by

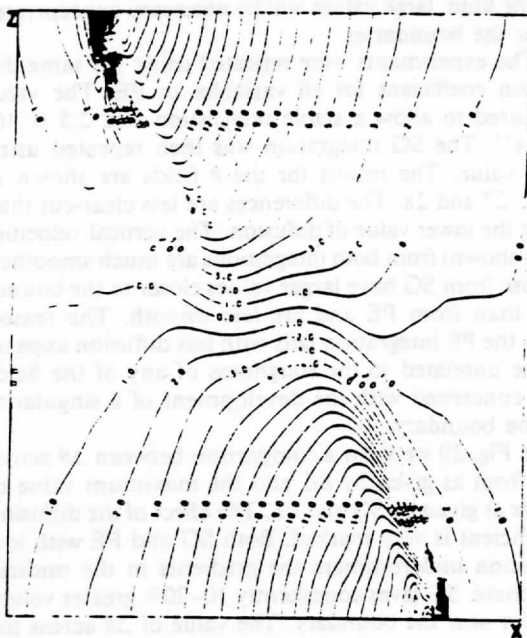


FIG. 22. The  $v$ -velocity after 13.9 h. model as in Fig. 21.

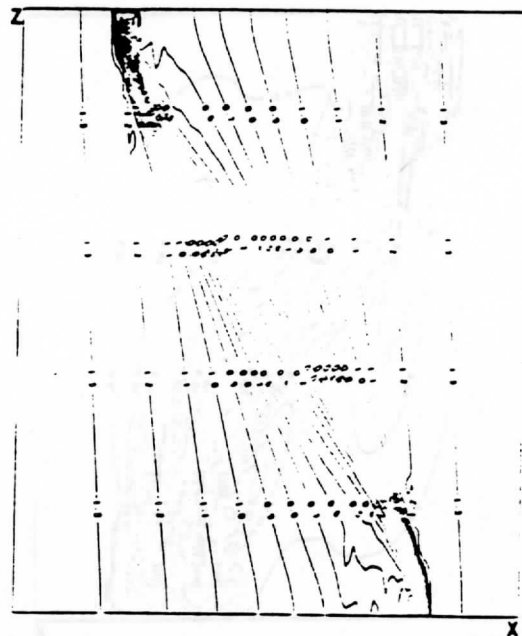


FIG. 24. Potential temperature after 13.9 h. SG.  $200 \times 20$  grid. diffusion coefficient:  $190 \text{ m}^2 \text{ s}^{-1}$ .

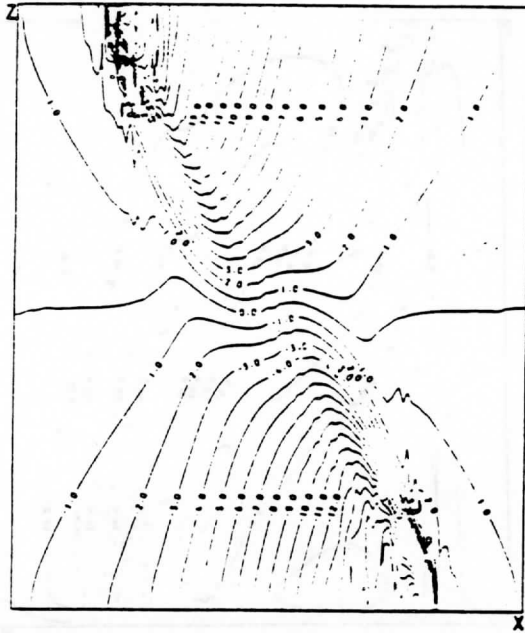
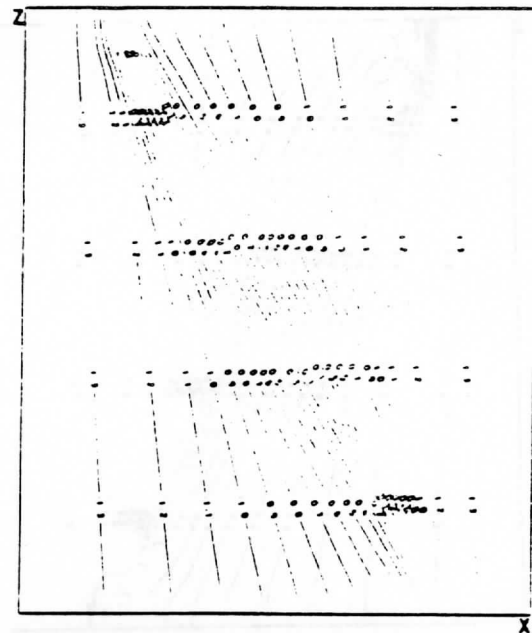


FIG. 25. As in Fig. 20, but model as in Fig. 24.

FIG. 27. Potential temperature after 13.9 h. PE, model as in Fig. 21 with diffusion coefficient  $2.5 \times 10^4 \text{ m}^2 \text{ s}^{-1}$  for all variables.

the validity of the SG equations discussed by Hoskins and Bretherton.

The vertical velocities are considerably different in character in PE and SG. In PE there are regions of large values on either side of the front. In Fig. 23, they fill much of the space between the vertical lines defining

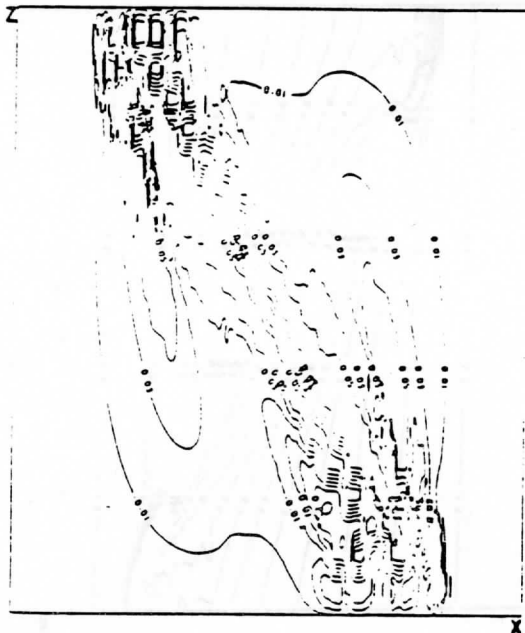


FIG. 26. Vertical velocity after 13.9 h. model as in Fig. 24

the overall width of the frontal zone. In SG (Fig. 26), the large values are confined much closer to the frontal zone and to separate regions extending almost vertically from the points where the frontal zone intersects the boundaries. There are very large values near the boundaries. It has not yet been possible to calculate vertical velocities from EC. However, in order to produce the effect of propagating the front into the interior of the fluid, large values will be necessary concentrated near the boundaries.

The experiments were repeated using the same diffusion coefficient for all variables in PE. The value required to allow a stable integration was  $2.5 \times 10^4 \text{ m}^2 \text{ s}^{-1}$ . The SG integration was then repeated using this value. The results for the  $\theta$  fields are shown in Figs. 27 and 28. The differences are less clear-cut than with the lower value of diffusion. The vertical velocities (not shown) from both integrations are much smoother. Those from SG have larger values closer to the boundary than from PE and are less smooth. The reason why the PE integration fails with less diffusion appears to be unrelated to the roughness of any of the fields but concerned with the development of a singularity at the boundary.

In Fig. 29 we show a comparison between  $\Delta\theta$  across the front as given by EC and the maximum value of  $\partial\theta/\partial x$  as given by SG and PE. The effect of the diffusion coefficient is very marked. Both SG and PE with low diffusion underestimate the gradients in the midtroposphere. SG gives consistently 10–20% greater values except near the boundary. The value of  $\Delta\theta$  across the jump decreases very rapidly away from the boundary.

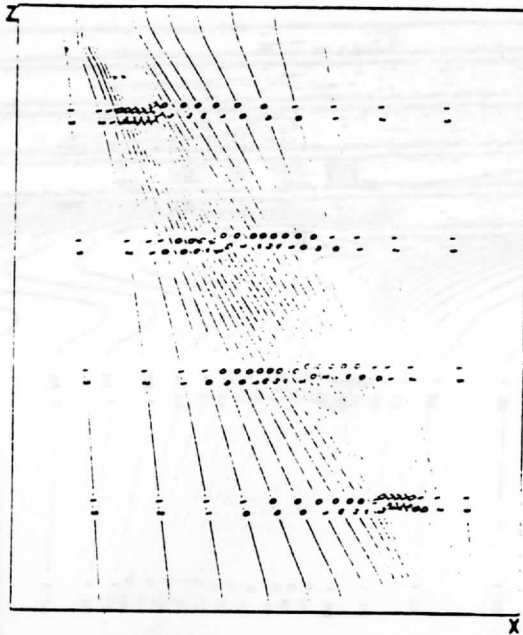


FIG. 28. Potential temperature after 13.9 h. SG. model as in Fig. 24 with diffusion coefficient  $2.5 \times 10^4 \text{ m}^2 \text{ s}^{-1}$ .

data has positive  $q$ . There is a danger that the case  $q = 0$  may present special problems in a numerical model. The data are only neutrally stable to symmetric instability, and numerical truncation error may create regions of negative  $q$ . Therefore, we present a comparison between the  $\theta$  fields given by SG and PE for positive  $q$  in Figs. 30 and 31. The same qualitative differences remain as in the  $q = 0$  case.

The final experiment shown is to solve SG using data with a discontinuity in  $q$ , representing a tropopause. The data used has zero potential vorticity for  $0 \leq z \leq 3/4$ , and large positive potential vorticity for  $3/4 < z < 1$ . A rigid wall condition is imposed at  $z = 1$ , and  $\theta$  is not constant on  $z = 1$ . This is intended as a comparison with the results of Hoskins and Bretherton on upper tropospheric fronts. In agreement with them, and with Theorem 3, no discontinuity is formed at the tropopause. The model produces a statically unstable profile just below the tropopause, (Fig. 32). This still occurs if the data are modified to have  $q \neq 0$  in the troposphere, and appears to be caused by the smearing of the sharp discontinuity in temperature gradient by the finite difference scheme. The long-front velocity field (Fig. 33) shows a well developed jet just below the tropopause with a secondary maximum near  $z = 1$ . There is no tendency to form a discontinuity in this field near the jets.

even in EC, in common with observations of frontal strength.

Though the use of data with  $q = 0$  was necessary because of the inability at present to implement the EC construction in any other case, typical atmospheric

### 7. Discussion

In this paper the extension to the model of Hoskins and Bretherton (1972) introduced in C is further de-

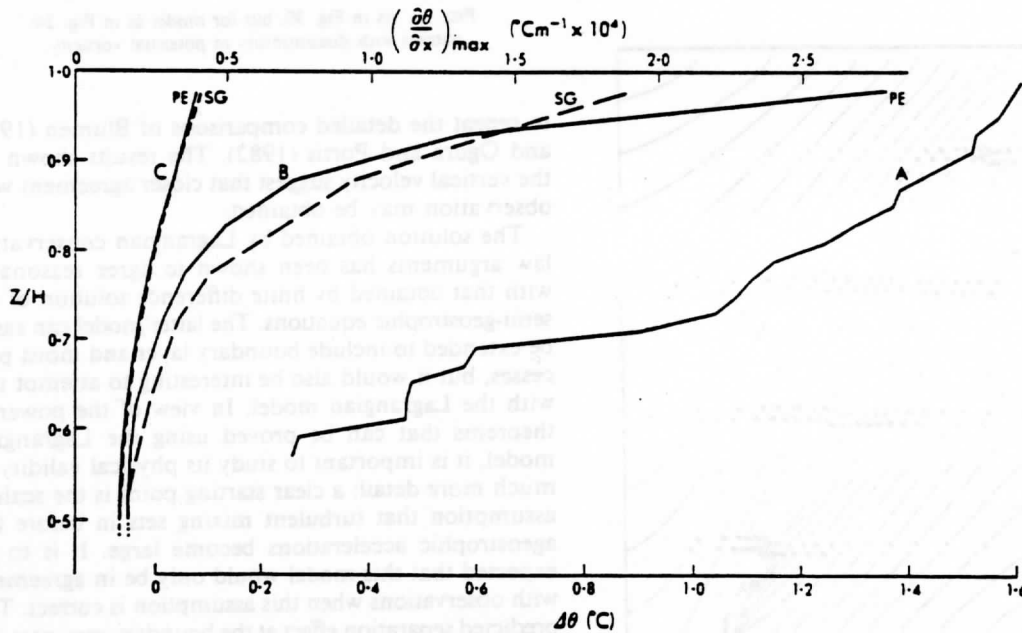


FIG. 29. (A) Graph of temperature difference across front. EC. (B) graph of the maximum  $\partial\theta/\partial x$  against  $z$  for SG and PE with diffusion coefficients  $190 \text{ m}^2 \text{ s}^{-1}$  for  $\theta$ , (C) as in (B) but for diffusion coefficients  $2.5 \times 10^4 \text{ m}^2 \text{ s}^{-1}$ .

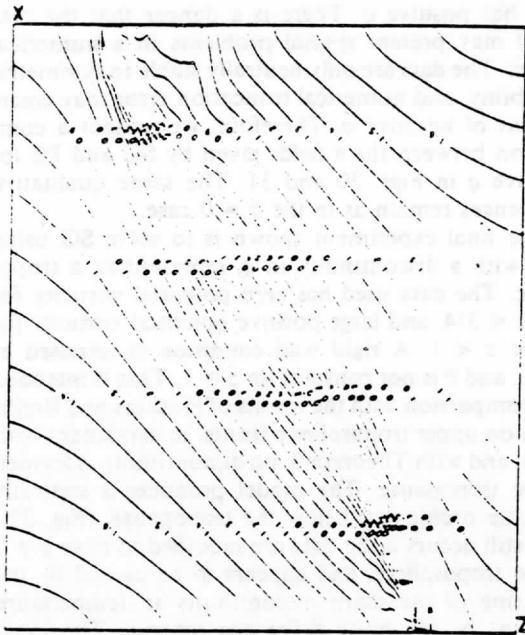


FIG. 30. Potential temperature after 13.9 h. model as in Fig. 21. data with  $q = \text{constant}$ .

veloped. By extending it beyond the initial formation of the front, we can obtain a solution which reflects a balance between frontogenetic and frontolytic forces. It is more reasonable to compare this solution with observations of a front than to use the solution before the front forms, and it would be interesting to use it

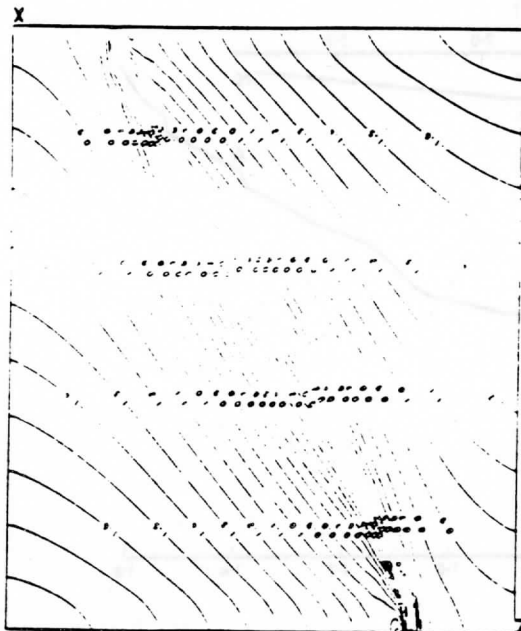


FIG. 31. As in Fig. 30, but for model as in Fig. 24. data as in Fig. 30.

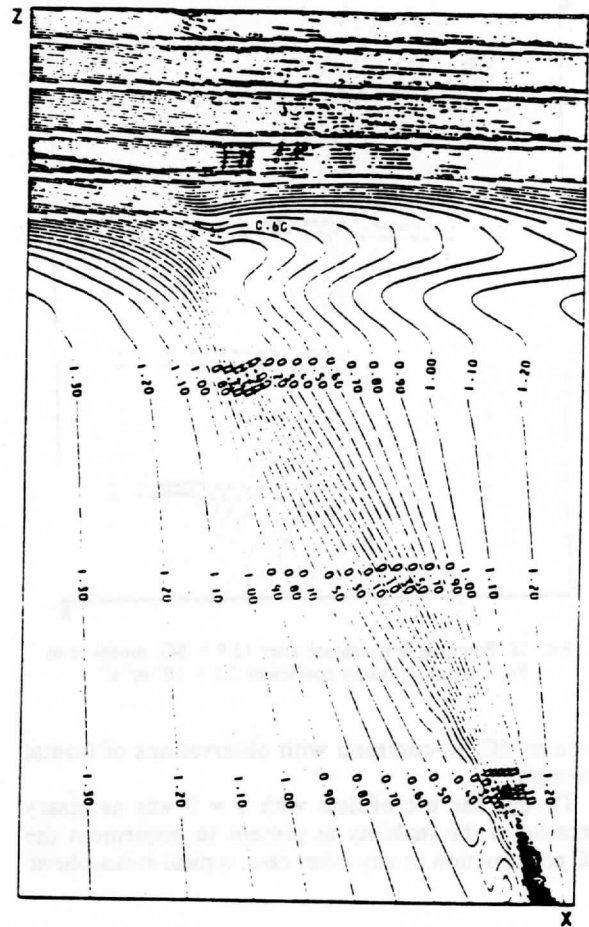


FIG. 32. As in Fig. 30, but for model as in Fig. 24; dataset with discontinuity in potential vorticity.

to repeat the detailed comparisons of Blumen (1980) and Ogura and Portis (1982). The results shown for the vertical velocity suggest that closer agreement with observation may be obtained.

The solution obtained by Lagrangian conservation law arguments has been shown to agree reasonably with that obtained by finite difference solution of the semi-geostrophic equations. The latter model can easily be extended to include boundary layer and moist processes, but it would also be interesting to attempt this with the Lagrangian model. In view of the powerful theorems that can be proved using the Lagrangian model, it is important to study its physical validity in much more detail; a clear starting point is the scaling assumption that turbulent mixing sets in before the ageostrophic accelerations become large. It is to be expected that this model would only be in agreement with observations when this assumption is correct. The predicted separation effect at the boundary may provide a good test.

The difference between the SG and PE finite difference solutions are disturbing. Some of the difficulty

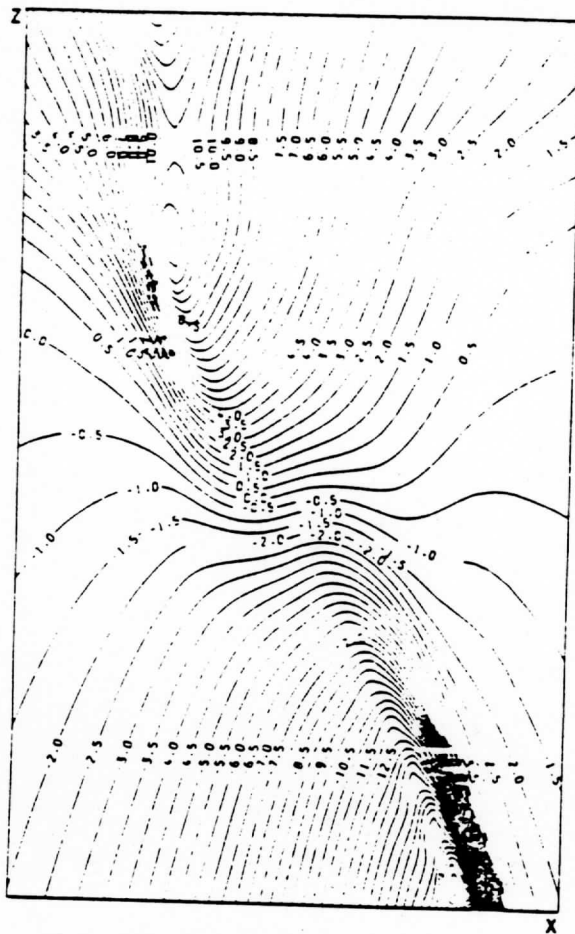


FIG. 33. The  $u$ -velocity after 13.9 h. model and data as in Fig. 32.

must be caused by the use of two-dimensional models. The real turbulent breakdown, which should be predicted by PE, is three dimensional. It would therefore be interesting to extend the comparison into three dimensions. However, since the PE can describe a scale collapse in three dimensions: the success of a PE model depends on a correct parameterization of subgrid-scale

turbulence, since the viscous dissipation scale cannot be resolved. It is, therefore, not surprising that it is difficult to model a solution where the small scales are generated in as organized a way as near a front.

*Acknowledgement.* The authors wish to thank two referees for constructive comments, and Mr. C. A. Parrett for carrying out some of the computer runs.

#### REFERENCES

- Blumen, W., 1980: A comparison between the Hoskins-Bretherton model of frontogenesis and the analysis of an intense surface frontal zone. *J. Atmos. Sci.* **37**, 64-77.
- Cullen, M. J. P., 1983: Solutions to a model of a front forced by deformation. *Quart. J. Roy. Meteor. Soc.* **109**, 565-573.
- Dey, C. H., 1978: Noise suppression in a primitive equation model. *Mon. Wea. Rev.* **106**, 159-173.
- Gadd, A. J., 1978: A split explicit integration scheme for numerical weather prediction. *Quart. J. Roy. Meteor. Soc.* **104**, 569-582.
- Heckley, W. A., and B. J. Hoskins, 1982: Baroclinic waves and frontogenesis in a nonuniform potential vorticity semi-geostrophic model. *J. Atmos. Sci.* **39**, 1999-2016.
- Hoskins, B. J., 1971: Atmospheric frontogenesis: some solutions. *Quart. J. Roy. Meteor. Soc.* **98**, 532-541.
- , 1982: The mathematical theory of frontogenesis. *Annual Reviews of Fluid Mechanics*, Vol. 14, Annual Reviews, 131-151.
- , and F. P. Bretherton, 1972: Atmospheric frontogenesis models: Mathematical formulation and solution. *J. Atmos. Sci.* **29**, 11-37.
- , and I. Draghici, 1977: The forcing of ageostrophic motion according to the semi-geostrophic equations and in an isentropic coordinate model. *J. Atmos. Sci.* **34**, 1859-1867.
- Lorenz, E. N., 1969: The predictability of a flow which possesses many scales of motion. *Tellus*, **21**, 289-307.
- Ogura, Y., and D. Portis, 1982: Structure of the cold front observed in SESAME-AVE III and its comparison with the Hoskins-Bretherton frontogenesis model. *J. Atmos. Sci.* **39**, 2773-2792.
- Orlanski, I., and B. B. Ross, 1977: The circulation associated with a cold front. Part I: Dry case. *J. Atmos. Sci.* **34**, 1619-1633.
- Ross, B. B., and I. Orlanski, 1982: The evolution of an observed cold front. Part I: Numerical simulation. *J. Atmos. Sci.* **39**, 296-327.
- Rockafellar, R. T., 1970: *Convex Analysis*. Princeton University Press, 451 pp.
- Sanders, F., 1955: An investigation of the structure and dynamics of an intense surface frontal zone. *J. Meteor.* **12**, 542-552.
- Williams, R. T., 1974: Numerical simulation of steady-state fronts. *J. Atmos. Sci.* **31**, 1200-1206.

7.15

## HURRICANE DEBBY--ANALYSIS AND NUMERICAL FORECASTS USING VAS SOUNDINGS

John F. Le Marshall  
Cooperative Institute for Meteorological Satellite Studies  
1225 West Dayton Street  
Madison, Wisconsin 53706

William L. Smith and Geary M. Callan  
NOAA/NESDIS Development Laboratory  
1225 West Dayton Street  
Madison, Wisconsin 53706

### 1. INTRODUCTION

The utility of VISSR Atmospheric Sounder (VAS) temperature and moisture soundings in defining the storm and its surroundings at subsynoptic scales has been examined using a numerical analysis and prognosis system. In particular, VAS temperature and moisture soundings and cloud and water vapor motion winds have been used in numerical analysis for three time periods. It is shown that the VAS temperature and moisture data which specify temperature and moisture well in cloud free regions are complimented by cloud and water vapor wind data which provide horizontal gradient information for the cloudy areas. The loss of analysis integrity due to the reduction of VAS data density in the cloudy regions associated with synoptic activity, is ameliorated by using cloud and water vapor motion winds. The improvement in numerical forecasts resulting from the addition of these data to the numerical analysis data base is also recorded.

### 2. BACKGROUND

Between 14 September 1982 and 20 September 1982 Hurricane Debby moved through the western Atlantic Ocean, 500 miles from the east coast of the U.S.A., providing a first opportunity for the VAS instrument on GOES-5 to observe a hurricane and its environs. During this period a data base was established from the usual conventional observations, VAS observations from GOES-5, HIRS and MSU observations from NOAA-6 and NOAA-7, cloud and water vapor motion wind observations and National Hurricane Research Laboratory dropwindsonde measurements. The utility of the various components of this data base in defining the storm and its surrounding environment has been examined. This study concentrates on the utility of the GOES-5, VAS temperature and moisture sounding data and cloud and water vapor motion data, because their timeliness, density and coverage make them well suited for analysis and forecast purposes in the western Atlantic Ocean.

### 3. THE DATA BASE

The data base used in this study had three components:

The usual conventional observations without ship reports, AIREPS, and the satellite components. These data were received in real time at the Space Science and Engineering Center (SSEC) at the University of Wisconsin in Madison.

VAS sounding data from GOES-5, which was processed using the physical retrieval scheme developed at the NESDIS Development Laboratory in the Space Science and Engineering Center at Madison (Smith, 1983). This scheme provides soundings which represent a full physical solution of the radiative transfer equation. It uses surface data to reduce sounding errors near the lower boundary and the temperature and moisture retrievals are made in a fully interactive Man-computer Interactive Data Access System (McIDAS) environment (Suomi, et al., 1983), which among other things, facilitates the removal of errors due to cloud contamination and noise. The first guess field used in the retrieval scheme was a 12 hour NMC global forecast and the retrievals were made approximately every 150 km.

Cloud and water vapor motion winds were also produced at the SSEC on the McIDAS using the technique described by Mosher (1978) which was applied to GOES-5 half hourly visible and infrared imagery and hourly water vapor imagery. This technique is based on manual selection of suitable cloud tracers from which pursuant programs generate wind vectors, using a correlation technique to determine the final position of the cloud tracers selected by the man.

A most important advantage of the latter two data types is that if during analysis some areas appear to be data sparse, a quick reexamination of the VAS radiance and cloud image fields often allows generation of supplementary sounding or wind data where it is required.

### 4. THE ANALYSIS-PROGNOSIS SYSTEM

The chief characteristics of both the analysis and prognosis schemes are listed in Table 1. The analysis and prognosis schemes have a horizontal grid spacing of either 67 km or 134 km (51 by 61 or 24 by 29 elements) on a Lambert Conformal Conic Projection. For this study the prognosis model integrations have been run at only 134 km resolution. (The model integrations are now being repeated at full (67 km) resolution.) The model also has the option to update boundary conditions using tendencies provided by a larger scale model. A brief summary of both the analysis and prognosis schemes are given below.

#### 4.1 The Analysis Scheme

The objective analysis scheme used in this study is an adaptation of a scheme written at

the Australian Numerical Meteorology Research Centre (ANMRC) by R. S. Seaman for limited area objective analysis over the Australian region (Mills et al., 1981). The scheme uses a combination of the successive correction method of Cressman (1959) and the variational blending techniques of Sasaki (1958, 1970) and is well suited to analysis of satellite temperature profiles and cloud and water vapor motion winds. It relies on an initial three dimensional blend of 1000 mb and 250 mb height, gradient and thickness data to specify the bulk atmospheric

analysis level. The model commences its integration using this non-divergent field.

#### 4.2 The Forecast Model

The forecast model is a primitive equation model originally written for the Australian region (McGregor et al., 1978) and later adapted to the North American region (NA) (Mills et al., 1981). The model has been used operationally by the Australian Bureau of Meteorology at a resolution of 250 km and in a research mode within the ANMRC at 125 km. The model for use over the NA region differs from the Australian version in three important respects. First, the finite differencing scheme of Corby et al., (1972) has been included to minimize truncation error over regions of steep topography. Second, a Kuo type convective parameterization scheme (Kuo 1965, 1974) has replaced the Arakawa-Shubert scheme described in McGregor et al. (1978). In addition, a comprehensive boundary layer scheme has also been added to the model (Mills et al., 1983) using similarity theory at the surface coupled with vertical diffusion of heat, moisture and momentum at the three lower model levels.

#### 5. THE ANALYSES

Three analyses have been done for each of the following time periods: 0000 GMT and 1200 GMT on 16 September 1982 and 0000 GMT on 17 September 1982. These analyses used conventional data (C), conventional plus VAS sounding data (C+V), and conventional plus VAS sounding plus cloud and water vapor drift wind data (C+V+CDW). The first guess fields for the 0000 GMT 16 September 1982 analysis was a blend of the NMC global and LFM analyses. The first guess fields for the other analyses were the global analyses alone because of the problems generated by the proximity of the storm to the LFM boundary and the better quality of the global analysis in the region of the storm because of its inclusion of satellite and other data due to its later cut-off time.

The mean sea level pressure (MSLP) analyses for the latter two analyses were slightly altered by the addition of 'bogus observations,' so that the cyclone center fitted the observed 'best track' reconnaissance data for the storm. By using these MSLP fields it was felt the study in some ways gauged the impact of VAS and CDW data used in conjunction with an 'operational' MSLP analysis. The MSLP field was the same for each of the three analyses done at a particular time.

Figures 1 and 2 show the conventional, conventional plus VAS and conventional plus VAS plus cloud and water vapor drift wind analyses at 500 mb and 250 mb at 0000 GMT on 12 September 1982. They illustrate the impact of increasing the data base and show a gradual correction of the geopotential fields to what one would hope to be an optimum analysis with all data (C+V+CDW) being used. Figures 3 and 4 show the 250 mb conventional plus VAS and conventional plus VAS plus CDW analyses for 0000 GMT in a little more detail, with the VAS sounding

TABLE 1  
PRINCIPLE FEATURES OF THE  
ANALYSIS SCHEME AND PROGNOSIS MODEL

Analysis System
Combination of successive correction method and variational blending in three dimensions.
Ten pressure levels, p=1000, 850, 700, 500, 400, 300, 250, 200, 150, and 100 mb.
Horizontal resolution: 67 km.
Fields analyzed or derived at each pressure level
--geopotential height
--temperature
--dewpoint
--wind components
--stream function
Prognosis Model
Primitive equations model in $\sigma$ -coordinates
Ten vertical levels at $\sigma=0.05, 0.15, 0.25, \dots, 0.95$
Horizontal resolution 67 km (134 km)
Staggered horizontal grid (Arakawa "C" grid)
Semi-implicit time differencing
Surface/boundary layer parameterization
Broad scale precipitation
Kuo-type convective parameterization
Updated boundary conditions

structure. Subsequent to this individual level geopotential analyses are performed by blending the geopotential gradient analyses at that level and the analyzed thicknesses immediately above and below the level in question. Geopotential thickness being a primary analysis variable facilitates assimilation of satellite temperature profiles into the objective analysis while the variational blending procedure ensures a consistent introduction of gradient information into the analysis. Different weights can also be given to scalar and gradient information in the blending procedure which determines geopotentials, allowing the geopotential gradient information inherent in satellite temperature data sets to be utilized more effectively than would be the case in a simple SCM analysis.

The wind fields are derived from the blended geopotential fields using a gradient/geostrophic relationship, and these wind components are used as input to a variational blending procedure (Seaman et al., 1977) to derive a stream function field at each



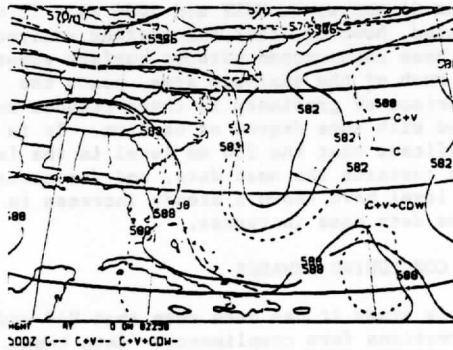


Fig. 1: Comparison of 500 mb geopotential analyses at 0000 GMT on 16 September 1982 using conventional, conventional plus VAS and conventional plus VAS plus cloud and water vapor drift wind observations.

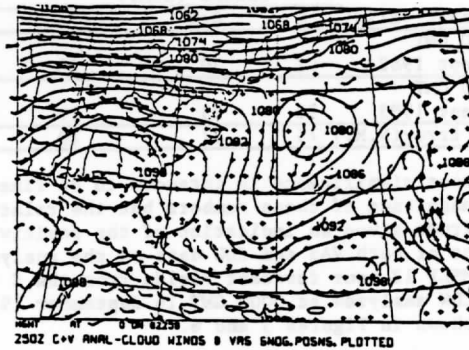


Fig. 3: The 250 mb geopotential analysis at 0000 GMT 16 September 1982 using conventional and VAS observations. Cloud drift winds and VAS sounding positions superimposed.

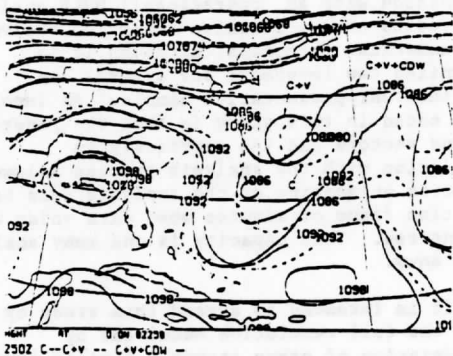


Fig. 2: Comparison of 250 mb geopotential analyses at 0000 GMT on 16 September 1982 using conventional, conventional plus VAS and conventional plus VAS plus cloud and water vapor drift wind observations.

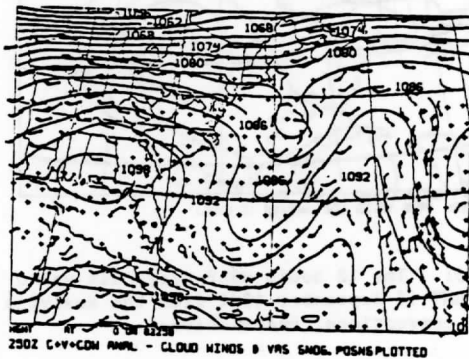


Fig. 4: The 250 mb geopotential analysis at 0000 GMT on 16 September 1982 using conventional, VAS and cloud drift wind observations. Cloud drift winds and VAS sounding positions superimposed.

positions (+) and CDW data plotted. The figures serve to illustrate two salient features of these analyses. The first is that the VAS sounding distribution and the CDW distribution are complementary and provide a quite uniform data base over the western Atlantic. This of course is anticipated as the VAS sounder provides soundings in the cloud free areas while suitable cloud tracers can often be found in the remaining areas. The second is that although the VAS data improves on the conventional analysis, the loss of VAS data caused by the intense cloudiness associated with hurricane Debby has masked two significant features in the analysis (Fig. 3). These are the exact positions of the cyclonic circulation centers near 70°W and the strength of the ridge at 60°W. It can be seen the addition of CDW data to this analysis (Fig. 4) has ameliorated the problem. In the 1200 GMT analyses on 16 September 1982 at 250 mb the VAS sounding and CDW distribution was again uniform, while the addition of cloud drift wind data again ameliorated the problem of defining ridge and trough positions in a data sparse region. It could also be pointed out that during the 1200 GMT analysis additional

cloud drift wind data was generated from imagery in a matter of minutes after it was found a data void was present near 38°N, 67°W.

## 6. THE FORECASTS

The analyses using C, C+V, and C+V+CDW data at 0000 GMT and 1200 GMT on 16 September 1982 have been used to initialize the primitive equation model, described in Section 4.2, over the analysis domain. The forecasts have been initially run at 137 km resolution. The integrations were run for a period of 12 hours, were non-nested and the C+V+CDW analyses were used for verification. It should be noted that with analyses and forecasts at these resolutions we can only examine the larger scale features associated with the hurricane.

The central position of the storm system has been measured from the 12 hour MSLP forecast and compared to the estimated best track position. The results are shown below.

Forecast valid	ERRORS (N.M.)		
	C	C+V	C+V+CDW
1200 GMT			
16 Sept 1982	91	30	28
0000 GMT			
17 Sept 1983	59	23	11
Mean Error(N.M.)	75	27	20

No great significance is intended to be fixed to the magnitude of these numbers but the relative magnitude gives an indication of the positive impact of both VAS and CDW data on the analyses. The MSLP 12 hour forecast fields from the C and C+V+CDW analyses at 0000 GMT 16 September 1982 are shown in Figures 5 and 6.

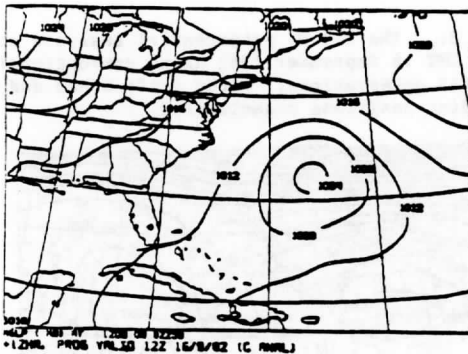


Fig. 5: The 12 hours MSLP prognosis valid 1200 GMT 16 September 1982 from the analysis using conventional observations.

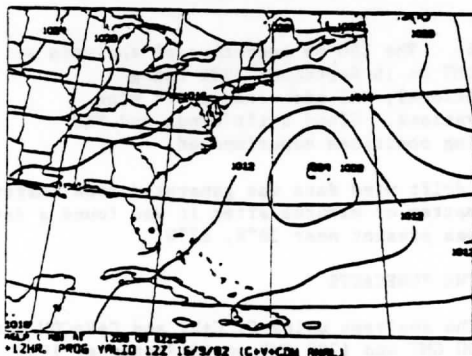


Fig. 6: The 12 hour MSLP prognosis valid 1200 GMT 16 September 1982 from the analysis using conventional, VAS and cloud and water vapor drift winds.

S1 skill scores (Teweles and Wobus, 1954) have also been calculated for each of the model integrations and are presented below.

Level	C	C+V	C+V+CDW
MSLP	48.6	46.4	46.2
1000	49.9	47.6	46.5
500	49.9	49.1	49.8
250	51.1	43.8	41.7

When examining these scores, it appears the difference in skill shown in the positioning of

the center of the storm is partially reflected in the S1 scores at MSLP and 1000 mb. It must be noted, however, that the surface analyses have been constructed without surface reports over much of the analysis area, hence the comparison of gradients in these regions must be viewed with some degree of caution. It is significant that the 250 mb level is the level which contains the most data, and forecasts at this level have shown a steady increase in skill as the data base increases.

## 7. CONCLUDING REMARKS

In this study it has been seen that VAS and CDW observations form complimentary data bases. In areas of extensive cloud, CDW data allowed full subsynoptic scale analysis at cloud tracer level by adding gradient information in areas devoid of VAS data. This often significantly changed the numerical analysis which had previously interpolated through the area. It has also been seen that the use of VAS and CDW data in conjunction with an 'operational' MSLP analysis, appeared to have a positive impact on twelve hour numerical forecasts, although it is recognized two forecasts are a small and sometimes unrepresentative sample. An important point noted in this study is that the generation of wind vectors and VAS retrievals in association with the analysis process allowed selective augmenting of the analysis data base in a time frame of minutes when data voids were encountered. This capacity is one many analysts would envy.

It is intended to extend this study by using the full resolution model and by consideration of other storms. Similar studies are now also being done over the mainland where careful account needs to be made of the relative quality of VAS temperature gradients and absolute values.

## ACKNOWLEDGMENTS

Many thanks are due to Tod Stewart for generating cloud and water vapor motion winds and to Mrs. Gail Turluck for her efforts in producing the manuscript.

## REFERENCES

- Corby, G. A., A. Gilchrist, and R. L. Newson, 1972: A general circulation model of the atmosphere suitable for long period integrations. *Quart. J. Roy. Meteor. Soc.*, 98, 809-832.
- Cressman, G., 1959: An operational objective analysis system. *Mon. Wea. Rev.*, 87, 367-374.
- Kuo, H. L., 1965: On formation and intensification of tropical cyclones through latent heat release by cumulus convection. *J. Atmos. Sci.*, 22, 40-63.
- Kuo, H. L., 1974: Further studies of the parameterization of the influence of cumulus convection on large scale flow. *J. Atmos. Sci.*, 31, 1232-1240.

- McGregor, J. L., L. M. Leslie, and D. J. Gauntlett, 1978: The ANMRC limited area model: Consolidated formulation and operational results. Mon. Wea. Rev., 106, 427-438.
- Mills, G. A., L. M. Leslie, J. L. McGregor and G. A. M. Kelly, 1981: A high resolution numerical analysis/forecast system for short term prediction over the North American region. Unpublished ANMRC Report, Australian Numerical Meteorology Research Centre, Melbourne, 76 pp.
- Mills, G., G. R. Diak and C. Hayden, 1983: The subsynoptic scale model and investigations of the value of satellite sounding data in numerical weather prediction. Internal report, Space Science and Engineering Center, University of Wisconsin, Madison, Wisconsin, 53706, 27 pp.
- Mosher, F. R., 1978: Cloud drift winds from geostationary satellites. Atmospheric Technology, 10, 53-60.
- Sasaki, Y., 1958: An objective analysis based on the variational method. J. Meteor. Soc. Japan, 36, 77-88.
- Sasaki, Y., 1970: Some basic formalisms in numerical variational analysis. Mon. Wea. Rev., 98, 875-910.
- Seaman, R. S., R. L. Flaconer, and J. Brown, 1977: Application of a variational blending technique to numerical analysis in the Australian region. Aust. Meteor. Mag., 25, 3-23.
- Smith, W. L., 1983: The retrieval of atmospheric profiles from VAS geostationary radiance observations. J. Atmos. Sci., 40, 2025-2035.
- Suomi, V. E., R. Fox, S. S. Limaye, and W. L. Smith, 1983: McIDAS III: A modern interactive data access and analysis system. J. Clim. and Applied Meteor., 22, 766-778.
- Teweles, S., and H. Wobus, 1954: Verification of prognostic charts. Bull. Amer. Meteor. Soc., 35, 455-463.

2/NESS19/05

Acknowledgement: This work was supported under NASA 8-34732. We acknowledge the enthusiastic support from the personnel of the NASA/ Marshall Space Flight Center.

The effect of variations in surface parameters on 24-hour forecasts  
forecast and surface temperatures have been examined on a day to day  
**The Influence of Variations in Surface Treatment on 24-Hour Forecasts**  
**with a Limited Area Model, Including a Comparison of**  
**Modelled and Satellite-Measured Surface Temperatures**

George Diak

Stacey Heikkinen

John Bates

University of Wisconsin-Madison  
Space Science and Engineering Center  
Madison, WI 53706

October 1984

The effect of variations in surface parameters on 24-hour limited area forecasts and surface temperatures have been examined on a day in July 1981. The vehicle for the study is a ten-level primitive equation model covering most of the continental U.S. Variations in ground wetness, surface roughness and soil flux treatment generally do not produce large differences in 24-hour forecasts of primary variables. Precipitation totals, however, are surprisingly sensitive to the surface treatment, especially in areas of significant large-scale precipitation evidenced in a control forecast. In these areas modulations of 10-30% of the 24-hour control amount due to changes in the surface treatment are common. Evidence in this case points to modulations in sensible heating and resulting convergence patterns with surface characteristics as the primary cause for the precipitation differences.

Diurnal surface temperature range measured by the VAS instrument on GOES-3 is compared to those generated in model experiments over the model grid. Good agreement is found in areas with moderate to large ground wetness and roughness heights. Poor agreement is evidenced in western U.S. where the daytime surface temperature and flux balance is shown to be critically sensitive to small errors in the ground wetness parameter.

## 1. Introduction

Parameterization of surface energy budget and momentum processes is one of the most difficult tasks in modelling of the planetary boundary layer. While intense in situ investigation can produce realistic values of surface parameters (moisture, momentum and submedium descriptors and albedo) valid at a particular site at a particular time, designating these parameters over the range of surfaces encountered in a global or even a limited area model is a formidable undertaking. Importantly, recent sensitivity studies (Zhang and Anthes 1982, Garrett 1982) using high-resolution PBL models show the sensitivity of boundary layer structure and convective activity to these surface parameters.

Advances are being made on several fronts to deal with the problems of designating surface variables. Comprehensive climatological land cover data sets (Matthews 1983, Kung et al. 1964, Hummel and Reck, 1979) are helpful in estimating their seasonal and geographical distribution, and may be used to infer climatological energy budget and momentum transfer descriptors.

Remote-sensing techniques are also offering some insight into parameterization of surface processes and may be useful in assessing shorter term fluctuations in surface variables than can be inferred from the climatological land cover and albedo data bases.

A persistent problem with remote-sensing efforts, however, is the lack of adequate verification, since no surface-based research effort to date has produced measurements with sufficient area-coverage to be used as ground-truth for large-area remote-sensing methods. Much of the verification must come from less direct indicators.

Our own interests are toward remote-sensing methods for land-surface energy budgets and also surface influences on short term (12-24 hour) forecasts of atmospheric state, convection, and precipitation. In this effort we are currently conducting experiments to evaluate the information in skin temperature and atmospheric soundings from the VISSR Atmospheric Sounder (VAS) instrument on board the current series of GOES satellites.

As a prelude, we have been investigating some of the surface energy budget and momentum parameterizations in common use in climate and limited-area models with the intent of providing some insight into how surface parameterizations and their variation affect surface temperature, atmospheric structure, and the development of precipitation. We also hope to acquire some experience as to how common simplifications made in limited-area models (for example, using average rather than area-specific surface parameters) can affect forecast outcome. Of particular interest to us is the sensitivity of surface temperature to surface variations and comparison of model generated surface temperatures to their remotely-sensed counterparts.

The experiments we will describe were run with a limited area model for one day in summer 1981. Obviously, one model and experiments on only one day cannot answer all questions in these areas. Except where obvious, we have tried to put our results in the framework of changes between forecasts rather than absolute forecast accuracy, and not to over generalize these findings.

## 2. The Model

The Subsynoptic Scale Model (SSM) is an adaptation of the Australian Region Primitive Equation Model which has been comprehensively documented

by McGregor et al. (1978). It has been thoroughly tested in operational conditions with a horizontal resolution of 250 km by the Australian Bureau of Meteorology and in a research mode with a 125 km resolution.

The model in the form used for the U.S. has been amended through the addition of a more comprehensive boundary layer parameterization (to be detailed), the inclusion of Corby differencing to better handle the high topographic regions of the continent and the replacement of the original Arakawa-Schubert convective parameterization with a modified Kuo scheme (Kuo 1968, 1974; Hammerstrand 1978). Two choices of resolution are available, 67 and 134 km. Forecast model characteristics are detailed in Table 1.

### 3. Boundary Layer Parameterization

#### a. Surface and Ekman Layer Treatments

Surface fluxes are calculated via the Monin-Obukhov similarity theory, using the stability functions of Businger et al. (1971) as integrated by Benoit (1976). Above the surface layer the vertical diffusion of heat, momentum, and moisture are parameterized using the Richardson number dependence functions of Blackadar (1977).

#### b. Surface Radiation

Shortwave flux at the top of the atmosphere is calculated as a function of geographical location and time of day. Cloud presence and fractional coverage are assessed at three levels as a function of relative humidity (Geylen 1981), and this cloudiness used to calculate the solar flux incident at the surface, using assigned bulk cloud properties (Katayama 1972).



Upwelling longwave flux from the surface is assessed using the surface temperature in the Stefan-Boltzmann relationship. Downwelling longwave flux is calculated as an empirical function of lowest level air temperature and humidity (Lettau and Lettau 1978) and is modified for the presence of clouds (Paltridge and Platt 1976). No direct shortwave or longwave heating/ cooling of the atmosphere is included.

c. Surface Temperature

Sea surface temperature is held constant through the forecast. Land surface temperature is calculated via a surface energy balance equation

$$SW\downarrow + (1-A) \cdot LW\downarrow + LW\uparrow + E_o + Q_o + S_o = 0 \quad (1)$$

$SW\downarrow$  = incident surface shortwave flux

$LW\downarrow$  = downwelling longwave flux

$LW\uparrow$  = upwelling longwave flux

$E_o$  = surface evaporative flux

$Q_o$  = surface sensible heat flux

$S_o$  = submedium flux (all  $W\cdot m^{-2}$ )

$A$  = surface albedo (dimensionless)

d. Soil flux treatment

Five different methodologies for designating the submedium energy flux are available with the SSM. These parameterizations, identical to Bhumralkar (1975) are

1) No soil flux  $S_o = 0$

2)  $S_o = \lambda/D \cdot (T_s - T_g)$

3)  $S_o = Cr \cdot (Rnet)$

4)  $S_o = C_q \cdot (Q_o)$

5)  $S_o = \text{"force restore" (Bhumralkar 1975)}$

where  $\lambda$  = soil thermal conductivity ( $\text{W}\cdot\text{m}^{-2}\cdot\text{K}^{-1}$ )

$D$  = damping depth (m)

$T_s$  = surface soil temperature (K)

$T_g$  = subsoil temperature (K)

$R_{\text{net}}$  = net radiation ( $\text{W}\cdot\text{m}^{-2}$ )

$C_r$  = net radiation constant (dimensionless)

$C_q$  = sensible heat constant (dimensionless)

Soil physical constants for methods 2 and 5 are specified as a function of ground wetness, GW, identical to Bhumralkar (1975). Empirical constants  $C_r$  and  $C_q$  are specified as a function of time of day from the research of Gadd and Keers (1970) and Kasahara and Washington (1971) respectively.

#### e. Surface Roughness

The Monin-Obukhov stability functions used to depict transfers in the surface layer require an estimate of the roughness height of the surface.

The roughness height for water surfaces is specified as a function of the lowest model level wind speed through the relationship researched by Garratt (1977).

For land surfaces the roughness height for momentum transfer can be designated as a constant value, as a function of the large-scale topography (Gates and Nelson 1975), or as a function of land use and vegetation character. As suggested by the research of Garratt and Hicks (1973) and Garratt (1978), we may differentiate between the roughness height for momentum transfer vs. those for heat and moisture transfer assuming  $Z_{0v} = Z_{0h} = Z_{0m}/\text{constant}$  where  $Z_0$  (h,v,m) are roughness heights for heat, vapor, and momentum transfer respectively.

#### f. Surface Evaporation

Land surface evaporation may be controlled through either a ground wetness (GW) or a Bowen ratio. Either of these moisture variables may be designated as a constant over the land area or allowed to vary geographically as a function of a land use and vegetation evaluation. For either option, the value of the surface moisture variable is held constant in time except where significant precipitation occurs, in which case a value appropriate for surface saturation replaces the original.

Sea surface evaporation is controlled by setting the surface humidity to saturation at the sea surface temperature.

#### g. Albedo

Surface albedo can be designated as a constant over the model grid or as a function of researched regional albedo values. These regional values come from Kung et al. (1964). While an albedo determined from satellite techniques (Gautier et al. 1980, Diak and Gautier 1983) was available, this measurement was limited to the spectral band of the GOES satellites ( $\sim 0.4-0.9 \mu\text{m}$ ). Spectral albedo values of both soil and vegetation can change dramatically with wavelength, especially in the near infrared (Norton et al. 1980). It was believed that the total solar albedo measurements from the Kung et al. research were more appropriate to determine net shortwave than the satellite measurements made in a limited spectral interval.

#### 4. The Experiments

All experiments were performed on the day of July 20, 1981 with the 134 km resolution model version. Some attention has been paid to this case (Smith et al. 1982, Peterson et al. 1983) due to the outbreak of severe tornadic storms which occurred at about 20 GMT in central Missouri. A

surface analysis at the initial time, 12 GMT, and analyzed 500 mb heights and temperatures are shown in Fig. 1a and b respectively.

At the surface, a cold front extends from Michigan southward to Colorado and drifts slowly southward during the course of the day. At 500 mb cold advection is evident into the upper Great Plains, associated with a jet streak propagating across Wyoming into Nebraska.

Measured precipitation amounts for the 24 hour period beginning 12Z July 20 are shown in Fig. 1c. An area of large scale precipitation in the northeastern and New England states is associated with the eastern Great Lakes low pressure center and leading warm front. Precipitation in the Midwest Plains is generally associated with convective outbreaks along the twin cold fronts propagating southward during the observation period. Southern Atlantic and Gulf Coast regions experience precipitation which is largely air-mass convective in nature.

A series of 24 hour forecasts were run, beginning at 12 GMT, July 20, 1981, employing various combinations of surface parameterizations as will be described. For comparison purposes it is convenient to describe a "nominal" (NOM) forecast for this time period, employing what we expect to be the best (most rigorous or complete) surface parameterizations available in the SSM. We define this forecast as follows:

- 1) full time dependent surface and PBL scheme
- 2) land use and vegetation survey used to designate ground wetness and roughness heights
- 3) soil flux calculated via force restore method
- 4) regional measurements used to designate albedo
- 5) differentiation between roughness heights for momentum vs. heat and vapor

a. Preliminary - PBL vs. No PBL Forecasts

Several authors have discussed the effects of a PBL parameterization addition to a limited-area model. Our first experiment in general verifies their qualitative results. The addition of surface drag has been noted to limit the intensification of low and high pressure systems (Anthes 1983) as evidenced in sea level pressure. Fig. 2(a-c) shows three 12-hour model forecasts of sea level pressure valid 0 GMT July 21. The first (NOPBL) is one which contains no PBL parameterization at all (no surface fluxes, no vertical diffusion); the second only a time independent drag coefficient (DRAG) for momentum at the surface (different for land and water); and the third the full time dependent NOM scheme previously described. Sea level pressure differences over the model grid range from approximately 0-2 mb between the NOPBL and NOM runs. In general, areas of large sensible heating (no clouds, low ground wetness) in the southwest and western states show the largest sea level pressure differences between these two runs. The differences are greatest after the 12 hour (daytime) period shown and are less-evident in the 24 hour forecast. Low level temperatures are noticeably warmer in the NOM experiment as would be expected with the inclusion of surface heating.

Differences in sea level pressure between the NOPBL and DRAG runs due to inclusion of surface drag are smaller than those reported in other investigations. Both the surface low located over the eastern Great Lakes and the high pressure system in west Colorado show almost no difference between these experiments. Compared to experiments reported by Danard (1969) and Anthes and Keyser (1979), the systems present on July 20 were dynamically weaker and characteristic of a summertime regime. As noted by Anthes (1983), the effect of friction over 24 hours varies from negligible

for lighter winds (this case) to extremely important for more vigorous systems. In this case, the role of surface sensible heating appears to be more important on sea level pressure variations than surface frictional effects.

Precipitation amounts over 24 hours between these runs vary, as would be intuitively expected. The NOPBL run shows the least precipitation, with slightly more (.5%) for the DRAG run.

The difference in precipitation between the NOM and NOPBL runs, however, is substantial (+26% average over the entire model grid). Increases are noted in existing areas of large-scale precipitation in the northeast and mid-Atlantic states. Some of the precipitation difference between these two runs also comes from additional diagnosed convective activity. The Kuo convective scheme, which is triggered by low level moisture convergence, and the augmentation of surface convergence due to surface heating and frictional effects in the NOM run, is likely responsible for the increase in convective precipitation.

Precipitation patterns from the 24-hour NOM forecast in general coincide well with those measured (Fig. 1C). The absolute maximum amount (>3.5cm) from the forecast is evidenced in central New York State somewhat west of the corresponding measured maximum. The positions of the local smaller measured maxima around North Carolina, Lake Michigan and Arkansas are also depicted in the NOM forecast with about 100 km accuracy. This forecast fails to capture the measured maxima in Wisconsin, Florida and Georgia.

##### 5. Soil Flux Experiments

The five methods for estimating soil flux outlined previously were evaluated in SSM runs for July 21 to assess their characteristics and

assess the sensitivities of forecasts to variations in this surface energy component. Of these methods, 2 and 3 ( $S_o = C_q(Q_o)$ ,  $S_o = C_r \cdot (Rnet)$ ) are highly empirical, basing the soil flux on another component of the surface energy budget. Methods 4 and 5 are simplifications of a fully physical description of the submedium.

Constants employed in the two empirical methods have been researched for both bare soil and vegetation-covered conditions while, strictly speaking, the two physical methods apply only to bare soil. It is common practice at this point in time in many limited area models, however, to employ them over all terrain types with only the roughness height of the surface as a vegetation descriptor, rather than a full canopy model such as Deardorff (1978). The response of all methodologies to this simplification will be of interest.

The magnitude of the soil flux for the four methodologies where this term is not equal to zero (2-5) are shown for one daylight and one nighttime period in the forecasts in Fig. 3. For these forecasts, all characteristics of the NOM experiment have been retained except for varying the soil flux treatment.

The magnitude and direction of the soil flux (positive toward the surface) show noteworthy differences between the four methods investigated. Of immediate note is the spatial uniformity of the  $Q_o = C_r \cdot (Rnet)$  (RNET experiment, Fig. 3a-b) at both times. With this method, the main spatial variation in submedium conduction is due to the presence of diagnosed clouds modifying the radiation field. The spatial variation, for example, in the eastern states for the two time periods coincides exactly with cloudy areas. Differences in energy balance components caused by differences in ground wetness and roughness heights over the model grid

show little, if any, effect on conduction for this method -- a highly unreasonable condition.

A second undesirable characteristic of the method is evidenced where net radiation becomes small (generally large negative surface-air temperature differences at night). Under these conditions the surface layer may become extremely stable with a cutoff of sensible and latent heat exchange with the atmosphere. The simplified energy budget equation (1) would then be

$$R_{net} = S_o \quad (2)$$

and a generalized nighttime constant for soil flux as a function of net radiation ( $|C_r| < 1$ ) is inadequate. Unrealistically low calculated surface temperatures are the result.

The submedium flux predicted by the sensible heat  $S_o = C_q \cdot (Q_o)$  (SENS experiment, Fig. 3c-d) shows variations in space which depend heavily on the spatial variation of ground wetness, the chief modulator of the ratio of sensible to latent heat. Variations with roughness height across the model grid are less pronounced since roughness height effects on the sensible/latent heat ratio are secondary to ground wetness. Thus, areas of large sensible heating in the western states during the daytime exhibit the largest soil flux magnitudes. At night these same areas are generally clear with low winds. The result is low and uniform values of conduction to the surface.

Some spatial variation and higher magnitude are maintained at night in the northeastern U.S. where clouds and somewhat higher winds keep the surface layer from becoming stable enough to damp sensible heating to the surface.



With the SENS experiment, when sensible heat flux approaches zero (nighttime stable conditions), submedium conduction also goes to zero. No energy from the submedium is available to maintain surface temperature and anomalously low calculated temperatures are the result.

Observations have shown that to a good approximation, the amount of energy entering the submedium during daytime hours is returned to the surface at night. While we made no explicit efforts in these forecasts to keep track of the 24-hour net conductive energy to the soil, it can be seen in principle that the SENS method may violate this observation. For example, as shown, clear areas during the daytime are those which conduct the most energy into the submedium, yet those same areas are the ones which tend to be the most stable at night and return the least flux to the surface.

Figs. 4(a-b) show the time trace of conduction flux for a grid point in the Texas Panhandle which was cloud-free and had negligible advective effects (e.g., periodic forcing) for the RNET and SENS experiments. It is clear that neither of these methods approach having the 24-hour net soil flux equal zero.

Both the  $Q_o = \lambda/D \cdot (T_s - T_g)$  and force restore (KDT and FRES experiments respectively) methodologies for submedium flux are simplified physical models of the submedium. Rigorously they apply to bare soil, although it has become common practice to apply them to the "active surface" (Oke 1978) which, in theory, is a height at which the atmosphere exchanges mass momentum and energy with the surface.

The KDT method relies on the calculated temperature difference between the surface and the sublayer temperature (usually kept constant) to estimate soil flux. A characteristic of this is that the surface

temperature, forcing, and soil flux are always in phase, which is disparate with observation of real systems. The FRES method corrects for this deficiency by allowing energy exchange between the surface and deep soil layer. The result is the proper phase relationship of soil flux, forcing, and surface temperature.

The patterns of the magnitude of soil flux for KDT and FRES experiments are generally very similar, as evidenced in Fig. 3(e-h). Relative maxima of conduction exist in western regions with low ground wetness and roughness heights, and minima in the Midwest and East where ground wetness and roughness is greater. An interesting feature of the FRES experiment is the large magnitude of the soil flux compared with all other methods (factors of 1-5) at all the shown observation times. Some of this can be explained by the nature of the method, which for periodic forcing, predicts larger magnitude of soil flux before local noon than after. However, looking at the methods in Fig. 2 (a, c, e, h) at 18 GMT (about local noon in the Midwest), we see that the larger magnitudes relative to other methods persist even in eastern states which are past local noon. The magnitude of the soil flux in the FRES experiment seems unrealistically large for areas of both low and high roughness height (dense and sparse vegetation), compared with observations of these regimes (Oke 1978, Sellers 1965).

By 24 GMT (about 6 pm local time in the Midwest), the soil flux from the FRES method is directed toward the surface over the entire model domain. This is quite consistent with the observational studies, and the only method which has this characteristic.

Graphically, in Fig. 4c, we see that this property is important in allowing the 24-hour net soil flux to be closest to zero of any of the methods investigated.

For the KDT experiment, magnitudes of soil flux as evidenced in Fig. 3 are much lower than the FRES experiment, and appear more consistent with the aforementioned observational studies over various terrain conditions. The KDT method does not appear to approximate well the condition that 24 hour net soil flux be approximately zero (Fig. 4d).

Both KDT and FRES methods are sensitive to designated roughness height variations, and behave qualitatively correctly to this simple vegetation designation. Fig. 5 (a-b) shows an example at 18 GMT for these two experiments where the roughness heights were lowered to a value appropriate to bare soil. Marked increases in conduction are noted here versus the base experiments in Fig. 3 (e, g). Of note again are the high magnitudes of soil flux predicted by the FRES experiments, which here can be greater than 70% of the net radiation and do not seem reasonable.

a. Forecast differences between conduction experiments

The differences which exist between 24 hour SSM forecasts using the no soil flux condition and the four discussed methods of parameterization of soil flux are small and subtle. While the methods may vary greatly among one another in the amount and timing of the energy exchange with the submedium, large energy differences relative to the soil energy budget are most often small (< 20% of the net shortwave forcing). As a result, there are small differences between these five experiments in the 24-hour forecasts of sea level pressure and primary variables (temperature, mixing ratio, wind).

Surprising differences, however, do exist in the precipitation amounts between certain of the methodologies. Averaged over the entire model grid, the differences generally are not large, but they tend to be concentrated in existing areas of large-scale predicted rainfall, in these experiments, the northeast and mid-Atlantic states.

Table 2 shows total precipitation and precipitation at six-hour intervals averaged over the entire model grid for the five soil flux experiments. The RNET, KDT, and SENS experiments, which have similar magnitude and phase of soil conduction, show precipitation amounts very similar to one another, both total and over time. The FRES experiment, which predicts the highest magnitude of soil flux during daytime hours, has the lowest precipitation and the So=0 (NOCOND) experiment, with no flux exchange with the soil, the most. Two possible explanations are offered for this difference between the two experiments. First is the possibility that the augmented sensible heating in the NOCOND vs. FRES experiments is responsible for augmented surface-air coupling and increased low-level convergence patterns with resulting increase in precipitation. The second possibility hinges on the fact that the NOCOND experiment also has more energy available for evaporation than the FRES run. This increase in evaporation could result in increased precipitation, made more pronounced in certain areas due to advective and convergence mechanisms.

Table 2 shows that differences in precipitation have already begun to develop at only six and twelve hours into the forecasts between the NOCOND and FRES experiments. This is before we would expect the small differences in surface evaporation between the two to make much of a difference. It suggests that surface heating and surface-air coupling are responsible for precipitation differences. Later experiments varying the ground wetness parameter will lend more evidence to this conclusion.

Calculated surface temperature spatial patterns are very similar in the FRES, KDT, SENS and RNET experiments except for the previously noted localized nighttime anomalies with the SENS and RNET runs. The extreme differences are in the FRES and NOCOND runs which have the most and least

submedium exchange respectively. Daytime differences between the methods average about  $+3^{\circ}\text{K}$  for NOCOND vs. FRES. At night, when soil temperature is more sensitive to soil flux variations, the NOCOND temperatures are as much as  $10\text{K}$  lower than FRES.

## 6. Ground Wetness Experiments

Several experiments were run varying the value of the ground wetness parameter, GW, in an attempt to assess the sensitivity of model forecasts and surface temperature response to this parameter. Forecasts were run, using a distribution of GW from land use and vegetation evaluation (the NOM forecast), the extremes of GW (that is,  $\text{GW}=1$  and  $\text{GW}=0$ ) over the entire model grid, and also a forecast setting GW to an average value of .1 over the grid. All other characteristics of the NOM forecast were retained in these experiments.

Differences in primary variables between these forecasts are not large and are as expected. Highest low level temperatures and lowest sea level pressures are found for the  $\text{GW}=0$  (GWO) experiment which has the most sensible heating of the atmosphere. The  $\text{GW}=1$  (GW1) experiment is the opposite extreme, with both the  $\text{GW}=.1$  (GW.1) and NOM experiments being close to one another and in the middle of the range for low level temperatures and sea level pressure.

As with the soil flux experiment, we find that precipitation is sensitive to the value of ground wetness. Table 3 shows total differences in precipitation and differences over time between these ground wetness experiments. It provides additional evidence that, in these 24 hour forecasts surface convergence, as influenced by surface heating and surface-atmosphere coupling, is important in modulating precipitation

amounts. The GW0 experiment (no evaporation) has by far the most precipitation of any experiment run and the GW1 run, the least amount.

Experiments NOM and GW.1 fall close to one another in total precipitation amounts and between the previously mentioned extremes. With some exceptions, precipitation is generally higher between the GW.1 and NOM runs where this .1 value of GW is lower than the corresponding value in the NOM experiment, again supporting the importance of surface heating and convergence processes on this short term precipitation forecast.

Large calculated surface temperature differences exist between the extreme GW0 vs. GW1 experiments. During daylight hours surface temperatures in western regions with low roughness heights show as much as +20K difference. Areas with larger roughness heights show typically +10-15K.

At night there is less systematic temperature difference between these experiments evidenced over the entire model grid. In areas where the lower atmosphere is not excessively stable (eastern regions with higher winds, roughness heights and some clouds), some latent heating is maintained in the GW1 experiment, even at night. The result is lower surface temperatures here than in the GW0 run. In the stable western regions, the increased magnitude of submedium conduction in the GW1 experiment holds surface temperatures somewhat above those in the GW0 run.

#### 7. Roughness Height Experiments

Several forecasts for July 20 were made, varying the value of the surface roughness over the model grid from the climatological value used in the NOM run. In addition to the climatological distribution, SSM runs were made, using a value of  $Z_0 = .1$  cm, typical of bare soil, and  $Z_0 = 10$  cm, ( $Z_{0.1}$  and  $Z_{010}$  experiments respectively).

The differences between these 24 hour forecasts are minimal for sea level pressure and primary variables. Again, precipitation amounts are sensitive to this surface parameter in the areas of heavy large-scale precipitation in northeast, and mid-Atlantic states this time for reasons which are not obvious. Table 4 shows the time history of precipitation for these runs. In this case, the most total precipitation is exhibited by the experiment with the intermediate value of surface roughness, the  $Z_{0.10}$  experiment, and as Table 4 shows, it is the large amount of precipitation in the last 6 hours of the forecast which puts it in first place.

Until the last 6 hours, precipitation totals for these experiments had been in decreasing order with increasing roughness height. Zhang and Anthes (1982) have shown decreased values of sensible vs. latent heating with increasing roughness height (all other factors constant), and this was also observed in our forecasts. Before the last 6 hours it was surmised that the additional sensible heating (shown to be important in prior experiments) in the  $Z_{0.1}$  experiment was responsible for keeping precipitation the largest of these experiments.

In the last 6 hours, a conjecture is that the time history of evaporation has also become important and the  $Z_{0.10}$  run, which has had intermediate values of both evaporation and surface heating in the first 18 hours, has the largest precipitation due to the combination of these effects. More investigation is required, however, to prove this theory or to provide an alternative explanation.

In the eastern and midwest states, roughness heights are approximately an order of magnitude larger for the NOM vs.  $Z_{0.10}$  experiments. Here, daytime surface temperature differences of about +3K are noted for the  $Z_{0.10}$  run. In the western regions the 10 cm value for the  $Z_{0.10}$  experiment more

closely matches the climatological value in the NOM run, but decreased ground wetness in the area keeps the temperature difference between these experiments about the same as in the East and Midwest. At night there is very little surface temperature difference between these two experiments.

The  $Z_{0.1}$  experiment exhibits daytime surface temperatures which are about 6K above the NOM experiment in the East and Midwest and as much as +15K in dry western regions. Once again, at night the  $Z_{0.1}$  run shows surface temperatures very similar to the other roughness height experiments.

## 8. Comparison of Modelled and Measured Surface Temperatures

### a. Surface temperature measurements

Measured surface temperatures were derived for July 20 from brightness temperature data in two VAS infrared window channels (channel 7 at 12.6  $\mu\text{m}$  and channel 8 at 11  $\mu\text{m}$ ), using an empirical algorithm derived by matching VAS clear field of view satellite radiances with reports of sea surface temperature (SST) from NOAA fixed environmental buoys (Bates 1983).

SST's derived from VAS data have undergone extensive evaluation as part of a workshop series sponsored by NASA's Jet Propulsion Laboratory (Njoko 1984). Results from these workshops showed that VAS SST's have a scatter of .8-1.0 K and a slight warm bias with respect to other remotely sensed and in situ measurements. The two-window channel algorithm was slightly modified over land surfaces to account for higher land surface temperatures and varying land emissivity. Temperature corrections for this two-channel algorithm compared with single window channel temperatures from the GOES satellite correspond well in magnitude with those reported by Zandlo et al. (1982) corrected using TIROS-N water vapor channel measurements.

*Paper 25*



b. Temperature comparisons

Model calculated surface temperatures are sensitive to the initial analysis of lowest level model air temperature. For this reason we place primary emphasis on comparison of diurnal surface temperature range which should be less influenced by initial conditions. It has the added benefit of reducing temperature retrieval errors due to estimation of surface emissivity.

Fig. 6a shows the measured diurnal surface temperature excursion from the VAS instrument, and 6b those calculated from the NOM model experiment previously detailed. Some of the "measured" surface temperatures, mostly in cloudy areas of the eastern third of the U.S., have been interpolated between clear regions where a satellite measurement was possible. As such, they are representative of clear-air surface temperatures. Much of the same area was diagnosed cloudy in the NOM model run and, therefore, the model surface temperatures in these regions are representative of a cloudy regime (reduced insolation), and should not be compared with their interpolated measurement counterparts. Regions of exclusion for temperature comparison are outlined in Figs. 6a and b.

Several observations are immediately apparent in the comparison of the measured and modelled surface temperature range. First, is the relatively good agreement of this range in the east through the midwest. Second is the poor agreement over the western third of the model grid. While measured and modelled surface temperatures in these regions have certain features in common (twin maxima in New Mexico and Wyoming areas, and the general westward increase in surface temperature range), values are

systematically lower predicted vs. observed, sometimes by as much as 15K. Nighttime predicted temperatures were quite close to those observed (usually  $\pm 3K$ ), and so it is the daytime predicted surface temperatures which are at fault for the large discrepancies.

Suggested causes for these discrepancies between measured and modelled temperatures lies in the climatological assessment of ground wetness and roughness heights used in the model. Some systematic overestimation of  $Z_0$  in western regions was noted in our survey compared with the more comprehensive analysis of Matthews (1983) which is probably a contributing factor.

Most of the failure of the NOM experiment in duplicating observed surface temperatures, however, comes from the extreme sensitivity of surface temperatures and the balance of surface fluxes to the ground wetness parameter in the dry range ( $GW \leq .1$ ). Fig. 7 shows the Bowen Ratio ( $B_0 = Q_0/E_0$ ) plotted at local noon for model grid point with varying values of ground wetness from the NOM experiment. While other differing parameters between grid point ( $Z_0$  and soil flux) can also influence the Bowen Ratio, similar plots for these variables showed ground wetness to be by far the dominating factor.

This graph points to several unsettling conclusions for the ground wetness as a moisture parameter and its evaluation. Within a range of about 0-.1 surface evaporation is critically dependent on the specification of GW, and differences as small as several hundredths make large differences in the flux balance and the daytime surface temperature excursion.

On the investigation day, July 20, 1981, notable dry anomalies existed in ground wetness in the western states, compared with climatological

values. The USDA Crop Moisture Index for this day, with small exceptions, varied from slightly dry to severely dry (vs. climatological) over the model grid west of a line extending from western North Dakota through the Texas Panhandle. Thus, to begin with, the climatological value of GW used in the model is probably an overestimation for this day, and contributes to observed temperature and flux errors.

Even if moisture conditions on this day matched climatological, however, the question remains whether it is possible to initialize GW to the approximately .02 tolerance required to accurately depict surface fluxes in this dry range.

We were able to well-approximate the observed maximum of temperature range in the western regions with the aforementioned reduction of roughness height and, most importantly, reducing ground wetness from .02 to 0.

## 9. Conclusions

The sensitivity of numerical forecasts to variations in ground wetness, roughness length, and soil flux treatment has been documented in a case study for summer, 1981. Generally, the differences in the 24-hour forecasts of primary variables with varying surface treatment were not large, and it is modulations in precipitation which stand out as the main difference between these forecasts. In all cases, maximum precipitation differences were in the areas of significant large-scale precipitation evidenced in the control (NOM) forecast and were typically 10-30% of the control amount. It appears that the main cause for the precipitation differences regime are modulations in sensible heating and associated convergence and surface coupling patterns between experiments.

The implications are that boundary layer and precipitation (convection) parameterizations must be developed and tuned in unison for precipitation prediction and that an accurate local representation of the surface will be required. Model sensitivity to surface variations also suggests that anomalies in surface properties from climatological values may be important in certain synoptically sensitive areas, and thus remote sensing of surface energy budgets may have a role in short term forecasting.

Of the soil flux methods examined, two, the RNET and SENS methods, are undesirable because of anomalous surface temperatures at night, poor response to surface roughness characteristics, and poor 24-hour flux conservation, which may have an impact in longer term (climate) forecasts. The KDT method also does not predict 24-hour net flux well, but does well for instantaneous flux magnitude. The FRES method well-conserves the 24-hour flux but over-predicts instantaneous values. Of the soil flux methods, it is FRES which has been most rigorously derived for bare soil conditions. Using the method with only a simple vegetation designation such as roughness height instead of a full canopy treatment, while commonly done, may be the cause of some of the inadequacy. Even terrain with sparse vegetation usually has a cover of rubble, organic matter, or its residue which influences energy transfer. Lowering the thermal conductivity in the FRES method to a value representative of these situations may well alleviate some of its over prediction.

Surface temperatures and temperature range were relatively well-predicted in areas with moderate to high roughness heights and ground wetnesses and are not very sensitive in those regions to errors in these parameters. However, in dry regions with low roughness heights, small

errors in the assessment of ground wetness (a moisture parameter in very common use in climate and limited-area models) cause very large errors in surface temperature and the surface flux balance. This suggests that a very careful climatological evaluation of ground wetness need be made, or that an alternative moisture variable be chosen for which small errors do not have such drastic effects.

Acknowledgements -- This work was conducted under the auspices of National Science Foundation Grant ATM-8218092.

8/DIAK2/04

## REFERENCES

- Anthes, R.A., 1983: Regional models of the atmosphere in middle latitude. Mon. Wea. Rev., 111, 1306-1355.
- \_\_\_\_\_ and D. Keyser, 1979: Tests of a fine mesh model over Europe and the United States. Mon. Wea. Rev., 110, 1187-1213.
- Bates, J.J., 1983: Satellite-derived sea surface temperature: Workshop I. JPL Publication 83-34. Jet Propulsion Laboratory, California Inst. of Technology, Pasadena, CA 91109.
- Benoit, R., 1976: A Comprehensive Parameterization of the Atmospheric Boundary Layer for General Circulation Models, NCAR Cooperative Thesis No. 39, National Center for Atmospheric Research, Box 3000, Boulder, CO 80307, 278 pp.
- Bhumralkar, C.M., 1975: Numerical experiments on the computation of ground surface temperature in an atmospheric circulation model. J. Appl. Meteor., 14, 1246-1258.
- Blackadar, A.K., 1977: High resolution models of the planetary boundary layer. Advances in Environmental Science and Engineering, Vol. 1. Gordon and Breach, 50-85.
- Businger, J.A., J.G. Wyngaard, Y. Izumi, and E.F. Bradley, 1971: Flux profile relationships in the atmospheric surface layer. J. Atmos. Sci., 28, 181-189.
- Danard, M.B., 1969: Numerical effects of surface friction on large scale atmospheric motions. Mon. Wea. Rev., 97, 835-844.
- Deardorff, J.W., 1978: Efficient prediction of ground surface temperature and moisture with inclusion of a layer of vegetation. J. Geophys. Res., 83, 1889-1903.
- Diak, G.R., and C. Gautier, 1983: Improvements to a simple physical model for estimating insolation from GOES data. J. Appl. Meteor., 22, 505-508.
- Gadd, A.J., and J.F. Keers, 1970: Surface exchange of sensible and latent heat in a 10-level model atmosphere. Quart. J. Roy. Meteor. Soc., 96, 297-308.
- Garratt, J.R., and B.B. Hicks, 1973: Momentum, heat, and water vapour transfer to and from natural surfaces. Quart. J. Roy. Meteor. Soc., 99, 680-687.
- \_\_\_\_\_, 1977: Review of drag coefficients over oceans and continents. Mon. Wea. Rev., 105, 915-928.

- \_\_\_\_\_, 1978: Transfer characteristics for a heterogeneous surface of large aerodynamic roughness. Quart. J. Roy. Meteor. Soc., 104, 491-502.
- Garrett, A.J., 1982: A parameter study of interactions between convective clouds, the convective boundary layer, and a forested surface. Mon. Wea. Rev., 110, 1041-1059.
- Gates, W.L., and A.B. Nelson, 1975: A new (revised) tabulation of the Scripps topography on a 1° global grid. Part I: Terrain heights. Rep. R-1276-1-ARPA. The Rand Corporation, 1700 Main St., Santa Monica, CA 90406, 132 pp.
- Gautier, C., G. Diak, and S. Masse, 1980: A simple physical model to estimate solar radiation at the surface from GOES satellite data. J. Appl. Meteor., 29, 1005-1012.
- Geylen, J.F., 1981: Some diagnostics of the cloud/radiation interaction in the ECMWF forecasting model. Workshop on Radiation and Cloud Interaction in Numerical Modelling, Shinfield Park, United Kingdom, 15-17 October 1980. European Center for Medium Range Weather Forecasting, Shinfield Park, U.K., 209 pp.
- Hammerstrand, U., 1977: On parameterization of convection for large scale numerical forecasts at mid latitudes. Beiträge zur Physik der Atmosphäre, 50, 78-88.
- Hummel, John R., and R.A. Reck, 1979: A global surface albedo model. J. Appl. Meteor., 18, 239-253.
- Kasahara, A., and W. Washington, 1971: General circulation experiments with a six-layer NCAR model, including orography, cloudiness, and surface temperature calculations. J. Atmos. Sci., 28, 657-701.
- Katayama, A., 1972: A simplified scheme for computing radiative transfer in the troposphere, Technical Report No. 6, Department of Meteorology, University of California at Los Angeles, 405 Hilgard Avenue, Los Angeles, CA 90024, 77 pp.
- Kung, E.C., R. Bryson, and D. Lenschow, 1964: Study of a continental surface albedo made on the basis of flight measurements and structure of the earth's surface cover over North America. Mon. Wea. Rev., 92, 543-564.
- Kuo, H.L., 1964: On formation and intensification of tropical cyclones through latent heat release by cumulus convection. J. Atmos. Sci., 22, 40-63.
- \_\_\_\_\_, 1974: Further studies of the parameterization of the interaction of cumulus convection on large-scale flow. J. Atmos. Sci., 31, 1232-1240.
- McGregor, J.L., L.M. Leslie, and D.J. Gauntlett, 1978: The ANMRC limited area model: consolidated formulation and operational results. Mon. Wea. Rev., 106, 427-438.

- Njoko, E.G., 1984: Satellite-derived sea surface temperature: workshop comparisons. Submitted to Bull. Amer. Meteor. Soc.
- Norton, C., F. Mosher, B. Hinton, D. Martin, D. Santek, and M. Kuhlow, 1980: A model for calculating atmospheric turbidity over the oceans from geostationary satellite data. J. Appl. Meteor., 19, 633-644.
- Oke, T.R., 1978: Boundary Layer Climates, John Wiley & Sons, 372 pp.
- Paltridge, G.W., and C.M.R. Platt, 1976: Radiative Processes in Meteorology and Climatology. Elsevier Scientific Publishing Company, 318 pp.
- Peterson, R.A., D. Keyser, A. Mostek, and L. Ucellini, 1983: Severe storms analysis and forecasting techniques using VAS satellite data. Proceedings 13th Conf. Severe Local Storms, Boston, Amer. Meteor. Soc., 375 pp.
- Sellers, W.D., 1965: Physical Climatology. University of Chicago Press, 272 pp.
- Smith, W.L., V.E. Suomi, F.X. Zhong, and W.P. Menzel, 1982: Nowcasting applications of geostationary satellite atmospheric sounding data. Nowcasting, Academic Press, 123-135.
- Zandlow, J.A., W.L. Smith, W.P. Menzel, and C.M. Hayden, 1982: Surface temperature determination from an amalgamation of GOES and TIROS-N radiance measurements. J. Appl. Meteor., 21, 44-50.
- Zhang, D., and R.A. Anthes, 1982: A high resolution model of the planetary boundary layer-sensitivity tests and comparisons with SESAME-79 data. J. Appl. Meteor., 21, 1595-1609.



### Table Captions

1. Forecast model characteristics
2. Precipitation per area vs. time for soil conduction experiments. Arbitrary units.
3. Same as 2, but for ground wetness experiments.
4. Same as 2, but for roughness length experiments.

Table 1.

Prognosis Model Characteristics

Primitive equations model in  $\sigma$ -coordinates  
Ten vertical levels at  $\sigma = .09, .19, .29, \dots, .99$   
Horizontal resolution: 67 km & 134 km  
Staggered horizontal grid (Arakawa "C" grid)  
Semi-implicit time differencing ( $\Delta t = 10$  min)  
Similarity theory surface layer  
Stability dependent vertical diffusion of momentum, heat,  
moisture above surface layer through depth of PBL  
Surface shortwave and longwave flux modified by cloudiness  
Surface energy balance equation  
Large-scale precipitation  
Kuo-type convective parameterization  
Horizontal diffusion of momentum, heat, moisture  
Updated boundary conditions

Table 2

<u>Forecast Length</u>	<u>Experiment</u>				
	<u>KDT</u>	<u>FRES</u>	<u>RNET</u>	<u>SENS</u>	<u>NOCOND</u>
6 hrs	7.3	7.2	7.2	7.3	7.4
12 hrs	26.3	25.0	26.0	26.2	27.2
18 hrs	52.5	49.6	51.3	52.5	54.7
24 hrs (total)	80.3	78.4	81.3	84.6	88.7

Table 3

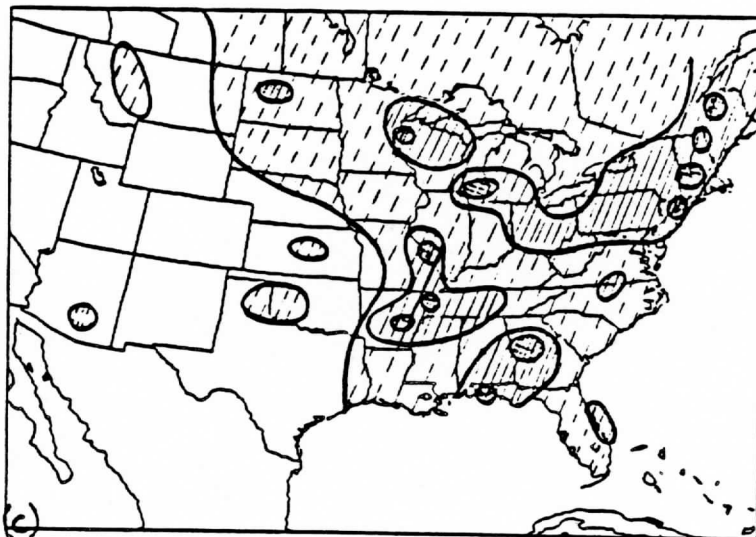
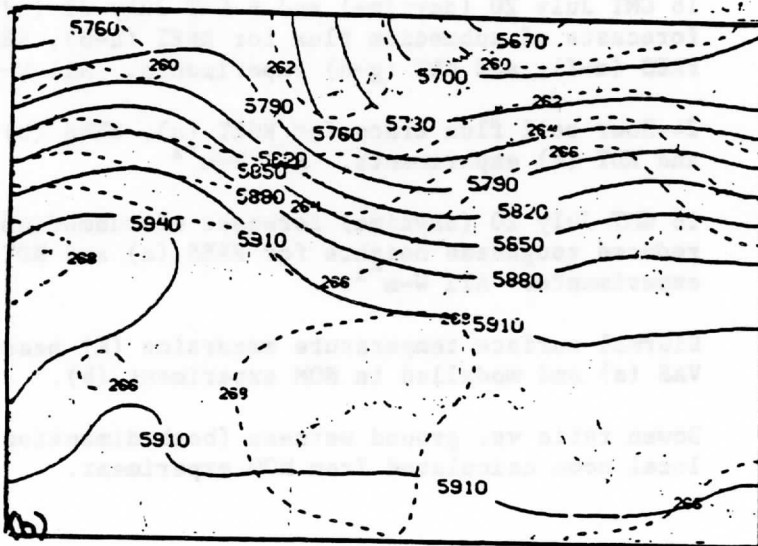
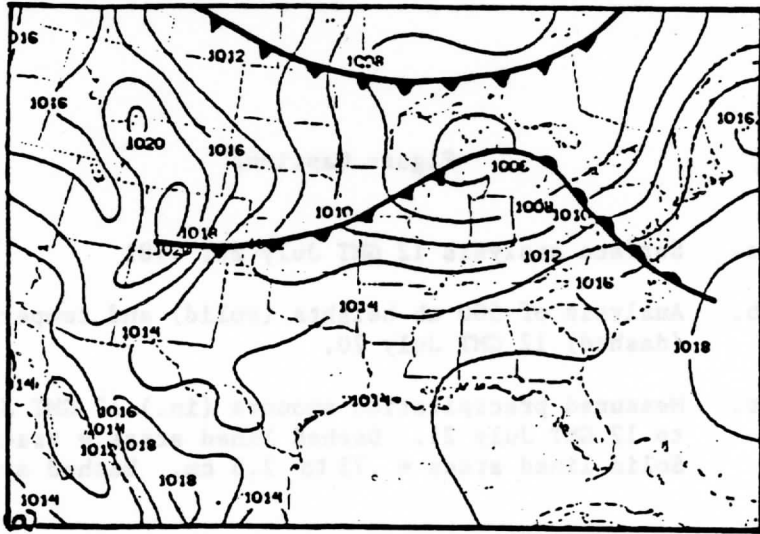
<u>Forecast Length</u>	<u>Experiment</u>			
	<u>NOM</u>	<u>GWO</u>	<u>GW1</u>	<u>GW.1</u>
6 hrs	7.2	10.5	6.5	7.3
12 hrs	25.0	49.0	22.0	26.3
18 hrs	49.6	96.0	44.3	53.7
24 hrs (total)	78.4	166.0	69.6	88.5

Table 4

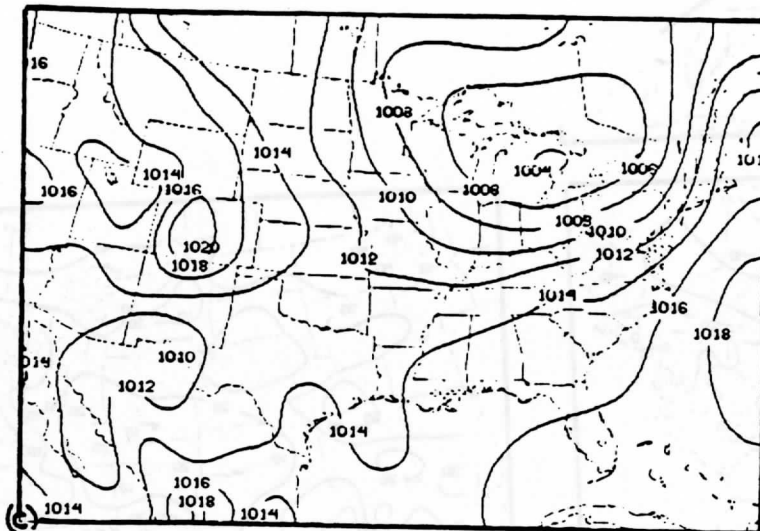
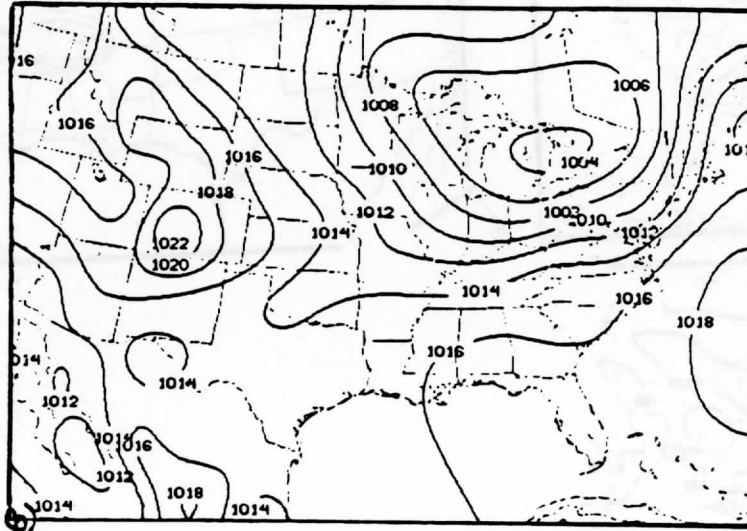
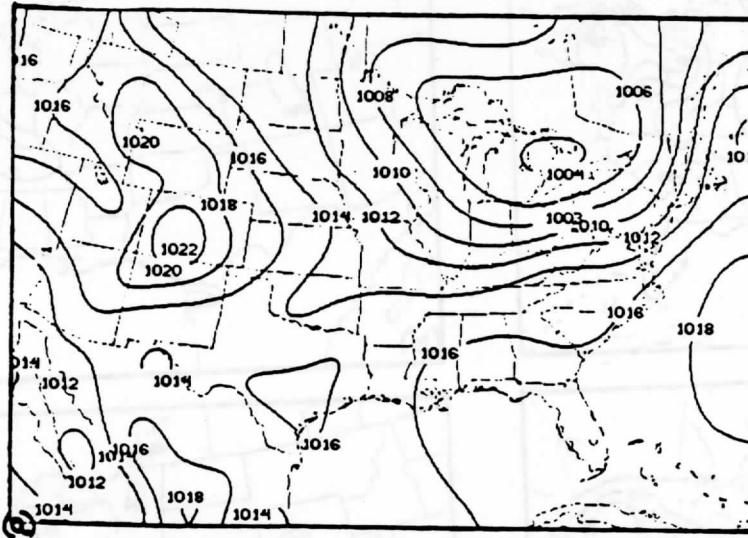
<u>Forecast Length</u>	<u>Experiment</u>		
	<u>NOM</u>	<u>Z<sub>0.1</sub></u>	<u>Z<sub>0.10</sub></u>
6 hrs	7.2	7.6	7.5
12 hrs	25.0	29.4	28.2
18 hrs	49.6	56.6	55.6
24 hrs (total)	78.4	86.4	90.2

Figure Captions

- Figure 1
- a. Surface analysis 12 GMT July 20, 1981
  - b. Analysis of 500 mb heights (solid) and temperatures (dashed) 12 GMT July 20.
  - c. Measured precipitation amounts (in.) 12 GMT July 20 to 12 GMT July 21. Dashed lined areas = trace to .75 cm. Solid lined areas = .75 to 2.5 cm. Hashed areas = > 2.5 cm.
- Figure 2 12-Hour forecasts of sea level pressure (mb) for NOPBL (a), DRAG (b), and NOM (c) experiments.
- Figure 3 18 GMT July 20 (daytime) and 6 GMT July 21 (nighttime) forecasts of submedium flux for RNET (a-b), SENS (c-d), FRES (e-f), and KDT (g-h) experiments. All  $W\text{-m}^{-2}$ .
- Figure 4 24-Hour soil flux trace for RNET (a), SENS (b), FRES (c), and KDT (d) experiments. All  $W\text{-m}^{-2}$
- Figure 5 18 GMT July 20 (daytime) forecast of submedium flux with reduced roughness heights for FRES (a) and KDT (b) experiments. All  $W\text{-m}^{-2}$ .
- Figure 6 Diurnal surface temperature excursion (K) measured from VAS (a) and modelled in NOM experiment (b).
- Figure 7 Bowen ratio vs. ground wetness (both dimensionless) at local noon calculated from NOM experiment.



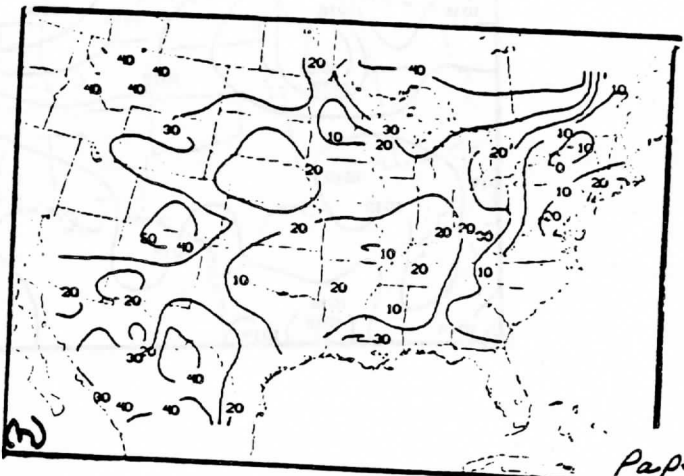
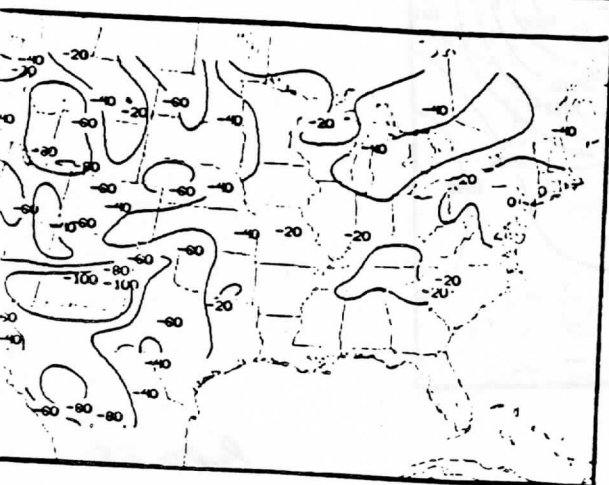
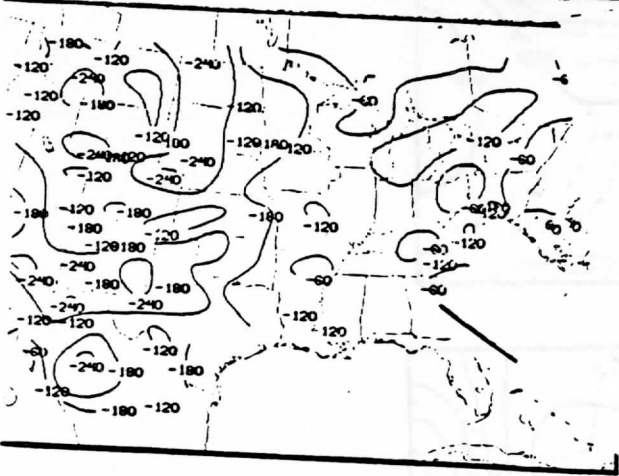
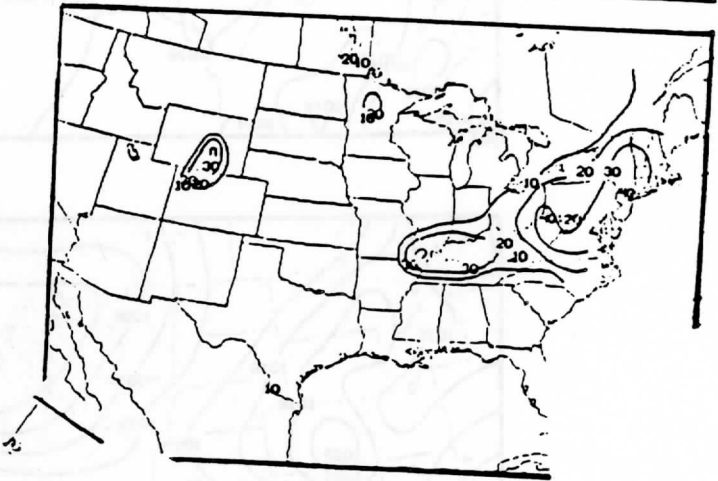
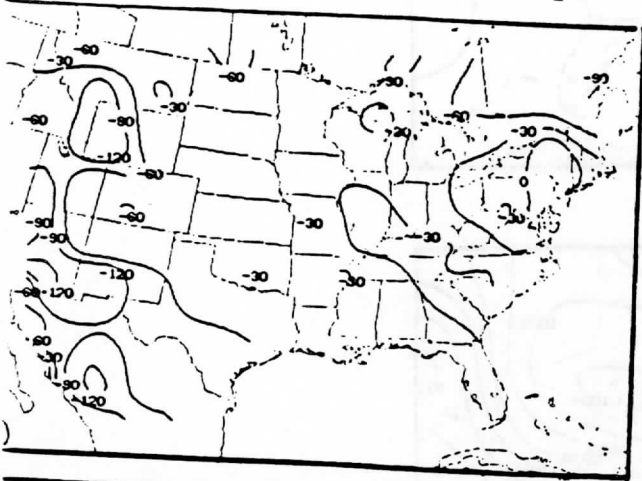
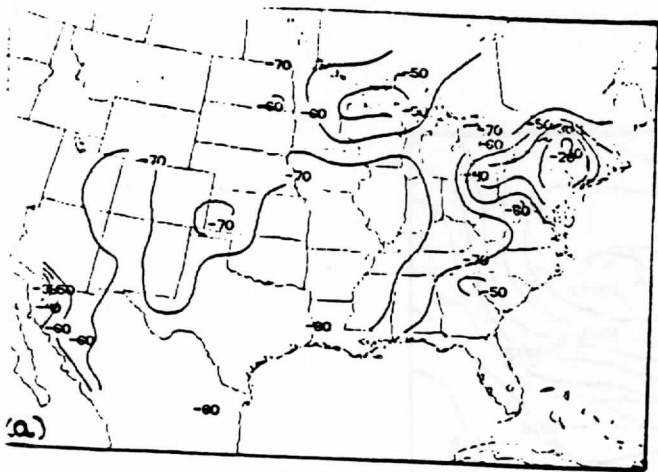
Paper 25  
Fig 1



Paper 25

Fig 2





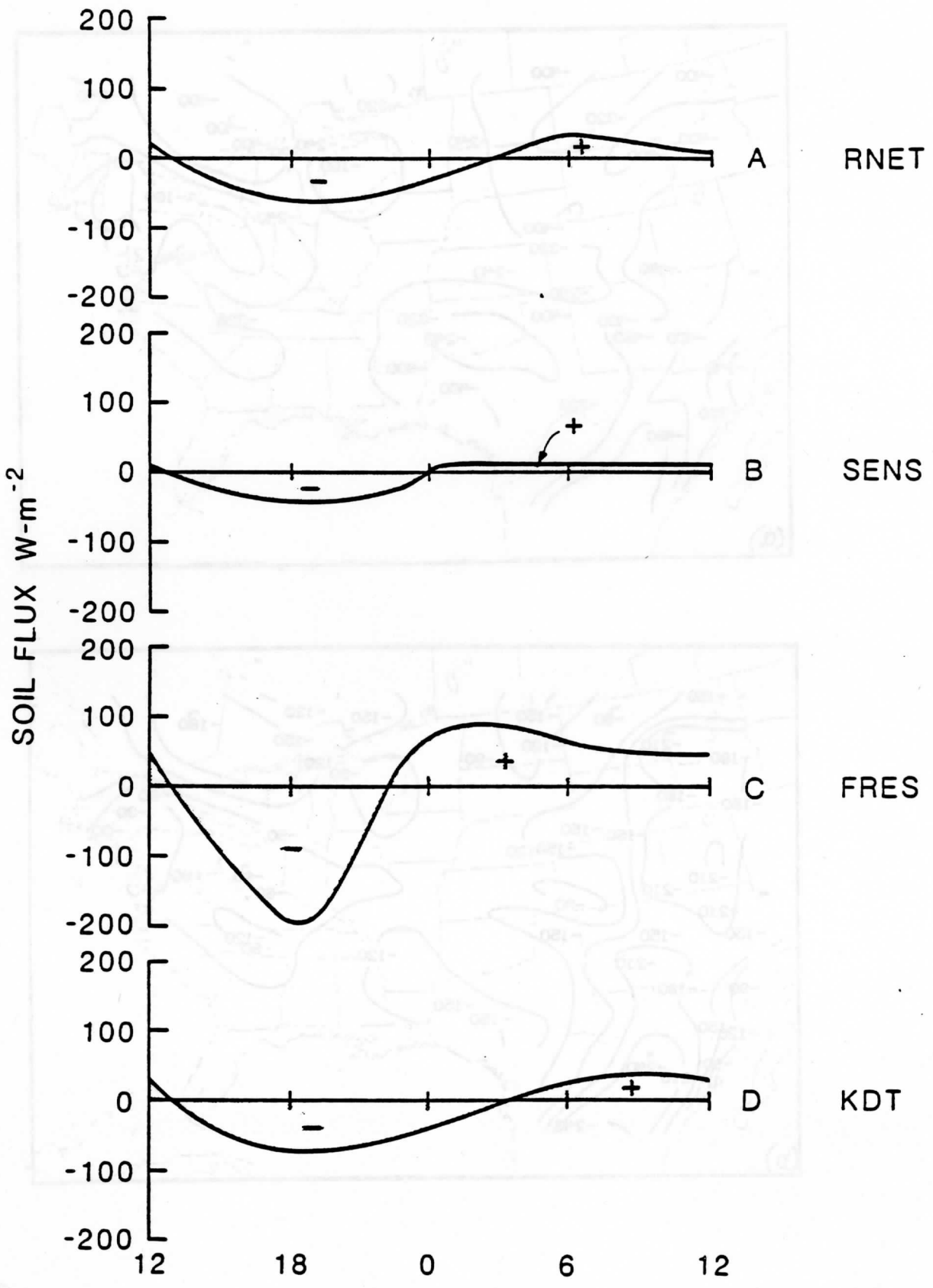
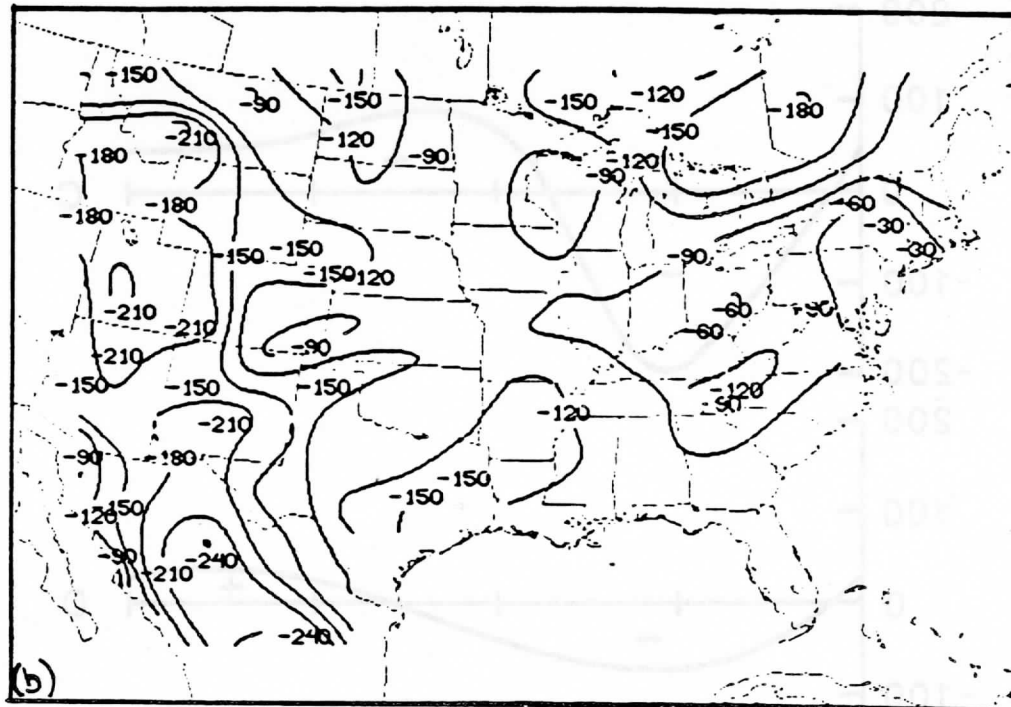
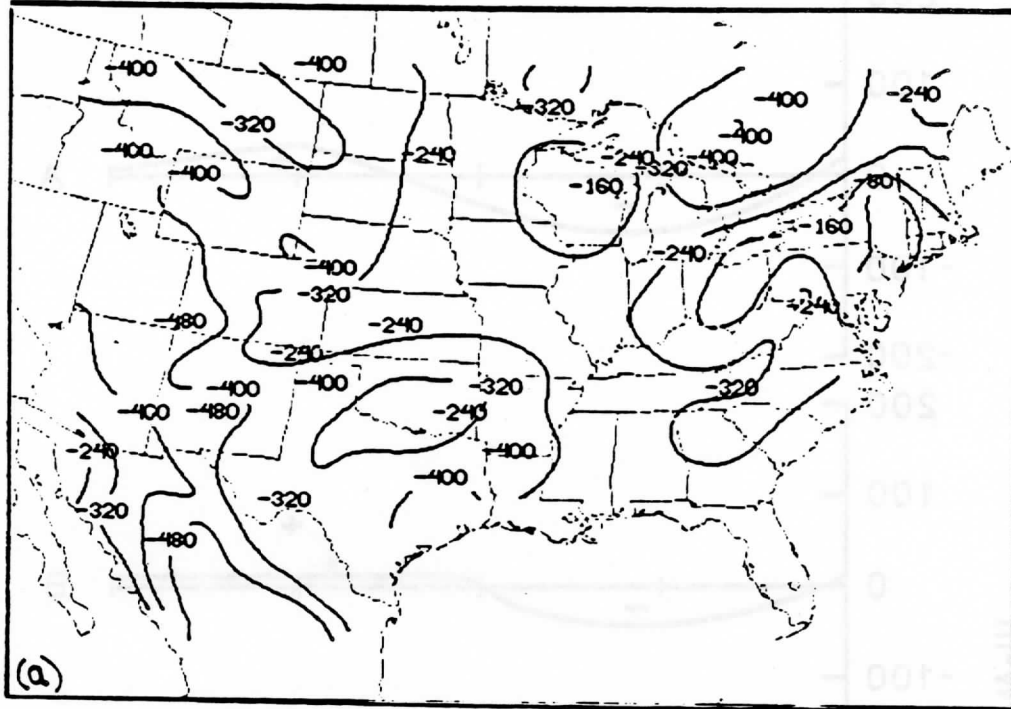
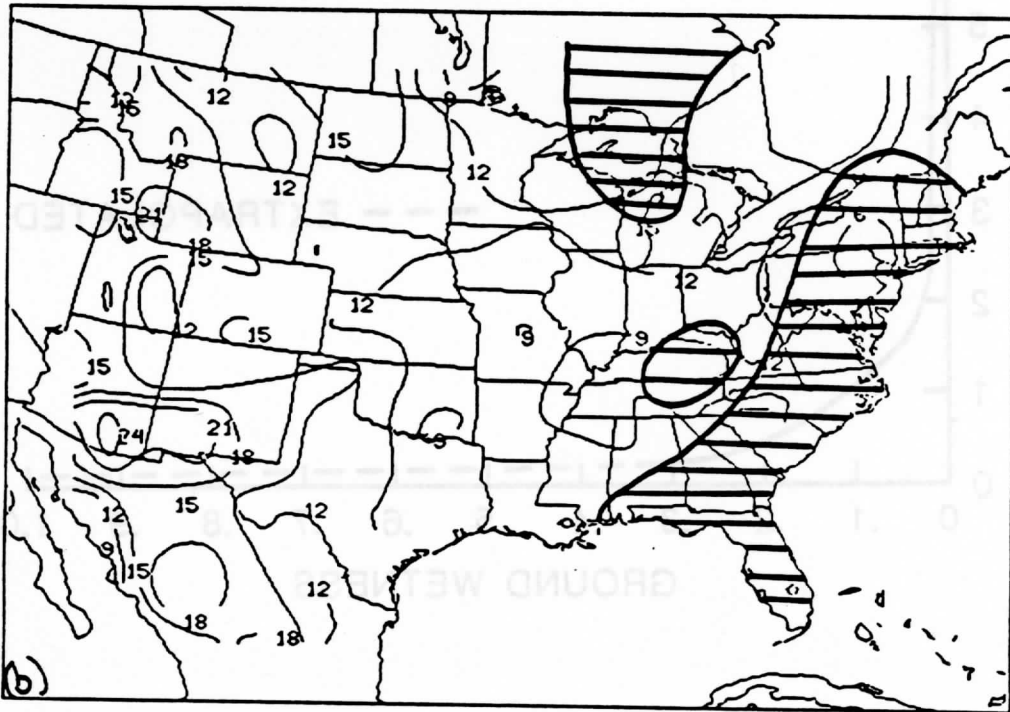
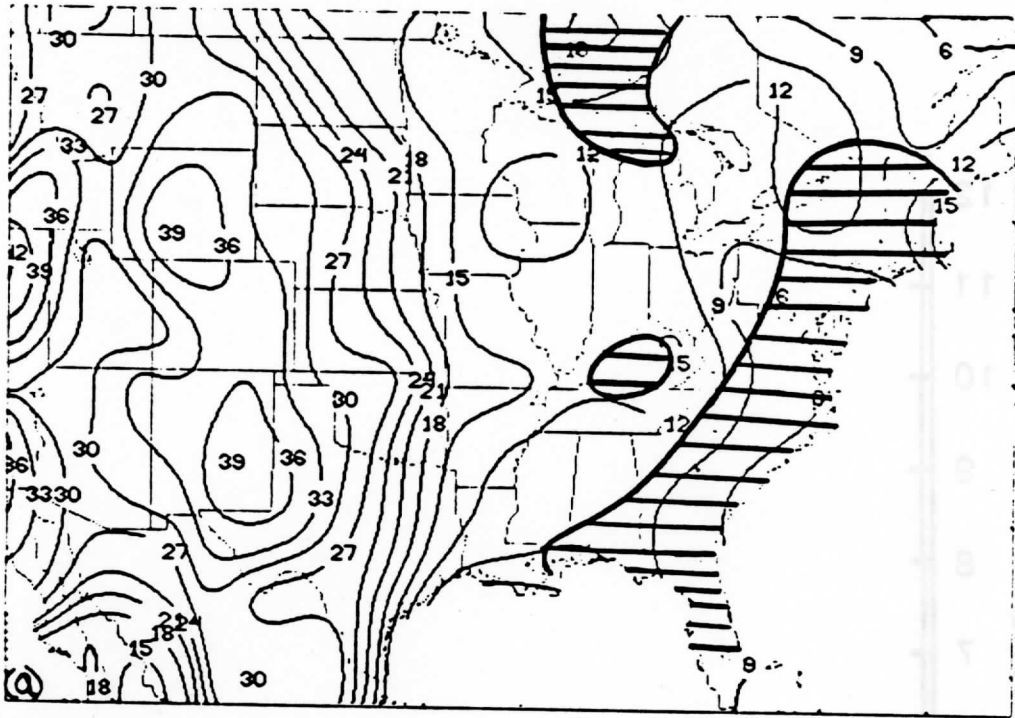


Fig. 4





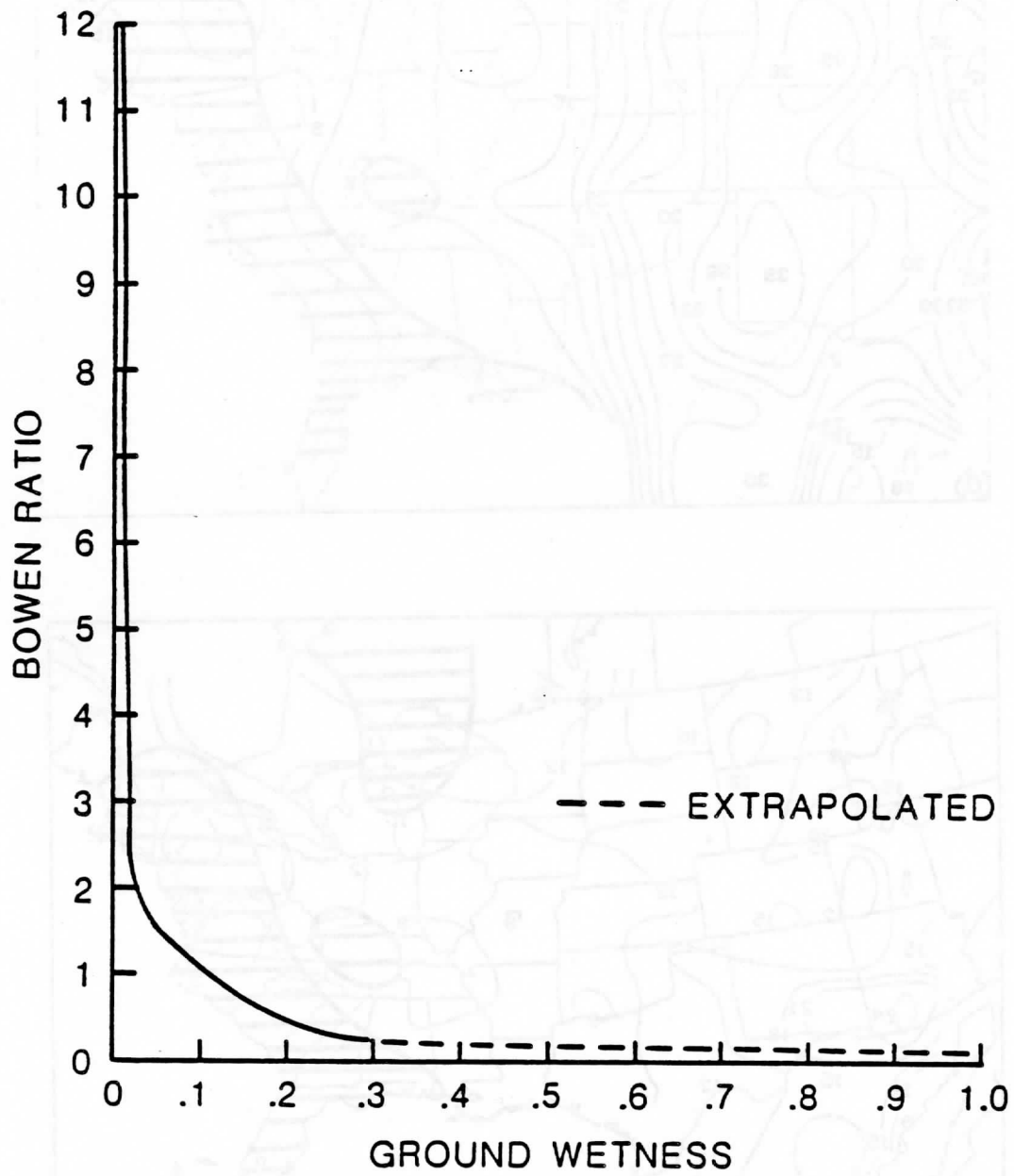


Fig 7

A NEW APPROACH TO THE OPTIMAL ASSIMILATION OF  
METEOROLOGICAL DATA BY ITERATIVE BAYESIAN ANALYSIS

R. James Purser  
Cooperative Institute for Meteorological Satellite Studies  
(On leave from United Kingdom Meteorological Office)  
University of Wisconsin  
1225 West Dayton Street  
Madison, Wisconsin 53706

1. INTRODUCTION

The requirement of modern objective data assimilation schemes to accommodate data of different types and variable reliability has led to an increasing emphasis on the use of statistically based methods of analysis in the preparation of initial fields for numerical prediction models. Notable contributions to the development of analysis schemes that are in some statistical sense optimal have been made by Sasaki (1958) and by Gandin (1963) who pioneered the technique of optimum interpolation. Developments by Rutberford (1972), Schlatter (1975), Bergman (1979), and Lorenc (1981) have established it as an effective practical technique.

This paper describes a method of analysis currently under development which generalizes the linear formulation of optimum interpolation to an essentially non-linear one, exploiting a statistical approach based on Bayes' theorem of conditional probabilities. While under special restricted conditions the Bayesian approach becomes identical to the linear optimum interpolation, a more general non-linear formulation appears formally to be able to handle in a statistically consistent and unified way several aspects of the data assimilation problem that have hitherto been dealt with separately. These include the problem of data "quality control," i.e., how to treat the occasional, but potentially damaging, occurrence of observations that, for unknown reasons, possess abnormally large errors; the consistent inclusion of non-linear balancing procedures or "initialization" and the direct insertion of satellite derived data avoiding the separate intermediate step of performing independent single-column retrievals of temperature and humidity. In addition, this formulation can accommodate a number of adaptive features that were sometimes present in empirical analysis methods, such as the stretching or bending of structure functions of "successive correction" schemes according to the local flow features that are intuitively desirable but which are lacking in conventional optimum interpolation.

The Bayesian scheme is presented in relation to conventional optimum interpolation. Being non-linear it demands the use of iterative methods and the recognition of this fact has strongly influenced the composition of the algorithms designed to achieve the desired optimal analysis. Consideration has been given to strategies that avoid where possible the explicit manipulation (e.g., inversion) of very large matrices which would consume an inordinate amount of computation, and an outline is sketched of the algorithmic structure developed to attain this objective.

2. OPTIMUM INTERPOLATION AND BAYESIAN GENERALIZATIONS

In optimum interpolation an analysis  $A_i$  consisting of one or more variables at each gridpoint  $i$ , is obtained as a linear combination of a "background" field  $B_i$  (also known as each gridpoint) and an incomplete scatter of observations  $O$  located at observations points  $a$ . The linear coefficients are chosen to minimize the expected mean square of the analysis error  $A_i'$  and are derived from knowledge or estimates of the covariances  $C_{ij}$  of background field errors  $B_i'$  and from the covariances  $E_{ab}$  of observational errors  $O'$ , assuming that all errors are unbiased and that the set  $\{O'\}$  are uncorrelated with set  $\{B_i'\}$ . It is convenient to use  $i, j, k, \dots$  to label standard gridpoint values and  $\alpha, \beta, \gamma, \dots$  to denote individual observables. Also a function  $D(B)$  will be used to express the composition of observable  $\alpha$  (e.g., a particular satellite radiance observation) in terms of the standard gridpoint values. With these conventions and assumptions it will be stated without proof that the analysis sought is given by the matrix equation

$$A_i = B_i + \int_{\alpha\beta} (CD)_{i\alpha} (D^T CD + E)_{\alpha\beta}^{-1} (O - D(B))_{\beta} \quad (1)$$

where

$$D_{i\alpha}(B) = \frac{\partial D(B)}{\partial B_i} \quad \text{and} \quad D_{\alpha\beta}^T = D_{i\alpha}$$

Using the above subscript convention no confusion will arise by identifying

$$C_{i\alpha} \equiv \int_j C_{ij} D_{j\alpha}$$

$$C_{\alpha\beta} \equiv \int_{ij} D_{i\alpha}^T C_{ij} D_{j\beta}$$

$$A_{\alpha} \equiv D_{\alpha}(A) = D_{\alpha}(B) + \int_i (A_i - B_i) D_{i\alpha}$$

A significant feature of (1) that is immediately evident is that a matrix inverse is required, the order of the matrix being formally equal to the number of observations considered. In a large scale analysis system based on the Gandin method it is of course impossible to solve the formal system (1) and it is customary to restrict severely the number of observations permitted to influence each grid point.

An alternative approach to analysis optimization can be developed from probabilistic principles. Imagine a "state" of the system, i.e., its  $N$  gridpoint values, as represented by a point in an  $N$ -dimensional space whose coordinates are the possible gridpoint values themselves, thus both the analysis  $A$  and background  $B$  can be regarded as position vectors in this "state-space." Similarly the  $M$  observables may be thought of as defining a point in an  $M$ -dimensional "observation space." Each individual observable  $a$  is associated with a continuous family of  $(M-1)$ -dimensional surfaces in state-space parametrized naturally by the values of  $D$ . In practice, knowledge of the state is always somewhat vague and may be formally regarded at any time as a probability density function in state-space, for example, the prior knowledge or assumptions of the "location" of the atmospheric state are summarized by a probability density,  $P_B(B')$  of the errors  $B'$  of the initial guess  $B$  comprising the locally most probable state. Note that this choice for  $B$  implies

$$\left. \frac{\partial P_B(B')}{\partial B_1'} \right|_{B'=0} = 0. \quad (2)$$

Similarly, the observations are known to contain random errors or to be contaminated by effects too small or too transient to be significant so it is natural to express this degree of vagueness also in probabilistic terms. For example, by assuming that the observation errors  $O'$  are each distributed independently by a probability density  $P(O')$ . Assuming the prior distribution  $P_B$  is obtained independently from the new observations (e.g., using climatology, a previous forecast together with dynamical constraints) then it is possible to combine the two sources of information into a single conditional probability distribution, say  $P_A$ , using Bayes' rule for conditional probabilities.

$$P_A(A) = \rho P_B(B-A) \prod_{\alpha=1}^M P_{\alpha}(O_{\alpha}-A_{\alpha}) \quad (3)$$

where  $\rho$  is a normalizing factor. Figure 1 illustrates schematically the typical application

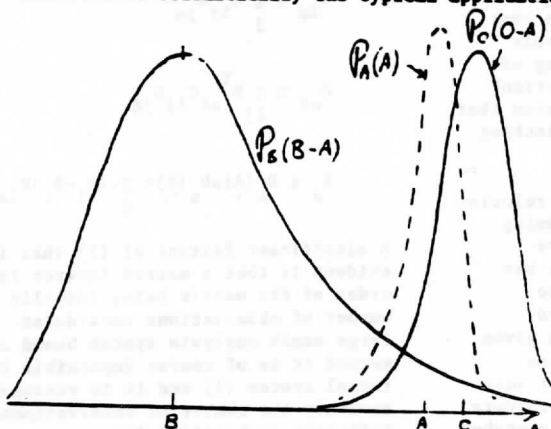


Figure 1: Schematic illustration of Bayes' rule in one dimension.

of this rule to one dimension, the conditional probability density  $P_A$  being peaked between the peaks of distributions  $P_B$  and  $P_C$ , to be narrower than either of them and to be closer to the narrower distribution  $P_C$  than to  $P_B$ . Following the spirit of Gandin's optimum interpolation one would consider the centroid of  $P_A$  as the optimal analysis since only at this location in state-space is the expectation squared error of each component of  $A$ , of the analysis simultaneously minimized. However, a simpler procedure, though one that is arguably less "optimal," is to redefine the optimal analysis as that which maximizes  $P_A$  itself (or equivalently, its logarithm) with respect to local variations of the components  $A_1$ , i.e.,

$$\frac{\partial}{\partial A_1} \log P_A = \frac{\partial}{\partial B_1} \log P_B(B') + \sum_{\alpha=1}^M D_{1\alpha} \frac{\partial}{\partial O_{\alpha}} \log P_{\alpha}(O_{\alpha}') = 0 \quad (4)$$

where

$$O_{\alpha}' = O_{\alpha} - A_{\alpha}$$

$$B_1' = B_1 - A_1$$

This general formulation can be shown to reduce to standard linear optimum interpolation with independent observational errors under the assumptions of Gaussian structures to  $P_B$  and  $P_{\alpha}$  and the linearity of function  $D$ .

Then

$$P_B(B') \propto \exp \left\{ -\frac{1}{2} \sum_{ij} C_{ij}^{-1} B_i' B_j' \right\} \quad (5)$$

$$P_{\alpha}(O_{\alpha}') \propto \exp \left\{ -\frac{1}{2} E_{\alpha}^{-1} O_{\alpha}'^2 \right\}$$

reducing (4) to

$$\sum_{ij} C_{ij}^{-1} B_j' + \sum_{\alpha} D_{1\alpha} E_{\alpha}^{-1} O_{\alpha}' = 0$$

hence

$$A_1 = B_1 + \sum_{ij} C_{ij}^{-1} D_{j\alpha} E_{\alpha}^{-1} (O_{\alpha} - A_{\alpha}) \quad (6)$$

which is equivalent to (1) when  $A_{\alpha}$  is eliminated from the right side.

Under more general circumstances "effective" statistics can be obtained to replace  $E_{\alpha}^{-1}$  and  $C_{ij}^{-1}$ . In principle these are obtained from the local behavior of the probability densities  $P_B$  and  $P_{\alpha}$  in the vicinity of  $B$  and  $O$  and formally yield a pseudo-covariance  $C_{ij}$  whose matrix inverse is

$$C_{ij}^{-1} = - \left( \frac{\partial^2 \log P_B(B')}{\partial B_i \partial B_j} \right) \frac{B_j}{\sum_k (B_k^2 R_k)} \quad (7)$$

and the pseudo-variance  $E_a$  whose inverse is

$$E_a^{-1} = - \frac{\partial}{\partial O_a^2} \frac{\log P_a(O_a^2)}{O_a^2} \quad (8)$$

An important point to make here is not that one should attempt to catalogue a comprehensive tabulation of probabilities  $P_a$  and  $P_0$  and extract effective statistics as in (7) but rather that one should recognize that the Bayesian method is flexible enough to accommodate effective statistics that are adaptive to the situation being analyzed and that it provides guidance as to how this might be done.

A suggestion of the versatility and potential of the adaptive formalism is provided by illustrating its handling of observations known occasionally to contain gross errors, i.e., those for which a traditional analysis method requires a separate quality control procedure. For simplicity suppose the errors of observable  $a$  have a probability density:

$$P_a(O_a^2) = \exp \left\{ E_0^{-1} a \left[ \exp \left( - \frac{O_a^2}{2a} \right) - 1 \right] \right\} \quad (9)$$

as illustrated in Figure 2a for  $a=2E_0^{-1}$ . Note the existence of non-vanishing tails in this distribution, consistent with the occasional appearance of gross errors. The impact of such an observable on the analysis as a function of its final departure from that analysis is given by the "forcing function:"

$$X_a(O_a^2) = E_0^{-1} O_a^2 - \frac{\partial}{\partial O_a^2} \log P_a(O_a^2)$$

i.e.,

$$X_a(O_a^2) = E_0^{-1} \exp \left( - \frac{O_a^2}{2a} \right) O_a^2 \quad (10)$$

(Figure 2b). It is evident that the impact of the observation is negligible if a large disparity persists between it and the analysis. To complete the picture (Figure 2c) the effective weight is, by (8):

$$E^{-1}(O_a^2) = E_0^{-1} \exp \left( - \frac{O_a^2}{2a} \right) \quad (11)$$

This artificial example demonstrates the ability of the formalism to incorporate in a natural way a form of quality control, but by continuous weighting rather than by an explicit rejection-acceptance criterion.

### 3. COMPUTATIONAL CONSIDERATIONS

The implicit optimal analysis equation (6) forms the core of the iterative methods. Since it contains no non-trivial matrix inverse it is simple to verify. Suppose an approximation  $A$  to the optimal analysis is obtained by replacing  $E^{-1}(O_a - A)$  in (6) by an approximation to the forcing,  $X_a$ . The degree of inconsistency between

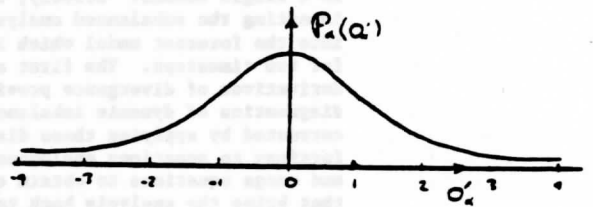


Figure 2a:  $P_a$  as a function of  $O_a^2$ .

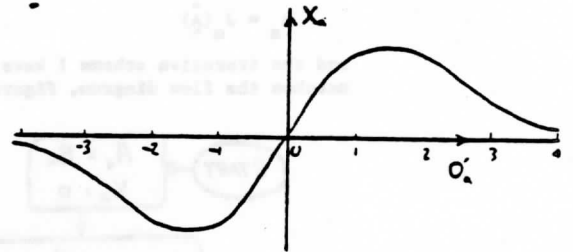


Figure 2b:  $X_a$  as a function of  $O_a^2$ .

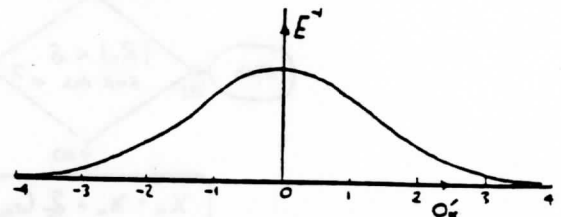


Figure 2c:  $E_a^{-1}$  as a function of  $O_a^2$ .

these approximations is measured by evaluating the residual,

$$R_a = E_a^{-1}(O_a - A_a) - X_a \quad (12)$$

for each observable (only when the residual vanishes for every observable is the analysis obtained in this way "optimal"). The sensitivity of  $R$  to changes in  $X$  is

$$\frac{\partial R_a}{\partial X_b} = -(E_a^{-1} C_{a\beta} + I_{a\beta})$$

where  $I_{a\beta}$  is the unit matrix. Then provided an approximation to the inverse of this matrix is available, one may obtain an improved estimate of  $X$  and hence of  $A$  by means of the correction:

$$X_a = X_a + \sum_{\beta} C_{a\beta} R_{\beta} \quad (13)$$

where

$$C_{a\beta} = (E^{-1} C + I)^{-1}$$

The repetition of this procedure will lead to successively better analyses. Adaptive features of the Bayesian method discussed earlier, i.e., the updating of  $C$ ,  $D$ ,  $E^{-1}$ , may be included. In addition, it becomes feasible to



incorporate periodically adjustments that insure that a state of dynamical balance is maintained, thereby combining "analysis" and "initialization" in a single scheme. Briefly, this is achieved by inserting the unbalanced analysis, now denoted  $A$  into the forecast model which is then run forward for two timesteps. The first and second time derivatives of divergence provide convenient diagnostics of dynamic imbalance which can be corrected by applying these diagnostic fields as forcings to equations analogous to the balance and omega equations to obtain correction fields that bring the analysis back towards a state of balance,  $\hat{A}$ . Symbolically this procedure is written,

$$A_a = J_a(\hat{A})$$

and the iterative scheme I have described then matches the flow diagram, Figure 3.

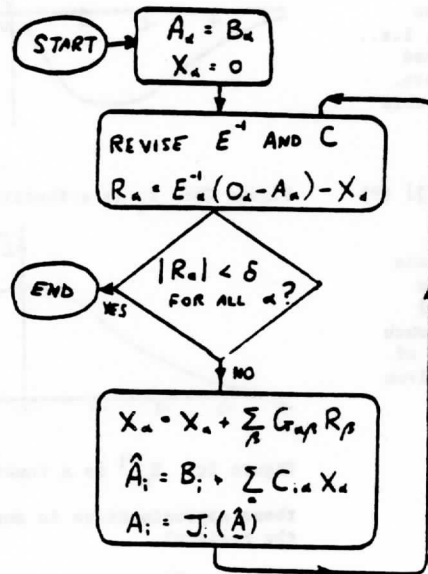


Figure 3: Flow chart for an iterative Bayesian analysis algorithm.

A major difficulty with this algorithm is obtaining an estimate for  $C$ , which is good enough to give a reasonably rapid convergence of the algorithm yet which does not require the direct computation of large matrix inverses. There are indications that the problem is alleviated by using a method able to discriminate between the different spatial scales at which analysis corrections are required and to treat these scales separately. One approach is to organize the observations into small clusters and to exploit the fact that the forcing,  $X$  formed by the sum of forcings  $X$  in a tight cluster  $\beta$  and acting at the centroid of this cluster, has an impact almost identical to that of the original forcings  $X$ . In this way it is possible to approximate the analysis problem by a coarser-scale representation containing fewer elements. The corrections deduced at the coarser scale are enforced as temporary strong constraints of a modified analysis problem when the iterative algorithm descends back to the finer scale. The clustering procedure, and the

associated adjustments to the analysis algorithm are readily extended to a hierarchy of levels of clustering. It is found that reliably good approximations  $C_a$  to the correction matrices at each level of the hierarchy may now be obtained without excessive computation. This strategy is analogous to the "multigrid" algorithm developed by Brandt (1977) and others to accelerate the convergence of iterative solutions of elliptic equations.

#### 4. CONCLUSION

An alternative statistical formalism for dealing with general problems in meteorological data assimilation has been introduced. This enables several aspects of the problem previously treated separately, notably those implicitly requiring nonlinear treatments, to be brought together within a unified framework. Methods of solving the resulting equations are necessarily iterative and this fact is used to advantage in the design of algorithms that avoid the direct and costly inversion of large matrix systems which appear in conventional optimum interpolation. By transforming the problem into a series of representations at progressively coarser scales it is possible to enhance the efficiency of the algorithm as a whole. A high-priority application of the technique is to the three dimensional assimilation of satellite radiances to circumvent the somewhat dubious custom of treating retrieved satellite temperatures in an analysis as if they comprise a set of observations with errors independent of those of the background field. If successful a unified and consistent approach to the analysis of mixed satellite and ground based observation would be of obvious benefit.

#### 5. REFERENCES

- Bergman, K. B., 1979: Multivariate analysis of temperatures and winds using optimum interpolation. *Mon. Wea. Rev.*, 107, 1423-1443.
- Brandt, A., 1977: Multi-level adaptive solutions to boundary-value problems. *Math. Comp.*, 31, 333-390.
- Gandin, L. S., 1963: Objective analysis of meteorological fields. Leningrad, Gidromet; (Jerusalem, Israel Program for Scientific Translations; 1965, 242 pp.).
- Lorenc, A., 1981: A global three dimensional multivariate statistical interpolation scheme. *Mon. Wea. Rev.*, 101, 701-721.
- Rutherford, I. D., 1972: Data assimilation by statistical interpolation of forecast error fields. *J. Atmos. Sci.*, 29, 809-815.
- Sasaki, Y., 1958: An objective analysis based on the variational method. *J. Meteor. Soc. Japan*, 36, 77-88.
- Schlatter, T. W., 1975: Some experiments with a multivariate statistical objective analysis scheme. *Mon. Wea. Rev.*, 103, 246-257.

THE USE OF VAS WINDS AND TEMPERATURES AS INPUT  
TO BAROTROPIC HURRICANE TRACK FORECASTING

John M. Lewis and Christopher M. Hayden  
NOAA/NESDIS Development Laboratory  
1225 West Dayton Street, 2nd Floor  
Madison, Wisconsin 53706

**DRAFT**

Christopher S. Velden, Tod R. Stewart and Raymond J. Lord  
Space Science and Engineering Center  
1225 West Dayton Street  
Madison, Wisconsin 53706

Lloyd Shapiro and Stanley Goldenberg  
NOAA/OAR/ERL/AOML Hurricane Research Division  
4301 Rickenbacker Causeway  
Miami, Florida 33149

Abstract

Wind and temperature observations from the GOES-East satellite are used to augment the normal input to the SANDers BARotropic (SANBAR) model that is routinely used to track hurricanes. The winds are obtained at three levels and amalgamated into a deep layer mean wind that is used to initialize the model. Cloud elements are tracked at upper (approximately 250 mb) and lower (approximately 850 mb) levels to get wind estimates and water vapor imagery is tracked at the middle levels (approximately 400 mb). These winds are combined with the VAS thermal gradient winds and coupled vertically by using geopotential thickness observations from VAS in conjunction with the gradient thermal wind law. A variational adjustment process has been used similar to one deployed at FNWC. Following the vertical coupling, a time coupling is accomplished using a sequence of three analyses of the deep layer mean that are six to twelve hours apart. The time coupling uses the absolute vorticity of the deep layer mean as a standard of comparison and makes changes to the vorticity (and associated streamfunction) by requiring a least squares adjustment subject to the SANBAR model constraint, conservation of absolute vorticity.

Deep layer mean winds are found for data collected for the case of Hurricane Debby in September 1982. Comparisons are made between the normal SANBAR forecasts and those initialized with VAS data.

Abstract

Regional cloud distribution parameters for the Arabian Sea region during the onset phase of the 1979 summer monsoon have been derived through analysis of three-dimensional radiance histograms constructed from near local noon visible and infrared imagery from GOES-I. The techniques and the limitations are discussed and the derived cloud distribution statistics corresponding to low, medium, high and cumulonimbus categories are presented.

THE REGIONAL CLOUD DISTRIBUTION DURING THE ONSET PHASE  
OF THE 1979 SUMMER MONSOON BASED ON GOES-I IMAGERY

by

Hassan Virji<sup>1</sup>  
Space Science and Engineering Center  
and  
Leroy D. Herman  
NOAA/NESDIS Development Laboratory  
University of Wisconsin  
1225 West Dayton Street  
Madison, Wisconsin 53706

<sup>1</sup>Current affiliation: National Science Foundation  
Washington, DC

Abstract

Regional cloud distribution parameters for the Arabian Sea region during the onset phase of the 1979 summer monsoon have been derived through analysis of bi-dimensional radiance histograms constructed from near local noon visible and infrared imagery from GOES-I. The technique and its limitations are discussed and the derived cloud distribution statistics corresponding to low, medium, high and cumulonimbus categories are presented.

THE REGIONAL CLOUD DISTRIBUTION DURING THE ONSET PHASE  
OF THE 1979 SUMMER MONSOON BASED ON GOES-I IMAGERY

BY

Wesley V. Kousky  
James R. Kousky and Engineering Center  
and  
Larry D. Herman  
NOAA NESDIS Development Laboratory  
University of Wisconsin  
1500 West Dayton Street  
Madison, Wisconsin 53706

Current Affiliation: National Science Foundation  
Washington, DC

## 1. Introduction

One objective of the 1979 Monsoon Experiment (MONEX) was to document the pattern of heating fields over main heat source and sink regions for various phases of the summer monsoon. A necessary ingredient for fulfilling this objective is the knowledge of cloud distribution over these regions. The cloud cover associated with the rapidly evolving onset vortex during the monsoon onset phase had a pronounced effect on the magnitude and spatial pattern of the earth and atmosphere radiation balance (Virji et al., 1982). Whereas few systematic conventional observations of cloud type, relative cover, top and bottom pressures were made over the Arabian Sea during the field phase of the summer MONEX, analysis of satellite imagery provides perhaps the best means for determining the regional cloud distribution parameters. This study examines the feasibility of such an approach.

Several investigators have considered the question of cloud classification from satellite imagery (Minnis and Harrison, 1983; Desbois et al., 1982; Smith et al., 1981; Fye, 1978; Reynolds and Vonder Haar, 1977). The usual technique for determination of cloud heights and amounts from satellite imagery involves objective analysis of multi-dimensional radiance histograms extracted from the imagery. The problem is to separate the many radiance classes of the histograms into cloud types, relative cloud cover, and to assign appropriate cloud top and base levels. A simplification generally made is that all observations producing a certain set of reflectance and brightness temperature values are assumed to result from a common cloud height, amount, and opacity. A schematic illustration of the resulting general empirical relationship between infrared and visual gray shades for various cloud and surface types is shown in Fig. 1.

Information on cloud types, depths, and amounts for various cloud modes are deduced from the radiance histograms using as empirical relations those formulated by Reynolds and Vonder Haar (1977) and Mosher (1976). The procedure used here to interpret the radiance histograms into information on cloud parameters has been summarized in Smith (1978). Realistic estimates of the relative accuracies to be expected from such analysis on a regional basis at a given time are 5% in cloud cover and 1 km in cloud top altitude.

During 1979, the GOES-I satellite was positioned at the equator and 58 E longitude. The infrared sensor (~~0.5-0.9~~<sup>11-12.5</sup>  $\mu\text{m}$ ) on board malfunctioned after 21 June 1979, but concurrent radiance observations in the visible and infrared channels are available for the onset phase of the 1979 summer monsoon and provide an opportunity to use the bi-dimensional histogram technique to deduce cloud distribution parameters during the evolution of the onset vortex over the Arabian Sea region. The purpose of this note is to report on cloud distribution during this period derived from the high resolution GOES-I imagery.

The analysis of bi-dimensional histograms from GOES-I satellite visible and infrared imagery for the onset phase of the 1979 summer monsoon is discussed in the next section. Estimates of the cloud distributions for the 1979 monsoon onset phase analyzed on a two degree grid are presented in Section 3.

## 2. Data and Analysis

The onset of the 1979 summer monsoon occurred during 11-20 June. For this period, hourly full resolution two channel Visible Infrared Spin-Scan Radiometer (VISSR) imagery for the region bounded by the equator to 28 N and 48 E to 84 E was displayed on the Man-computer Interactive Data Access System Data Access (McIDAS) facility at the University of Wisconsin-Madison. The GOES-I VISSR observations were calibrated using in-situ radiance measurements made by NASA

CV-990 instrumented aircraft in order to obtain representative measurements of reflectance from the satellite data (Smith et al., 1981). The reflectance ( $r_g$ ) for the GOES-I spectral region 0.5-0.9  $\mu$ m was obtained from the calibration relation:

$$r_g = 0.0000164 C_g - 0.00077$$

where  $C_g$  is the square of the digital brightness count (range 0-255) from the GOES-I visible channel divided by the cosine of the solar zenith angle and the earth-sun distance factor. The brightness temperature was determined from the standard calibration of the GOES-I infrared channel supplied by the National Environmental Satellite, Data, and Information Service (NESDIS). With the exception of poor quality infrared data between 0600-1500 GMT on 13 June 1979 all data at resolution 4 mi. from near local noon hour over the central Arabian Sea (approximately 1830 GMT) was used in the bi-dimensional radiance histogram analysis described below.

For each consecutive two degree square box within the study domain, a two-dimensional histogram of reflectivity and brightness temperature was computed. The four mile resolution data yielded a total of over 900 pixel values in each grid box along the northern edge of the domain and over 1000 pixel values in each grid box along the equator. The histogram values were coded in frequency class intervals of 10% units of reflectivity (visible grayshade) ranging between 0-100% and 10K degrees brightness temperature (infrared grayshade) over the total range 190-330 K. For typical 2 X 2 degree regions around selected grid points within the study domain shown in Fig. 2 (labeled A-F), the corresponding bi-dimensional histograms are displayed in Fig. 3. The clusters over different frequency classes in these examples corresponding to different cloud types conform with the schematic representation of Fig. 1.

The sea surface reflectivity under clear sky conditions (e.g., Fig. 2,

location A), is generally less than 10%, except in regions of specular reflection over the ocean. Land surface under similar conditions has higher reflectivity (greater than 15%) and generally higher brightness temperature (greater than 300 K). Exceptions could be land/sea areas under cloud shadows or where it has recently rained. Topography variations can cause further indeterminacy in the bi-dimensional radiance histogram frequencies. Most of the terrain within the study domain is under 3 km altitude, an exception being the northeastern corner where the permanent snow cover over the Himalayan mountain ranges would be in the high reflectivity and low surface temperature classes of the histogram.

The large variability in the histogram frequencies depending upon the variety of surface and atmospheric conditions observed by the satellite is evident in the radiance histograms shown in Fig. 3. In particular, the radiance frequencies are spread over a broad spectrum of histogram classes at those grid locations where several cloud types are present (Fig. 3D). Several relative maxima can be identified in the cases corresponding to a mixture of different cloud types. A reduction of this spread into distinct clusters of observations, assumed to result from similar cloud height, amount, and opacity, can be achieved in several ways. For example gaussian distribution type least square fits have been used (Smith, 1978; Desbois et al., 1982). For the purposes of this preliminary analysis, the following somewhat simpler and faster approach was used.

An iterative search of the entries in the radiance histogram was used to identify principal and other local maxima. On the first pass, all entries adjacent to and including the principal maxima were summed at the class location of the maxima. The adjacent class entries were then set to zero. In subsequent passes, maxima in descending order were similarly processed. Allowance was made for two or more adjacent classes being equal, in which case the order of adding



the entries into a maxima was decided by the relatively larger sum computed. Ten iterations were generally sufficient to reduce the entries into distinct classes accounting for over 99% of the total population of the histogram. Remaining entries (totaling less than 1%) were merged into the nearest cloud category.

An empirical calibration (table 1) of the bi-dimensional radiance histogram classes was used to assign cloud top and bottom pressure levels and thus appropriate vertical depths to the various cloud types. This calibration procedure, discussed by Mosher (1976) and Peslen, 1980, has been successfully used during the operational cloud tracking program of MONEX to assign pressure heights to the cloud wind data. The essential steps are as follows. First, optical thickness is computed from the observed visible brightness. The cloud depth is then calculated from the relation  $T = \sigma p z$ , where  $T$  is the optical thickness,  $z$  is the physical depth,  $\tau$  is the scattering cross-section typical of the cloud type, and  $p$  is the number density of cloud particles. The plane-parallel doubling model of Hansen (1971) is assumed to be valid for the tropical standard atmosphere and the standard drop size distribution given in Deirmendjian (1969) is used. The minimum and maximum levels are set at 950 and 100 mb, and earth's surface temperature value for the calibration is fixed at 305 K. The resulting calibration is summarized in Table 1 where cloud top and bottom pressure levels are shown as a function of reflectivity and cloud top temperature.

The assumptions implicit in the conversion of the histogram categories into cloud depths limit the accuracy of the method. In particular, the use of the plane parallel model ignores the fact that clouds have different shapes. The leakage of radiation from the sides of finite clouds is not taken into consideration and the resulting indeterminacy in the cloud depth estimates can be significant (Suchman et al., 1981). Therefore, in this study the cloud types of

figure 1 are combined into four general categories corresponding to low, medium, high, and cumulonimbus clouds. This combination reduces some of the indeterminacy. The final product of the analysis for the selected cases from Fig. 3 is shown in Table 2. A careful comparison of the derived cloud populations over the region with ground based observations is not possible in view of sparse surface based observations. Few available ship and aircraft observations during this period seem to indicate that the above analysis produces a reasonable depiction of the cloud layers present. A comparison of this analysis with the nephanalysis of the Air Force Global Weather Central is currently in progress.

Note that when only two-dimensional radiance histograms based on visible and infrared imagery are used to compute cloud depths, semi-transparent clouds such as thin cirrus (emissivity  $\ll 1$ ) can be misclassified due to infrared flux upwelling through the cloud, as is the case at location F (Fig. 2). In this case a small amount of thin cirrus cloud (around 5%) was present and misclassified as cumulus. Use of additional channels (e.g., water vapor channel, 5,7-7.1  $\mu$ m) can help reduce such indeterminacy (Desbois et al., 1982). However, for GOES-I data, we are restricted to availability of observations in only two channels.

An obvious problem in satellite determination of cloud parameters relates to the fact that overcast sky conditions at a higher levels mask clouds at lower levels. Though several different cloud types can be recognized in the histogram, it is very difficult to delineate clouds which in reality are vertically stacked. A satisfactory resolution of this difficulty has not yet been achieved. The above deficiencies of the model should be kept in mind during the following discussion of the regional cloud distribution during the onset phase of the summer MONEX.

### 3. Cloud distribution

During the beginning of the onset of the 1979 summer monsoon, a major cloud cluster formed on 12 June at 8-12 N/75 E within a well defined 700 mb shear line (Sikka and Grossman, 1980). This shear line intensified and moved northward over the next two days. Concurrently, a significant increase in cloudiness occurred around 8-15 N/55-80 E leading to the formation of the onset vortex at 10 N/70 E. A tropical depression formed in the central Arabian Sea during 16-18 June which over the next four days drifted gradually northwestward toward Oman. Well defined cloud clusters developed within the vortex near 19 N/85 E toward the end of the onset phase.

The satellite derived cloud distributions are shown in Figures 4 and 5. for various cloud types at the beginning and end of the onset phase are shown in Figs. 4 and 5. The zonally averaged total cloud cover (Fig. 4) is seen to evolve northward over the Arabian Sea. While no significant change in the total cover occurred around the Horn of Africa (figure 5), the percent cover in the southwestern sector along the region of the low level jet axis underwent at least a two-fold increase during the onset phase. The cloud cover associated with the tropical depression which drifted to Oman by 20 June contributed to the 100% increase in the cover over this region of the Saudi Arabian peninsula. In contrast, in the region of the onset vortex, the total cover increased by at least two-fold. Concurrently, the total cloud cover over central India also increased two-fold, while southward over Sri Lanka, the total cover remained the same as at the beginning of the onset phase.

The breakdown of the total cover into various cloud types at the beginning and the end of the onset phase is also shown in Fig. 5. The northward transition of various cloud types as the onset phase progressed is clearly evident. In particular, a substantial increase in low level cloudiness occurs

in the western Arabian Sea in the region of the mean low level jet axis. Elsewhere, the signal in the low level cloudiness may have been obscured by increases in cloudiness at higher levels. The maxima in middle level cloudiness occur primarily along the boundaries of the regions of deep convection. The high level cloudiness represents the cirrus outflow from the cumulonimbus clouds and is maximized towards the end of the onset phase over the entire region consistent with the increase in the convective activity as the onset progressed northward. Perhaps the most interesting distribution is that of cumulonimbus clouds. At the beginning of the onset phase over the Arabian Sea (June 12), no two degree square region contains 100% coverage of the cumulonimbus-type. In contrast, at the end of the onset (June 20), 100% coverage occurs at a number of grid locations in the two convectively active regions of the onset vortex and the tropical depression.

The evolution of these convective regions is easily evident on a composite plot of the regions where significant cumulonimbus occurrence takes place (Fig. 6). Here, maximum values of cumulonimbus coverage taken from daily analyses at local noon have been replotted in sequence for each of the ten days of the onset phase. Besides the northward transition and increase in the cumulonimbus activity, two major regions of intense convection (Cb clusters) are evident from the beginning of the onset phase. The western Cb cluster was easily tracked on a sequence of images of the last five days of the onset as it developed into a tropical depression which drifted toward the coast of Oman. Considering the high-frequency pulsations in the cumulonimbus activity (more frequent than once a day), the depiction of cumulonimbus clusters in the eastern Arabian Sea are not reflective of continuous transitions, but generally represent discrete development of the intense convective activity progressively northward.

#### 4. Further Remarks

The calibrated data from GOES-1 satellite during the 1979 monsoon onset period has been used to specify evolution of cloudiness distribution. The derived distribution has further been utilized together with thermodynamic state parameters to estimate tropospheric radiative heating distribution, a report on which is under preparation. The 2X2 degree cloudiness distribution parameters described for the period 11-20 June 1979 are available on computer compatible tapes at the Space Science and Engineering Center at the University of Wisconsin-Madison.

#### Acknowledgments

Drs. Fred Mosher and Paul Menzel's contribution in developing the calibration (Table 1) was indispensable in this analyses. The work was funded by the National Science Foundation under Grant ATM 8205386.

5. References

- Chou, M.-D., and A. Arking, 1980: Computation of infrared cooling rates in the water vapor bonds. J. Atmos. Sci., 37, 855-867.
- Deirmendjian, D., 1969: Electromagnetic Scattering on Spherical Polydispersions. American Elsevier Publishing Company, Inc., New York, 290 pp.
- Desbois, M., G. Seze, and G. Szejwach, 1982: Automatic classification of clouds on METEOSAT imagery: Application to high level clouds. J. Applied Meteor., 21, 401-412.
- Fye, F. K., 1978: The AFGWC automated cloud analysis model. AFGWC Technical Memorandum 78-002, HQ AFGWC, Offutt Air Force Base, Nebraska, 97 pp.
- Hansen, J. E., 1971: Multiple scattering of polarized light in planetary atmospheres, Part I. The doubling method. J. Atmos. Sci., 28, 120-125.
- Minnis, P., and E. F. Harrison, 1983: Diurnal variability of regional cloud and surface radiative parameters derived from GOES data. J. Climate & Appl. Met., in press.
- Mosher, F. R., 1976: Cloud height determination. Proceedings of the Symposium on Meteorological Observations from Space: Their Contribution to the First GARP Global Experiment, Proceedings of the 19th COSPAR Meeting, Philadelphia, Published by NCAR, Boulder, Colorado, pp. 201-204.
- Peslen, C. A., 1980 Short-Interval SMS Wind Vector Determination for a Seven Local Storm Area. Mon. Wea. Rev., 108, 1407-1418.
- Reynolds, D. W., and T. H. Vonder Haar, 1977: A bispectral method for cloud parameter determination. Mon. Wea. Rev., 105, 446-457.

- Sikka, D. R. and B. Grossman, 1980: Summer MONEX chronological Weather Summary. Published by the International Monex Management Center, New Dehli, India, 49 pp.
- Smith, W. L., 1978: Status and plans for a cloud climatology programme. JOC Study Conference on the Parameterization of Extended Clouds and Radiation for Climate Models, September 27-October 9, 1978, Oxford, England. Published by the W.M.O.
- Smith, W. L., L. D. Herman, A.J. Schreiner, H. W. Howell and W. P. Menzel, 1981: Radiation budget characteristics of the onset of the summer monsoon. Proc. of the International Conference on Early Results of FGGE and large-scale aspects of its monsoon experiments, Tallahassee, FL. Published by W. M. O., pp. 6-16 to 6-26.
- Suchman, D., B. Auvine, R. Lord, D. Martin, F. Mosher and D. A. Santek, 1981: Improvements in the use of meteorological satellite data: Some techniques developed for GATE. Technical Report, Space Sci & Eng Ctr, University of Wisconsin-Madison, pp 1-24.
- Virji, H., W. L. Smith, A. J. Schreiner, and L. D. Herman, 1982: Earth-atmosphere radiation balance from geostationary satellite data for the summer monsoon onset region. An Atlas, available from the Space Sci & Eng Ctr., University of Wisconsin-Madison, 254 pp.

Figure Captions

- Fig. 1: A schematic illustration of the general empirical relationship between infrared and visual grayshades corresponding to various cloud and surface types (adapted from Fye, 1978)
- Fig. 2: GOES-1 visible and infrared satellite photographs over the Arabian Sea for 1000 GMT, June 20, 1979. Locations A-F refer to the bi-dimensional histograms shown in Fig. 3.
- Fig. 3: Histograms of temperature (degrees Kelvin) versus reflectivity (percent) corresponding to the locations A-F identified in Fig. 2.
- Fig. 4: Zonally averaged total cloud cover along selected latitude bands in the Arabian Sea region during the onset phase of the monsoon.
- Fig. 5: Breakdown of cloud cover into various types for June 12 and June 20, 1979.
- Fig. 6: Evolution of principal cumulonimbus clusters during the monsoon onset. The center of maximum cumulonimbus cover is shown as a star or a circle. The coded numbers (xx-yy) correspond to the percent x 10 cover (xx), and date (yy) during June 1979.



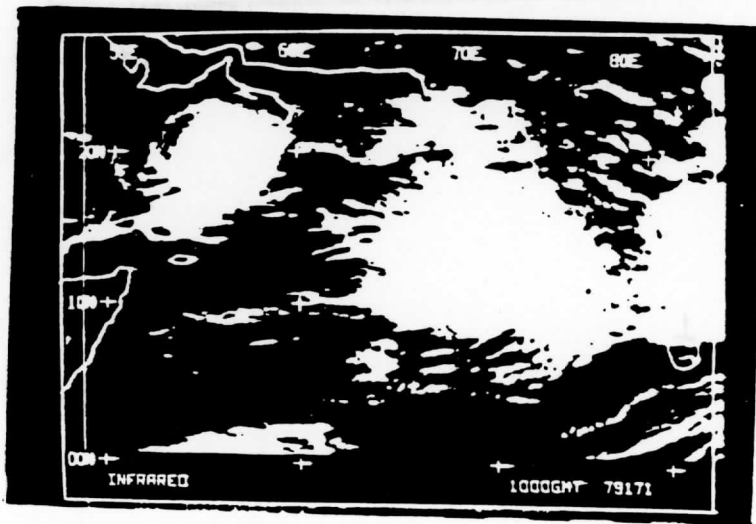
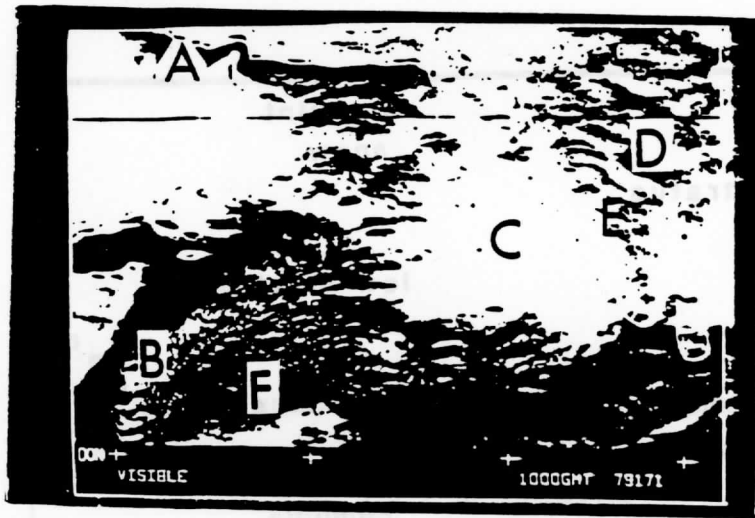


FIG 2

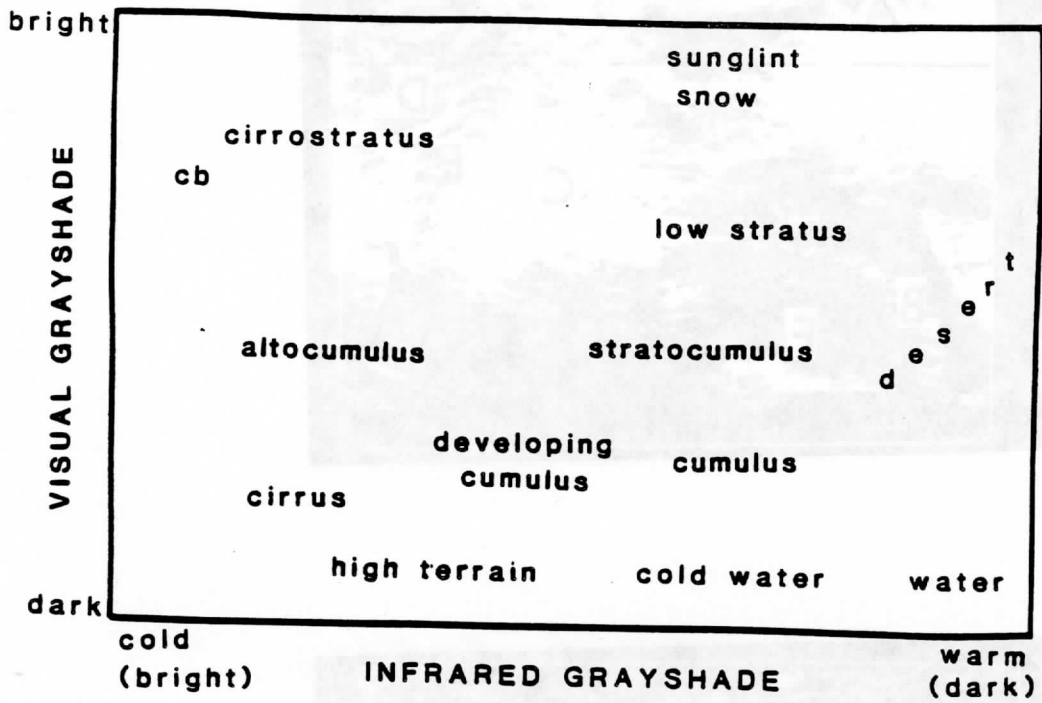
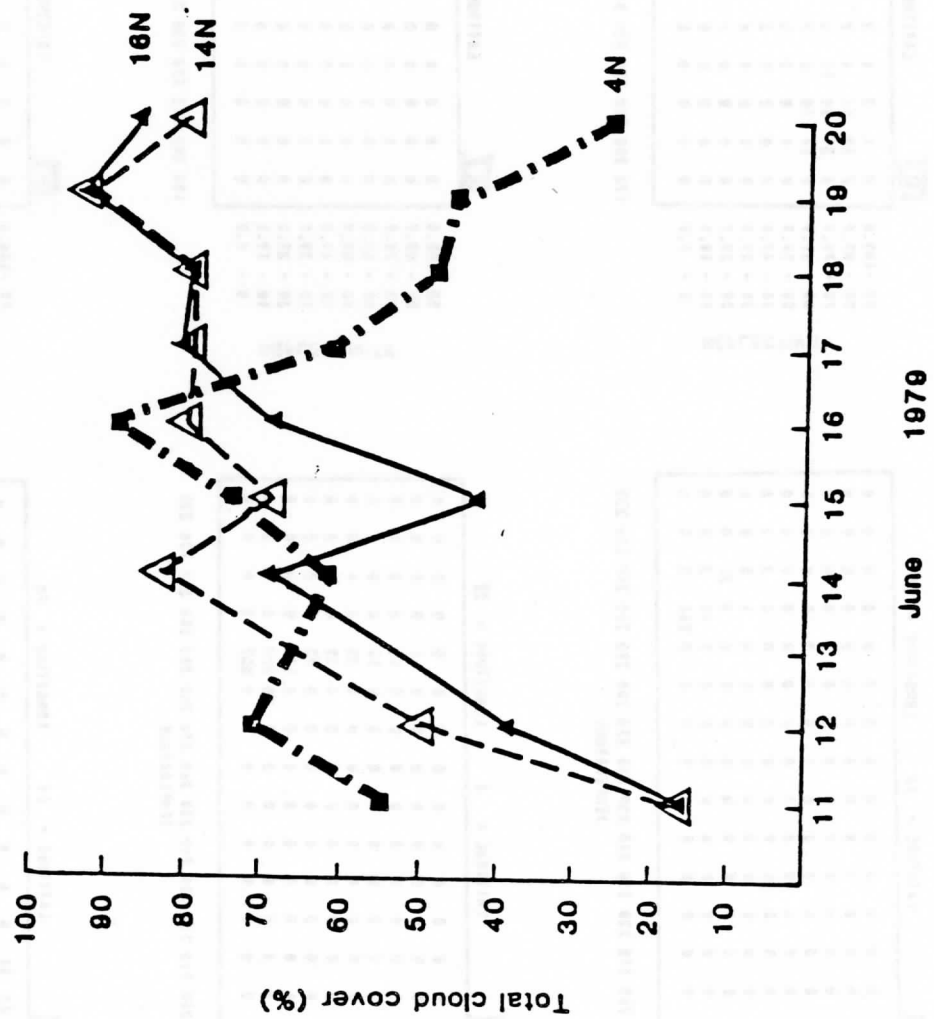


Fig 1





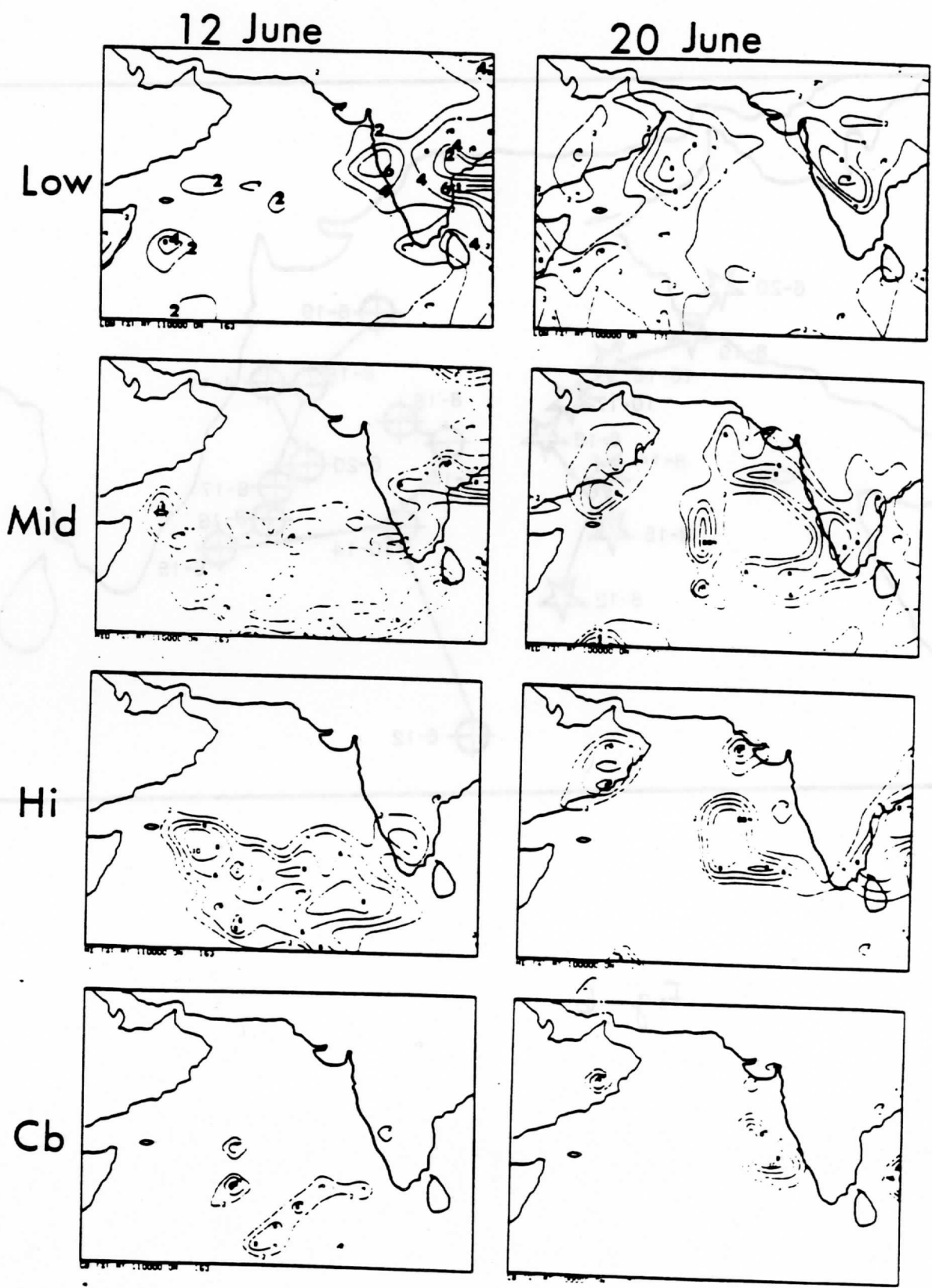


Fig 5

[% x 10]

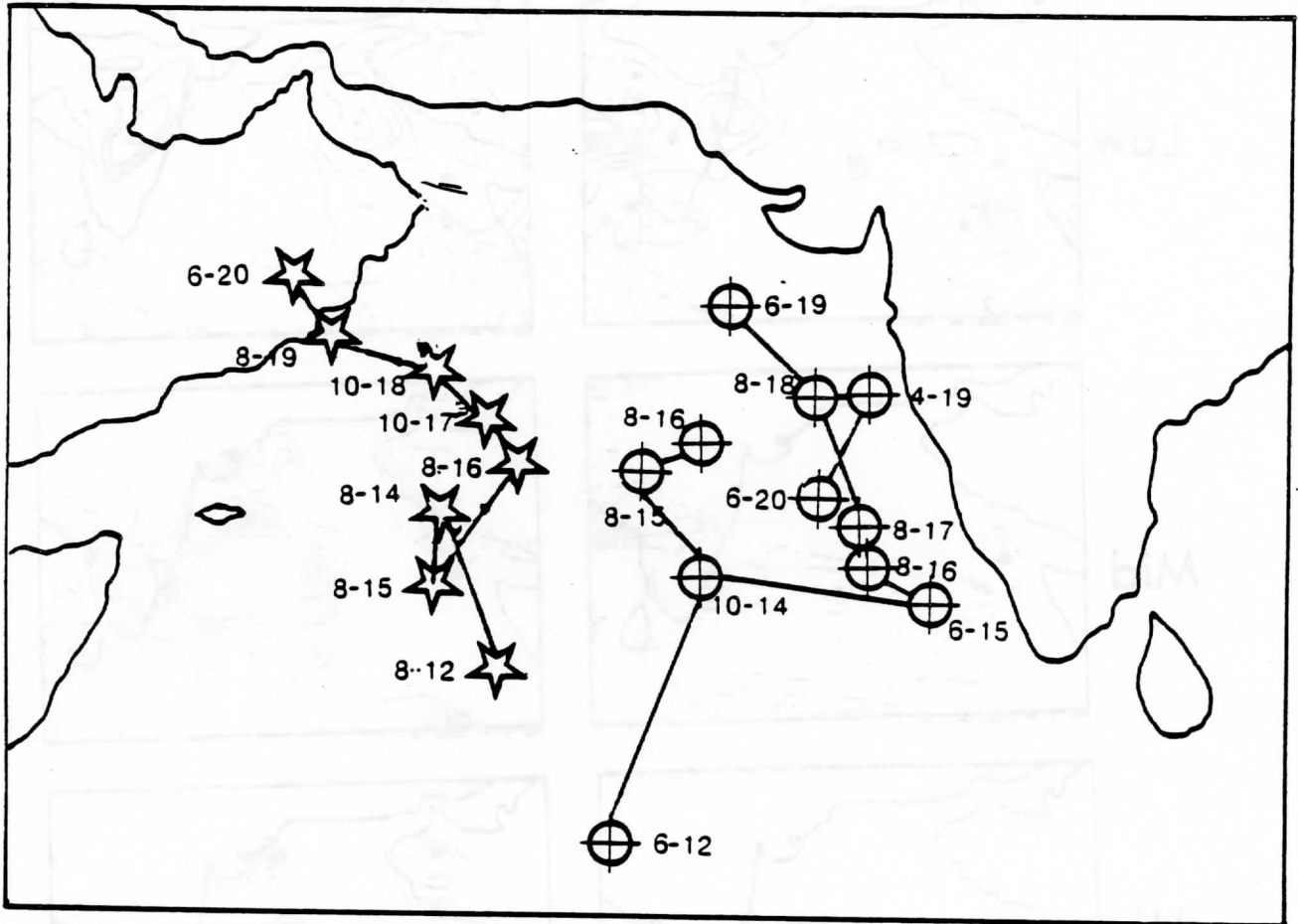


Fig 6

TABLE 1

AN EMPIRICAL CALIBRATION OF BI-DIMENSIONAL RADIANCE HISTOGRAM CLASSES  
 INTO CLOUD TOP AND BOTTOM PRESSURE LEVELS (AFTER MOSHER, 1976)

CLOUD TOP PRESSURE: (mb)	107	137	174	220	274	336	412	498	608	738	918
REFLECTIVITY (%)	CLOUD BOTTOM PRESSURE (mb)										
95	950	950	950	950	950	950	950	950	950	950	950
85	950	950	950	950	950	950	950	950	950	950	950
75	890	911	934	950	950	950	950	950	950	950	950
65	392	433	474	526	580	637	702	766	861	950	950
55	243	283	330	379	438	502	570	648	757	909	950
45	191	227	271	322	378	441	515	595	704	848	950
35	157	192	233	283	338	401	476	558	671	809	950
25	135	169	206	255	311	375	452	538	646	781	950
15	114	146	185	230	285	345	423	511	615	645	928
CLOUD TOP TEMPERATURE (deg. K)	195	205	215	225	235	245	255	265	275	285	295

TABLE 2

CLOUD DISTRIBUTION AT THE SELECTED LOCATIONS

SHOWN IN FIGS. 2 AND 3

CLOUD TYPE	% CLOUD COVER AT LOCATIONS					
	A	B	C	D	E	F
LOW (950-700 mb)	0	52	0	30	15	23
MIDDLE (699-400 mb)	0	0	0	12	85	0
HIGH (399-100 mb)	0	0	6	8	0	0
CUMULONIMBUS (950-100 mb)	0	0	94	19	0	0

Abstract

During the first Global Experiment (GAGE), observations of  
temperature and moisture were made from TIROS-N and NOAA-6 satellites  
and microwave sounding radiance measurements. The data were processed by two  
methods differing principally in their horizontal resolution. At the National  
Earth Satellite Service (NESS) in Washington, D.C., the data were processed

**SATELLITE OBSERVED THERMODYNAMICS DURING FGGE**

Level II-b data sets for application to large-scale numerical models and  
prediction models. High horizontal resolution (75 km sounding data sets were  
produced using one-degree isentropic surfaces for the "special observation  
periods" of GAGE at the National Center for Environmental Prediction and received as

**WILLIAM L. SMITH**

**NOAA/NESDIS Development Laboratory  
at the University of Wisconsin  
1225 West Dayton Street  
Madison, Wisconsin 53706**

**Lecture Prepared for the FGGE Workshop  
Woods Hole, Massachusetts  
July 9-20, 1984**

JUNE 1984



## Abstract

During the First GARP Global Experiment (FGGE), determinations of temperature and moisture were made from TIROS-N and NOAA-6 satellite infrared and microwave sounding radiance measurements. The data were processed by two methods differing principally in their horizontal resolution. At the National Earth Satellite Service<sup>1</sup> (NESS) in Washington, D.C., the data were produced operationally with a horizontal resolution of 250 km for inclusion in the FGGE Level II-b data sets for application to large-scale numerical analysis and prediction models. High horizontal resolution (75 km) sounding data sets were produced using man-machine interactive methods for the "Special Observing Periods" of FGGE at the NASA/Goddard Space Flight Center and archived as supplementary level IIb. The procedures used for sounding retrieval and the characteristics and quality of these thermodynamic observations are given in this report.

---

<sup>1</sup>Now known as National Environmental Satellite, Data, and Information Service (NESDIS).

## 1. Introduction

The TIROS-N satellite was the first of a new series of operational polar orbiting satellites launched into orbit on 13 October 1978, just prior to the beginning of FGGE. The second spacecraft in the series, NOAA-6, was launched into orbit on 27 June 1979, midway through the FGGE year. The complement of infrared and microwave instruments aboard each of the polar orbiting spacecraft provided a complete global coverage of vertical temperature and moisture profile data every 12 hours. With the two spacecraft, complete coverage was achieved every six hours. Table 1 provides the characteristics and purpose of the radiance observations provided by the various spectral channels of each of the three sounding instruments: 1) the High-resolution Infrared Radiation Sounder (HIRS), 2) the Microwave Sounding Unit (MSU), and 3) the Stratospheric Sounding Unit (SSU). The spatial resolution and scan geometry are different for each instrument, but it suffices to state that nearly complete coverage of sounding radiance data is achieved in a swath that below the spacecraft is 2250 km wide. The meteorological soundings which were produced globally have a horizontal resolution and spacing of 250 km. Higher horizontal resolution of 75 km is achieved for limited geographical regions during special observation periods using man-machine interactive processing methods (Greaves et al., 1979).

The purpose of this paper is to summarize the data processing techniques and describe the characteristics and quality of the TIROS Operational Vertical Sounder (TOVS) soundings as produced for the FGGE. For a more complete description of the TIROS-N sounding instruments and their associated data processing techniques, the reader is referred to papers by Smith et al. (1976, 1979, 1981) and McMillin et al. (1982, 1983).

TABLE I. Characteristics of TOV sounding channels.

Channel number	Channel central wave-number	Central wave-length ( $\mu\text{m}$ )	Principal absorbing constituents	Level of peak energy contribution (mb)
	1	668	CO <sub>2</sub>	30
	2	679	CO <sub>2</sub>	60
	3	691	CO <sub>2</sub>	100
	4	704	CO <sub>2</sub>	400
	5	716	CO <sub>2</sub>	600
	6	732	CO <sub>2</sub> /H <sub>2</sub> O	800
	7	748	CO <sub>2</sub> /H <sub>2</sub> O	900
	8	898	Window	Surface
	9	1028	O <sub>3</sub>	25
HIRS	10	1217	H <sub>2</sub> O	900
	11	1364	H <sub>2</sub> O	700
	12	1484	H <sub>2</sub> O	500
	13	2190	N <sub>2</sub> O	1000
	14	2213	N <sub>2</sub> O	950
	15	2240	CO <sub>2</sub> /H <sub>2</sub> O	700
	16	2276	CO <sub>2</sub> /H <sub>2</sub> O	400
	17	2361	CO <sub>2</sub>	5
	18	2512	Window	Surface
	19	2671	Window	Surface
20	14367	0.70	Window	Cloud
Frequency (GHz)				
MSU	21	58.31	Window	Surface
	22	53.73	O <sub>3</sub>	700
	23	54.96	O <sub>3</sub>	300
	24	57.95	O <sub>3</sub>	90
Wavelength ( $\mu\text{m}$ )				
SSU	25	15.0	CO <sub>2</sub>	15.0
	26	15.0	CO <sub>2</sub>	4.0
	27	15.0	CO <sub>2</sub>	1.5

## 2. Global Operational Soundings

A global coverage of vertical temperature and moisture soundings were produced with 250 km spatial resolution by NESS operations. The operational data processing system, originally developed by Smith and Woolf (1976), had undergone continuous refinement during FGGE. These refinements dealt principally with safeguarding the output against erroneous soundings produced by cloud attenuated microwave observations (Phillips, 1980) and minimizing horizontal discontinuities resulting from the geographical stratifications of the statistical data used in the profile retrieval process. Since the FGGE, significant improvements in the operational system for handling cloud influences have been implemented (McMillin et al., 1982, 1983).

a) Processing Characteristics

The details of the operational processing system are presented by Smith et al. (1979), Broderick et al. (1981), and McMillin and Dean (1982). The two polar orbiting satellites operating during FGGE, TIROS-N and NOAA-6 respectively, possessed an equator crossing time (local) of 1500 and 1900 when northbound and approximately 0300 and 0700 when southbound. Each satellite completed 14 orbits per day with a westward shift of about 25.5° longitude between adjacent orbits. The scan width of the sounding instruments resulted in overlapping views poleward of 38°. Each HIRS measurement (scan spot) resolves a circular area that is 25 km diameter at the subsatellite point, whereas the MSU resolves a circular area of 110 km diameter at the satellite subpoint. The fields of view enlarge and become elliptical as the instruments scan away from the satellite subpoint. Fifty-six HIRS spots are contained within each scan line covering a linear distance of about 2250 km. The MSU instrument has 11 fields of view along its swath having the same linear extent. A sounding is made for every array of seven HIRS scan lines and scan spots, resulting in 5 x 6 array of profiles for each 40 x 56 array of scan spots. The nominal horizontal resolution of soundings from TOVS is about 250 km.

The conversion of measured radiances to temperature and moisture profiles requires several adjustments to produce the final radiances from which temperatures and dewpoints are produced using linear regression coefficients. These include adjustments for the changing scan angle, surface emissivity, and clouds. (There was no account for terrain elevation in the operational system so their results are unreliable in mountainous regions.)

The operational method of processing the TOVS sounding data during FGGE was developed by Smith and Woolf (1976). Temperature and water vapor profiles were produced from "clear radiances" that have been corrected for any clouds that are

inferred to be present. The processing program that produces clear radiances first attempts to identify scan spots that are completely clear. Failing in this, the program then attempts to extract clear radiances from scan spots that are only partly covered with clouds. If this too fails, it attempts to produce temperatures from the four microwave channels and the four stratospheric HIRS channels, since the latter measurements are not as significantly affected by clouds as are the tropospheric HIRS channels. These are in essence the three retrieval paths which are identified as "clear," "partly cloudy," and "overcast," respectively. In the "clear" and "partly cloudy" paths, retrievals use radiances from all 24 HIRS and MSU channels, and identical coefficients are used to convert from radiance to temperature and dewpoint. However, the "overcast" path retrievals utilize a different set of coefficients, since only stratospheric HIRS radiances and MSU radiances are used.

One would expect "clear" retrievals to be more accurate than "partly cloudy" retrievals because of certain assumptions regarding cloud height uniformity involved in the "partly cloudy" method. However, the difference between the "overcast" retrievals and either the "clear" or "partly cloudy" retrievals is much greater than the difference between "clear" and "partly cloudy" retrievals. In addition, the relative accuracies of the three types are sensitive to limits in tests used to accept or reject the attempted retrievals. For example, inclusion of some "partly cloudy" measurements in the ones selected as "clear" will decrease the accuracy of this group of soundings. Also, the decision about the retrieval method selected involves tests that are only indirectly related to cloud amounts. These tests involve comparisons between measured and expected albedo and surface temperatures, and between a measured microwave radiance and a microwave radiance predicted from those infrared radiances that are subject to cloud contamination.

The second important feature of the processing procedure is the regression for atmospheric temperature and water vapor mixing ratio alluded to above. Regression coefficients for a given latitude zone are updated weekly using collocated radiosonde and satellite data uniformly distributed over the preceding two weeks. Coefficients are then used for the following week. This procedure results in an average time lag ranging from one and one-half weeks in a data-rich region (e.g., 30-60°N) to two and one-half weeks in a data sparse region (e.g., 30-60°S). Separate regression coefficients are calculated for each of five latitude zones: 90°N-60°N, 60°N-30°N, 30°N-30°S, 30°S-60°S, 60°S-90°S.

To eliminate temperature discontinuities that would otherwise occur at 30° and 60°, the coefficients used for a retrieval are interpolated from those for the five zones. In the interpolation, the highest probing microwave channel (57.95 GHz), which senses the lower stratosphere, is used as the interpolating variable. The instrumentation and the processing of the radiances from the sounders on the two satellites were essentially the same, with the notable exception that the MSU channel 3 on NOAA-6 was not used after early December 1979 because it was considered too noisy.

An example coverage of operational TIROS-N retrievals are shown in Fig. 1. The symbols indicate the type of retrieval path used; open circles for "clear," solid circles for "overcast" cloud, and stars for "partly cloudy." During the FGGE, generally 80% of the soundings were produced according to either the "clear" or "partly cloudy" path, with the remaining 20% produced according to the infrared channel deficient "overcast" path.

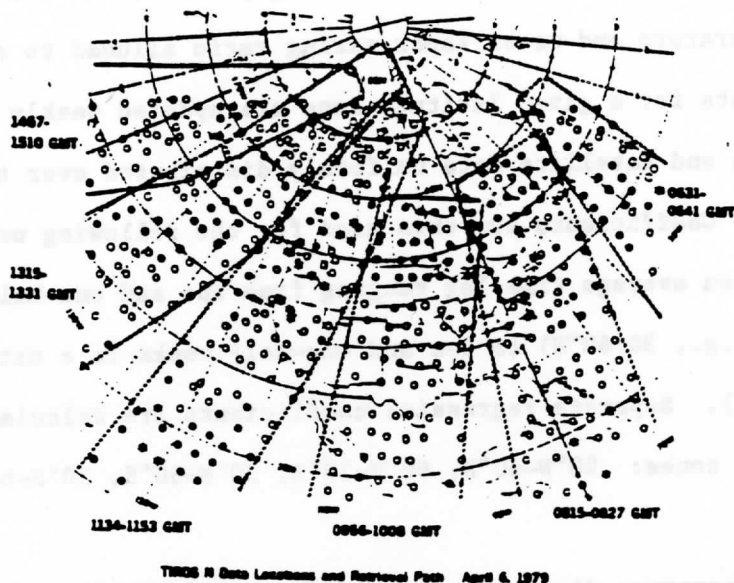


Fig. 1: TIROS-N retrieval locations for April 6, 1979. Broken lines delineate orbital swaths with times as indicated. Open circles indicate clear path, stars indicate partly cloudy path, and solid circles indicate cloudy path retrievals (after Broderick et al., 1981).

#### b) Radiosonde Temperature Comparisons

When evaluating satellite retrievals, radiosondes are often used as a comparison. The comparisons given here were computed by a program at the National Meteorological Center that was designed by A. Desmarais. Comparisons are calculated from radiosondes within  $\pm 3$  hours and within  $3^\circ$  of great circle arc from the satellite observation. These time and space discrepancies limited the utility of these comparisons for error assessments. In addition, the comparisons are mainly representative of the Northern Hemisphere even though the data are global. This bias toward the Northern Hemisphere is a consequence of the large number of radiosondes and, thus, comparisons in that area. The comparisons in this study include both land and sea areas. However, radiosondes are more numerous over land, thus the land cases dominate. Because there is no method to account for terrain elevation in the operational retrieval method, the

radiosonde comparison statistics exaggerate the "retrieval errors" in the lower troposphere.

The number of comparisons also varies with the satellite (i.e., TIROS-N or NOAA-6) and the type of retrieval. However, comparisons for a single satellite for a month typically total over 2000 for cloudy soundings, 7000 for partly cloudy soundings, and over 10,000 for clear soundings.

Table 2 shows the RMS difference between NESS operational temperature soundings and radiosondes for the FGGE year. This statistic was obtained from more than 150,000 clear sounding comparisons, 100,000 partly cloud comparisons and 35,000 overcast cloud comparisons. Similar statistics have been provided elsewhere by Smith (1979, 1981), Phillips et al. (1979), Schlatter (1980), Broderick et al. (1981), Gruber and Watkins (1982) and Koehler et al. (1983). The main point to be made from all these statistics is that "clear" and "partly cloudy" retrievals are of similar accuracy and "overcast" cloud retrievals are of greatly reduced accuracy throughout the troposphere. The reduced accuracy of the "overcast" retrievals is due to the limited number of tropospheric sounding microwave channels and their deficient vertical resolution in the low troposphere due to non-unity surface emissivity.

It should be remembered that the "error" implied in Table 2 is due mainly to the poor vertical resolution of the TOVS. Consequently much of the error is a synoptic scale systematic error. Consequently errors in horizontal temperature gradients are much smaller, generally 1°C or less depending upon the depth of the atmospheric layer (Schlatter, 1980).



Table 2. RMS differences ( $^{\circ}\text{K}$ ) between satellite retrievals and radiosondes during FGGE

Layer (mb)	Clear	Partly Cloudy	Overcast Cloud
100--70	2.2	2.2	2.2
200-100	2.1	2.2	2.3
300-200	2.3	2.5	2.8
400-300	2.3	2.4	3.0
500-400	2.3	2.4	3.0
700-500	2.0	2.1	2.7
850-700	2.4	2.7	3.4
1000-850	2.8	3.1	3.8

c) Geopotential Thickness Comparisons

Fig. 2 presents analyses of TOVS derived 1000-500 mb geopotential thickness for a 12 hour time period (Fig. 2a) on 29 and 30 April 1979. Shown for comparison is the National Meteorological Center (NMC) analysis (Fig. 2b), devoid of TOVS data, for 0000 GMT on 30 April. The NMC analysis is of historical significance in that it is the last analysis performed without the inclusion of TIROS-N data (i.e., the 1200 GMT analysis on 30 April included TIROS-N soundings). (TIROS-N sounding data was included in operational analyses on 6 March, but only over water south of  $10^{\circ}\text{S}$ . On 30 April, all oceanic soundings were introduced in the analysis at all latitudes.) The correspondence between the "pure" satellite analyses and the NMC analysis, which did not incorporate the TOVS data at this time, is striking. The agreement over the continents validates the TOVS data. The agreement over the oceanic regions pays tribute to the NMC analysis-forecast system since the analyses in these regions are largely constructed from surface and aircraft observations with a 12 hour forecast used as a first guess in the analysis cycle. The most notable differences between the "TIROS" and "conventional" analyses are in the low pressure areas over the northeastern Pacific and eastern Europe, both of which are more intense in the TIROS analysis.

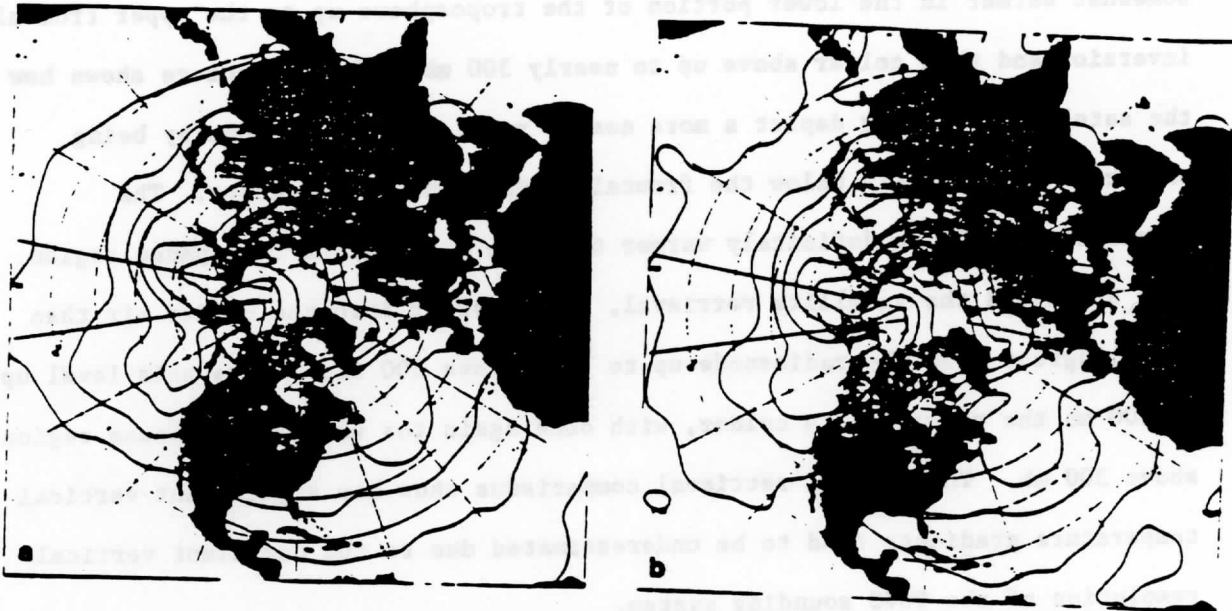


Fig. 2: Comparison of 1000-500 mb thickness charts obtained solely from TIROS-N sounding data (a) and from conventional data (b). (a) TIROS-N, 29 April, 1800 GMT-30 April, 0600 GMT, (b) NMC, 30 April, 0000 GMT (after Smith et al., 1981).

#### d) Vertical Temperature Structure

Fig. 3 is given to illustrate the vertical resolution of the TOVS soundings produced during FGGE. Two of the NOAA-6 soundings are collocated with the Omaha, Nebraska and St. Cloud, Minnesota radiosondes. These two pairs of soundings, shown in Fig. 3, illustrate graphically the fact that horizontal gradients tend to be weakened due to inadequate vertical resolution. The base of an upper level front can be seen in the radiosondes sloping from near 600 mb at Omaha up to 475 mb at St. Cloud. The surface inversion at Omaha is probably evidence of the slightly cooler and drier air mass, although it is difficult to distinguish it from a normal nocturnal inversion. At St. Cloud this cooler air mass may be associated with the slightly stable layer just above 700 mb up to 570 mb. The intrusion of Arctic air may be evidenced by the lower stab-

portion of the radiosonde profile. At Omaha, the NOAA-6 retrieval is clearly somewhat warmer in the lower portion of the troposphere up to the upper frontal inversion and then colder above up to nearly 300 mb. This structure shows how the satellite sounding depict a more nearly vertical frontal zone by being warmer in the cold air below the frontal surface and colder above. The retrieval profile is definitely warmer than the raob in the tropopause region. Near St. Cloud the satellite retrieval, being deeper into the colder air than Omaha, agrees with the radiosonde up to just above 500 mb. Above this level up to 300 mb the retrieval is colder, with once again the warmer tropopause region above 300 mb. This set of retrieval comparisons show how significant vertical temperature gradients tend to be underestimated due to the deficient vertical resolution of the TOVS sounding system.

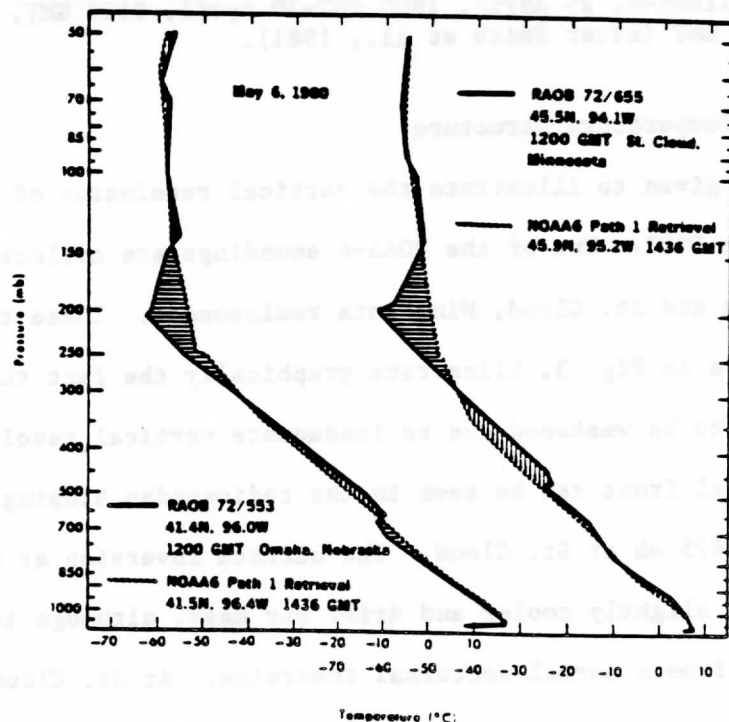


Fig. 3: Radiosonde (1200 GMT) and NOAA-6 retrieval (1436 GMT) pairs for 6 May 1980. Radiosonde temperatures in solid line and retrievals in broken line (after Broderick et al., 1981).

The deficient vertical resolution of TOVS soundings is responsible for the reduced horizontal variance and horizontal error correlation of the satellite temperature profiles noted by Phillips et al. (1979), Phillips (1980), Schlatter (1981), and McMillin and Dean (1982). The fact that empirical regression coefficients are used for the retrieval also greatly contributes to horizontal smoothing and error correlation because of the inherent space and time collocation noise in the regression sample. Also, Le Marshall and Schreiner (1984) have shown that much of the horizontal variance loss by the operational regression retrieval method is due to the manner in which the radiance data is "corrected" for view angle. Physical methods of retrieval which do not require "limb corrected" data have proven to be superior in accuracy to the empirical regression method used during FGGE.

e) Water Vapor Retrievals

Unfortunately there has been very little evaluation of the TIROS-N/NOAA-6 water vapor retrievals during FGGE. This is in part due to the very difficult task of evaluating water vapor estimates using radiosonde comparisons because of the large space and time variability of atmospheric moisture. Theoretical expectations of the water vapor profile retrieval performance have been given by Smith and Woolf (1976).

The most extensive use of the operational water vapor retrievals during FGGE has been to define the precipitable water over the Indian Ocean during the 1979 summer monsoon (Cadet, 1983). In this application, water vapor bogus was used in disturbed cloudy areas since no operational TOVS water vapor retrievals are provided. The cloud bogus is based upon TOVS "overcast" path temperature soundings and the assumption of a relative humidity of 90% between the surface and 700 mb, 80% between 700 and 400 mb and 70% above.

Fig. 4a shows a typical coverage of operational TIROS-N water vapor soundings over the Indian Ocean. The data void areas are due to overcast cloud where temperature but no water vapor profiles are retrieved. Fig. 4b shows an analysis of precipitable water for the lower troposphere (surface-700 mb) based on the TIROS-N water vapor retrievals and cloud bogus data. The detail is noteworthy. Cadet (1983) has verified these analyses using aircraft dropsonde data and shows that the accuracy for the surface-700 mb, 700-500 mb, and 500-300 mb layers is better than 10-20%, depending upon atmospheric layer.

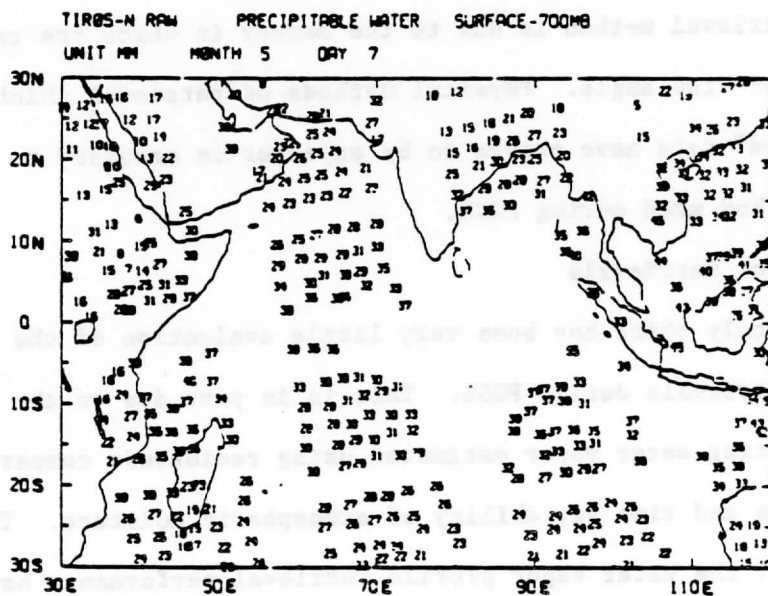


Fig. 4a: TIROS-N soundings obtained around 1030 GMT over the Indian Ocean on 7 May 1979. Precipitable water within the layer surface-700 mb (after Cadet, 1983).

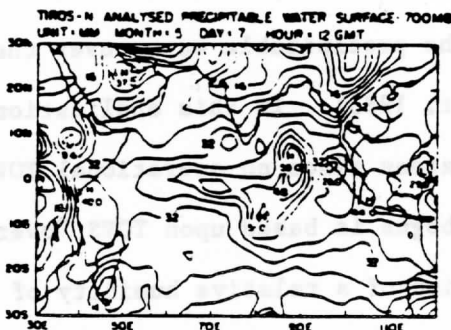


Fig. 4b: Analyzed field of precipitable water for layer surface-700 mb on 7 May 1979 from TIROS-N water vapor retrievals and bogus data (after Cadet, 1983).

### 3. "Special Effort" High Resolution Soundings

The special effort (Greaves et al., 1979, Atlas, 1981) was conducted for the special observing periods of FGGE (January-March and May-July 1979) as a joint project between NASA, NOAA, and the University of Wisconsin. Man-computer Interactive Data Access System (McIDAS) videographic terminals developed by the Space Science and Engineering Center (SSEC) of the University of Wisconsin were utilized by experienced meteorologists at the National Meteorological Center (NMC) for data evaluation and quality assessment, and at the Goddard Laboratory for Atmospheric Sciences (GLAS) for satellite data enhancements. The interactive programs for this purpose were developed by the National Environmental Satellite Service Development Laboratory at the University of Wisconsin and the SSEC (Smith et al., 1978, 1979, 1981).

For each synoptic period there was an initial editing of FGGE data by NMC. At this stage, quality indicators were assigned to temperature soundings. The determination of data quality was made on the basis of synoptic considerations, including horizontal, vertical and temporal consistency. Regions where data deficiencies exist or where higher resolution data was needed to adequately represent the atmospheric thermal structure were then selected for enhancement. The eastern North Pacific was routinely enhanced because of the importance of this region to forecasting for North America. In addition, cases of blocking, cut off low development, cyclogenesis, and tropical circulations were preselected for enhancement by an ad-hoc international committee of participating scientists.

The sounding data enhancement was aimed at supplementing the operational satellite sounding data set with higher resolution soundings in meteorologically active regions, and with new soundings where data voids or soundings of questionable quality exist. The algorithm for retrieving temperature profiles

from the TIROS-N observations of radiance displayed on McIDAS, was the same regression algorithm used by NESS for the objective generation of operational temperature and water vapor profiles. The operational profiles have a horizontal resolution of 250 km whereas special effort profiles can be retrieved at the resolution of the measurements (25 km for HIRS and 150 km for MSU) but is nominally 75 km.

The sounding enhancement process at GLAS was performed as follows: once an area had been selected, the McIDAS operator began by displaying the locations of all available conventional and special FGGE data for that area, the Level III analysis, and visible, infrared, and microwave images from TIROS-N. At this stage, the operator noted where data deficiencies exist and from the TIROS-N images, determines the extent of cloudiness and where the most intense atmospheric thermal gradients were located. High resolution temperature retrievals were then generated for the area. This was followed by a manual editing of the retrievals to remove small-scale discontinuities due to cloud-induced noise while retaining significant meteorological structures. Enhanced microwave retrievals, consistent with neighboring infrared retrievals, were then generated in cloudy areas.

After the entire enhancement process is completed a final editing and quality assessment of the enhanced data was performed at NMC. The data was then archived as supplementary Level IIb.

Subjective comparisons of enhanced soundings and radiosonde reports were performed after the enhancement process was completed. These comparisons showed that the enhanced and operational retrievals tended to be similar in cloud free areas. However, large differences occasionally occur. The differences are accentuated in and around cloudy areas where the interactive processing at high resolution allows for the generation of substantially more infrared retrievals,

and where the microwave retrievals show greater internal consistency than the operational retrievals.

An example illustrating some of the effects of the sounding data enhancement is presented in Fig. 5. In Fig. 5, 1000-300 mb thickness analyses of operational (solid line) and special effort retrievals (dashed lines), and plotted radiosonde reports are shown for a section of the North Pacific at 0000 GMT 7 January 1979. Large differences in the orientation, gradient, and absolute value of the enhanced and operational thickness contours are evident. In addition, the errors relative to the colocated radiosondes have been reduced in this case by 30-80 geopotential meters.

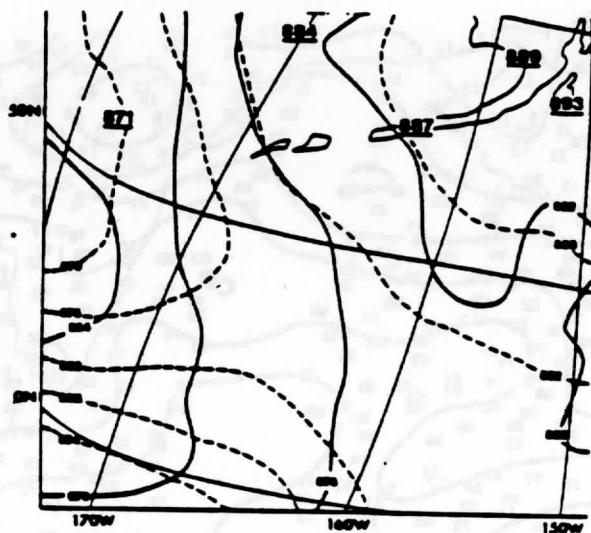


Fig. 5: 1000-300 mb thickness analyses of operational soundings (solid lines) and special effort soundings (dashed lines) for 0100 GMT 7 January 1979. Radiosonde observations of 1000-300 mb thickness in decameters are plotted as large numbers (after Atlas, 1981).

Finally, Fig. 6 shows the coverage and an analysis of high spatial resolution total precipitable water estimates derived from TOVS data during the MONEX using a "physical" as opposed to a "statistical" algorithm (Smith et al., 1983). In the "physical" algorithm the resulting temperature and moisture profile are obtained by numerical solution of the radiative transfer equation. Water vapor



profiles are achieved to the earth's surface under cloudy conditions utilizing the microwave temperature profile and relative humidity profile obtained by interpolation between cloud level and the surface. Comparisons between physical retrievals and those achieved using operational empirical regression coefficients reveal that the gradient accuracy and horizontal variance is much improved in the physical solutions (Menzel, 1984). Note the much greater density and improved coverage of the physical high resolution retrievals shown in Fig. 6 as compared to the operational TOVS soundings shown in Fig. 4a.

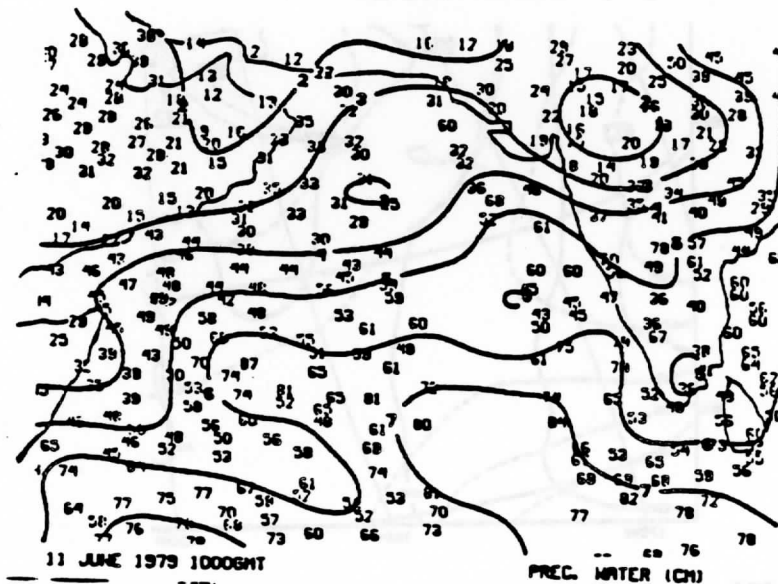


Fig. 6: Total precipitable water values (mm) and a contour analysis (cm) for 11 June 1979 in the MONEX special observation region. This example is taken from an extensive set of soundings derived during Summer MONEX by A. J. Schreiner at the University of Wisconsin.

#### 4. Summary

The thermodynamic observations from satellites during FGGE consisted of globally produced temperature and water vapor soundings at 250 km resolution and

limited area "special effort" soundings at 75 km resolution. The accuracy of the temperature profiles is better than 2.5°C, depending upon level, as judged from comparisons with radiosondes. The accuracy of the layer mean precipitable water retrievals is 10-20% as judged from comparisons with aircraft dropsondes. The higher resolution "special effort" enhanced soundings tend to improve the accuracy and occasionally intensify the temperature and water vapor gradients in a realistic manner. Also, the interactive "special effort" soundings fill in major gaps in the operational coverage. The main deficiencies of the FGGE satellite sounding data are:

1. Deficient accuracy in overcast cloud areas,
2. Deficient horizontal gradient definition due to the TOVS inherently low vertical resolution (approximately 5 km),
3. Lack of globally produced moisture profiles in overcast cloud regions,
4. Inability of the operational regression method to account for variable terrain conditions thereby yielding unreliable results in mountainous regions,
5. Poor accuracy near the earth's surface due to the lack of utilization of conventional surface observations in the sounding retrieval process.

It should be noted that many of the FGGE time period sounding deficiencies have been alleviated through improved processing procedures; in particular, methods for handling clouds and the use of physical solutions rather than empirical regression procedures (McMillin et al., 1983 and Smith et al., 1983). Because of the unique coverage of in-situ observations (e.g., buoy and aircraft observations) during the FGGE, it may be worthwhile at some future time to reprocess the TOVS observations during the FGGE time period in order to take advantage of the processing algorithm improvements.

## References

- Brodrick, H., C. Watkins, and A. Gruber, 1981: Statistical and synoptic evaluations of TIROS-N and NOAA-6 retrievals. NOAA Technical Report NESS 86, Washington, D.C., 48 pp.
- Cadet, D. L., 1983: Mean fields of precipitable water over the Indian Ocean during the 1979 summer monsoon from TIROS-N soundings and FGGE data. Tellus, 35B, 329-345.
- Greaves, J. R., G. DiMego, W. L. Smith, and V. E. Suomi, 1979: A special effort to provide improved sounding and cloud motion wind data for FGGE. Bull. Amer. Meteor. Soc., 60, 124-127.
- Gruber, A., and C. D. Watkins, 1982: Statistical assessment of the quality of TIROS-N and NOAA-6 satellite soundings. Mon. Wea. Rev., 110, 867-876.
- Koehler, T. L., J. C. Derber, B. D. Schmidt, and L. H. Horn, 1983: An evaluation of soundings, analyses, and model forecasts derived from TIROS-N and NOAA-6 satellite data. Mon. Wea. Rev., 111, 562-571.
- Le Marshall, J. F., and A. J. Schreiner, 1984: Limb effects in satellite temperature sounding. Submitted to J. Clim. and Applied Meteor.
- McMillin, L. M., and C. Dean, 1982: Evaluation of a new operational technique for producing clear radiances. J. Applied Meteor., 21, 1005-1014.
- McMillin, L. M., and C. A. Dean, 1982: Variance ratios, loss of energy and regression in satellite temperature retrievals. Mon. Wea. Rev., 110, 296-299.
- McMillin, L. M., D. G. Gray, H. F. Drahos, M. W. Chalfant, and C. S. Novak, 1983: Improvements in the accuracy of operational satellite soundings. J. Clim. and Applied Meteor., 22, 1948-1955.
- Menzel, W. P. (editor), 1983: Technical Proceedings of the First International TOVS Study Conference. A report from the Cooperative Institute for Meteorological Satellite Studies, 1225 West Dayton Street, Madison, Wisconsin, 53706.
- Phillips, N., 1980: Two examples of satellite temperature retrievals in the North Pacific. Bull. Amer. Meteor. Soc., 61, 712-717.
- Phillips, N., L. McMillin, A. Gruber, and D. Wark, 1979: An evaluation of early operational temperature soundings from TIROS-N. Bull. Amer. Meteor. Soc., 60, 1188-1197.
- Schlatter, T. W., 1981: An assessment of operational TIROS-N temperature retrievals over the United States. Mon. Wea. Rev., 109, 110-119.
- Smith, W. L., and H. M. Woolf, 1976: The use of eigenvectors of statistical covariance matrices for interpreting satellite sounding radiometer observations. J. Atmos. Sci., 33, 1127-1140.

- Smith, W. L., C. M. Hayden, H. M. Woolf, H. B. Howell, and F. W. Nagle, 1978: Interactive processing of TIROS-N sounding data. Preprints, AMS Conference on Weather Forecasting and Analysis and Aviation Meteorology, Silver Spring, Maryland, 16-19 October 1978, pp. 390-395. Published by the American Meteorological Society, Boston, Massachusetts.
- Smith, W. L., H. M. Woolf, C. M. Hayden, D. Q. Wark, and L. M. McMillin, 1979: The TIROS-N operational vertical sounder. Bull. Amer. Meteor. Soc., 60, 1177-1187.
- Smith, W. L., F. W. Nagle, C. M. Hayden, and H. M. Woolf, 1981: Vertical mass and moisture structure from TIROS-N. Bull. Amer. Meteor. Soc., 62, 388-393.
- Smith, W. L., H. M. Woolf, C. M. Hayden, A. J. Schreiner, and J. F. Le Marshall, 1983: The physical retrieval TOVS export package. In W. P. Menzel (editor), Technical Proceedings of the First International TOVS Study Conference. A report from the Cooperative Institute for Meteorological Satellite Studies, 1225 West Dayton Street, Madison, Wisconsin, 53706.

The Technical Proceedings of  
The First International TOVS Study Conference

Igls, Austria

29 August through 2 September 1983

Edited by

W. P. Menzel

Cooperative Institute for Meteorological Satellite Studies  
Space Science and Engineering Center  
University of Wisconsin  
1225 West Dayton Street  
Madison, Wisconsin 53706  
(608) 262-0544

March 1984

## FOREWORD

These proceedings detail the technical presentations at the First International TOVS Study Conference held in Igls, Austria, 29 August-2 September 1983. A summary of the conference objectives, conclusions, and plans for future action is contained in an executive report available from the CIMSS, University of Wisconsin-Madison.

The technical presentations deal mainly with the methods used for obtaining and processing TOVS data at the institutions of the participants. In this conference, emphasis was placed on algorithms found useful for the specification of the temperature profile and the associated methods required to alleviate the influences of cloud on the profile retrieval. (The specification of the water vapor profile will be emphasized at a future meeting.) The technical proceedings imply that the state of the art of atmospheric radiance computation and the analytical techniques of profile retrieval have advanced to the point where "physical" methods can replace the more traditional statistical regression methods of radiosonde temperature and satellite radiance observations. This result has very important implications for the future World Weather Watch program. Also important is the conclusion that the effects of cloud can be largely alleviated using the TOVS microwave radiance observations and the very high resolution (1 km) visible and infrared observations of the AVHRR available at the same time as TOVS from the same satellite.

One important aspect of the technical work of the participants is the evolution toward a single universally accepted method of processing TOVS data. Although such a method does not yet exist, the rapid evolution towards one that is (a) physical, (b) analytically direct, and (c) computationally efficient is obvious from these proceedings.

In summary, a world-wide coordinated effort is underway to improve the process of specifying atmospheric profiles from TOVS observations. The work of the participants will continue until a common technique is defined that is universally acceptable. The initial contributions contained in this report indicate that this objective may be achieved within the next two or three years.



William L. Smith  
Chairman  
The First International TOVS  
Study Conference

TABLE OF CONTENTS

ACKNOWLEDGMENTS

The publication of these proceedings has been possible through the financial support from the National Oceanic and Atmospheric Administration to the Cooperative Institute for Satellite Studies in Madison, Wisconsin.

The careful retyping of the complete edited manuscript was accomplished by Jan Waite, several of the figures were drafted by Tony Wendricks, and the production was handled by Ann North. We thank them for their quality work.

## TABLE OF CONTENTS

Clear Radiance Retrieval of HIRS Channels with the Use of AVHRR Data .....	1
Tadao Aoki	
TIP Data Processing Activities in Poland .....	10
Les Baranski	
Improved Initialization Inversion Procedure ("3I") .....	14
A. Chedin and N. A. Scott	
Mesoscale Analysis Using Satellite Information .....	80
Y. Durand and R. Juvanon du Vachat	
High-Resolution Temperature Retrievals at the U.K. Meteorological Office ..	94
J. R. Eyre	
Precipitable Water Vapor and Thickness Fields Over the Tasman Sea on .....	101
28 October 1982	
Donald W. Hillger and Thomas H. Vonder Haar	
TOVS-Data Preprocessing in Maly Javornik .....	109
M. Jusko, F. Kostal, O. Olsina, D. Podhorsky	
The Australian Operational Direct Readout and TOVS Processing System .....	111
and its Application to the Tasman Sea Intercompanion Study	
G. A. Kelly and J. F. LeMarshall	
Temperature Retrievals Over Mountains Using One FOV .....	132
F. Loechner	
The Operational TOVS Retrieval Method .....	142
Larry McMillin	
A Study of Several Different Numerical Iteration Solutions of the .....	148
Radiative Transfer Equation (RTE)	
W. P. Menzel	
W.A.I.T. Tasman Sea Study .....	155
W. P. Menzel and M. J. Lynch	
Improvement of MSU Temperature Retrievals by Use of Tropopause Heights ....	165
Derived from TOMS Ozone Measurements	
M. J. Munteanu, E. R. Westwater, and N. C. Grody	
Determination of Clear HIRS-2 Pixels and Clear Radiances Retrieval by .....	173
Using AVHRR	
T. Phulpin, A. Brard and M. Derrien	
An Appraisal of Retrieval Methods Used for Obtaining Temperature .....	184
Profiles from TOVS Radiances	
A. J. Prata	



Experiments on TOVS Data at the Freie Universitat Berlin .....	204
E. Reimer and H. Billing	
Satellite Soundings Over the Alpex Area .....	210
Rolando Rizzi	
Numerical Study of Vertical Temperature Profile with Satellite Data .....	219
G. Rochard	
The Physical Retrieval TOVS Export Package .....	227
W. L. Smith, H. M. Woolf, C. M. Hayden, A. J. Schreiner, J. F. LeMarshall	
Comments on TOVS Transmittances .....	279
D. Spänkuch, W. Dohler and J. Guldner	
The GLAS Physical Numerical Algorithm for Analysis of HIRS 2/MSU Data ....	285
J. Susskind and M. T. Chahine	
A Non-Linear Approach for Derivation of Temperature Profiles .....	300
from TOVS-Data	
J. Svensson	
The First International TOVS Study Conference Case Study Report .....	304
B. F. Taylor	
Temperature Retrievals from Typical Shape Functions .....	316
D. Q. Wark	
Use of TOVS in Canada .....	321
Tsoi-Ching Yip, P. King, B. Greaves, and D. Steenbergen	
Some Preliminary Results from the Polar-Orbiting Satellite .....	345
Data Retrieval	
Fengxian Zhou and Gaoxiang Zhao	

\* \* \* \* \*

Only the Table of Contents is included here. Copies of any of these papers are available from CIMSS upon request.

A REPORT ON  
THE FIRST INTERNATIONAL TOVS  
STUDY CONFERENCE

Igls, Austria

29 August - 2 September, 1983

(Edited by W. P. Menzel and M. J. Lynch)

First draft  
10 October, 1983

Final draft  
12 December, 1983

TABLE OF CONTENTS

FORWARD ..... 1

I. EXECUTIVE SUMMARY ..... 1

    A. Introduction ..... 1

    B. Conclusions ..... 7

    C. Future Concerns ..... 3

II. SPECIFIC RECOMMENDATIONS AND ACTIONS ..... 4

III. THE DATA ANALYSES COMPARISONS ..... 8

    A. ALPEX ..... 8

    B. Tasman Sea ..... 9

    C. Structure of Future Comparisons .....11

IV. SUMMARY OF THE WORKING GROUP DISCUSSIONS .....12

    A. Data Preparation .....12

        1. Calibration .....12

        2. Angular Correction .....12

        3. Earth Location .....13

    B. Transmission Function Calculation .....13

    C. Retrieval Methods .....15

    D. Effect of Clouds and Surface Properties .....16

    E. Use of Ancillary Data .....18

V. ABSTRACTS FROM TOVS STUDY CONFERENCE .....20

APPENDICES .....A-1

    A. Events Leading to TOVS Study Conference .....A-1

    B. Technical Information .....A-2

    C. List of Acronyms .....A-9

    D. Addresses of TOVS Study Conference Participants .....A-10

\* \* \* \* \*

Only the Table of Contents is included here. Copies of any of these papers are available from CIMSS upon request.

## The First International TOVS Study Conference

Organizer and Host  
H. J. Bolle (Austria)

### Co-Chairmen

W. L. Smith (USA)  
R. Rizzi (Italy)

### WMO Representative

J. Giraytys (USA)

### Participants

T. Aoki (Japan)	W.P. Menzel (USA)
L.A. Baranski (Poland)	M.J. Munteanu (USA)
H. Billing (FRG)	K. Paetzold (FRG)
H.J. Bolle (Austria)	T. Phulpin (France)
M.T. Chahine (USA)	F. Prata (UK)
A. Chedin (France)	G. Rochard (France)
Y. Durand (France)	H. Rott (Austria)
J.R. Eyre (UK)	N. Scott (France)
H. Fischer (FRG)	D. Spänkuch (GDR)
G.A. Kelly (Australia)	J. Susskind (USA)
P. King (Canada)	J. Svensson (Sweden)
T.J. Kleespies (USA)	B.F. Taylor (New Zealand)
J.F. LeMarshall (Australia)	R.J. du Vachat (France)
F. Loechner (FRG)	H.M. Woolf (USA)
M.J. Lynch (Australia)	F.X. Zhou (PRC)
L. McMillin (USA)	

## FORWARD

The inference of atmospheric temperature profiles from spectral radiances measured by satellite borne radiometers has a history of about 25 years. Probably the first paper on this topic was published by Kaplan in 1959. Within this relatively short time period, this technique has been developed into a powerful observational tool for meteorology. To arrive at this level, it was necessary to install highly sophisticated instrumentation on board satellites, to perform extremely accurate transmission measurements of atmospheric gases in laboratories and in the open air, and to develop the mathematical inversion theory to a degree where it could be applied to the ill conditioned cases of cloudy atmospheres.

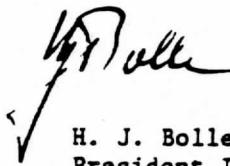
For many years, COSPAR, the Radiation Commission of IAMAP, and WMO have been trying to stimulate scientists to contribute to the improvement of this unique system. Thanks to the dedicated work of mainly a few individual scientists, we now see that a broad community from all over the world is using the satellite data and is working on the removal of limitations in the method. What is even more encouraging is that this community has decided to approach remaining problems jointly and to intercompare their findings in workshops.

An immense benefit can be foreseen from such cooperation for the WWW system. More recently it has also become evident that improved measurement and evaluation techniques increase the feasibility of applying the data to climate studies, which require a very high long term stability of both the instrumentation and the algorithms to infer temperature fields. This application could result in the detection of global temperature trends and thus contribute significantly to the objective of the World Climate Programme.

Substantial work still must be done to make the inferences of humidity profiles as reliable and useful as temperature profile determinations. Therefore, it is hoped that the First International TOVS Study Conference will soon be followed by others, addressing different aspects of the system.

Drs. W. L. Smith and R. Rizzi have invested many years of long effort to organize this Study Conference and to make it the success it was. We are very grateful for their initiative as we are to Drs. W. P. Menzel and M. J. Lynch for the fine work they did in editing this material.

Innsbruck, 7 December 1983



H. J. Bolle  
President IAMAP